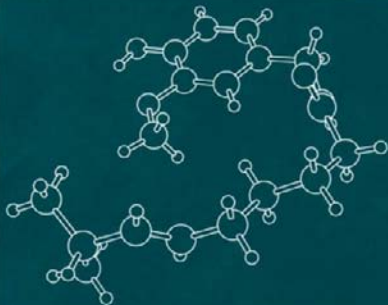


IUCr MONOGRAPHS ON CRYSTALLOGRAPHY • 13

Structure Determination from Powder Diffraction Data

Edited by
W. I. F. David, K. Shankland,
L. B. McCusker, and Ch. Baerlocher



INTERNATIONAL UNION OF CRYSTALLOGRAPHY
OXFORD SCIENCE PUBLICATIONS



INTERNATIONAL UNION OF CRYSTALLOGRAPHY
BOOK SERIES

IUCr BOOK SERIES COMMITTEE

E. N. Baker, *New Zealand*
J. Bernstein, *Israel*
P. Coppens, *USA*
G. R. Desiraju, *India*
E. Dodson, *UK*
A. M. Glazer, *UK*
J. R. Helliwell, *UK*
P. Paufler, *Germany*
H. Schenk (*Chairman*), *The Netherlands*

IUCr Monographs on Crystallography

- 1 *Accurate molecular structures*
A. Domenicano, I. Hargittai, editors
- 2 *P. P. Ewald and his dynamical theory of X-ray diffraction*
D. W. J. Cruickshank, H. J. Juretschke, N. Kato, editors
- 3 *Electron diffraction techniques, Vol. 1*
J. M. Cowley, editor
- 4 *Electron diffraction techniques, Vol. 2*
J. M. Cowley, editor
- 5 *The Rietveld method*
R. A. Young, editor
- 6 *Introduction to crystallographic statistics*
U. Shmueli, G. H. Weiss
- 7 *Crystallographic instrumentation*
L. A. Aslanov, G. V. Fetisov, G. A. K. Howard
- 8 *Direct phasing in crystallography*
C. Giacovazzo
- 9 *The weak hydrogen bond*
G. R. Desiraju, T. Steiner
- 10 *Defect and microstructure analysis by diffraction*
R. L. Snyder, J. Fiala and H. J. Bunge
- 11 *Dynamical theory of X-ray diffraction*
A. Authier
- 12 *The chemical bond in inorganic chemistry*
I. D. Brown
- 13 *Structure determination from powder diffraction data*
W. I. F. David, K. Shankland, L. B. McCusker, Ch. Baerlocher, editors

- 14 *Polymorphism in molecular crystals*
J. Bernstein
- 15 *Crystallography of modular materials*
G. Ferraris, E. Makovicky, S. Merlino
- 16 *Diffuse x-ray scattering and models of disorder*
T. R. Welberry
- 17 *Crystallography of the polymethylene chain: an inquiry into the structure of waxes*
D. L. Dorset
- 18 *Crystalline molecular complexes and compounds: structure and principles*
F. H. Herbstein
- 19 *Molecular aggregation: structure analysis and molecular simulation of crystals and liquids*
A. Gavezzotti

IUCr Texts on Crystallography

- 1 *The solid state*
A. Guinier, R. Julien
- 4 *X-ray charge densities and chemical bonding*
P. Coppens
- 5 *The basics of crystallography and diffraction, second edition*
C. Hammond
- 6 *Crystal structure analysis: principles and practice*
W. Clegg, editor
- 7 *Fundamentals of crystallography, second edition*
C. Giacovazzo, editor
- 8 *Crystal structure refinement: a crystallographer's guide to SHELXL*
P. Müller, editor

Structure Determination from Powder Diffraction Data

Edited by

W. I. F. DAVID

Rutherford Appleton Laboratory, Oxfordshire, UK

K. SHANKLAND

Rutherford Appleton Laboratory, Oxfordshire, UK

L. B. McCUSKER

Laboratory of Crystallography, ETH Zurich, Switzerland

Ch. BAERLOCHER

Laboratory of Crystallography, ETH Zurich, Switzerland

OXFORD
UNIVERSITY PRESS

OXFORD

UNIVERSITY PRESS

Great Clarendon Street, Oxford OX2 6DP

Oxford University Press is a department of the University of Oxford.
It furthers the University's objective of excellence in research, scholarship,
and education by publishing worldwide in

Oxford New York

Auckland Cape Town Dar es Salaam Hong Kong Karachi
Kuala Lumpur Madrid Melbourne Mexico City Nairobi
New Delhi Shanghai Taipei Toronto

With offices in

Argentina Austria Brazil Chile Czech Republic France Greece
Guatemala Hungary Italy Japan Poland Portugal Singapore
South Korea Switzerland Thailand Turkey Ukraine Vietnam

Oxford is a registered trade mark of Oxford University Press
in the UK and in certain other countries

Published in the United States
by Oxford University Press Inc., New York

© Oxford University Press 2002

The moral rights of the author have been asserted
Database right Oxford University Press (maker)

First published 2002

First published in paperback 2006

All rights reserved. No part of this publication may be reproduced,
stored in a retrieval system, or transmitted, in any form or by any means,
without the prior permission in writing of Oxford University Press,
or as expressly permitted by law, or under terms agreed with the appropriate
reprographics rights organization. Enquiries concerning reproduction
outside the scope of the above should be sent to the Rights Department,
Oxford University Press, at the address above

You must not circulate this book in any other binding or cover
and you must impose the same condition on any acquirer

British Library Cataloguing in Publication Data

Data available

Library of Congress Cataloging in Publication Data

Structure determination from power diffraction data/edited by W. I. F. David ... [et al.].

p. cm—(IUCr monographs on crystallography; 13)

Includes bibliographical references and index.

1. X-ray crystallography. 2. Crystals—Structures. 3. Powders—
Measurement. I. David, W. I. F. (William I. F.) II. International Union of

Crystallography monographs on crystallography; 13.

QD945.S88 2002 548—dc21 2001047555

Typeset by Newgen Imaging Systems (P) Ltd., Chennai, India

Printed in Great Britain

on acid-free paper by

Biddles Ltd., King's Lynn

ISBN 0-19-850091-2 978-0-19-850091-9

ISBN 0-19-920553-1 (Pbk.) 978-0-19-920553-0 (Pbk.)

1 3 5 7 9 10 8 6 4 2

Preface to the Paperback Edition

In the few years that have elapsed since this book first appeared in hardback, structure determination from powder diffraction data (SDPD) methods have been refined and accepted into the structural communities as a powerful alternative for use when single-crystal diffraction methods are not appropriate. This is clearly reflected in the number of papers being published that involve the use of SDPD and it is particularly gratifying to see SDPD-derived structures appearing regularly in volumes of *Acta Crystallogr. B, C, and E*, confirming the truly routine nature of the technique in many instances. This surely also reflects the fact that instrumental developments, both in laboratories and at synchrotron sources, have made measuring very high-quality X-ray powder diffraction data easier than ever before.

Many of the more recent developments in methods, algorithms and computer programs are covered in a special issue of *Zeitschrift Für Kristallographie* (volume 219, 12, 2004) which is dedicated to the subject of SDPD. It is probably true to say that the majority of developments have been incremental rather than revolutionary; there has been no step change in the level of structural complexity that can be tackled as a result of the introduction of, for example, novel optimisation methods, new evaluation functions or the closer coupling of direct methods/global optimisation. The change in complexity represented by the study of protein structures using powder diffraction still lies more in the domain of structure *refinement* than determination but regardless, it represents an exciting new research topic.

Preface

The art of solving a structure from powder diffraction data has developed rapidly over the last ten years. Prior to 1990, very few unknown crystal structures had been determined directly from powder diffraction data, and each structure solved could be regarded as a *tour de force* of ingenuity and perseverance. Today, the situation is quite different and numerous crystal structures, both organic and inorganic, have been solved from powder data. Developments in instrumentation, computer technology and powder diffraction methodology have all contributed to this increased success rate. However, the route to a successful structure determination is still by no means as straightforward and routine as it is with single-crystal diffraction data.

In the chapters that follow, experts in the field discuss both the fundamental and applied aspects of structure solution from powder diffraction data. The process is sequential, with any particular stage depending crucially on the successful completion of all the previous steps, and the ordering of the chapters within the book essentially reflects this flow. Although the Rietveld method of structure refinement from powder diffraction data is often loosely considered to be synonymous with structure determination, it is not. The Rietveld method only comes into play in the final stage of the structure solution process when an approximate structural model has been found. The subject of this book is how that structural model is determined.

Despite the sequential nature of the structure determination process, there are nevertheless various paths that can be taken through it. The art of structure solution from powder diffraction data lies not only in the correct application of a specific technique or computer program, but also in the selection of the optimal path for the problem at hand. The limitations inherent to the data available and to each of the methods used must be recognized. This book is designed to help the reader find his or her way through the maze of possibilities.

Readers will find that while every effort has been made to ensure that the chapters present a consistent and coherent approach to structure determination, no attempt has been made to gloss over differences of opinion, as expressed by individual authors, regarding the benefits or limitations of particular methods. This is particularly apparent in the case of the key step of intensity extraction,

where the relative merits of the Pawley and Le Bail methods are raised in several chapters. Such differences are, however, minor and should not overly concern the reader. Indeed, probably the most significant legacy of the past decade lies in the diversity of methods that have been developed.

William I. F. David
Kenneth Shankland
Lynne B. McCusker
Christian Baerlocher

This page intentionally left blank

Contents

| | |
|---|------|
| List of contributors | xvii |
| 1 Introduction | |
| <i>William I. F. David, Kenneth Shankland, Lynne B. McCusker and Christian Baerlocher</i> | 1 |
| 1.1 Crystal structures from powder diffraction data | 1 |
| 1.2 The structure determination process | 4 |
| 1.3 Adapting single-crystal structure solution methods to powder diffraction data | 7 |
| 1.4 Direct-space methods that exploit chemical knowledge | 8 |
| 1.5 Hybrid approaches | 9 |
| 1.6 Outlook | 10 |
| Acknowledgements | 11 |
| References | 11 |
| 2 Structure determination from powder diffraction data: an overview | |
| <i>Anthony K. Cheetham</i> | 13 |
| 2.1 Introduction | 13 |
| 2.2 Early history of powder diffraction | 14 |
| 2.3 Early <i>ab initio</i> approaches | 15 |
| 2.4 Pre-Rietveld refinement methods | 15 |
| 2.5 Rietveld refinement | 16 |
| 2.6 Solving unknown structures from powder data | 19 |
| 2.7 Trial-and-error and simulation methods | 21 |
| 2.8 Some examples of structure determination from powder data | 22 |
| 2.9 Conclusions | 24 |
| References | 26 |
| 3 Laboratory X-ray powder diffraction | |
| <i>Daniel Louër</i> | 29 |
| 3.1 Introduction | 29 |
| 3.2 The reflection overlap problem | 29 |
| 3.2.1 Instrumental broadening— $g(2\theta)$ | 30 |
| 3.2.2 Sample broadening— $f_{hkl}(2\theta)$ | 32 |
| 3.2.3 $H(x)$ profiles | 33 |

| | | |
|-------|---|----|
| 3.3 | Instrumentation and experimental considerations | 34 |
| 3.3.1 | Diffractometer geometries | 34 |
| 3.3.2 | Monochromatic radiation | 36 |
| 3.3.3 | Data quality | 37 |
| 3.4 | Examples of crystal structure solution | 40 |
| 3.4.1 | Bragg–Brentano powder diffraction data | 40 |
| 3.4.2 | Debye–Scherrer powder diffraction data | 43 |
| 3.5 | Conclusions | 46 |
| | Acknowledgements | 46 |
| | References | 46 |
| 4 | Synchrotron radiation powder diffraction | |
| | <i>Peter W. Stephens, David E. Cox and Andrew N. Fitch</i> | 49 |
| 4.1 | Introduction | 49 |
| 4.2 | Synchrotron powder diffraction instruments in use for <i>ab initio</i> structure determination | 51 |
| 4.3 | Angular resolution, lineshape and choice of wavelength | 54 |
| 4.4 | Data preparation and indexing | 59 |
| 4.5 | Pattern decomposition and intensity extraction | 61 |
| 4.6 | Systematic errors | 64 |
| 4.6.1 | Particle statistics | 64 |
| 4.6.2 | Preferred orientation | 65 |
| 4.6.3 | Absorption | 65 |
| 4.6.4 | Extinction | 66 |
| 4.7 | Examples of structure solution | 66 |
| 4.7.1 | Pioneering studies | 66 |
| 4.7.2 | Organic compounds | 70 |
| 4.7.3 | Microporous materials | 75 |
| 4.7.4 | Organometallics | 78 |
| 4.7.5 | More difficult problems | 80 |
| 4.8 | Conclusions | 83 |
| | Acknowledgements | 84 |
| | References | 84 |
| 5 | Neutron powder diffraction | |
| | <i>Richard M. Ibberson and William I. F. David</i> | 88 |
| 5.1 | Introduction | 88 |
| 5.2 | Instrumentation | 89 |
| 5.3 | Autoindexing and space group assignment | 89 |
| 5.4 | Patterson methods | 91 |
| 5.5 | Direct methods | 91 |
| 5.6 | X-n structure solution | 92 |
| 5.7 | Future possibilities | 93 |
| | References | 97 |

| | | |
|-------|---|-----|
| 6 | Sample preparation, instrument selection and data collection | |
| | <i>Roderick J. Hill and Ian C. Madsen</i> | 98 |
| 6.1 | Introduction | 98 |
| 6.2 | Issues and early decisions—experimental design | 99 |
| 6.3 | Multiple datasets | 100 |
| 6.4 | The sample | 101 |
| 6.4.1 | Sources of sample-related errors | 101 |
| 6.4.2 | Number of crystallites contributing to the diffraction process | 101 |
| 6.4.3 | Increasing the number of crystallites examined | 103 |
| 6.4.4 | Generating random orientation | 105 |
| 6.4.5 | Removing extinction | 105 |
| 6.5 | The instrument | 105 |
| 6.5.1 | What radiation to use—X-rays or neutrons? | 106 |
| 6.5.2 | What wavelength to use? | 106 |
| 6.5.3 | Number of ‘independent’ observations (integrated intensities) | 106 |
| 6.5.4 | What geometry to use? | 108 |
| 6.5.5 | Sources of instrument-related error | 111 |
| 6.6 | Data collection | 112 |
| 6.6.1 | Step time and width recommendations | 113 |
| 6.6.2 | Variable counting time data collection | 114 |
| 6.7 | Conclusions | 116 |
| | References | 116 |
| 7 | Autoindexing | |
| | <i>Per-Erik Werner</i> | 118 |
| 7.1 | Introduction | 118 |
| 7.2 | Basic relations | 118 |
| 7.3 | The indexing problem | 120 |
| 7.4 | The dominant zone problem | 122 |
| 7.5 | Geometrical ambiguities—derivative lattices | 122 |
| 7.6 | Errors in measurements | 123 |
| 7.7 | Indexing programs | 125 |
| 7.7.1 | ITO | 125 |
| 7.7.2 | DICVOL91 | 126 |
| 7.7.3 | TREOR90 | 128 |
| 7.7.4 | Why more than one indexing program? | 129 |
| 7.8 | Computing times | 130 |
| 7.9 | The PDF 2 database | 131 |
| 7.10 | Comments | 132 |
| | Appendix: (Most likely) unit-cell dimensions for selected PDF-2 powder patterns | 133 |
| | References | 134 |

| | | |
|------|---|-----|
| 8 | Extracting integrated intensities from powder diffraction patterns | |
| | <i>William I. F. David and Devinderjit S. Sivia</i> | 136 |
| 8.1 | Introduction | 136 |
| 8.2 | The Le Bail method | 138 |
| | 8.2.1 The origins of the Le Bail method | 138 |
| | 8.2.2 The iterative Le Bail algorithm | 140 |
| 8.3 | The Pawley method | 143 |
| | 8.3.1 Introduction | 143 |
| | 8.3.2 Mathematical background | 144 |
| 8.4 | Space group determination | 148 |
| 8.5 | Overcoming Bragg peak overlap | 151 |
| 8.6 | Incorporating crystallographic information | 154 |
| 8.7 | Conclusions | 160 |
| | Acknowledgements | 160 |
| | References | 161 |
| 9 | Experimental methods for estimating the relative intensities of overlapping reflections | |
| | <i>Thomas Wessels, Christian Baerlocher, Lynne B. McCusker and William I. F. David</i> | 162 |
| 9.1 | Introduction | 162 |
| 9.2 | Anisotropic thermal expansion | 162 |
| | 9.2.1 A simple two-peak analysis | 163 |
| | 9.2.2 Mathematical aspects of the analysis of integrated intensities collected at more than one temperature | 164 |
| | 9.2.3 An example of differential thermal expansion—chlorothiazide | 165 |
| 9.3 | Texture | 168 |
| | 9.3.1 Concept | 168 |
| | 9.3.2 Sample preparation | 169 |
| | 9.3.3 Texture description | 170 |
| | 9.3.4 Instrumentation | 171 |
| | 9.3.5 Data collection | 173 |
| | 9.3.6 Data analysis | 173 |
| | 9.3.7 Example | 175 |
| 9.4 | Conclusions | 177 |
| | References | 177 |
| 10 | Direct methods in powder diffraction—basic concepts | |
| | <i>Rene Peschar, Anke Etz, Jouk Jansen and Hendrick Schenk</i> | 179 |
| 10.1 | Introduction | 179 |
| 10.2 | Basics of Direct methods | 179 |
| 10.3 | Direct methods in practice | 181 |

| | | |
|--------|--|-----|
| 10.3.1 | Normalization and setting up phase relations | 181 |
| 10.3.2 | Selection of starting-set phases | 182 |
| 10.3.3 | Active phase extension | 182 |
| 10.3.4 | Selection of most likely numerical starting set (criteria) | 183 |
| 10.4 | Whole-pattern fitting | 183 |
| 10.4.1 | The Pawley whole-pattern refinement | 184 |
| 10.4.2 | The two-step LSQPROF whole-pattern fitting procedure | 184 |
| 10.5 | Estimation of the intensity of completely overlapping reflections: the DOREES program | 185 |
| 10.6 | Direct methods for powder data in practice: the POWSIM package | 186 |
| | References | 188 |
| 11 | Direct methods in powder diffraction—applications <i>Carmelo Giacovazzo, Angela Altomare, Maria Cristina Burla, Benedetta Carrozzini, Giovanni Luca Casciarano, Antonietta Guagliardi, Anna Grazia G. Moliterni, Giampiero Polidori and Rosanna Rizzi</i> | 190 |
| 11.1 | Introduction | 190 |
| 11.2 | A set of test structures | 191 |
| 11.3 | Performance of extraction algorithms | 191 |
| 11.4 | Some warnings about the use of powder data | 195 |
| 11.5 | Powder pattern decomposition using supplementary prior information | 196 |
| 11.5.1 | Pseudo-translational symmetry | 197 |
| 11.5.2 | Expected positivity of the Patterson function in reciprocal space | 198 |
| 11.5.3 | The expected positivity of the Patterson function in direct space | 198 |
| 11.5.4 | A located molecular fragment | 198 |
| 11.6 | Applications | 200 |
| | References | 200 |
| 12 | Patterson methods in powder diffraction: maximum entropy and symmetry minimum function techniques <i>Michael A. Estermann and William I. F. David</i> | 202 |
| 12.1 | Introduction | 202 |
| 12.2 | The crystal structure and its Patterson function | 203 |
| 12.2.1 | Patterson maps calculated from X-ray powder diffraction data | 204 |
| 12.2.2 | Patterson maps calculated from neutron powder diffraction data | 204 |
| 12.3 | Conventional methods for improving the | |

| | | |
|------|--|-----|
| | interpretability of the Patterson map | 205 |
| 12.4 | Maximum entropy Patterson maps | 205 |
| 12.5 | Decomposition of overlapping Bragg peaks using the Patterson function | 207 |
| 12.6 | Solving a crystal structure directly from a powder Patterson map | 208 |
| 12.7 | Automatic location of atomic positions with the symmetry minimum function | 210 |
| 12.8 | Examples of structure solution using automated Patterson superposition techniques | 212 |
| | 12.8.1 Bismuth nitride fluoride Bi_3NF_6 | 212 |
| | 12.8.2 Synthetic CaTiSiO_5 | 214 |
| | Acknowledgements | 216 |
| | References | 217 |
| 13 | Solution of Patterson-type syntheses with the Direct methods sum function | |
| | <i>Jordi Rius</i> | 219 |
| 13.1 | Introduction | 219 |
| 13.2 | Definition of the modulus sum function | 220 |
| 13.3 | The modulus sum function in reciprocal space | 223 |
| 13.4 | The sum function tangent formula, $S' - \text{TF}$ | 226 |
| 13.5 | Application of the sum function tangent formula to powder diffraction data | 227 |
| | Acknowledgements | 232 |
| | References | 232 |
| 14 | A maximum entropy approach to structure solution | |
| | <i>Christopher J. Gilmore, Kenneth Shankland and Wei Dong</i> | 233 |
| 14.1 | Introduction | 233 |
| 14.2 | Data collection, range and overlap | 233 |
| 14.3 | Starting set choices: defining the origin and enantiomorph | 235 |
| 14.4 | Basis set expansion and the phasing tree | 236 |
| 14.5 | Log-likelihood gain | 237 |
| 14.6 | Centroid maps | 241 |
| 14.7 | Fragments and partial structures | 241 |
| 14.8 | Using likelihood to partition overlapped reflections | 242 |
| | 14.8.1 The overlap problem defined in terms of hyperphases and pseudophases | 242 |
| | 14.8.2 Duncan's procedure for multiple significance tests | 243 |
| | 14.8.3 The determination of pseudophases using the maximum entropy-likelihood method and Duncan's procedure | 245 |
| 14.9 | The maximum entropy method and the need for | |

| | |
|--|-----|
| experimental designs | 247 |
| 14.9.1 Error correcting codes and their use in MICE | 247 |
| 14.10 Conclusions and other possibilities | 249 |
| Acknowledgements | 250 |
| References | 250 |
| | |
| 15 Global optimization strategies | |
| <i>Kenneth Shankland and William I. F. David</i> | 252 |
| 15.1 Introduction | 252 |
| 15.2 Background | 253 |
| 15.3 Describing a crystal structure | 256 |
| 15.4 Calculating the odds | 258 |
| 15.5 Beating the odds—global optimization algorithms | 261 |
| 15.5.1 A search method with a physical basis—simulated annealing | 262 |
| 15.5.2 A search method with a biological basis—genetic algorithms | 263 |
| 15.5.3 Search methods with a social basis—the swarm | 266 |
| 15.5.4 The downhill simplex algorithm—a ‘semi-global’ optimizer | 267 |
| 15.5.5 Other approaches | 268 |
| 15.5.6 Which algorithm is best? | 269 |
| 15.5.7 Use of molecular envelope information | 269 |
| 15.5.8 Hybrid DM—global optimization approaches | 270 |
| 15.6 Structure evaluation—the cost function | 270 |
| 15.6.1 Efficiency of function evaluations | 270 |
| 15.6.2 Multi-objective optimization | 272 |
| 15.6.3 Maximum likelihood | 273 |
| 15.7 Examples | 273 |
| 15.8 Influence of crystallographic factors | 275 |
| 15.9 Caveats and pitfalls | 279 |
| 15.10 Conclusions | 282 |
| Acknowledgements | 282 |
| References | 283 |
| | |
| 16 Solution of flexible molecular structures by simulated annealing | |
| <i>Peter G. Bruce and Yuri G. Andreev</i> | 286 |
| 16.1 Introduction | 286 |
| 16.2 Simulated annealing | 288 |

| | | |
|--------|---|-----|
| 16.3 | Constraints and restraints | 289 |
| 16.3.1 | Non-structural constraints | 290 |
| 16.3.2 | Structural restraints | 290 |
| 16.3.3 | Molecular crystals | 291 |
| 16.4 | Examples | 293 |
| 16.4.1 | (PEO) ₃ :LiN(SO ₂ CF ₃) ₂ | 294 |
| 16.4.2 | PEO:NaCF ₃ SO ₃ | 298 |
| 16.4.3 | PEO ₆ :LiAsF ₆ | 302 |
| 16.5 | Discussion | 303 |
| | Acknowledgements | 305 |
| | References | 305 |
| 17 | Chemical information and intuition in solving crystal structures | |
| | <i>Lynne B. McCusker and Christian Baerlocher</i> | 307 |
| 17.1 | Introduction | 307 |
| 17.2 | Data collection | 308 |
| 17.3 | Indexing and choice of space group | 308 |
| 17.4 | Model building | 309 |
| 17.5 | Computer generation of structural models | 314 |
| 17.6 | Using chemical information actively in an automated structure determination process | 314 |
| 17.7 | Recognizing a structure solution | 316 |
| 17.8 | Interpretation of Fourier maps | 317 |
| 17.9 | Elucidation of refinement difficulties | 320 |
| 17.10 | Evaluation of the final structure | 321 |
| 17.11 | Conclusion | 321 |
| | References | 322 |
| | Index of symbols | 325 |
| | Index of abbreviations | 327 |
| | Computer programs | 328 |
| | Index | 331 |

Contributors

Angela Altomare, Istituto di Ricerca per lo Sviluppo di Metodologie Cristallografiche, Dipartimento Geomineralogico, Via Orabona 4, Campus Universitario, I-70125 Bari, Italy

Yuri G. Andreev, School of Chemistry, University of St. Andrews, St. Andrews, Fife KY16 9ST, Scotland

Christian Baerlocher, Laboratory of Crystallography, ETH, CH-8092 Zürich, Switzerland

Peter G. Bruce, School of Chemistry, University of St. Andrews, St. Andrews, Fife KY16 9ST, Scotland

Maria C. Burla, Istituto di Ricerca per lo Sviluppo di Metodologie Cristallografiche, Dipartimento Geomineralogico, Via Orabona 4, Campus Universitario, I-70125 Bari, Italy

Benedetta Carrozzini, Istituto di Ricerca per lo Sviluppo di Metodologie Cristallografiche, Dipartimento Geomineralogico, Via Orabona 4, Campus Universitario, I-70125 Bari, Italy

Giovanni L. Casciarano, Istituto di Ricerca per lo Sviluppo di Metodologie Cristallografiche, Dipartimento Geomineralogico, Via Orabona 4, Campus Universitario, I-70125 Bari, Italy

Anthony K. Cheetham, Materials Research Laboratory, University of California, Santa Barbara, CA 93106, USA

David E. Cox, Department of Physics, Brookhaven National Laboratory, Upton, NY 11973 USA

William I. F. David, ISIS Facility, Rutherford Appleton Laboratory, Chilton, Didcot, Oxon OX11 0QX, England

Wei Dong, Department of Chemistry, University of Glasgow, Glasgow G12 8QQ, Scotland

Michael A. Estermann, Laboratory of Crystallography, ETH, CH-8092 Zürich, Switzerland

Anke Etz, Laboratory of Crystallography, University of Amsterdam, Nieuwe Achtergracht 166, NL-1018 WV Amsterdam, The Netherlands

Andrew N. Fitch, European Synchrotron Radiation Facility, B.P. 220, F-38042 Grenoble, France

Carmelo Giacobozzo, Istituto di Ricerca per lo Sviluppo di Metodologie Cristallografiche, Dipartimento Geomineralogico, Via Orabona 4, Campus Universitario, I-70125 Bari, Italy

Christopher Gilmore, Department of Chemistry, University of Glasgow, Glasgow G12 8QQ, Scotland

Antonietta Guagliardi, Istituto di Ricerca per lo Sviluppo di Metodologie Cristallografiche, Dipartimento Geomineralogico, Via Orabona 4, Campus Universitario, I-70125 Bari, Italy

Roderick J. Hill, CSIRO Division of Minerals, P.O. Box 124, Port Melbourne 3207, Victoria, Australia

Richard M. Ibberson, ISIS Facility, Rutherford Appleton Laboratory, Chilton, Didcot, Oxon OX11 0QX, England

Jouk Jansen, National Centre of HREM, Delft University of Technology, Rotterdamseweg 137, NL-2628 Al Delft, The Netherlands

Daniel Louër, Laboratoire de Chimie du Solide et Inorganique Moléculaire, Université de Rennes I, F-35042 Rennes, France

Ian C. Madsen, CSIRO Division of Minerals, P.O. Box 124, Port Melbourne 3207, Victoria, Australia

Lynne B. McCusker, Laboratory of Crystallography, ETH, CH-8092 Zürich, Switzerland

Anna Grazia G. Moliterni, Istituto di Ricerca per lo Sviluppo di Metodologie Cristallografiche, Dipartimento Geomineralogico, Via Orabona 4, Campus Universitario, I-70125 Bari, Italy

Rene Peschar, Laboratory of Crystallography, University of Amsterdam, Nieuwe Achtergracht 166, NL-1018 WV Amsterdam, The Netherlands

Giampiero Polidori, Istituto di Ricerca per lo Sviluppo di Metodologie Cristallografiche, Dipartimento Geomineralogico, Via Orabona 4, Campus Universitario, I-70125 Bari, Italy

Jordi Rius, Instituto de Ciencia de Materiales de Barcelona, CSIC, Campus UAB, E-08193 Bellaterra, Spain

Rosanna Rizzi, Istituto di Ricerca per lo Sviluppo di Metodologie Cristallografiche, Dipartimento Geomineralogico, Via Orabona 4, Campus Universitario, I-70125 Bari, Italy

Hendrik Schenk, Laboratory of Crystallography, University of Amsterdam, Nieuwe Achtergracht 166, NL-1018 WV Amsterdam, The Netherlands

Kenneth Shankland, ISIS Facility, Rutherford Appleton Laboratory, Chilton, Didcot, Oxon OX11 0QX, England

Devinderjit S. Sivia, ISIS Facility, Rutherford Appleton Laboratory, Chilton, Didcot, Oxon OX11 0QX, England

Peter W. Stephens, Department of Physics, State University of New York, Stony Brook, NY 11794, USA

Per-Erik Werner, Department of Structural Chemistry, Stockholm University, S-10691 Stockholm, Sweden

Thomas Wessels, Laboratory of Crystallography, ETH, CH-8092 Zürich, Switzerland

This page intentionally left blank

Introduction

*William I. F. David, Kenneth Shankland, Lynne B. McCusker
and Christian Baerlocher*

1.1 Crystal structures from powder diffraction data

Powder diffraction has played a central role in structural physics, chemistry and materials science over the past twenty years. Important advances in structural studies of materials ranging from high temperature superconductors and fullerenes to zeolites and high-pressure research have relied heavily on the powder diffraction technique. By far the majority of these structures have been analysed using the Rietveld method (Rietveld 1969), a development which has greatly enhanced the power of powder diffraction experiments (Young 1993). However, the Rietveld method is a refinement process and, as such, requires that an approximation to the correct structure be known in advance. If a structural model is not available, it must first be determined.

Unfortunately, structure determination from powder diffraction data is much more difficult than from single crystal data. This is associated almost entirely with the collapse of the three dimensions of crystallographic information onto the single dimension of a powder diffraction pattern. The resulting ambiguity in the data creates particular problems in the determination of the unit cell and in the application of traditional Direct methods or Patterson techniques. Indeed, all parts of the structure solution process are less straightforward than their single-crystal equivalents. Nevertheless, with improvements in instrumentation and algorithm developments coupled with greater computing power, increasingly complex crystal structures are being solved from powder diffraction data alone. Ironically, for some larger structures, the weak link in the structure determination chain is becoming the final structure refinement itself. It can be easier to determine a structure with more than 50 independent atoms than to provide an accurate and precise refinement of its crystal structure. Algorithm advances in powder diffraction data have come full circle with structure determination now providing an impetus for the further development of the Rietveld method.

Why should powder diffraction be used for structure solution when the single-crystal approach is much more straightforward? The answer is simple: there are many materials for which no single crystals are easily available. If representative single crystals are available, then single crystal diffraction is the

preferred method. For structures with less than 100 atoms in the asymmetric unit, single-crystal techniques are almost guaranteed to be successful and the final refined structure will almost always be more reliable than its powder diffraction equivalent. Indeed, the most recent developments in Direct methods of structure solution from single-crystal data (Weeks *et al.* 1994; Burla *et al.* 2000) have seen stunning successes, with structures containing up to 2000 atoms now tractable. If only powder samples are available, there may still be small crystallites that are large enough to be used for microcrystalline diffraction. This will usually give a higher likelihood of success, particularly for larger crystal structures, and will enable a more precise and accurate crystal structure to be obtained. Microcrystals do, however, suffer from the obvious disadvantage that they may not be representative of the bulk powder. Thus, for such samples, it is essential to collect a powder diffraction pattern as well to verify that the structure obtained from the microcrystal corresponds to that of the bulk material.

With the techniques described in this book, however, it is clear that a powder diffraction pattern on its own can provide enough structural information to allow fairly complex structures to be solved. Indeed, even relatively poor diffraction patterns can yield successful structure solutions. This is illustrated in Fig. 1.1, where the crystal structure of 1,4-diethynyl-2,5-bis(octyloxy)benzene (Fig. 1.1(a)) has been determined from the rather poor laboratory X-ray diffraction data shown in Fig. 1.1(b).

Although most of the structures determined from powder diffraction data have been solved in the last few years, there are, nevertheless, important examples that go back to the very earliest days of X-ray crystallography. Many of these structures are relatively straightforward but, nevertheless, represent significant *tours-de-force* for their time. Notable contributions include those of Zachariasen (1948) and Werner and co-workers in the 1970s (e.g. Berg and Werner 1977). Zachariasen, in particular, used a number of ingenious methods to solve crystal structures from powders. His work on β -plutonium (Zachariasen and Ellinger 1963), for example, utilized differential thermal expansion to resolve Bragg peak overlap (see Chapter 9). Many of the early zeolite structures that were solved from powder diffraction data involved model building and significant chemical intuition (e.g. zeolite A, Breck *et al.* 1956; ZSM-5, Kokotailo *et al.* 1978), and these concepts are now being implemented in computer algorithms. More details about the fascinating history of structure solution from powder data can be found in Chapter 2.

Today, structures of much higher complexity have become accessible to powder diffractionists. A number of different research groups are now applying the increasingly powerful techniques to a wide range of problems. Just a few recent examples are given here to illustrate the diversity and richness of the field. Conventional single-crystal approaches adapted to cope with the vagaries of powder diffraction data have been used to solve structures as complicated as the sulfathiazole polymorph V (32 non-H atoms in the asymmetric

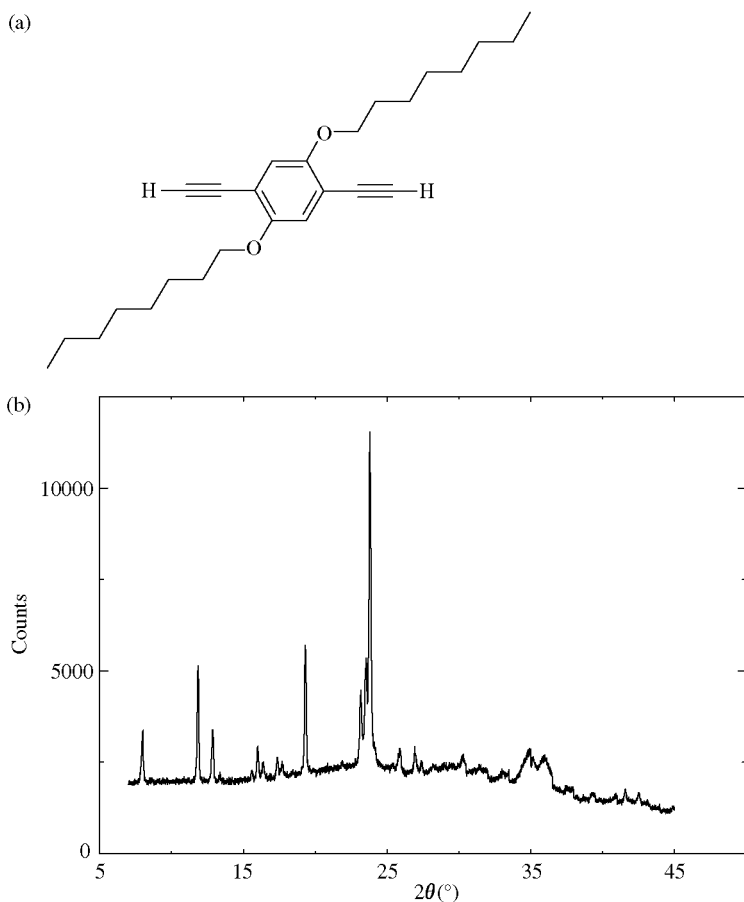


Fig. 1.1. (a) The molecular formula of 1,4-diethynyl-2,5-bis(octyloxy) benzene (b) Diffraction data collected at 1.5406 Å from a sample of 1,4-diethynyl-2,5-bis(octyloxy) benzene using a Stoe X-ray powder diffractometer equipped with a linear position sensitive detector.

unit; Chan *et al.* 1999), fluorescein diacetate (31 non-H atoms; Knudsen *et al.* 1998), and the mineral tincite with a complex structural disorder (Rius *et al.* 2000). With better estimates of reflection intensities obtained by collecting multiple datasets on a textured polycrystalline sample, the power of Direct methods could even be extended to solve the structure of the zeolite UTD-1F (117 non-H atoms; Wessels *et al.* 1999). Heavy atom methods followed by Fourier recycling have allowed a complex tubular uranyl phenylphosphonate to be solved from laboratory X-ray data (50 non-H atoms; Poojary and Clearfield 1997; Poojary *et al.* 1996). Global minimization procedures operating in direct (model-building) space have been applied successfully to some very large

molecular compounds, including β -haematin (43 non-H atoms and eight variable torsion angles; Pagola *et al.* 2000), an organometallic bipyridine polymer (29 non-H atoms and five variable torsion angles; Dinnebier *et al.* 2000), and $\text{Ph}_2\text{P}(\text{O})(\text{CH}_2)_7\text{P}(\text{O})\text{Ph}_2$ (35 non-H atoms and 12 variable torsion angles; Kariuki *et al.* 1999). On the non-molecular side, a zeolite-specific method that operates in both direct and reciprocal space was used to elucidate the structure of the zincosilicate VPI-9 (59 non-H atoms; McCusker *et al.* 1996). These are just a few examples of the state-of-the-art of structure solution from powder diffraction data. Many more are given in the following chapters. Indeed, new ones are appearing in the open literature with increasing frequency.

1.2 The structure determination process

The structure determination process can be viewed as a search for the best way through a maze (Fig. 1.2). Although there are many paths leading to the centre (i.e. the final structure), not all are appropriate or even feasible for a given problem.

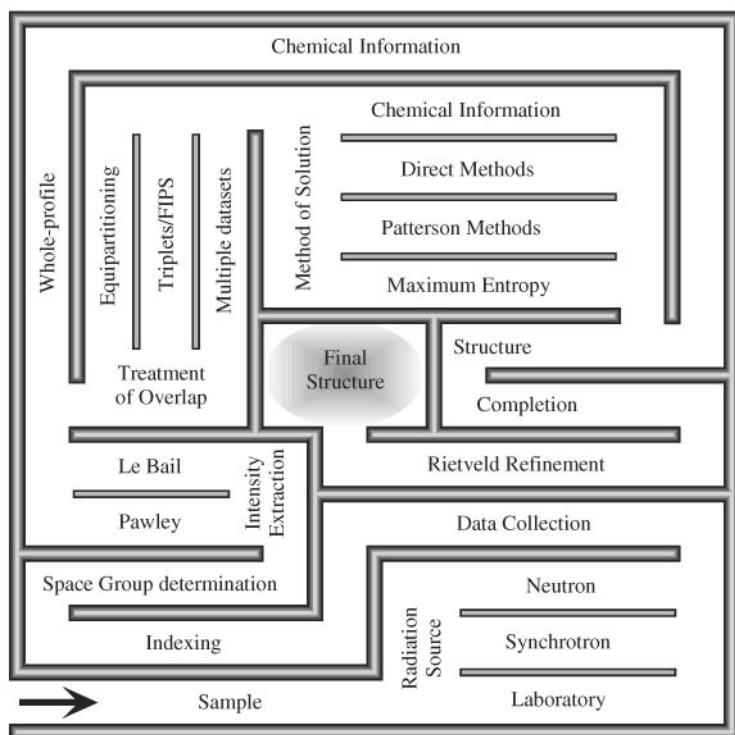


Fig. 1.2. The structure determination maze.

It is immediately apparent from Fig. 1.2 that everything depends upon the sample itself. Even if a material cannot be crystallized in the form of single or even microcrystals, time invested in producing a high-quality polycrystalline sample (e.g. high purity and crystallinity) prior to a structural investigation is time well spent. All subsequent steps in the structure determination process will depend upon the quality of the data and these in turn depend upon the quality of the sample.

The first choice in finding a path through the maze is which radiation source and instrument geometry is best suited to the problem. Are high-resolution data collected on a laboratory X-ray instrument (Chapter 3) sufficient, or does the complexity of the problem require the higher resolution or tunability offered by a synchrotron source (Chapter 4)? Or does the nature of the material make a neutron experiment (Chapter 5) more appropriate? Of course, once the type of experiment has been established, the data collection parameters (e.g. step size, counting times, data range) must be evaluated and optimized for the problem in hand (Chapter 6).

Whichever path is chosen for the data collection, the first step in data analysis is the indexing of the diffraction pattern (Chapter 7). While modern indexing programs work extremely well with good data, the user needs to be aware of the potential pitfalls. Even with excellent diffraction patterns, conventional auto indexing programs will sometimes fail to yield the correct unit cell. For example, the synchrotron diffraction pattern shown in Fig. 1.3 was not indexed correctly, despite the fact that (a) all of the first 40 reflections were indexed, (b) the average absolute difference between observed and calculated 2θ was only 0.00034° , and (c) the F_{40} figure of merit was 2178 (for a definition of F_{40} see Chapter 7).

All but one of these first 40 reflections can in fact be accounted for by a single plane in reciprocal space with corresponding lattice constants $a = 23.4891(4) \text{ \AA}$, $c = 21.3685(4) \text{ \AA}$, $\beta = 116.485(2)^\circ$. The length of the b axis ($b = 3.7698(2) \text{ \AA}$) is determined by a single peak position, and is, unfortunately, completely spurious. It is essential to realise that if the unit cell is wrong, all effort expended in the subsequent search for the correct structure will be pointless. It is ironic that progress in our ability to solve larger structures takes us into a region where unit cells inevitably become larger, thus creating problems at the indexing stage. In the case shown in Fig. 1.3, it is the combination of two long axes and one very short axis that creates the problem.

Once the unit cell has been found, the associated space group must be determined. This is also a critical step, and is often difficult and rarely unambiguous. In many cases, several space groups will need to be investigated and the possibility of a further reduction in the symmetry always borne in mind. This is one area of powder diffraction where subjective judgements remain the norm, though a probabilistic approach (Markvardsen *et al.* 2001; Chapter 8) has recently been proposed.

From the unit cell and the selected space group, the positions of the reflections in the diffraction pattern can be calculated. The diffracted intensity associated with each reflection can then be determined by applying a whole-profile-fitting

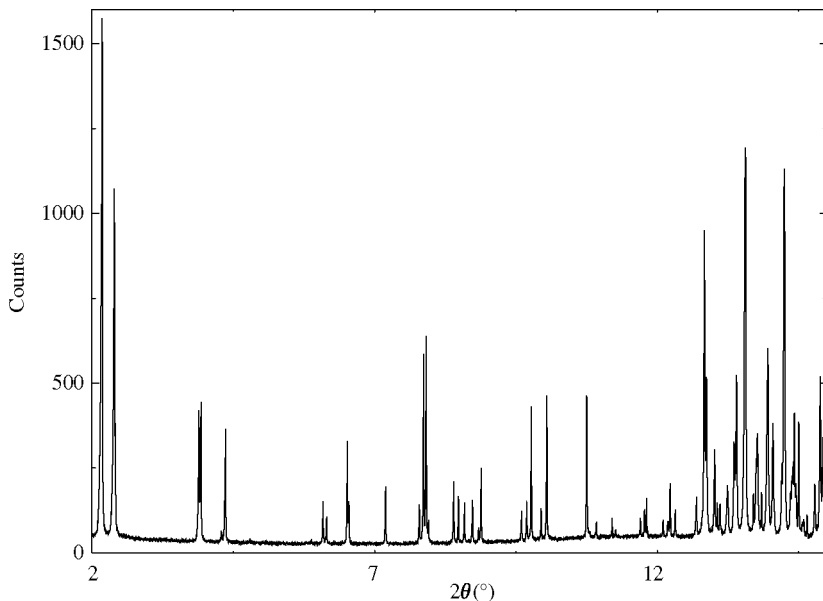


Fig. 1.3. High-resolution X-ray powder diffraction data collected using an incident wavelength of 0.8266 \AA on BM16 of the ESRF. The sample is a material of pharmaceutical interest contained in a 1.0 mm capillary.

technique similar to that used in a Rietveld refinement but with the intensities of the reflections rather than the structural parameters being the non-profile variables (Chapter 8). This procedure, known as intensity extraction, can be performed using either a least-squares method (Pawley 1981) or an iterative approach (Le Bail *et al.* 1988). Even if integrated intensities are not used in subsequent steps, this procedure is still necessary to establish the appropriate profile parameters for whole-profile applications.

Those reflections that are too close to one another to be considered independently (i.e. strongly overlapping reflections) must be recognized and treated in some way. The simplest approach is to equipartition the total intensity over all contributing reflections (taking the peak-shape function into consideration), but several methods for obtaining better estimates of the relative intensities of overlapping reflections have been developed and these are strongly recommended (Chapters 8–11). Keeping track of the correlations between reflection intensities is also advantageous. Of course, the partitioning step can be bypassed if the whole profile is to be used in combination with direct-space techniques, but for the application of Patterson and Direct methods, partitioning cannot be avoided.

The option of collecting multiple datasets to obtain a more reliable partitioning of these reflections and more single-crystal-like intensities (Chapter 9) might be chosen if the structure under study is complex. Data collected at

different temperatures for a material displaying anisotropic thermal expansion or at different sample orientations for samples with a preferred orientation of the crystallites can provide additional information about the relative intensities of overlapping reflections. Whichever method of partitioning is applied, the result is a pseudo-single-crystal dataset (i.e. list of hkl and I_{hkl}).

Only at this point can the actual determination of the structure begin. The methods currently available can be grouped into three main categories: (a) adaptations of single-crystal techniques, (b) direct-space methods that exploit prior chemical knowledge, and (c) hybrids of the two. These are discussed in more detail in the next three sections.

The final and often most time-consuming step in the structure determination maze is the completion of the structure (e.g. finding any missing atoms by Fourier analysis, resolving disorder problems, etc.) and the refinement of the structural parameters using the Rietveld method (Rietveld 1969; Young 1993). Only when the refinement has been brought to a successful conclusion can the structure proposal from the structure determination step be considered to be confirmed. Throughout the whole procedure, chemical information and intuition play an important role in guiding the user through the maze (Chapter 17).

1.3 Adapting single-crystal structure solution methods to powder diffraction data

Conventional crystallographic approaches to structure solution such as Direct, Patterson and maximum-entropy methods have been modified to address the problems posed by the deficiencies inherent to powder diffraction data (Giacovazzo 1998). The basic concepts of Direct methods and the difficulties involved in their application to powder data are outlined in Chapter 10, and the more practical aspects of their application are discussed in Chapter 11. Patterson techniques, including maximum entropy Patterson maps and the use of the symmetry minimum function in structure solution, are discussed in Chapter 12, and a derivation of how the Direct methods sum function can be used to solve structures from Patterson syntheses is presented in Chapter 13. Finally, the adaptation of the maximum entropy approach to structure solution for the case of powder diffraction data is described in Chapter 14.

In the standard Direct methods approach to crystal structure solution, a density map of the unit cell is generated using the Fourier transform of a set of *measured* structure factor magnitudes and a corresponding set of *calculated* phase angles, that is,

$$\rho(\mathbf{r}) = \frac{1}{V} \sum_{\mathbf{h}} |F(\mathbf{h})| e^{i\phi} e^{-2\pi i \mathbf{h} \cdot \mathbf{r}}. \quad (1.1)$$

Assuming that the structure factors have been collected to atomic resolution from a single crystal and the calculated phase angles are approximately correct,

the resultant density map is composed of discrete ‘blobs’ of electron or nuclear density within the unit cell, corresponding to the atomic positions in the structure. It is then a straightforward matter to connect these ‘blobs’, using the rules of chemical bonding, in order to visualize the crystal structure. If the complete structure is not elucidated in a single pass, a series of difference Fourier or fragment recycling calculations will normally reveal the remaining atoms.

However, it is relatively rare in powder diffraction, particularly when dealing with organic crystal structures, for good quality diffraction data to be obtained to atomic resolution. Accordingly, one is typically faced with the prospect of interpreting low-resolution density maps in ways analogous to those employed so successfully by protein crystallographers. There is, however, one very important difference. In the case of protein crystallography, the low-resolution density maps are generally based upon a large number of well-determined structure factor magnitudes. Furthermore, the phases are normally derived from one or more single-crystal experiments involving isomorphous replacement or anomalous dispersion measurements. Compare this with the situation in powder diffraction, where we typically have a small number of poorly determined structure factor magnitudes and are restricted to phases derived from Direct methods probability relationships or from heavy atom positions gleaned from a Patterson map. It should, therefore, come as no surprise that the quality of the density maps obtained from a powder diffraction experiment can be quite poor and their interpretation a non-trivial matter.

Nonetheless, single-crystal methods have been applied quite successfully to both inorganic and organic structures with up to several tens of atoms in the asymmetric unit. Continuing developments in Direct methods (Altomare *et al.* 2000) are likely to push these numbers even higher.

1.4 Direct-space methods that exploit chemical knowledge

Direct-space methods have evolved from traditional model building in which all available information about the material is used to construct a chemically feasible structural model. The diffraction pattern calculated from this model is then compared with the measured one to evaluate the model’s viability. As this approach takes advantage of prior chemical knowledge and not just the diffraction data, it is a very powerful one, but it is time consuming and uncomfortably dependent upon the intuition and ingenuity of the model builder. However, with modern computing power, large numbers of feasible models can be generated, evaluated and modified automatically once the chemical information has been suitably encoded. The encoding is the crucial point.

Naturally, the encoding makes an algorithm specific to a chemical class of materials, but this class can be as general as organic molecules. In fact, the most successful algorithms to date have been developed for molecular compounds,

where the connectivity of the atoms is known. Given the connectivity and typical bond lengths and angles, it is relatively straightforward to describe the molecule in terms of internal coordinates (i.e. bond distances, bond angles and torsion angles). Then, the only variables are the position and orientation of the molecule as a whole plus any variable torsion angles. Using this information, thousands or even millions of chemically feasible trial structures can be generated automatically and their powder patterns calculated. The only problem is finding the structure corresponding to the best fit between the observed and calculated diffraction data (i.e. the global minimum).

A number of algorithms, ranging from simple grid searches (Chernyshev and Schenk 1998) to simulated annealing and genetic algorithms (Kariuki *et al.* 1997; Shankland *et al.* 1997; Turner *et al.* 2000) have been developed. Global optimization procedures for the solution of molecular structures are described in Chapter 15, and the specific use of a simulated annealing approach for this purpose is discussed in Chapter 16.

For inorganic structures, or those where connectivity is not known, other approaches are needed. In fact, Deem and Newsam (1989) were the first to introduce the concept of simulated annealing in the context of structure solution from powder diffraction data, and they did so for zeolite structures, not molecular compounds. The chemical information they used was the fact that zeolites and related materials have three-dimensional framework structures composed of corner-connected tetrahedral units (TO_4 , where $\text{T} = \text{Si}, \text{Al}, \text{P}$, etc.). They encoded this information in the form of pseudo-potentials for T–T distances, T–T–T angles and coordination number (derived from related structures). The variables were simply the positions of the T-atoms in the unit cell. These were moved around the asymmetric unit in a search for a global minimum corresponding to the best fit of the pseudo-potentials and the observed and calculated diffraction patterns. Falconi and Deem (1999) have since refined that simulated annealing minimization procedure to include a parallel tempering algorithm.

Another option for structures in which the connectivity is not known is to introduce the chemical information in the form of chemical potentials. This approach has been implemented, for example, in the program ENDEAVOUR (Putz *et al.* 1999).

1.5 Hybrid approaches

Approaches that work in both reciprocal and real space have also been developed. The program FOCUS, for example, uses chemical information about zeolite framework structures in real space in combination with intensities and (random) phases in reciprocal space to solve zeolite structures (Chapter 17). Another combination involves the use of a structure envelope (Brenner *et al.* 1997; Brenner 1999), derived from just a few strong low-resolution (high

d-spacing) reflections, to restrict a direct-space search for the structure to the most likely areas of the unit cell.

The latest release of EXPO attempts to take the best elements of the Direct methods based approaches and combine them with elements of the global optimization strategies outlined above. In particular, expected coordination geometry is taken into account in the interpretation of density maps (Altomare *et al.* 2000). It seems entirely logical that continuing software developments will see an equivalent flow of important features from Direct methods into the global optimization based programs.

1.6 Outlook

It is generally unwise to make predictions about how a particular research field will develop in the future. After all, few foresaw the arrival and impact of the ‘Shake-and-Bake’ methodology (Weeks *et al.* 1994) upon the field of single-crystal diffraction. However, the last few years have seen structure determination from powder diffraction data move quickly from simple demonstrations of underlying principles to real-life applications. It is interesting to consider the complexity of many of the structure solution examples contained in this book in the general context of organic molecular structures solved by single-crystal diffraction methods. It is clear from Fig. 1.4 that powder diffraction is now in a

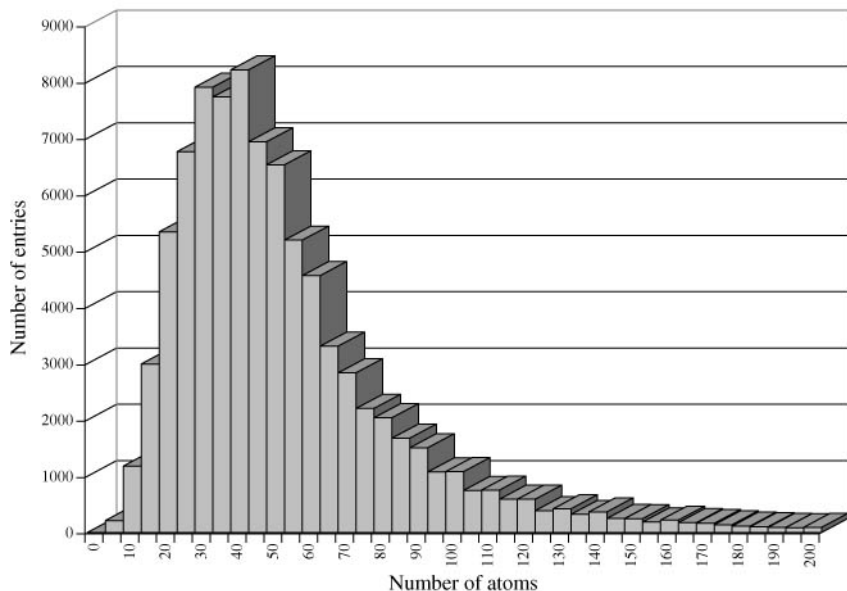


Fig. 1.4. Distribution of the number of organic (excluding organometallic) molecular crystal structures in the October 2000 release of the Cambridge Structural Database versus the number of atoms (including hydrogens where reported) in each structure.

position to contribute valuable crystal structures to the peak of the distribution, rather than simply adding to its leading edge.

Acknowledgements

We would like to thank Paul Attfield and Paul Raithy of Cambridge University for permission to use the data shown in Fig. 1.1. We would also like to thank Robert Lancaster of Glaxo Wellcome, Stevenage for permission to use the data shown in Fig. 1.3. and Alastair Florence of Strathclyde University for his help in preparing Fig. 1.4.

References

- Altomare, A., Giovacazzo, C., Guagliardi, A., Moliterni, A. G. G. and Rizzi, R. (2000). *J. Appl. Crystallogr.*, **33**, 1305–10.
- Berg, J.-E. and Werner, P.-E. (1977). *Z. Kristallogr.*, **145**, 310–20.
- Burla, M. C., Camalli, M., Carrozzini, B., Cascarano, G. L., Giovacazzo, C., Polidori, G. and Spagna, R. (2000). *Acta Crystallogr. A*, **56**, 451–7.
- Breck, D. W., Eversole, W. G., Milton, R. M., Reed, T. B. and Thomas. T. L. (1956). *J. Am. Chem. Soc.*, **78**, 5963–71.
- Brenner, S., McCusker, L. B. and Baerlocher, Ch. (1997). *J. Appl. Crystallogr.*, **30**, 1167–72.
- Brenner, S. (1999). *Ph.D. Thesis*, ETH, Zürich, Switzerland.
- Chan, F. C., Anwar, J., Cernik, R., Barnes, P. and Wilson, R. M. (1999). *J. Appl. Crystallogr.*, **32**, 436–41.
- Chernyshev, V. V. and Schenk, H. (1998). *Z. Kristallogr.*, **213**, 1–3.
- Deem, M. W. and Newsam, J. M. (1989). *Nature*, **342**, 260–2.
- Dinnebier, R. E., Wagner, M., Peters, F., Shankland, K. and David, W. I. F. (2000). *Z. Anorg. Allg. Chemie*, **626**, 1400–5.
- Falcioni, M. and Deem, M. W. (1999). *J. Chem. Phys.*, **110**, 1754–66.
- Giacovazzo, C. (1998). *Direct phasing in crystallography*, pp. 410–44, Oxford Science Publications.
- Kariuki, B. M., Calcagno, P., Harris, K. D. M., Philp, D. and Johnston, R. L. (1999). *Angew. Chem. Int. Ed.*, **38**, 831–5.
- Kariuki, B. M., Serrano Gonzalez, H., Johnston, R. L. and Harris, K. D. M. (1997). *Chem. Phys. Lett.*, **280**, 189–95.
- Knudsen, K. D., Pattison, P., Fitch, A. N. and Cernik, R. J. (1998). *Angew. Chem. Int. Ed.*, **37**, 2340–3.
- Kokotailo, G. T., Lawton, S. L., Olson, D. H. and Meier, W. M. (1978). *Nature*, **272**, 437–8.
- Le Bail, A., Duroy, H. and Fourquet, J. L. (1988). *Mater. Res. Bull.*, **23**, 447–52.
- Markvardsen, A., David, W. I. F., Johnson, J. C. and Shankland, K. (2001). *Acta Crystallogr. A*, **57**, 47–54.
- McCusker, L. B., Grosse-Kunstleve, R. W., Baerlocher, Ch., Yoshikawa, M. and Davis, M. E. (1996). *Microporous Mater.*, **6**, 295–309.

- Pagola, S., Stephens, P. W., Bohle, D. S., Kosar, A. D. and Madsen, S. K. (2000). *Nature*, **404**, 307–10.
- Pawley, G. S. (1981). *J. Appl. Crystallogr.*, **14**, 357–61.
- Poojary, D. M. and Clearfield, A. (1997). *Acc. Chem. Res.*, **30**, 414–22.
- Poojary, D. M., Cabeza, A., Aranda, M. A. G., Bruque, S. and Clearfield, A. (1996). *Inorg. Chem.*, **35**, 1468–73.
- Putz, H., Schön, J. C. and Jansen, M. (1999). *J. Appl. Crystallogr.*, **32**, 864–70.
- Rietveld, H. M. (1969). *J. Appl. Crystallogr.*, **2**, 65–71.
- Rius, J., Louër, D., Louër, M., Gali, S. and Melgarejo, J. C. (2000). *Eur. J. Mineral.*, **12**, 581–8.
- Shankland, K., David, W. I. F. and Csoka, T. (1997). *Z. Kristallogr.*, **212**, 550–2.
- Turner, G. W., Tedesco, E., Harris, K. D. M., Johnston, R. L. and Kariuki, B. M. (2000). *Chem. Phys. Lett.*, **321**, 183–90.
- Weeks, C. M., DeTitta, G. T., Hauptman, H. A., Thuman, P. and Miller, R. (1994). *Acta Crystallogr. A*, **50**, 210–20.
- Wessels, T., Baerlocher, Ch., McCusker, L. B. and Creyghton, E. J. (1999). *J. Am. Chem. Soc.*, **121**, 6242–7.
- Young, R. A., ed. (1993). *The Rietveld method.*, Oxford University Press.
- Zachariasen, W. H. (1948). *Acta Crystallogr.*, **1**, 265–8, 277–87
- Zachariasen, W. H. and Ellinger, F. H. (1963). *Acta Crystallogr.*, **16**, 369–75.

Structure determination from powder diffraction data: an overview

Anthony K. Cheetham

2.1 Introduction

The explosion of interest in powder diffraction methods during the last 30 years has been driven by a number of factors. The major one was most certainly the development of the Rietveld method (Rietveld 1969) in the late 1960s, since, at a stroke, this extended the scope of powder techniques from simple, high-symmetry materials to compounds of substantial complexity in any space group. Within five years, for example, the method was being used to refine the structures of orthorhombic and monoclinic materials with as many as 22 atoms in the asymmetric unit (Von Dreele and Cheetham 1974), and by 1977, Cheetham and Taylor were able to review the application of the Rietveld method to over 150 compounds (Cheetham and Taylor 1977). The majority of these early applications involved the use of neutrons, but the field received a further boost in the late 1970s and early 1980s with the extension of the Rietveld method to X-ray data (Malmros and Thomas 1977; Young *et al.* 1977), time-of-flight neutron data (Von Dreele *et al.* 1982), and then synchrotron X-ray data (Cox *et al.* 1983). These instrumental advances were accompanied by software developments, such as the availability of the DBWS (Wiles and Young 1981) and GSAS (Larson and Von Dreele 1987) packages, making possible the analysis of data from complex mixtures or the simultaneous analysis of more than one dataset. Another major area of interest has been the development of methods for solving unknown structures from powder diffraction data, a subject that is the primary focus of this book.

The developments in powder diffraction have been driven by a growing need for tools that are able to probe the structures of materials that are only available in powder form, or can only be studied as powders (e.g. under difficult *in situ* conditions). Such materials include many zeolite catalysts, as well as certain high T_c cuprates and fullerenes. Table 2.1 lists some of the many areas in which powder diffraction methods have had a major impact; clearly, modern materials science and many other areas have been major beneficiaries of the developments in this area during the last 30 years, and this trend will surely continue well into the twenty-first century.

Table 2.1 Impact of powder diffraction methods in materials science and other areas

| | |
|----------------------------|---|
| Hydrogen storage | Superconductivity |
| Metal hydrides | High T_c cuprates |
| Magnets | Batteries/fuel cells |
| Magnetoresistance, GMR | β -alumina solid electrolytes |
| Heterogeneous catalysts | Ferroelectrics |
| Zeolites, clays | PbTiO ₃ etc. |
| Ceramics | Electro-optics |
| Zirconias | Non-linear optics, e.g. KTiOPO ₄ |
| Novel materials | Biominerals |
| C ₆₀ fullerenes | Apatites |
| Coordination compounds | Organic materials |
| Homogeneous catalysts | Pharmaceuticals |

The aim of this overview is to trace the key developments in powder diffraction methods from their discovery in the early twentieth century to the present day. The evolution of tools for solving unknown structures will be emphasized, while remembering, of course, that the refinement step is also an important component of this process.

2.2 Early history of powder diffraction

The possibility of using powder diffraction methods to study materials was recognized shortly after the discovery of X-ray diffraction by Laue and von Knipping in 1910. In particular, the construction of a simple powder diffractometer was described by Hull in 1917 (Hull 1917), and the instrument was used to obtain patterns from a number of simple materials such as diamond, graphite and iron. Even at this early stage, the use of metal foils to remove $K\beta$ radiation from the X-ray beam was well understood. Within a few years, many others, including the Braggs and Pauling, had exploited the powder method to study a wide range of materials, including metals, minerals, and simple organic solids. It could reasonably be argued that the first *ab initio* structure determinations were performed during this period, since the crystal structures of many simple materials (e.g. rocksalt) were obtained from powder diffraction data alone.

The first systematic attempts to determine unknown structures of non-cubic materials were probably those of Zachariasen, reported in the late 1940s. For example, the hexagonal structure of UCl₃, in space group $P6_3/m$, was determined by first placing the heavy atom and then estimating the position of the chlorine by careful inspection of the intensities of different classes of reflections (Zachariasen 1948a). In the same issue of *Acta Crystallographica*, a series of

papers by Zachariasen describe the structures of eight uranium halides and oxohalides from X-ray powder data (Zachariasen 1948*b*), and in the following year a similar approach was used by Mooney to solve the tetragonal structure of UCl_4 (Mooney 1949).

These early approaches might be regarded as trial-and-error methods, though they reveal great insight into the relationships between trends in the integrated intensities of different classes of reflections and the locations of the scattering centres. They certainly laid the foundations for the systematic approaches that evolved during subsequent decades.

2.3 Early *ab initio* approaches

There are at least two papers in the 1960s that describe systematic attempts to use the structure-solving tools of modern crystallography, Direct methods and Patterson techniques, to solve structures from powder data. In a remarkable paper by Zachariasen and Ellinger (1963), the monoclinic structure of β -plutonium, in space group $I2/m$, was solved by using a manual Direct methods phasing procedure. There are seven Pu atoms in the asymmetric unit, underlining the complexity of this task. A particularly interesting aspect of this work was the clever use of the anisotropic thermal expansion of β -plutonium to unscramble the individual Bragg intensities of overlapping reflections from patterns collected at different temperatures (see Chapter 9). As will become clear later, the treatment of overlapping reflections remains one of the major issues in structure determination from powder data.

Another eye-catching paper from the 1960s is that by Debets (1968) in which the orthorhombic structure of UO_2Cl_2 in space group $Pnma$ was determined by Patterson methods. As in the work of Zachariasen and Ellinger, their approach is not radically different from that which has been used widely in the late 1980s and 1990s. An interesting difference between these early studies and the more recent work, however, is that the structure refinement step did not take advantage of least-squares methods, which, of course, are used routinely today. Nevertheless, the essential correctness of the UO_2Cl_2 structure has since been confirmed by Taylor and Wilson (1973).

2.4 Pre-Rietveld refinement methods

The development of least-squares crystallographic structure-refinement methods in the 1960s, which was facilitated by the growing availability of digital computers, was applied not only to single-crystal data but also to powder data. A number of laboratories, such as UKAEA, Harwell, made widespread use of single-crystal codes for refining structures from powder data, and some of the codes were adapted to handle groups of non-equivalent overlapping reflections that could not be resolved experimentally. Table 2.2 shows an example of such a

Table 2.2 Integrated-intensity structure refinement for $\text{Fe}_{0.923}\text{O}$ at 800°C , based upon powder neutron diffraction data. There were 12 observations and four variable parameters: the scale factor, the occupancy number for the tetrahedral interstitial site, and independent isotropic temperature factors for the iron and oxygen atoms (Cheetham *et al.* 1970). The R_I value is 0.78 per cent

| hkl | I(obs) | I(calc) |
|---------|--------|---------|
| 111 | 6092 | 6315 |
| 200 | 89 766 | 89 604 |
| 220 | 79 186 | 79 285 |
| 311 | 3378 | 3484 |
| 222 | 26 340 | 26 139 |
| 400 | 12 697 | 13 094 |
| 331 | 1540 | 1377 |
| 420 | 31 104 | 31 301 |
| 422 | 23 695 | 23 438 |
| 333/511 | 1061 | 898 |
| 440 | 5831 | 6042 |
| 600/442 | 10 394 | 10 308 |

refinement, carried out at Harwell shortly before a Rietveld program that would run on the computer there became available. The paucity of data and the poor observation-to-parameter ratio make it hard to believe that this was essentially the state-of-the-art in the late 1960s, but it is important to stress that such studies played an important role at the time in the quantitative structural characterization of high-symmetry inorganic materials. A particular class of materials that benefited from this approach was that of non-stoichiometric compounds, which are typically high-symmetry phases that are found at high temperatures. Nevertheless, the limitation of the integrated intensity method, at the time, was that it could not be applied to the complex patterns obtained from low-symmetry materials. The advent of the Rietveld refinement method, however, was soon to solve this problem.

2.5 Rietveld refinement

In response to the need to develop enhanced procedures for obtaining structural information from powder samples, in the late 1960s, Rietveld (1969) proposed a method for analysing the more complex patterns obtained from low-symmetry materials by means of a curve-fitting procedure. The least-squares refinement minimizes the difference between the observed and calculated profiles, rather

than individual reflections. In the first instance, this procedure was carried out with constant wavelength neutrons, rather than X-rays, because of the simpler peak shape of the Bragg reflections. With constant wavelength neutrons, it can normally be assumed that the reflections are Gaussian in shape, and the calculated intensity at each point (say, $0.05^\circ 2\theta$ steps) on the profile is obtained by summing the contributions from the Gaussian peaks that overlap at that point. In addition to the conventional parameters in the least-squares procedure (i.e. scale factor, atomic coordinates and temperature factors), additional parameters are required: the lattice parameters (which determine the positions of the reflections), a zero-point error for the detector, and three parameters that describe the variation of the Gaussian half-width (full width at half maximum intensity) with scattering angle. The technique has been applied to a wide range of solid-state problems and has been reviewed by several authors during the last 25 years (Cheetham and Taylor 1977; Hewat 1986; Young 1993).

The application of the Rietveld method to neutron data in the early 1970s was soon followed by its extension to laboratory X-ray diffractometer data (Malmros and Thomas 1977; Young *et al.* 1977). The problem of the more complex peak shape was resolved by employing alternative peak-shape functions, such as the Lorentzian and the pseudo-Voigt. Other problems that can plague X-ray studies include preferred orientation and poor powder averaging (graininess), both of which arise from the fact that X-rays probe a smaller sample volume than do neutrons; these were addressed by paying closer attention to the data collection strategy.

The accuracy and precision of a structure refinement from X-ray data can normally be optimized by collecting high-resolution data at a synchrotron source (Cox *et al.* 1983). The resolution of the powder diffractometers at second and third generation sources is so good that sample imperfections now play a major role in determining the shape of the Bragg peaks. This presents both challenges and opportunities. For the crystallographer, the subtle variations in peak shape from one class of reflection to another (which may stem from, say, anisotropic particle size or strain effects) may be an irritation if the sole aim is to obtain a high-quality refinement of the crystal structure. However, the materials scientist may be delighted to retrieve a wealth of additional information pertaining to the microstructure of the sample.

Refinement by the Rietveld method is now commonplace with both laboratory and synchrotron X-ray data, although it is not, in general, as precise as the neutron method (Table 2.3). There are three reasons for this. First, as mentioned above, it is more difficult to collect X-ray data that are essentially free from systematic errors. Consequently, it is not unusual to find that the precision, as measured in terms of the estimated standard deviations (e.s.d.s), gives a misleading impression of the real accuracy of the structure. Second, the fall-off of intensity with scattering angle due to the X-ray form factor reduces the quality of the information that can be retrieved from the high-angle region of an X-ray pattern. Third, the wide variation in X-ray scattering factors between

elements from different parts of the periodic table leads to considerable differences in the sensitivities with which atoms can be located; in particular, heavy atoms will be better defined than light atoms. In Table 2.3, for example, the y coordinate of Cr(2) is determined with greater precision than the y coordinate of O(2) by X-ray powder diffraction. This problem does not arise to the same extent with neutrons because their scattering amplitudes (or scattering lengths, as they are known) fall within a relatively narrow range of values (Bacon 1975).

The Rietveld method was also extended to the analysis of time-of-flight neutron powder data collected at pulsed sources. The procedure is essentially the same as that used in constant-wavelength experiments, except that the peak shape function is considerably more complex, due in part to the shape of the neutron pulse, and wavelength-dependent corrections (e.g. absorption and extinction) must be taken into account (Von Dreele *et al.* 1982). One advantage

Table 2.3 Structural parameters for α -CrPO₄ refined using synchrotron X-ray (marked X) and neutron (N) data in *Imma* with e.s.d.s in parentheses (Attfield *et al.* 1988). Values from the reported single-crystal study (marked S) are given for comparison (Glaum *et al.* 1986)

| Atom | x | y | z | B_{iso}^a |
|-------|---|---|--|-----------------------|
| Cr(1) | 1/2 | 1/2 | 0 | 0.3(2)N 0.283(6)S |
| Cr(2) | 1/4 | 0.3660(3)X 0.3650(4)N 0.36611(3)S | 1/4 | 0.0(1)N 0.316(4)S |
| P(1) | 1/2 | 1/4 | 0.0819(12)X 0.0790(8)N 0.0825(2)S | 0.0(1)N 0.30(1)S |
| P(2) | 1/4 | 0.5738(4)X 0.5739(2)N 0.57358(5)S | 1/4 | 0.47(8)N 0.345(7)S |
| O(1) | 0.3790(10)X 0.3766(3)N 0.3773(2)S | 1/4 | 0.2269(17)X 0.2280(5)N 0.2268(3)S | 0.53(8)N 0.42(2)S |
| O(2) | 0.3603(6)X 0.3610(2)N 0.3611(1)S | 0.4914(5)X 0.4907(1)N 0.4902(1)S | 0.2145(11)X 0.2142(3)N 0.2146(2)S | 0.62(6)N 0.42(1)S |
| O(3) | 0.2263(6)X 0.2240(1)N 0.2238(1)S | 0.6352(5)X 0.6368(2)N 0.6363(1)S | 0.0576(10)X 0.0546(3)N 0.0552(2)S | 0.68(5)N 0.56(1)S |
| O(4) | 1/2 | 0.3509(8)X 0.3486(2)N 0.3496(2)S | -0.0457(15)X -0.0422(4)N -0.0432(3)S | 0.31(7)N 0.50(2)S |

^aFor the powder X-ray refinement, overall $B_{iso} = 0.24(7) \text{ \AA}^2$

of time-of-flight powder methods is that the whole diffraction pattern is collected simultaneously since the counter, or bank of counters, remains stationary, making it an attractive way of following structural changes that evolve as a function of time, temperature or pressure. In addition, since the incident and scattered beams can pass through small apertures in, say, a high-pressure apparatus, the design of special environments is clearly easier for such measurements (Jorgensen 1988). A further advantage is that it is relatively easy to obtain high-resolution data by using a long incident flight path and placing the detectors in the back scattering position.

The Rietveld method is a powerful tool, but it is limited by the same drawback that affects powder methods in general: the loss of information that arises from the compression of the three-dimensional diffraction pattern into a single dimension. It is also important to underline the fact that the Rietveld method, though an excellent technique for *refining* structures, requires a good starting model if it is to converge successfully and does not, by itself, constitute a method for *structure determination*. We shall now return to the question of solving unknown structures and examine the state-of-the-art in this area.

2.6 Solving unknown structures from powder data

There has been a great deal of interest concerning the determination of unknown structures from powder diffraction data during the last decade and there have been several reviews of the subject (Cheetham 1986; Cheetham 1993; Harris and Tremayne 1996). The process may conveniently be broken down into a series of steps, though there may be considerable overlap between the different stages:

- (1) determination of the unit cell;
- (2) decomposition of the powder pattern into integrated intensities, I_{hki} ;
- (3) assignment of space group from systematic absences;
- (4) solution of the phase problem;
- (5) refinement of the structure, typically by the Rietveld method.

Most of these stages are discussed in detail in more specialized chapters in this book, so only a few general comments will be made at this stage.

Step 1, the indexing of the powder pattern to yield a unit cell, is normally carried out by autoindexing methods, for which a number of powerful computer programs are now available (see Chapter 7). These include ITO (Visser 1969), TREOR (Werner *et al.* 1985) and DICVOL (Boultif and Louër 1991). Access to more than one of these programs is desirable since they work in different ways and successful indexing may not always be achieved with one particular program; the key point is that successful indexing is facilitated by collecting high-quality data. In practice, with careful instrument alignment, careful data collection and accurate peak-position determination, it seems that few structure

determinations stumble at the point of determining the unit cell. Of course, as mentioned in Section 1.2 of Chapter 1, this situation may well change.

We should also note that the identity of the space group may become apparent following the autoindexing stage, though uncertainties frequently remain and must be resolved at a later stage (see below). In cases where the unit-cell determination is proving difficult, it might be worthwhile to obtain selected area electron diffraction patterns from microcrystals, noting that an electron diffraction pattern is the equivalent of a zero-level precession photograph with X-rays. The feasibility of this approach will depend upon the stability of the sample in the beam, but the extra effort that it entails may be rewarded, especially if there is a subtle superstructure to which powder X-ray methods may not be sensitive.

The second step of the structure determination, the decomposition of the pattern into individual integrated intensities, is often the most challenging one because it is here that severe ambiguities may arise due to overlapping of peaks (see Chapter 8). Such overlapping may be accidental or may be an unavoidable consequence of the symmetry (e.g. the exact overlap of non-equivalent reflections in certain high-symmetry Laue groups). A number of powerful single-step strategies that have been developed to address the pattern-decomposition problem are now embodied in computer programs such as ALLHKL (Pawley 1981), WPPF (Toraya 1986), GSAS (Larson and Von Dreele 1987, incorporating the Le Bail method (Le Bail *et al.* 1988)), LSQPROF (Jansen *et al.* 1992*a*) and EXTRA (Altomare *et al.* 1995). The earliest development in this area, due to Pawley (1981), was based upon a Rietveld fitting procedure in which the integrated intensities were refined in addition to the lattice parameters, peak-shape parameters, etc. Le Bail's method is closely related, but is somewhat more robust in its treatment of overlapping data.

From this stage onwards, the analysis can mirror that of a single-crystal study. In stage 3, the possible space groups can be assigned from the systematic absences, although in cases of uncertainty it may be useful to carry out the pattern decomposition in a number of alternative space groups (or to obtain a series of electron diffraction patterns, as discussed above). Uncertainties often remain (as they do with single-crystal methods) and may have to be resolved during the structure solution and/or refinement steps. The phase problem is then solved in stage 4 by conventional crystallographic methods, that is, Patterson or Direct methods, the choice being dictated by the chemical nature of the material. Early work in this area utilized programs that had been developed for the analysis of single-crystal data, but some Direct methods codes that are optimized for powder data are now available, including EXPO (Altomare *et al.* 1999) and SIMPEL (Jansen *et al.* 1993) (see Chapters 10 and 11). Patterson determinations are also benefiting from vector-search algorithms (see Chapters 12 and 13).

As with the solution of structures from single-crystal data, light atom problems will normally respond better to Direct methods, while structures containing a subset of heavy atoms will be more amenable to Patterson

techniques. The principal difficulty is that, even if there are no ambiguities due to peak overlap, the data set will be considerably smaller than that obtained in a single-crystal study and the phasing procedure will be less straightforward. It is a tribute to the robustness of modern structure-solving techniques that it is still possible to determine structures under these unfavourable circumstances. Once a suitable starting model has been obtained, stage 5, the refinement of the structure, can proceed by using the Rietveld method. Quite commonly, the starting model will be incomplete and additional atoms will be found during the refinement procedure by using difference Fourier methods.

More recently, the probability of solving a structure from powder data has improved because there has been a move towards the development of pattern-decomposition methods that are more sophisticated. Typically, these new methods are not single-step procedures, but involve an iteration between the pattern-decomposition step and the subsequent Patterson or Direct methods calculations. For example, the observed intensities that are obtained from a successful pattern decomposition should yield a Patterson map that fulfils certain requirements; for example, it should be positive at all points. Some of the codes that link the pattern decomposition and the structure-solving stage are DOREES (Jansen *et al.* 1992*b*) and FIPS (Estermann *et al.* 1992; Estermann and Gramlich 1993), and those based upon maximum entropy (David 1987, 1990) and Bayesian fitting procedures (Sivia and David 1994). A potentially powerful approach is the use of entropy maximization and likelihood ranking (Bricogne and Gilmore 1990; Gilmore *et al.* 1993), a method that has been used in other areas of crystallography and has now been adapted for powder data in the MICE computer program (Gilmore *et al.* 1990; see also Chapter 14).

2.7 Trial-and-error and simulation methods

In addition to the systematic approaches described above, there has been a long-standing tradition of solving unknown structures from powder data by trial-and-error methods. A typical example can be seen in the work of Titcomb *et al.* (1974), who solved the superstructure of the metal hydride phase, CeH_{2+x} , by exploring all of the possible arrangements of the interstitial hydrogens in the fluorite-related parent structure. The fluorite-related structure of Bi_3ReO_8 was solved in a similar manner (Cheetham and Rae Smith 1985). The starting models obtained by trial-and-error were then refined by the Rietveld method. In this approach, it is clearly advantageous (and often essential) to use information that may be available from other studies on the material of interest. In Bi_3ReO_8 , for example, it was known from infra-red measurements that the oxygen coordination around the rhenium atom was tetrahedral. Similarly, model-building, together with information from electron microscopy and ^{29}Si magic angle spinning NMR, was used to elucidate the structure of the molecular sieve zeolite, ZSM-23 (Wright *et al.* 1985).

The manual trial-and-error strategy is not very attractive, since it can be very time-consuming and the chances of success are not particularly high. However, modern simulation methods, together with the power of modern computers, can be used to remove much of the labour and uncertainty from this approach by automating the way in which previous knowledge of a system, or related systems, is used. In the zeolite area, for example, Deem and Newsam (1989) have developed a simulated annealing method that can be used to predict unknown zeolite structures from a knowledge of the unit cell, the space group, and the number of tetrahedral Si/Al (T) sites in the cell. In cases where the space group or number of T sites is uncertain, the calculation is sufficiently fast for alternative possibilities to be tested. The simulation procedure employs cost functions that depend upon the T–T distances and T–T–T angles in a large body of known zeolitic structures. Further refinement of this approach involving the implementation of a biased Monte Carlo scheme was reported recently (Falcioni and Deem 1999).

Molecular crystals, too, lend themselves naturally to simulation methods, since their molecular structures (or fragments thereof) are often known with some confidence. We can use prior knowledge of the molecular structure (or an energy-minimized molecular structure obtained by quantum mechanical calculations) and move the molecular fragment by translations and rotations within the unit cell using algorithms ranging from simple grid search to simulated annealing and genetic algorithms (see Chapters 15 and 16). Knowledge of the space group is again required, of course. The crystal structure can be predicted by using energy functions based upon appropriate inter- and intra-molecular potentials, or by comparison between the calculated and observed X-ray powder patterns. Approximate models can then be refined by the Rietveld method. Examples of structures solved in this manner include piracetam, $C_6H_{10}N_2O_2$ (Louër *et al.* 1995) and 1-methylfluorene, $C_{14}H_{12}$ (Tremayne *et al.* 1996). The approach is very straightforward for rigid molecules, but becomes considerably more difficult as the number of degrees of freedom increases. Nevertheless, algorithmic developments have led to a situation where the crystal structures of relatively flexible molecular moieties can be solved quite straightforwardly (see Section 2.8 and Chapters 15 and 16).

2.8 Some examples of structure determination from powder data

A great deal of the development work in the field of structure determination from powder data has relied on the use of conventional, laboratory X-ray sources, and there were a number of important early successes in the area (Berg and Werner 1977; Clearfield *et al.* 1984). However, synchrotron X-ray data has profound advantages over conventional X-ray data for structure determination. In particular, the combination of the high brightness and excellent vertical collimation can be harnessed to construct diffractometers with unparalleled

angular resolution, as in the case of the instrument at the National Synchrotron Light Source (NSLS), Brookhaven National Laboratory (Cox *et al.* 1986), where the resolution at the focusing position is $<0.02^\circ$ in 2θ . This is partly achieved by constructing the instrument in the vertical plane, since the vertical divergence, θ_v , is only $\sim 0.01^\circ$ at 2.5 GeV. With high-resolution data, the solution of structures from powder data is greatly facilitated because ambiguities due to peak overlap are minimized and the information content of the dataset is optimized. Many successful structure solutions and refinements have now been performed, a selection of which is given in Table 2.4. On the other hand, relatively few structures have been solved from powder neutron diffraction data. This is partly a consequence of the lower resolution of most neutron diffractometers, but it is mainly due to the near equivalence of the neutron scattering lengths for most elements, as a result of which the phase problem cannot be solved on the basis of locating a small subset of atoms. Some recent examples of structure solutions from neutron diffraction data, obtained by the application of both Direct methods and global optimization strategies, are discussed in Chapter 5.

Table 2.4 Some examples of *ab initio* structure determinations from synchrotron X-ray powder data

| Compound | Space group | No. of atoms in asymmetric unit | Ref. |
|---|---------------------------|---------------------------------|------|
| α -CrPO ₄ | <i>Imma</i> | 8 | 1 |
| I ₂ O ₄ | <i>P2₁/c</i> | 6 | 2 |
| Al ₂ Y ₄ O ₉ | <i>P2₁/c</i> | 15 | 2 |
| MnPO ₄ · H ₂ O | <i>C2/c</i> | 6 | 3 |
| PbC ₂ O ₄ | <i>P1</i> | 7 | 4 |
| Clathrasil, Sigma-2 | <i>I4₁/amd</i> | 17 | 5 |
| LaMo ₅ O ₈ | <i>P2₁/a</i> | 14 | 6 |
| BeH ₂ | <i>Ibam</i> | 4 | 7,8 |
| UPd ₂ Sn | <i>Pnma</i> | 4 | 9 |
| C ₅ H ₁₁ NO ₂ | <i>Pna2₁</i> | 19 | 10 |
| NaCD ₃ | <i>I222</i> | 10 | 11 |
| C ₁₀ N ₆ SH ₁₆ | <i>P2₁/n</i> | 33 | 12 |
| BaBiO _{2.5} | <i>P2₁/c</i> | 5 | 13 |
| (VO) ₃ (PO ₄) ₂ · 9H ₂ O | <i>P2₁/n</i> | 13 non-H | 14 |
| CuPt ₃ O ₆ | <i>Pn2₁m</i> | 10 | 15 |
| Ga ₂ (HPO ₃) ₃ · 4H ₂ O | <i>P2₁</i> | 29 | 16 |
| La ₃ Ti ₅ Al ₁₅ O ₃₇ | <i>Cc</i> | 60 | 17 |

1 = Attfield *et al.* 1986; 2 = Lehmann *et al.* 1987; 3 = Lightfoot *et al.* 1987; 4 = Christensen *et al.* 1989; 5 = McCusker 1988; 6 = Hibble *et al.* 1988; 7 = Smith *et al.* 1987; 8 = Smith *et al.* 1988; 9 = Marezio *et al.* 1988; 10 = Kurahshi *et al.* 1989; 11 = Weiss *et al.* 1990; 12 = Cernik *et al.* 1991; 13 = Lightfoot *et al.* = 1991; 14 = Teller *et al.* 1992; 15 = Hriljac *et al.* 1991; 16 = Morris *et al.* 1992; 17 = Morris *et al.* 1994

In the first example of a structure solved from synchrotron X-ray powder data, carried out in 1986 by Attfield *et al.* (1986), the orthorhombic structure of α -CrPO₄, with eight atoms in the asymmetric unit, was solved by Patterson methods using a vector-search procedure; 68 well-resolved peaks were utilized. A relatively poor R_p -factor (19.3 per cent) was obtained for the final Rietveld refinement with the synchrotron data, no doubt due to problems with preferred orientation and hkl -dependent line-broadening effects, but a subsequent medium resolution neutron study (on D1a at ILL Grenoble) gave an excellent fit ($R_p = 8.3$ per cent), confirming the correctness of the X-ray model. A comparison of the coordinates obtained from the X-ray and neutron refinements, and a subsequent single-crystal study, was given in Table 2.3. In particular, we note that the neutron refinement gives improved precision for almost all atoms, in spite of the modest resolution of the neutron data.

During the last decade, there has been widespread use of synchrotron powder methods to solve unknown structures (Table 2.4), the most striking development being the extension of the method to systems of very considerable complexity, with as many as 60 atoms in the asymmetric unit of the cell (Morris *et al.* 1994). Such complex structures normally require a combination of both synchrotron X-ray and neutron data for their solution and refinement, since they lie at the limit of what can currently be done with a single dataset. With the advent of global optimization methods, challenging 'equal atom' organic structures are also being solved. However, subsequent refinement is not trivial. Some recent examples include forms A and B of famotidine and the nitrate and acetate salts of remacemide (Admans 2000), and the disordered structure of tetraferrocenyl-[3]-cumulene (Dinnibier *et al.* 2000).

The ease of access to good laboratory diffractometers, however, has encouraged an even greater effort with laboratory data. Structures of high complexity have been solved (e.g. β -Ba₃AlF₉, with 29 atoms in the asymmetric unit (Le Bail 1993)), and there has been extensive use of the methodologies in the areas of molecular organic crystals, coordination compounds and organometallic materials (most of the effort in the powder diffraction area has traditionally been in the realm of non-molecular inorganic materials). Eye-catching examples include recent work on bipyridyl complexes of nickel and copper (Masciocchi *et al.* 1996), the carbonyl cluster compound [HgRu(CO)₄]₄ (Masciocchi *et al.* 1993) and Ph₂P(O)-(CH₂)₇-P(O)Ph₂ (Kariuki *et al.* 1999).

2.9 Conclusions

The role of powder diffraction in the structural characterization of materials has expanded dramatically during the last 30 years. A number of developments have played important roles: (a) the advent of the Rietveld refinement method, (b) improvements in laboratory X-ray instrumentation, (c) the availability of

high-resolution powder diffractometers at pulsed neutron sources and synchrotron sources, (d) advances in computational methods for structure solution, and (e) improvements in computer hardware (e.g. personal computers that are capable of running Rietveld codes). The power of powder techniques is such that they have had an impact in most of the major developments in the field of new materials during recent years; solid electrolytes, high-temperature superconductors, fullerenes, zeolites and giant magnetoresistance (GMR) materials are obvious examples. As a consequence, powder diffraction has been transformed from the ugly duckling of crystallography into one of the most exciting and fast-moving areas.

Notwithstanding the remarkable progress, much work remains to be done. The solution of unknown structures from powder data is by no means routine, and the methods need to be further automated before they can be used by non-specialists, even those with crystallographic experience. Furthermore, there is considerable scope for advances in refinement procedures, in spite of the power of the Rietveld method. For example, some of the complex structures that are now being solved are at the limit of what can be refined by current procedures. As a consequence, the accuracy of many of these more complex structures falls well short of what we would hope for and aspire towards. This can easily be seen by looking at the bond lengths that are obtained from refinements of complex organic or zeolitic materials; it is not unusual to find interatomic distances that are clearly outside the range that would be considered to be chemically acceptable.

The solution to this problem will no doubt come from several areas. First, it will become possible to collect better data, and more of it, especially with access to short X-ray wavelengths at the third-generation synchrotron sources (systematic errors in X-ray data can be dramatically reduced at shorter wavelengths). Second, the simultaneous analysis of X-ray and neutron data is already having an impact, but we shall no doubt see the use of data from other techniques such as solid state NMR and EXAFS. In addition, advances in computation are taking us towards a scenario where energy minimization will become a part of the refinement procedure. For example, it is already clear that we can sometimes calculate the structure of an all-silica zeolite with better accuracy than we can determine it experimentally by powder X-ray diffraction (Cheetham *et al.* 1997). Finally, we shall see the use of more subtlety in the refinement process, such as the more extensive use of maximum-entropy methods (Sakata *et al.* 1990, 1993).

This overview would not be complete without reference to the developments in single crystal methods that may have an impact on powder crystallography. The construction of third-generation synchrotron sources has, once again, focused attention on the possibility of collecting X-ray data from micron-size crystals. Progress in this area has not been as rapid as many had expected, but a recent example from the European Synchrotron Radiation Facility (ESRF) in Grenoble (Noble *et al.* 1997) may offer a glimpse of future possibilities in this

area. Certainly, the use of dedicated synchrotron X-ray stations equipped with CCD type detectors (such as Station 9.8 at the Daresbury Synchrotron Radiation Source (SRS)) is transforming expectations of what can be achieved in terms of structure determination from very small crystals. Nor should we forget the power of the electron microscope for interrogating small crystals. There have been several examples (e.g. Vincent *et al.* 1984; Tsuda and Tanaka 1995) of structure refinements by using higher-order Laue zones (HOLZ) from convergent beam electron diffraction patterns, and this area is likely to attract further attention. Nevertheless, the current capabilities and the exciting opportunities for the future can leave us in no doubt that powder diffraction will continue to play a dominant role in this area for the foreseeable future.

References

- Admans, G., ed. (2000). *ESRF Highlights 1999*, ESRF, Grenoble.
- Altomare, A., Burla, M. C., Camalli, M., Carrozzini, B., Cascarano, G. L., Giacovazzo, C., Guagliardi, A., Moliterni, A. G. G., Polidori, G. and Rizzi, R. (1999). *J. Appl. Crystallogr.*, **32**, 339–40.
- Altomare, A., Burla, M. C., Cascarano, G., Guagliardi, A., Moliterni, A. G. G. and Polidori, G. (1995). *J. Appl. Crystallogr.*, **28**, 842–6.
- Attfield, J. P., Cheetham, A. K., Cox, D. E. and Sleight, A. W. (1988). *J. Appl. Crystallogr.*, **21**, 452–7.
- Attfield, J. P., Sleight, A. W. and Cheetham, A. K. (1986). *Nature (London)*, **322**, 620–2.
- Bacon, G. E. (1975). *Neutron diffraction*, 3rd edn. Clarendon Press, Oxford.
- Berg, J.-E. and Werner, P.-E. (1977). *Z. Kristallogr.*, **145**, 310–20.
- Boultif, A. and Loüer, D. (1991). *J. Appl. Crystallogr.*, **24**, 987–93.
- Bricogne, G. and Gilmore, C. J. (1990). *Acta Crystallogr. A*, **46**, 284–97.
- Cernik, R. J., Cheetham, A. K., Prout, C. K., Watkin, D. J., Wilkinson, A. P. and Willis, B. T. M. (1991). *J. Appl. Crystallogr.*, **24**, 222–6.
- Cheetham, A. K. (1986). *Mater. Sci. Forum*, **9**, 103–12.
- Cheetham, A. K. (1993). In *The Rietveld method* (ed. R. A. Young), pp. 276–92, Oxford University Press.
- Cheetham, A. K., Bull, L. M. and Henson, N. J. (1997). *Studies Surf. Sci. Catal.*, **105**, 2267–74.
- Cheetham, A. K., Fender, B. E. F. and Taylor, R. I. (1970). *J. Phys. C (Solid State Phys.)*, **4**, 2160–5.
- Cheetham, A. K. and Rae Smith, A. R. (1985). *Acta Crystallogr. B*, **41**, 225–30.
- Cheetham, A. K. and Taylor, J. C. (1977). *J. Solid State Chem.*, **21**, 253–75.
- Christensen, A. N., Cox, D. E. and Lehmann, M. S. (1989). *Acta Chem. Scand.*, **43**, 19–25.
- Clearfield, A., McCusker, L. B. and Rudolf, P. R. (1984). *Inorg. Chem.*, **23**, 4679–82.
- Cox, D. E., Hastings, J. B., Cardoso, L. P. and Finger, L. W. (1986). *Mater. Sci. Forum*, **9**, 1–20.
- Cox, D. E., Hastings, J. B., Thomlinson, W. and Prewitt, C. T. (1983). *Nucl. Instrum. Methods*, **208**, 573–8.

- David, W. I. F. (1987). *J. Appl. Crystallogr.*, **20**, 316–19.
- David, W. I. F. (1990). *Nature*, **346**, 731–4.
- Debets, P. C. (1968). *Acta Crystallogr. B*, **24**, 400–2.
- Deem, M. W. and Newsam, J. M. (1989). *Nature*, **342**, 260–2.
- Dinnebier, R. E., Schweiger, M., Bildstein, B., Shankland, K., David, W. I. F., Jobst, A. and van Smaalen, S. (2000). *J. Appl. Crystallogr.*, **33**, 1199–207.
- Estermann, M. A. and Gramlich, V. (1993). *J. Appl. Crystallogr.*, **26**, 396–404.
- Estermann, M. A., McCusker, L. B. and Baerlocher, Ch. (1992). *J. Appl. Crystallogr.*, **25**, 539–43.
- Falcioni, M. and Deem, M. W. (1999). *J. Chem. Phys.*, **110**, 1754–66.
- Gilmore, C. J., Bricogne, G. and Bannister, C. (1990). *Acta Crystallogr. A*, **46**, 297–308.
- Gilmore, C. J., Shankland, K. and Bricogne, G. (1993). *Proc. Royal Soc. Ser. A*, **442**, 97–111.
- Glaum, R., Gruehn, R. and Moller, M. (1986). *Z. Anorg. Allg. Chem.*, **543**, 111–16.
- Harris, K. D. M. and Tremayne, M. (1996). *Chem. Mater.*, **8**, 2554–70.
- Hewat, A. W. (1986). *Chem. Scripta*, **26A**, 119–30.
- Hibble, S. J., Cheetham, A. K., Bogle, A. R. L., Wakerley, H. R. and Cox, D. E. (1988). *J. Am. Chem. Soc.*, **110**, 3295–6.
- Hriljac, J. A., Parise, J. B., Kwei, G. H., Shannon, R. and Schwartz, K. (1991). *J. Phys. Chem. Solids*, **52**, 1273–9.
- Hull, A. W. (1917). *Phys. Rev.*, **9**, 84–7.
- Jansen, J., Peschar, R. and Schenk, H. (1992a). *J. Appl. Crystallogr.*, **25**, 231–6.
- Jansen, J., Peschar, R. and Schenk, H. (1992b). *J. Appl. Crystallogr.*, **25**, 237–43.
- Jansen, J., Peschar, R. and Schenk, H. (1993). *Z. Krist.*, **206**, 33–43.
- Jorgensen, J. D. (1988). *NATO ASI Series, Series C*, **221**, 159–84.
- Kariuki, B. M., Calcagno, P., Harris, K. D. M., Philp, D. and Johnston, R. L. (1999). *Angew. Chem.*, **38**, 831–5.
- Kurahashi, M., Honda, K. and Goto, M. (1989). *Photon Factory Activity Report*, **7**, 170.
- Larson, A. C. and Von Dreele, R. B. (1987). *GSAS, Los Alamos National Laboratory Report No. LA-UR-86-748*.
- Le Bail, A. (1993). *J. Solid State Chem.*, **103**, 287–91.
- Le Bail, A., Duroy, H. and Fourquet, J. L. (1988). *Mater. Res. Bull.*, **23**, 447–52.
- Lehmann, M. S., Christensen, A. N., Fjellvag, H., Feidenhans'l, R. and Nielsen, M. (1987). *J. Appl. Crystallogr.*, **20**, 123–9.
- Lightfoot, P., Cheetham, A. K. and Sleight, A. W. (1987). *Inorg. Chem.*, **26**, 3544–7.
- Lightfoot, P., Hriljac, J. A., Pei, S., Zheng, Y., Mitchell, A. W., Richards, D. R., Dabrowski, B., Jorgenson, J. D. and Hinks, D. G. (1991). *J. Solid State Chem.*, **92**, 473–9.
- Louër, D., Louër, M., Dzyabchenko, V. A., Agafonov, V. and Ceolin, R. (1995). *Acta Crystallogr. B*, **51**, 182–7.
- Marezio, M., Cox, D. E., Rossel, C. and Maple, M. B. (1988). *Solid State Commun.*, **67**, 831–5.
- Malmros, G. and Thomas, J. O. (1977). *J. Appl. Crystallogr.*, **10**, 7–11.
- Masciocchi, N., Cairati, P., Carlucci, L. and Mezza, G. (1996). *J. Chem. Soc., Dalton Trans.*, **13**, 2739–46.
- Masciocchi, N., Cairati, P., Ragaini, F. and Sironi, A. (1993). *Organometallics*, **12**, 4499–502.

- McCusker, L. B. (1988). *J. Appl. Crystallogr.*, **21**, 305–10.
- Mooney, R. (1949). *Acta Crystallogr.*, **2**, 189–91.
- Morris, R. E., Harrison, W. T. A., Nicol, J. M., Wilkinson, A. P. and Cheetham, A. K. (1992). *Nature (London)*, **359**, 519–22.
- Morris, R. E., Owen, J. J., Stalick, J. K. and Cheetham, A. K. (1994). *J. Solid State Chem.*, **111**, 52–7.
- Noble, G. W., Wright, P. A., Lightfoot, P., Morris, R. E., Hudson, K. J., Kvik, Å. and Graafsma, H. (1997). *Angew. Chemie*, **36**, 81–3.
- Pawley, G. S. (1981). *J. Appl. Crystallogr.*, **14**, 357–61.
- Rietveld, H. M. (1969). *J. Appl. Crystallogr.*, **2**, 65–71.
- Sakata, M., Mori, S., Kumazawa, S., Takata, M. and Toraya, M. (1990). *J. Appl. Crystallogr.*, **23**, 526–34.
- Sakata, M., Uno, T., Takata, M. and Howard, C. J. (1993). *J. Appl. Crystallogr.*, **26**, 159–65.
- Sivia, D. S. and David, W. I. F. (1994). *Acta Crystallogr. A*, **50**, 703–14.
- Smith, G. S., Johnson, Q. C., Cox, D. E., Snyder, R. L., Smith, D. K. and Zalkin, A. (1987). *Adv. X-ray Anal.*, **30**, 383–8.
- Smith, G. S., Johnson, Q. C., Smith, D. K., Cox, D. E., Snyder, R. L. and Zhou, R.-S. (1988). *Solid State Commun.*, **67**, 491–4.
- Taylor, J. C. and Wilson, P. W. (1973). *Acta Crystallogr. B*, **29**, 1073–6.
- Teller, R. G., Blum, P., Kostiner, E. and Hriljac, J. A. (1992). *J. Solid State Chem.*, **97**, 10–18.
- Titcomb, C. G., Cheetham, A. K. and Fender, B. E. F. (1974). *J. Phys. C, Solid State Phys.*, **7**, 2409–16.
- Toraya, H. (1986). *J. Appl. Crystallogr.*, **19**, 440–7.
- Tremayne, M., Kariuki, B. M. and Harris, K. D. M. (1996). *J. Mater. Chem.*, **6**, 1601–4.
- Tsuda, K. and Tanaka, M. (1995). *Acta Crystallogr. A*, **51**, 7–19.
- Vincent, R., Bird, D. M. and Steeds, J. W. (1984). *Philos. Mag. A*, **50**, 745–65.
- Visser, J. W. (1969). *J. Appl. Crystallogr.*, **2**, 89–95.
- Von Dreele, R. B. and Cheetham, A. K. (1974). *Proc. Roy. Soc. A*, **338**, 311–26.
- Von Dreele, R. B., Jorgensen, J. D. and Windsor, C. G. (1982). *J. Appl. Crystallogr.*, **15**, 581–9.
- Weiss, E., Corbelin, S., Cockcroft, J. K. and Fitch, A. N. (1990). *Angew. Chem. Int. Ed. Engl.*, **29**, 650–2.
- Werner, P.-E., Eriksson, L. and Westdahl, M. J. (1985). *J. Appl. Crystallogr.*, **18**, 367–70.
- Wiles, D. B. and Young, R. A. (1981). *J. Appl. Crystallogr.*, **14**, 149–51.
- Wright, P. A., Thomas, J. M., Millward, G. R., Ramdas, S. and Barri, S. A. I. (1985). *J. Chem. Soc. Chem. Comm.*, 1117–19.
- Young, R. A., ed. (1993). *The Rietveld method*, Oxford University Press.
- Young, R. A., Mackie, P. E. and Von Dreele, R. B. (1977). *J. Appl. Crystallogr.*, **10**, 262–9.
- Zachariasen, W. H. (1948a). *Acta Crystallogr.*, **1**, 265–8.
- Zachariasen, W. H. (1948b). *Acta Crystallogr.*, **1**, 277–87.
- Zachariasen, W. H. and Ellinger, F. H. (1963). *Acta Crystallogr.*, **16**, 369–75.

Laboratory X-ray powder diffraction

Daniel Louër

3.1 Introduction

The majority of moderately complex crystal structures determined using powder diffraction data have been obtained from conventional laboratory-based X-ray diffractometers. Indeed, it was laboratory-based instrumentation that provided the impetus in the early stages of the modern development of the powder method. Although synchrotron radiation offers higher resolution and higher count-rates, modern in-house X-ray powder diffractometers with optimized optics offer sufficient resolution, precision and count rate to permit successful structure solution. Adequate resolution and peak precision are crucial in the three principal stages involved in crystal structure determination from powder data: (a) the determination of lattice constants and use of systematic absences to give space group information, (b) the extraction of structure factor magnitudes for solving the phase problem and elaborating a structure model, and (c) the refinement of structural parameters such as atomic coordinates to give the best fit to the observed data.

This chapter describes the performance and limitations of laboratory-based X-ray diffraction instrumentation for solving crystal structures *ab initio* from powder data. Examples are presented to illustrate the methods and to indicate the precision of the results obtained. The impact of conventional X-ray powder diffraction structure solution is discussed and compared with single-crystal analysis.

3.2 The reflection overlap problem

The essential difference between single-crystal and powder diffraction is the loss of information that results from the rotational projection of the three-dimensional grid of reciprocal lattice points on to the one dimension of a powder diffraction pattern. This feature is often aggravated by line broadening arising from structural imperfections. The degree of reflection overlap becomes increasingly severe with increasing angle, because the number of diffraction points varies as d^{*3} ($d^* = 2 \sin \theta / \lambda$). This theoretical number (N) is given by the number of possible lattice points for which d^* is less than d_N^* and is

approximately equal to the volume of a sphere with radius d_N^* divided by the volume V^* of the reciprocal unit cell, weighted by the number of symmetry-equivalent reflections m (e.g. $m = 2$ for triclinic symmetry):

$$N \approx \frac{4\pi(d_N^*)^3}{3mV^*}. \quad (3.1)$$

Extracting integrated intensities is thus a pattern decomposition process (see also Chapter 8). The intensity of each reflection in reciprocal space has a three-dimensional shape, which is projected onto the single 2θ dimension of a powder diffraction pattern to yield a peak profile with the contribution $H_{hkl}(2\theta_i)$ at point $2\theta_i$. Thus, the discrete intensity y measured at point $2\theta_i$ is given by summing the contributions of all Bragg reflections to this point

$$y(2\theta_i) = \sum_{hkl} H_{hkl}(2\theta_i). \quad (3.2)$$

Recovering the individual components, $H_{hkl}(2\theta)$, is a systematic procedure involving the decomposition of a powder pattern into its individual reflection profiles, without any reference to a structural model. This approach is used in the course of the structure analysis at two stages: (a) to extract peak positions for pattern indexing, and (b) to obtain integrated intensities for structure-model determination.

Obviously, the degree of peak overlap can be substantially exacerbated by line broadening. This takes the form of a convolution of the instrumental profile function $g(2\theta)$, including the wavelength-dispersion contribution, with a sample profile function $f_{hkl}(2\theta)$ that contains information on the microstructure of the sample. The breadth and shape of the individual components observed in the pattern are then influenced by the combination of instrumental broadening and the microstructure of the sample:

$$H_{hkl}(2\theta) = f_{hkl}(2\theta) * g(2\theta). \quad (3.3)$$

The use of the pattern decomposition technique in the preliminary stages of the structural study may give an indication of the hkl -dependence of line breadths and shapes, which ideally should also be incorporated into the refinement step.

3.2.1 Instrumental broadening— $g(2\theta)$

Instrumental resolution is a major factor in structure determination from powder data. Good resolution can help to minimize the reflection overlap problem as long as sample broadening is not significant. Instrumental line profiles arise from the distribution of wavelengths in the incident beam, convoluted with several functions resulting from the geometry of the instrument, such as beam divergence, the finite width of source and receiving slit, specimen transparency and residual misalignment. Both the breadth and shape of

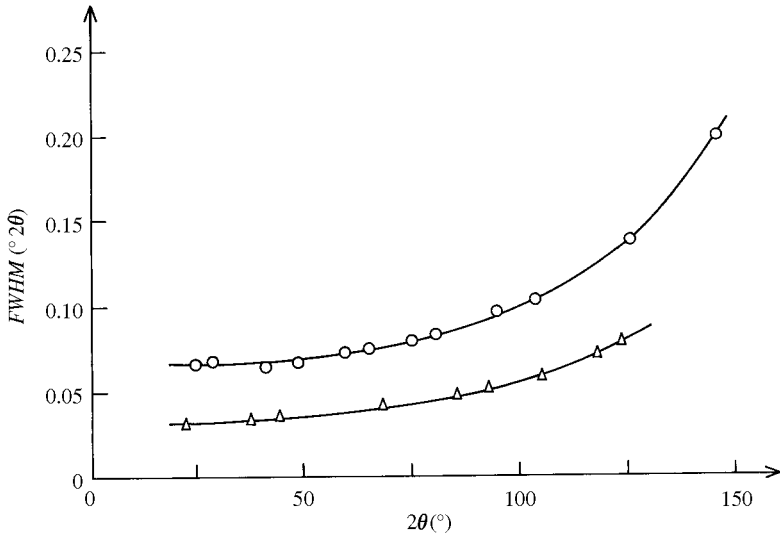


Fig. 3.1. *FWHM* versus 2θ for annealed BaF_2 standard specimen. (○) Conventional diffractometer with an incident-beam monochromator tuned to $\text{Cu K}\alpha_1$ radiation (from Louër and Langford 1988), (△) High resolution powder diffractometer on station 9.1 at the Daresbury Laboratory SRS, $\lambda = 1.4188 \text{ \AA}$ (from Langford, Cernik and Louër 1991).

instrumental line profiles vary continuously with 2θ for conventional angle-dispersive X-ray diffractometers. An example of the angular variation of full-width at half-maximum (*FWHM*) for the commonly used Bragg–Brentano geometry is shown in Fig. 3.1.

This instrumental resolution function (IRF) (*FWHM* versus 2θ) has been obtained with monochromatic radiation ($\text{Cu K}\alpha_1$) from a sample of annealed BaF_2 (Louër and Langford 1988) and shows a minimum of $0.062^\circ 2\theta$ at intermediate angles, increasing to twice this value at $130^\circ 2\theta$ as a consequence of spectral dispersion. For comparison, the IRF obtained from the same standard material on the high-resolution powder diffractometer on station 9.1 at the Daresbury Synchrotron Radiation Source (SRS) is given in Fig. 3.1.

In Rietveld structure refinement programs, the angular dependence of *FWHM* is commonly modelled using a quadratic form in $\tan\theta$. There are, however, further subtleties in the angular dependence of the various components of the instrumental profile, which can be revealed with the analytical functions used to model the observed diffraction line profiles (see Table 1.2 in Young (1995) for an overview of profile functions). Modern fundamental parameters approaches offer a more rigorous peak-shape formulation (Cheary and Coelho 1998). Whatever method is used, however, it must be stressed that an accurate peak description is highly desirable if structure solution is to be

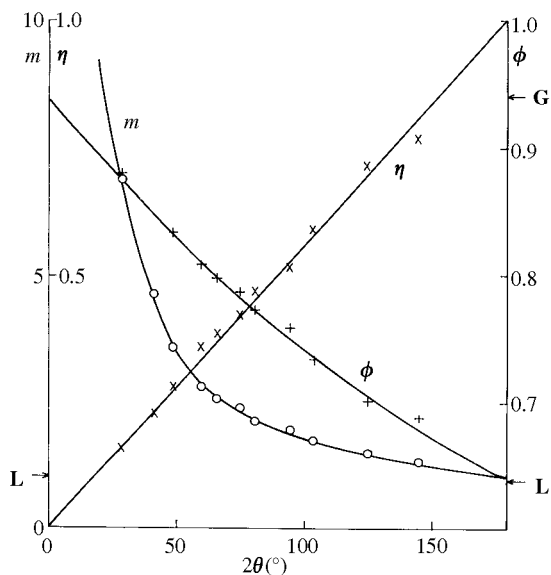


Fig. 3.2. Variation of line-profile shape parameters with 2θ for the Bragg–Brentano geometry with monochromatic X-rays (see Fig. 3.3). m : Pearson VII index; η : pseudo-Voigt mixing parameter; ϕ : Voigt parameter ($=FWHM/\beta$, where β is the integral breadth), L: Lorentzian, G: Gaussian (from Louër and Langford 1988).

attempted. In Fig. 3.2, the variation of peak-shape parameters for Bragg–Brentano optics with monochromatic X-rays reflects the Gaussian character of $g(2\theta)$ profiles at low angles, where geometric aberrations are dominant, and the almost Lorentzian contribution arising from the wavelength distribution at high angles. Similar curves can be obtained for other sources of radiation and geometries (e.g. Langford *et al.* 1991).

3.2.2 Sample broadening— $f_{hkl}(2\theta)$

Sample microstructure often contributes to diffraction line broadening. In fact, samples with no physical line broadening are likely to contain crystals large enough to perform single-crystal microdiffraction. The contribution resulting from ‘size’ broadening is independent of the order of reflection, while ‘strain’ broadening is order-dependent. This means that broadening effects will become increasingly severe at high angles and that the limit in $\sin \theta/\lambda$, from which there is no reliable diffraction information, is directly influenced by the microstructural properties of the sample.

‘Size’ effects arise from the finite size of domains over which diffraction is coherent, measured in the direction of the scattering vector. This can be the mean thickness of individual crystallites, but it can also be related to a subdomain

structure such as the distance between stacking faults in layer structures or the distance between dislocations. The breadth of ‘size’ profiles is inversely proportional to the mean apparent size in the direction of the scattering vector. The true crystallite size can only be calculated if the crystallite shape is known. The form of ‘size’ profiles depends on the crystallite size distribution, and for unimodal distributions, the shape is generally not Lorentzian (Langford *et al.* 2000).

‘Strain’ broadening represents a variation of d -spacing between planes perpendicular to the direction of the scattering vector and is related to lattice distortions arising from internal stress distributions, dislocations (see, e.g. Ungár and Borbély 1996) or deviation from ideal stoichiometry.

Severe diffraction line broadening reduces the number of reliable integrated intensities extracted from pattern decomposition, which can generally affect the efficiency of the Direct methods for structure determination. The extraction of integrated intensities being implicitly avoided with direct space approaches, such methods may be less sensitive to line broadening (see, e.g. Bataille *et al.* 2004).

3.2.3 $H(x)$ profiles

A variety of line shapes can be generated from the microstructure of the sample. The observed profiles usually range from the Gaussian to the Lorentzian limits, but high and ultra-high-resolution data have revealed profiles for which the intensity in the tails decreases more slowly than a Lorentzian (e.g. Hastings *et al.* 1984; Plévert and Louër 1990). Such super-Lorentzian shapes must be correctly modelled for intensity extraction or Rietveld refinement either through a fundamental parameters approach or through the use of empirical functions such as the Pearson VII with $m < 1$ or the pseudo-Voigt with $\eta > 1$. Moreover, to reduce the loss of integrated intensity arising from truncation effects, the observed intensity distribution, normally defined as $\pm k \times FWHM$ relative to the Bragg peak position, must be adapted to the line shape to incorporate most of the line profile, for example, $k = 63$ to include 99 per cent of a Lorentzian function, or $k = 3$ for a Gaussian function (Toraya 1985). Residual truncation is undesirable but often inevitable in the case of Lorentzian and super-Lorentzian line shapes.

The precision of a structure determination will depend on how well the complete powder diffraction pattern has been modelled. The physical parameters that describe the origin of sample-dependent line broadening should ideally be considered as far as possible in pattern modelling. This is not an easy task for anisotropic ‘size’ and ‘strain’ broadening (Delhez *et al.* 1995), particularly for low-crystal symmetry, but some progress in this direction has been made recently (Popa 1998; Stephens 1999).

3.3 Instrumentation and experimental considerations

High resolution, good counting statistics and precise modelling of peak positions and peak shapes are essential for structure solution. The additional information that they provide compensates to some extent for the loss of information resulting from line broadening. The relative merits of different X-ray optics used for collecting powder data have been discussed in some reviews (e.g. Werner 1992; Baerlocher and McCusker 1994; Langford and Louër 1996). Some of these instrumentation aspects are discussed in this section with particular reference to their impact in structure solution.

3.3.1 *Diffraction geometries*

Guinier focusing cameras were regularly used for obtaining structures in the early period of *ab initio* structure determination from powder data. This was because of their high resolution, the accuracy of measured diffraction angles and the use of monochromatic radiation (e.g. Werner 1986). A representative example of this early success is the complex structure determination of the organomolybdate $(\text{NH}_4)_4[(\text{MoO}_2)_4\text{O}_3](\text{C}_4\text{H}_3\text{O}_5)_2 \cdot \text{H}_2\text{O}$ (Berg and Werner 1977). Powder diffractometers, however, have now largely replaced film cameras in most laboratories. Both reflection and transmission geometries are available for laboratory diffractometers.

Although reflection geometry using parafocusing Bragg–Brentano optics is more popular, transmission geometry with thin film or capillary samples presents some definitive advantages for structural analysis and requires only a small amount of sample. The technique is well suited to materials containing only light atoms, but is less appropriate for strongly absorbing materials. Furthermore, preferred orientation effects can be reduced significantly with a capillary set-up. Representative examples of data collected in transmission mode with monochromatic X-rays and a position-sensitive detector are: (a) *p*- $\text{CH}_3\text{C}_6\text{H}_4\text{SO}_2\text{NH}_2$ (Lightfoot *et al.* 1992*a*), $\text{C}_2\text{H}_4\text{N}_2\text{O}_2$ (Lightfoot *et al.* 1992*b*) and lithium triflate LiCF_3SO_3 (Tremayne *et al.* 1992), which were studied using thin flat samples, and (b) piracetam (Louër *et al.* 1995), three stereoisomers of the cyclic tetramer of 3-aminobutanoic acid (Seebach *et al.* 1997), and lithium borate $\text{LiB}_2\text{O}_3(\text{OH}) \cdot \text{H}_2\text{O}$ (Louër *et al.* 1992), which were studied using capillary samples.

On the other hand, reflection geometry is suitable for strongly absorbing materials since there is no absorption correction for a sample with an apparent ‘infinite’ thickness. The instrument configuration most commonly used with conventional divergent-beam X-ray sources is based on the Bragg–Brentano parafocusing geometry shown in Fig. 3.3.

The source (or focal point of an incident beam monochromator i.e. F in Fig. 3.3), sample and receiving slit lie on the ‘focusing circle’, which has a radius dependent on θ . Coherently scattered X-rays from a flat sample then converge

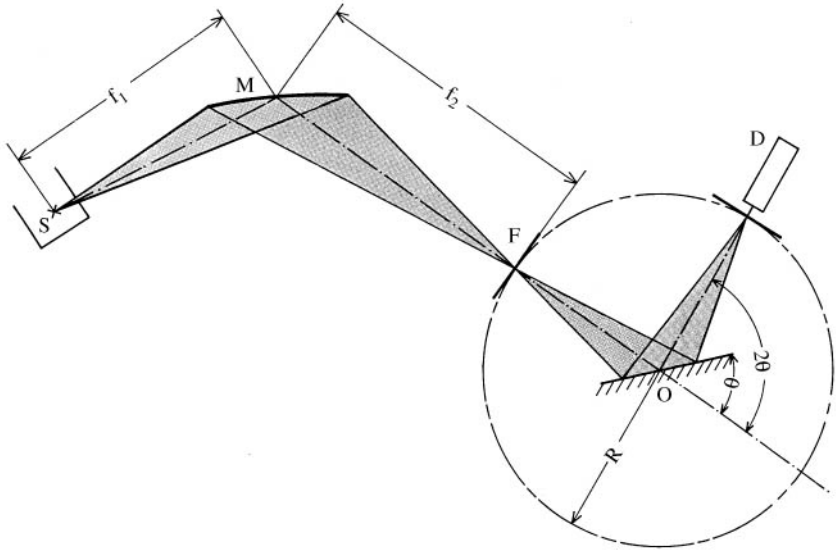


Fig. 3.3. Geometry of Bragg-Brentano diffractometer with incident beam monochromator (M). X-ray tube focus (S), adjustable knife edge to cut off residual $K\alpha_2$ component (F), axis of rotation (O), and detector (D).

on a receiving slit located in front of the detector. The detector rotates about the goniometer axis through twice the angular rotation of the sample ($\theta/2\theta$ scans). Use of this geometry requires that several important points be considered.

During a scan, the angle between the sample surface and the incident beam changes, that is, the illuminated area of the sample changes. As a consequence, the intensities are incorrectly measured at low angles if part of the incident beam overshoots the sample and therefore cannot be diffracted. Hence, it is wise to determine the angle above which the incident beam falls completely on the sample surface and to collect the data below this angle using a narrower divergence slit before the sample. This slit should be selected to ensure that the incident beam does not extend beyond the sample area. The two (or more) ranges then have to be scaled to one another. This procedure can be useful for both intensity extraction and structure refinement.

In addition, the use of a flat sample tends to increase the impact of preferred orientation. To reduce this effect, it is recommended that a side-loading sample holder be used in order to avoid a smoothing action of the front surface of the sample (Swanson *et al.* 1964). Other techniques can also be used to reduce preferred orientation; these include sieving to produce crystallites with sizes in the range 5–10 μm (Parrish and Huang 1983), spray drying (Smith *et al.* 1979) or the admixture of an amorphous material.

There is also increasing interest in applications for parallel X-ray beams in the laboratory using, for example, graded multilayer reflective mirrors or polycapillary optics. It seems likely that they will have an impact upon structure solution at the laboratory level in the near future.

3.3.2 Monochromatic radiation

Although the use of monochromatic radiation is desirable in diffraction experiments operating in the angle-dispersive mode, the most widely used radiation in conventional powder diffractometry is still the $\text{Cu K}\alpha_{1,2}$ doublet. Two diffraction patterns are thus recorded simultaneously, which contributes to a further loss in resolution with increasing angle, particularly at moderate to high angles. The favourable effect of monochromatic radiation can be seen from the slightly broadened diffraction pattern of monoclinic $\text{Nd}(\text{OH})_2\text{NO}_3 \cdot \text{H}_2\text{O}$ (Fig. 3.4), whose structure was solved from data collected with monochromatic radiation (Louër and Louër 1987). However, $\text{Cu K}\alpha_{1,2}$ radiation has been used successfully for structure determination of a number of materials. Representative examples are $\text{Zr}(\text{HPO}_4)_2 \cdot \text{H}_2\text{O}$ (Rudolf and Clearfield 1985) and the complex structure of $\beta\text{-Ba}_3\text{AlF}_6$ (Le Bail 1993).

Better resolution can be obtained by means of a focusing monochromator (Louër and Langford 1988). There is some reduction in the intensity of the $\text{K}\alpha_1$ line, but this can be partially compensated for by using high-power X-ray tubes. Some residual $\text{K}\alpha_2$ component (a few percent of the original component) is often observed at the focal point of the monochromator. This can be eliminated

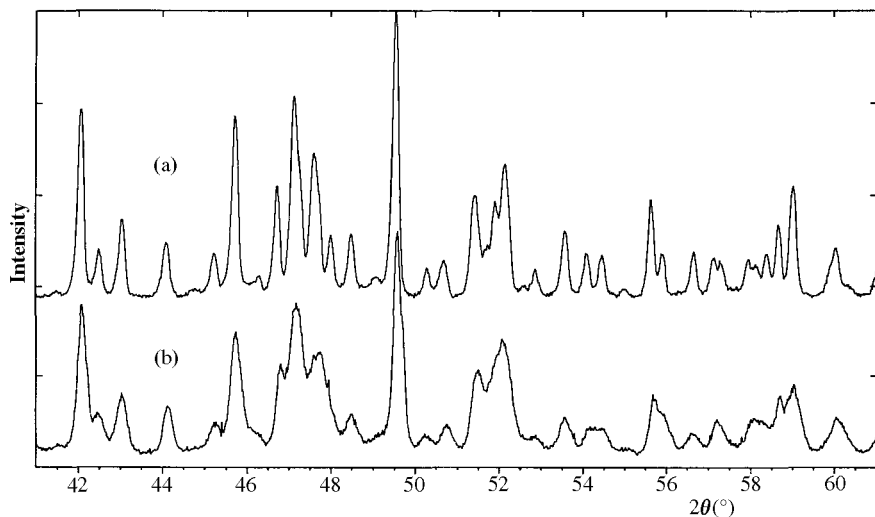


Fig. 3.4. Diffraction pattern of monoclinic $\text{Nd}(\text{OH})_2\text{NO}_3 \cdot \text{H}_2\text{O}$. (a) Germanium incident-beam monochromator, $\text{Cu K}\alpha_1$. (b) Graphite diffracted-beam monochromator, $\text{Cu K}\alpha_{1,2}$.

by incorporating a knife-edge (slit F in Fig. 3.3) that leaves the $K\alpha_1$ component unaffected. Typically, powder data up to $150^\circ 2\theta$ can be collected with good counting statistics within 48 h. An example of powder diffraction data for $U_2O(PO_4)_2$, used for *ab initio* structure solution (Bénard *et al.* 1996), is shown in Fig. 3.5.

Several advantages of using monochromatic radiation have been listed by Louër and Langford (1988). These include (a) the number of contributing reflection positions is halved with respect to the $K\alpha_{1,2}$ radiation, (b) instrumental line profiles can be readily modelled with a single analytical function and a minimum *FWHM* of $\sim 0.06^\circ 2\theta$ can be obtained (Fig. 3.1), (c) the shape of instrumental $g(x)$ profiles varies with angle in a straightforward manner (Fig. 3.2), and (d) the background is low and is essentially constant over a wide angular range.

3.3.3 Data quality

High-quality data are essential for structure solution. Diffractometers must be well-aligned and tested using standard materials. In addition to high instrumental resolution, peak positions must also be precise, for both indexing and Rietveld refinement. The principal errors in peak position are zero-point shift and displacement of the specimen. If they are not eliminated at source or properly modelled, experimental imperfections are introduced in the Rietveld refinement.

The quality of the diffractometer alignment can be evaluated from standard reference materials. For example, synthetic fluorophlogopite mica (SRM 675 from NIST, basal spacing $d_{001} = 9.98104 \pm 0.00007 \text{ \AA}$), is suitable for diffraction in reflection geometry. With a thin sample and a high degree of preferred orientation of the crystallites, ten $00l$ reflections are observed in the angular range $8\text{--}135^\circ 2\theta$ for $Cu K\alpha_1$ radiation. Differences between observed and calculated peak positions of less than $\sim 0.005^\circ 2\theta$ can be reasonably obtained with a conventional, well-aligned powder diffractometer (Louër 1992). This precision is excellent for routine indexing of most powder diffraction patterns for materials with moderate unit-cell volumes ($< \sim 3000 \text{ \AA}^3$).

Although precision in peak position and good diffractometer alignment are essential, counting statistics should not be neglected (a relative standard deviation of 1 per cent is obtained for a counting rate of 10 000). Good counting statistics contribute to stable pattern decomposition and Rietveld refinement. High-quality data can reveal subtle structural details such as the influence of hydrogen atoms on the precision of bond lengths within an oxalate group in the structure of $YK(C_2O_4)_2 \cdot 4H_2O$, which was solved *ab initio* from powder diffraction data (Bataille *et al.* 1999).

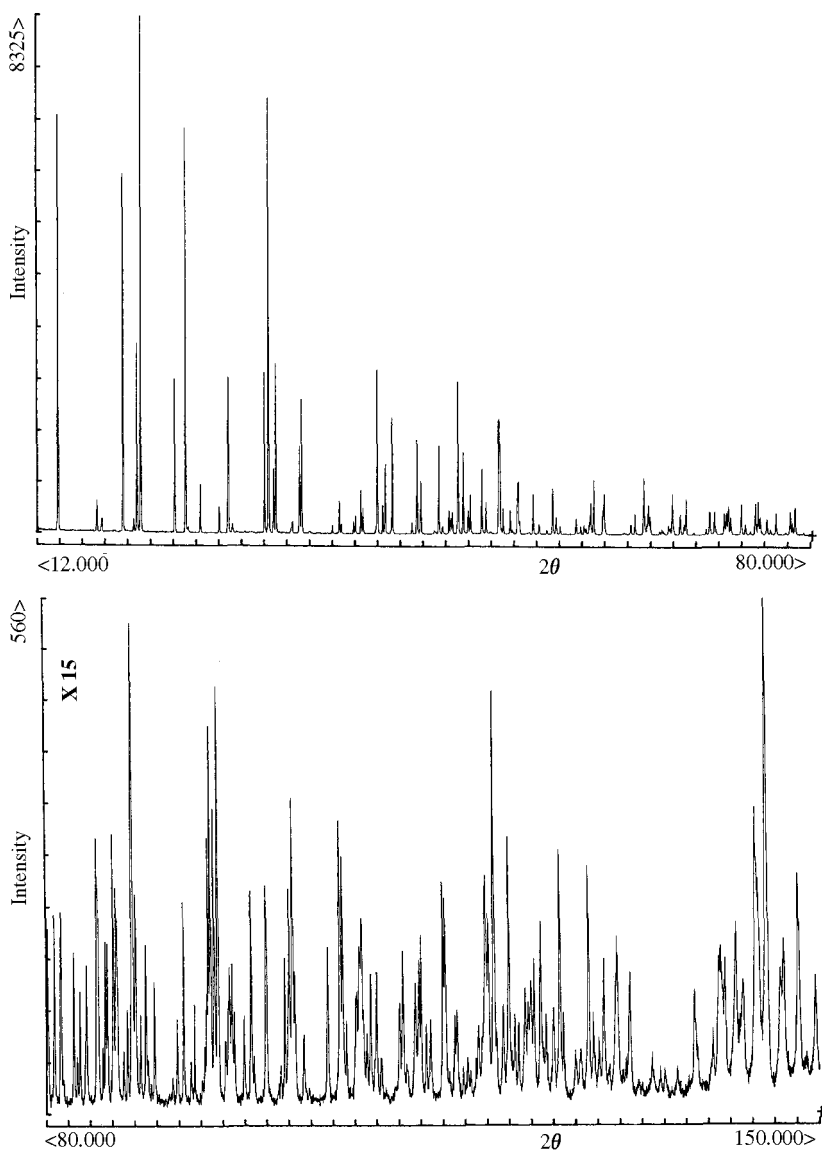


Fig. 3.5. Powder diffraction pattern of diuranium oxide phosphate, $U_2O(PO_4)_2$, collected with a high-resolution Bragg–Brentano diffractometer (see Fig. 3.3) with an incident-beam monochromator tuned to $Cu K\alpha_1$ radiation.

3.3.3.1 *Unit-cell determination*

Instrumental resolution, particularly at low angles, and the accuracy of observed peak positions are the two crucial prerequisites for powder pattern indexing. This can be understood from the definition of the figures of merit M_{20} and F_{20} (eqns (7.7) and (7.8) respectively in Chapter 7) used to assess the reliability of an indexing solution. With higher resolution, more peaks can be detected, particularly for low crystal symmetry. Lower discrepancies between observed and calculated Q ($=1/d^2$) and 2θ values will result if the diffractometer is correctly aligned and care has been taken in determining peak positions. With the performance of in-house powder diffractometers using monochromatic radiation, the quality of data is good enough to index most powder diffraction patterns (see Louër 1992).

Examples of successful indexing of patterns of materials with large unit-cell volumes include monoclinic $\text{BaTiO}(\text{C}_2\text{O}_4)_2 \cdot 4.5\text{H}_2\text{O}$ ($V = 2597 \text{ \AA}^3$) (Louër *et al.* 1990), monoclinic sotalol ($V = 3131 \text{ \AA}^3$) (Shankland and Sivia 1996) and cubic $[(\text{CH}_3)_4\text{N}]_4\text{Ge}_4\text{S}_{10}$ ($V = 7471 \text{ \AA}^3$) (Pivan *et al.* 1994). In general, the higher angular precision and accuracy of powder diffractometers at synchrotron sources give an additional improvement in the quality of the unit cell parameters derived from the indexing procedures. Two examples of pattern indexing based on both monochromatic ($\text{Cu K}\alpha_1$ radiation) Bragg–Brentano data and data collected on the two-circle diffractometer on station 2.3 at the SRS ($\lambda = 1.4039 \text{ \AA}$) are reported in Table 3.1 (Cernik and Louër 1993).

Higher figures of merit and lower average angular discrepancies ($\langle \Delta 2\theta \rangle$) are observed with the synchrotron data. However, the values obtained with conventional high-resolution diffractometers remain excellent, that is, $\langle \Delta 2\theta \rangle = 0.0059^\circ$ and 0.0038° 2θ for laboratory data versus 0.0012° and 0.0016° 2θ for the synchrotron data. The powder data collected with conventional monochromatic X-rays were in fact used to solve the crystal structure *ab initio* once the correct space group had been assigned from scrutiny of the diffraction pattern (Bénard *et al.* 1991; Louër *et al.* 1988). For further discussion of space group assignment, see Chapter 8, Section 8.4.

Table 3.1 Indexing comparisons from Bragg–Brentano (B–B) and synchrotron (SRS) X-ray powder diffraction data ($\langle FWHM \rangle$ is the average full width at half-maximum, in $^\circ 2\theta$, for the 20 lines) (from Cernik and Louër 1993)

| | $V(\text{\AA}^3)$ | M_{20} | F_{20} | $\langle FWHM \rangle$ |
|---|-------------------|----------|----------------|------------------------|
| Zr(OH)₂(NO₃)₂ · 4.7H₂O (triclinic) | | | | |
| B–B | 530 | 54 | 112(0.0059,30) | 0.100 |
| SRS | 533 | 295 | 635(0.0012,26) | 0.047 |
| KCaPO₄ · H₂O (monoclinic) | | | | |
| B–B | 460 | 72 | 107(0.0038,49) | 0.077 |
| SRS | 460 | 156 | 259(0.0016,47) | 0.044 |

3.3.3.2 *Data set of structure-factor magnitudes*

Both Patterson and Direct methods of structure solution can be very sensitive to the accuracy and resolution of the extracted structure factors. For example, the Direct methods solution of the crystal structure of cubic thiogermanate $[(\text{CH}_3)_4\text{N}]\text{Ge}_4\text{S}_{10}$ with a unit-cell volume of 7471 \AA^3 [$a = 19.5490(4) \text{ \AA}$, $M_{20} = 60$, $F_{30} = 112(0.0051, 52)$, $\text{SG} = P\bar{4}3n$] (Pivan *et al.* 1994) exhibited sensitivity to the resolution of the data set. Most of the E -maps derived from the extracted structure factors revealed small but unconvincing fragments of the structure. However, one data set collected up to $80^\circ 2\theta$ yielded a partial model. By taking into consideration the tetrahedral configuration of the GeS_4 group, eight of the 26 E -map peaks could be identified as being likely to be correct. The model was completed from subsequent Fourier analysis. This type of sensitivity to high-angle data is not unique to laboratory-based diffraction data—see, for example, Chan *et al.* (1999) for a synchrotron-based example. One useful indicator of the quality of the diffraction data is an estimate of the number of statistically independent reflections present in the pattern. Altomare *et al.* (1995) and David (1999) have proposed such measures, based on a detailed study of reflection overlap.

3.4 Examples of crystal structure solution

Partial compilations of *ab initio* structure determinations from laboratory X-ray powder diffraction data have been reported by several authors (Cheetham 1995; Langford and Louër 1996; Harris and Treymane 1996; Masciocchi and Sironi 1997). They include inorganic, organic and coordination materials. To illustrate the different approaches available for data collection and their treatment, a few representative examples are described here. Where appropriate, the precision of results is also discussed. In all of these examples, powder pattern indexing was carried out with the program DICVOL91 (Boulton and Louër 1991), using high-resolution data collected in Bragg–Brentano mode. Space group assignments were derived using the program NBS*AIDS83 (Mighell *et al.* 1981). Different instrumental setups were used for collecting powder data for structure solution purposes, and different methods were used for solving the structures. All calculations were carried out on a desktop computer using programs listed elsewhere (see, e.g. Louër and Louër 1994).

3.4.1 *Bragg–Brentano powder diffraction data*

The structure of $\text{Zr}(\text{OH})_2\text{SO}_4 \cdot 3\text{H}_2\text{O}$ was solved from powder data collected with monochromatic X-rays ($\text{Cu K}\alpha_1$) and Bragg–Brentano geometry (Gascoigne *et al.* 1994). The pattern was indexed with a monoclinic unit cell ($a = 8.3645(4) \text{ \AA}$, $b = 15.1694(9) \text{ \AA}$, $c = 5.4427(3) \text{ \AA}$, $\beta = 103.145(5)^\circ$, $M_{20} = 120$,

Table 3.2 List of the highest Patterson peaks (arbitrary scale) of $\text{Zr}(\text{OH})_2\text{SO}_4 \cdot 3\text{H}_2\text{O}$ and their interpretation in terms of vectors between Zr atoms and Zr and S atoms

| Peak | <i>u</i> | <i>v</i> | <i>w</i> | <i>H</i> | Interpretation |
|--------|----------|----------|----------|----------|----------------|
| Origin | 0 | 0 | 0 | 1000 | |
| 1 | 0 | 0.1486 | 0.5 | 232 | Zr–Zr |
| 2 | 0.6644 | 0.5 | 0.3592 | 202 | Zr–Zr |
| 3 | 0.3464 | 0.3538 | 0.149 | 104 | Zr–Zr |
| 4 | 0.0811 | 0.1388 | 0.518 | 78 | Zr–S |

$F_{30} = 170(0.0037, 48)$, $Z = 4$, $\text{SG} = P2_1/c$). Using the Le Bail pattern-decomposition technique (Le Bail *et al.* 1988; see Chapter 8), 579 integrated intensities were extracted in the angular range $10\text{--}84^\circ 2\theta$. The Zr and S atoms were located by Patterson methods and the structure completed by Fourier recycling.

A list of the five highest Patterson peaks and their interpretation in terms of vectors between Zr atoms and between Zr and S atoms is given in Table 3.2. The presence of a Harker line at $0, \frac{1}{2} - 2y, \frac{1}{2}$ (peak 1) and of a Harker section of type $2x, \frac{1}{2}, \frac{1}{2} + 2z$ (peak 2) gives direct information about atomic coordinates. Peak 3, with half-multiplicity, corresponds to the components $-2x, 2y, -2z$, and peak 4 is a vector between Zr and S. The final coordinates in the refined structure are $x = 0.8321$, $y = 0.1757$, $z = 0.4241$ for Zr and $x = 0.7566$, $y = 0.0360$ and $z = 0.9030$ for S.

The electron density map, computed with the signs derived from the contribution of the Zr and S atoms only, allowed all other non-hydrogen atoms to be located. The refinement of the complete structure model, using data in the range $15\text{--}135^\circ 2\theta$, converged to give an $R_F = 0.03$. The final Rietveld plot is shown in Fig. 3.6. The maximum deviation of the S–O distances from the mean value 1.477 \AA was $\pm 0.014 \text{ \AA}$ and the O–S–O angle varied in the range $107.3\text{--}111.4^\circ$, values close to the distances and tetrahedral angles normally observed in a sulphate group. In this example, the ratio of atomic numbers of Zr and O is small and this explains why the atomic coordinates of the atoms are determined with roughly equal accuracy.

In contrast, in the case of $\text{U}(\text{UO}_2)(\text{PO}_4)_2$ (Bénard *et al.* 1994), the X-ray powder data were dominated by the scattering contribution of the metal atoms (the ratio of the atomic numbers of U and O is greater than 11). The quality of the diffraction pattern was, however, satisfactory and the structure could still be solved. At the end of the final Rietveld refinement ($R_F = 0.04$, $R_{wp} = 0.14$), a significant distortion of the phosphate group was observed, with P–O distances ranging from 1.46 to 1.62 \AA . By using neutron diffraction data, where the neutron scattering lengths for U and O are in the more favourable ratio of ~ 1.45 , Rietveld refinement yielded P–O distances in the range $1.510\text{--}1.565 \text{ \AA}$, which are in good agreement with the distances usually found in structures solved from single-crystal data.

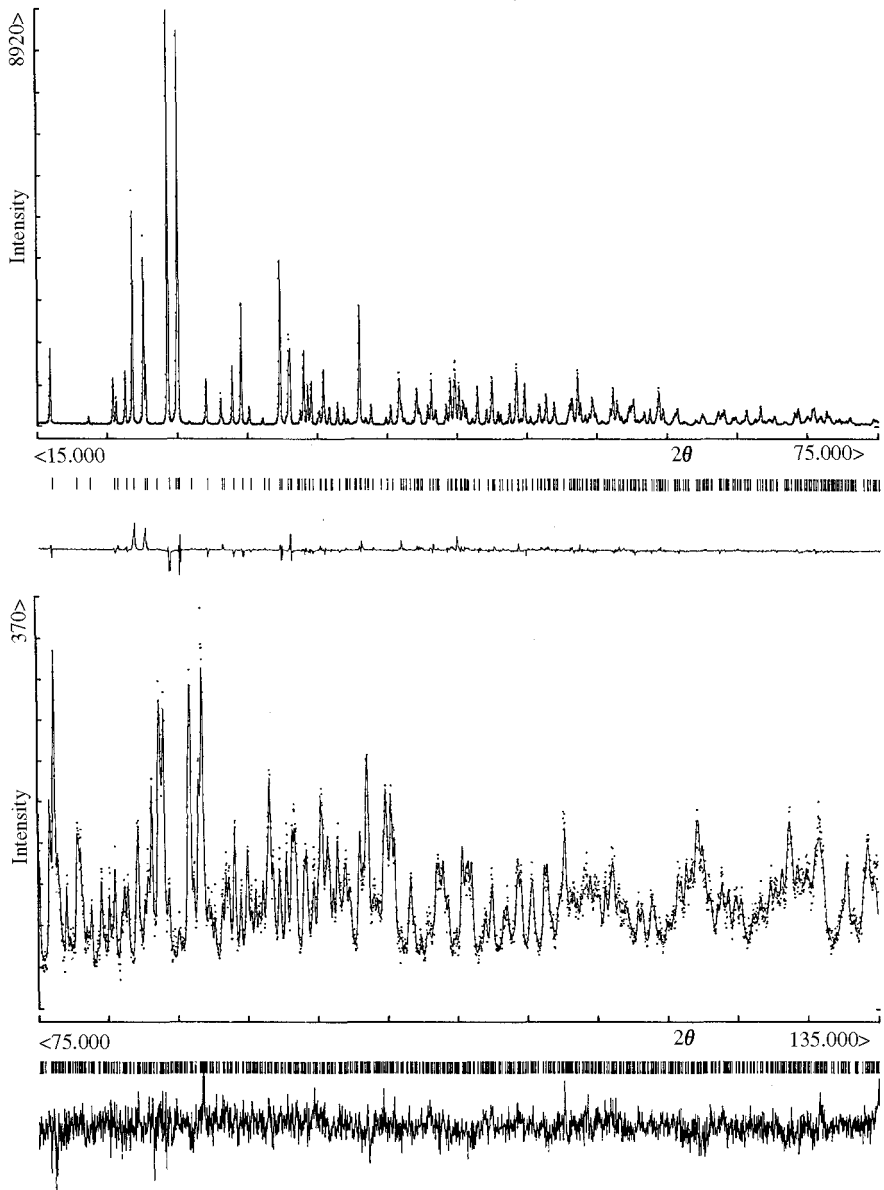


Fig. 3.6. The final Rietveld plot of $\text{Zr(OH)}_2\text{SO}_4 \cdot 3\text{H}_2\text{O}$, $\text{Cu K}\alpha_1$ radiation ($R_F=0.03$, $R_{wp}=0.11$) (from Gascoigne *et al.* 1994).

3.4.2 Debye–Scherrer powder diffraction data

Transmission geometry is suitable for weakly absorbing specimens (typically materials containing only light atoms) and Debye–Scherrer geometry with focusing optics was used for both examples in this section. Monochromatic radiation ($\text{Cu K}\alpha_1$) was selected with an incident-beam curved-quartz monochromator with asymmetric focusing (short focal distance 130 mm, long focal distance 510 mm). A 0.5 mm diameter glass capillary was mounted at the centre of the goniometer and data were collected using a cylindrical position-sensitive detector (INEL CPS120), which allows a simultaneous recording of a powder pattern over a 120° 2θ range. This wide-angle detector consists of 4096 channels with an angular step of $\sim 0.03^\circ$ and requires careful angular calibration. To minimize angular errors, a self-calibration by the materials themselves was carried out after collecting reference data sets from thin deposits of the materials on silicon plates using a high-resolution Bragg–Brentano diffractometer.

3.4.2.1 Lithium diborate hydrate

The diffraction pattern of lithium diborate hydrate, $\text{LiB}_2\text{O}_3(\text{OH})\cdot\text{H}_2\text{O}$, was indexed with an orthorhombic unit cell ($a = 9.798(1)\text{ \AA}$, $b = 8.2759(7)\text{ \AA}$, $c = 9.6138(8)\text{ \AA}$, $M_{20} = 56$, $F_{30} = 109(0.0081, 34)$, $\text{SG} = Pnna$). Structure-factor moduli were extracted for $\sin\theta/\lambda < 0.48\text{ \AA}^{-1}$ using the Le Bail pattern-decomposition procedure and the structure was solved using Direct methods. Although the solution was originally obtained with the program MULTAN, the powder data have since been reanalysed with SIRPOW92 (Altomare *et al.* 1994). The number of ‘independent observations’ (Altomare *et al.* 1995) in the dataset was calculated to be 173, about 47 per cent of the total number of reflections present.

All non-hydrogen atoms were found in the top E -map, with (a) peaks corresponding to O atoms exhibiting a relative intensity in the range 99–100, (b) peaks corresponding to B atoms exhibiting a relative intensity in the range 56–53 and (c) the Li atom exhibiting a relative intensity of 27. The corresponding R factor obtained from SIRPOW was 0.07. A projection of the structural model found by the Direct methods is compared to the final refined structural model in Fig. 3.7. Large fragments of the structure are clearly recognizable in Fig. 3.7(a). For example, tetrahedra 9 and 4 correspond to the boron atoms B(3) and B(1) (Fig. 3.7(b)) and peak 7 corresponds to the triangle centred on B(2). The final Rietveld refinement converged to the structure-model indicator $R_F = 0.05$.

More recently, the crystal structure of $\text{LiB}_2\text{O}_3(\text{OH})\cdot\text{H}_2\text{O}$ has been solved again from single-crystal data collected up to $\sin\theta/\lambda = 0.807\text{ \AA}^{-1}$ (Louër *et al.* 1997), which is considerably higher than the limit of the powder data (0.48 \AA^{-1}). The results were essentially the same at each of the three stages of the structural analysis. However, due to the higher resolution of the single-crystal data set, a higher precision on the atomic coordinates was obtained and, on

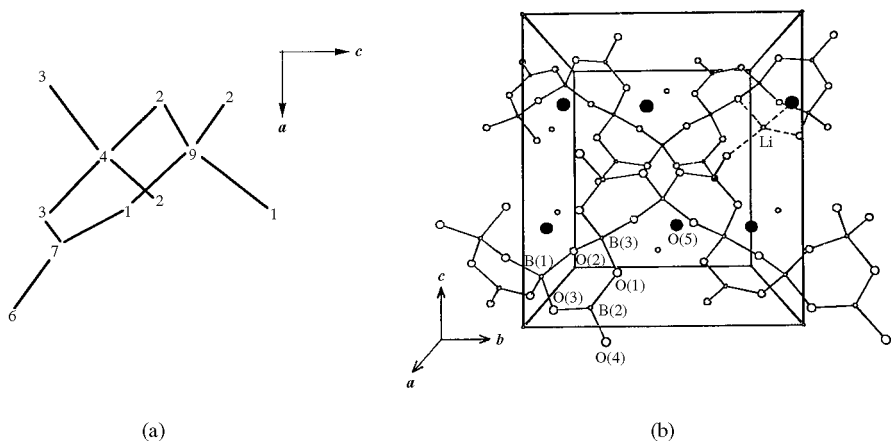


Fig. 3.7. (a) Representation and interpretation of the *E*-map computed with the best sign set obtained by application of the direct methods. (b) Final structure model of $\text{LiB}_2\text{O}_3(\text{OH}) \cdot \text{H}_2\text{O}$.

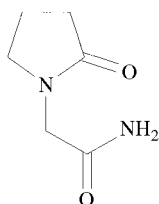


Fig. 3.8. The molecular structure of piracetam.

average, the results agreed within 1 combined standard uncertainty (s.u.) for *x* and *z* and 2 combined s.u. values for *y*.

3.4.2.2 Piracetam

The organic compound (2-Oxo-1-pyrrolidinyl)acetamide (piracetam, Fig. 3.8) is a drug substance with potential applications in a number of therapeutic areas (Goulliaev and Senning 1994).

Three polymorphs are known. The structures of the triclinic ($P\bar{1}$) and monoclinic ($P2_1/n$) phases have been determined from single-crystal data, showing that the conformation of the piracetam molecule is nearly identical in both phases. The third phase (form I) is formed as a result of a phase transformation of one of the stable phases upon heating at 135°C. At room temperature, this third phase is stable for only about 2 h. Powder diffraction data could, however, be collected using Debye–Scherrer geometry combined with a curved position-sensitive detector. For organic materials such as piracetam,

diffraction peaks usually fade quickly with increasing angle, vanishing at moderate angles ($\sim 60^\circ$ 2θ with $\text{CuK}\alpha_1$ radiation). Thus, whilst pattern indexing and space group assignment were successful ($a = 6.747(2)\text{ \AA}$, $b = 13.418(3)\text{ \AA}$, $c = 8.090(2)\text{ \AA}$, $M_{20} = 25$, $F_{30} = 49(0.0145, 42)$, $\text{SG} = P2_1/n$), the application of Direct methods failed to solve the structure of the metastable polymorph.

An alternative approach for the crystal structure solution of such organic phases is to use real-space methods in which structure models are postulated and either (a) optimized with respect to the powder diffraction data or (b) optimized with respect to another function and then verified against the powder diffraction data. These real-space approaches are discussed further in Chapters 15 and 16. For the metastable polymorph of piracetam, the atom-atom potential method, introduced by Kitaigorodsky (1973), was used (Louër *et al.* 1995). The method assumes that the molecular conformation is known and involves searching for the most favourable crystal packing constrained by the known unit-cell dimensions and space group symmetry. The six-parameter space of molecular rigid-body translations and rotations is explored globally in order to find the lowest minima of crystal-lattice potential energy. The unique region of this space (Hirshfeld 1968), an analogue to the asymmetric unit cell, is used to span the grid of starting points for energy minimization. The energy is calculated using empirical atom-atom potential functions fitted to predict the known crystal structures of the given chemical class (Pertsin and Kitaigorodsky 1986). While the systematic search normally requires extensive computer work, further restrictions imposed on the searchable space, and even its dimensionality, are frequently possible due to chemical intuition. For example, considerable computational effort is saved in the case of molecular organic compounds by incorporating the knowledge that only some hydrogen-bonded motifs are probable. Computational details and examples have been reported in several articles (e.g. Williams 1991; Dzyabchenko *et al.* 1996). The method was first applied to the two known piracetam polymorphs, showing that the optimized and observed structures were in fair agreement with one another (Dzyabchenko and Agafonov 1995). This information was then used to predict the structure of the metastable phase. As a result of packing calculations, two distinct energy minima (-100.78 and $-87.29\text{ kJ mol}^{-1}$) were found, suggesting the existence of two additional polymorphs of piracetam. However, only the higher energy structure matched the experimental powder data, the structure rapidly converging to an $R_B = 0.04$ in a Rietveld refinement (Louër *et al.* 1995). (Recently, Fabbiani *et al.* (2005) succeeded in obtaining single-crystal X-ray diffraction data at 150 K from a single crystal of form I. From their structure determination, the authors concluded that '*our crystal structure of form I is in very good agreement with the structure obtained from the previous powder diffraction study.*') This approach was also applied in a recent study, in which crystal-packing calculations and laboratory X-ray powder data were combined to elucidate the structure of a modification of 4-amidinoindanone

guanylhydrazone (Karfunkel *et al.* 1996). Alternative direct-space methods, employing search methods such as simulated annealing, are now popular in the study of organic materials. Sophisticated software is available and it has been proved that high-quality laboratory (capillary) powder X-ray diffraction data are sufficient for successful structure solution of flexible molecules (e.g. Andreev and Bruce 1998; Engel *et al.* 1999; Giovannini *et al.* 2001).

3.5 Conclusions

Laboratory-based X-ray powder diffractometers are sufficient for structure solution of moderately complex crystal structures. Even if higher resolution proves to be essential, in-house diffractometers still offer an inexpensive preliminary stage in the study of more complex structures. For example, better use of valuable synchrotron beamtime is assured if the material under study can be indexed and the space group determined using a laboratory source. Tuneable synchrotron radiation, coupled with ultra-high instrumental resolution, clearly dominates the frontiers of structure solution. However, the sheer number of in-house diffractometers relative to synchrotron-based powder diffractometers means the impact of *ab initio* structure determination from conventional X-ray sources will continue to be considerable.

Acknowledgements

The author is grateful to Prof. A. V. Dzyabchenko and Prof. V. Agafonov for the informative discussions on the atom–atom potential method and Prof. M. Louër for critically reading the manuscript.

References

- Altomare, A., Cascarano, G., Giacovazzo, C., Guagliardi, A., Burla, M. C., Polidori, G. and Camalli, M. (1994). *J. Appl. Crystallogr.*, **27**, 435–6.
- Altomare, A., Cascarano, G., Giacovazzo, C., Guagliardi, A., Moliterni, A. G. G., Burla, M. C. and Polidori, G. (1995). *J. Appl. Crystallogr.*, **28**, 738–44.
- Andreev, Y. G. and Bruce, P. G. (1998). *JCS Dalton Trans.*, 4071–80.
- Baerlocher, C. and McCusker, L. B. (1994). *Stud. Surf. Sci. Catal.*, **85**, 391–428.
- Bataille, T., Auffrédic, J.-P. and Louër, D. (1999). *Chem. Mater.*, **11**, 1559–67.
- Bataille, T., Audebrand, N., Boultif, A. and Louër, D. (2004). *Z. Kristallogr.* **219**, 881–91.
- Bénard, P., Louër, M. and Louër, D. (1991). *J. Solid State Chem.*, **94**, 27–35.
- Bénard, P., Louër, D., Dacheux, N., Brandel, V. and Genet, M. (1994). *Chem. Mater.*, **6**, 1049–58.

- Bénard, P., Louër, D., Dacheux, N., Brandel, V. and Genet, M. (1996). *Anales Quim. Int. Ed.*, **92**, 79–87.
- Boultif, A. and Louër, D. (1991). *J. Appl. Crystallogr.*, **24**, 987–93.
- Berg, J. E. and Werner, P.-E. (1977). *Z. Kristallogr.*, **145**, 310–20.
- Cernik, R. J. and Louër, D. (1993). *J. Appl. Crystallogr.*, **26**, 277–80.
- Chan, F. C., Anwar, J., Cernik, R., Barnes, P. and Wilson, R. M. (1999). *J. Appl. Crystallogr.*, **32**, 436–41.
- Cheary, R. W. and Coelho, A. A. (1998). *J. Appl. Crystallogr.*, **31**, 862–8.
- Cheetham, A. K. (1995). In *The Rietveld method* (ed. R. A. Young), pp. 277–92. Oxford University Press.
- David, W. I. F. (1999). *J. Appl. Crystallogr.*, **32**, 654–63.
- Delhez, R., Keijsers, Th. H. de, Langford, J. I., Louër, D., Mittemeijer, E. J. and Sonneveld, E. J. (1995). In *The Rietveld method* (ed. R. A. Young), pp. 132–66. Oxford University Press.
- Dzyabchenko, A. V. and Agafonov, V. (1995). In *Proc. 28th Hawaii Int. Conf. on System Sciences* (ed. L. Hunter and B. D. Shriver), pp. 237–45. IEEE Computer Soc. Press, Los Alamitos, California.
- Dzyabchenko, A. V., Pivina, T. S. and Arnautova, E. A. (1996). *J. Mol. Struct.*, **378**, 67–82.
- Engel, G. E., Wilke, S., König, O., Harris, K. D. M. and Leusen, F. J. J. (1999). *J. Appl. Cryst.*, **32**, 1169–79.
- Fabbiani, P. A., Allan, D. R., Parsons, S. and Pulham, C. R. (2005). *Cryst. Eng. Comm.*, **7**, 179–86.
- Gascoigne, D., Tarling, S. E., Barnes, P., Pygall, C. F., Bénard, P. and Louër, D. (1994). *J. Appl. Crystallogr.*, **27**, 399–405.
- Giovannini, J., Perrin M.-A., Louër, D. and Leveiller, F. (2001). *Mat. Sci. Forum*, **378–81**, 582–7.
- Gouliayev, A. H. and Senning, A. (1994). *Brain Res. Rev.*, **19**, 180–222.
- Harris, K. D. M. and Tremayne, M. (1996). *Chem. Mater.*, **8**, 2554–70.
- Hastings, J. B., Thomlinson, W. and Cox, D. E. (1984). *J. Appl. Crystallogr.*, **17**, 85–95.
- Hirshfeld, F. L. (1968). *Acta Crystallogr. A*, **24**, 301–11.
- Karfunkel, H. R., Wu, Z. J., Burkhard, A., Rihs, G., Sinnreich, D., Buerger, H. M. and Stanek, J. (1996). *Acta Crystallogr. B*, **52**, 555–61.
- Kitaigorodsky, A. I. (1973). *Molecular crystals and molecules*. Academic Press, New York.
- Langford, J. I., Cernik, R. J. and Louër, D. (1991). *J. Appl. Crystallogr.*, **24**, 913–19.
- Langford, J. I. and Louër, D. (1996). *Rep. Prog. Phys.*, **59**, 131–234.
- Langford, J. I., Louër, D. and Scardi, P. (2000). *J. Appl. Crystallogr.*, **33**, 964–74.
- Le Bail, A. (1993). *J. Solid State Chem.*, **103**, 287–91.
- Le Bail, A., Duroy, H. and Fourquet, J. L. (1988). *Mater. Res. Bull.*, **23**, 447–52.
- Lightfoot, P., Glidewell, C. and Bruce, P. G. (1992a). *J. Mater. Chem.*, **2**, 361–36.
- Lightfoot, P., Tremayne, M., Harris, K. D. M. and Bruce, P. G. (1992b). *J. Chem. Soc. Chem. Commun.*, 1012–13.
- Louër, D. (1992). *NIST Spec. Pub.*, **846**, 92–104.
- Louër, D., Boultif, A., Gotor, F. J. and Criado, J. M. (1990). *Powder Diffraction*, **5**, 162–4.
- Louër, D. and Langford, J. I. (1988). *J. Appl. Crystallogr.*, **21**, 430–7.

- Louër, D. and Louër, M. (1987). *J. Solid State Chem.*, **68**, 292–9.
- Louër, D., Louër, M., Dzyabchenko, V. A., Agafonov, V. and Ceolin, R. (1995). *Acta Crystallogr.*, **B51**, 182–7.
- Louër, D., Louër, M. and Touboul, M. (1992). *J. Appl. Crystallogr.*, **25**, 617–23.
- Louër, M. and Louër, D. (1994). *Adv. X-ray Anal.*, **27**, 21–5.
- Louër, M., Louër, D., Bétourné, E. and Touboul, M. (1997). *Adv. X-ray Anal.*, **40**, CD-ROM. Newtown Square, USA: ICDD.
- Louër, M., Plévert, J. and Louër, D. (1988). *Acta Crystallogr. B*, **44**, 463–7.
- Masciocchi, N. and Sironi, A. (1997). *J. Chem. Soc., Dalton Trans.*, 4643–50.
- Mighell, A. D., Hubbard, C. R. and Stalick, J. K. (1981). NBS * AIDS80: a FORTRAN program for crystallographic data evaluation. US Technical Note 1141, National Bureau of Standards, Washington, D.C.
- Parrish, W. and Huang, T. C. (1983). *Adv. X-ray Anal.*, **26**, 35–44.
- Pertsin, A. J. and Kitaigorodsky, A. I. (1986). *The atom–atom potential method in the physics and chemistry of organic molecular solids*, Springer, Berlin.
- Pivan, J. Y., Achak, O., Louër, M. and Louër, D. (1994). *Chem. Mater.*, **6**, 827–30.
- Plévert, J. and Louër, D. (1990). *J. Chim. Phys.*, **87**, 1427–40.
- Popa, N. C. (1998). *J. Appl. Crystallogr.*, **31**, 176–80.
- Rudolf, P. and Clearfield, A. (1985). *Acta Crystallogr. B*, **41**, 418–25.
- Seebach, D., Matthews, J. L., Meden, A., Wessels, T., Baerlocher, C. and McCusker, L. B. (1997). *Helv. Chim. Acta*, **80**, 173–82.
- Shankland, K. and Sivia, D. S. (1996). *Int. J. Pharm.*, **139**, 9–14.
- Smith, S. T., Snyder, R. L. and Brownell, W. E. (1979). *Adv. X-ray Anal.*, **22**, 77–87.
- Stephens, P. W. (1999). *J. Appl. Crystallogr.*, **32**, 281–9.
- Swanson, H. E., Morris, M. C., Evans, E. H. and Ulmer, L. (1964). *Natl. Bur. Stand. (US), Monograph*, **25**, 1–3.
- Toraya, H. (1985). *J. Appl. Crystallogr.*, **18**, 351–8.
- Tremayne, M., Lightfoot, P., Mehta, M. A., Bruce, P. G., Harris, K. D. M. and Shankland, K. (1992). *J. Solid State Chem.*, **100**, 191–6.
- Ungár, T. and Borbély, A. (1996). *Appl. Phys. Lett.*, **69**, 3173–5.
- Werner, P.-E. (1986). *Chem. Scr.*, **26A**, 57–64.
- Werner, P.-E. (1992). *NIST Spec. Pub.*, **846**, 503–9.
- Williams, D. E. (1991). In *Reviews in computational chemistry II* (ed. K. B. Lipkowitz and D. B. Boyd), pp. 219–71. VCH Publishers, New York.
- Young, R. A. (1995). In *The Rietveld method* (ed. R. A. Young), pp. 1–38. Oxford University Press.

Synchrotron radiation powder diffraction

Peter W. Stephens, David E. Cox and Andrew N. Fitch

4.1 Introduction

Synchrotron radiation is the most powerful source of X-rays currently available for powder diffraction experiments. The combination of high intensity, intrinsic collimation and a continuous wavelength spectrum leads to a large number of significant advantages over laboratory sources. The basic properties of synchrotron radiation and their concomitant features for X-ray diffraction are covered in many reviews (see, e.g. Coppens 1992). The spectral intensity (photons/s per solid angle per fractional bandwidth) of several synchrotron sources currently in use for powder diffraction experiments are compared with a typical fixed-target X-ray tube in Fig. 4.1. The advantages of the former are clear. There is an even greater discrepancy between the brightness (intensity divided by source size) of X-ray tubes and synchrotrons, not to mention that between the various synchrotron radiation sources. Furthermore, special insertion devices, known as undulators, which produce far greater spectral brightness in the X-ray regime, are available, especially at so-called third-generation storage rings. While most structure solutions from powder diffraction data are currently performed with samples sufficiently large that intensity, rather than brightness, is the figure of merit for the source, it is likely that improved source characteristics will have a significant impact on powder diffraction in the future.

In principle, one might use such a source to illuminate a sample to obtain a signal several orders of magnitude larger than that produced with a standard laboratory source. However, it is more often applied to increase the resolution (in 2θ) beyond that of a conventional laboratory diffractometer. The flux at the sample position of a sealed-tube diffractometer is typically 2.0×10^9 photons/s compared with 1.0×10^{11} at a typical synchrotron powder diffraction station. The difference between the ratios of source intensity to flux at the sample position is due to differences in the optics.

This chapter is devoted to a discussion of how powder diffraction experiments can take advantage of the properties of a synchrotron source, and to considerations of how the data are best processed, with a particular emphasis on structure solution. The final part of the chapter reviews a number of 'typical' structure solutions utilizing synchrotron powder datasets.

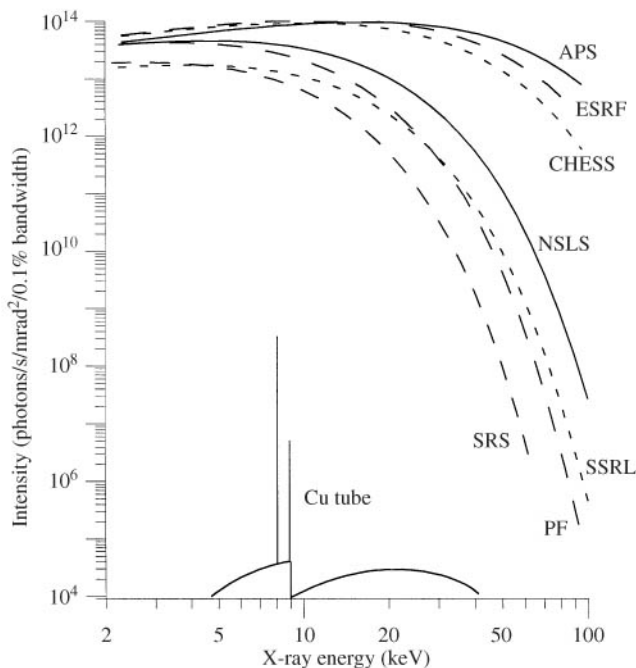


Fig. 4.1. Spectral intensity versus energy for several synchrotron sources, compared with that of a Cu X-ray diffraction tube. Computations courtesy of Steve Hulbert (storage rings) and John Gilfrich and Charles Dozier (X-ray tube) according to the techniques described in Hulbert and Weber (1992), Brown and Gilfrich (1971), and Brown *et al.* (1975).

The higher resolution leads (sample permitting) to sharper, better-resolved peaks. Peak positions can thus be determined more accurately. This is particularly favourable for indexing powder patterns and assigning the correct space group in the initial stages of structure solution. In profile fitting and analysis, precise knowledge and consequent control of lineshape is important for Rietveld refinement, but essential for *ab initio* structure solution. The entire philosophy of Rietveld analysis is to minimize the impact of overlapping reflections; unresolved peaks may reduce the amount of information to some degree, but do not generally compromise the ability of the technique to reach a satisfactory state of convergence. However, because many of the techniques of structure solution, for example, Patterson maps and Direct methods, are based on knowing the intensity of each individual reflection, they are much more sensitive to the loss of this information. Similarly, if there are systematic differences between the experimental data and the theoretical lineshape used in a refinement, these will degrade the profile *R*-factor achievable in a Rietveld refinement without necessarily introducing significant bias in the result. When intensities

are extracted for structure solution, however, the same systematic peak-shape differences are likely to produce incorrect extracted intensities and introduce additional unwanted correlations between the intensities of nearby peaks.

4.2 Synchrotron powder diffraction instruments in use for *ab initio* structure determination

The most widely-used configurations for synchrotron powder diffractometers that are best suited for *ab initio* structure solution are shown in Fig. 4.2. A feature common to all of these instruments is that they use a crystal monochromator, typically Si or Ge, to select a given wavelength from the synchrotron beam. Another feature that is frequently encountered is a means of focusing the X-ray beam on the sample, such as a mirror or bent-crystal optics. While no environmental chambers are illustrated, such instruments can usually accommodate sample cryostats, ovens, and pressure cells. The intensity of the X-ray beam from a storage ring decays with time, so the beam incident on the sample must be monitored and the diffracted signal normalized accordingly.

The simplest configuration for a synchrotron radiation X-ray powder diffractometer uses a single receiving slit as the resolution-determining element, and is illustrated in Fig. 4.2(a). This is the configuration, for example, of

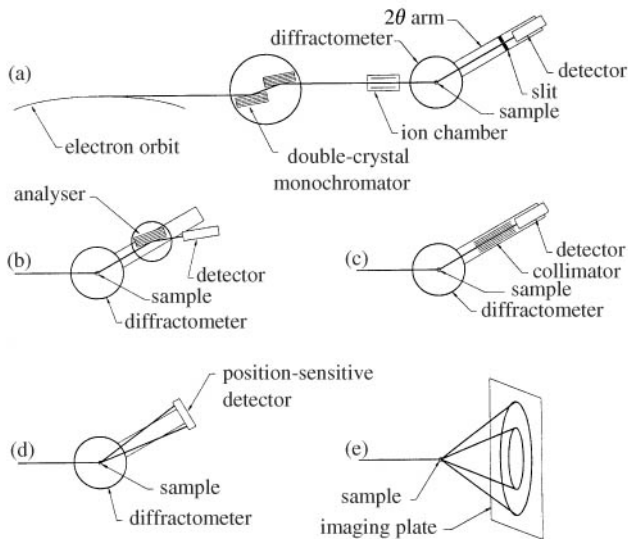


Fig. 4.2. Sketches of several popular geometries for synchrotron powder diffraction setups. (a) illustrates the basic components of a typical synchrotron beamline with a simple detector slit, (b) is the analyser crystal geometry, (c) shows a parallel-blade collimator, (d) an electronic position sensitive detector, and (e) an X-ray image plate.

beamline 9.1 at the SRS in Daresbury (Langford *et al.* 1991). Either a small sample (such as a capillary), the image of the source on an extended sample (such as a flat plate), or a second upstream slit on the detector arm can be used to limit the angular divergence of the diffracted beam. Note that this is not equivalent to the parafocusing condition of a typical laboratory X-ray powder diffractometer, because the incident beam is not diverging. This design gives the highest intensity, but does not have the high resolution and the insensitivity to sample misalignment or transparency of the setups described below.

Fig. 4.2(b) shows a crystal analyser configuration, pioneered by Hastings *et al.* (1984), in which the X-rays diffracted from the sample powder are diffracted again from an analyser crystal before reaching the detector. This use of a single crystal as a receiving slit offers the highest angular resolution, less than 0.01° full width at half maximum (FWHM), and discrimination against fluorescence from the sample; the angular resolution is much better than the intrinsic widths from samples usually encountered, so the widths of diffraction peaks are generally determined by the sample.

One improvement on the basic configuration of Fig. 4.2(b) is to couple several detectors to the same axis, allowing the pattern to be recorded in several (generally overlapping) segments simultaneously. Two such multiple analyser systems are currently in use. On beamline BM16 at the European Synchrotron Radiation Facility (ESRF), the detector bank consists of nine scintillation counters, each behind a separate Ge(111) analyser crystal, with the nine crystals mounted on a single rotation stage on the 2θ arm (Hodeau *et al.* 1998). The angular separation between each channel is close to 2° . Consequently, nine diffraction patterns, offset from one another by *c.* 2° , are measured simultaneously. This beamline often works with short wavelength X-rays (0.3–1.0 Å), and thus a diffraction pattern is usually complete by 50° in 2θ . This is one of the reasons it is desirable to minimize the separation between channels, so the detectors are concentrated in the region of interest. Data are collected in a continuous scanning mode, where the encoder on 2θ and the counts accumulated in the electronic scalers are read (without resetting) at up to 100 times/s, depending on the rate of scanning. Following data collection, the counts from the nine channels are rebinned, taking account of the exact separation between the channels, the different detector efficiencies, and the decrease in the beam current during the scan, to produce the equivalent normalized step scan, which is more suitable for analysis with standard programs. The five detectors of the powder diffractometer operated on beamline 4B at the Photon Factory are separated by 25° (Toraya *et al.* 1996), and one must make a correction for sample illumination, because the angles between the incident and diffracted X-ray beams and the sample are not equal.

Three groups have described the construction of parallel-blade collimators with angular acceptance of 0.03 – 0.07° for powder diffraction, schematically illustrated in Fig. 4.2(c) (Parrish *et al.* 1987; Cernik *et al.* 1990; Toraya *et al.* 1995); collimators with comparable specifications are also available

commercially. The theoretical transmission of such collimators is typically 50–75 per cent. This is a better match to the angular width from typical samples, and so the intensity available from such a setup is generally significantly larger than from an analyser crystal configuration. An energy-sensitive detector, such as cryogenically cooled intrinsic germanium gives a degree of discrimination against X-ray fluorescence background, but such detectors generally have a longer dead time than do the scintillation counters in typical use, and so are limited to signal rates of less than *c.* 30 000 counts/s. A further advantage of the parallel-blade configuration is that the wavelength can be changed rapidly, because there is no analyser crystal to be aligned. One point to be considered with parallel-blade collimators is that the effective sample size should be several times the spacing between foils, so that slight movements of the diffracted beam, caused by imperfect alignment or specimen opacity, are averaged over a number of blades; the detector then views a proper statistical sample.

For more rapid data collection, it is advantageous to use a linear position-sensitive detector (PSD) as illustrated in Fig. 4.2(d). Both flat and curved detectors are available commercially; the angular resolution that can be achieved depends on the detector resolution ($\sim 100\ \mu\text{m}$), the width of the sample or incident beam, and the distance between sample and detector, and typically ranges between 0.05° and 0.1° . Flat detectors are mounted on the 2θ arm and stepped at appropriate intervals during data collection; they have the advantage that they can be moved further from the sample if higher resolution is needed, and can be used with both narrow-diameter capillaries and flat-plate samples in essentially symmetric reflection or transmission geometry. However, simultaneous data collection is only possible over a few degrees with flat detectors, whereas curved detectors may cover as much as 120° . Because most linear PSDs rely on delay-line readout and time-to-amplitude converters, their maximum counting rates are limited to around 30 000 counts/s over the entire angular range. However, an order-of-magnitude increase is possible with the use of time-to-digital converters (Smith 1991). Gas proportional detectors also have sufficiently good energy resolution to allow discrimination against fluorescent radiation or higher order harmonics. They may also be used in the ‘escape-peak’ mode with Kr gas (Smith 1991). With this technique, an angular resolution of $\sim 0.03^\circ$ can readily be obtained (Jephcoat *et al.* 1992).

Another version of a position sensitive detector for recording powder diffraction patterns is the X-ray imaging plate, a form of electronic film originally developed for diagnostic radiography (Miyahara *et al.* 1986; Ito and Amemiya 1991). This is a flexible sheet, typically $20 \times 40\ \text{cm}$ in size, which uses a metastable phosphor to store the electronic energy when an X-ray is absorbed, and releases it as fluorescence when a laser beam is scanned over its surface. Imaging plates offer parallel data collection over a large area (a) without the limited count rate typical of electronic PSDs, (b) with a very large dynamic range and convenient readout relative to conventional film, and (c) with a spatial resolution on the order of $100\ \mu\text{m}$. On the other hand, the recorded intensity decays somewhat

between exposure and readout, and for best results, they must be handled in the dark. One can either collect a powder pattern over the entire imaging plate at one time, as shown in Fig. 4.2(e), or scan the imaging plate behind a fixed slit to obtain time-resolution. The former technique, of integrating around the Debye–Scherrer rings, is particularly useful with small or granular samples. Sophisticated analysis techniques (Hammersley *et al.* 1996) are required to reduce the data to a one-dimensional pattern with the angular accuracy required for structure refinement or solution with imaging plates from powder samples, but there have been some impressive successes at the Photon Factory (Honda *et al.* 1990; Takata *et al.* 1992, 1995) and the NSLS (Norby 1997). The angular resolution available in an imaging plate camera is improved by increasing the sample to plate distance, and a large instrument with a 56.3 cm diameter is in use at the Australian National Beamline Facility at the Photon Factory (Sabine *et al.* 1995).

Both the crystal analyser and the parallel-blade collimator share the advantage that the instrument measures the *angle* of the diffracted X-ray, rather than its position through a receiving slit. This ensures that the system is immune to parallax errors due to sample displacement or the partial transparency of the sample to X-rays, which are encountered with simple receiving slits (Fig. 4.2(a)) or PSDs (Fig. 4.2(d) or 4.2(e)). This is particularly important for indexing and other aspects of structure solution, where peak locations must be determined accurately.

4.3 Angular resolution, lineshape and choice of wavelength

The instrumental contribution to the width of a reflection at a synchrotron source arises from a combination of many factors. The angular width of a synchrotron X-ray beam near the critical energy is of the order of the electron rest mass (0.511 MeV) divided by the electron energy (e.g. 0.20 mrad (0.01°) for the 2.58 GeV NSLS machine), but the angular size of the sample may be much smaller, perhaps 1 mm/15 m = 0.0038°. The X-ray source size from a storage ring (e.g. 0.2 mm FWHM at ESRF) is generally smaller than the samples in typical use, so it makes a negligible contribution to the angular width. The Darwin widths of the monochromating (and analysing) crystals are of the same order of magnitude as these geometric effects (e.g. 0.0015° for Si(111) at 10 keV). The intrinsic width is a minimum at the point where the diffraction angle is the same as that of the monochromator, and it grows at larger diffraction angles due to chromatic dispersion. The Darwin curves of the monochromator (and analyser) have tails proportional to the inverse square of the distance from the Bragg angle. This contributes to the largely Lorentzian character of the lineshape, which is in contrast to the nearly Gaussian lineshape obtained with typical neutron and laboratory X-ray diffractometers. The sample-to-detector parallax for PSDs and imaging plates generally outweighs

the source and monochromator contributions in such configurations, so a nearly Gaussian or even more rectangular lineshape is obtained. In all, an analytical prediction of the instrumental lineshape by convoluting the contribution of each element is a difficult exercise.

Experimental measurement of the instrumental lineshape is also problematical, because there is no test sample free of finite size or strain broadening. Certain materials such as Si and LaB_6 are frequently used as lineshape standards, but they really only provide an upper limit to the diffractometer resolution. Indeed, the peaks from any useful powder diffraction experiment must be much broader than the intrinsic resolution of the instrument, because, in order for kinematic scattering intensities to be observed, the grains must be much smaller than the extinction length, and therefore produce diffraction peaks much broader than the Darwin width. The widths of several experimentally measured peaks from LaB_6 are plotted vs. energy in Fig. 4.3(a), and the variation of peak width vs. scattering angle at one particular X-ray wavelength in Fig. 4.3(b).

A priori knowledge of the intrinsic instrumental lineshape is not especially important for the task of structure solution, because the techniques of peak fitting and intensity extraction or modelling generally fit the observed lineshape with a sufficient number of adjustable parameters. Sample dependent contributions are typically broken down into size and strain effects: the former gives an angular width $\Gamma_{2\theta}$ proportional to $1/\cos(\theta)$ while the latter grows in

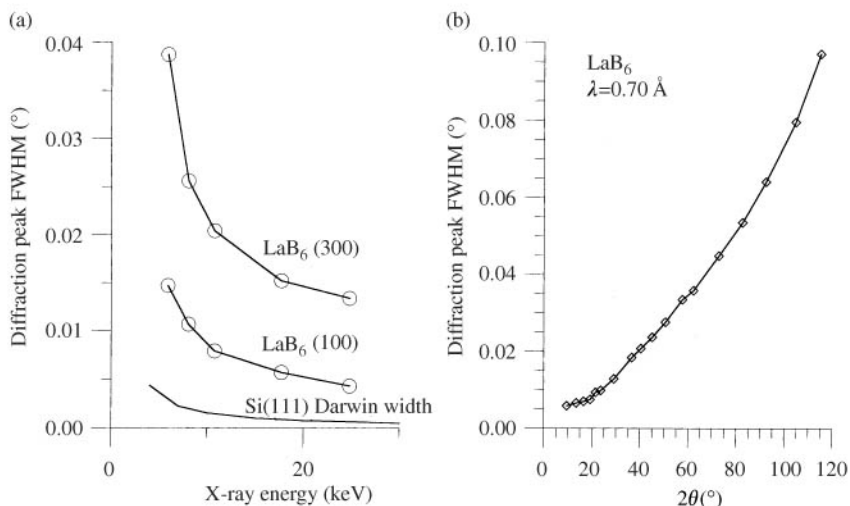


Fig. 4.3. (a) Fitted FWHM of the (100) and (300) peaks from LaB_6 (National Institute of Standards and Technology Standard Reference Material 660) at various photon energies. Also shown are the Darwin widths (full width between $y = \pm 1$) of the Si(111) Bragg reflections. (b) Fitted FWHM of several LaB_6 peaks at an X-ray wavelength of 0.70 \AA . (Data taken at NSLS beamline X3B1 with Si(111) monochromator, Ge(111) analyser, in flat-plate sample geometry.)

proportion to diffraction order, so that $\Gamma_{2\theta}$ increases as $\tan(\theta)$. The considerable literature on sample broadening and the choice of appropriate lineshapes is reviewed elsewhere, for example in Young (1993).

In any powder diffraction measurement, the low-angle peaks are asymmetrically broadened to the low-angle side, due to the intersection of the curved Debye–Scherrer cone with a flat receiving slit. This is equally true with analyser crystal geometry, where the receiving slit is in momentum, rather than physical space. The issue frequently appears to be more serious with synchrotron data, because the peaks are intrinsically sharper. The analytical computation of the correct broadening profile is straightforward (van Laar and Yelon 1984; Eddy *et al.* 1986; Finger *et al.* 1994), but many Rietveld and Le Bail extraction programs contain only an empirical approximation to the lineshape. The tradeoff between the lineshape and integrated intensity, as controlled by the transverse slit size is illustrated in Fig. 4.4. Note that the high-angle sides of the peaks are equally sharp, so that increased transverse slit width only broadens the low-angle side of the peak. Therefore, accepting a larger solid angle (or sample illuminated size) increases the peak signal with only a partial reduction in resolution. Since one cannot completely remove the effect by narrowing the beam to any finite value, it is important to view it as a parameter which is under the experimentalist's control, and which should be chosen to be appropriate for the specific measurement. One should also note that the peak asymmetry effect becomes more serious at decreasing Bragg angles, which occur for either increasing unit-cell sizes or decreasing X-ray wavelengths. In our experience, the semi-empirical asymmetry corrections used in most extraction and refinement programs create serious systematic errors. While some Rietveld programs have implemented the correct geometry for many years (David *et al.* 1992), at the time of this writing, only two of the widely-used Rietveld programs contain the correct geometry: GSAS (Larsen and Von Dreele 1985–94), and FullProf (Rodríguez-Carvajal 1997). We hope that the increased use of advanced powder techniques will motivate more people to incorporate the correct geometry into their codes.

One important choice faced by the synchrotron powder diffractionist is that of the wavelength at which the measurement should be performed. The source intensity corrected for the transmission of the windows and optical elements generally has a broad peak, but is useful over a wide range, for example, between 5 and 25 keV at the NSLS, and from 5 to 40 keV at the ESRF ($E \text{ (keV)} \times \lambda(\text{\AA}) = 12.398 \text{ keV \AA}$). The photon energy also affects the angular width of the diffraction peaks. A given pair of peaks will have a greater angular separation at long wavelength, but they also become broader, so that the resolution in $\delta d/d$ does not improve. For example, Fig. 4.5 compares the lineshape observed from a quartz sample at various wavelengths, for analyser crystal and collimator geometries. This shows that for a typical, somewhat strain-broadened sample, the ability of an analyser-geometry diffractometer to separate nearby lines does not depend strongly on the wavelength. The data

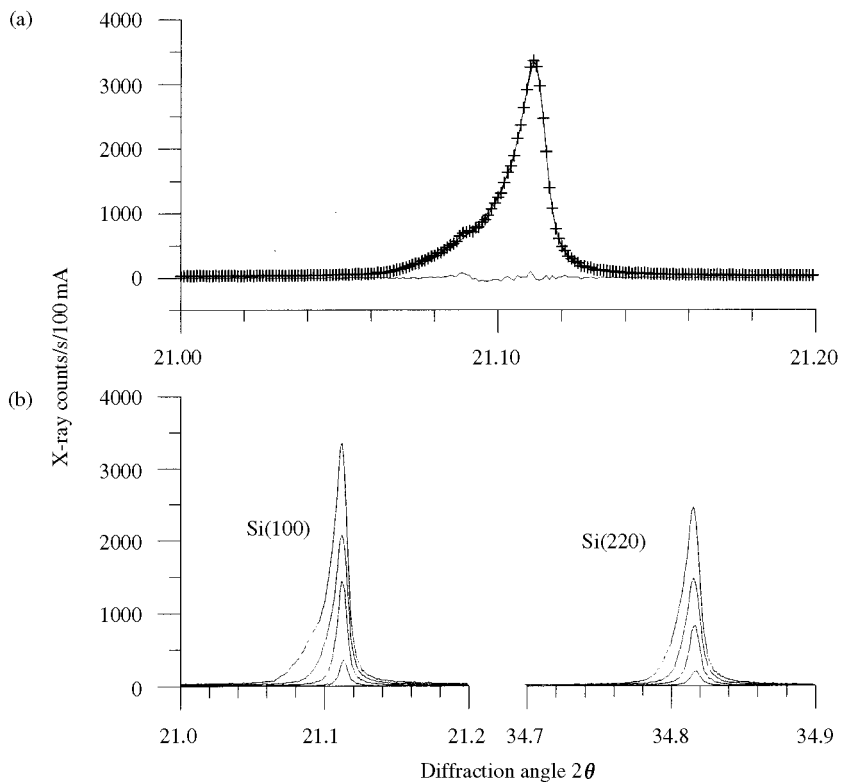


Fig. 4.4. (a) Si(111) reflection at $\lambda = 1.15 \text{ \AA}$, showing pronounced peak asymmetry. The sample was 'gently crushed' Si powder in a capillary. The illuminated part of the sample and the detector slit were both 8 mm wide, and the sample to detector distance was 33 cm. The smooth curve is a fit to a pseudo-Voigt lineshape corrected for axial divergence, as described in the text; also shown is the difference curve. (b) Si(111) and (200) peaks with equal source and detector slit widths of 8, 6, 4 and 2 mm, showing the evolution of the asymmetric broadening.

plotted in Fig. 4.5 show that the constant angular width of the collimator degrades the $\delta d/d$ resolution as the energy is increased, whereas that of the analyser remains approximately constant. At the same time, the intensity of collimator relative to the analyser increases with increasing photon energy, because the Darwin width (and therefore the integrated intensity) of the analyser crystal decreases roughly in proportion to λ .

The continuous spectrum from a synchrotron radiation source also allows the exploitation of anomalous scattering in powder diffraction experiments. The topic has been reviewed at length elsewhere (Materlik *et al.* 1994; Cox and Wilkinson 1994); here we only touch on the fundamentals. The scattering factor f for an atom is a function of scattering angle 2θ and photon wavelength λ , but

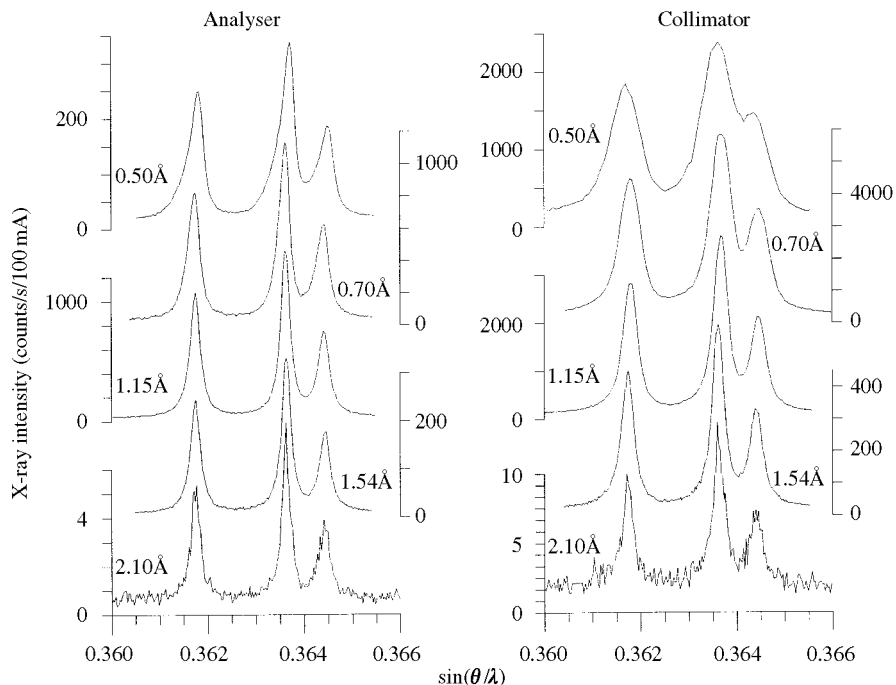


Fig. 4.5. Powder reflections of quartz. {212}, {203}, and {301} reflections at various X-ray wavelengths for analyser and collimator geometries. Data taken at NSLS beamline X3B1 with Si(111) monochromator and sample in 1.0 mm diameter capillary. The analyser crystal is Ge(111), and the collimator has 0.03° FWHM. All scans have the same vertical units of X-ray counts/s/100 mA of electron beam current. Note the different vertical scale factors.

to a good approximation, it can be separated into the form

$$f(\theta, \lambda) = f_0(\sin \theta / \lambda) + f'(\lambda) + if''(\lambda). \quad (4.1)$$

Here f_0 is the usual atomic scattering factor, dependent only on the magnitude of the scattering vector; in the limit of low angles, it approaches the number of electrons in the atom or ion. f' and f'' are the real and imaginary parts of the anomalous scattering term, which arise from resonances between the X-ray and the atomic energy levels, that is, at the K , L , and (for heavy atoms) M absorption edges. Variations of f' and f'' with X-ray energy are illustrated for several elements in Fig. 4.6(a). Tabulated values of f' and f'' are conveniently available in the compilation by Sasaki (1988), or they can readily be computed with the GSAS program (Larson and Von Dreele 1985–94). The positions of the absorption edges are shown in Fig. 4.6(b), showing that resonant effects from

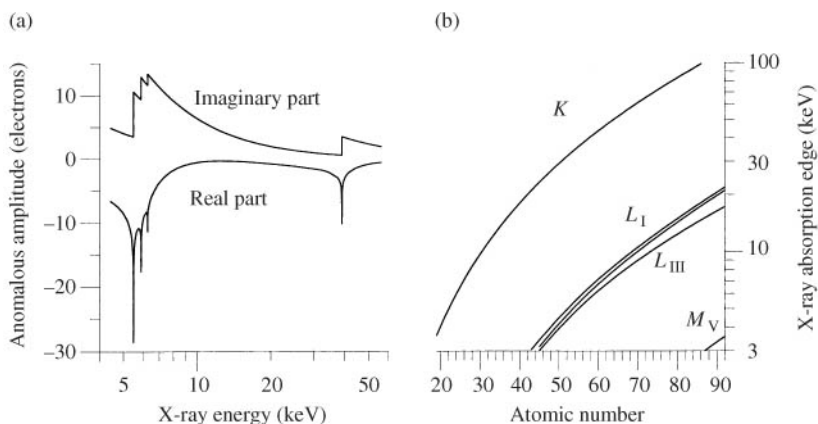


Fig. 4.6. (a) Variation of the anomalous scattering factors f' and f'' with photon energy for Bi. (b) Energy of K, L and M edges versus atomic number.

many elements are available in the typical range for powder diffraction (5–40 keV).

Anomalous scattering amplitudes can be used in two ways for the determination of structures from powder data: for phasing the reflections and for distinguishing atoms at specific sites in cases where the atomic numbers are close or there are mixed occupancies. The principles of using anomalous amplitudes to phase a powder pattern were described by Prandl (1990, 1994). The concept is demonstrated in an example of SrSO_4 given later in this chapter. In contrast to the importance of multiple anomalous diffraction (MAD) phasing techniques in macromolecular crystallography, recently reviewed, for example, by Hendrickson and Ogata (1997), we are not aware of any work where the determination of phases in a powder data set by anomalous diffraction was essential to the solution. The latter application, of assigning cation occupancies to disordered sites, is nicely illustrated by two studies of high-temperature superconductors. Site distributions of specific samples were assigned as $(\text{Tl}_{0.47}\text{Pb}_{0.53})(\text{Sr}_{1.58}\text{Ca}_{0.42})(\text{Ca}_{1.94}\text{Tl}_{0.06})\text{Cu}_3\text{O}_9$ ($T_c = 118.2\text{K}$) (Marcos *et al.* 1994) and $(\text{Tl}_{1.72}\text{Cu}_{0.28})\text{Ba}_2(\text{Ca}_{1.86}\text{Tl}_{0.14})\text{Cu}_3\text{O}_{10}$ ($T_c = 127\text{K}$) (Sinclair *et al.* 1994), based on data collected near several different absorption edges for each sample.

4.4 Data preparation and indexing

In contrast to the usual procedure for processing laboratory X-ray powder data, the raw intensity data obtained at a synchrotron source with a scintillation detector or a linear PSD must first be normalized with respect to the incident

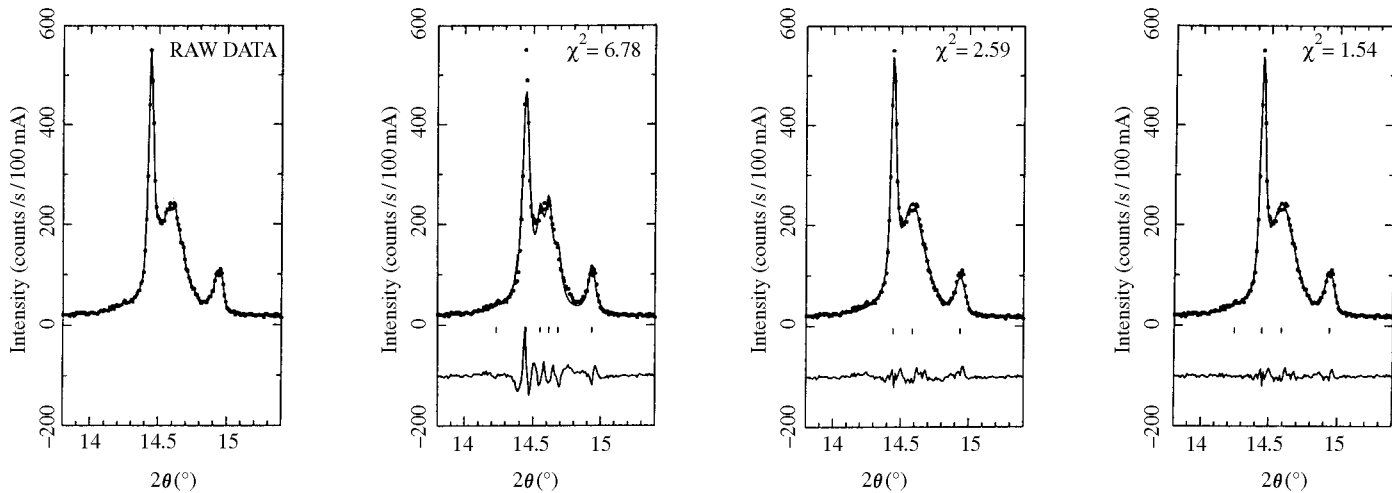


Fig. 4.7. Example of fits to a pseudo-Voigt function illustrating anisotropic peak broadening. χ^2 is the goodness of fit. From left to right; raw data; six peaks with the same FWHM (Γ) and Pseudo-Voigt mixing parameter (η); three peaks with individually-fitted Γ 's and η 's; four peaks with individually-fitted Γ 's and η 's.

beam intensity recorded by the monitor, and corrected for dead time losses. It is important to note that the statistical errors in the observations (usually taken as the square root of the raw counts) must also be properly scaled, since these will be required for the weighting scheme used in the subsequent least-squares fitting procedure. Data obtained with an imaging plate or a charge-coupled detector do not need to be normalized in this way as long as multiple frames are exposed on a constant-monitor-count basis, but they do require rather specialized software for conversion into a form suitable for profile analysis (Hammersley *et al.* 1996). At present, there seems to be no standard method for estimating the observational errors for such data, and unit weights are often assigned.

A careful visual inspection of the pattern should first be made for features such as (a) sets of weaker peaks that are much broader (or sharper) than the rest, which may be the signature of an impurity phase, (b) peaks that are split, which might be indicative of a slightly distorted unit cell, and (c) peaks with a systematically asymmetric shape, which might reflect slight inhomogeneities in composition. If the unit cell is not known, the next requirement is a set of 20–30 peak positions suitable for input into an autoindexing program (see Chapter 7). One of the many advantages of synchrotron radiation is that with a well-calibrated diffractometer it is routinely possible to determine low-angle peak positions with an absolute accuracy of $0.002\text{--}0.005^\circ$, and this greatly improves the chances of a successful outcome. In many cases, it is quite straightforward to extract the first 20–30 peak positions from single peaks or small clumps of peaks in the low-angle region of the pattern. However, ambiguities may arise when the lineshapes of nearby peaks are found to differ significantly. This might be due to the superposition of overlapping peaks but could also reflect the presence of anisotropic microstrain or particle size effects. In such cases, the evolution of the least-squares goodness-of-fit χ^2 values and the difference plots provide valuable information when fitting clumps of peaks; for example, whether or not there are extra peaks lurking within the profile. Fig. 4.7 shows (from left to right) a narrow region of low-angle data collected from a sample with an unknown structure where clearly there are at least four peaks of varying width; a very dubious fit to six peaks based on a pseudo-Voigt function with a single FWHM Γ and mixing parameter η ; a much-improved fit to three peaks with individually-refined Γ 's and η 's; and a further significant improvement with the addition of a fourth peak at the low-angle end, at which point the low value of χ^2 and the lack of structure in the difference plot indicate there is little prospect of any further improvement.

4.5 Pattern decomposition and intensity extraction

Once the pattern has been indexed successfully, the next step is to attempt to determine the possible space groups by looking for systematic absences. The answer is often ambiguous, and one must therefore return to the question of

possible space groups throughout the process of structure solution. Next, one must extract as many integrated intensities as possible for structure solution. This, for the general case where the peak width is a smooth function of d -spacing alone, is the subject of Chapter 8.

Here, we address the non-ideal case. High-resolution measurements frequently reveal deviations from ideal behaviour, and a number of different approaches to deal with this problem have been put forward (Le Bail 1992).

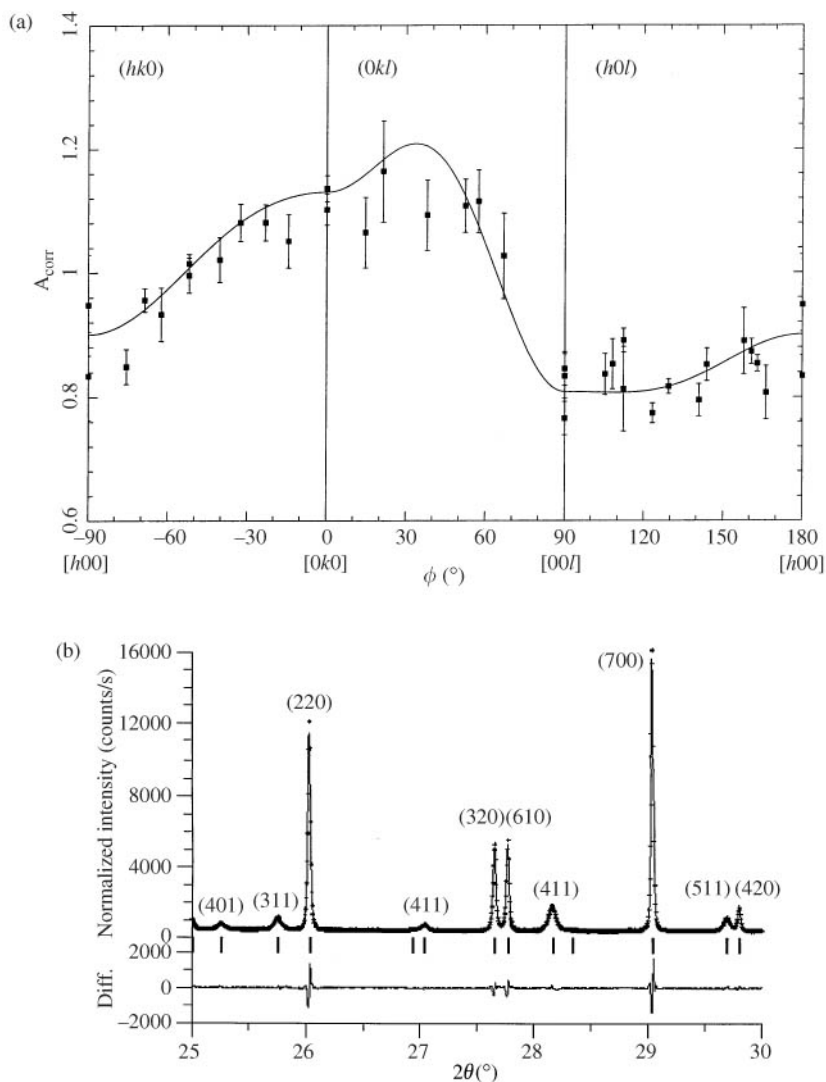


Fig. 4.8. See caption opposite.

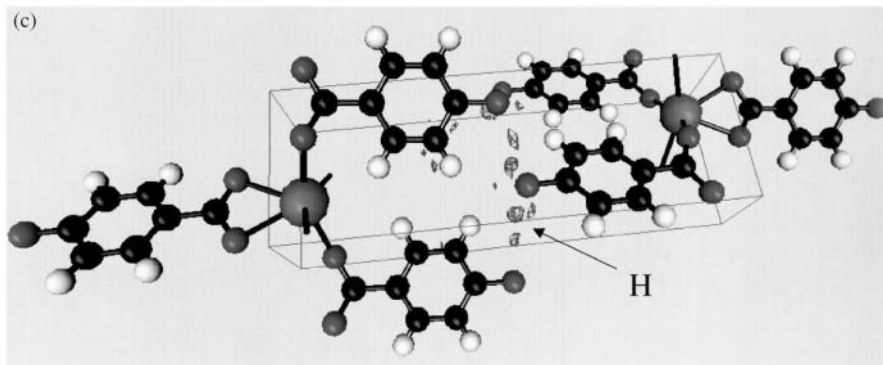


Fig. 4.8. (a) Peak widths (FWHM) versus diffraction angle for a sample of sodium para-hydroxy benzoate. Plotted are both the widths of pseudo-Voigt fits to individual peaks (circles) and widths to a Le Bail fit of the full profile, using the anisotropic broadening formalism of Stephens (1999). (b) Portion of the Rietveld refinement of sodium para-hydroxy benzoate incorporating anisotropic strain broadening (Dinnebier *et al.* 1999). (c) Structure of sodium para-hydroxy benzoate determined from powder data, from Dinnebier *et al.* (1999). The contours indicate hydrogen atoms, found from Fourier difference maps.

Many of the attempts at general formulations for this problem, such as expanding the Caglioti parameters (Caglioti *et al.* 1958) as ellipsoids in the three-dimensional reciprocal space, do not respect the symmetry of the reciprocal lattice, and so cannot claim to correctly model the effect, even though they may allow the diffractionist to draw a relatively smooth curve through the data. A commonly observed case is anisotropic strain broadening, in which the diffraction-peak width increases in proportion to the diffraction order, producing a contribution to $\delta d/d$ which depends only on the direction in reciprocal space. (Other cases, such as anisotropic size broadening (see Popa 1998) or stacking faults are also observed in practice, but will not be discussed here.) Several authors have developed models to deal with anisotropic strain broadening based on moments of a multi-dimensional distribution of lattice metrics within a powder sample (Thompson *et al.* 1987; Rodriguez-Carvajal *et al.* 1991; Popa 1998; Stephens 1999). In its general form, this produces contributions to strain broadening for certain allowed quartic combinations of Miller indices, which results in a few (2–15) anisotropic strain parameters which can be refined in a Le Bail or Rietveld fit. This has been incorporated into the Rietveld analysis package GSAS (Larson and Von Dreele 1985–94). Fig. 4.8(a) shows the widths of well-resolved peaks as a function of diffraction angle from a sample of sodium para-hydroxybenzoate, and Fig. 4.8(b) shows a portion of a Rietveld refinement of the structure of that material (Dinnebier *et al.* 1999). These illustrate that nearby diffraction peaks can differ by a factor of four in their widths,

and that this phenomenological model of anisotropic strain broadening can model the effect very well, and is invaluable for analysis of such data. Subsequently, Ungar and Tichy (1999) have shown that the same quartic combinations of Miller indices arise from a general treatment of elastic strain caused by lattice defects, at least in the cubic system. Therefore, this treatment of strain broadening appears to be more fundamental than its phenomenological roots.

4.6 Systematic errors

As already emphasized, the likelihood of a successful outcome to an *ab initio* structure problem depends very much on the accuracy and quality of the intensity data, and we will now consider some common systematic errors and how to correct for or avoid them. With care, it should be routinely possible to collect synchrotron X-ray data with an overall error level no more than 1–2 per cent.

4.6.1 Particle statistics

If the effective sample volume is small and the average size of individual crystallites is large, say $\geq 1 \mu\text{m}$, there may not be enough grains satisfying the diffraction conditions for a particular reflection to ensure a proper statistical powder average (see Chapter 6). Very narrow peak widths comparable to the instrumental resolution provide an early warning signal of a potential problem, which in extreme cases can manifest itself in the form of ragged or saw-tooth peak shapes, but is more likely to escape detection altogether except as indicated by a lack of success in the structure solution or poor results for the structure refinement.

Examination by optical and scanning-electron microscopy should give a good indication of the crystallite size, making allowance for the fact that the latter is not necessarily the same as the size of the individual aggregates. Another useful check is to measure the rocking-curves of a few strong reflections with the detector fixed at the peak position; fluctuations of more than 20 per cent are an indication of possible trouble ahead. Problems of this type can almost always be eliminated by the use of capillary samples which are rotated at several Hz, but if this option is not a viable one, the sample should at least be rocked through several degrees during data collection. The volume of sample exposed to the incident beam should be optimized by choosing a suitable wavelength with due regard for absorption edges (typically in the range 0.4–1.3 Å), selecting an appropriate diameter for the capillary (a useful rule-of-thumb is $\mu R(\rho/\rho_0) \leq 2.5$, where ρ/ρ_0 is the packing fraction), and using as wide a horizontal aperture for the beam as is practicable. If absorption considerations make it necessary to use flat-plate samples, the latter should be spun (along the sample normal) if possible, or rocked through a range of a few degrees about the symmetric position.

Imaging plates can also be used to overcome the problem of inadequate particle statistics, because the intensity can be integrated over the whole Debye–Scherrer ring, or at least a large segment of it. This technique is especially well-suited for very small samples, and is widely used for structural studies at high pressure in diamond-anvil cells, but generally yields data with more modest resolution and peak-to-background discrimination. Another technique to obtain a better powder average from a marginal sample is to use a Gandolfi spinner with a small (say 1 mm × 1 mm) X-ray beam. A more drastic remedy is to further grind the sample, but this should be done very carefully to avoid unwanted consequences such as degradation of the peak shapes and widths, the formation of disordered regions or extended defects, or even partial transformation into a second phase.

4.6.2 Preferred orientation

The presence of significant preferred orientation effects is often a consequence of using flat-plate geometry, which should normally be avoided if a preliminary microscopic examination indicates a platy or acicular crystal habit. Debye–Scherrer (capillary) geometry is superior in this respect, since preferred orientation effects are vastly reduced. Nevertheless, as pointed out in Chapter 9, in some cases it may be possible to take advantage of preferred orientation in crystal structure solution, and these specialized techniques of data collection should not be ruled out.

4.6.3 Absorption

When capillary geometry is used, a correction for absorption should be made if the effective value of $\mu R \geq 1$. If uncorrected, absorption effects are likely to lead to a negative overall thermal parameter (Hewat 1979). For larger values, a correction can be made by parameterization of the transmission factors in the International Tables (Maslen 1995); either Chebyshev polynomials (Toby 1997) or double Gaussian functions analogous to those used for scattering factors are suitable for this purpose. In order to make this correction, the packing density must be estimated, or better still, determined from direct measurements of the weight and dimensions of the sample (the latter procedure is strongly recommended not just for structure solution but for *all* studies involving capillary samples). If absorption corrections are made carefully, negative thermal factors should not be obtained.

For ideal flat-plate samples, the absorption factor is $\mu/2$ independent of 2θ and no correction is necessary. However, for very granular and highly-absorbing materials there could be a significant reduction in intensity at low scattering angles due to surface roughness as discussed by Suortti (1972), and careful attention should be given to the preparation of flat-plate specimens of

this type and the choice of wavelength, since there is no a priori way to correct the raw data for this kind of microabsorption effect.

4.6.4 Extinction

Although extinction effects are seldom considered in the analysis of X-ray powder data, they can be surprisingly large in highly-crystalline materials such as diamond and silicon, especially at longer wavelengths. If an examination by optical or electron microscopy reveals crystallites that are several microns in size, the wavelength chosen for the experiment should be short enough to eliminate possible extinction effects based on an order-of-magnitude estimate from the expressions given by Sabine (1993), because there is no a priori method to correct the data for effects of this type either.

4.7 Examples of structure solution

This book contains many examples of structure solutions that have utilized synchrotron data. Rather than present a comprehensive review of recent results obtained using the powerful and rapidly-evolving techniques in SDPD, we have chosen problems that highlight the specific areas where synchrotron radiation has made a key contribution. The earliest crystal structure determinations from synchrotron powder diffraction data were of inorganic materials, such as α -CrPO₄, MnPO₄·H₂O, Al₂Y₄O₉ and I₂O₄. Since then, a full range of materials, including inorganics, organics, organometallics, microporous compounds, hydrates, fullerenes, etc., have yielded to the power of synchrotron radiation. Table 4.1 summarizes the lattice parameters and number of atoms in the irreducible cell for those mentioned in this chapter.

4.7.1 Pioneering studies

4.7.1.1 α -CrPO₄

The first example of a structure solved from synchrotron data (α -CrPO₄, Attfield *et al.* 1986, 1988) is discussed in Chapter 2 and the techniques employed in this work set a pattern that was to be followed for several years.

4.7.1.2 MnPO₄·H₂O

The unit cell of MnPO₄·H₂O (Lightfoot *et al.* 1987) was determined by auto-indexing from 20 reflections using the program of Visser (1969). A figure of merit M_{20} of 196 indicated unambiguously that the correct unit cell had been found. Such high figures of merit are not unusual with synchrotron studies, because the peak positions are determined so accurately. Systematic absences indicated the space groups Cc or $C2/c$ and a Patterson map calculated from

Table 4.1 Summary of examples discussed in this chapter. N_A refers to the number of independent atoms, and N_C to the number of refined positional parameters

| Compound | Space group | N_A | N_C | a (Å) | b (Å) | c (Å) | β (°) | V (Å ³) |
|---|---|-------|-------|------------|------------|------------|-------------|-----------------------|
| α -CrPO ₄ | <i>Imma</i> | 8 | 13 | 10.4058(1) | 12.8995(1) | 6.29933(6) | | 845.6 |
| MnPO ₄ · H ₂ O | <i>C2/c</i> | 6 | 11 | 6.912(1) | 7.470(1) | 7.357(1) | 112.3(1) | 351.4 |
| Al ₂ Y ₄ O ₉ | <i>P2₁/c</i> | 15 | 45 | 7.3781(1) | 10.4735(1) | 11.1253(1) | 108.540(1) | 815.1 |
| I ₂ O ₄ | <i>P2₁/c</i> | 6 | 18 | 8.4879(2) | 6.7010(2) | 8.3407(2) | 124.713 | 390.0 |
| BeH ₂ | <i>Ibam</i> | 4 | 7 | 9.082(4) | 4.160(2) | 7.707(3) | | 291.2 |
| Sigma-2 | <i>I4₁/amd</i> | 17 | 33 | 10.2387(1) | | 34.3829(1) | | 3604.4 |
| SrSO ₄ | <i>Pnma</i> | | | 8.361 | 5.352 | 6.871 | | 307.5 |
| 5-aminovaleric acid | <i>Pna2₁</i> | 8 | 23 | 17.358(7) | 4.523(2) | 7.447(3) | | 584.7 |
| C ₆ F ₆ :C ₆ D ₆ | <i>P2₁/a</i> | 12 | 36 | 9.4951(3) | 7.4235(2) | 7.5262(2) | 95.630(2) | 527.9 |
| Norbornane | <i>P2₁/m</i> | 4 | 11 | 5.9365(3) | 9.6818(1) | 5.7116(3) | 116.356(5) | 294.2 |
| RS-camphor | <i>Cmcm</i> | 11 | 33 | 6.8341(2) | 11.6585(4) | 11.5000(3) | | 916.3 |
| S-camphor | <i>P2₁2₁2₁</i> | 22 | 66 | 9.9276(1) | 27.0636(3) | 7.3815(2) | | 1783.2 |
| C ₂₄ H ₁₆ O ₇ | <i>P-1</i> | 31 | 93 | 11.044 | 11.730 | 7.371 | triclinic | 937.5 |
| Beryllphosphate-H | <i>P321</i> | 25 | 63 | 12.5815(4) | | 12.4508 | | 1706.9 |
| LiZnPO ₄ | <i>Pn2₁a</i> | 10 | 30 | 10.0207(2) | 6.6731(2) | 4.96548(8) | | 332.0 |
| Na ₄ Ti ₂ Si ₈ O ₂₂ · 4H ₂ O | <i>P4₂12</i> | 8 | 16 | 7.3673(1) | | 10.6998(1) | | 580.8 |
| UiO-7 | <i>Pbca</i> | 30 | 90 | 14.533(3) | 15.334(6) | 16.601(4) | | 3699.8 |
| NH ₄ -VPI-9 | <i>P4₂/ncm</i> | | | 9.8946 | | 36.8715 | | 3609.8 |
| Rb-VPI-9 | <i>P4₁2₁2</i> | 57 | 165 | 9.8837(1) | | 73.6505(6) | | 7194.7 |
| NaCD ₃ | <i>I222</i> | 11 | 29 | 6.7686(1) | 18.6016(4) | 6.5762(1) | | 828.0 |
| RbC ₃ H ₅ I | <i>Pnma</i> | 4 | 10 | 10.7990(2) | 8.6923(2) | 5.7061(2) | | 535.6 |
| RbC ₃ H ₅ II | <i>Pbcm</i> | 8 | 19 | 9.3396(1) | 10.9666(1) | 10.5490(1) | | 1080.5 |
| β -haematin | <i>P-1</i> | 41 | 14 | 12.196(2) | 14.684(2) | 8.040(1) | triclinic | 1416 |
| Mg ₆ Co ₂ H ₁₁ | <i>Pnma</i> | 24 | 63 | 8.1000(2) | 10.0643(2) | 18.5664(4) | | 1513.5 |
| Ga ₂ (HPO ₃) ₃ · 4H ₂ O | <i>P2₁</i> | 29 | 87 | 8.0947(2) | 10.0336(2) | 7.6711(2) | 111.392(2) | 580.1 |
| La ₃ Ti ₅ Al ₁₅ O ₃₇ | <i>Cc</i> | 60 | 178 | 22.5655(3) | 10.9863(2) | 9.7189(1) | 98.569(2) | 2382.5 |
| (CH ₃) ₂ SBr ₂ | <i>P2₁/a</i> | 5 | 15 | 11.4090(1) | 7.3819(1) | 7.4510(10) | 92.824(1) | 626.8 |
| (CH ₃) ₂ SBr _{2.5} | <i>Cmca</i> | 7 | 17 | 21.9676(2) | 11.1972(1) | 11.0531(1) | | 2718.8 |
| (CH ₃) ₂ SBr ₄ | <i>P2₁/a</i> | 7 | 21 | 9.0381(1) | 11.6589(1) | 8.8859(1) | 90.134(1) | 936.3 |
| Zn Insulin T ₃ R ₃ DC | <i>R3</i> | 1630 | 4893 | 81.278 | | 73.0389 | | 417 860 |

61 extracted intensities showed the location of a Mn atom. Subsequent difference Fourier maps revealed the remaining non-hydrogen atoms and hydrogen was positioned after refinement of the structure on the basis of bond-length and bond-strength calculations. In the final cycles, the hydrogen was allowed to refine unrestrained, resulting in an O–H bond length of 1.00(4) Å and an H–O–H angle of 100(1)°. The water content of one molecule per formula unit differs from the previously assumed composition of this phase (1.5 H₂O), but is in agreement with TGA measurements. The octahedrally coordinated Mn(III) ion has a marked Jahn–Teller distortion, in contrast to those observed in various related M^{II}SO₄·H₂O structures.

4.7.1.3 *Al₂Y₄O₉ and I₂O₄*

The structures of Al₂Y₄O₉ and I₂O₄ were solved from data collected with a small linear PSD (Lehmann *et al.* 1987). Al₂Y₄O₉ is isostructural with Al₂Eu₄O₉, so a good estimate of the unit cell and space group was available as prior information. From 573 reflections extracted by a Pawley refinement, 252 with $|F| > 3\sigma$ were used with the Direct methods program MULTAN77 to reveal the positions of the four Y atoms. Least-squares refinement followed by the calculation of a Fourier map revealed the locations of the nine O and two Al atoms. In the case of I₂O₄, a probable unit cell and a space group were known from Guinier measurements. Pawley refinement of the data gave 157 reflections with $|F| > 3\sigma$ and the two I atoms were located from a Patterson map and by the program MULTAN. Fourier maps based on the intensities extracted by the Pawley refinement were very noisy, but after Rietveld refinement with just the two I atoms, the four O atoms could be found easily. The structure was confirmed by a refinement using neutron diffraction data.

4.7.1.4 *BeH₂*

The structure of BeH₂ (illustrated in Fig. 4.9) was solved without any prior knowledge (Smith *et al.* 1988), via autoindexing, space-group identification from systematic absences, and then the calculation of the Patterson map. Two Be atoms were identified, and the hydrogens were positioned using a trial-and-error approach. The structure is composed of a network of corner-sharing BeH₄ tetrahedra, rather than hydrogen-bridged chains as previously suggested. The crystal-analyser geometry allowed a relatively large capillary to be used (0.7 mm) without any loss of resolution, so more of the weakly scattering sample could be placed in the beam.

4.7.1.5 *Sigma-2*

The first microporous structure determined from synchrotron data was that of the 17-atom clathrasil Sigma-2 reported by McCusker (1988). With a series of programs assembled for the task, peaks positions were identified and the pattern

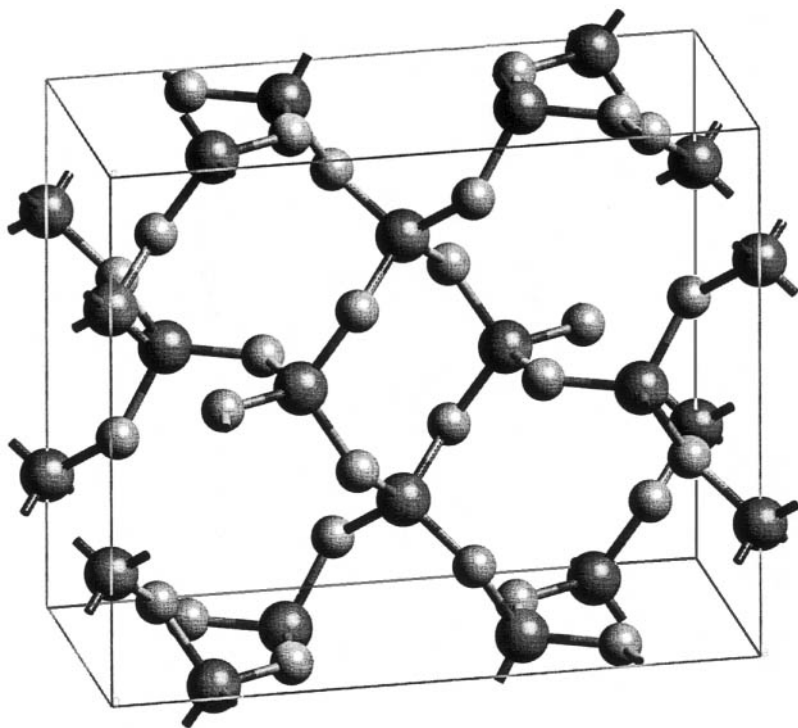


Fig. 4.9. View of the structure of BeH_2 showing the network of corner-sharing BeH_2 tetrahedra (Smith *et al.* 1988).

indexed using TREOR (Werner *et al.* 1985). Systematic absences showed the space group to be $I4_1md$, $I42d$ or $I4_1/amd$, and the latter centrosymmetric space group was assumed on the basis of intensity statistics. Two hundred and fifty-eight reflections extracted by the Pawley method were used as input to the single-crystal package XTAL, and all four Si atoms and five of the eight O atoms were correctly located. The three remaining framework O atoms were located in a difference Fourier map. Following Rietveld refinement of the structure, the disordered organic template was located in the large cage. The large and small cages that characterize the structure had not been encountered previously in microporous materials.

4.7.1.6 SrSO_4

In a recent paper, Prandl (1994) proposed a method for *ab initio* structure solution based on partial Patterson maps of anomalous scatterers derived from powder data collected at three wavelengths, two close to an absorption edge and one off-edge. This is analogous to the well-known multiple anomalous dispersion method widely used in protein crystallography, but differs insofar as the

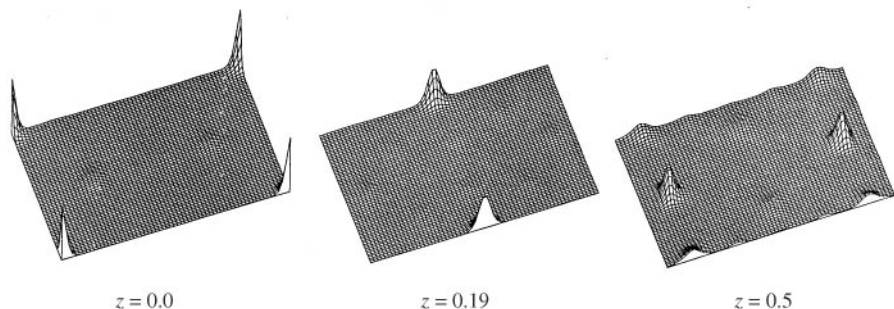


Fig. 4.10. Maximum-entropy reconstruction of partial Patterson maps for Sr atoms in SrSO_4 obtained from anomalous scattering measurements, showing three sections at different heights z along the c -axis (Burger *et al.* 1998).

Bijvoet pairs of reflections are coincident in a powder pattern. As a demonstration test of this proposed technique, data were collected from a reference sample of SrSO_4 at wavelengths of 0.7702, 0.7820 and 1.1294 Å, that is, about 13, 256 and 5132 eV below the Sr K-edge (Burger *et al.* 1998). Diamond dust was added to the sample as an internal standard in order to scale the data on an absolute basis in the subsequent derivation of the partial Patterson maps, which are shown in Fig. 4.10. From the latter, the coordinates of the Sr atom were readily determined as (0.16, 0.25, 0.19) and used to complete the structure determination from the off-edge data set. A key feature of this work was the use of maximum entropy methods to allow both overlapped and non-overlapped peaks to be used in the reconstruction of Patterson maps, which were as free of noise and truncation effects as possible. This technique might prove to be useful in cases where conventional methods of structure solution have failed, but clearly requires very accurate data and careful attention to experimental details.

4.7.2 Organic compounds

The crystal structures of organic compounds are often more difficult to solve than inorganic structures. This is because there is usually no heavy atom present for identification in a Patterson map, to provide phasing of the reflections, and the scattering is usually weak, especially at the higher angles essential for Direct methods. Furthermore, the crystallinity can be poorer, leading to peak broadening and hence, more problems for indexing and extracting individual intensities from overlapping reflections. On the other hand, the molecular structure is usually well known and this can be put to good use, once a unit cell has been determined, by considering the most efficient packing of the molecules.

In studies of organic materials, it is often necessary to use either a deep flat-plate sample or (preferably) a fat capillary, 1–2 mm in diameter. Thin flat-plate

samples are not normally suitable as there is a very strong tendency for preferred orientation. Thin capillaries are quite difficult to fill, particularly when the materials are hygroscopic, waxy, or electrostatically charged. Use of an analyser crystal or Soller collimators is therefore essential, in order to avoid large peak shifts caused by specimen transparency with the deep flat-plate sample, or to avoid the broad peaks that would arise using a conventional receiving slit with a fat capillary.

4.7.2.1 *5-aminovaleric acid*

5-aminovaleric acid ($\text{NH}_2(\text{CH}_2)_4\text{CO}_2\text{H}$) was solved from data collected using a cylindrical imaging-plate system (Honda *et al.* 1990). The data were recorded in only 6 min, digitized, and reduced to the equivalent one-dimensional scan up to 65° in steps of 0.01° of 2θ . The fact that FWHM of 0.07° is not particularly narrow when compared with standard synchrotron diffractometers operating with Debye–Scherrer slits or an analyser crystal did not preclude structure solution via a combination of Patterson maps, trial-and-error C–C chain positioning and difference Fourier maps. It is particularly impressive that a full structure can be obtained from data collected in such a short time.

4.7.2.2 *C₆H₆–C₆F₆ adduct*

The solid adduct that forms between benzene and hexafluorobenzene at room temperature undergoes three phase transitions, at 272, 247.5 and 199 K. The ambient structure of phase I was solved from single-crystal data and comprises cylindrically disordered columns of alternating benzene and hexafluorobenzene molecules (Overell and Pawley 1982) held together by the quadrupole moments of the two molecules, which are of opposite sign. The phase transitions are associated with ordering of the columns, and large volume changes lead to the fracture of single crystals. Powder diffraction patterns of phases II, III, and IV were all indexed, with figures of merit greater than 200 (Williams *et al.* 1992).

The monoclinic cell of the lowest temperature phase IV was indexed despite the presence of some weak peaks attributable to residual phase III arising from the sluggish phase transition (even low levels of such impurities are generally easily observed with synchrotron data). Intensities extracted by the Le Bail method were input to the single-crystal program SIR88, which solved the complete non-hydrogen structure comprising six C and three F atoms. The structure, shown in Fig. 4.11, was refined by the Rietveld method, but the presence of the phase III impurity led to a somewhat high value for R_{wp} . A deuterated sample had also been measured by neutron diffraction, and refinement of the X-ray structure using this pattern, which contains very little phase III, gave a satisfactory fit. The structure of phase III was subsequently deduced (Cockcroft 1995) in conjunction with the neutron data using the triclinic cell determined from the synchrotron study.

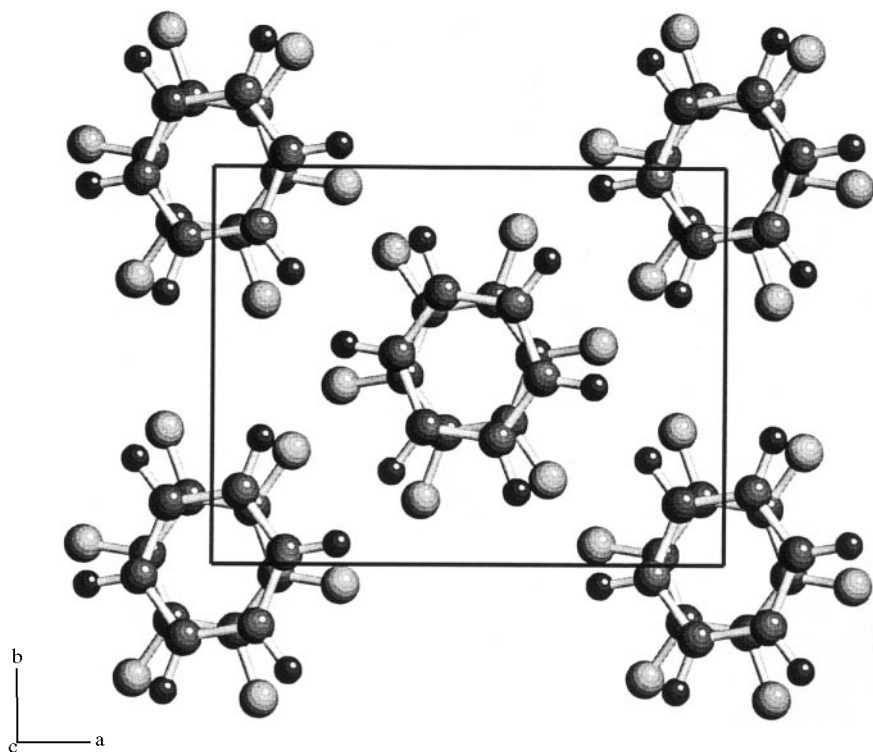


Fig. 4.11. View down the columns of alternating benzene and hexafluorobenzene molecules in the lowest-temperature phase IV of the solid adduct. The molecules appear to be intermediate between a staggered and an eclipsed configuration (Williams *et al.* 1992).

4.7.2.3 Bicyclics

Bicyclic molecules frequently have orientationally disordered cubic or hexagonal structures under ambient conditions, but order at low temperature under the influence of the weak steric and van der Waals interactions between molecules. The low-temperature structures of two such systems, norbornane (bicyclo [2.2.1] heptane— C_7H_{12}) (Fitch and Jovic 1993), and RS-camphor ($C_{10}H_{16}O$) (Mora and Fitch 1997) were solved from synchrotron data. In each case, unit cells were readily obtained by autoindexing, but attempts to solve the structures by Direct methods were not successful.

The norbornane molecule has $mm2$ symmetry (C_{2v}) and it is apparent that there are two molecules per unit cell. Alignment of one of the molecule's mirror planes with the mirror plane of the most probable space group ($P2_1/m$) was followed by manual manipulation of the molecule's position within the unit cell in an effort to generate a calculated diffraction pattern resembling the observed

one—a process of ‘manual global optimization’. Once the correct molecular mirror plane had been selected, satisfactory agreement was eventually obtained.

For RS-camphor, which is an equimolar solid solution of enantiomeric molecules, the apparent space group is $Cmcm$, which has 16 general (x, y, z) positions. The number of molecules per unit cell is four, implying a residual disorder of the molecules, because they have symmetry I . The output from SHELXS indicated fragments of molecules in the vicinity of the $(0, 1/4, \sim 0.25)$ position with symmetry $m2m$, but no clear picture was obtained. The correct orientation of the molecule was obtained by a grid search of all possible molecular orientations, centred at $(0, 1/4, \sim 0.25)$ using the Rietveld method to assess the models. In the refinements, the molecule was also given freedom to move its centre away from $(0, 1/4, \sim 0.25)$. From an initial search of orientational space using coarse 10° steps, successively finer steps were used around the orientation that gave a minimum in R_{wp} until the correct molecular orientation was clear. The structure has fourfold disorder in the position of the molecule. Twofold disorder comes from the superposition of the two enantiomeric forms of the molecule, with each possessing an additional twofold orientational disorder.

More recently, the structure of the pure enantiomeric form of camphor in the ordered, lowest-temperature phase was solved. A powder pattern was collected from a spinning capillary cooled to 100 K and the pattern indexed with an orthorhombic cell. The volume of the unit cell ($V = 1782 \text{ \AA}^3$) indicates that there are eight molecules per cell, hence two molecules in the asymmetric unit for the most probable space group $P2_12_12_1$. Attempts to solve the structure by using the Direct methods package EXPO (Altomare *et al.* 1999) to locate the 22 non-hydrogen atoms constituting the two independent molecules were not successful. In contrast, global optimization using simulated annealing as implemented in *PowderSolve* (Engel *et al.* 1999) returned the correct structure after a 10-day run on a Silicon Graphics O2 computer, utilizing 1.1×10^8 cycles of simulated annealing, performed in two distinct steps. In the first SA runs, both molecules were allowed to rotate and translate independently, but no structure solution was obtained. In the second round of annealing, the molecular locations were fixed (in a sense emulating the approach used for the racemic solid solution) and only their orientations allowed to vary. This second SA run improved the match between the calculated and the observed diffraction pattern significantly and a subsequent Rietveld refinement of this solution converged rapidly, indicating this to be the correct structure for S-camphor.

4.7.2.4 *Fluorescein diacetate*

Fluorescein diacetate, $C_{24}H_{16}O_7$, contains five connected aromatic and alicyclic rings. A high-resolution diffraction pattern, collected from a spinning 1.5 mm capillary at room temperature, could be indexed with a triclinic cell with a

volume indicative of two molecules in the cell. Structure solution using EXPO (Altomare *et al.* 1999) and SIRPOW (Altomare *et al.* 1995) failed to find a sensible solution. Accordingly, the diffraction pattern was recollected at 100 K and the high-angle region of the pattern scanned twice as often as the low-angle region to improve the statistical quality of the high-angle data. Again, structure solution attempts failed until the 'fwhm' parameter (which controls whether adjacent reflections are considered to be overlapping or not) was increased from its default value of 0.1 to 0.2. At that point, 14 atoms appeared in a solution that had a combined figure of merit of 0.988. Subsequent cycles of Fourier synthesis and refinement yielded the complete molecular structure, with carbon and oxygen atoms correctly assigned and bond distances to within about 0.1 Å of the values expected (Knudsen *et al.* 1998). The packing of the fluorescein diacetate molecules in the crystal reveals a network of intermolecular C–H···O hydrogen bonds, 10 per molecule, holding the structure together (Fig. 4.12).

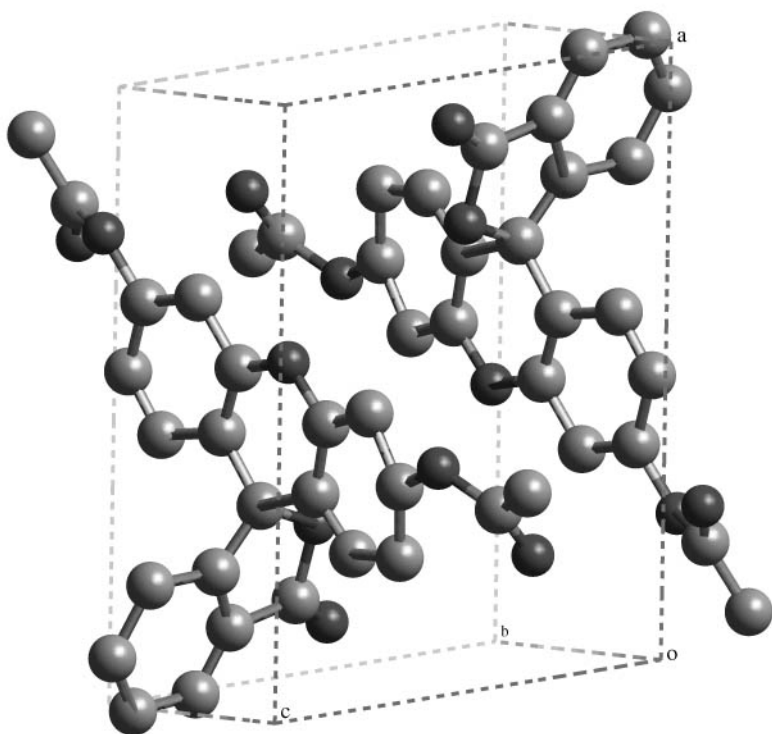


Fig. 4.12. View of the crystal structure of fluorescein diacetate as solved from powder data using Direct methods. The two molecules shown are related by inversion (Knudsen *et al.* 1998).

4.7.3 Microporous materials

A number of impressive structures of microporous materials have been solved using synchrotron radiation.

4.7.3.1 Beryllphosphate-H

Beryllphosphate-H, $\text{NaKBe}_2\text{P}_2\text{O}_8 \cdot 3\text{H}_2\text{O}$, in which sodium and potassium cations balance the negative charge of the microporous beryllphosphate framework (Harvey *et al.* 1992), was indexed on a hexagonal unit cell with no systematic absences. Due to the multitude of possible space groups (16), no attempt was made to solve the structure using Direct methods. Rather, the similarity of the lattice parameters to those of MAPSO-46 was used to solve the structure. The unit cell for MAPSO-46 was halved along c and its c -glide removed to give space group $P321$, and the calculated powder diffraction pattern of that model matched the observed pattern. The framework was then optimized by distance least-squares refinement. After Rietveld refinement with restrained framework bond lengths and angles, the two Na and two K atoms were located from difference Fourier maps, along with disordered water molecules.

4.7.3.2 LiZnPO_4

LiZnPO_4 is one of a number of novel materials that are formed between the alkali metals, zinc, phosphate and water. It may be formed by dehydration of the monohydrate, or synthesised directly (Harrison *et al.* 1995). After deduction of the unit cell and space group ($Pn2_1a$) from a combination of lab, synchrotron and second-harmonic-generation measurements, attempts to transform the framework of $\text{LiZnPO}_4 \cdot \text{H}_2\text{O}$ via a displacive non-bond-breaking procedure proved unsuccessful. In contrast, a Direct methods solution using 342 $|F|^2$ values as input to SHELX-86 revealed the positions of the Zn and P atoms. Structure completion and refinement followed along conventional lines. The structure deduced in this study confirms that dehydration of $\text{LiZnPO}_4 \cdot \text{H}_2\text{O}$ leads to the breaking and remaking of Zn–O–P linkages, transforming a framework that contains 4-, 6- and 8-rings into one that has only 6-rings, but maintaining the alternation of ZnO_4 and PO_4 units. This is unusual behaviour, as dehydration in microporous compounds normally proceeds with only small distortions to the framework, though rearrangement of cations is frequently encountered.

4.7.3.3 $\text{Na}_4\text{Ti}_2\text{Si}_8\text{O}_{22} \cdot 4\text{H}_2\text{O}$

Titanosilicates are often good catalysts, and are of particular importance in the petrochemical industry. A novel compound, of composition $\text{Na}_4\text{Ti}_2\text{Si}_8\text{O}_{22} \cdot 4\text{H}_2\text{O}$, synthesised hydrothermally, was solved via autoindexing, Le Bail

decomposition, and Direct methods using SHELX-86 (Roberts *et al.* 1996). The solution, in the non-centrosymmetric space group $P4_21_2$, confirmed EXAFS results that had suggested five-fold coordination of Ti by oxygen, in a square-pyramidal coordination, with the apical oxygen having a shorter Ti–O distance. The structure is layered, and is a double-sheet titanosilicate, in contrast to fresnoite which has single sheets.

4.7.3.4 Aluminophosphate UiO-7

The high-resolution powder diffraction pattern of the aluminophosphate UiO-7 was indexed using TREOR90 on an orthorhombic cell, with systematic absences suggesting the space groups $Pbcm$ or $Pbc2_1$ (Akpориaye *et al.* 1996). An approach to solving the structure via model building, based on intuitive knowledge from known-framework topologies, failed to produce structures consistent with the data. However, an approach using simulated annealing (Deem and Newsam 1989) based on structural knowledge about four-connected networks combined with the symmetry restrictions imposed by the space group was successful. Framework topologies are generated and then ranked in terms

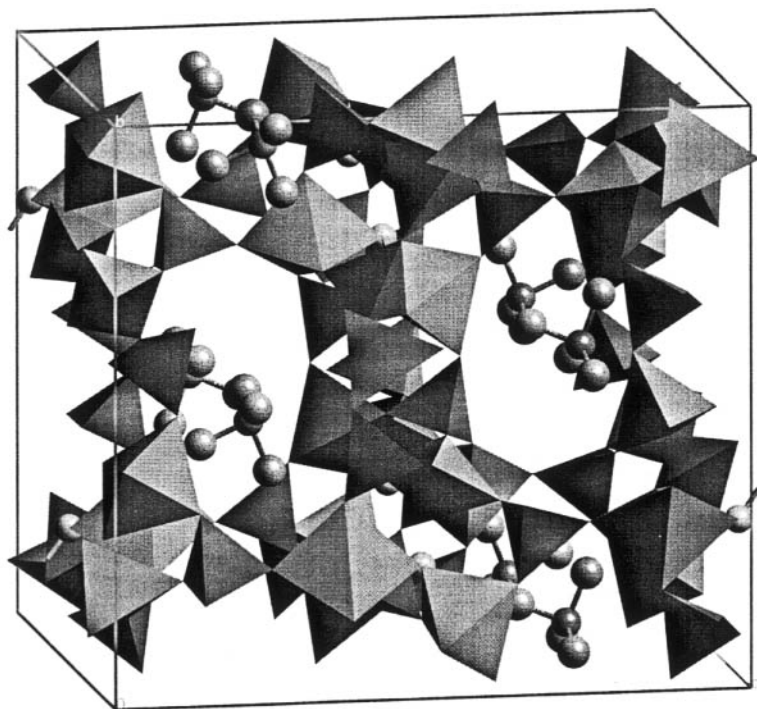


Fig. 4.13. View of the structure of UiO-7 (Akpориaye *et al.* 1996).

of a figure of merit, by applying a penalty factor based on deviations from prescribed connectivities, bond lengths and angles, and site occupancies. The match with the observed diffraction data is also included. Information required in the procedure includes the number of tetrahedral atoms in the unit cell N_T and in the asymmetric unit N_U . The former was obtained from the known relationship of the framework density and the micropore volume obtained from the water adsorption isotherm, and the latter was obtained from analysis of the ^{31}P and ^{27}Al MAS NMR spectra, yielding the most likely value as 6, but with 8 or 4 also as possibilities. A solution with a high figure of merit was found only for $N_U=4$, in space group $Pbcm$. However, to obtain P and Al ordering, the unit cell must be doubled along a and the space group changed to $Pbca$. The structure (Fig. 4.13) was completed by Rietveld refinement, and the location of the organic template was determined from Fourier maps. The final refinements included 30 atoms. This is the first published use of the simulated annealing approach for the solution of a completely unknown framework topology.

4.7.3.5 VPI-9

Following optimization of the sample preparation to obtain a pure phase and ammonium ion exchange, the unit cell of the zirconosilicate VPI-9 was indexed definitively from synchrotron data on a tetragonal unit cell with $a=9.8946\text{ \AA}$ and $c=36.8715\text{ \AA}$ in the space group $P4_2/nm$ (McCusker *et al.* 1996). The unit cell of the as-synthesised Rb-containing material has a doubled c parameter, so structure solution was not attempted with those data. The structure of the ammonium form was solved using a new approach (FOCUS) in which a large number of electron density maps were generated from the extracted integrated intensities, with randomly assigned phases. These were subjected to a Fourier recycling procedure combined with a search for a three-dimensional 4-connected framework with appropriate bond distances and angles (see Chapter 17). The framework identified has seven tetrahedral sites (T-sites), and initial Rietveld refinements indicated that the correct structure had been found. This represents one of the most complex zeolite-like structures solved from powder data using an automated procedure.

The refinement was not pursued, as it was apparent that the exchange of NH_4^+ for Rb^+ was incomplete. Refinement was therefore attempted for the as-synthesised Rb-analogue. Doubling the c -axis leads to the space group $P4_12_12$ and requires 15 tetrahedral and 30 oxygen atoms. The distribution of Zn atoms could not be obtained by refining the T-site occupancies. Therefore zinc atoms were placed in the 3-rings, because this is where they are found in related zirconosilicates, and the population parameters of just these nine T-sites were refined, starting from population parameters corresponding to $2/3$ Si and $1/3$ Zn. Refinement of this model led to localization of Zn into three pure sites in the 3-rings. The channel contents were obtained from Fourier maps whose

interpretation relied on chemical considerations. The final structure involves 59 atoms (45 of which describe the framework) and 170 structural parameters.

4.7.4 Organometallics

4.7.4.1 NaCD_3

The complementary use of synchrotron X-ray and neutron data to solve a structure is illustrated by the case of deuterated methylsodium, NaCD_3 (Weiss *et al.* 1990). Neutron data were collected and the pattern could be indexed as body-centred orthorhombic ($a = 6.7686 \text{ \AA}$, $b = 18.6016 \text{ \AA}$, and $c = 6.5762 \text{ \AA}$). Due to the similarity between a and c , it was not possible to resolve reflections adequately to assess with confidence whether any systematic absences other than those required for body centring were present. A synchrotron data set showed clearly that no extra extinction conditions applied, indicating space groups $I222$, $I2_12_12_1$, $Imm2$, $Im2m$, $Im22$, or $Immm$. The latter is centrosymmetric and was excluded on the basis of intensity statistics. Using SHELX-86, each space group was investigated, and a sensible non-hydrogen-atom structure obtained in $I222$. There are three crystallographically distinct Na atoms and two C atoms in the structure. The six distinct D-atom positions were obtained from the neutron diffraction data. Half the ions are arranged in $(\text{NaCD}_3)_4$ tetramers with the D atoms staggered with respect to the three neighbouring sodium ions, (similar to methyl lithium). The remaining Na^+ ions are arranged in zig-zag chains and the remaining CD_3^- ions interconnect the tetramers via Na–C contacts. The structure, therefore, appears to be intermediate between that of methyl lithium and methylpotassium, in which discrete ions are present.

4.7.4.2 RbC_5H_5

The high resolution of a synchrotron radiation experiment was instrumental in the solution of the structures of two polymorphic phases of RbC_5H_5 present in a single sample (Dinnebier *et al.* 1997). Noting that the low-angle peaks fell into two families (Fig. 4.14) the authors were able to index the two sets of peaks separately. Thereafter, SIRPOW92 gave direct solutions of the two different structures, the first in space group $Pbcm$ ($a = 9.3396 \text{ \AA}$, $b = 10.9666 \text{ \AA}$, $c = 10.5490 \text{ \AA}$) and the second in $Pnma$ ($a = 10.7990 \text{ \AA}$, $b = 8.6923 \text{ \AA}$, $c = 5.7061 \text{ \AA}$). Both phases have polymeric zig-zag chains consisting of an array of bent Rb-Cp sandwiches (Cp = cyclopentadiene, C_5H_5). The first has two independent chains perpendicular to each other running along b and c , whereas the second has a single type of chain, running along the a -axis.

4.7.4.3 β -haematin

Another recent application of powder diffraction to organometallic compounds relates to malaria, a disease that kills more than a million people annually. The

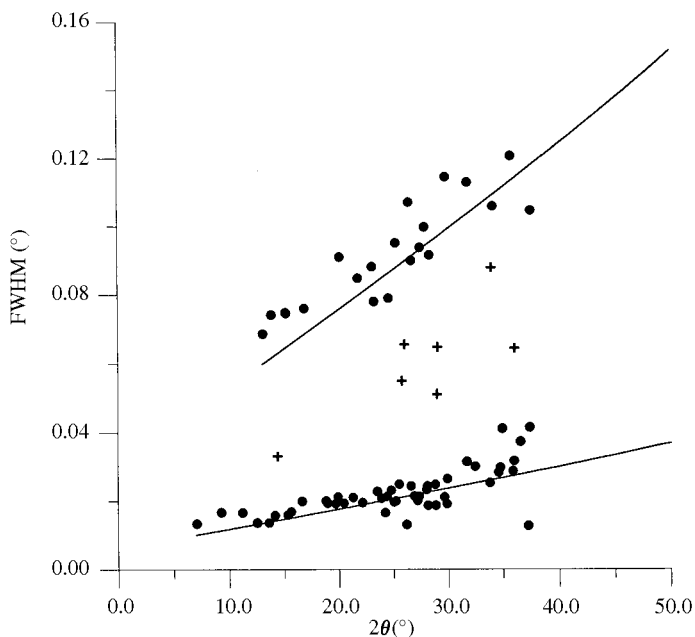


Fig. 4.14. Diffraction peak width versus angle 2θ from a sample comprising two polymorphs of RbC_5H_5 . The smooth curves represent the fitted FWHM from the final Rietveld refinements. Crosses represent groups of peaks that were not visually resolved in the raw data (Dinnebier *et al.* 1997).

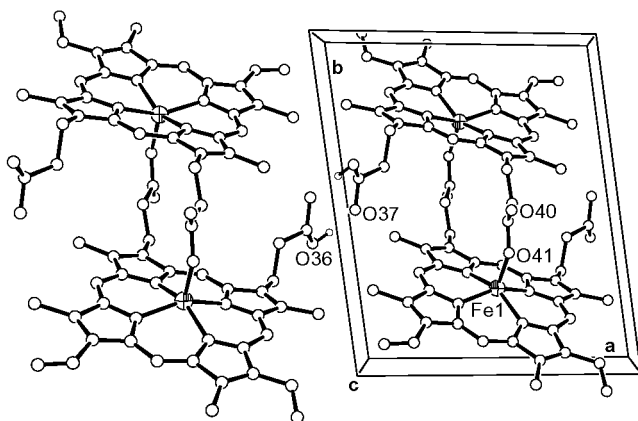


Fig. 4.15. Structure of β -haematin (malaria pigment) determined from powder X-ray diffraction. Formation of dimers, by the inversion operation within each triclinic cell, occurs through the Fe1–O41 bond, whereas dimers are linked into chains by hydrogen bonds through O36 and O37. All other hydrogens are omitted for clarity. From Pagola *et al.* (2000).

haem groups released from the digestion of haemoglobin of malaria-infected red blood cells are aggregated into an insoluble material called haemozoin or malaria pigment. It is suspected that the antimalarial action of quinoline drugs is associated with an inhibition of growth of haemozoin crystals in the digestive vacuole of the malaria parasite *Plasmodium*. β -haematin is a synthetic analogue of malarial haemozoin, known to be chemically and crystallographically identical, but available in powder samples with higher crystallinity. The structure was solved using the simulated annealing program *PSSP*. Previously, it had been believed that haemozoin was a coordination polymer, but in fact, the structure turned out to be a novel dimer of reciprocally esterified porphyrin rings (Fig. 4.15).

4.7.5 More difficult problems

With the exception of some of the structures of microporous materials described above, most solutions are of structures containing less than 20 crystallographically distinct atoms. To go further requires samples (and instrumentation) of the highest quality to yield data with narrow peaks throughout the whole angular range: at low angles for indexing, and at higher angles for accurate profile decomposition. Even then, structures are still usually solved in several steps, though this is changing with the advent of global optimization methods (see Chapters 15 and 16).

4.7.5.1 $Mg_6Co_2H_{11}$

The diffraction pattern of $Mg_6Co_2H_{11}$ was indexed from Guinier photographs, taken with $Co K\alpha_1$ radiation (Cerny *et al.* 1992). A few weak peaks were incompatible with the *C*-centred orthorhombic cell. To check for the presence of a superstructure, synchrotron data were recorded, and these indicated a quadrupling of the cell along *a*, yielding *Pnma* as the true space group. The synchrotron data were collected at three wavelengths close to the Co K edge, so that the changes in the values of f' and f'' could be used to provide better contrast between Co and Mg atoms. The structure was solved in the *C*-centred orthorhombic subcell, from Patterson and Fourier maps, using the contrast provided by the resonant scattering of Co. There are two Co and eight Mg sites in the full structure. Positions for hydrogen atoms were located from neutron diffraction measurements on a deuterated specimen. Twenty possible sites for D were identified by assuming minimum Co–D and Mg–D distances of 1.55 and 1.90 Å, respectively. Refinement showed that 14 of these sites are occupied. The final refinements used neutron and synchrotron data simultaneously. One Co atom has four D ligands, and the other has four or five D ligands because one of the five surrounding sites is half occupied. The structure is therefore partially disordered, and has a three-to-one mixture of $[CoD_4]^{5-}$ and $[CoD_5]^{4-}$ complex

anions, with the limiting ionic formula



This description implies that the compound conforms to the 18-electron rule.

4.7.5.2 $\text{Ga}_2(\text{HPO}_3)_3 \cdot 4\text{H}_2\text{O}$

Another example where neutron diffraction was used to complete a structure whose heavy-atom structure was solved from synchrotron data is $\text{Ga}_2(\text{HPO}_3)_3 \cdot 4\text{H}_2\text{O}$ (Morris *et al.* 1992). A monoclinic unit cell was determined by TREOR from laboratory powder diffraction data. Thermogravimetric analysis and the observation of three distinct P sites from ^{31}P MAS NMR, led to a postulated composition of $\text{Ga}_2(\text{HPO}_3)_3 \cdot 3\text{H}_2\text{O}$. Systematic absences in the synchrotron data were indicative of a two-fold screw axis, which, when combined with SHG measurements, indicated $P2_1$. Following a Le Bail extraction of the intensities, the two Ga atoms were located by Direct methods using SHELX-86. After structure completion using Fourier synthesis, Rietveld refinement and molecular modelling, the final structure, comprising 29 atoms, was refined against the neutron data.

4.7.5.3 $\text{La}_3\text{Ti}_5\text{Al}_{15}\text{O}_{37}$

The laboratory X-ray pattern of $\text{La}_3\text{Ti}_5\text{Al}_{15}\text{O}_{37}$ was indexed in space group $C2/c$ or Cc with $a = 22.54 \text{ \AA}$, $b = 10.97 \text{ \AA}$, $c = 9.67 \text{ \AA}$, and $\beta = 98.49^\circ$ (Morris *et al.* 1994). The intensities were extracted from the high-resolution synchrotron data using the Le Bail method and input to MULTAN84. The positions of the three La atoms and two of the Ti atoms were found in Cc . No sensible solution was found in $C2/c$. Difference Fourier maps revealed nine more metal atoms (assigned to Al) and 27 oxygens. No more atoms could be found with the X-ray data, so neutron data were collected. Following Rietveld refinement using the partial model, ten O and seven more Al atoms were located by difference Fourier synthesis. Following reassignment of one of the Al atoms designated with the X-ray data as Ti, the remaining two Ti atoms were located in a Fourier map. The structure has 60 atoms in the asymmetric unit. The final Rietveld refinement was performed using two neutron diffraction patterns simultaneously. They were collected using different monochromator crystals (Cu (311) and Si (531)) and wavelengths to adjust the optimum resolution to different parts of the diffraction pattern. Restraints were applied to the tetrahedrally coordinated Al atoms to improve the stability of the final refinement. This is one of the most complex structures solved from powder diffraction data to date.

4.7.5.4 $(\text{CH}_3)_2\text{SBr}_2$

$(\text{CH}_3)_2\text{SBr}_2$ was believed to exist in a stable and a metastable form, depending on the method of preparation. Over a period of time, the metastable form

transforms into the stable form as monitored by infrared and Raman spectroscopy. The stable and metastable compounds appear to correspond to a charge-transfer form, $(\text{CH}_3)_2\text{S} \rightarrow \text{Br}_2$, and an ionic form, $(\text{CH}_3)_2\text{SBr}^+\text{Br}^-$, respectively. The crystal structure of the stable form was solved via Direct methods from synchrotron data in space group $P2_1/a$, with a unit-cell volume of 628 \AA^3 (Mora *et al.* 1996). The structure confirmed the postulated charge-transfer nature of the bonding to the bromine molecule giving a near-linear S–Br–Br angle.

In contrast, the high-quality diffraction data collected from the metastable form (Fig 4.16) could not be indexed as a single phase despite concerted efforts. The pattern was eventually indexed as a mixture of two phases using TREOR. By running the program many times, systematically increasing the maximum values of the unit-cell lengths and volume, and allowing a large number of unindexed reflections, but imposing a stringent condition on the agreement between observed and predicted peak positions, a monoclinic cell with a high figure of merit ($M_{20} = 122$) was eventually obtained. Removing the peaks predicted by this cell led to a subset of reflections that could also be indexed with M_{20} of 198 (Vaughan *et al.* 1999).

One phase is monoclinic (unit-cell volume of 936 \AA^3) and the other is orthorhombic (unit-cell volume of 2719 \AA^3). Both crystal structures were solved using Direct methods. The orthorhombic phase corresponds to an ionic form, but with additional bromine molecules in the structure whose presence was not anticipated, giving a composition of $(\text{CH}_3)_2\text{SBr}_{2.5}$. The monoclinic phase resembles the charge-transfer form, and the structure also contains additional bromine atoms, giving $(\text{CH}_3)_2\text{SBr}_4$. Thus, the overall nature and composition

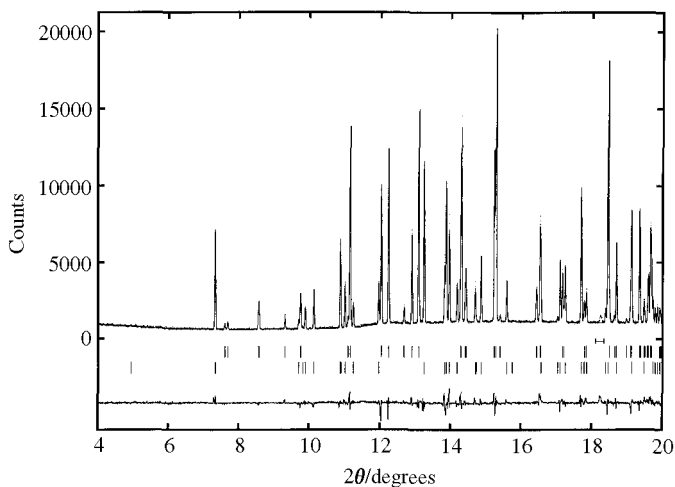


Fig. 4.16. Part of the Rietveld fit to the synchrotron X-ray diffraction pattern of the two metastable forms of $(\text{CH}_3)_2\text{SBr}_x$. From Vaughan *et al.* (1999). The positions of the peaks from the two phases illustrate how interwoven the two patterns are.

are quite different from those expected from the sample preparation. The true character of this sample was learned only when the structures were solved, and it is clear that data of the highest quality was required for this success.

4.7.5.5 *Human insulin–zinc complex*

The structure of human insulin–zinc complex, is truly enormous relative to the small-molecule crystallography usually practised with powder diffraction. Motivated by the observation that powders of protein crystals often have very sharp peaks, indicating crystallite size of $\sim 1\ \mu\text{m}$ and negligible micro-strain, Von Dreele (1999) has adapted the data analysis techniques used in protein crystallography into the Rietveld package GSAS. In practice, the number of stereochemical restraints exceeds the number of points in a diffraction profile.

In an investigation of the human insulin–zinc complex by powder diffraction, it was discovered that grinding crystals of the well-known $\text{T}_3\text{R}_3\text{Zn}$ –insulin complex in mother liquor produced a transformation to a new structure, dubbed $\text{T}_3\text{R}_3\text{DC}$. The biologically active insulin unit consists of an AB pair of polypeptide chains. The $\text{T}_3\text{R}_3\text{Zn}$ –insulin complex is rhombohedral, in which the hexagonal cell contains three $(AB)_2$ dimers (810 non-H atoms per dimer, excluding solvent). Upon grinding, the hexagonal axis approximately doubles, although the molar cell volume decreases by 2.1 per cent. The structure solution started with two independent rigid bodies of the previously known T_3R_3 structure, displaced by half of the c -axis and rotated about it. Once this had converged (with one of the groups rotating by 25° relative to its original position during the refinement), a full stereochemical restraint and Rietveld refinement completed the $\text{T}_3\text{R}_3\text{DC}$ structure. The structure passes the protein stereochemistry tests usually performed during crystallographic refinement. The final refinement was of a pattern with 4800 data points up to $3.22\ \text{\AA}$ resolution (minimum d -spacing), with 2927 reflections, 7981 restraints, and 4893 structural parameters (Von Dreele *et al.* 2000).

4.8 Conclusions

The above discussions and examples illustrate the advantages of using synchrotron radiation to solve crystal structures from powder diffraction data. Narrow peaks, accurate peak positions and excellent signal-to-background ratios mean that these data are ideal for indexing, space group determination and intensity extraction. This, coupled with the flexibility that a modern powder diffractometer at a synchrotron source provides (e.g. sample environment, multiple detectors) means that synchrotron data are ideal for structure solution and refinement. Sadly, despite the excellent quality of synchrotron data and the ingenuity of the scientists who collect it, not all structures can be solved. Every laboratory has a supply of powder data sets which stubbornly refuse to yield to

structure solution. It is the existence of these sets that will act as a continual challenge to both instrumental and algorithmic developments.

Acknowledgements

We gratefully acknowledge G. M. Bendele, R. E. Dinnebier, and B. H. Toby for permission to quote some of their work prior to publication. The calculations in Fig. 4.1 were furnished by J. Gilfrich and S. Hulbert. Work by P. W. Stephens was supported by the National Science Foundation under grant DMR 95-03525 and by the U.S. Department of Energy, Division of Basic Energy Sciences under grant DE-FG02-86ER-45231. Work by D. E. Cox was supported by the US Department of Energy, Division of Materials Sciences, under contract no. DE-AC02-98CH10886.

References

- Akporiaye, D. E., Fjellvåg, H., Halvorsen, E. N., Hustveit, J., Karlsson, A. and Lillerud, K. P. (1996). *J. Phys. Chem.*, **100**, 16641–6.
- Altomare, A., Burla, M. C., Cascarano, G., Giacovazzo, C., Guagliardi, A., Moliterni, A. G. G. and Polidori, G. (1995). *J. Appl. Crystallogr.*, **28**, 842–6.
- Altomare, A., Burla, M. C., Camalli, M., Carrozzini, B., Cascarano, G., Giacovazzo, C., Guagliardi, A., Moliterni, A. G. G., Polidori, G. and Rizzi, R. (1999). *J. Appl. Crystallogr.*, **32**, 339–40.
- Attfield, J. P., Sleight, A. W. and Cheetham, A. K. (1986). *Nature*, **322**, 620–2.
- Attfield, J. P., Cheetham, A. K., Cox, D. E. and Sleight, A. W. (1988). *J. Appl. Crystallogr.*, **21**, 452–7.
- Brown, D. B. and Gilfrich, J. V. (1971). *J. Appl. Physics*, **42**, 4044–6.
- Brown, D. B., Gilfrich, J. V. and Peckerar, M. C. (1975). *J. Appl. Physics*, **46**, 4537–40.
- Burger, K., Cox, D. E., Papoular, R., and Prandl, W. (1998). *J. Appl. Crystallogr.*, **31**, 789–97.
- Caglioti, G., Paoletti, A. and Ricci, F. P. (1958). *Nuclear Instruments and Methods*, **3**, 223–8.
- Cernik, R. J., Murray, P. K., Pattison, P. and Fitch, A. N. (1990). *J. Appl. Crystallogr.*, **32**, 292–6.
- Cerny, R., Bonhomme, F., Yvon, K., Fischer, P., Zolliker, P., Cox, D. E. and Hewat, A. (1992). *J. Alloys Comp.*, **187**, 233–41.
- Cockcroft, J. K. (1995). Private communication.
- Coppens, P. (1992). *Synchrotron radiation crystallography*, Academic Press, New York.
- Cox, D. E. and Wilkinson, A. P. (1994). In *Resonant anomalous X-ray scattering: theory and applications* (ed. G. Materlik, C. J. Sparks and K. Fischer) pp. 195–219, Elsevier Science B.V., Amsterdam.
- David, W. I. F., Ibberson, R. M. and Matthewman, J. C. (1992). *Rutherford Appleton Laboratory Report RAL-92-032*.
- Deem, M. W. and Newsam, J. M. (1989). *Nature*, **342**, 260–2.

- Dinnebier, R. E., Olbrich, F., van Smaalen, S. and Stephens, P. W. (1997). *Acta Crystallogr. B*, **53**, 153–8.
- Dinnebier, R. E., Von Dreele, R., Stephens, P. W., Jelonek, S. and Sieler, J. (1999). *J. Appl. Crystallogr.*, **32**, 761–9.
- Eddy, M. M., Cheetham, A. K. and David, W. I. F. (1986). *Zeolites*, **6**, 449–54.
- Engel, G. E., Wilke, S., König, O., Harris, K. D. M. and Leusen, F. J. J. (1999). *J. Appl. Crystallogr.*, **32**, 1169–79.
- Finger, L. W., Cox, D. E. and Jephcoat, A. P. (1994). *J. Appl. Crystallogr.*, **27**, 892–900.
- Fitch, A. N. and Jobic, H. (1993). *J. Chem. Soc. Chem. Commun.*, 1516–17.
- Hamilton, W. C. (1965). *Acta Crystallogr.*, **18**, 502–10.
- Hammersley, A. P., Svensson, S. O., Hanfland, M., Fitch, A. N. and Häusermann, D. (1996). *High Pressure Res.*, **14**, 235–48.
- Harrison, W. T. A., Gier, T. E., Nicol, J. M. and Stucky, G. (1995). *J. Solid State Chem.*, **114**, 249–57.
- Harvey, G., Baerlocher, C. and Wroblewski, T. (1992). *Z. Kristallogr.*, **201**, 113–23.
- Hastings, J. B., Thomlinson, W. and Cox, D. E. (1984). *J. Appl. Crystallogr.*, **17**, 85–95.
- Hendrickson, W. and Ogata, C. (1997). In *Methods in enzymology*, **276A** (ed. C. W. Carter, Jr. and R. M. Sweet), pp. 494–523, Academic Press.
- Hewat, A. W. (1979). *Acta Crystallogr. A*, **35**, 248.
- Hodeau, J. L., Bordet, P., Anne, M., Prat, A., Fitch, A. N., Doorhyee, E., Vaughan, G. and Freund, A. (1998). *Proceedings SPIE*, **3448**, 353–61.
- Honda, K., Goto, M. and Kurahashi, M. (1990). *Chem. Lett.*, 13–16.
- Hulbert, S. L. and Weber, J. M. (1992). *Nucl. Instrum. Methods Phys. Res. A*, **319**, 25–31.
- Ito, M. and Amemiya, Y. (1991). *Nucl. Instrum. Methods Phys. Res. A*, **310**, 369–72.
- Jephcoat, A. P., Finger, L. W. and Cox, D. E. (1992). *High Pressure Res.*, **8**, 667–76.
- Knudsen, K. D., Pattison, P., Fitch, A. N. and Cernik, R. J. (1998). *Angew. Chem. Int. Ed.*, **37**, 2340–3.
- Langford, J. I., Cernik, R. J. and Louër, D. (1991). *J. Appl. Crystallogr.*, **24**, 913–19.
- Larson, A. C. and Von Dreele, R. B. (1985–94). *GSAS: General Structure Analysis System* (Los Alamos National Laboratory report LAUR 86-748, available by anonymous FTP from mist.lansci.lanl.gov).
- Le Bail, A. (1992). *NIST Spec. Pub.*, **846**, 142–53.
- Lehmann, M. S., Christensen, A. N., Fjellvåg, H., Freidenhans, R. and Nielsen, M. (1987). *J. Appl. Crystallogr.*, **20**, 123–9.
- Lightfoot, P., Cheetham, A. K. and Sleight, A. W. (1987). *Inorganic Chemistry*, **26**, 3544–47.
- Marcos, M. D., Aranda, M. A. G., Sinclair, D. C. and Attfield, J. P. (1994). *Physica C*, **235–40**, 967–8.
- Maslen, E. N. (1995). In *International tables for X-ray crystallography, Vol. C* (ed. A. J. C. Wilson), pp. 520–9. Kluwer Academic Publishers, Dordrecht.
- Materlik, G., Sparks, C. J. and Fischer, K., ed. (1994). *Resonant anomalous X-ray scattering: theory and applications*, Elsevier Science B.V.
- McCusker, L. (1988). *J. Appl. Crystallogr.*, **21**, 305–10.
- McCusker, L. B., Grosse-Kunstleve, R. W., Baerlocher, C., Yoshikawa, M. and Davis, M. E. (1996). *Microporous Mater.*, **6**, 295–309.
- Miyahara, J., Takahashi, K., Amemiya, Y., Kamiya, N. and Satow, Y. (1986). *Nucl. Instrum. Methods Phys. Res. A*, **246**, 572–8.

- Mora, A. J. and Fitch, A. N. (1997). *J. Solid State Chem.*, **134**, 211–14.
- Mora, A. J., Fitch, A. N., Gates, P. N. and Finch, A. (1996). *Mater. Sci. Forum*, **228–31**, 601–6.
- Morris, R. E., Harrison, W. T. A., Nicol, J. M., Wilkinson, A. P. and Cheetham, A. K. (1992). *Nature*, **359**, 519–22.
- Morris, R. E., Owen, J. J., Stalicj, J. K. and Cheetham, A. K. (1994). *J. Solid State Chem.*, **111**, 52–7.
- Norby, P. (1997). *J. Appl. Crystallogr.*, **30**, 21–30.
- Osborn, R. S. and Rogers, D. (1975). *Acta Crystallogr. B*, **31**, 359–64.
- Overell, J. S. W. and Pawley, G. S. (1982). *Acta Crystallogr. B*, **38**, 1966–72.
- Pagola, S., Stephens, P. W., Bohle, D. S., Kosar, A. D. and Madsen, S. K. (2000). *Nature*, **404**, 307–10.
- Parrish, W., Hart, M., Huang, T. C. and Bellotto, M. (1987). *Adv. in X-ray Anal.*, **30**, 373–81.
- Popa, N. C. (1998). *J. Appl. Crystallogr.*, **31**, 176–80.
- Prandl, W. (1990). *Acta Crystallogr. A*, **46**, 988–92.
- Prandl, W. (1994). *Acta Crystallogr. A*, **50**, 52–5.
- Roberts, M. A., Sankar, G., Thomas, J. M., Jones, R. H., Du, H., Chen, J., Pang, W. and Xu, R. (1996). *Nature*, **381**, 401–4.
- Rodriguez-Carvajal, J. (1997). *FullProf version 3.3 (Aug. 1997)* Institut Laue Langevan, unpublished. Available by anonymous FTP from bali.saclay cea.fr.
- Rodriguez-Carvajal, J., Fernandez-Diaz, M. T. and Martinez, J. L. (1991). *J. Phys.: Condens. Matter*, **3**, 3215–34.
- Sabine, T. M. (1993). In *The Rietveld method* (ed. R. A. Young), pp. 53–60, Oxford University Press.
- Sabine, T. M., Kennedy, B. J., Garrett, R. F., Foran, G. J. and Cookson, D. J. (1995). *J. Appl. Crystallogr.*, **28**, 513–17.
- Sasaki, S. (1988). Numerical tables of anomalous scattering factors calculated by the Cromer and Liberman's method, KEK Report 88–14.
- Sinclair, D. C., Aranda, M. A. G., Attfield, P. and Rodrigues-Carvajal, J. (1994). *Physica C*, **225**, 307–16.
- Smith, G. C. (1991). *Synchrotron Radiat. News*, **4(3)**, 24–30.
- Smith, G. S., Johnson, Q. C., Smith, D. K., Cox, D. E., Snyder, R. L., Zhou, R.-S. and Zalkin, A. (1988). *Solid State Commun.*, **67**, 491–4.
- Stephens, P. W. (1999). *J. Appl. Crystallogr.*, **32**, 281–9.
- Suortti, P. (1972). *J. Appl. Crystallogr.*, **5**, 325–31.
- Takata, M., Yamada, M., Kubota, Y. and Sakata, M. (1992). *Adv. X-ray Anal.*, **35**, 85–90.
- Takata, M., Umeda, B., Nishibori, E., Sakata, M., Saito, Y., Ohno, M. and Shinohara, H. (1995). *Nature*, **377**, 46–49.
- Thompson, P., Reilly, J. J. and Hastings, J. B. (1987). *J. Less-Common Metals*, **129**, 105–14.
- Toby, B. H. (1997). Private communication.
- Toraya, H., Takata, M., Hibino, H., Yoshino, J. and Ohsumi, K. (1995). *J. Synchrotron Radiat.*, **2**, 143–7.
- Toraya, H., Hibino, H. and Ohsumi, K. (1996). *J. Synchrotron Radiat.*, **3**, 75–83.
- Ungar, T. and Tichy, G. (1999). *Phys. Status Solidi A*, **171**, 425–34.

- van Laar, B. and Yelon, W. B. (1984). *J. Appl. Crystallogr.*, **17**, 47–54.
- Vaughan, G. B. M., Mora, A. J., Fitch, A. N., Gates, P. N. and Muir, A. S. (1999). *J. Chem. Soc. Dalton Trans.*, 79–84.
- Visser, J. W. (1969). *J. Appl. Crystallogr.*, **2**, 89–95.
- Von Dreele, R. B. (1999). *J. Appl. Crystallogr.*, **32**, 1084–89.
- Von Dreele, R. B., Stephens, P. W., Smith, G. D. and Blessing, R. H. (2000). *Acta Crystallogr. D*, **26**, 1549–53.
- Weiss, E., Corbelin, S., Cockcroft, J. K. and Fitch, A. N. (1990). *Angew. Chem. Int. Ed.*, **29**, 650–2.
- Werner, P. E., Eriksson, L. and Westdahl, J. (1985). *J. Appl. Crystallogr.*, **18**, 367–70.
- Williams, J. H., Cockcroft, J. K. and Fitch, A. N. (1992). *Angew. Chem. Int. Ed.*, **31**, 1655–7.
- Young, R. A., ed. (1993). *The Rietveld method*, Oxford University Press.

Neutron powder diffraction

Richard M. Ibberson and William I. F. David

5.1 Introduction

There is an old adage in powder diffraction that ‘neutron powder diffraction is the technique of choice for structure refinement while X-rays should be used for structure determination’. While this is an over-simplification, it is generally true that the essentially constant nuclear scattering lengths for neutron powder diffraction that are beneficial for refinement are also detrimental for structure solution, because the effective number of visible atoms is higher for neutrons than for X-rays. Accordingly, the vast majority of crystal structure determinations are undertaken using X-ray diffraction data. There are, however, some cases in which neutron diffraction data are to be preferred. In this chapter, we review the technique and instrumentation of modern neutron powder diffraction with emphasis on its role in the determination of crystal structures.

Thermal neutrons are useful as a crystallographic probe because their wavelength spectrum is of the same magnitude as interatomic distances. Neutrons scatter relatively weakly from matter, which means that large samples may be used. This penetrating power leads to several advantages. Diffraction experiments may be performed using complex sample environments such as cryostats and pressure cells and the use of large samples reduces many of the systematic errors commonly associated with X-ray powder diffraction.

Neutrons are scattered by the atomic nucleus but also interact, through magnetic dipolar forces, with unpaired electrons, thus enabling the investigation of magnetic structures. In the area of powder diffraction, neutrons are the technique of choice for the structure determination of magnetic structures. Since the nucleus is a point scatterer, the neutron cross-section is essentially independent of neutron energy and, therefore, can generally be considered to be independent of scattering angle or wave-vector $\kappa = \sin \theta / \lambda = Q / 4\pi$. As a result, strong reflections are commonly observed at both long and short d -spacings. This is of particular value to structure refinement and can also be useful in structure solution. Furthermore, the neutron scattering length varies as an essentially irregular function of atomic number, whereas the comparable X-ray scattering factor relates directly to the number of electrons. X-ray diffraction, in consequence, is dominated by the presence of a heavy atom in a structure, whereas for neutron diffraction, scattering from both light and heavy elements

is of a similar magnitude. X-ray diffraction thus possesses an advantage for structure solution since there are fewer ‘visible’ atoms. As a corollary, neutron diffraction is capable of elucidating the complete structure with greater precision. Arguably, the main role of neutron powder diffraction in structure determination is the validation and completion of structures determined using X-rays. However, there are a number of circumstances, outlined below, in which it can be advantageous to use neutron diffraction data as the principal tool for structure solution.

5.2 Instrumentation

High-resolution neutron time-of-flight powder diffractometers operating at pulsed sources such as HRPD at ISIS and high-resolution instruments on constant wavelength sources such as D2B at the Institut Laue-Langevin (ILL) Grenoble, permit the routine collection of data with a resolution, $\Delta d/d$, better than 10^{-3} . In the case of time-of-flight instruments, this resolution is effectively constant across the whole diffraction pattern. As a direct result of this inherently high resolution, high-quality powder diffraction patterns that contain a large number of well-resolved reflections and consequently a high-information content can be recorded. These high-resolution diffraction data may be collected for Bragg reflections at d -spacings of well below 1 \AA because of the lack of form-factor fall-off. This combination of high resolution and access to high $\sin \theta/\lambda$ is the principal reason that HRPD at ISIS in particular can provide an alternative to single-crystal neutron diffraction for obtaining both accurate and precise structural parameters in relatively simple crystal structures. Low-temperature structure solution has also proven to be more straightforward, because the data collection is technically much simpler with neutrons than with X-rays.

5.3 Autoindexing and space group assignment

In the early stages of structure solution, such as the determination of unit-cell dimensions and the assignment of the correct space group, neutron powder diffraction can, in some cases, offer significant benefits.

Unit-cell determination by autoindexing techniques (see Chapter 7) is, in general, crucially dependent on the availability of the longest d -spacing information from a single-phase powder pattern, regardless of the type of radiation used. High-resolution data provides more precise d -spacing information leading to higher figures of merit and more reliable indexing solutions, but again, these factors are largely independent of the radiation used. The ease of lattice-parameter determination from first principles in the case of high-resolution time-of-flight powder diffraction experiments, however, is impressive. The

technique offers a particular advantage over other methods because in time-of-flight measurements, the fixed instrument geometry leads to a zero-point error which is not only small but becomes progressively less important at large d -spacings, in contrast to the situation in constant-wavelength measurements.

The sensitivity of neutrons to light atoms can be critical to the correct assignment of space group. For example, neutrons are particularly sensitive to the tilting of octahedral TiO_6 groups in perovskites or to the orientation of methyl groups in small organic molecules, both of which may subtly affect the appropriate space group. This is well illustrated by the study of the structure and phase transition in methylammonium tin chloride (Yamamuro *et al.* 1995). This is one of a large family of compounds that have interesting structural and dynamic properties associated with phase transitions. Within the ' $R\bar{3}m$ ' phase of all these compounds, a subtle phase transition occurs between 100 and 200 K. All of the structural and spectroscopic properties change only slightly, but there is a clear heat-capacity anomaly. Significantly, a single crystal X-ray study (Kitahama *et al.* 1979) found the structure to be $R\bar{3}m$ at all temperatures, although the hydrogen atom positions were not determined directly. In contrast, the neutron powder diffraction study carried out on HRPD confirmed an order-disorder transition associated with the CD_3 and ND_3 groups of the methylammonium ion at 156 K, and the true low-temperature space group was shown to be $R\bar{3}$. The high- and low-temperature structures of the CD_3NH_3^+ cations are shown in Fig. 5.1. The two alternative methyl rotations in the disordered phase are separated by about 1 Å and are easily resolved using HRPD.

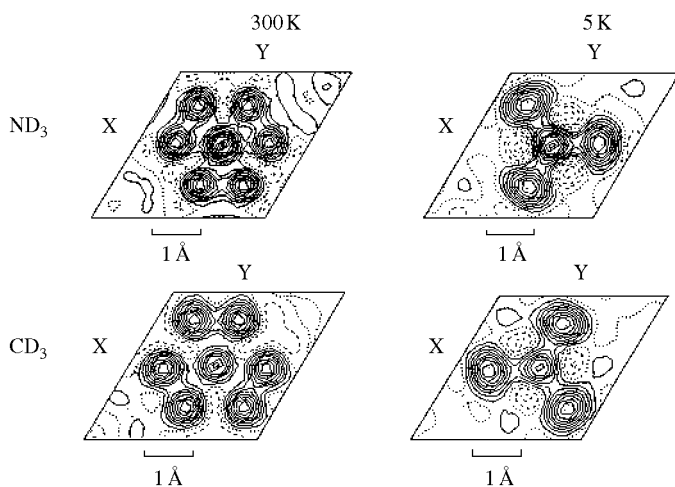


Fig. 5.1. Fourier maps of the CD_3ND_3^+ cations in the high-temperature disordered phase of methylammonium tin chloride at 300 K and the low-temperature ordered phase at 5 K. The sections are shown perpendicular to c at the level of the D atoms.

5.4 Patterson methods

Patterson methods are most effective when there are a limited number of strong scatterers that dominate the interatomic vector map (Chapter 12). This situation is rarely the case with neutron diffraction studies. However, there are cases where the scattering characteristics of neutrons benefit this technique. For example, the sensitivity in neutron diffraction data to the hydrogen atoms decorating, for example, a benzene ring is useful in Patterson methods to emphasize the planarity of the group to be located. For powder studies of organic compounds, hydrogen is ideally replaced by deuterium, which has essentially the same scattering length as carbon. The scattering dependence of neutrons upon the nucleus is a combination of potential and resonance scattering and it is the sum of these two factors that facilitates differentiation between isotopic species of an element. Of more potential interest is the occurrence of negative scattering factors for some elements. This phenomenon offers the unique concept of Patterson techniques using negative-channel pattern decomposition. This is discussed further in Chapter 12, where the particular case of the synthetic mineral sphene, CaTiSiO_5 , is outlined.

5.5 Direct methods

The more uniform nature of scattering lengths and the ability to record data out to high Q values make Direct methods a more attractive technique than Patterson methods for structure solution using neutron powder diffraction data. The practicability of *ab initio* determination from neutron powder data was demonstrated by Cheetham *et al.* as early as 1986 with the structure of ferric arsenate, FeAsO_4 . The structure is monoclinic, space group $P2_1/n$, with a unit-cell volume of 296.55 \AA^3 and six atoms in the asymmetric unit, and its solution by Direct methods was a *tour de force*. Given that structure solution of inorganic compounds using X-rays is relatively straightforward, the literature for *ab initio* solution from neutron powder data alone is, in this particular field, restricted (see for example Balsys and Davis 1994, 1997, for studies of layered alkali-transition metal oxides, and Harrison *et al.* (1995a) on the structure of $\text{Sr}_6\text{Co}_5\text{O}_{15}$).

In recent years, the majority of crystal structures that have been determined solely from neutron powder data are molecular. These include *ortho*-xylene (Ibberson *et al.* 2000b), acetaldehyde (Ibberson *et al.* 2000c), dimethyl sulphide (Ibberson *et al.* 1997), methyl fluoride (Ibberson and Prager 1996), dimethyl acetylene (Ibberson and Prager 1995), trichlorofluoromethane (Cockcroft and Fitch 1994), rhenium heptafluoride (Vogt *et al.* 1994), trifluoriodomethane (Clarke *et al.* 1993), malonic acid (Delaplane *et al.* 1993), tribromofluoromethane (Fitch and Cockcroft 1992), trifluorobromomethane (Jouanneux *et al.* 1992) and cyanamide (Torrie *et al.* 1992). This success is due to a number of

factors. Many of these structure solutions and space group assignments depend crucially on accurate hydrogen atom location. With neutron diffraction data, this can be done with ease, particularly if the sample is deuterated. Moreover, the low melting point of the majority of the examples cited above presents additional technical problems for X-ray studies, either in terms of producing and handling small single crystals, or producing small volumes of polycrystalline materials that exhibit a good powder average.

The complexity of structure solution by Direct methods tenable by neutron powder diffraction remains modest even with recourse to the sophisticated intensity extraction procedures detailed in Chapters 8–11. The monoclinic structure of *ortho*-xylene, $V = 634 \text{ \AA}^3$, with 18 atoms in the asymmetric unit and the triclinic structure of dimethyl sulphide, $V = 179 \text{ \AA}^3$, with nine atoms in the asymmetric unit represent some of the most complex examples tackled to date.

5.6 X-n structure solution

The limits of structural complexity that can be solved and refined from powder data have been substantially increased by harnessing the combined power of X-ray and neutron diffraction. For example, in the study of the non-aluminosilicate open framework material LiZnPO_4 , Harrison *et al.* (1995*b*) used synchrotron X-ray data and Direct methods in order to establish the framework structure. Having established the location of the framework species, neutron data were then used to locate and refine locations for the lithium and water molecule guests. A similar approach was used by Morris *et al.* (1992) in order to elucidate the novel framework structure of monoclinic $\text{Ga}_2(\text{HPO}_3)_3 \cdot 4\text{H}_2\text{O}$ (space group $P2_1$) with a total of 29 atoms in the asymmetric unit and a unit-cell volume of 580 \AA^3 . Synchrotron X-ray data were collected on beam line X7A at the NSLS, Brookhaven National Laboratory and structure factors for 551 reflections were extracted from the powder pattern. Structure solution using Direct methods produced an *E*-map with two large peaks that were assigned as gallium atoms. Fourier recycling revealed a further four atoms that were assigned to be two phosphorus and two oxygen atoms. The atomic coordinates were then refined using the Rietveld method and subsequent Fourier syntheses revealed the positions of a further phosphorous atom and 10 more oxygen atoms. Thus, a total of 17 atoms were located in the asymmetric unit from the X-ray data. In order to complete the structure solution and improve the overall quality of the structure refinement, neutron diffraction data were recorded on diffractometer BT-1 at the National Institute of Standards and Technology. Computer graphics techniques were used to add the positions of phosphite deuteriums and two of the water deuteriums to the model. Rietveld refinement against the neutron data was then possible. An additional water oxygen and the remaining deuterium

atoms were located from subsequent cycles of refinement and Fourier synthesis. This complementary use of synchrotron X-ray and neutron powder diffraction data illustrates well the potential for tackling considerably more complex structures using what may be described as traditional crystallographic methods.

Following their work on gallium phosphite, Morris *et al.* (1994) proceeded to solve the structure of $\text{La}_3\text{Ti}_5\text{Al}_{15}\text{O}_{37}$ that has 60 atoms in the asymmetric unit, again using a combination of synchrotron X-ray and neutron powder diffraction. The overall results are impressive; the structure is non-centrosymmetric (space group Cc) with a unit-cell volume of 2383 \AA^3 . X-ray data were used to locate the bulk of the metal atoms and 27 of the oxygen atoms. The role then played by the neutron data is of particular interest since, in addition to providing the location of the remaining oxygen atoms, it proved crucial in resolving an incorrect assignment of aluminium for titanium in the analysis of the synchrotron data. In the final analysis, a joint-Rietveld refinement of the structure was carried out using two neutron data sets recorded at on BT-1 at NIST with Cu(311) and Si(531) monochromators ($\lambda = 1.539$ and 1.589 \AA , respectively). The higher take-off angle for the Si(531) crystal compared with the Cu(311) monochromator yields greater resolution for the high-angle data that is especially important for precise structure refinement.

5.7 Future possibilities

As the desire to solve more complex structures from powder diffraction data grows, the need to combine X-ray and neutron powder diffraction data will increase. The remarkable success of Morris *et al.* with $\text{La}_3\text{Ti}_5\text{Al}_{15}\text{O}_{37}$, described in the previous section, will become more commonplace as X-ray powder diffraction data alone prove to be inadequate. The recently developed global optimization techniques (see Chapter 15) will also benefit from the availability of neutron powder diffraction data. These techniques often utilize diffraction data to molecular ($d_{\text{min}} \sim 1.5$ to 2.5 \AA) rather than true atomic resolution ($d_{\text{min}} \sim 1 \text{ \AA}$), and this can leave a degree of ambiguity in the location of some of the atoms within the crystal structure. The availability of neutron powder diffraction data provides essentially an independent verification of the correctness of the proposed crystal structure. If the proposed crystal structure agrees with both X-ray and neutron powder diffraction data, one can be confident that the structure is correct. Moreover, the neutron powder diffraction data can help in the location of light atoms such as hydrogen and lithium and in the discrimination between atoms such as nitrogen and oxygen in a molecular crystal structure. A typical example is illustrated in Fig. 5.2 where two structures of tetracycline hydrochloride are shown.

This material was used as part of an unofficial ‘SDPD Round-Robin challenge’ issued in 1998. Both structures have essentially equivalent goodness of fit

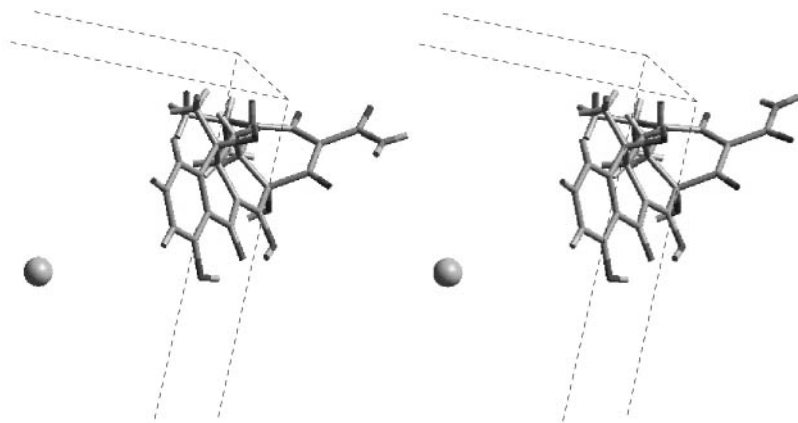


Fig. 5.2. Two crystal structures for tetracycline hydrochloride obtained by simulated annealing. The structures differ only in the orientation of the small planar fragment [C–CO–NH₂] to the right of the fused-ring system. It is difficult to distinguish between them on the basis of X-ray powder diffraction data but with neutron data the difference is substantial.

to the powder X-ray diffraction data. The only difference is the 180° rotation of the NH₂ and the oxygen atom about the C–C bond on the right-hand ring. It is difficult to distinguish between the two alternatives with X-ray diffraction alone as the number of electrons is so similar for the NH₂ and O. With 1.5–2 Å resolution data, it is also difficult to discriminate on the basis of bond lengths. With neutron diffraction data there is no such problem. The hydrogen atoms are immediately visible and the nitrogen scattering length is some 60 per cent larger than that of oxygen.

The uses of neutron powder diffraction data in global optimization methods are not, however, restricted to the ‘end-game’ of structure solution. For example, the orthorhombic structure of *meta*-xylene, with 18 atoms in the asymmetric unit and a cell volume of 1280 Å³, was solved routinely using global optimization methods applied to neutron data (Ibberson *et al.* 2000*a*). Other more recent examples of this technique include solution of the phase III structure of methane (Neumann *et al.* 2003) and the phase II structure of dimethyl sulfate (Ibberson *et al.* 2006).

The negative scattering lengths of hydrogen can actively be used to discriminate between the outer-molecular envelope (corresponding to the hydrogen atom positions) and the molecular backbone. A two-channel, positive–negative maximum entropy (ME) map phased from a small number of reflections provides superior contrast to a map containing only positive scattering density. This is exemplified by the example of sulphamide. Data were collected on

Table 5.1 The phased-structure factors used in the construction of the $hk0$ projection of sulphamide. The phases of the weak reflections are not known. However the bimodal distribution can be well approximated by a single Gaussian distribution centred at zero

| h | k | l | F | $\sigma(F)$ |
|-----|-----|-----|------|-------------|
| 6 | 12 | 0 | 0.0 | 0.1 |
| 4 | 14 | 0 | 0.0 | 0.1 |
| 4 | 8 | 0 | 0.0 | 0.1 |
| 10 | 4 | 0 | 11.4 | 0.4 |
| 6 | 6 | 0 | 13.9 | 0.1 |
| 2 | 8 | 0 | 14.7 | 0.1 |

HRPD at ISIS. The crystal structure is orthorhombic with space group $Fdd2$ and lattice constants $a = 9.6479$, $b = 16.7624$ and $c = 4.4939$ Å. With the active use of only six centric $hk0$ reflections, it is possible to locate the molecule within the ab plane. Three strong and three weak $hk0$ reflections were used in the construction of the scattering density. These are listed in Table 5.1.

In contrast with traditional Fourier methods, the weak reflections have a valuable role to play. ME maps are consistent with the observed structure factor data and are not precluded from containing non-zero Fourier components associated with unobserved data. The addition of weak reflection information forces the ME map to have only very small Fourier components associated with these reflections. Remarkably, in the positive channel of the Fourier projection shown in Fig. 5.3(a), the nitrogen atoms are revealed very clearly along with the oxygen atoms. The sulphur atom is invisible. This is to be expected since nitrogen is the relatively 'heavy atom' for neutrons, while sulphur is a weak scatterer. The relative scattering lengths of the main atoms in organic molecules are listed in Table 5.2 with their 'X-ray equivalent' scattering—oxygen is taken to be the reference standard. The negative ME map is less clear cut. Although the hydrogen atom positions are clearly indicated, the strongest feature is related to the positive scattering density associated with the nitrogen. This is perhaps not unexpected since so few Fourier components are being used.

The potential presence of both positive and negative scattering density in a neutron diffraction Fourier map is commonly considered to be disadvantageous, because the positivity premise (and, consequently, triplet relationships) of Direct methods is violated. However, this example of sulphamide illustrates that there is extra information when negative scattering occurs, since two maps rather than one can be constructed. The contrasting visibility of different atoms for neutrons and X-rays can also be harnessed to good advantage. Although neutron powder diffraction data will always be used less frequently than X-ray data for structure solution, the complementary information available from

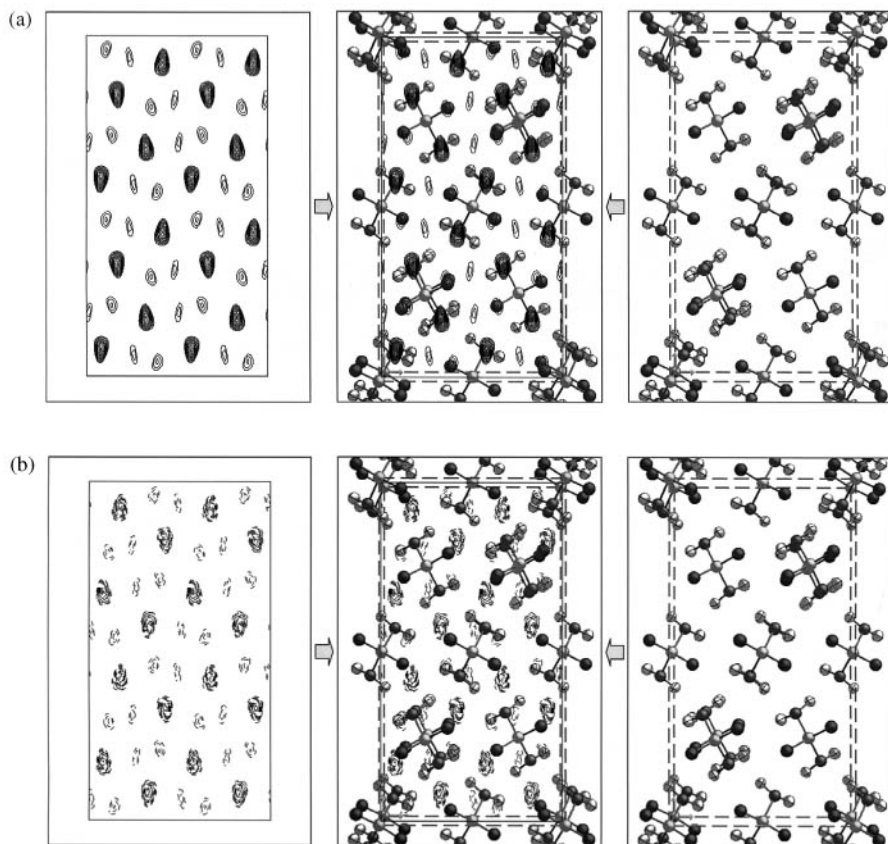


Fig. 5.3. (a) Positive and (b) negative channel ME projections for sulphamide. Using only three phased strong reflections and three unphased weak reflections, all the atoms in the projected structure of sulphamide are clearly determined. The latter map shows only hydrogen positions while nitrogen and oxygen positions (sulphur scatters weakly) are clearly located in the positive channel. The figures are arranged as follows: projection only (left), projection plus overlaid structure (centre), structure only (right).

Table 5.2 Common elements in organic materials and their neutron scattering lengths. The element associated with the effective equivalent X-ray scattering factor is shown in the third column (the scattering factors are scaled relative to oxygen)

| Atom | b (10^{-15} m) | X-ray 'equivalent' |
|------|---------------------|--------------------|
| C | 6.65 | F |
| N | 9.40 | Al |
| O | 5.80 | O |
| S | 2.87 | Be |
| H | -3.74 | B |
| D | 6.67 | F |

neutron diffraction data will become increasingly important as more complex crystal structures are tackled. In particular, neutron powder diffraction may prove to be an invaluable additional technique for crystal structures that have more than one molecule within the asymmetric unit, where molecular-envelope information can provide a significant constraint upon the complex search space that needs to be explored by global optimization methods.

References

- Balsys, R. J. and Davis, R. L. (1994). *Solid State Ionics*, **69**, 69–74
- Balsys, R. J. and Davis, R. L. (1997). *Solid State Ionics*, **93**, 279–82.
- Cheetham, A. K., David, W. I. F., Eddy, M. M., Jakeman, R. J. B., Johnson, M. W. and Toradi, C. C. (1986). *Nature*, **320**, 46–8.
- Clarke, S. J., Cockcroft, J. K and Fitch, A. N. (1993). *Z. Kristallogr.*, **206**, 87–95.
- Cockcroft, J. K. and Fitch, A. N. (1994). *Z. Kristallogr.*, **209**, 488–90.
- Delaplane, R. G., David, W. I. F., Ibberson, R. M. and Wilson, C. C. (1993). *Chem. Phys. Lett.*, **201**, 75–8.
- Fitch, A. N. and Cockcroft, J. K. (1992). *Z. Kristallogr.*, **202**, 243–50.
- Harrison, W. T. A., Hegwood, S. L. and Jacobson, A. J. (1995a). *J. Chem. Soc. Chem. Commun.*, 1953–4.
- Harrison, W. T. A., Gier, T. E., Nicol, J. M. and Stucky, G. D. (1995b). *J. Solid State Chem.*, **114**, 249–57.
- Ibberson, R. M. and Prager, M. (1995). *Acta Crystallogr. B*, **51**, 71–6.
- Ibberson, R. M. and Prager, M. (1996). *Acta Crystallogr. B*, **52**, 892–5.
- Ibberson, R. M., McDonald, P. J. and Pinter-Krainer, M. J. (1997). *J. Mol. Struct.*, **415**, 259–66.
- Ibberson, R. M., David, W. I. F., Parsons, S., Prager, M. and Shankland, K. (2000a). *J. Mol. Struct.*, **524**, 121–8.
- Ibberson, R. M., Morrison, C. and Prager, M. J. (2000b). *J. Chem. Soc. Chem. Commun.*, 539–40.
- Ibberson, R. M., Yamamuro, O. and Matsuo, T. (2000c). *J. Mol. Struct.*, **520**, 265–72.
- Ibberson, R. M., Telling, M. F. T. and Parsons, S. (2006). *Acta Crystallogr. B*, **62**, 280–6.
- Jouanneaux, A., Fitch, A. N. and Cockcroft, J. K. (1992). *Molecular Physics*, **71**, 45–50.
- Kitahama, K., Kiriya, H. and Baba, Y. (1979). *Bull. Chem. Soc. Jpn*, **52**, 324–8.
- Morris, R. E., Harrison, W. T. A., Nicol, J. M., Wilkinson, A. P. and Cheetham, A. K. (1992). *Nature*, **359**, 519–22.
- Morris, R. E., Owen, J. J., Stalick, J. K. and Cheetham, A. K. (1994). *J. Solid State Chem.*, **111**, 52–7.
- Neumann, M. A., Press, W., Nöldeke, C., Asmussen, B., Prager, M. and Ibberson, R. M. (2003). *J. Chem. Phys.*, **119**, 1586–9.
- Torrie, B. H., Von Dreele, R. and Larson, A. C. (1992). *Molecular Physics*, **76**, 405–10.
- Vogt, T., Fitch, A. N. and Cockcroft, J. K. (1994). *Science*, **263**, 1265–7.
- Yamamuro, O., Matsuo, T., Suga, H., David, W. I. F., Ibberson, R. M. and Leadbetter, A. (1995). *Physica B*, 213–214, 414–16.

Sample preparation, instrument selection and data collection

Roderick J. Hill and Ian C. Madsen

6.1 Introduction

The importance of careful sample preparation and data collection in powder diffraction studies has been described on several previous occasions (Hill and Madsen 1987; Bish and Post 1989; Hill 1993; and references therein). Nevertheless, the process of collecting diffraction data is often entered into without adequate forethought about the purpose of the data collection or its impact on the outcomes of the experiment. Laboratory instruments normally have a 'favoured' configuration which is used for a wide range of experiments. While this is convenient, it is often not suitable for all of the data collections that take place in the laboratory. Even at large installations, folklore and/or time pressures, rather than a considered approach, often dictate data collection protocol.

In designing a powder diffraction experiment, it should be remembered that there are a multitude of possible reasons for collecting diffraction data on a sample. These include the qualitative and quantitative phase analysis of a multi-phase mixture, the determination of unit-cell dimensions through pattern indexing, the solution of an unknown crystal structure, or the refinement of a partially known structure using the Rietveld method. In the context of this book, structure determination lies in the foreground, so its requirements will be emphasized. Considerations specific to Rietveld refinement have been discussed previously (Hill 1993; McCusker *et al.* 1999).

For the solution and/or refinement of a crystal structure, the peak intensities must accurately represent the inherent scattering from the crystal lattice, free from aberrations that might be introduced by the sample or the instrument. In other words, the diffraction pattern must be an unbiased representation of the intensity-weighted reciprocal lattice. If, however, unit-cell determination and indexing (see Chapter 7) is the primary purpose of the experiment, the peak intensities are of less concern than the peak positions. In this case, the positions of the peaks must accurately reflect the d -spacing of the reflections involved and their widths and shapes need to be such that they can be readily

modelled with existing peak profile functions. Thus, the experiment might be constructed differently, depending on the information required.

6.2 Issues and early decisions—experimental design

There are three central issues to be addressed before data collection begins. The first relates to the sample itself. What is the form of the sample? Is it a powder or can it be processed into a powder? How much sample is there? Is there enough for neutron analysis (if required) or only enough for a small capillary or a thin-film sample mount? Will the data be free of sample-related aberrations, such as preferred orientation or extinction, due to size and shape effects?

The second main issue involves the selection of the most appropriate diffraction instrument for the experiment. What radiation should be used? Are X-rays the most appropriate radiation? Is access to a synchrotron facility required for additional intensity or resolution (see Chapter 4)? If neutron data are better suited, perhaps because of sample absorption or the need to determine light atom positions (see Chapter 5), should a high- or low-resolution instrument be used? Having decided on the radiation, it is necessary to consider the instrument geometry. Most laboratory diffractometers are set up in reflection mode, but an increasing number of laboratories are equipped with capillary transmission mode setups. At neutron and synchrotron facilities, capillary mode is almost universal.

The third and final issue relates to the desirable characteristics of the data. What d -spacing range is required? What should the step width between the data points be? How intense should the pattern be? That is, what exposure time is required, or how long should the counter dwell at each point? Should a fixed or variable counting time strategy be employed?

All of the factors mentioned above are within the control of the experimentalist and all have the potential to affect the outcome of the data analysis. Since the choice of experimental conditions will also be partly governed by the total time available on the instrument of choice, this may require that the optimum data collection conditions be compromised, or, in some cases, the speed of data collection may be governed by the sample itself. If, for example, the sample is unstable, or if it is used in a dynamic study, there may be a need to collect the data more rapidly than normal. In this case, it may be necessary to choose between a conventional detector system and one that collects the whole pattern simultaneously using a position sensitive detector, an image plate or a film.

In this chapter, the following issues are addressed: (a) the need for multiple datasets, (b) the effect of sample characteristics, (c) the diffraction instrument and (d) data collection strategies and the manner in which they influence the diffraction pattern and the quality of data analysis. The discussion relates equally to pattern indexing, structure solution, Rietveld refinement and phase

analysis, although it is clear that the emphasis will vary in each of these applications.

6.3 Multiple datasets

During the course of a full structure determination and refinement from powder data it can be advantageous to collect several diffraction patterns under conditions optimized for each of the analytical steps involved. This addresses and corrects the common practice in which all operations are performed using a single dataset. The latter leads to compromises being made, and has the potential to cause errors in the final result. The set of recommended patterns includes:

1. *A reconnaissance pattern* for the identification of phases by search-match methods, for the preliminary investigation of the suitability of the sample (e.g. purity), and to decide on future data collection conditions (d -spacing range, step width and pattern intensity). Such a pattern can be collected quite rapidly over a limited d -spacing range.
2. *An indexing pattern* to be used in the determination of the unit-cell dimensions via pattern indexing. Ideally, in a laboratory X-ray experiment, this pattern should be collected with an internal standard (for accurate 2θ calibration) and a thin-film sample mount (to minimize sample-related aberrations in a Bragg-Brentano setup) and would be limited to the 20–40 largest d -spacings.
3. *The pattern decomposition pattern* to be used for the extraction of integrated intensities for subsequent structure solution. This pattern needs to be collected over a wide d -spacing range with the highest possible resolution to allow a maximum separation of adjacent peaks and with high intensities to ensure the good counting statistics required for the decomposition of both strong and weak reflections. Step size should be selected according to the characteristics of the pattern (see Section 6.6.1).
4. *The structure refinement pattern* to be used for the Rietveld refinement of the structure. This pattern has the same requirements as the previous one, but should also include the smallest practical d -spacings. These low d -spacing reflections are essential for a precise refinement of the structure parameters.
5. *A second refinement pattern* might be collected with a different wavelength or radiation source to resolve problems in the structure refinement. For example, if most of the work has been carried out using laboratory X-ray data, a neutron dataset may be required to obtain accurate refinement of light atoms, selected atom site occupation factors or thermal parameters.

Specific discussion of the need for, and requirements of each of these data sets will be described at appropriate points in the discussion below.

6.4 The sample

One of the most critical steps in diffraction analysis is to minimize systematic sample-related effects and instrumental aberrations *before* data collection begins. Very often the models for the correction of aberrations are only approximations, which do not adequately correct for large errors in the data. A computer program should never be used to make gross corrections for poor sample preparation or inappropriate instrument configuration. Rather than persisting with poor data, it is better to (a) re-prepare or remake the sample, (b) find a more suitable sample, or (c) change to another instrumental configuration and/or wavelength.

6.4.1 Sources of sample-related errors

A summary of some of the typical sample-related problems and their possible solutions can be found in Table 6.1. It should be noted that sometimes a sample ‘problem’ can actually provide useful information. For example, while preferred orientation can often cause difficulties in the measurement of unbiased powder intensities, the same effect can be used to obtain more information in an intensity extraction process (see Chapter 9).

6.4.2 Number of crystallites contributing to the diffraction process

For structure refinement, it is generally accepted that the peak intensities need to be measured to a precision of about ± 2 per cent because this is a reasonable target for the agreement between observed and calculated intensities in the structure refinement step. As indicated in Table 6.2, the ability to achieve this precision is strongly governed by the size of the crystallites in the sample. Reproducible diffraction intensities require a small crystallite size in order to ensure that all parts of the Debye–Scherrer cone are equally populated by the diffracted beams.

Table 6.3 shows that for a typical sample volume of 20 mm^3 there can be as few as 12 crystallites diffracting if their size is about $40 \mu\text{m}$, but this figure increases by more than three orders of magnitude if the crystallite size is reduced to $1 \mu\text{m}$. It should be noted, of course, that single-crystal diffraction patterns can now be collected on crystallites with volumes of less than $1000 \mu\text{m}^3$ at synchrotron microcrystal facilities, so if there are large crystallites in the sample, this alternative route to structure solution should be considered before the sample is ground.

Elton and Salt (1996) have used both theoretical and experimental methods to estimate the number of crystallites diffracting (N_{diff}) in a sample. They have shown that variations in line intensity between replicate samples arise largely from the statistical variation in the number of particles contributing to the diffraction process and that small changes to the instrumental and/or sample

Table 6.1 A list of some sample related problems, their cause and possible solutions

| Effect | Cause | Possible solution |
|---|---|---|
| Inaccurate peak intensity measurement | Not enough crystallites contributing to the diffraction process | Reduce the crystallite size Spin the sample Increase beam divergence |
| Poor reproducibility of peak intensities | Sample not representative of the 'bulk'—not enough crystallites in the sample | Adopt better sub-sampling strategies Reduce the crystallite size |
| Enhanced or reduced peak intensities along particular crystallographic directions | Preferred orientation | Reduce the crystallite size Change sample presentation (side-mount rather than back-press; use capillary geometry) Include randomizing sample movements Introduce a diluent Average the intensity around the Debye-Scherrer 'rings' |
| Low-angle intensities observed with lower than expected intensity | Incident beam 'footprint' too large; surface roughness; extinction | Match footprint of beam and sample by correct selection of slits Smooth the sample surface Reduce crystallite size Introduce crystal strain Use a shorter wavelength of radiation |
| High background | Sample fluorescence; incoherent scattering; air scatter | Change wavelength Deuterate the sample Evacuate the beam path Use a diffracted beam monochromator |

configuration can significantly improve the sample statistics. An estimate of the fractional particle statistics error, σ_{PS} , is given by:

$$\sigma_{PS} = \frac{\sqrt{N_{\text{diff}}}}{N_{\text{diff}}} \quad (6.1)$$

Estimated values of N_{diff} are dependent on the number of particles being irradiated and the solid angular range over which the particle can diffract.

Table 6.2 Typical intensity reproducibility for quartz (113) reflection using Cu K α (from Klug and Alexander 1974)

| | | | | |
|---------------------------|---------------------|--------------------|--------------------|-------------------|
| Crystallite size range | 15–20 μm | 5–50 μm | 5–15 μm | < 5 μm |
| Intensity reproducibility | 18.2% | 10.1% | 2.1% | 1.2% |

Table 6.3 Relationship between crystallite diameter and number of crystallites diffracting (from Smith 1992)

| | | | |
|---------------------------------|--------------------|--------------------|-----------------------|
| Crystallite diameter | 40 μm | 10 μm | 1 μm |
| Crystallites/20 mm ³ | 5.97×10^5 | 3.82×10^7 | 3.82×10^{10} |
| No. crystallites diffracting | 12 | 760 | 38 000 |

6.4.3 Increasing the number of crystallites examined

For a given sample, several methods can be used to increase the number of crystallites contributing to the diffraction pattern.

1. Use an instrument with wider beam divergence (σ_{PS} reduced by a factor of about two). However, it should be noted that this will reduce the overall instrumental resolution and lead to greater peak overlap, so might not be appropriate if structure determination is planned.
2. Rotate the sample about the normal to the sample surface for a flat-plate sample or about the sample axis for a capillary sample (σ_{PS} reduced by a factor of about five or six).
3. Oscillate the sample about the theta axis (flat plate only). Note that this motion defeats the exact $\theta/2\theta$ relationship between sample and receiving slit and may lead to aberrations in the peak intensities, positions and profile shapes when using a Bragg–Brentano setup with a non-parallel X-ray beam.
4. Repack the sample, recollect and reanalyse the diffraction data. Averaging the results from each analysis will produce more meaningful parameter values and will allow better determinations of their estimated standard deviations (e.s.d.s).
5. Average the data sets collected in (4). This will increase the precision of the final estimates.

For heavily absorbing materials, the beam will not penetrate as far into the sample and the overall volume of diffracting material will therefore be smaller. Equation (6.2) shows the relationship between linear absorption coefficient (μ) and penetration depth (t):

$$t = \frac{3.45}{\mu} \sin \theta \quad (6.2)$$

For quartz (SiO₂) with a Cu K α source and a diffraction angle of 30° 2θ , $\mu = 95 \text{ cm}^{-1}$ and t is approximately = 95 μm . For hematite (Fe₂O₃), with $\mu = 1146 \text{ cm}^{-1}$, the penetration depth is only 7.8 μm .

The most effective method of increasing the number of crystallites examined is simply to reduce the average crystallite size by carefully grinding the sample. However, while too little grinding results in an inadequate reduction of size, over-grinding often changes the sample. This can result in (a) generation of amorphous layers at the surface, (b) peak-broadening related to crystallite size and strain effects, and (c) solid-state phase transitions. These problems are significantly reduced by grinding in a liquid (e.g. alcohol or acetone), which tends to reduce local heating of the sample in the grinding vessel.

It should be noted that all methods of grinding will cause some contamination from the grinding vessel unless the vessel and sample have the same phase composition. The aim should always be to minimize the contamination, or at least to ensure that the contaminating material does not significantly interfere with the diffraction pattern. Materials commonly used in grinding vessels include agate (SiO_2), tungsten carbide (WC), tool steel (Fe), corundum (Al_2O_3)

Table 6.4 A comparison of different methods of crystallite size reduction with their potential benefits and shortcomings

| Technique | Benefits | Drawbacks |
|-----------------------------|--|--|
| Hand mortar and pestle | Cheap and readily available | Tedious to use, especially if small particle sizes are required |
| Automatic mortar and pestle | Can produce small sizes ($\sim 3\ \mu\text{m}$) in reasonable times (several minutes) Can be used for 'dry' or 'wet' grinding | |
| McCrone micronising mill | Capable of routinely producing sizes of $\sim 10\ \mu\text{m}$ with a small spread of sizes Use of grinding fluid minimizes structural damage | The use of 48 grinding elements can make it tedious to clean |
| Rotary (Sieb-Technik) mills | Effective for initial grinding of very large grains ($> \text{a few mm}$) | Can cause severe structural damage Not suitable for fine grinding; broad range of particle sizes produced |
| Ball mills | Rapid reduction of particle size | Can be tedious to clean Cannot easily accommodate liquids so can cause severe structural damage |

and zirconia (ZrO_2). A summary of some of the commonly used methods of size reduction is given in Table 6.4.

6.4.4 *Generating random orientation*

In order to generate peak intensities that are representative of the intensity-weighted reciprocal lattice, the crystallites in the powder must not only be sufficient in number, but they must also be randomly oriented. That is, each crystal orientation should have the same probability of diffracting.

A number of sample preparation methods can be used to minimize preferred orientation. For flat specimens, back-pressing and side-loading into the sample holder tend to produce much less preferred orientation than front-mounted samples. However, they tend not to be very effective for phases with extreme morphologies like clays. The addition of solid diluents such as gum arabic, glass, gelatin or the use of a binder material can reduce preferred orientation, but will contaminate the sample, increase the average transparency, and produce amorphous scatter (resulting in an increase in the pattern background) or the appearance of extra peaks in the pattern. Spray drying is quite effective in reducing preferred orientation, but is not suited to small samples (<1 g). To work effectively, the particles used in a spray drier should be < 5 μm . Sample motion at 90° to the diffraction vector produces the most effective reduction of preferred orientation. The added benefit is that the sample motion also improves particle statistics, but it should be borne in mind that rocking changes the $2:1\ 2\theta:\theta$ relationship in the Bragg–Brentano case.

6.4.5 *Removing extinction*

Multiple diffraction of the X-ray or neutron beam within the crystallites (extinction) can result in the systematic attenuation of the high-intensity, low-angle data. The effect is most commonly observed in a material with larger perfect crystallites and is rarely a problem with fine powders. Hence, the effect can be reduced by fine grinding to decrease the mosaic size and/or introduce lattice strain. Extinction can also be reduced by decreasing the wavelength used in the experiment. Care must be taken in interpreting the presence of extinction in a sample as it is often confused with other effects that cause similar decreases in large peak intensities, such as detector dead time, preferred orientation or surface roughness (for reflection geometry).

6.5 **The instrument**

The choice of diffraction instrument is often governed by availability rather than by careful consideration of the instrument most suited to the needs of the experiment. While it is always easier to collect data on a laboratory instrument than to travel to the large, and often difficult to access, neutron and synchrotron sources, this should not be the governing criterion in selecting the instrument.

6.5.1 *What radiation to use—X-rays or neutrons?*

Structure solution is generally easier with X-rays because (a) the phase problem is more likely to be solved for a particular subset of the atoms in the asymmetric unit (i.e. the heavy atoms) and (b) the resolution of X-ray instruments is generally better than that available at neutron sources (Hill and Cranswick 1994). However, for structure refinement, precise structural parameters are more likely to be derived from neutron data because (a) the distribution of scattering power is more uniform between elements and (b) the fall-off in reflection intensities with decreasing d -spacing is not as severe.

Some of the issues and recommendations to be considered prior to the selection of the instrument are summarized in Table 6.5. Further details are also given in Chapters 3–5.

6.5.2 *What wavelength to use?*

Once the instrument has been selected, an appropriate choice of wavelength, which is not merely dictated by the usual laboratory setup, also needs to be made. The essential criteria to be considered are that (a) for structure solution using Direct methods, more than 10 $|E|$ values of reasonable magnitude should be collected for every atom in the asymmetric unit (Cheetham and Wilkinson 1991), (b) for structure refinement, more than 10 reflection intensities should be collected for every structural parameter in the model (Hill and Cranswick 1994), and (c) for X-rays, some elements in the sample may cause excessive fluorescence or absorption when exposed to certain wavelengths.

The observations to parameters ratio should be maximized for best results, so a short wavelength may have to be selected to ensure that sufficient reflections fall within the accessible diffraction sphere or a longer one to attain a better separation of the reflections. For transmission geometry, the effects of absorption in the sample and the beam path should be kept to a minimum. This is best achieved by selecting a very short wavelength or a wavelength on the low-absorption side of an absorption edge. If the experiment is making use of the effects of anomalous dispersion for structure solution or site-occupancy refinement (Attfield 1992), fine tuning of the wavelength and hence access to a synchrotron source will be required. The presence of components in the sample that produce fluorescence may require the selection of a wavelength that avoids this effect and its adverse influence on background levels. If a special sample environment is required in which only a limited range of diffraction data can be observed (for example, in a pressure cell), the use of a short wavelength is recommended.

6.5.3 *Number of 'independent' observations (integrated intensities)*

The number and density of reflections in a diffraction pattern is governed not only by the wavelength used to collect the data but also by crystal symmetry and unit-cell size. For example, cubic and triclinic cells each with a volume of

Table 6.5 Summary of the issues which need to be addressed in the collection of diffraction data and recommendation of the most appropriate source to use

| Issue | Conventional laboratory X-rays ^a | High-resolution laboratory X-rays ^b | Synchrotron X-rays | Low-resolution neutrons ^c | High-resolution neutrons ^d |
|--------------------------------------|---|--|--------------------|--------------------------------------|---------------------------------------|
| Intensity at sample | ✓ | no | ✓ | no | some third generation instruments |
| Unit cell determination | fair | ✓ | ✓ | poor | ✓ |
| Heavy X-ray absorber | short λ reflection geometry | short λ reflection geometry | short λ | ✓ | ✓ |
| Light atom in presence of heavy atom | no | no | no | ✓ | ✓ |
| Hydrogen atoms | no | maybe | maybe | when deuterated | when deuterated |
| Large unit cell (complex structure) | no | ✓ | ✓ | no | ✓ |
| Magnetic structure | no | no | no | ✓ | ✓ |
| Thermal parameters | poor | ✓ | ✓ | poor | ✓ |
| Line-broadened sample | ✓ | compromised | compromised | ✓ | compromised |
| Availability at low cost | ✓ | ✓ | competitive access | competitive access | competitive access |
| Very small sample size | ✓ | ✓ | ✓ | ✓ | no |
| Non-ambient environment | maybe | maybe | ✓ | ✓ | ✓ |

^aCharacteristic doublet present, minimum FWHM $\approx 0.12^\circ 2\theta$

^bSingle wavelength (incident beam monochromator), minimum FWHM $\approx 0.06^\circ 2\theta$

^cFirst generation neutron facilities with minimum FWHM $\approx 0.1025^\circ 2\theta$ at low angles, but rising rapidly thereafter

^dSecond and third generation instruments with minimum FWHM $\approx 0.10^\circ 2\theta$ at 110° – 135° . At time-of-flight sources, the equivalent FWHM in 2θ is $\alpha \tan \theta$ where α ranges from 0.05 to 0.25.

1000 \AA^3 and one lattice point per unit cell produce markedly different numbers of reflections and reflection density in a pattern (Table 6.6).

Since the intensities of overlapping reflections are correlated with each other, the available information in a powder diffraction pattern is rarely equivalent to

Table 6.6 Calculation of the reflection density and total number of reflections in a diffraction pattern up to 110° and $140^\circ 2\theta$, respectively for 1000 \AA^3 cubic and triclinic unit cells, using a wavelength of 1 \AA (Hill 1993)

| Symmetry | Average reflection multiplicity | Maximum reflection density at $110^\circ 2\theta$ (reflections/degree) | Total reflections up to $140^\circ 2\theta$ |
|-----------|---------------------------------|--|---|
| Cubic | 24 | 14 | 1150 |
| Triclinic | 2 | 170 | 13 900 |

that of a full single-crystal dataset. At one extreme, when reflections completely overlap, as for Friedel pairs and those with systematic or accidentally exact redundancies in their d -spacings, the information that is extractable from the pattern is reduced to a single observation for the overlapping set. As the centroids of the overlapping reflections move apart, progressively more information about the individual components is realizable in the deconvolution process. This leads to greater confidence in the determination of the individual reflection intensities and therefore, to a higher chance of success in structure solution. Clearly, the amount of independent information (i.e. reflections) can be substantially reduced if the unit cell is large, if the cell dimensions are accidentally related (e.g. $a \sim 2b$) and/or the resolution of the instrument is poor. Altomare *et al.* (1995) have suggested a method for quantitatively estimating the amount of reflection overlap, whilst David (1999) has suggested an alternative method. Either method can be used to make a quick estimate of the number of ‘independent’ reflections in a diffraction pattern, for use as a guide for assessing whether or not a problem is tractable and, if so, what data collection conditions are appropriate.

6.5.4 What geometry to use?

The selection of which diffraction geometry to use will be largely governed by sample related considerations that include (a) the amount of material available, (b) whether aberrations such as preferred orientation are present, and (c) whether the sample will remain stable over the duration of the data collection. A small amount of weakly diffracting material may require simultaneous detection of the entire pattern using a position sensitive detector or an image plate system in order for the data collection to be made within a reasonable period of time. These and other sample-related conditions and recommendations for instrument geometry are summarized in Table 6.7.

6.5.4.1 Flat-plate sample

This is still the most common geometry used in laboratory X-ray facilities. Detailed discussion of its relative merits can be found in Cullity (1978),

Table 6.7 Details of sample related problems and recommendations for appropriate instrument geometry

| Sample Condition | Recommended Geometry |
|---|--|
| Preferred orientation present | Transmission—capillary (Debye–Scherrer) with sample spinning (preferably Gandolffi-type) Area detector with averaging or integration of intensity around the Debye cone |
| Heavy absorber | Reflection geometry with X-rays, or use neutrons |
| Medium to low absorber | Transmission—capillary or thin film Absorption can be decreased further by diluting sample or using shorter wavelength |
| Large crystallite size, but sample cannot be ground | If the crystallites are single, consider microcrystal diffraction, otherwise Transmission—capillary with Gandolffi-type sample motion |
| Small sample | Transmission—capillary or thin film |
| Weakly scattering or multi-phase | Position sensitive detector Multiple detectors Film or image-plate system |
| Unstable sample or dynamic study | Position sensitive detector Multiple detectors Film or image-plate system |

Klug and Alexander (1974) and Jenkins and Snyder (1996) and will not be repeated here.

In summary, the important points to remember for reflection geometry include:

1. For accurate measurement of peak intensity, the sample must be ‘infinitely’ thick to the radiation employed or an intensity correction must be applied. Equation (6.2) shows the relationship between sample linear absorption coefficient and sample thickness.
2. For a sample with a low absorption coefficient, the penetration of the beam into the sample will result in a significant peak shift and asymmetric broadening unless the incident beam has zero, or very low, divergence (as at a synchrotron X-ray source).
3. The collection of representative intensities requires that the footprint of the incident beam fall on the sample at all values of 2θ .
4. Other aberrations can cause loss of intensity at low 2θ in patterns collected on laboratory instruments. These include (a) sample transparency, (b) anode self absorption, (c) axial divergence and (d) curvature of the Debye–Scherrer conic section entering the receiving slit. An additional

intensity correction has been proposed to calibrate the instrument for these effects (Matulis and Taylor 1993).

6.5.4.2 *Thin sample*

This is an optimal geometry for the determination of accurate peak positions for pattern indexing and unit-cell refinement on a laboratory source, because it eliminates most of the aberrations associated with 'thick' samples (Klug and Alexander 1974). However, thin sample mounts are not uniform or infinitely thick, so they are not suitable for the collection of intensity data. Furthermore, this technique may induce preferred orientation in the sample making the peak-intensity estimates unreliable.

The best substrate for thin sample presentation is a 'zero-background' plate consisting of single crystals of silicon or quartz cut at an angle that ensures that no diffraction peaks are observed in the diffraction range of interest (Narasimha Rao *et al.* 1996). Thin sample mounts can be prepared by (a) sprinkling a small amount of the sample onto a substrate coated with a viscous material (grease, oil, etc), or (b) placing a small amount of powder on a clean substrate and mixing it with a few drops of a suitable solvent (e.g. ethanol) to form a 'slurry'. Evaporation of the solvent leaves the sample as a thin film on the surface. Suitable patterns can be obtained from very small amounts of material. Care needs to be taken with this type of mount to ensure that the sample is at the correct height in the diffractometer so that aberrations due to sample offset are minimized, although this is not a problem for parallel beam geometry.

6.5.4.3 *Capillary sample*

Transmission (capillary) geometry is used almost universally for neutron and synchrotron data collection but is less common for laboratory X-ray sources. However, high-resolution transmission diffractometers with a focused Debye-Scherrer geometry and a small position-sensitive detector are gaining in popularity, especially in the structure solution community. The primary advantage of a capillary mount is the virtual elimination of preferred orientation effects that are the bane of flat-specimen geometry.

Another advantage of capillary geometry is that very small amounts of sample can be examined, down to a few milligrams with careful sample handling. However, particle statistics can become a problem since very little material is examined in the experiment. The sample should be finely ground to facilitate packing in the capillary and should be spun during the data collection to minimize particle statistics errors.

While changes in sample absorption as a function of diffraction angle can be neglected in symmetrical flat-plate geometry, absorption of the X-ray beam in capillary geometry diminishes the low-angle intensities relative to the high-angle data. A correction, based on μ (the linear absorption coefficient), R (the

sample radius) and the packing density ratio, is required to adjust the calculated intensities during pattern decomposition or refinement (Hill and Madsen 1991).

In the case of very high absorption, it is recommended that the problem be addressed prior to the collection of data by diluting the sample with an appropriate low-absorption-coefficient material. For example, diamond powder has a low absorption coefficient for most useable wavelengths and has a paucity of lines, resulting in minimum interference with the pattern. Figure 6.1 shows the effect of sample absorption on patterns collected for (a) pure LaB_6 and (b) LaB_6 diluted with 77 weight per cent diamond powder. The few diamond peaks can be either excluded from the subsequent structure solution and refinement or included as an internal standard.

6.5.5 Sources of instrument-related error

Detailed discussion of the sources of error in laboratory X-ray applications of Bragg–Brentano and Debye–Scherrer geometry can be found in Klug and Alexander (1974) and Jenkins and Snyder (1996). In summary, the major points to consider in the configuration of a Bragg–Brentano instrument with divergent beam optics include:

1. View the X-ray tube focus laterally (with a small take-off angle) for the highest resolution. The use of an incident beam monochromator to eliminate the $K\alpha_2$ component further enhances the resolution (Madsen *et al.* 1996; Löwer and Langford 1988).
2. Sample displacement error causes peak shifts with a maximum at low values of 2θ . To minimize this effect, ensure that the sample is positioned accurately at the centre of the diffractometer.
3. Flat-specimen error causes minor peak asymmetry and peak shifts except at low values of 2θ . Reduce the irradiated sample length to reduce the impact.
4. Axial divergence causes asymmetric peak-broadening with maximum effect at low and high 2θ . Insertion of Soller slits into both incident and diffracted beam positions will reduce the effect (Madsen and Hill 1988).
5. A mis-setting of the 2:1 relationship between the 2θ : θ axes causes peak-broadening with a maximum effect at low values of 2θ .
6. Sample transparency in low-absorption-coefficient samples causes asymmetric broadening and peak shifts with maximum effect near $90^\circ 2\theta$.

The use of parallel beam geometry (such as at a synchrotron source) eliminates the effects of the displacement, transparency and flat-specimen errors that plague focusing geometry. Recent advances have seen the development of multilayer mirrors capable of producing (a) parallel beams from the normally diverging laboratory source, or (b) focused beams for specific applications (Göbel 1995; Schuster and Göbel 1996). They can be used to produce high

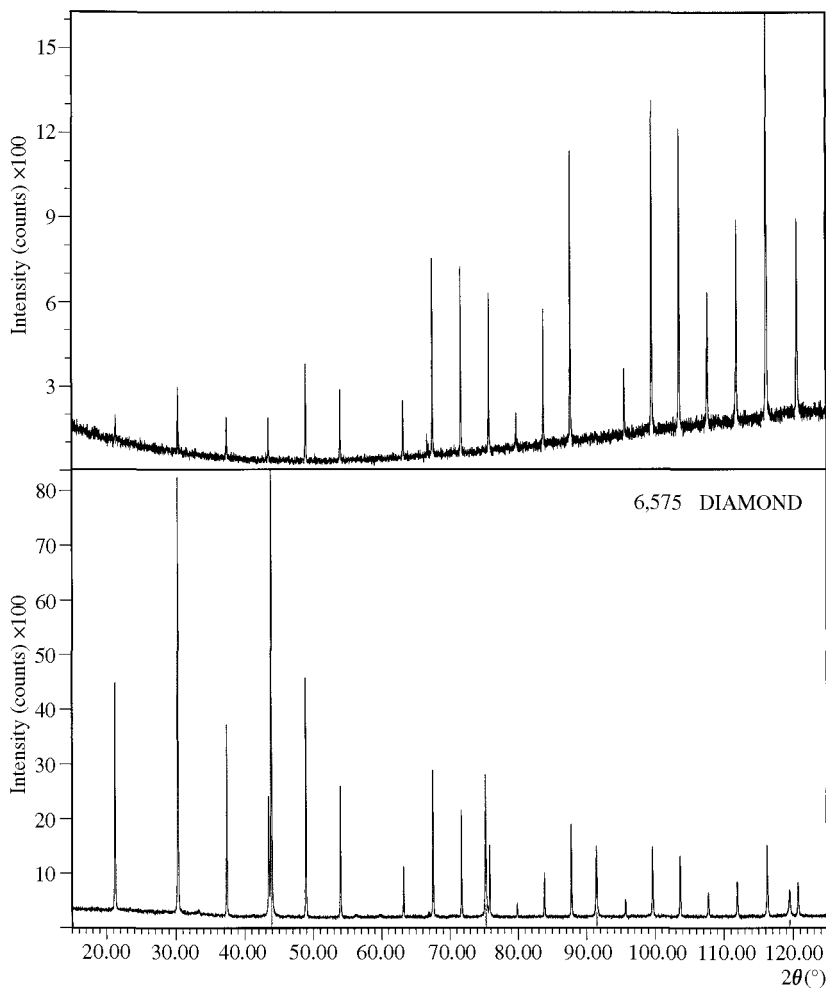


Fig. 6.1 X-ray diffraction patterns ($\text{Cu K}\alpha$) for NIST SRM660 LaB_6 in a 0.3 mm capillary (top) and LaB_6 diluted with 77 wt % diamond powder (bottom).

intensities from the small sample volumes encountered with capillary geometry and can be expected to have considerable impact on laboratory instrumentation in the future.

6.6 Data collection

Once the sample has been prepared and the instrument configuration selected, only the conditions under which the diffraction data will be collected remain to

be determined. What range of d -spacings (diffraction angles or energy) should be scanned? How frequently should the pattern be sampled? That is, what angular or energy step interval should be used? How many counts should be accumulated at each step? This determines the overall pattern intensity, and hence the counting statistics, which can vary markedly across the pattern and between individual reflections. Will a constant step counting time suffice, or will the use of a variable step counting time regime (Madsen and Hill 1994; David 1996) be necessary to provide more uniform, or specifically customized, counting statistics across the pattern?

Hill and Madsen (1987) have shown that variation in all of these factors have the potential to influence the outcome of a Rietveld refinement substantially. Judicious selection of data collection conditions can provide significant improvement in the accuracy and precision of pattern decomposition and structure refinement from conventional X-ray diffractometers, and this could decrease the need to resort to the use of synchrotron or neutron data.

It must be remembered that the fundamental measured quantities (observations) in a diffraction pattern are the *integrated* intensities of the reflections. The intensities collected at each step serve only as multiple, variably-weighted, estimates of these values. The precision of peak-intensity measurement can be improved by increasing (a) the counts accumulated at each step, that is increasing the step counting time T , and (b) the number of points, N , measured across the peak. Often, the temptation is to collect the data with large values of N and T to maximize counting statistics across the pattern. However, the resulting increased precision is only useful up to the point where counting variance becomes negligible in relation to other sources of error; thereafter experiment time is wasted. For example, if the sample is affected by the presence of severe preferred orientation, the collection of highly precise data will not help. Time would be better spent in remaking the sample and recollecting the data.

6.6.1 *Step time and width recommendations*

Hill and Madsen (1984, 1986) have undertaken systematic studies on the effect of step counting time and step width on Rietveld refined parameters obtained from constant-wavelength laboratory X-ray data. They have concluded that, for many relatively simple materials such as corundum, olivine and rutile-type compounds, it is sufficient to collect from 5000 to 20 000 counts on the top of the largest peak in the pattern. Beyond this, errors in the preparation and presentation of the sample and limitations of the model used for fitting the data dominate the counting errors. However, if one or two large peaks dominate the pattern, or the pattern is particularly complex, with a high level of peak overlap, it may be necessary to collect more counts to ensure adequate counting statistics in the weaker peaks.

For Rietveld analysis, the step width should be selected to be about 0.2–0.3 times the minimum observed FWHM in the pattern (Hill and Madsen 1984, 1986). This is again based on the fact that at shorter step widths, insignificant advantages accrue in relation to the precision of the integrated peak intensities, at a considerable cost in data collection times. Note that the exact value of step width should decrease with increasing complexity of the diffraction pattern and the degree of overlap between adjacent peaks. The optimum step width is a compromise between (a) increasing serial correlation and unnecessarily long data collection times at short step widths and (b) decreasing intensity precision at long step widths.

For pattern decomposition, the step width might be less than 0.1 times the minimum observed FWHM in the pattern for complex materials. A smaller step width than that used for Rietveld refinement is required since, in pattern decomposition based only on a unit-cell model for peak positions, it is not possible to take account of the interactions between the intensities of strongly overlapping reflections.

6.6.2 *Variable counting time data collection*

The intensity in constant-wavelength X-ray diffraction patterns is observed to decrease strongly up to angles of about $100^\circ 2\theta$ with a small recovery at higher angles. There are several physical factors which cause this variation, including the atomic scattering factors and thermal vibration, but the dominant term (for X-rays) is the effect of the Lorentz-polarization factor (Madsen and Hill 1994). While other factors, including reflection multiplicity and absorption (for capillary geometry), partially compensate for this decrease, there is an overall change in intensity across the pattern that can be as much as two orders of magnitude. While neutron patterns also show a decrease in intensity with diffraction angle, the variation is not as large as for X-rays since there is no angular dependence for the nuclear scattering factors.

As a result of this severe decrease in X-ray peak intensity at higher Bragg angles, the high-angle data is often deemed to be too 'weak' to contribute to the analysis and is not collected at all. However, the density of peaks in the mid- to high-angle region of the pattern is much greater than at low angles. Thus the high-angle region is potentially able to contribute more information per degree than the low-angle data. In addition, the high-angle data is more likely to be largely free from the aberrations (such as surface roughness and instrumental aberrations) that affect the low-angle data. Furthermore, these data can be critical to structure solution, especially if a Direct methods approach is used.

The conclusion is that, not only should the high-angle data be collected, but they should be collected with appropriate counting statistics. Advantages can accrue if the data are collected in such a way that each reflection receives approximately the same weighting during data analysis. This can be achieved by using a variable counting time (VCT) strategy that adjusts the step counting

time during data collection so that short step counting times are used at low 2θ where the average peak intensity is large, and progressively longer times are used at high 2θ to compensate for the intensity fall-off. This ensures that all moderately-sized peaks have approximately equal intensity, thus providing near-constant counting statistics across the entire diffraction pattern. Figure 6.2

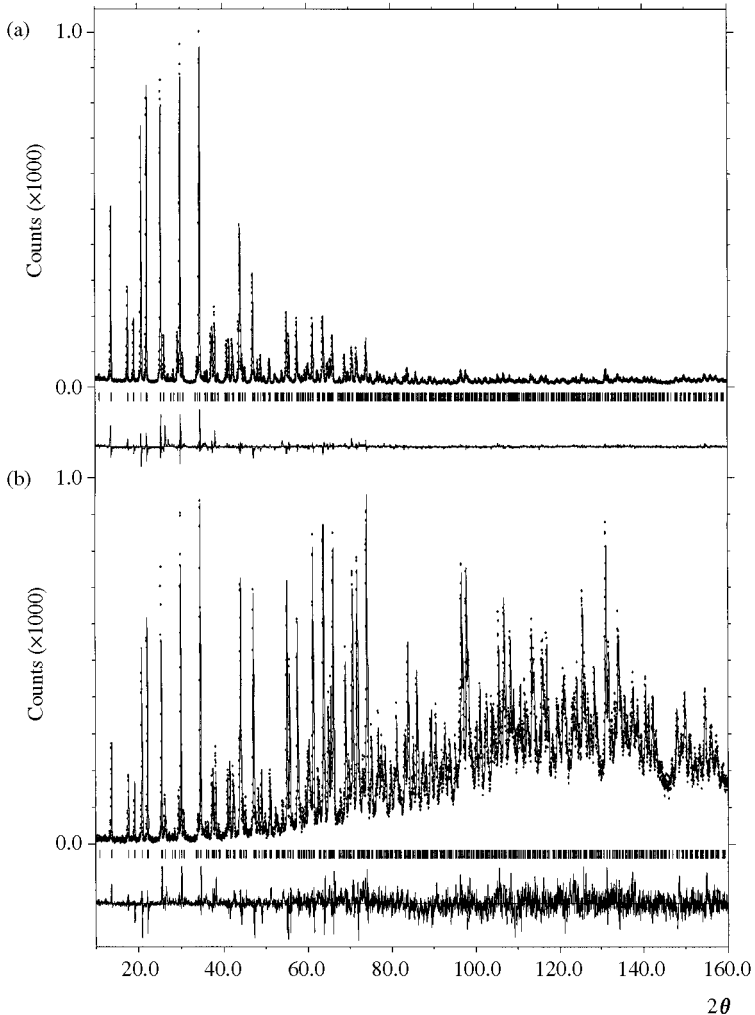


Fig. 6.2. Rietveld refinement output plots for tourmaline collected with (a) fixed and (b) variable step counting times using Cu $K\alpha$ X-rays, Bragg-Brentano geometry. The observed data are indicated by the points, the calculated profile as the continuous line overlying them. The lower curve is the difference between calculated and observed while the short vertical tick marks represent the positions of the allowable Bragg reflections.

shows plots of fixed and variable counting time X-ray diffraction data collected using Cu K α radiation from a sample of tourmaline. The advantages of employing a VCT strategy as a specific part of the structure solution process have been demonstrated clearly for both Direct methods of structure solution (Shankland *et al.* 1997) and global-optimization-based methods (David *et al.* 1998).

6.7 Conclusions

Sample preparation, selection of an appropriate wavelength and instrumental configuration, consideration of the number of reflections to be collected, and choosing the optimum step width and intensity with which to sample the powder pattern are all crucial aspects of the process of structure solution and refinement. Furthermore, different stages of the process place different demands on the experiment so that these conditions are unlikely to be satisfied by a single dataset. Thus, it is recommended that separate patterns be collected for reconnaissance, indexing, decomposition and refinement, each collected with due consideration of the instrumental configuration and data collection conditions outlined in this chapter.

References

- Altomare, A., Cascarano, G., Giacovazzo, C., Guagliardi, A., Moliterni, G. G., Burla, M. C. and Polidori, G. (1995). *J. Appl. Crystallogr.*, **28**, 738–44.
- Attfield, J. P. (1992). *NIST Spec. Publ.*, **846**, 175–82.
- Bish, D. L. and Post, J. E., ed. (1989). *Modern powder diffraction*, Reviews in mineralogy Vol. 20, Mineralogical Society of America, Washington, DC.
- Cheetham, A. K. and Wilkinson, A. P. (1991). *J. Phys. Chem. Solids*, **52**, A10, 1199–208.
- Cullity, B. D. (1978). *Elements of X-ray Diffraction*, 2nd edition, Addison Wesley, Reading, MA.
- David, W. I. F. (1996). Abstr MS 10.08.01, XVII IUCr Congress, Seattle, USA, August 9–17, 1996.
- David, W. I. F., Shankland, K. and Shankland, N. (1998). *J. Chem. Soc. Chem. Commun.*, 931–2.
- David, W. I. F. (1999). *J. Appl. Crystallogr.*, **32**, 654–63.
- Elton, N. J. and Salt, P. D. (1996). *Powder Diffraction*, **11**, 218–29.
- Goebel, H. E. (1995). In *Abstracts of the Fourth European Powder Diffraction Conference, Chester, England*, p. 11. CCL Daresbury Laboratory.
- Hill, R. J. (1993). In *The Rietveld method* (ed. R. A. Young), pp. 61–101. Oxford University Press.
- Hill, R. J. and Cranswick, L. M. D. (1994). *J. Appl. Crystallogr.*, **27**, 802–44.
- Hill, R. J. and Madsen, I. C. (1984). *J. Appl. Crystallogr.*, **17**, 297–306.
- Hill, R. J. and Madsen, I. C. (1986). *J. Appl. Crystallogr.*, **19**, 10–18.

- Hill, R. J. and Madsen, I. C. (1987). *Powder Diffraction*, **2(3)**, 146–62.
- Hill, R. J. and Madsen, I. C. (1991). *Z. Kristallogr.*, **196**, 73–92.
- Jenkins, R. and Snyder, R. (1996). *Introduction to X-ray powder diffractometry*, John Wiley & Sons, New York.
- Klug, H. P. and Alexander, L. E. (1974). *X-ray diffraction procedures for polycrystalline materials*, 2nd edn, John Wiley & Sons, New York.
- Löuer, D. and Langford, J. I. (1988). *J. Appl. Crystallogr.*, **21**, 430–7.
- Madsen, I. C. and Hill, R. J. (1988). *J. Appl. Crystallogr.*, **21**, 398–405.
- Madsen, I. C. and Hill, R. J. (1994). *J. Appl. Crystallogr.*, **27**, 385–92.
- Madsen, I. C., Hill, R. J. and Stereff, G. (1996). *Powder Diffraction*, **11**, 290–6.
- Matulis, C. and Taylor, J. (1993). *Adv. X-ray Anal.*, **36**, 301–7.
- McCusker, L. B., Von Dreele, R. B., Cox, D. E., Louër, D. and Scardi, P. (1999). *J. Appl. Crystallogr.*, **32**, 36–50.
- Narasimha Rao, G. V., Sastry, V. S., Gopala Krishana Murthy, H. S., Seshagiri, V. and Radhakrishnan, T. S. (1996). *Powder Diffraction*, **11**, 200–3.
- Schuster, M. and Göbel, H. (1996). *Adv. X-ray Anal.*, **39**, 57–71.
- Shankland, K., David, W. I. F. and Sivia, D. S. (1997). *J. Mater. Chem.*, **7**, 569–72.
- Smith, D. K. (1992). *Adv. X-ray Anal.*, **35**, 1–15.

Autoindexing

Per-Erik Werner

7.1 Introduction

In principle, all information available in a single-crystal diffraction pattern is also present in a powder diffraction pattern. Suppose all the pages in a book have been printed on top of each other on one single sheet. Obviously everything written in the book is present on the paper, but this does not mean that we are able to extract the information. Fortunately, however, there are some special features in a powder diffraction pattern that make it possible to extract its three-dimensional information in a step-wise manner. Thus, we can distinguish three different kinds of information: the peak positions, the peak shapes and the integrated intensities. If not only the peak positions but also the peak shapes or the intensities had been functions of the unit-cell dimensions, we would probably never have been able to index powder patterns.

Powder indexing is important not only in order to find unit-cell dimensions. It is a way to reconstruct the three-dimensional lattice that produced the one-dimensional spacing information. Thus, if we want to make use of the integrated intensities to solve the crystal structure or of the peak shapes to study size and strain properties of the sample, indexing is a necessary first step.

The lattice of a crystalline material is also highly diagnostic. Thus, a material can be registered or identified once any primitive cell that defines the lattice has been determined. The NBS Crystal Data File contains unit-cell data for many more substances than the total number of patterns, indexed and non-indexed, in the PDF 2 database (Mighell and Stalick 1980).

7.2 Basic relations

For reasons to be discussed later, it is often desirable to form the dot product of a reciprocal-lattice vector with itself:

$$\mathbf{r}_{hkl}^* \cdot \mathbf{r}_{hkl}^* = (h\mathbf{a}^* + k\mathbf{b}^* + l\mathbf{c}^*) \cdot (h\mathbf{a}^* + k\mathbf{b}^* + l\mathbf{c}^*). \quad (7.1)$$

Carrying out the dot products and collecting terms yields:

$$\begin{aligned}
 (\mathbf{r}_{hkl}^*)^2 &= \frac{1}{d_{hkl}^2} = h^2 a^{*2} + k^2 b^{*2} + l^2 c^{*2} + 2hka^*b^* \cos \gamma^* \\
 &\quad + 2klb^*c^* \cos \alpha^* + 2hla^*c^* \cos \beta^*,
 \end{aligned}
 \tag{7.2}$$

where d_{hkl} is the interplanar spacing related to the diffraction angle by Bragg's law:

$$2 d_{hkl} \sin \theta = \lambda. \tag{7.3}$$

For powder indexing, the quantity $1/d_{hkl}^2$ or $10^4/d_{hkl}^2$ is often designated Q_{hkl} . We shall here use the designation:

$$Q_{hkl} = \frac{10^4}{d_{hkl}^2}, \tag{7.4}$$

but it should be noted that from eqns (7.3) and (7.4) it follows that the difference between Q_{hkl} and $\sin^2 \theta$ is only a scale factor $(200/\lambda)^2$.

For the following discussion, eqns (7.2) and (7.4) are used to define the six a_{ij} parameters in the following equation:

$$Q_{hkl} = h^2 a_{11} + k^2 a_{22} + l^2 a_{33} + hka_{12} + kla_{23} + hla_{13}. \tag{7.5}$$

The parameters a_{ij} are related to the reciprocal cell, as shown above, and thus, also to the direct cell parameters. The number of a_{ij} -parameters to determine varies from one to six, depending on the symmetry (see Table 7.1).

These linear relations between observed Q -values and the a_{ij} -parameters form the basis for a large number of powder-indexing procedures.

Table 7.1 Quadratic forms and relations between a_{ij} and reciprocal unit-cell parameters

| Symmetry | Quadratic form |
|--------------|--|
| Cubic | $Q = (h^2 + k^2 + l^2) \cdot a_{11}$ |
| Tetragonal | $Q = (h^2 + k^2) \cdot a_{11} + l^2 \cdot a_{33}$ |
| Hexagonal | $Q = (h^2 + hk + k^2) \cdot a_{11} + l^2 \cdot a_{33}$ |
| Orthorhombic | $Q = h^2 \cdot a_{11} + k^2 \cdot a_{22} + l^2 \cdot a_{33}$ |
| Monoclinic | $Q = h^2 \cdot a_{11} + k^2 \cdot a_{22} + l^2 \cdot a_{33} + hl \cdot a_{13}$ |
| Triclinic | $Q = h^2 a_{11} + k^2 a_{22} + l^2 a_{33} + hka_{12} + kla_{23} + hla_{13}$ |

$a_{11} = K \cdot a^{*2}$; $a_{22} = K \cdot b^{*2}$; $a_{33} = K \cdot c^{*2}$; $a_{12} = K \cdot 2a^*b^* \cos \gamma^*$; $a_{13} = K \cdot 2a^*c^* \cos \beta^*$;
 $a_{23} = K \cdot 2b^*c^* \cos \alpha^*$; $K = 10^4$

7.3 The indexing problem

For each observed Q -value we need to find three crystallographic indices (hkl) for which, in the general triclinic case, the following inequalities are fulfilled:

$$Q_{\text{obs}} - \Delta < h^2 a_{11} + k^2 a_{22} + l^2 a_{33} + hka_{12} + kla_{23} + hla_{13} < Q_{\text{obs}} + \Delta. \quad (7.6)$$

If the measured Bragg angles, θ , have the same accuracy for all reflections, Δ should be a function of θ . In modern least-squares unit-cell refinement programs, the accuracy in 2θ is usually given as an input parameter. However, indexing programs for unknown powder patterns, where several hundred thousand trial indexings may be tested, sometimes operate with fixed Δ -values. Unit-cell dimensions found by an indexing program for unknown cells should always be refined later with a separate program where *all* lines and *all* conditions for absences are used. At that stage, the allowed deviations between observed and calculated values can be given in 2θ .

In this chapter, individual least-squares refinement programs, not included in autoindexing programs for unknown unit-cell dimensions, are not discussed. It should be noted, however, that flexible dialogue programs, where *alternative* refinements can be carried out (by using generated single-indexed lines, variable error bounds, various conditions for systematic absences (hkl)'s fixed in agreement with calculated intensities etc.) are very useful tools for checking and refining unit cells derived by autoindexing procedures.

The conditions in eqn (7.6) are necessary but not sufficient for a physically plausible indexing. This is easy to understand from the fact that any powder pattern can be indexed formally with a cubic unit cell having a cell axis of say 10^5 \AA , that is, $a_{11} \approx 10^{-6}$. Then it should be possible to find large integers h , k and l for which the inequalities (7.6) are fulfilled, with extremely small Δ values, for all observed Q -values. Obviously, however, this will not be a physically plausible indexing. We expect the low-angle lines in a powder pattern to have (hkl)s that are small integers. Thus, regardless of *how* we index a powder pattern, we need a simple criterion for the physical plausibility of the indexing. One of the most important contributions to the field of powder indexing was made by P. M. de Wolff (1968), who successfully derived a figure-of-merit test for this purpose. The de Wolff figure of merit M_{20} is defined by the expression:

$$M_{20} = \frac{Q_{20}}{2 \cdot \langle Q \rangle \cdot N_{20}}. \quad (7.7)$$

Here N_{20} is the number of different calculated Q values up to Q_{20} , which is the Q value for the 20th observed and indexed line; $\langle Q \rangle$ is the average discrepancy in Q for these 20 lines. There are few exceptions from the rule that, if all of the first 20 lines are indexed and $M_{20} > 10$, the indexing is physically reliable. Note that the term 'correct' here may also include indexing with common factors in the quadratic forms (see Table 7.1). For example, a pattern indexed with all $h = 2n$ is

not regarded as incorrect. The a -axis may of course be divided by 2 in the final least-squares refinement of the unit cell. A less obvious but frequently occurring example is the indexing of a tetragonal pattern with all $h^2 + k^2 = 5n$. Two kinds of exceptions, geometrical ambiguities and dominant zone problems, will be discussed below.

De Wolff also stated that if the number of unindexed lines below Q_{20} is not more than two, a value of $M_{20} > 10$ guarantees that the indexing is substantially correct, that is, it may be confirmed by single-crystal data. De Wolff's experience was limited to a large number of manual tests, and exceptions to this rule can be found with computer programs for powder indexing, especially in the case of dominant zone patterns (see below). Experience shows, however, that such unindexed lines are often found to be impurity lines or represent errors of measurement. Unless better solutions are found, it may, therefore, be worth checking solutions with one or two unindexed lines if the de Wolff figure of merit is high.

Another figure of merit, the F index, has been defined by Smith and Snyder (1979):

$$F_N = \frac{1}{\langle \Delta 2\theta \rangle} \cdot \frac{N}{N(\theta_g)}, \quad (7.8)$$

where $N(\theta_g)$ is the number of different calculated Q values up to θ_g , which is the θ value for a selected limit, $\langle \Delta 2\theta \rangle$ is the average discrepancy in 2θ for the number of observed lines, N , below θ_g .

The F index is probably superior to de Wolff's M_{20} index for ranking solutions, but it has a disadvantage when estimating the physical plausibility of a suggested unit cell. The fact that the M index increases systematically with symmetry is not a disadvantage. A cubic trial indexing of a powder pattern is more likely to be correct than a triclinic one, the fraction of observed lines and accuracy being equal. It should be noted that the de Wolff figure of merit is defined for exactly 20 lines. According to experience, the F_N index does not vary with the number of lines as much as a generalized M_N figure of merit. This may be the reason F_{30} is often reported on the PDF-2 cards.

The de Wolff figure of merit is defined to become (statistically) equal to 1 for a completely arbitrary indexing. This is the reason for the factor 2 in the denominator. There is no upper limit for M_{20} , as the discrepancies between observed and calculated Q values may become infinitely small. Powder diffraction patterns recorded by synchrotron radiation have sometimes been found to give M_{20} values in the range 500–700. Values in the range 20–60 are often obtained for good routine work on pure, well-crystallized samples, when focusing cameras and an internal standard substance are used, or when diffractometer measurements are made in the way described by NBS. Although $\langle Q \rangle$ may decrease with increasing cell dimensions, N_{20} will increase. The de Wolff figure of merit is not only a test for accuracy in the diffraction data but

also a test for how well the calculated pattern will cover the observed one. The quantity M_{20} takes account of the amount of 'coverage' (i.e. the fraction of lines actually observed).

Index triples falling under obvious general absences should be disregarded in computing N_{20} . Therefore, the M_{20} values calculated by indexing programs for unknown patterns should normally be recalculated by a least-squares refinement program where all systematic absences are taken into account. The choice made by de Wolff to use the first 20 lines is a compromise based on experience. The number of observed lines should be reasonably large in relation to the number of unit-cell parameters. On the other hand, the indexing of high-angle lines is always much more ambiguous, thus adding less to the reliability than the low-angle lines. It is also a general experience that the error of the measurement tends to increase with Q .

It is impossible to make a rigorous statistical test of the reliability of powder indexing. Although recent experience has shown that there are cases when $M_{20} > 10$ is no guarantee of correctness, the importance of the de Wolff figure-of-merit test in powder indexing can hardly be overestimated.

7.4 The dominant zone problem

The main situation in which the de Wolff figure-of-merit test may fail is when a dominant zone is present in the pattern, that is, one cell axis is much shorter than the other two. This has been extensively illustrated by Shirley (1980). The obvious reason for failure in the figure-of-merit test in such cases is that with one index equal to zero for most of the low-angle lines, an extra degree of freedom is introduced in the calculations. The problem may be circumvented, however, if the indexing program used is designed to start with a dominant zone test. In extreme cases, when only a few of the first 20 lines depend on the short axis, one may at least get a clear indication of the existence of a short axis, even if a reliable indexing is difficult to find.

Another way to circumvent the dominant-zone problem is to use an indexing procedure that takes advantage of the fact that low-volume solutions are more likely to be correct. Pseudo solutions may also be revealed by analysing *all* lines in the pattern.

7.5 Geometrical ambiguities—derivative lattices

The fact that only the length of the reciprocal-lattice vector, but not the three-dimensional vector itself, is observed in a powder pattern may cause some lattices with different, though related, reduced cells to give geometrically identical powder patterns. Such geometrical ambiguities can only occur between cells of orthorhombic or higher symmetry. Perhaps the best-known example is when a hexagonal pattern is (falsely) indexed by an orthorhombic cell having

the cell dimensions $a/2$, $a\sqrt{3}/2$ and c , where a and c are the hexagonal cell dimensions. Fortunately, it is easily detected, because of the square-root-of-three relation between two of the orthorhombic unit-cell axes. The problem has been described and analysed in detail by Mighell and Santoro (1975).

Autoindexing programs will often find a superlattice with twice the volume of the true lattice or a sublattice with one half of the volume. Super and sublattices are two forms of derivative lattices as defined by Santoro and Mighell (1972). Unindexed peaks can occur either from a second phase or from a derivative lattice. Usually superlattices are easily detected from the occurrence of common factors in the quadratic forms (see Table 7.1). In order to avoid sublattices—other than geometrical ambiguities—it is important to include all weak reflections, especially in the low-angle region (Mighell and Stalick 1980).

7.6 Errors in measurements

Powder indexing would be quite easy if errors in measurements did not exist. As stated by Shirley (1980): 'Powder indexing is not like structure analysis, which works well on good data, and will usually get by on poor data given a little more time and attention. Powder indexing works beautifully on good data, but with poor data it usually will not work at all.' This has been expressed in several ways by different authors. Smith and Kahara (1975) stated: 'Our experience with data recorded by Debye–Scherrer technique has been especially disappointing. The far greater success with data from focusing cameras reflects greater accuracy and resolution *per se*, smaller systematic errors, and greater detectability of weak reflections. For high-quality diffractometer data, such as the NBS patterns, our experience has likewise been good. However, for data sets having non-trivial systematic errors, successes have been as limited as with Debye–Scherrer data.' Shirley (1980) also stated: 'The paramount importance of resolution for indexing work explains the high success rate for focusing camera data, especially from Guinier–Hägg instruments, whose resolution can only be described as superb. It is rather less common (and considerably more expensive) to obtain as good resolution with diffractometer data.' As shown by the present author (Werner 1992) both precision and accuracy in 2θ are normally better than 0.01° in routine measurements of Guinier photographs, if an internal standard and an automated film scanner system are used. It has been shown by Louër and Langford (1988), however, that a conventional diffractometer with an incident-beam monochromator may have an instrumental resolution function with a minimum FWHM as small as 0.065° (2θ).

Average deviations between observed and calculated 2θ -values, determined by using synchrotron radiation, are often less than 0.002° . Such high data quality is extremely useful for powder indexing, but normally, indexing problems must be solved from ordinary laboratory data prior to data collection at a synchrotron source. With the high peak/background ratio obtained with

synchrotron radiation, extremely minor impurity contributions may also give observable diffraction peaks. If intensity differences are very large in the low-angle range, it may help to omit the very weak lines in a trial indexing. As soon as a plausible indexing is found, all lines should be tested with a separate dialogue program as discussed above.

In the instruction manual for the indexing program ITO, the program author, J. W. Visser writes: 'Do not use a Debye-Scherrer camera unless the unit cell to be expected is small. Would you like to solve a jigsaw puzzle when half the pieces are missing'. From the same manual may also be quoted: 'Finding the unit cell depends for 95 per cent on the quality of the input data. A random error of 0.03 degrees two theta can usually be tolerated, but a systematic (zero-point) error of 0.02 degrees is probably disastrous. Check your input lines against their higher orders.'

It is well known that it is possible to obtain accurate d -values by using an external standard technique. From the frequency of occurrence of low quality data in the PDF-2 database, however, it may be concluded that unless an internal standard technique is used, experimentalists often have very limited knowledge of the data quality they have obtained. The internal standard method is recommended for powder indexing, as it can be used not only to correct the zero-point error but also to correct for sample-dependent 2θ -error functions.

In the following, the strategies used by three different indexing programs will be briefly discussed. They represent three completely different methods. The programs to be discussed are ITO, DICVOL and TREOR, listed by McCusker (1992) in a review about integrated software for structure solution from powder data.

In the programs, different ways are used to express the maximum allowed discrepancies between observed and calculated data. In ITO and DICVOL, discrepancies are given in $^\circ 2\theta$, whereas in TREOR, one low-angle and one high-angle maximum deviation is given in $\sin^2\theta$. In Table 7.2, the maximum accepted deviations for all three programs are converted to Q values for comparison. If the input data to TREOR are given as d values (in Å) they are normally converted to $\sin^2\theta$ values for Cu $K\alpha_1$ radiation.

Table 7.2 Maximum accepted discrepancy between observed and calculated Q values versus 2θ for Cu $K\alpha_1$ radiation. The values are calculated for the default parameter settings used by the programs. In all programs the tolerances may easily be changed

| $2\theta(^\circ)$ | ITO | DICVOL91 | TREOR90 |
|-------------------|-----|----------|---------|
| 10 | 1.5 | 1.2 | 3.4 |
| 20 | 3.0 | 2.3 | 3.4 |
| 30 | 4.4 | 3.3 | 6.8 |
| 60 | 7.6 | 5.7 | 6.8 |

As only the first 20 lines are necessary for the calculation of M_{20} , it is rare that diffraction angles above 30° (60° in 2θ) are used to determine the reliability of the indexing if Cu $K\alpha_1$ radiation is used for the data collection.

7.7 Indexing programs

7.7.1 ITO

Reciprocal lattice points lying in a plane through the origin constitute a central zone in reciprocal space, and the corresponding powder lines are said to belong to the same zone. Any such zone may be described by two variable indices h and k , and needs only three parameters:

$$Q_{hk0} = h^2 a_{11} + k^2 a_{22} + hka_{12}. \quad (7.9)$$

Any two points in the reciprocal lattice, unless they are both on the same line through the origin, may be used to define such a plane. If they are on the same line, they may both be described as $h00$. The basic idea proposed by de Wolff (1958) and programmed by Visser (1969) in the indexing program ITO is to make a systematic search in the array of observed Q values to find as many points as possible in such a zone. Two Q values, Q' and Q'' , are selected and used to define two reciprocal lattice vectors \mathbf{a}^* and \mathbf{b}^* , respectively (i.e. $Q' = Q_{100}$ and $Q'' = Q_{010}$). The lengths of the vectors may be written $1/d'$ and $1/d''$. Then from the cosine law, it follows that for any point $hk0$ in the zone:

$$\frac{1}{d^2} = \left(\frac{h}{d'}\right)^2 + \left(\frac{k}{d''}\right)^2 + 2\left(\frac{h}{d'}\right)\left(\frac{k}{d''}\right)\cos\gamma^*, \quad (7.10)$$

where d equals the length of the reciprocal lattice vector and γ^* is the angle between (the arbitrarily chosen) vectors \mathbf{a}^* and \mathbf{b}^* . Thus:

$$Q_{hk0} = h^2 \cdot Q_{100} + k^2 \cdot Q_{010} + 2 \cdot hk \cdot (Q_{100} \cdot Q_{010})^{1/2} \cdot \cos\gamma^*. \quad (7.11)$$

Let

$$R = 2 \cdot (Q_{100} \cdot Q_{010})^{1/2} \cdot \cos\gamma^*. \quad (7.12)$$

Then

$$R = \frac{-(h^2 \cdot Q_{100} + k^2 \cdot Q_{010} - Q_{hk0})}{hk}. \quad (7.13)$$

By inserting all observed Q values up to a reasonable limit for Q_{hk0} and a few positive integers for h and k , and by storing the absolute value of R , we get

a great number of $|R|$ values, some of which are equal within the limits of error. From the list of R values, the most obvious concentrations are selected and the zone angles γ^* are calculated. The accepted discrepancies used for this zone-finding part of ITO is not the same as shown in Table 7.2. The default value is $3.0Q$ units, independent of the diffraction angle. For Q_{100} and Q_{010} , combinations of the first two or three lines are usually the most powerful choices. When the multiplicity factor of a powder line is greater than two, its Q value represents more than one point in the reciprocal lattice. Therefore, combination of a line with itself is sometimes very useful, as the corresponding orthogonal zone occurs rather frequently.

An important feature in ITO is that the zones found are checked for the length of \mathbf{a}^* and \mathbf{b}^* and thereafter reduced. Just a brief list of the steps in the program is given here. For details see Visser (1969) and the ITO instruction manual.

1. Find zones and reduce them.
2. Check the lengths of the base vectors and refine the three zone-parameters with a least-squares method. Calculate an approximate probability, C , that the zone is found by pure chance:

$$C = \frac{N_c!}{N_0!(N_c - N_0)!} \cdot p^{N_0}(1 - p)^{N_c - N_0}, \quad (7.14)$$

where N_c is the number of calculated Q values in the zone of which N_0 give a fit, $p = (\sum \Delta Q)/Q_{\max}$. The reciprocal values $1/C$ are used as quality values for the zones.

3. Find pairs of zones with a common row and determine the angle between these zones. This is probably the most difficult step, but it should be realised that even when ITO does not find a reliable solution to the three-dimensional indexing problem, it often finds correct zones.
4. Reduce the lattices found and transform if necessary so that the lattice is described in a standard way.
5. Try to index the first 20 lines of the pattern and repeat this after a least-squares refinement of the parameters. Calculate M_{20} and print out the list.

The program has a very flexible input and contains several options, for example advanced procedures for zero-point correction, not discussed in this short review.

7.7.2 DICVOL91

DICVOL uses a successive dichotomy method for indexing accurate powder patterns. The first version of the program was written for orthorhombic and higher symmetries by Louër and Louër (1972). The method has been extended to include monoclinic (Louër and Vargas 1982) and triclinic symmetries in

DICVOL91 (Boultif and Louër 1991). The search of unit-cells is exhaustive within input parameter limits, although a few restrictions for the hkl indices of the first five diffraction lines have been introduced in the study of triclinic symmetry.

The dichotomy method for automatic indexing of powder diffraction patterns is based on the variation of the lengths of cell edges and interaxial angles in direct space for finite ranges, which are progressively reduced by means of a dichotomy procedure if they contain a possible solution. With this strategy, an exhaustive search in an n -dimensional space (n being the number of unknown unit cell parameters) is performed.

In order to illustrate the method, the procedure used for the cubic search is described. The cell edge can be investigated from a value a_0 up to a maximum value a_M . The variation is made, for example, in steps of $p = 0.5 \text{ \AA}$. The a ($= b = c$) axis length is tested in intervals of $[a_0 + np]$ to $[a_0 + (n + 1) \cdot p]$ up to the chosen a_M . For each interval, limits in Q are defined as a function of hkl :

$$Q_-(hkl) = \frac{h^2 + k^2 + l^2}{a_0 + (n + 1) \cdot p}, \quad (7.15)$$

$$Q_+(hkl) = \frac{h^2 + k^2 + l^2}{a_0 + np}. \quad (7.16)$$

If, within error limits and for all observed Q values (usually the first twenty), hkl can be found for which:

$$Q_-(hkl) \leq Q_{\text{obs}} \leq Q_+(hkl), \quad (7.17)$$

then the interval $[a_0 + np]$ to $[a_0 + (n + 1) \cdot p]$ is divided into two equal parts and the test procedure is repeated. The procedure is repeated six times. Thus, the final step length is $p/2^6 = 78 \cdot 10^{-4} \text{ \AA}$.

The search strategy is to go from high to low symmetries and to use partitions of volume space, scanning successive 400 \AA^3 shells of volume, except for triclinic symmetry, where the shells are based on an estimated unit-cell volume V_{est} .

It has been shown by Smith (1977), from the examination of $1/N$ vs d^3 plots for accurate triclinic patterns, that a simple approximate relation can be derived for the unit-cell volume as a function of the number of lines N :

$$V_{\text{est}} = \frac{0.60 \cdot d^3}{1/N - 0.0052} \quad (7.18)$$

Corresponding relations can also be derived for higher symmetries, but they are not very reliable, mainly because the conditions for absences are unknown.

The presence of a common zero index for the first lines of the pattern does not impede finding the correct cell. As low-volume solutions are likely to be correct,

pseudo solutions are usually avoided by the fact that small-volume tests are made prior to large-volume tests.

The monoclinic symmetry is complicated by the fact that only a_{22} (see Table 7.1) is independent of the monoclinic angle β . Furthermore, if all observed lines are located within some limits, each domain has to be divided into 2^4 sub-domains by halving the intervals, as the total domain is four-dimensional. In the triclinic case, the dichotomy method is applied in Q space directly, because the general relation of Q to the direct cell parameters is too complicated. In order to reduce the computing times, some restrictions representative of the majority of experimental patterns with triclinic symmetry are imposed on the first five lines.

The unit-cell parameters are refined by a least-squares method, and figures of merit (M_N and F_N) are displayed. In order to help the user, the number of solutions retained at each level of the dichotomy procedure is printed. An examination of these numbers can be useful if too strict an absolute error limit relative to the accuracy of the data has been applied to the input data. An important feature of the program is its insistence that every observed line must be indexed, which penalizes data containing impurity lines. It is, of course, possible to rerun the program several times, omitting suspect lines in a successive manner, in order to identify spurious lines due to impurities. The strategy used by DICVOL, not to index patterns containing impurity lines, has the advantage that the user is not allowed to ignore unindexed lines.

7.7.3 *TREOR90*

TREOR searches for solutions in index space by varying the Miller indices, and Shirley (1980) has classified it as semi-exhaustive. The term was proposed for programs containing 'judicious deductions to limit the size of the solution field in order to gain speed.' The first parts of the program were written and described by Werner (1964), but the computer technology of that time did not allow a rigorous implementation of the principles. A more complete program version was written and published by Werner, Eriksson and Westdahl (1985). The present version of the program is described in the TREOR90 documentation file.

Although the general principles used for trial-and-error indexing are relatively simple and straightforward, the success of the method is a function, not only of data quality, but also of a large number of crystallographic decisions put into the program. Thus, an essential part of the program is a standard set of parameter values. They are termed normal values and represent accumulated experience from several hundreds of indexing problems. The parameters are referred to by keywords, and the user may easily change them. All keywords and their normal values are listed in a documentation file.

The program will normally start with cubic symmetry and, in a step-wise manner, test for lower symmetries. Higher order lines automatically correct the first low-angle lines if present. Trial parameters a_{ij} (see Table 7.1) are derived from base-line sets and it is therefore important that especially the

low-order lines are accurately measured. Solutions are ranked primarily according to the number of indexable lines among the first 19, and secondarily according to the smallest cell volume. Therefore, if no solution is found with more than, for example, 16 lines indexed in a trial phase, such unit cells may be saved temporarily and later refined by a least-squares method. Trial cells are not rejected because one or more lines cannot be indexed. This is avoided because of the experience that it is usually impossible to identify an extraneous line a priori. Furthermore, a small error in one or more of the base-lines may seriously affect the trial parameters. The fact that several different base-line sets are tested usually makes it possible, however, to find a correct solution. Dominant zone tests are made for orthorhombic and lower symmetries. An algorithm for successive reduction of trial-cell volume is used in monoclinic and triclinic tests, and therefore, the user does not normally need to restrict cell volumes to values below 2000 \AA^3 or cell edge maxima below the default value of 25 \AA .

If a satisfactory solution is found (i.e. normally an indexed pattern with $M_{20} > 10$ and not more than one unindexed line among the first twenty), a short output list containing only this solution is printed after least-squares refinement. If the unit cell is monoclinic or triclinic, the reduced and the conventional cells are derived. The reduction is only valid, however, if the cell is primitive. Instructions are also given on how to rerun the program in order to test for better solutions. This is important, because although the first solution found is often the best one, this is not always the case.

If no satisfactory solution is found, the user can inspect the general output list. This list may contain a large number of more-or-less possible indexing solutions with $M_{20} > 6$ and not more than three unindexed lines among the first twenty. This often makes it possible to identify impurity or badly measured lines in the pattern.

7.7.4 *Why more than one indexing program?*

As stated above, all indexing procedures are strongly dependent on the quality of the input data. Crystallographers working in the field of powder indexing have also often focused on accurate measuring systems. The indexing programs are dependent on the data quality in somewhat different ways, however. Furthermore, derivative lattices, which are often found by indexing programs, are sometimes detected by comparing output lists from different programs.

The programs ITO and TREOR are especially dependent on accurate low-angle data, because the first lines play an important role in the indexing strategies, whereas for DICVOL, data errors play a role independent of the diffraction angle. A multitude of non-systematic absences can make it impossible to find a solution with ITO, but is of much less importance for DICVOL or TREOR. As ITO employs a general triclinic approach to the indexing problem, whereas DICVOL and TREOR use relatively strong restrictions in the triclinic tests, it can be expected that ITO will sometimes solve triclinic problems that

cannot be solved by the other two programs. DICVOL is less dependent on dominant zone problems than TREOR, although this part of the program has been improved in the TREOR90 version. ITO and TREOR contain many options not described in this short presentation, which make them very efficient for a user who is familiar with all details in the programs. In order to take advantage of these opportunities, however, the user will need some experience with the programs.

Given the exhaustive strategy used by DICVOL, one would expect that all patterns of monoclinic and higher symmetries would be correctly indexed, if the measurement is of reasonable quality. Unfortunately, however, impurity lines and/or individual lines strongly affected by overlaps occur frequently. Other programs sometimes identify such lines via solutions with high M_{20} values and one or two unindexed lines, whereas DICVOL will not pinpoint a possible impurity line. As stated above, however, the number of solutions retained at each dichotomy level may be a useful error indicator. In the program version DICVOL04 (Boultif and Louër 2004) a tolerance to the presence of impurity lines has been added.

A mistake that is often made is to use more than the first 20–25 lines in the indexing programs DICVOL and TREOR. It is important to include *all* lines and *all* systematic extinction conditions in the final least-squares refinement of the unit-cell dimensions. At that stage, all lines should be carefully checked. The reason one should avoid using high-angle data in the first trials to *find* the basic solution to the indexing problem is that errors, which are much more frequent in the high-angle region, may completely rule out the possibility of finding a solution. DICVOL will not accept *any* unindexed line and TREOR may use erroneously indexed lines in trial refinements and thus lose correct solutions. The strategy used by ITO, however, is probably optimal for about 35 lines.

Powder indexing is only partly a mathematical problem. The chemical and structural information contained in the pattern is also of importance. The main reason that indexing programs allow for one or two lines to be discarded if they cannot be indexed is that impurities are often present. An unindexed line should be carefully checked from a chemical point of view. If it can be identified as the strongest line from a chemically possible impurity, the validity of the unit cell found is strengthened. It may be added that this is a frequently occurring situation, as can also be seen from the fact that several complete structure determinations from powder patterns during recent decades have been made from two-phase samples.

7.8 Computing times

With modern computers, all three indexing programs discussed above are very fast for orthorhombic and higher symmetries. CPU times for lower symmetries usually increase in the order: ITO < TREOR90 < DICVOL91. ITO is very fast regardless of the symmetry. For TREOR90, computing times may vary from

less than one second to around thirty seconds on a 1GHz Pentium-4 based PC. For DICVOL91, CPU times for the monoclinic symmetry can be rather long. As stated above, if a solution is found by TREOR, the problem should be run again with stronger restrictions in order to test for better solutions. One may agree, however, with the statement by Boultif and Louër (1991) that 'if a solution is found for the time-consuming examples, time is probably unimportant, particularly if an *ab initio* structure determination follows this geometrical reconstruction of the reciprocal lattice.'

7.9 The PDF 2 database

A search of the 59 847 non-deleted patterns in the PDF 2 database, sets 1–44, to determine the frequencies of different unit-cell symmetries shows that the group of unindexed patterns is indeed the largest one (Table 7.3).

In dataset 44, there are 521 unindexed patterns, that is, 26 per cent. The lowest number of unindexed patterns, is found in dataset 25 (297, i.e. 12 per cent). The ACA subcommittee's final report, standard for the publication of powder patterns (Calvert *et al.* 1980), comprises an investigation of inaccuracies of d -values in PDF 2. It was found that the average value of $|\Delta 2\theta|$ for all 1638 cubic patterns in sets 1–24 is 0.091° , whereas especially for the cubic patterns published by NBS, the average of $|\Delta 2\theta|$ is 0.015° . Hopefully, data quality has improved since 1980. Although examples can be given of non-indexed powder patterns in PDF 2 that can be indexed with reasonable confidence with modern programs (e.g. PDF no: 37–166 [deleted patterns], 36–21, 36–22, 38–668, 40–66, 43–603, 43–604 and 43–913), there are probably not very many. It seems reasonable, however, to assume that the main reason for the large number of non-indexed patterns in the database is to be found in the low quality of the data. This statement is also strongly supported by the fact that computer indexing of powder patterns published by NBS is successful almost 100 per cent of the time. However, impurity lines in these patterns are (probably?) omitted in the editorial procedure.

Table 7.3 PDF 2, sets 1–44

| Symmetry | Number | % |
|--------------|--------|------|
| Cubic | 6669 | 11.1 |
| Rhombohedral | 2187 | 3.7 |
| Tetragonal | 5396 | 9.0 |
| Hexagonal | 5540 | 9.3 |
| Orthorhombic | 8510 | 14.2 |
| Monoclinic | 8063 | 13.5 |
| Triclinic | 1666 | 2.8 |
| Unindexed | 21816 | 36.4 |

Table 7.4 Differences in 2θ as a function of change in d -value

| $d(\text{\AA})$ | $\Delta(^{\circ}2\theta)$ |
|--------------------------------|---------------------------|
| 3.00 \rightarrow 3.01 | 0.10 |
| 2.50 \rightarrow 2.51 | 0.15 |
| 2.00 \rightarrow 2.01 | 0.24 |
| 1.800 \rightarrow 1.801 | 0.03 |
| (1.7995 \rightarrow 1.80149) | 0.06 |

Table 7.5 Changes in d -values for some selected 2θ if $\Delta(2\theta) = 0.03^{\circ}$

| $2\theta(^{\circ})$ | $d(\text{\AA})$ |
|---------------------------|-----------------------------|
| 9.00 \rightarrow 9.03 | 9.82 \rightarrow 9.78 |
| 20.00 \rightarrow 20.03 | 4.436 \rightarrow 4.429 |
| 36.00 \rightarrow 36.03 | 2.4927 \rightarrow 2.4909 |
| 72.00 \rightarrow 72.03 | 1.3105 \rightarrow 1.3100 |

For training, the reader can try to find the most likely unit-cell dimensions for the examples listed above.

If the observed d -values are given with too few decimal places (as in Table 7.4), it is usually a waste of time to try any indexing procedure (Werner 1976). Even if a correct solution can sometimes be found by using wide error bounds, the risk of obtaining false solutions is high. The data in the Tables 7.4 and 7.5 are calculated on the assumption that the radiation used is Cu $K\alpha_1$.

It is recommended that $d > 5.00 \text{\AA}$ be reported to 2 decimal places, $5.00 \text{\AA} \leq d < 2.500 \text{\AA}$ to 3 decimal places and $d \leq 2.5000 \text{\AA}$ to 4 decimal places.

7.10 Comments

The indexing programs discussed above have not been chosen in an objective way, although they represent three different approaches to the problem. It should be mentioned, for example, that other programs working in index space have been written by Taupin (1973), by Kohlbeck and Hörll (1976, 1978) and by Smith and Kahara (1975). An indexing program using dichotomy methods has also been written by Neumann (2003). A special search procedure proposed by Smith and Kahara for the (020) reflection in monoclinic patterns has also been implemented in TREOR. Quite recently, Kariuki and co-workers (1999) have described an approach that involves indexing powder diffraction data by using a whole-profile fitting technique and a genetic-algorithm-based global-optimization method. Altomare and co-workers (2000) have also incorporated the

TREOR90 program into a more extensive peak search and cell-refinement framework.

A subroutine named 'biblio', containing a large number of useful references about powder indexing up to 1984, is included in the Fortran source code of the ITO program, and more recently, Louër (1992) has written a general article about automatic indexing.

It is not the intention of the present work to recommend or to judge the efficiency of specific indexing programs. It is strongly recommended, however, that it is better to have different programs using quite distinct and complementary methods available. A list of indexing programs is given on the Internet at <http://www.ccp14.ac.uk/solution/indexing/>. The CRYSFIRE program of Shirley, which generates input for the most common indexing programs, can also be found there. As discussed above, the limitations tend to affect different programs in different ways. Although deductive and semi-exhaustive programs may require more experience to take full advantage of all facilities, it is important in all computerized indexing procedures to know *how to change the error limits* in a step-wise manner if indexing is not successful. This is also strongly related to experience with the actual sample and measuring system.

Appendix: (Most likely) unit-cell dimensions for selected PDF-2 powder patterns

PDF 37-166

$\text{Cs}_2\text{V}_6\text{O}_{16}$ (deleted pattern) (see PDF 40-454 and 40-456)

Monoclinic: $a = 8.169 \text{ \AA}$, $b = 8.508 \text{ \AA}$, $c = 4.985 \text{ \AA}$, $\beta = 95.52^\circ$, $V = 344.6 \text{ \AA}^3$, $M_{20} = 16$, $F_{23} = 18(0.021, 63)$.

A B-centred cell ($V = 688 \text{ \AA}^3$) can be found. It can be transformed to (an arbitrary) primitive cell by MODCELL. The cell can then be reduced and rewritten to the conventional cell given above by REDUCT. Finally, the dialogue program PIRUM can be used for refinement. (Several other programs listed by S. Gorter and D. K. Smith in the *World directory of powder diffraction programs. Release 2.12* (1993) can be used. The programs discussed here, as well as a stand-alone version of N-TREOR, are available from the present author.) PIRUM can be used for analysis and least-squares refinement of all examples reported below.

PDF 36-21

$\text{NaAl}(\text{HPO}_4)_2$

Monoclinic: $a = 7.820 \text{ \AA}$, $b = 9.427 \text{ \AA}$, $c = 8.427 \text{ \AA}$, $\beta = 108.83^\circ$, $V = 587.9 \text{ \AA}^3$, $M_{20} = 22$ (C-centred cell), $F_{30} = 31(0.017, 58)$

PDF 36-22

$\text{NaGaH}_5(\text{AsO}_4)_3 \cdot \text{H}_2\text{O}$

Orthorhombic: $a = 15.968 \text{ \AA}$, $b = 14.008 \text{ \AA}$, $c = 4.6632 \text{ \AA}$, $V = 1043 \text{ \AA}^3$
 $M_{20} = 72$, $F_{30} = 163$ (0.004, 31)

PDF 38–668

$\text{Ba}_2\text{Mo}_5\text{O}_{17}$

Monoclinic: $a = 14.690 \text{ \AA}$, $b = 7.564 \text{ \AA}$, $c = 6.958 \text{ \AA}$, $\beta = 100.39^\circ$, $V = 760.5 \text{ \AA}^3$
 $M_{20} = 23$, $F_{24} = 43$ (0.011, 52)

Figures of merit are dependent on the number of lines used in the refinement. The cell parameter values change gradually with the number of lines (up to 66) included in the refinement. The pattern has a curved θ scale. The line at $d = 3.4500 \text{ \AA}$ can be identified as an impurity line. On the PDF-card it is reported that MoO_3 was used for the synthesis and has its strongest line at this d -value (see PDF 21–569).

PDF 40–66

$\text{Mg}(\text{H}_2\text{PO}_4)_2$

Monoclinic: $a = 7.381 \text{ \AA}$, $b = 15.237 \text{ \AA}$, $c = 5.313 \text{ \AA}$, $\beta = 97.84^\circ$, $V = 591.9 \text{ \AA}^3$
 $M_{20} = 13$ ($0k0 = 2n$), $F_{21} = 18$ (0.021, 56)

PDF 43–603

$\text{Eu}_2\text{O}(\text{CO}_3)_2 \cdot \text{H}_2\text{O}$

Orthorhombic: $a = 8.454 \text{ \AA}$, $b = 7.097 \text{ \AA}$, $c = 4.8969 \text{ \AA}$, $V = 293.8 \text{ \AA}^3$
 $M_{20} = 30$, $F_{30} = 34$ (0.014, 63)

Note: $a/c = 1.7267$, see PDF 43–604 (geometrical ambiguity?)

PDF 43–604

$\text{Gd}_2\text{O}(\text{CO}_3)_2 \cdot \text{H}_2\text{O}$

Hexagonal: $a = 9.744 \text{ \AA}$, $c = 7.063 \text{ \AA}$, $V = 580.8 \text{ \AA}^3$
 $M_{20} = 29$, $F_{30} = 28$ (0.022, 49)

A possible geometrical ambiguity.

Orthorhombic: $a = 7.070 \text{ \AA}$, $b = 8.435 \text{ \AA}$, $c = 4.878 \text{ \AA}$, $V = 290 \text{ \AA}^3$
 $M_{20} = 53$ Note $b/c = \sqrt{3}$ (see PDF 43–603)

PDF 43–913

$\text{Bi}_{12}\text{Ni}_{58}\text{S}_{30}$

Orthorhombic: $a = 11.394 \text{ \AA}$, $b = 7.813 \text{ \AA}$, $c = 6.351 \text{ \AA}$, $V = 565 \text{ \AA}^3$
 $M_{20} = 17$, $F_{27} = 20$ (0.017, 81)

References

- Altomare, A., Giacovazzo, C., Guagliardi, A., Moliterni, A. G. G., Rizzi, R. and Werner, P.-E. (2000). *J. Appl. Crystallogr.*, **33**, 1180–6.
 Boulton, A. and Louër, D. (1991). *J. Appl. Crystallogr.*, **24**, 987–93.

- Boultif, A. and Louër, D. (2004). *J. Appl. Crystallogr.*, **37**, 724–31.
- Calvert, L. D., Flippen-Anderson, J. L., Hubbard, C. R., Johnson, Q. C., Lenhart, P. G., Nichols, M. C., Parrish, W., Smith, D. K., Smith, G. S., Snyder, R. L. and Young, R. A. (1980). *NBS Spec. Publ.*, **567**, 513–35.
- de Wolff, P. M. (1958). *Acta Crystallogr.*, **11**, 664–5.
- de Wolff, P. M. (1968). *J. Appl. Crystallogr.*, **1**, 108–13.
- Kariuki, B. M., Belmonte, S. A., McMahon, M. I., Johnstone, R. L., Harris, K. D. M. and Nemes, R. J. (1999). *J. Synchrotron Rad.*, **6**, 87–92.
- Kohlbeck, F. and Hörl, E. M. (1976). *J. Appl. Crystallogr.*, **9**, 28–33.
- Kohlbeck, F. and Hörl, E. M. (1978). *J. Appl. Crystallogr.*, **11**, 60–1.
- Louër, D. (1992). *NIST Spec. Publ.*, **846**, 92–104.
- Louër, D. and Langford, J. I. (1988). *J. Appl. Crystallogr.*, **21**, 430–7.
- Louër, D. and Louër, M. (1972). *J. Appl. Crystallogr.*, **5**, 271–5.
- Louër, D. and Vargas, R. (1982). *J. Appl. Crystallogr.*, **15**, 542–5.
- McCusker, L. B. (1992). *NIST Spec. Publ.*, **846**, 75–9.
- Mighell, A. D. and Santoro, A. (1975). *J. Appl. Crystallogr.*, **8**, 372–4.
- Mighell, A. D. and Stalick, J. K. (1980). *NBS Spec. Publ.*, **567**, 393–403.
- Neumann, M. A. (2003) *J. Appl. Crystallogr.*, **36**, 356–65.
- Santoro, A. and Mighell, A. D. (1972). *Acta Crystallogr.*, **A28**, 284–7.
- Shirley, R. (1980). *NBS Spec. Publ.*, **567**, 361–82.
- Smith, G. and Kahara, E. (1975). *J. Appl. Crystallogr.*, **8**, 681–3.
- Smith, G. S. (1977). *J. Appl. Crystallogr.*, **10**, 252–5.
- Smith, G. S. and Snyder, R. L. (1979). *J. Appl. Crystallogr.*, **12**, 60–5.
- Taupin, D. (1973). *J. Appl. Crystallogr.*, **6**, 380–5.
- Visser, J. W. (1969). *J. Appl. Crystallogr.*, **2**, 89–95.
- Werner, P.-E. (1964). *Z. Kristallogr.*, **120**, 375–87.
- Werner, P.-E. (1976). *J. Appl. Crystallogr.*, **9**, 216–19.
- Werner, P.-E. (1992). *NIST Spec. Publ.*, **846**, 51–61.
- Werner, P.-E., Eriksson, L. and Westdahl, M. (1985). *J. Appl. Crystallogr.*, **18**, 108–13.

Extracting integrated intensities from powder diffraction patterns

William I. F. David and Devinderjit S. Sivia

8.1 Introduction

This chapter deals with the theoretical aspects of extracting integrated intensities from a powder diffraction pattern and with the ancillary issue of space group determination. Extracting integrated intensities is a relatively straightforward stage in the structure solution process. Two principal techniques have been developed. The first of these, the iterative Le Bail method (Le Bail *et al.* 1988) based upon Rietveld's original method (Rietveld 1969) for determining observed structure-factor magnitudes, is discussed in Section 8.2. The second method originally proposed by Pawley (1981) is a constrained linear least-squares approach and is outlined in Section 8.3. A comprehensive review of the origins of whole powder pattern decomposition methods and their application to structure solution has been undertaken by Le Bail (2005).

Although extracting integrated intensities is, in principle, not difficult, it is this stage in the structure solution process that highlights most clearly the loss of information in a powder diffraction measurement. This loss comes from the inevitable overlap of Bragg reflections resulting from the collapse of the three dimensions of reciprocal space onto the single dimension of a powder diffraction pattern. Overlap may be exact because of the equivalence of reflection d -spacings or accidental resulting from near-equivalent d -spacings that are separated from one another by an amount less than the resolving power of the instrument. Exact overlap occurs in crystal systems with higher than orthorhombic symmetry; typical examples include the $43l$ and $50l$ reflections in the tetragonal system, the $70l$ and $53l$ reflections in the trigonal or hexagonal systems, and the 333 and 511 reflections in the cubic system. Accidental overlap can occur in high-symmetry systems, but mainly occurs in orthorhombic or lower systems because of the increased number of independent reflections. The excellent resolution available at modern X-ray synchrotron and neutron powder diffractometers can result in up to several hundred resolved Bragg peaks. However, as $\sin \theta/\lambda$ is increased, accidental overlap must occur and this limits the complexity of problems that may be tackled. Although Bragg peak overlap is inevitable in a powder diffraction experiment, several theoretical and

experimental methods have been put forward to overcome this difficulty. Theoretical approaches are discussed later in this chapter in Section 8.5. Two successful experimental methods for overcoming Bragg peak overlap are described in Chapter 9.

How severe is the problem of Bragg peak overlap? Consider a reciprocal lattice with volume, $V^* = 1/V$. The number, N , of Bragg reflections is simply the number of reciprocal lattice points with $d^* = (1/d)$ less than a maximum reciprocal distance d_{\max}^* and is given by $N = \frac{4}{3}\pi d_{\max}^{*3}/V^*$. Clearly, in a powder diffraction pattern, all reflections with the same d -spacing are overlapped and so the number of reflections, assuming that Friedel's law is obeyed, between d^* and $d^* + \Delta d^*$ is given by the number in the corresponding shell in reciprocal space, $\Delta N(d^*) = 2\pi V d^{*2} \Delta d^*$. This formula presumes triclinic symmetry but is also approximately valid for monoclinic and orthorhombic symmetries if V is considered to be the volume of the asymmetric unit. Multiplication by the appropriate Jacobian leads to a number density as a function of 2θ given by

$$\Delta N(2\theta) = \frac{\pi^2 V \sin \theta \sin 2\theta}{45\lambda^3} \Delta(2\theta). \quad (8.1)$$

This formula highlights the overlap problem for the solution of moderately large crystal structures. The number of peaks scales linearly with the unit-cell volume and varies inversely with d^2 for long d ($\gg \lambda$).

It can be seen from Fig. 8.1 that there is a clear maximum in the peak density. The precise theoretical position of this maximum occurs at $2\theta = 2 \tan^{-1}(\sqrt{2}) = 109.47^\circ$ and can be calculated by differentiating eqn (8.1)

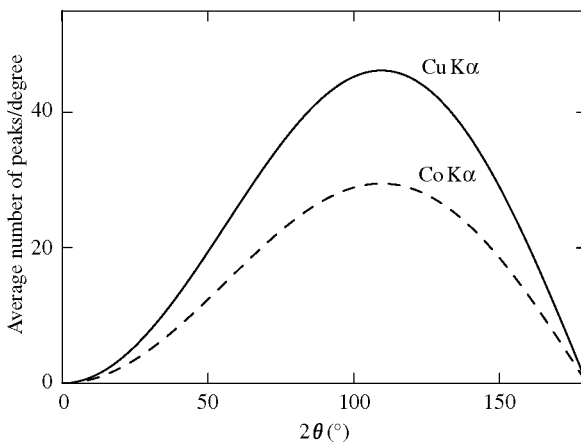


Fig. 8.1. The average number density of peaks as a function of $2\theta^\circ$ for copper radiation (solid line) and cobalt radiation (dashed line) for a unit cell of volume 1000 \AA^3 .

with respect to 2θ . The maximum peak density is then found to be equal to

$$\Delta N_{\max}(2\theta) = \frac{4\pi^2 V}{(135\sqrt{3})\lambda^3} \approx \frac{0.169V}{\lambda^3}. \quad (8.2)$$

Sheldrick's rule (<http://shelx.uni-ac.gwdg.de/SHELX>) states that, for routine structure solution by Direct methods, diffraction data should be collected down to around 1 \AA . For standard laboratory data ($\lambda = 1.54 \text{ \AA}$), d -spacings of 1 \AA occur at 100° near the maximum peak density. The number of peaks in a one-degree range at $d = 1 \text{ \AA}$ is then approximately equal to

$$\Delta N \approx \frac{V}{20}. \quad (8.3)$$

Peak separations, $\Delta 2\theta$, for low-symmetry systems are essentially random and thus follow an exponential probability distribution, $p(\Delta 2\theta < \delta) = 1 - \exp(-\Delta N\delta)$. Assuming no sample broadening and a best full width at half maximum (FWHM) resolution of 0.06° implies that over 60 per cent of the peaks are within one FWHM of another Bragg peak for an asymmetric unit volume of only 360 \AA^3 . For organic structures, this signals problems for modest molecules containing as few as 20 non-hydrogen atoms. This overlap problem may be to some extent resolved by using longer wavelengths such as cobalt radiation (see Fig. 8.1) although sample-broadening effects may diminish this potential improvement. Of course, the best resolutions are achieved at synchrotron sources (see Chapter 4). Take, for example, BM16 at the European Synchrotron Radiation Facility (ESRF). However, even with $\lambda = 0.8 \text{ \AA}$ and a FWHM of 0.01° , the limiting volume of the asymmetric unit only doubles to around 800 \AA^3 . Although giving access to molecules with up to 40 non-hydrogen atoms, this is still a rather modest volume for organic structures.

8.2 The Le Bail method

8.2.1 The origins of the Le Bail method

The origins of the Le Bail method are to be found in the early pioneering work of Rietveld (1969). Rietveld proposed a simple yet elegant summation approach to the evaluation of an observed structure-factor magnitude for partially and indeed completely overlapped reflections. It is worth considering in detail Rietveld's summation method with a simple two-peak example. Figure 8.2 shows a portion of a diffraction pattern with two overlapping peaks.

The calculated diffraction pattern is good but not excellent and it is clear that the observed and calculated structure-factor magnitudes are different from one another. In this example, the observed value for the first reflection is significantly larger than the calculated value; the observed value for the second reflection is slightly smaller than has been calculated. Rietveld's approach was simple. The peak area is proportional to the square of the structure-factor

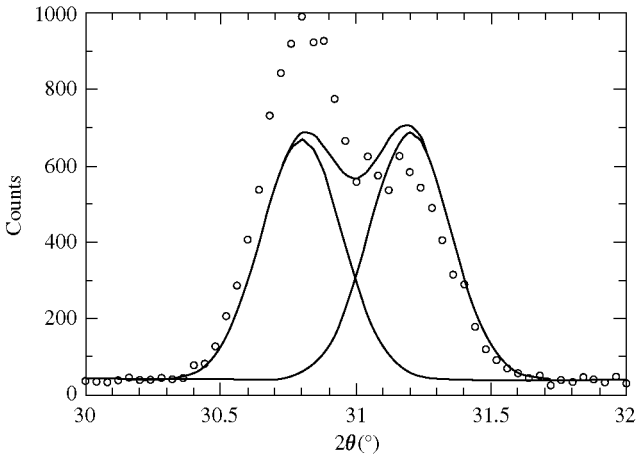


Fig. 8.2. A Rietveld fit for two overlapping peaks. The observed data are shown as circles while the fitted pattern and solid lines represent individual calculated peaks.

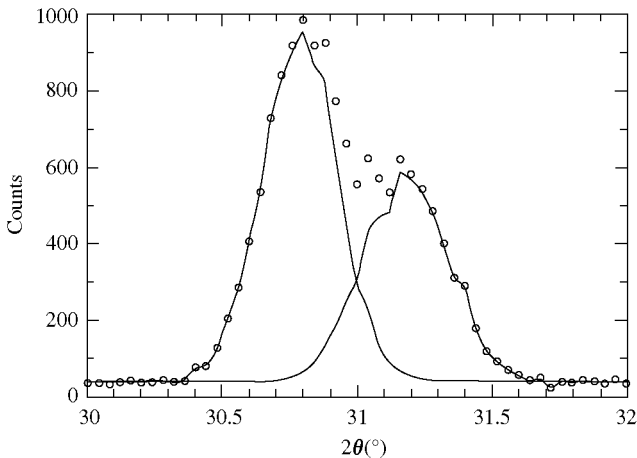


Fig. 8.3. The individual peaks contributions (solid lines) towards the observed peak area as calculated by the method originally proposed by Rietveld (1969).

magnitude and the problem thus reduces to finding the peak area. For an isolated peak, the observed peak area is easy to evaluate. All that needs to be done is to add together the background-subtracted profile points. For overlapping peaks, the contribution for a given reflection is weighted by the calculated peak contribution for that reflection divided by the sum of the calculated peak values for each contributing reflection. This is illustrated for the two-peak example in Fig. 8.3.

The ‘observed’ integrated intensities for the two reflections are given by the following formulae:

$$A_1(obs) = \sum_i \frac{A_1(calc) \times q_1(i)}{(A_1(calc) \times q_1(i) + A_2(calc) \times q_2(i))} (obs(i) - back(i)), \quad (8.4)$$

$$A_2(obs) = \sum_i \frac{A_2(calc) \times q_2(i)}{(A_1(calc) \times q_1(i) + A_2(calc) \times q_2(i))} (obs(i) - back(i)), \quad (8.5)$$

where $A_k = j_k |F_k|^2$ are the integrated intensities, (j_k and $|F_k|$ are the reflection multiplicity and structure-factor magnitude respectively), $q_k(i) = c_k(i)H_k(i)$ is the product of $c_k(i)$ (which contains Lorentz-polarization, absorption and extinction terms) and $H_k(i)$, the normalized k th peak shape, and $obs(i) - back(i)$ is the observed peak contribution at the i th point in the diffraction pattern.

Combining eqns (8.4) and (8.5) gives

$$A_1(obs) + A_2(obs) = \sum_i (obs(i) - back(i)), \quad (8.6)$$

which indicates that the sum of the observed peak areas evaluated by Rietveld’s algorithm is always equal to the background-subtracted area of the observed Bragg peaks in the powder diffraction pattern. This has been the standard approach for thirty years for extracting estimates of structure-factor magnitudes and has been successfully applied to numerous problems.

8.2.2 The iterative Le Bail algorithm

Le Bail *et al.* (1988) noted that the Rietveld approach to obtaining estimates of structure-factor magnitudes could be extended to the situation where there is no initial structural model. If the structure is unknown and, as a result, no calculated structure factors can be generated, then the simplest thing to presume is that all the integrated intensities are initially equal.¹ The particular initial value does not matter as the sum rule expressed in eqn (8.6) ensures that the observed integrated intensities are correctly scaled. Clearly, after one iteration, isolated peaks will have an observed intensity equal to the observed area under the Bragg peak. For overlapping reflections, the procedure has to be tackled iteratively. The Le Bail method is, thus, a recursive version of the original Rietveld approach to observed structure-factor magnitude evaluation where the observed peak areas for the r th iteration are used as the calculated peak areas for the $(r + 1)$ th

¹ Strictly speaking, without prior knowledge of the crystal structure, the expectation values of the peak areas of neighbouring Bragg reflections are the same and not the structure-factor magnitudes (Bricogne 1991).

iteration. Generalizing to N -peak overlap, this may be written mathematically as

$$A_m^{(r+1)}(obs) = \sum_i \frac{A_m^{(r)}(obs) \times q_m(i)}{\left(\sum_{n=1}^N A_n^{(r)}(obs) \times q_n(i)\right)} (obs(i) - back(i)), \quad (8.7)$$

where $A_n^{(r=1)}(obs) = 1 \forall n = 1, \dots, N$.

Applying this recursive algorithm to the two-peak example shown in Fig. 8.2 rapidly leads to good estimates of the Bragg peak areas. Figure 8.4(a) shows the

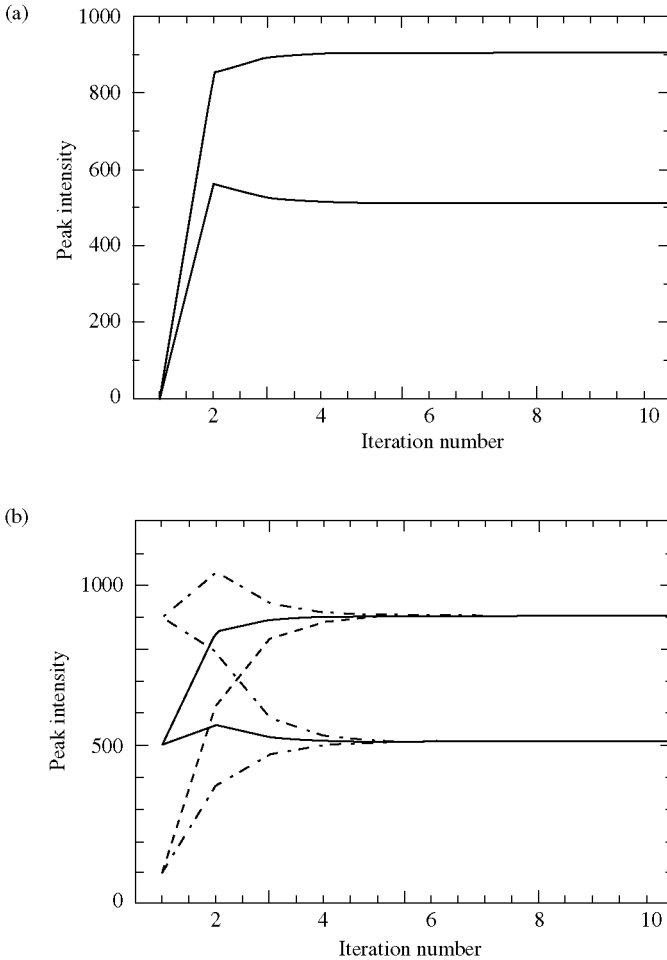


Fig. 8.4. The individual peak intensities for the two overlapping peaks shown in Figs 8.2 and 8.3 evaluated iteration by iteration by the Le Bail method, (a) with initial values of 1 for both peaks and (b) with different initial values of (500, 500) (solid line), (100, 900) (dashed line) and (900, 100) (dot-dash line).

rapid convergence of the Le Bail method in a few iterations despite the initial assumption of unit-peak area. Indeed, Fig. 8.4(b) illustrates that the Le Bail algorithm in this well-conditioned example is robust with respect to the initial starting values of the Bragg peak areas. In only five iterations, the Le Bail algorithm has lost all memory of the initial starting values. This robustness is valuable since it implies that the integrated intensity estimates derived from the Le Bail method may generally be treated with confidence.

As a corollary, however, it highlights the difficulty of using the recursive Le Bail method for incorporating prior knowledge about structure-factor magnitudes by using these values as the starting point for the iterative process. Figure 8.4(b) shows that for differing starting points, very different values are obtained for first, second and third iterations. Since there is no statistical preference for any particular iteration, it is difficult to know which iteration to select and so the Le Bail method cannot be considered to be a robust method for incorporating prior structure-factor-magnitude information. Nevertheless, some authors have used this approach to some advantage (Altomare *et al.* 1996)—see also Chapter 11.

Although the Le Bail method is generally robust and converges relatively rapidly, there are occasional instabilities. Figure 8.5(a) illustrates such a situation.

The two peaks are in the same positions and have the same widths as those in Fig. 8.2 but are ten times weaker. Furthermore, the background has been slightly overestimated. For weak peaks, this is not an uncommon occurrence. The Le Bail estimates, iteration by iteration, are shown in Fig. 8.5(b) and are chaotically oscillatory with the appearance of negative intensities upon occasion. Mathematically, this occurs because the overestimated background leads to both positive and negative contributions (and, as a consequence, occasionally contributions that are very small) to the denominator in eqn (8.7). In general, however, with strong peaks and correctly determined backgrounds this does not occur, and the Le Bail method offers a pragmatic and successful approach to extracting integrated intensities from a powder diffraction pattern.

Perhaps, the single most important aspect concerning the popularity of the Le Bail method is its ease of incorporation into standard Rietveld codes since it is an iterative adaptation of Rietveld's original method for estimating observed structure-factor magnitudes. Most main Rietveld codes include this small modification, which has in turn ensured the wide use of the Le Bail method. Although the estimated standard deviations of observed intensities are not normally included as part of the standard Le Bail approach, they may nevertheless be evaluated. Indeed, the fully correlated integrated intensities weight matrix (the inverse of the integrated intensities covariance matrix) may be easily evaluated in exactly the same way as in the least-squares Pawley method (see Section 8.3.2). Access to this matrix allows rapid calculation of the powder diffraction pattern for structure solution based upon integrated intensities extracted by the Le Bail method. This approach has been used successfully by Pagola *et al.* (2000).

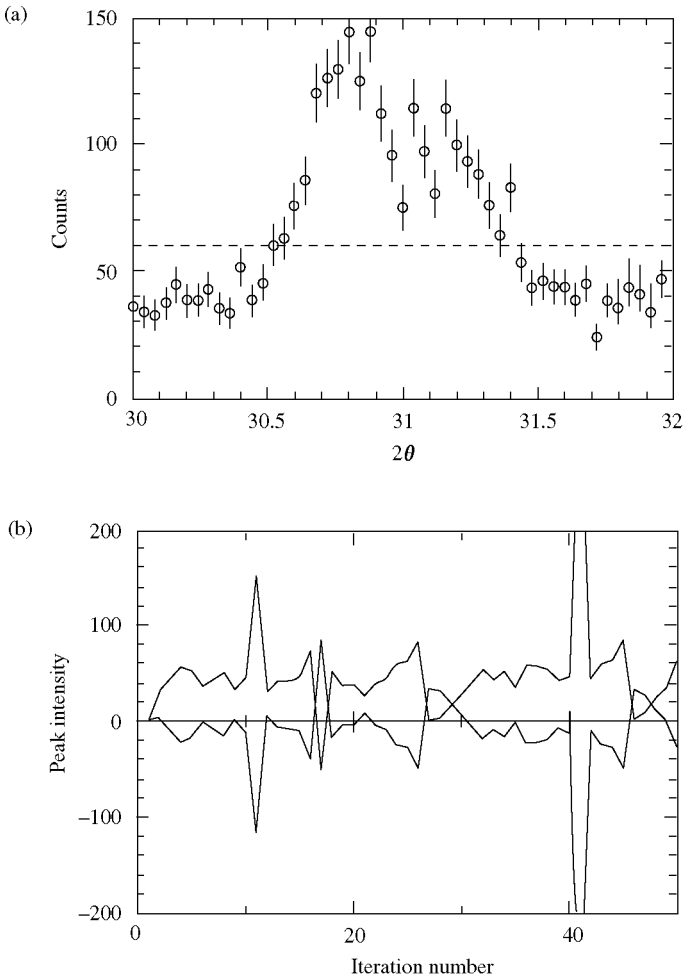


Fig. 8.5. (a) Two weak overlapping peaks. The observed data are represented as circles with lines representing the estimated standard deviations. The background (dashed line) has been slightly over estimated. (b) The Le Bail estimates of the two peak areas shown in Fig. 8.4(a) show wild, chaotic behaviour iteration by iteration.

8.3 The Pawley method

8.3.1 Introduction

Pawley (1981) published a method for determining Bragg peak intensities from powder diffraction data in the absence of a structural model. The principle behind the Pawley method is quite simple. The Rietveld method involves

the least-squares analysis of a powder diffraction pattern where the variables are (a) peak position parameters (cell parameters and zero-point), (b) peak-shape parameters and (c) parameters dependent on the peak area (i.e. atomic coordinates, anisotropic displacement parameters, absorption and extinction parameters). The Pawley method is also a least-squares analysis of a powder diffraction pattern but while the variables associated with peak positions and widths are the same, the variables associated with the peak areas are simply the peak areas themselves. Thus, no structural model is required. Despite the fact that the statistical basis of the Pawley method is far more robust than the Le Bail iterative method and, although the Pawley method was introduced some six years earlier than its counterpart, the Le Bail method is currently still the more popular approach. There are two reasons for this—availability of code and perceived weaknesses in the Pawley method. These are addressed in the following section.

8.3.2 *Mathematical background*

The mathematical description of the model value for a point in a powder diffraction pattern may be written as

$$M(i) = \text{back}(i) + \sum_{\{k\}_i} A_k q_k(i), \quad (8.8)$$

where the summation is over all peaks that contribute to the i th point in the pattern and the symbols are the same as in Section 8.2.

In the Rietveld method, explicit functional forms and derivatives for the structure factors with respect to structural parameters must then be evaluated. For the Pawley method, the structure-factor magnitudes may be evaluated simply by minimizing the summed weighted difference between observed ($y(i)$) and model ($M(i)$) diffraction patterns:

$$\chi^2 = \sum_{i=1}^N \frac{1}{\sigma_i^2} (y(i) - M(i))^2. \quad (8.9)$$

The derivatives with respect to $A_k = j_k |F_k|^2$ are easy to evaluate and when set to zero give the best-fit criterion with respect to peak areas.

$$\frac{\partial \chi^2}{\partial A_k} = -2 \sum_{i=1}^N \frac{1}{\sigma_i^2} q_k(i) \left(y(i) - \sum_{\{h\}_i} q_h(i) A_h \right) = 0. \quad (8.10)$$

Obtaining peak areas is a linear least-squares problem and may be achieved by a single matrix inversion:

$$A_k = (H_{hk})^{-1} B_h, \quad (8.11)$$

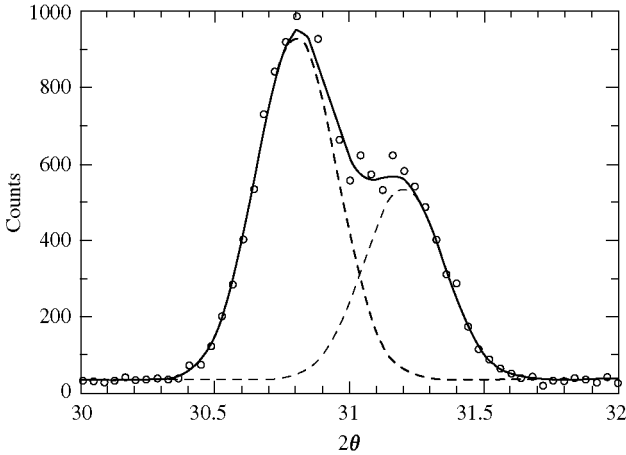


Fig. 8.6. A linear least-squares Pawley fit (solid line) for the two overlapping peaks illustrated also in Figs 8.2 and 8.3. The dashed lines show the individual peak shapes.

where

$$H_{hk} = \sum_{i=1}^N \frac{1}{\sigma_i^2} q_k(i) q_h(i) \quad \text{and} \quad B_h = \sum_{i=1}^N \frac{1}{\sigma_i^2} q_h(i) y(i). \quad (8.12)$$

All the important statistical quantities are immediately available. The integrated-intensities covariance matrix, for example, is given by $C_{hk} = (H_{hk})^{-1}$.² Indeed, instead of being an iterative approach, the Pawley method solves the integrated intensity extraction problem in a single matrix inversion. When peak-shape parameters and lattice constants are known, the integrated intensities are obtained in a single least-squares cycle. In the two-peak example discussed in the previous section, this linear least-squares approach returns peak intensities of 897 ± 3 and 499 ± 1 (see Fig. 8.6). The -3 per cent correlation between the two peak areas is very small indicating that the peaks are essentially independent of one another (David 1999).

The simplicity of the mathematics associated with the Pawley method, however, belies a number of practical problems. Perhaps the most straightforward of these is that the algebra outlined above necessitates more substantial modifications to existing Rietveld codes than the Le Bail method. As a consequence, there are fewer generally used computer programs based upon the Pawley approach. More significantly, the matrix H_{hk} is large (order = the number of

² A discussion of the use of integrated intensities for structure solution is given in Chapter 15. Note that a large matrix inversion is required to obtain the integrated-intensities covariance matrix irrespective of whether the Le Bail or Pawley methods are being used.

reflections) and usually degenerate. The size of the matrix is not a serious problem because the matrix itself is highly sparse (all the non-zero terms are close to the matrix diagonal as they can only arise from overlapping peaks) and thus, can be easily inverted in block diagonal form. From a practical point of view, however, most Pawley programs do not invoke sparse matrix inversion and thus, are limited to a few hundred reflections which, though small compared with the number of reflections in many powder diffraction patterns, are sufficient for structure solution.

The degenerate nature of the matrix again, in principle, is easy to overcome but has, in practice, proved to be more difficult to handle. Degeneracy occurs when two rows (or columns since the matrix is symmetrical) are identical to one another and happens when two or more peaks are almost exactly overlapping. This can be avoided by grouping together reflections that are closer than a particular criterion such as a quarter of a FWHM. Experience with our own algorithms suggests that a better criterion is a proportion of the step size in the powder diffraction pattern. It might reasonably be considered that peaks that lie less than one step size apart when treated separately lead to ill-conditioning on matrix inversion. Experience, however, has shown that stable inversions are obtained when peak separations are as little as 0.5 step sizes (corresponding to less than 0.1 FWHM) apart. Other authors have found a two-stage approach to be successful (Jansen *et al.* 1992a).

Although stable refinements are achieved, close peak separation often leads to the appearance of highly negative intensities, which have generally been considered to be problematical by the powder diffraction community. How, for example, can one take the square root of a negative number to obtain a meaningful structure-factor magnitude? Various approaches have been elaborated to deal with this problem. Pawley, in his original implementation of his program, introduced Waser-type constraints (Waser 1963) to minimize the differences between neighbouring integrated intensities. This ingenious approach can eliminate negative intensities but does increase the number of iterations and can lead to instabilities. Other authors (Sivia and David 1994; Engel *et al.* 1999; Coelho 2000) have enforced positivity by refining not on the integrated intensities but on the structure-factor magnitudes themselves. The least-squares process is no longer linear and thus, convergence is slower and can take many iterations to complete.

Sivia and David (1994) proposed another method based upon probability theory that enforced positivity through a Bayesian prior probability approach. The procedure is rapid, robust and reliable and leads to all positive intensities that can be used successfully for structure solution (Shankland *et al.* 1997). The method is illustrated by a two-peak example taken from the paper of Sivia and David (1994). The results of a Pawley refinement are shown graphically as a probability distribution function in Fig. 8.7(a). The contours represent the results of the Pawley refinement that give refined values of -5 ± 25 and 14 ± 11 for the two peak intensities.

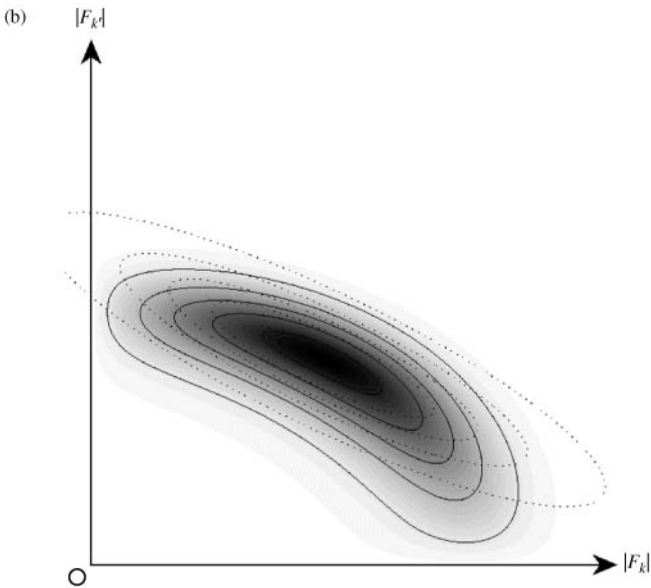
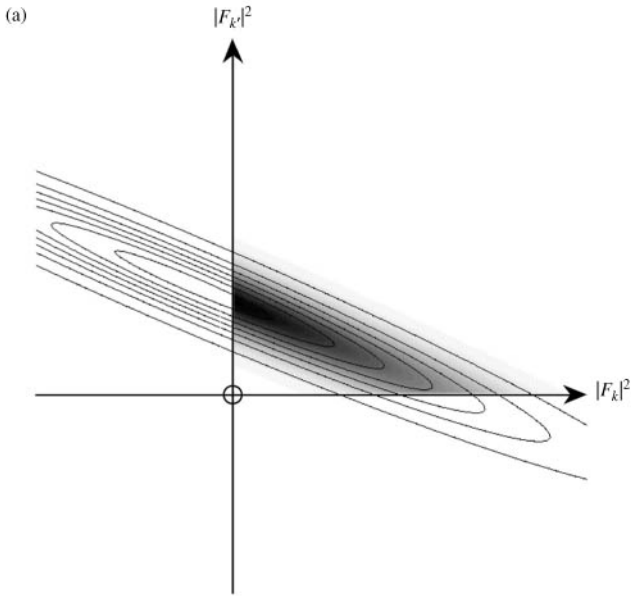


Fig. 8.7. The probability distribution function derived from a Pawley refinement for two strongly overlapping peaks shown (a) as a function of $|F|^2$ and (b) as a function of $|F|$. The grey contours represent the combined information from the Pawley refinement and enforcement of positivity. The dotted contours in (b) are the best-fit multivariate Gaussian distribution to the probability distribution function.

The peaks are extremely close together and this is reflected in the high negative statistical correlation of -97 per cent between the two peaks. The appearance of a negative intensity is usually taken to be problematical. Figure 8.7(a), however, illustrates that the refined negative intensity only indicates the top of the probability distribution. There is significant probability that both peaks are positive. The Bayesian approach incorporates precisely this prior assumption—namely that the peaks must be positive. The only acceptable part of the probability distribution is then, the grey-shaded area in the positive quadrant of Fig. 8.7(a). This truncated probability distribution is now highly non-Gaussian. However, transforming to $|F|$ space (which is allowed as only the positive quadrant has a finite probability) results in a banana-shaped distribution shown in Fig. 8.7(b) that is more closely Gaussian and can indeed be approximated by a multivariate Gaussian distribution (dotted contours in Fig. 8.7(b)). This transformation is stable and rapid and yields $|F|$ values of 3.2 ± 1.8 and 2.8 ± 0.9 with a correlation of -87 per cent. At first sight it is rather unexpected to find that the first $|F|$ value is larger than the second as the average $|F|^2$ value for the first peak was negative. However, the large estimated standard deviation of the first peak implies a high probability of relatively large structure-factor values which propagate through to the final $|F|$ result. After structure solution, the calculated $|F|$ values for the two peaks were 3.1 and 2.6, which provides satisfactory evidence of the efficacy of the Bayesian approach.

This section would not, however, be complete without a final caveat for all integrated intensity extraction methods. When the Bragg peak overlap is so substantial at high angle that no clear Bragg peak-shapes are visible against the background, all methods must be considered unreliable. Unlike the Rietveld method, where the crystal structure constrains the size of the Bragg peaks, the ability to discriminate between peak and background disappears. Although this can be accommodated mathematically using the full covariance matrix that includes both peak intensities and background coefficients, there is little information content in these reflections and they are best left unused for structure solution.

8.4 Space group determination

Traditionally, space group determination from powder diffraction data is performed manually by inspection of the systematically absent reflections. In monoclinic symmetry, for example, it is usually relatively easy to distinguish between the small number of space group options. Strictly speaking, examination of the space group absences in a powder diffraction pattern only indicates the extinction symbol (Vos and Buerger 1993) often leaving a small ambiguity about the precise space group. For example, the extinction symbol associated with the space group, $P 2_1$ (*b*-axis unique), is $P - 2_1$ - which is shared with space group $P 2_1/m$ (*b*-axis unique). In other words, both space groups

share the same systematic absences which are $k = 2n + 1$ for $0k0$. On the other hand, the extinction symbol, $P - 2_1/c -$, is unique to the common space group, $P 2_1/c$ (b -axis unique); the absences $0k0$, $k = 2n + 1$ and $h0l$, $l = 2n + 1$ uniquely determine that space group. Although it is, in principle, possible to distinguish between different space groups that possess the same extinction symbol by evaluating intensity statistics, it is a much more difficult task than the equivalent process with single crystal data. This is because the substantial degree of Bragg peak overlap in a powder diffraction pattern generally makes the differences between centric and acentric reflection distributions effectively impossible to detect.

Bragg peak overlap can clearly cause difficulties with determining absences. For low Miller indices associated with long d -spacing reflections, the problem is rarely severe even for low-resolution laboratory powder diffraction data. However, for higher Miller indices (typically 5 and above) reflections that may be absent often overlap with reflections that are present for all space groups. This means that the manual decision about a particular space group is often made on the basis of a small number of low-index reflections; most of the information in the diffraction pattern is rejected in the visual determination of a space group. One obvious way forward is to profile fit the diffraction data using either the Le Bail or Pawley methods. These give a stronger indication of the presence or absence of a Bragg peak. Full use of the integrated-intensities covariance matrix gives the best evidence for the presence or absence of a peak. The profile R -factor or integrated intensities chi-squared value gives a global measure of the goodness of fit to a powder diffraction pattern and can be used as a test for space group discrimination. In particular, if a space group predicts an absence where there is a strong Bragg peak, then the various goodness-of-fit quantities will be substantially poorer than for space groups where the peak is allowed. This profile refinement method does indeed reduce the space group choice, but still leads to a large number of possible space groups. This is because all space groups with extinction conditions that are a subset of the conditions for the correct space group will fit with equal or better goodness-of-fit values. In the example of dopamine hydrobromide, which is discussed below, all the profile refinements with extinction symbols above $P - - -$ fit as well or better than the refinement with the correct symbol $P b c -$ (see Table 8.1). One needs to bias towards more restrictive models that involve more stringent extinction conditions. Markvardsen *et al.* (2001) have recently developed such an approach, based upon Bayesian probability theory, that quantifies the penalty costs for relaxing extinction conditions.

In the case of space group determination, Bayesian probability theory goes beyond the question of 'How well are the data fitted given a particular extinction symbol?' to address the more appropriate question of 'Which is the most probable extinction symbol given the data that have been collected?'. The first question turns out to be half the answer. Additionally, one has to construct prior probability distributions for reflections that are conditional on whether

Table 8.1 Extinction symbol probabilities for dopamine hydrobromide. The probabilities are expressed as a ratio of the log(probability) of the extinction symbol to the log(probability) of $P - - -$. The diffraction pattern used to determine the space group of dopamine hydrobromide was collected on Station BM16 at the ESRF, from a 1 mm capillary using an incident wavelength of 0.6528 Å

| Symbol | Probability | hkl | $0kl$ | $h0l$ | $hk0$ | $h00$ | $0k0$ | $00l$ |
|------------|-------------|-------|-------|-------|-------|-------|-------|-------|
| $Pbc-$ | 97.98 | | k | l | | | k | l |
| $Pb--$ | 50.34 | | k | | | | k | |
| $P-c-$ | 43.96 | | | l | | | | l |
| $P-2_12_1$ | 21.17 | | | | | | k | l |
| $P-2_1-$ | 15.21 | | | | | | k | |
| $P--2_1$ | 5.96 | | | | | | | l |
| $P---$ | 0 | | | | | | | |
| $Pbc b$ | -388.55 | | k | l | k | | k | l |
| $P-c b$ | -423.68 | | | l | k | | k | |
| $Pb-b$ | -436.18 | | k | | k | | k | |
| $P--b$ | -471.32 | | | | k | | k | |

the reflection is present or absent. The probability of a space group absence is simply a delta function (i.e. the assumption is made that the peak intensity is precisely zero) whereas a presence follows a Wilson-type intensity distribution. Combining these prior probabilities with the quality of fit to the data makes simpler models with fewer reflections present more probable in a quantifiable way.

Table 8.1 illustrates this for the case of dopamine hydrobromide. Of the top six possibilities shown, it is clear that $Pbc-$ is much more probable, given the data, than the next choice $Pb--$, which is in turn much more probable than $P-c-$, etc. As stated previously, it is not surprising that the second-to-sixth-ranked choices are more probable than $P---$, since all contain subsets of the reflection conditions for the most probable choice $Pbc-$. Similarly, those that are less probable than $P---$, all contain additional conditions that are not met by the data. Indeed for face-centred extinction symbols, the probabilities range from -94800 ($F---$) to -111200 ($Fddd$) which may all be considered to be extremely remote.

A more difficult case of space group determination is provided by the example of 1,4-dimethanol benzene (P. W. Stephens, personal communication). The crystal structure is monoclinic with lattice constants $a = 9.844$ Å, $b = 15.484$ Å, $c = 4.845$ Å and $\beta = 101.20^\circ$. From visual inspection of the systematic absences, it was not possible to distinguish between the space group extinction symbols $P12_1/a1$, $P12_1/n1$ and $P12_1/c1$. The Bayesian approach confirms this difficulty in space group determination since all three options are significantly more probable than $P1-1$ (see Table 8.2).

Table 8.2 Extinction symbol probabilities for 1,4-dimethanol benzene. The probabilities are expressed as a ratio of the log(probability) of the extinction symbol to the log(probability) of $P 1 - 1$. The diffraction pattern used to determine the space group of 1,4-dimethanol benzene was collected on beamline X3B1 at the NSLS, Brookhaven using an incident wavelength of 1.149896 Å

| Symbol | Probability | hkl | $h0l$ | $0k0$ |
|---------------|-------------|---------|-------|-------|
| $P 1 2_1/n 1$ | 25.36 | | $h+l$ | k |
| $P 1 n 1$ | 19.53 | | $h+l$ | |
| $P 1 2_1/a 1$ | 18.04 | | h | k |
| $P 1 2_1/c 1$ | 17.82 | | l | k |
| $P 1 a 1$ | 12.02 | | h | |
| $P 1 c 1$ | 11.98 | | l | |
| $P 1 2_1 1$ | 6.02 | | | k |
| $P 1 - 1$ | 0 | | | |
| $I 1 - 1$ | -1760.87 | $h+k+l$ | $h+l$ | k |
| $I 1 a 1$ | -1768.75 | $h+k+l$ | h,l | k |
| $A 1 n 1$ | -3398.06 | $k+l$ | h,l | k |
| $A 1 - 1$ | -3407.11 | $k+l$ | l | k |
| $C 1 - 1$ | -4682.25 | $h+k$ | h | k |
| $C 1 c 1$ | -4707.09 | $h+k$ | h,l | k |

The order of probability in Table 8.2 does, however, make space group $P 2_1/n$ more likely than either space groups $P 2_1/a$ or $P 2_1/c$. This assignment is confirmed by structure solution since only space group $P 2_1/n$ yields an acceptable structure. The discrimination between space groups involves not only the identification of single absent or present reflections, but also the evaluation of presences and absences within a group of reflections. While this is difficult by eye, the Pawley extraction of peak intensities and their correlations leads to a quantifiable assignment of peak absence/presence even in cases of substantial overlap.

8.5 Overcoming Bragg peak overlap

Although it is clearly impossible simply from profile refinement methods to determine the intensities of completely overlapping reflections, the use of basic crystallographic constraints such as positivity and atomicity can provide some discriminatory power. David (1987, 1990) showed that, by using all the available Bragg intensity data, information about the separation of overlapped intensities could be obtained from the non-overlapped reflections. Two strategies were proposed: one involved the use of a maximum-entropy Patterson map algorithm and the other a modification of Sayre's (1952) squaring method.

When high-resolution data are available, the maximum entropy method is powerful (David 1990), particularly when the Patterson map is used directly. The Sayre's squaring method has been substantially developed by the work of Estermann, Baerlocher and McCusker (1992) and Estermann and Gramlich (1993) to include an iterative redistribution of intensity statistics. This FIPS (Fast Iterative Patterson Squaring) method has been successfully used to solve several zeolite structures from powder data (see Section 12.5).

In order to understand how basic constraints such as positivity and atomicity can help in the separation of completely overlapping reflections, consider the Sayre's squaring method developed by David (1987). Electron density is concentrated on atomic sites and is everywhere positive in a crystal structure. The Patterson map, which is simply the autocorrelation function of the crystal structure, will have similar attributes. Fig. 8.8(a) shows a one-dimensional section of a Patterson map.

When this Patterson map is squared (Fig. 8.8(b)) the squared result still bears a strong resemblance to the original Patterson function. The Fourier transforms of the Patterson map and its square are given by

$$g_{\mathbf{h}} = \int_V P(\mathbf{r}) \cos(2\pi\mathbf{h} \cdot \mathbf{r}) dV = |F_{\mathbf{h}}|^2, \quad (8.13)$$

$$G_{\mathbf{h}} = \int_V P^2(\mathbf{r}) \cos(2\pi\mathbf{h} \cdot \mathbf{r}) dV = \sum_{\mathbf{k}} g_{\mathbf{k}} g_{\mathbf{h}-\mathbf{k}}. \quad (8.14)$$

Writing the Patterson map as a sum of Gaussian functions leads to

$$P(\mathbf{r}) = \sum_{n=1}^{N(N-1)} \exp\left[-(\mathbf{r} - \mathbf{r}_0^n)^2/2\sigma^2\right], \quad (8.15)$$

and

$$\begin{aligned} P^2(\mathbf{r}) &= \left(\sum_{n=1}^{N(N-1)} \exp\left[-(\mathbf{r} - \mathbf{r}_0^n)^2/2\sigma^2\right] \right)^2 \\ &\approx \sum_{n=1}^{N(N-1)} \exp\left[-(\mathbf{r} - \mathbf{r}_0^n)^2/\sigma^2\right]. \end{aligned} \quad (8.16)$$

The approximation holds if the overlaps between the peaks in the Patterson map are small and is a reasonable working assumption. This is because the Patterson map, though containing $N(N-1)$ peaks, is still relatively sparse and is dominated by vectors associated with heavy atoms that will generally be well-separated from one another. Combining eqns (8.13 and 8.14) and (8.15 and 8.16) leads to the relationship

$$|F_{\mathbf{h}}|^2 \propto \exp\left[-\frac{1}{2}\sigma^2/d_h^2\right] \sum_{\mathbf{k}} |F_{\mathbf{k}}|^2 |F_{\mathbf{h}-\mathbf{k}}|^2. \quad (8.17)$$

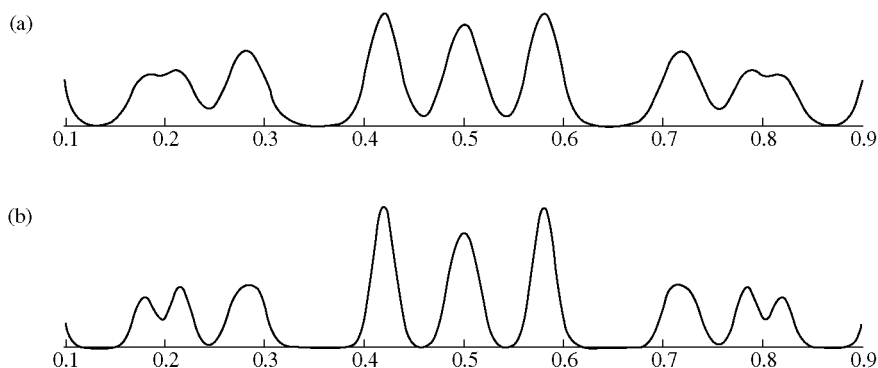


Fig. 8.8. A one-dimensional section of (a) a synthesized Patterson function and (b) its square.

For overlapping reflections, the coefficient is a constant as it is only a function of d -spacing and thus, the fractional integrated-intensity contribution of the m th of M overlapping reflections is given by

$$\frac{j_m |F_{\mathbf{h}_m}|^2}{\sum_{i=1}^M j_i |F_{\mathbf{h}_i}|^2} \cong \frac{j_m \sum_{\mathbf{k}} |F_{\mathbf{k}}|^2 |F_{\mathbf{h}_m - \mathbf{k}}|^2}{\sum_{i=1}^M j_i \left(\sum_{\mathbf{k}} |F_{\mathbf{k}}|^2 |F_{\mathbf{h}_i - \mathbf{k}}|^2 \right)}. \quad (8.18)$$

New estimates for the overlapped integrated intensities may be obtained using this equation with the initial presumption that overlapped intensities are equipartitioned. These new estimates can then be recycled through eqn (8.18) to provide improved values. This iterative process continues until convergence is achieved. This approach does provide superior results over equipartitioning. However, being based upon the approximate assumption that Patterson and squared Patterson maps look similar in structure, the algorithm is not exact. Examination of results (David 1987) suggests that the squaring method shifts the relative intensities in the correct sense but, in the majority of cases, to a degree often substantially less than the true amount.

Other techniques based upon semi-exhaustive intensity permutations of overlapped reflections have met with success (Jansen *et al.* 1992b; Cascarano *et al.* 1991). Perhaps the most rigorous development to date, however, is the theoretical work of Bricogne (1991) who showed that the effects of overlapped reflections may be treated as an extension of the phase ambiguities of centric (1 dimension) and acentric (2 dimensions) to a $(2n_a + n_c)$ -dimensional space, where n_a and n_c are the number of acentric and centric reflections contained within a completely overlapped group of reflections. The need to phase permute within a multi-dimensional hyperspace is computationally daunting and yet is an oversimplification of the problem as due account must also be taken of the

often high correlation between neighbouring reflections that almost overlap. This theoretical approach is discussed extensively in Chapter 14.

8.6 Incorporating crystallographic information

In the previous section, it was shown that the simple restrictions of positivity and atomicity could bring some discriminatory power to the separation of completely overlapping reflections. Clearly, if a part of the structure is already known then the estimated values of overlapping integrated intensities can be better determined. Various groups have developed strategies to incorporate such fragment information into the extraction of integrated intensities (Jansen *et al.* 1992*b*; Altomare *et al.* 1996, 1999) and these approaches are discussed elsewhere in this book (see Sections 10.5 and 11.5). In this section, we continue to use probability theory in a consistent Bayesian manner to show that substantial improvements can be made in the separation of integrated intensities if a part of the structure is already known.

Consider that the initially extracted integrated intensities have been used to determine, for example, the location of a heavy atom or an aromatic ring through Patterson methods. Phased structure factors can easily be calculated for this component of the crystal structure and then used in conjunction with the diffraction data to constrain further the structure-factor intensities. Take the case of two centric reflections, k and k' , depicted in Fig. 8.9(a) and (b).

The solid contours indicate the goodness of fit obtained with the diffraction data for various possible combinations of the two structure factors, F_k and $F_{k'}$, so that (a) corresponds to two isolated Bragg peaks (with $|F_k|^2 = 9 \pm 2$ and $|F_{k'}|^2 = 7 \pm 2$ with no correlation) and (b) depicts the situation for complete overlap ($|F_k|^2 + |F_{k'}|^2 = 16 \pm 3$). The toroidal probability distribution in Fig. 8.9(b) reflects the fact that only the sum of the integrated intensities (i.e. the quadratic sum of F_k and $F_{k'}$) is determined well by the measurements. The dotted contours represent the prediction for the two structure factors based solely on knowledge of the recognised fragment and the chemical composition of the full-crystal structure. The best estimate is the peak of this distribution and is given by the structure factors, F_k (known) and $F_{k'}$ (known), calculated from the positions of the known atoms, while the uncertainty, $\sigma = \sigma_k = \sigma_{k'}$, is governed by scattering density from the unlocated components. Indeed,

$$\sigma = \sqrt{\sum_{n=1}^{N_{\text{unlocated}}} f_n^2} \quad (8.19)$$

where f_n is the atomic scattering factor for one of the $N_{\text{unlocated}}$ atoms in the crystal structure. For this particular example, F_k (known) = 2 ± 2 and $F_{k'}$ (known) = 4 ± 2 . Observed and model probability distributions are multiplied together since they form two independent pieces of information. This final

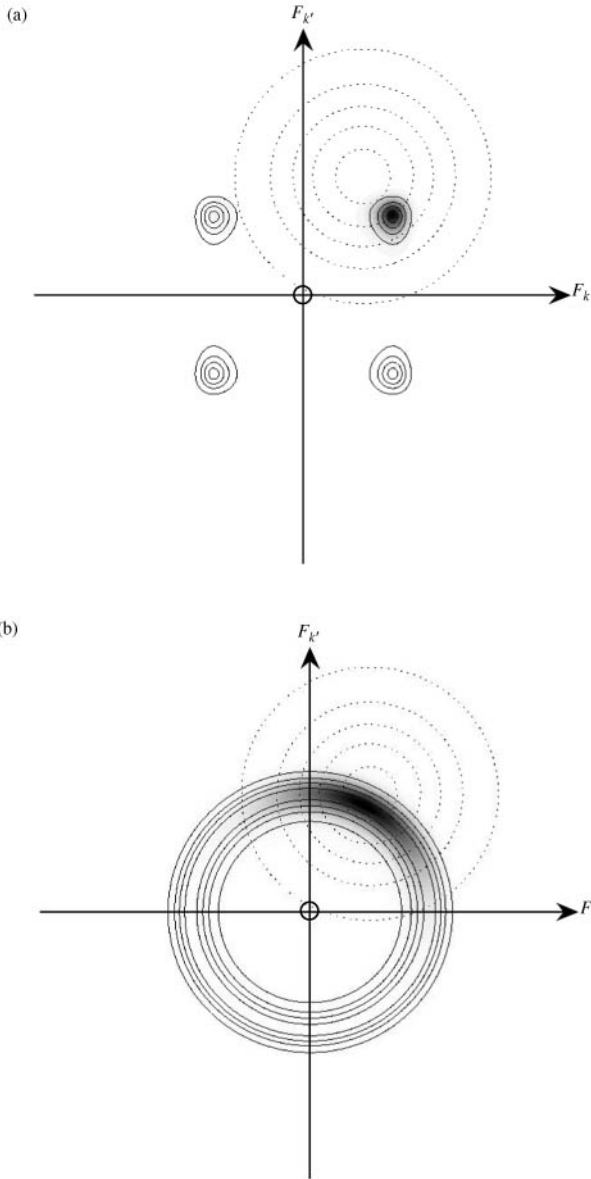


Fig. 8.9. The joint probability distribution for two phased structure factors (a) for two isolated Bragg peaks, and (b) for two completely overlapping Bragg peaks. The solid contours correspond to the probability distribution associated with the Pawley refinement of the observed data. The dotted contours are associated with the calculated structure factor, which is centred on the structure factor value of the known fragment and has a Gaussian blur related to the scattering from unlocated atoms. The grey-scale represents the combined probability distribution.

probability is indicated in the figures by the grey-scale shading. In the top example, although the model constraints are relatively weak, positive phases for both structure factors are highly preferred although there is still a small probability that F_k is negative. It is worth pointing out that this approach has not only confirmed intensities but also indicated probable phase values as well. Indeed, in general, located fragments contain powerful phase information that should be used to maximum advantage in structure solution. This is discussed further in the second half of this section. However, from a practical viewpoint, an updated estimate of the structure-factor magnitudes is useful as modified input to traditional Direct methods programs. In principle this process can proceed iteratively with structure factor estimates improving as the known fragment size increases until the complete structure is solved. An estimate of the structure-factor magnitudes can be obtained from the joint probability distribution shown in Fig. 8.9(a) and (b) by integrating it over regions where either $|F_k|$ or $|F_{k'}|$ are constant. The result of such a marginalization is shown in Fig. 8.10(a) and (b) and gives for case (a) $|F_k| = 2.97 \pm 0.34$ and $|F_{k'}| = 2.69 \pm 0.36$ with no correlation and for case (b) $|F_k| = 0.5 \pm 8.7$ and $|F_{k'}| = 4.0 \pm 1.2$ with a correlation of -94 per cent.

It should be noted that the error-bars quoted for case (b) have to be treated with caution, as the Gaussian approximation of the probability distribution upon which they are based is clearly a poor one in this instance. In the analysis above, both reflections have been presumed to be centric. As a further illustration of how this formal probabilistic analysis automatically makes full use of all the information that is presented to it, Fig. 8.10(c) shows how the estimate of the magnitudes of the structure factors would have changed for the case of two completely overlapping acentric peaks. The optimal estimates would then have been $|F_k| = 2.2 \pm 1.3$ and $|F_{k'}| = 3.4 \pm 0.9$ with a correlation of -86 per cent. In this situation of completely overlapping peaks, irrespective of whether the reflections are centric or acentric, there is a strong indication that both reflections have a positive phase and thus direct structure solution from this stage is possible if a sufficiently large structure fragment is known.

It is clear from the previous discussion in this section that knowledge of the partial crystal structure can be used to improve the estimates of the intensities of the reflections, $|F_k|^2$ and $|F_{k'}|^2$ particularly for strongly overlapped peaks. However, it was also shown that located atoms give an indication not only of the amplitude, but also of the phase of each structure factor. Ignoring the latter is tantamount to throwing away useful, if not vital, information. Indeed, Fig. 8.10(a) illustrates that for isolated and well-determined Bragg peaks, the fragment information has little effect on the intensities of the structure factors but does provide a strong preference for a particular phase assignment. In practice, this approach can be used successfully for structure completion when as little as one third of the scattering density in the crystal structure has been located. This is illustrated by the particular example of chlorothiazide that was solved by Direct methods (Shankland *et al.* 1997).

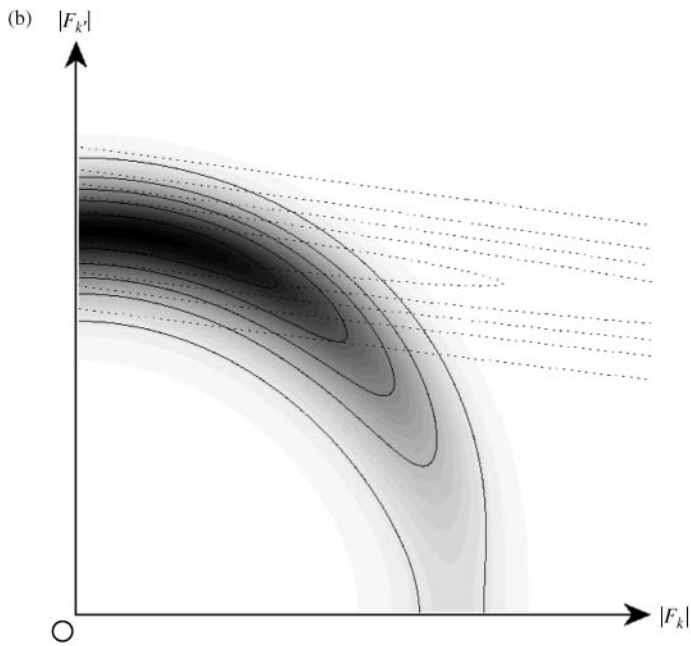
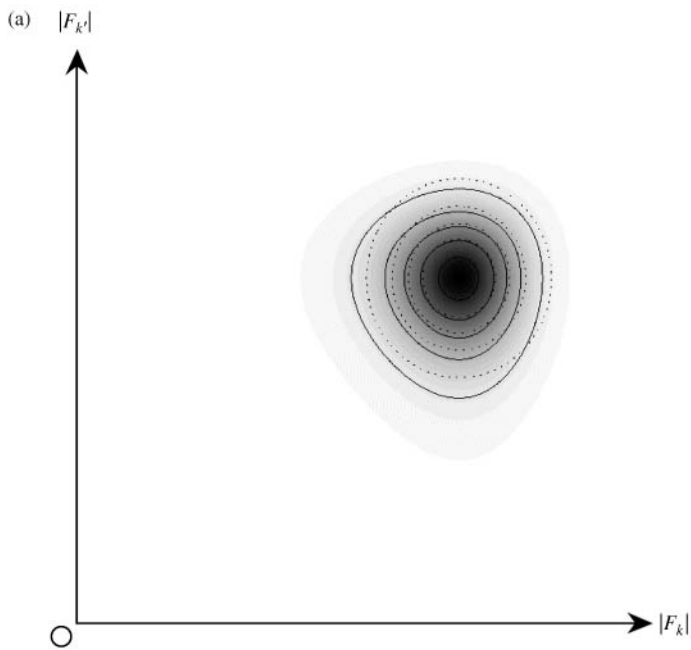


Fig. 8.10. See next page for caption.

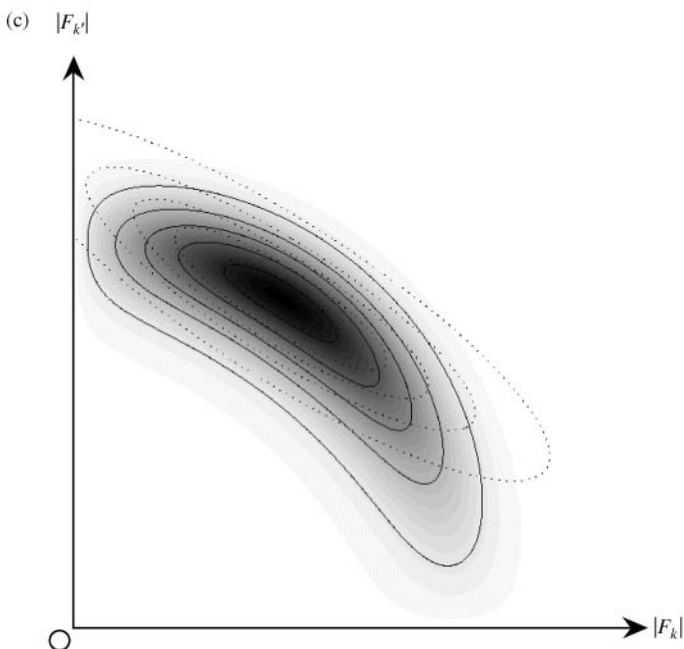


Fig. 8.10. The final probability distribution illustrated in Fig. 8.9 but represented in this diagram as a function of $|F|$ (hence only the positive quadrant is shown). This $|F|$ distribution must be calculated if the known fragment information is to be utilized in traditional direct methods. (a) The anticipated $|F|$ distribution for the reflections shown in Fig. 8.9(a)—the reflections are clearly centric. (b) The anticipated $|F|$ distribution for the reflections shown in Fig. 8.9(b) assuming the reflections are centric, (c) and as for (b) but assuming the reflections are acentric.

The molecular structure of chlorothiazide, $C_7H_6N_3O_4S_2Cl$, is shown in Fig. 8.11.

The crystal structure is triclinic (space group PI) with lattice constants $a = 6.372 \text{ \AA}$, $b = 8.916 \text{ \AA}$, $c = 4.855 \text{ \AA}$, $\alpha = 96.13^\circ$, $\beta = 99.48^\circ$, $\gamma = 74.41^\circ$ ($Z = 1$). The three heavy atoms ($2S + Cl$) constitute one third of the scattering density of the structure and are easily located using Patterson methods. The integrated intensities were extracted from the powder diffraction pattern using the Pawley method with due account taken of Bragg peak overlap by retaining the weight matrix, H_{hk} , given in eqn (8.12). The missing structure was then taken as an additional unknown contribution to the heavy-atom structure that was assumed to be known exactly. Mathematically, this corresponds to minimizing the correlated integrated intensity differences between the observed structure-factor magnitude squared, $|F_{\text{obs}}|^2$ and the magnitude squared of the sum of

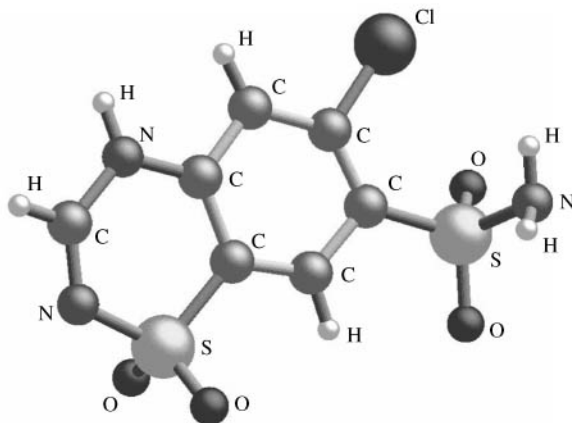


Fig. 8.11. The molecular structure of chlorothiazide, $C_7H_6N_3O_4S_2Cl$.

known + difference $|F_{\text{known}} + \Delta F|^2$, while enforcing positivity in the difference Fourier map. The quantity

$$\chi_{Cr}^2 = \sum_{\mathbf{h}} \sum_{\mathbf{k}} \left[|F_{\text{obs}}(\mathbf{h})|^2 - |F_{\text{known}}(\mathbf{h}) + \Delta F(\mathbf{h})|^2 \right] \times (\mathbf{C}_{\mathbf{hk}}^{-1}) \left[|F_{\text{obs}}(\mathbf{k})|^2 - |F_{\text{known}}(\mathbf{k}) + \Delta F(\mathbf{k})|^2 \right], \quad (8.20)$$

is minimized (where $\Delta F(\mathbf{h}) = \sum_{\mathbf{r}} \Delta\rho(\mathbf{r}) \exp(-2\pi i\mathbf{h} \cdot \mathbf{r})$ is the Fourier transform of the electron density, $\Delta\rho(\mathbf{r})$) while the entropic term $\sum_{\mathbf{r}} \Delta\rho(\mathbf{r}) \ln(\Delta\rho(\mathbf{r}))$ is simultaneously maximized. In this way, the observed integrated-intensities constraint is rigorously obeyed, the phase information from the heavy atoms is used and no constraints are imposed on the phases of unknown difference Fourier components. In the case of chlorothiazide, all non-hydrogen atoms were unambiguously located in the maximum entropy Fourier map (see Figs 8.12 and 8.13) implying that up to two-thirds of a crystal structure may be reconstructed using this approach. Many of the correct features associated with the unlocated atoms are visible in the standard Fourier map. However, the standard Fourier map also contains false features of a similar magnitude to the correct features making atom location a task that involves a substantial amount of chemical intuition. In the maximum entropy Fourier map, the correct atomic features are easily discriminated from the surrounding low background density. In conclusion, it is clear from this example that the correct treatment of overlap and correlations between integrated intensities combined with the active use of fragment information can be a powerful tool for complete structure solution from powder diffraction data.

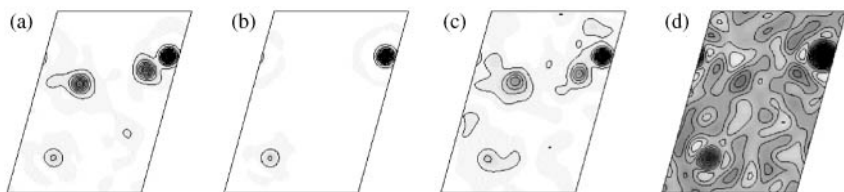


Fig. 8.12. Two-dimensional section of the scattering density for chlorothiazide (a) calculated using the full crystal structure, (b) calculated using only the heavy atom (two sulphur and one chlorine) sub-structure, (c) synthesized from a maximum entropy map based upon fitting the correlated integrated intensities, with due account taken of the structure factors associated with the heavy atoms and the structure factor blur corresponding to the unlocated atoms, and (d) taken from a standard powder diffraction Fourier map derived from the observed structure factors (assuming the heavy atom model) obtained by applying Rietveld's original method. Note that two heavy atoms (*c.f.* (b)) are visible in this section.

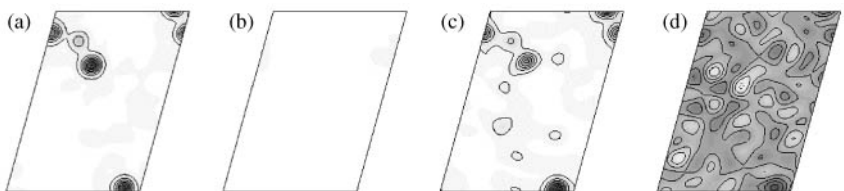


Fig. 8.13. A second, different two-dimensional section of the scattering density for chlorothiazide taken from the same maps as those shown in Fig. 8.12. Note that despite the fact that no heavy atoms are to be found in this section, the Bayesian approach (c) reveals all the other atoms, whereas the standard map (d) is ambiguous.

8.7 Conclusions

Well-developed computer programs based upon the Le Bail and Pawley methods are available for extracting integrated intensities from powder diffraction data. The challenge that faces this stage in the structure solution process is obtaining the best structure-factor magnitudes as input to structure-solving programs. The incorporation of a known partial structure has substantial benefits and there is significant potential for future algorithms to exploit this information.

Acknowledgements

The authors wish to thank Dr. K. Shankland for useful discussions on many aspects of extracting integrated intensities from powder diffraction data and to Dr A J Markvardsen for discussions on space group determination.

References

- Altomare, A., Carrozzini, B., Giacobazzo, C., Guagliardi, A., Moliterni, A. G. G. and Rizzi, R. (1996). *J. Appl. Crystallogr.*, **29**, 667–73.
- Altomare, A., Burla, M. C., Camalli, M., Carrozzini, B., Cascarano, G. L., Giacobazzo, C., Guagliardi, A., Moliterni, A. G. G., Polidori, G. and Rizzi, R. (1999). *J. Appl. Crystallogr.*, **32**, 339–40.
- Bricogne, G. (1991). *Acta Crystallogr. A*, **47**, 803–29.
- Cascarano, G., Giacobazzo, C., Giuagliardi, A. and Steadman, A. (1991). *Acta Crystallogr. A*, **47**, 480–4.
- Coelho, A. A. (2000). *J. Appl. Crystallogr.*, **33**, 899–908.
- David, W. I. F. (1987). *J. Appl. Crystallogr.*, **20**, 316–19.
- David, W. I. F. (1990). *Nature*, **346**, 731–4.
- David, W. I. F. (1999). *J. Appl. Crystallogr.*, **32**, 654–63.
- Engel, G. E., Wilke, S., König, O., Harris, K. D. M. and Leusen, F. J. J. (1999). *J. Appl. Crystallogr.*, **32**, 1169–79.
- Estermann, M. A., McCusker, L. B. and Baerlocher, Ch. (1992). *J. Appl. Crystallogr.*, **25**, 539–43.
- Estermann, M. A. and Gramlich, V. (1993). *J. Appl. Crystallogr.*, **26**, 396–404.
- Jansen, J., Peschar, R. and Schenk, H. (1992*a*). *J. Appl. Crystallogr.*, **25**, 231–6.
- Jansen, J., Peschar, R. and Schenk, H. (1992*b*). *J. Appl. Crystallogr.*, **25**, 237–43.
- Le Bail, A., Duroy, H. and Fourquet, J. L. (1988). *Mater. Res. Bull.*, **23**, 447–52.
- Le Bail, A. (2005). *Powder Diffraction.*, **20**, 316–26.
- Markvardsen, A., David, W. I. F., Johnson, J. C. and Shankland, K. (2001). *Acta Crystallogr. A*, **57**, 47–54.
- Pagola, S., Stephens, P. W., Bohle, D. S., Kosar, A. D. and Madsen, S. K. (2000). *Nature*, **404**, 307–10.
- Pawley, G. S. (1981). *J. Appl. Crystallogr.*, **14**, 357–61.
- Rietveld, H. M. (1969). *J. Appl. Crystallogr.*, **2**, 65–71.
- Sayre, D. (1952). *Acta Crystallogr.*, **5**, 60–5.
- Sivia, D. S. and David, W. I. F. (1994). *Acta Crystallogr. A*, **50**, 703–14.
- Shankland, K., David, W. I. F. and Sivia, D. S. (1997) *J. Mater. Chem.*, **7**, 569–72
- Vos, A. and Buerger, M. J. (1993). *International tables for crystallography, Space group symmetry* (ed. T. Hahn), Vol. A, pp. 40–48. Kluwer Academic Publishers, Dordrecht.
- Waser, J. (1963). *Acta Crystallogr.* **16**, 1091–4.

Experimental methods for estimating the relative intensities of overlapping reflections

*Thomas Wessels, Christian Baerlocher, Lynne B. McCusker
and William I. F. David*

9.1 Introduction

The better the estimate of the individual reflection intensities from a powder diffraction pattern, the better are the chances of solving the structure. All of the approaches to structure determination described in the remaining chapters become more powerful as the quality of the diffraction data improves. Extra effort to produce more single-crystal-like data can facilitate structure determination considerably, and can even make the difference between solving and not solving the structure. A number of ingenious computational methods have been developed to improve the estimation of the relative intensities of overlapping reflections, and these have been described in the previous chapter and Chapters 10 and 11. However, it is also possible to modify the data collection procedure to obtain better intensity information experimentally.

By collecting several datasets on the same sample under different but controlled conditions, more information about the relative intensities of overlapping reflections can be deduced. The relationship between the datasets must be known or determined, and then, using this information, a set of more single-crystal-like reflection intensities can be extracted from the patterns. Two such methods have been developed and applied successfully, and these are described in more detail in the following sections. The first requires a material that undergoes anisotropic thermal expansion, and the second a sample in which a homogeneous texture (preferred orientation of the crystallites) has been induced.

9.2 Anisotropic thermal expansion

If a material expands or contracts as a function of temperature without undergoing a phase transition, the positions of the reflections in the diffraction pattern change but their relative intensities remain more or less the same. If the

expansion is anisotropic (say, for example, the a -axis expands, the b -axis contracts and the c -axis remains the same), the positions of the lines relative to one another will change, and this means that the pattern of reflection overlap will also change. Reflections that overlap at one temperature may not overlap to the same extent at another and so by measuring the diffraction pattern of such a material at two or more temperatures, more information about the relative intensities of overlapping reflections can be extracted. For complex structural problems, the additional information that can be obtained from these extra datasets can be extremely valuable.

As this phenomenon of anisotropic thermal expansion is not uncommon, the method can be applied to a number of different types of materials. During the data collection, apparatus for heating or cooling the sample is required, but the experiment is otherwise straightforward.

9.2.1 *A simple two-peak analysis*

The essential benefits of anisotropic thermal expansion may be analysed by consideration of a simple two-peak example. A high quality diffraction pattern has been collected and the intensities extracted by a Pawley linear-least-squares analysis. Two peaks (with intensities I_1 and I_2) are essentially completely overlapped. Both individual intensities are poorly determined and indeed one is refined to be negative: $I_1 = -500 \pm 1000$ and $I_2 = 1500 \pm 1000$. The negative correlation ($c = -0.999$) is, however, extremely high reflecting the fact that the sum of the two-peak intensities has been well determined: $I_{\text{total}} = I_1 + I_2 = 1000 \pm 20$. Concern is often expressed when negative intensities occur. In a Pawley analysis, however, this situation is always associated with substantial peak overlap (and/or high correlation of the intensities with the background parameters) and does not prejudice the intensity extraction process. It merely indicates that individual intensities are poorly determined while sums of intensities are still well-behaved quantities.

Now consider a second rapid experiment where the temperature has been changed so that the peaks, through differential thermal expansion, are now no longer overlapping. As a result of the speed of the experiment, the overall statistics are poorer with $I_1 = 180 \pm 50$ and $I_2 = 720 \pm 150$. Importantly, however, there is now no statistical correlation between the intensities ($c = 0$). These measurements may be merged together to give the best estimate of $I_1 = 189 \pm 50$ and $I_2 = 804 \pm 60$ with $c = -0.733$. Note that the sum of the intensities $I_{\text{total}} = 993$ is much closer to the first experimental value since this has been determined substantially better than in the second measurement where $I_{\text{total}} = I_1 + I_2 = 900 \pm 170$. The second intensity I_2 is, as expected from the second experiment, substantially larger than I_1 . The intensity ratio of 4.25:1 does, however, differ from the value of 4:1 suggested by the second experiment. This is not on account of any ratio discrimination in the first measurement but because of (a) the fact that the estimated standard deviation (e.s.d.) of I_2 is

larger than that of I_1 and (b) the requirement that the summed intensity should be closer to 1000 than 900. Hence both experiments have brought valuable information to the analysis. The first, despite the presence of negative intensities, gives a better measure of the total intensity of the two peaks, whereas the second experiment provides the discrimination between the individual intensities.

Usually, when performing experiments at different temperatures, the same counting time is used in each case. In the example discussed above, the first experiment was taken to be longer than the second in order to highlight the fact that negative intensities are not problematical and indeed, when combined with the appropriate correlations, can bring important information about Bragg peak intensities.

9.2.2 *Mathematical aspects of the analysis of integrated intensities collected at more than one temperature*

In a standard powder diffraction measurement, the experimentally determined Bragg peak intensities are linearly related to the square of the structure-factor magnitudes of a Bragg reflection. Structure-factor magnitudes belonging to isolated reflections can thus be straightforwardly estimated. As discussed in Chapter 8, the most popular techniques are the iterative Le Bail method (Le Bail *et al.* 1988) and the Pawley least-squares method (Pawley 1981). In dealing with anisotropic thermal expansion and multiple datasets, the least-squares Pawley procedure is used since it gives access to the integrated intensities covariance matrix. In an ideal situation where a strong Bragg peak is isolated from other Bragg peaks, least-squares analysis returns a best-fit value of the intensity $\langle I \rangle$, and a measure, σ , of the range of values which give reasonable agreement with the data. This is equivalent mathematically to the assumption that the likelihood is roughly Gaussian with mean I_0 and standard deviation σ . This may be written as:

$$\text{prob}(\text{Data}|I) = \frac{1}{\sigma\sqrt{2\pi}} \exp[-(I - \langle I \rangle)^2/2\sigma^2]. \quad (9.1)$$

In powder diffraction patterns, the considerable overlap that commonly occurs between neighbouring Bragg peaks makes it impossible to consider individual reflections in isolation. The likelihood function of eqn (9.1) must, therefore, be generalized to a multivariate Gaussian:

$$\text{prob}(\text{Data}|I) \propto \exp \left[-\frac{1}{2} \sum_{i,j} (I_i - \langle I \rangle_i) (C^{-1})_{i,j} (I_j - \langle I \rangle_j) \right], \quad (9.2)$$

where I_j is the intensity of the j th reflection with the best-fit value $\langle I \rangle_j$. The matrix, C^{-1} , is the inverse of the covariance matrix representing the

correlations induced by the overlaps:

$$C_{ij} = \langle (I_i - \langle I \rangle_i)(I_j - \langle I \rangle_j) \rangle. \quad (9.3)$$

In considering anisotropic thermal expansion, several such sets of diffraction data need to be collected for the same sample at different temperatures $\{T_k\}$. It is assumed that there is little change in the fractional atomic coordinates. The intensity, $I_j\{T_k\}$, of the j th reflection at temperature, T_k , can be related to the intensity of the reflection at a reference temperature, $I_j\{T = T_0\}$, by introducing a small change to an overall Debye–Waller factor. In this simplest approximation, this gives:

$$I_j(T_k) = I_j(T_0) \exp[-(B(T_k) - B(T_0))d_j^{*2}(T_k)], \quad (9.4)$$

where $d^*(T_k)$ is the modulus of the reciprocal lattice vector at temperature T_k , and $B(T_k)$ is the initially unknown overall atomic displacement parameter, whose temperature dependence may be well modelled in terms of a single Einstein oscillator. Over a limited temperature range at temperatures well away from very low temperatures, $B(T_k)$ will vary linearly with temperature.

If there are substantial changes in fractional coordinates as a result of, for example, the rotation of a structural fragment, then the above assumptions may be modified to allow for a smooth variation in structure factor as a function of temperature. In practice, this is generally a small effect and can be neglected. In principle, such variations may be accommodated in a more general mathematical formalism. If even more severe changes occur as a result of effects such as a structural phase transition, then clearly even these approximations will fail. The simple solution to such a situation is to select a different temperature region.

The joint likelihood function for the intensities $\{\hat{I}\}$, conditional on the value of the overall atomic displacement parameter, is given by the product of the likelihood functions for the individual datasets:

$$\text{prob}(\{\text{Data}\}|\{\hat{I}\}, B(T_k)) = \prod_k \text{prob}(\text{Data}_k|\{\hat{I}\}, B(T_k)). \quad (9.5)$$

This equation is a multivariate generalization of the two-peak example in Section 9.2.1. Once overall atomic displacement parameter effects have been removed, the resulting integrated intensities may be extracted with significantly reduced correlations.

9.2.3 An example of differential thermal expansion—chlorothiazide

Diffraction data were collected for the diuretic compound, chlorothiazide, contained in a 1 mm capillary on beamline 9.1 at Daresbury SRS. The data were collected at 90 K, 130 K and 160 K at a wavelength 1.09852 Å. Sections of all three datasets, corresponding to an angular range of 25.5° to 34.5° 2θ , are shown in Fig. 9.1.

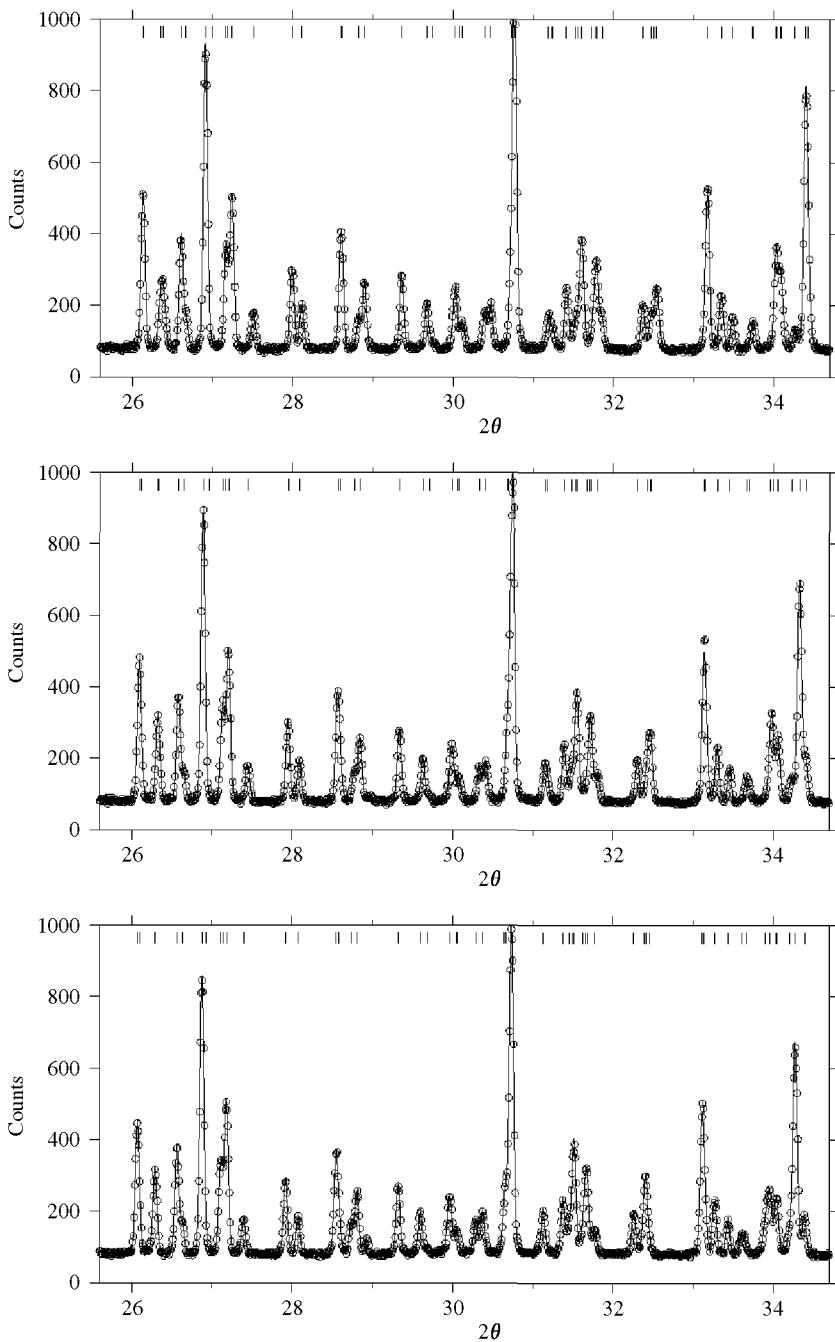


Fig. 9.1. Diffraction patterns of chlorothiazide collected at 90 K (top), 130 K (middle) and 160 K (bottom). The 9° range highlights the similarities between the diffraction patterns at the different temperatures.

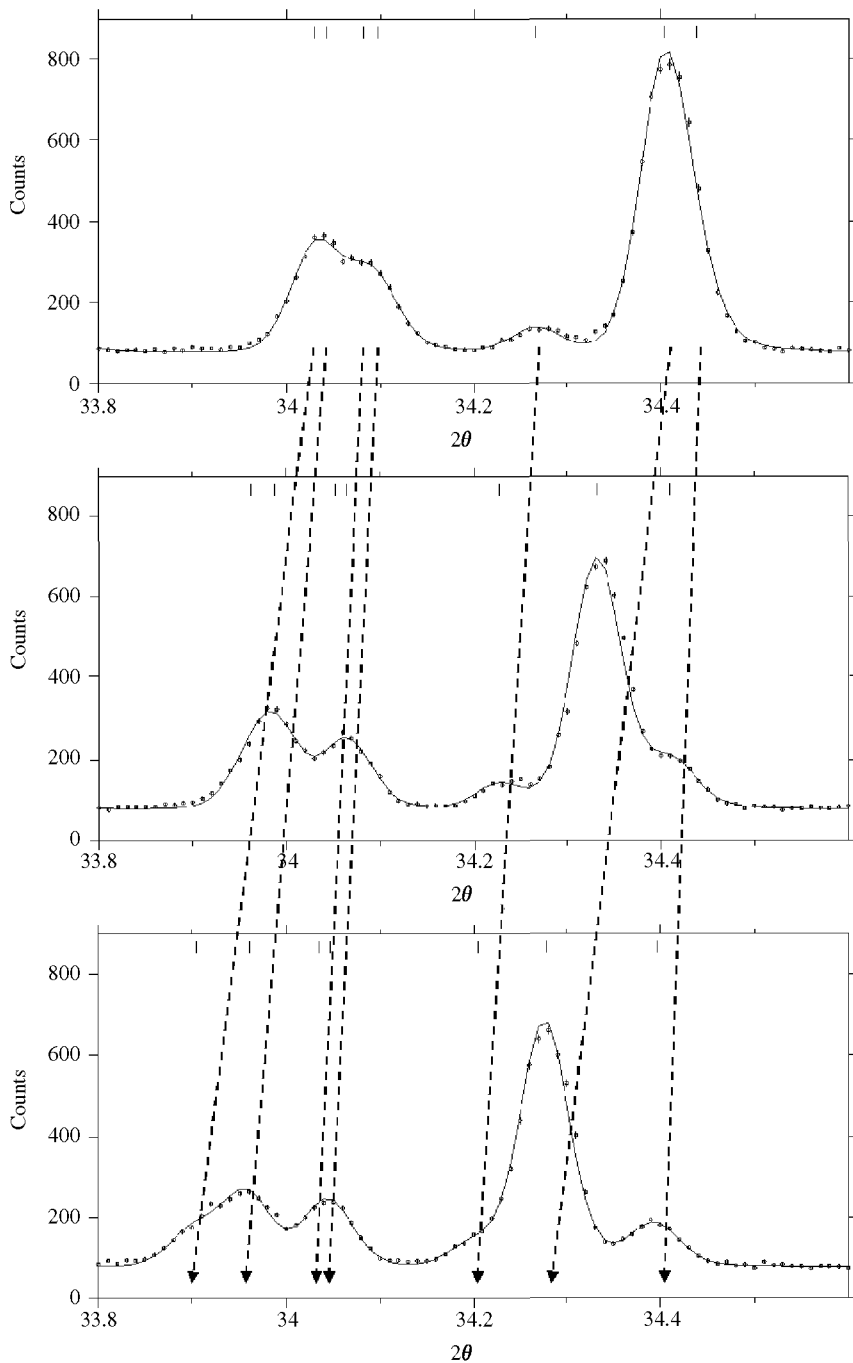


Fig. 9.2. Diffraction patterns of chlorothiazide collected at 90 K (top), 130 K (middle) and 160 K (bottom). The 0.8° range highlights the effects of anisotropic thermal expansion. The dashed lines indicate the different angular changes for the reflections as a function of temperature.

It is clear from a superficial assessment of Fig. 9.1 that little has changed in the diffraction pattern as a function of temperature. The distributions of peak intensities are essentially the same; the three most intense peaks are at approximately 27° , 31° and 34° in all datasets. However, a more detailed examination (Fig. 9.2) indicates that the extent of peak overlap does indeed vary as a function of temperature.

The dashed lines not only indicate that the crystal structure expands as a function of temperature but that the expansion is substantially different for different reflections. In particular, the 34.4° overlapping doublet at 90 K is split by 0.1° at 160 K, where it becomes clear that the higher angle reflection is substantially the weaker. A Pawley analysis of the individual datasets indicated that the 420 reflections in the chlorothiazide dataset were grouped into 360 groups comprising 60 completely overlapping doublets (i.e. 120 reflections). On merging all three datasets, the number of groups increased to 410 with only 10 completely overlapping doublets (20 reflections). The resulting set of reflection intensities is effectively non-overlapped and pseudo-single-crystal in nature. Unsurprisingly, since the data were collected to atomic resolution ($d_{\min} \cong 1 \text{ \AA}$), subsequent structure solution by Direct methods was straightforward (Shankland *et al.* 1997). More recently, Brunelli *et al.* (2003) have exploited anisotropic thermal expansion to solve larger molecular crystal structures.

9.3 Texture

Powder diffractionists usually take great care to ensure that a sample is free of preferred orientation effects, so they can be sure that the relative intensities of the peaks in the diffraction pattern are not distorted. However, in principle, a textured sample (one with preferred orientation) can be used to obtain additional information about the relative intensities of overlapping reflections.

9.3.1 Concept

The diffraction patterns of a single crystal, an 'ideal' powder sample (i.e. one with no preferred orientation) and a textured powder sample are shown in Fig. 9.3. For simplicity, a two-dimensional case is illustrated, but extrapolation to three dimensions is straightforward.

For the single crystal (Fig. 9.3(a)), all reflections are well-separated in space, and their individual intensities can be measured easily. For the 'ideal' powder (Fig. 9.3(b)), millions of crystallites with all possible orientations are present, so the diffraction pattern is simply a superposition of millions of differently oriented single-crystal diffraction patterns. As a result, reflections with similar d -spacings overlap in space and only the sum of their intensities can be measured. For example, the three reflections highlighted in the single-crystal pattern fall on top of one another in the 'ideal' powder diffraction pattern, so their

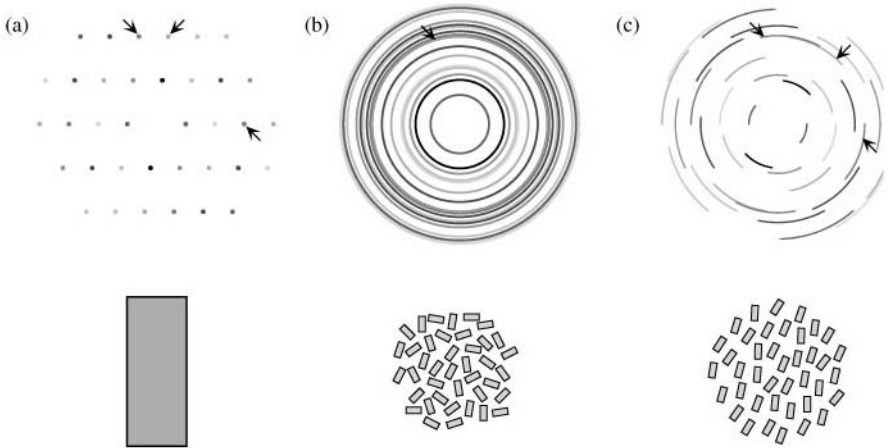


Fig. 9.3. Diffraction pattern (above) and schematic drawing of the sample (below) for a two-dimensional (a) single crystal, (b) powder with randomly oriented crystallites, and (c) textured powder. A gray scale has been used to represent the reflection intensities. The arrows highlight three reflections with similar diffraction angles (2θ) that are separate in the single-crystal pattern, but overlap in the normal powder pattern. In the textured powder pattern, these reflections can be separated if the pattern is measured appropriately. The diffraction angle (2θ) increases radially from the center of each diffraction pattern.

individual intensities cannot be determined. The textured powder sample (Fig. 9.3(c)) lies somewhere between these two extremes. As not all crystallite orientations are equally represented, the reflections are concentrated in certain directions, so by measuring the diffraction pattern along different directions (e.g. by orienting the sample appropriately), additional intensity information can be extracted.

The texture of the sample must be determined to establish which set of sample orientations will yield the most useful information, and to quantify the relationship between the diffraction patterns collected for these orientations. Then, by combining the texture information with the measured diffraction patterns, an improved set of individual reflection intensities can be generated.

9.3.2 *Sample preparation*

There are many ways of preparing textured samples, and all are sample-dependent. Advantage can be taken of electrical or magnetic properties by applying an appropriate field to align the crystallites, but it is usually the morphology of the crystallites that is exploited. If the crystallites are platelets, sedimentation techniques can be applied, and if they are needles, a smear approach, with or without a matrix, can be used.

Before any technique is applied, it is important that any non-oriented aggregation of the crystallites in the sample be minimized. This can be done by grinding the sample to reduce the size of the particles to a maximum of $c.50\ \mu\text{m}$, suspending these particles in a liquid medium, and then subjecting the suspension to a high-energy ultrasonic treatment. For an aluminophosphate sample, adding a dispersant (0.01 per cent solution of $\text{Na}_3(\text{PO}_4)_2$) to the suspension was found to help reduce flocculation.

Excellent results have been obtained by mixing disaggregated powder samples of needle-like crystallites with polystyrene dissolved in tetrahydrofuran (THF), and then applying a smear technique. The layer dries rapidly as the THF evaporates, and then additional layers can be added until the sample is thick enough. The matrix does contribute to the background of the powder diffraction patterns, but it is amorphous so no additional diffraction peaks are observed. Its use allows robust, relatively uniform, highly-textured specimens to be prepared. A polyvinyl alcohol / water mixture has also been used successfully as a matrix. In this case, more of the matrix material is used and the needles are aligned by rolling and stretching the rubbery mixture before it dries. More detailed descriptions of sample preparation techniques can be found in Wessels (1999).

9.3.3 *Texture description*

The preferred orientation of crystallites in a powder sample is often described in terms of a single vector. For example, platelets tend to be preferentially oriented with the plate axis (short dimension of the crystallite) aligned along the sample normal, whereas needles tend to be aligned with the needle axis perpendicular to the sample normal. While such descriptions can be useful if only an approximate characterization of the texture is needed, they are limited in quantitative applications because most real samples have much more complex textures. Nonetheless, simple functions have been used by Lasocha and Schenk (1997) and by Cerny (1998, 2000) to obtain better intensity information from textured samples.

To take full advantage of the additional information offered by a textured sample though, a full texture analysis of the sample is required. This approach was first proposed and demonstrated by Hedel *et al.* (1997) for simulated data. This full texture analysis requires that pole-figure data for several single (non-overlapping) reflections are measured. That is, the intensity of the reflection is measured at all sample orientations in 5° rotation (ϕ) and tilt (χ) steps (see Fig. 9.4(a)). An idealized crystallite orientation distribution is shown in Fig. 9.4(b) for a crystallite morphology with the dimensions $D_{[100]} \ll D_{[010]} \ll D_{[001]}$ and some pole figures simulated for that distribution in Fig. 9.4(c). Most of the crystallites will lie with the (100) planes approximately parallel to the specimen surface, but a significant number will lie with the (010) planes

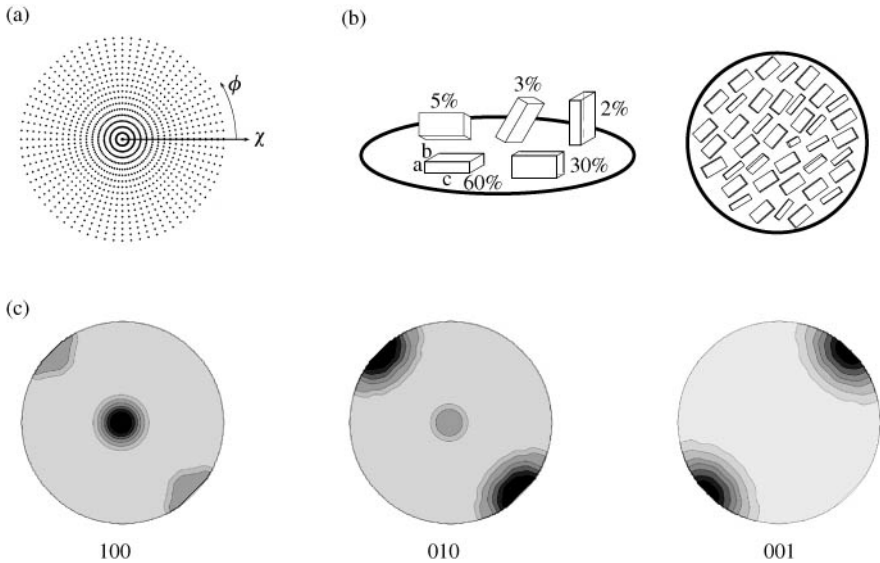


Fig. 9.4. (a) Schematic drawing of the 1296 points in χ and ϕ space that are measured to produce a pole figure for a single reflection. The χ (tilt) axis goes from 0° at the center to 90° at the perimeter, and the ϕ (rotation) axis runs counterclockwise around the perimeter. (b) An idealized crystallite distribution showing the volume percentages on the left and a schematic view of the sample from the top on the right. (c) Simulated pole figures for the 100, 010 and 001 reflections for the crystallite distribution given in (b). The intensity is proportional to the degree of grayness.

parallel to the surface, and some will adopt other orientations. A preferred orientation in the plane of the sample that might be induced by a smear technique (the long dimension is preferentially oriented at approximately 45°) has also been assumed.

A set of measured pole figures such as those simulated above can be used to determine the orientation distribution of the crystallites within the sample. This information can then be used to calculate the so-called 'pole-figure value' $P_{hkl}(\chi, \phi)$ for every reflection in the diffraction pattern for any sample orientation. $P_{hkl}(\chi, \phi)$ has a value of one for all sample orientations (χ, ϕ) if the crystallites are oriented randomly. For crystallites oriented preferentially, its value is proportional to the volume fraction of crystallites contributing to the intensity of the reflection hkl for the sample orientation (χ, ϕ) .

9.3.4 Instrumentation

For the measurement of the pole figures and for subsequent orientation of the sample at specific χ and ϕ angles, a controlled way of tilting and rotating the

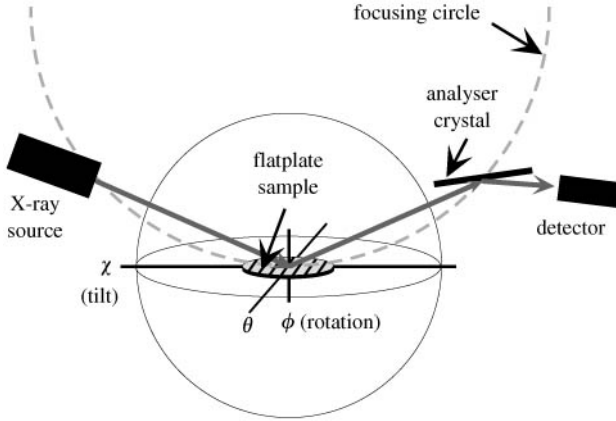


Fig. 9.5. Schematic diagram of the experimental setup showing the sample tilt (χ) and rotation (ϕ) axes and the predetector analyser crystal.

sample is necessary. Consequently, two additional circles (χ and ϕ) are attached to the powder diffractometer, to produce an experimental setup very similar to that of a standard four-circle single-crystal diffractometer. A schematic drawing of the instrument for reflection geometry is shown in Fig. 9.5.

On a conventional Bragg–Brentano laboratory diffractometer with a divergent X-ray beam, tilting a flat-plate specimen leads to a violation of the parafocusing condition, because parts of the sample are moved off the focusing circle. This defocusing results in severe line broadening and a corresponding increase in reflection overlap. However, by combining a highly collimated parallel beam (at a synchrotron source, for example) with a crystal analyser, which acts as a very fine receiving slit, Hastings *et al.* (1984) have shown that all sample displacement aberrations can be eliminated. All X-rays that are diffracted from the sample and fulfil the Bragg condition at the analyser are recorded simultaneously by the detector, independent of their point of origin in the sample. This phenomenon is essential to the success of the texture approach to structure determination described here. It means that complete 2θ scans can be measured for any sample orientation without any additional line broadening.

It is also possible to measure the data in transmission mode with a very small sample and an area detector (Prokic 2004; Baerlocher *et al.* 2004). This setup has the advantage that complete rings are measured simultaneously, so data collection times are an order of magnitude faster. Furthermore, complete pole figure data are collected for all reflections automatically. The main drawbacks of this geometry are that (a) the 2θ range is limited by the size of the image plate, and (b) the resolution of the diffraction patterns in FWHM is somewhat poorer. However, experiments indicate that the advantages of the setup probably outweigh the

disadvantages. Nonetheless, the remaining sections will concentrate on the reflection setup, because that geometry was used to develop the method.

9.3.5 Data collection

Data collection for the texture approach entails (a) the measurement of an untextured sample of a standard material to calibrate the instrumental setup, (b) the measurement of pole-figure data for several single reflections of the textured sample, and (c) the measurement of complete diffraction patterns for several selected sample orientations.

The calibration curve is used to correct for the decline in measured intensity caused by (a) the shape of the footprint of the incident beam on the sample as a function of tilt (χ) and 2θ angles (low 2θ and/or high χ cause the beam to 'overshoot' the sample), (b) the fact that as the tilt angle increases, so does the vertical dimension of the diffracted beam (this means that at some point the full diffracted beam no longer passes through the vertical slit in front of the analyser crystal), and (c) the sample transparency (if the sample is not 'infinitely thick'). To do the calibration, the diffracted intensity from an untextured sample of a material with an absorption coefficient, packing density and thickness similar to those of the sample of interest is measured for all tilt angles (5° steps) at a series of 2θ values (*c.* 5° apart). As the factors affecting this curve are closely related to the specific setup used and its current state of alignment, it is recommended that the calibration curve be measured before each data collection series.

The number of pole figures required to describe the texture depends upon the sample symmetry and the crystal symmetry. The lower these symmetries, the more pole figures needed. The final selection of reflections is usually dictated in part by the pattern itself, because only a limited number are free of overlap with neighbouring reflections.

Once the pole figures have been measured and an approximate texture established, the set of sample orientations that will yield the largest intensity contrasts can be deduced. Full diffraction patterns are then collected with the sample set at each of these orientations.

9.3.6 Data analysis

The deconvolution approach described here is based on the assumption that textured powder samples have a three-dimensional intensity distribution in reciprocal space. The diffracted intensity of a textured powder sample at step 2θ , can be expressed as a function of the sample orientation (χ, ϕ) in the form:

$$y(2\theta, \chi, \phi) = \sum_{hkl} I_{hkl} P_{hkl}(\chi, \phi) H(2\theta - 2\theta_{hkl}), \quad (9.6)$$

where the summation is over all reflections contributing to the intensity at that step, I_{hkl} is the true integrated intensity of reflection hkl (single-crystal value), $P_{hkl}(\chi, \phi)$ is its pole-figure value for the sample orientation (χ, ϕ) , and $H(2\theta - 2\theta_{hkl})$ is the peak profile function. Before any data analysis can be performed, all intensities must first be corrected with the intensity calibration curve described in the previous section.

To solve eqn (9.6) for the I_{hkl} , a two-step procedure is applied. First, the texture in the sample is determined from the pole-figure data. From the texture, all the required $P_{hkl}(\chi, \phi)$ values can be calculated, so the I_{hkl} are the only unknown quantities remaining in eqn (9.6). In the second step, the full diffraction patterns measured for different sample orientations (χ, ϕ) are used to unravel the overlapping reflections. These two steps of texture determination and extraction of integrated intensities are discussed in more detail below.

The pole figures $P_{hkl}(\chi, \phi)$ of the different reflections hkl are not independent of one another. All are related by the texture of the sample, which is defined as the Orientation Distribution Function (ODF) of its crystallites. To describe the texture, a local orthogonal coordinate system is assigned to each crystallite in the sample (strictly speaking to each volume element) and its orientation is specified with respect to a sample-fixed orthogonal coordinate system. This can be done by transforming one frame into the other by a sequence of three rotations. These three angles can be displayed in a Cartesian coordinate system, which defines the orientation space. Each crystal orientation is represented by a point in this space and the complete set of orientations is then called the texture. Pole-figure values $P_{hkl}(\chi, \phi)$ can be calculated by integrating the ODF along a certain path and can therefore be considered to be a two-dimensional projection of the ODF along this path. However, the inverse problem of calculating the ODF given a few pole figures, is the main problem in quantitative texture analysis. This problem is similar to that of reconstructing a three-dimensional object from two-dimensional projections.

There are two common approaches to the determination of the ODF from a few pole figures. Bunge (1965) and Roe (1965) introduced the harmonic method in which the texture and the pole figures are expressed as a series of spherical harmonics in Fourier space, while in the discrete or direct methods (e.g. the WIMV method developed by Matthies and Vinel (1992)), calculations are performed directly in orientation space. Computer programs for both approaches are available, and either can be used to determine the texture from pole-figure data and to obtain the pole-figure values required to solve eqn (9.6).

Either the Pawley method (Pawley 1981) or the Le Bail method (Le Bail *et al.* 1988) (see Chapter 8) are suitable for a multi-pattern deconvolution procedure. Equation (9.6) can be used directly if the Pawley approach is applied. As diffraction data from a textured powder sample provide more information than do those from an 'ideal' powder, the correlation of intensity values of reflections overlapping in 2θ is generally reduced. However, if reflections cannot be

resolved in either 2θ or orientation space, their intensities will still be highly correlated and the individual intensities can vary wildly between positive and negative values. To overcome this problem, which is inherent to the Pawley method, a Bayesian approach (Chapter 8; Sivia and David 1994), which includes the requirement that intensities be positive, can be applied to the extracted intensity values.

While the application of the Pawley method in a multi-pattern deconvolution procedure allows eqn (9.7) to be solved for the unknown I_{hkl} values in a straightforward manner, the Le Bail method does not. However, satisfactory results have been obtained with an iterative procedure in which the I_{hkl} for each of the measured powder patterns are first extracted separately using the standard Le Bail approach. For each reflection hkl , a set of intensities I_i^{hkl} , which correspond to the integrated intensities measured for different orientations of the sample, is obtained. To obtain a unique set of I_{hkl} values, these intensities are merged using:

$$I_{hkl} = \frac{\sum_i P_i^{hkl} I_i^{hkl}}{\sum_i P_i^{hkl}}, \quad (9.7)$$

where the summation is over all different sample orientations i . These values are then used as the new starting intensities for the next Le Bail extraction procedure and the intensities I_i^{hkl} obtained are merged again using eqn (9.7). The procedure is then repeated until convergence is reached.

9.3.7 Example

This texture approach has been applied successfully in reflection mode to three real polycrystalline materials with complex crystal structures (Wessels *et al.* 1999a). In all cases, it was possible to extract a set of intensities that was sufficiently single-crystal-like for the crystal structure to be solved *ab initio* by applying standard crystallographic methods. None of these structures could be solved from intensities extracted from a conventional diffraction pattern collected on an untextured powder sample. Two further structures have since been solved from data collected in transmission mode (Baerlocher *et al.* 2004; Jordá *et al.* 2005).

The solution of the previously unknown crystal structure of UTD-1F is presented here to illustrate the method (Wessels *et al.* 1999b). UTD-1 was the first extra-large pore silica-based zeolite ever synthesized (Balkus *et al.* 1995; Freyhardt *et al.* 1996), but initial structural investigations showed it to be orthorhombic and disordered (Lobo *et al.* 1997). By modifying the synthesis procedure, a sample of better quality (called UTD-1F) was prepared, and its diffraction pattern could be indexed on a monoclinic unit cell ($P2_1/c$, $a = 14.9633$, $b = 8.4704$, $c = 30.0098 \text{ \AA}$, $\beta = 102.667^\circ$, $V = 3711 \text{ \AA}^3$). The very

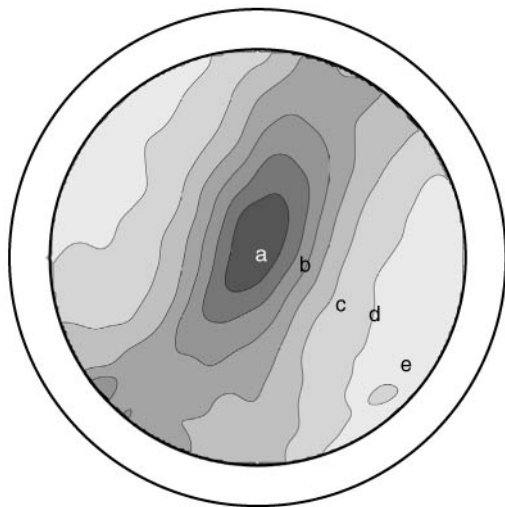


Fig. 9.6. Pole figure for the $10\bar{2}$ reflection of the high-silica zeolite UTD-1. Intensity is proportional to the degree of grayness. The sample tilt and rotation angle settings selected for the collection of full diffraction patterns are indicated with letters (see Fig. 9.7).

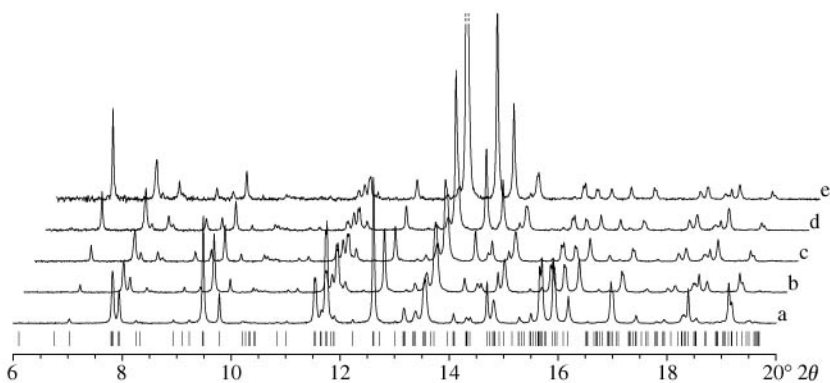


Fig. 9.7. Small sections of the five diffraction patterns collected on UTD-1 at different sample orientations (see Fig. 9.6). (a) $\chi = 0^\circ$, $\phi = 0^\circ$; (b) $\chi = 20^\circ$, $\phi = 345^\circ$; (c) $\chi = 35^\circ$, $\phi = 335^\circ$; (d) $\chi = 50^\circ$, $\phi = 335^\circ$; (e) $\chi = 70^\circ$, $\phi = 325^\circ$. The variations in intensity as a function of sample orientation are readily apparent.

fine needle-like crystallites of this material were aligned within a polystyrene matrix by applying a smear technique.

Pole-figure data for seven reflections and full diffraction patterns at five different sample orientations were measured. Figure 9.6 shows the $10\bar{2}$ pole figure while Fig. 9.7 shows small sections of the five diffraction patterns collected at the sample

orientations indicated on the pole figure. The differences in the relative intensities at the five sample settings are readily apparent and give a visual impression of the increased information content in the set of measured powder patterns.

The texture was determined using the WIMV method (computer program BEARTEX, Wenk *et al.* 1998), and then the iterative procedure outlined in the previous section was used to obtain a set of single-crystal-like reflection intensities. The application of a standard Direct methods program to these intensities revealed a complete three-dimensional, four-connected framework with 14-ring pores. All 16 Si atoms in the asymmetric unit and even 17 of the bridging oxygens were found on the top *E*-map. Subsequent difference Fourier maps calculated using the extracted intensity values allowed the remaining 15 oxygens and the (non-framework) Co atom and cyclopentadienyl rings to be located. Further structural analysis was performed using a powder diffraction pattern collected on an untextured sample. Rietveld refinement then showed the true symmetry to be *Pc* rather than *P2₁/c* and the final model to have a full ordering of the Co complex in the channels and a total of 117 atoms in the asymmetric unit.

9.4 Conclusions

By collecting several different, but related, diffraction patterns on a single material, more information about the relative intensities of overlapping reflections can be obtained. Two cases have been described. If a sample undergoes anisotropic thermal expansion, the relative positions of the reflections in the diffraction pattern will change as a function of temperature, but as long as the structure does not undergo a phase transition, their intensities will remain very similar. Thus, the relationship between the patterns is the fact that the reflection intensities are the same and the reflection positions are a function of the small changes in the unit cell dimensions. If a sample exhibits a preferential orientation of the crystallites, diffraction patterns measured with the sample at different orientations will differ in reflection intensity, but not in reflection position. In this case, the relationship between the patterns is the orientation distribution of the crystallites. These multi-pattern data collections require an appropriate sample and somewhat more experimental effort. However, for difficult cases, such experimental approaches to the solution of the overlap problem may be the only viable ones.

References

- Baerlocher, Ch., McCusker, L. B., Prokic, S. and Wessels, T. (2004). *Z. Kristallogr.*, **219**, 803–12.
- Balkus Jr, K. J., Gabrielov, A. G. and Sandler, N. (1995). *Mater. Res. Symp. Proc.*, **368**, 369–75.

- Brunelli, M., Wright, J. P., Vaughan, G. B. M., Mora, A. J. and Fitch, A. N. (2003). *Angewandte Chemie International Edition*, **42**, 2029–32.
- Bunge, H. J. (1965). *Z. Metallkunde*, **56**, 872–4.
- Cerny, R. (1998). *Adv. X-ray Anal.*, **40**, CD-ROM.
- Cerny, R. (2000). *Mat. Sci. Forum*, **321–324**, 22–7.
- Freyhardt, C. C., Tsapatsis, M., Lobo, R. F., Balkus, K. J. and Davis, M. E. (1996). *Nature*, **381**, 295–8.
- Hastings, J. B., Thomlinson, W. and Cox, D. E. (1984). *J. Appl. Crystallogr.*, **17**, 85–95.
- Hedel, R., Bunge, H. J. and Reck, G. (1997). *Textures Microstruct.*, **29**, 103–26.
- Jordá, J. L., Prokic, S., McCusker, L. B., Baerlocher, Ch., Xue, C. F. and Dong, J. (2005). *Comptes-rendus Chimie*, **8**, 331–9.
- Lasocha, W. and Schenk, H. (1997). *J. Appl. Crystallogr.*, **30**, 561.
- Le Bail, A., Duroy, H. and Fourquet, J. L. (1988). *Mater. Res. Bull.*, **23**, 447–52.
- Lobo, R. F., Tsapatsis, M., Freyhardt, C. C., Khodabandeh, S., Wagner, P., Chen, C. Y., Balkus, K. J., Zones, S. I. and Davis, M. E. (1997). *J. Am. Chem. Soc.*, **119**, 8474–84.
- Matthies, S. and Vinel, G. W. (1992). *Phys. Stat. Sol. (b)*, **112**, K111–K120.
- Pawley, G. S. (1981). *J. Appl. Crystallogr.*, **14**, 357–61.
- Prokic, S. (2004). *Ph.D. Thesis*, University of Zürich, Switzerland.
- Roe, R. J. (1965). *J. Appl. Phys.* **36**, 2024–31.
- Shankland, K., David, W. I. F. and Sivia, D. S. (1997) *J. Mater. Chem.*, **7(3)**, 569–72.
- Sivia, D. S. and David, W. I. F. (1994). *Acta Crystallogr. A*, **50**, 703–14.
- Wenk, H.-R., Matthies, S., Donovan, J. and Chateigner, D. (1998). *J. Appl. Crystallogr.*, **31**, 262–9.
- Wessels, T. (1999). *Ph.D. Thesis*, ETH, Zürich, Switzerland.
- Wessels, T., Baerlocher, Ch. and McCusker, L. B. (1999a). *Science*, **284**, 477–9.
- Wessels, T., Baerlocher, Ch., McCusker, L. B. and Creyghton, E. J. (1999b). *J. Am. Chem. Soc.*, **121**, 6242–47.

Direct methods in powder diffraction—basic concepts

Rene Peschar, Anke Etz, Jouk Jansen and Hendrick Schenk

10.1 Introduction

Direct methods (DM) are *ab initio* structure determination techniques that handle the crystallographic phase problem via phase processing in reciprocal space, starting from only the observed intensities. The main initial developments in DM started in 1948; the following twenty years witnessed rapid progress in the field. With the advent of sufficiently powerful computers and semi-automated computer programs in the 1970s, DM became the method of choice for structure solution. Nowadays, these software packages are capable of automatically solving molecular crystal structures with more than 100 independent atoms in the asymmetric unit from single-crystal diffraction data.

It has been shown recently that DM can also be applied to powder diffraction data, which lack the single-crystal-like quality, and in the following sections some aspects of DM in this process will be discussed. First, some basic DM concepts will be introduced (Section 10.2), and then the focus will be on DM in practice (Section 10.3). More detailed information on these topics can be found in textbooks on DM (e.g. Giacovazzo 1980; Schenk 1991). DM rely heavily on the availability of a sufficient number of single-crystal(-like) intensities, so the decomposition of the powder pattern into the individual intensities is very important (see also Chapters 8, 9 and 11). Consequently, two whole-pattern fitting techniques, the Pawley and the LSQPROF method, will be discussed (Section 10.4), and the estimation of the relative intensities of completely overlapping reflections via DM-based techniques as implemented in the program DOREES will be presented (Section 10.5). The routines LSQPROF and DOREES together with the DM program SIMPEL88 are the heart of the structure determination package POWSIM. In the final section, an outline of this package is given and some practical examples are discussed.

10.2 Basics of Direct methods

From a product of structure factors relative to two different origins, it is easily shown that the corresponding sum of phases is independent of the choice of origin whenever the reciprocal vectors add up to zero. This class of phase sum

relations are called the *structure invariants*. In DM, the most important invariants are the three-phase structure invariants, also known as the triplets:

$$\Psi_3 = \varphi_{\mathbf{h}_1} + \varphi_{\mathbf{h}_2} + \varphi_{-\mathbf{h}_1-\mathbf{h}_2} \quad (10.1)$$

and the four-phase invariants or quartets:

$$\Psi_4 = \varphi_{\mathbf{h}_1} + \varphi_{\mathbf{h}_2} + \varphi_{\mathbf{h}_3} + \varphi_{-\mathbf{h}_1-\mathbf{h}_2-\mathbf{h}_3}. \quad (10.2)$$

A second class of phase sum relations, the semi-invariants, arises if the choice of origin is limited to the *allowed origins*, as implied by space-group symmetry (see Giacovazzo 1980 for complete tables of semi-invariant conditions). Since the numerical values of the (semi-)invariants are determined solely by the crystal structure and do not depend on the (allowed) origins, they can be used to determine the crystal structure. Experimental phase sums are not obtained easily, so phase sums are estimated theoretically. A successful technique to achieve this is to assign random variables R_i and Φ_i ($i = 1, \dots, n$) to the structure factor moduli $|F_i|$ and phases φ_i respectively, and to set up a joint probability distribution $P(\Phi_1, R_1, \dots, \Phi_n, R_n)$ of the random variables (e.g. Karle and Hauptman 1958). In addition to the random variables R_i and Φ_i , a choice of primitive random variables and their prior distribution is also required to calculate the Fourier transform of the joint probability distribution. If primitive random variables are associated with atomic coordinates, while the indices of the reflections are fixed, $P(\Phi_1, R_1, \dots, \Phi_n, R_n) d\Phi_1 \cdots dR_n$ becomes the probability that a particular combination of phase values and magnitudes occurs, given the chosen prior distribution of the atoms. If only the contents of the unit cell are assumed to be known and no preference concerning the atomic positions can be stated, a model of N atoms that are uniformly and independently distributed in the unit cell and that have the same (overall) isotropic displacement parameter B can be adopted. Under these conditions, the Cochran distribution (Cochran 1955) can be derived. A conditional probability distribution of Ψ_3 , the random variable assigned to a sum of phases like eqn (10.1), given the three structure factor moduli:

$$P(\Psi_3 | R_1, R_2, R_3) \propto \exp[2G_3 \cos(\Psi_3)], \quad (10.3)$$

where $G_3 = |E_1 E_2 E_3| \sigma_{123} [\sigma_1 \sigma_2 \sigma_3]^{1/2}$, $|E_n| = R_n \sigma_n^{-1/2}$, $\sigma_n = \sum_{j=1}^N f_{jn}^2$ for $n = 1, 2, 3$ and $\sigma_{123} = \sum_{j=1}^N f_{j1} f_{j2} f_{j3}$.

According to eqn (10.3), $\Psi_3 \approx 0$ (modulo 2π), but this indication becomes less likely to be correct as G_3 becomes small. For identical scatterers, σ_{123} reduces to $N^{-1/2}$ and this quantity dominates G_3 if N becomes large. In this mathematical model, no feasible structure is excluded, so eqn (10.3) is expected to be generally applicable given the contents of the unit cell. On the other hand, chemically unfeasible and unwanted structures are not excluded and this may turn out to be

a weakness. More specific structural knowledge can be used as well (Main 1976; Heinerman 1977), in particular in the calculation of $|E_{\mathbf{h}}|$'s.

The Cochran expression is readily generalized to an expression of a phase $\Phi_{\mathbf{h}}$ that takes part in p triplets, and from the resulting expression, the tangent formula (Karle and Hauptman 1956; Karle and Karle 1966) can be derived. The tangent formula is used in practice to calculate a numerical phase value if a number of $\Phi_{\mathbf{k}} + \Phi_{\mathbf{h}-\mathbf{k}}$ and their statistical weights $W_{\mathbf{k}}$ and $W_{\mathbf{h}-\mathbf{k}}$ are available:

$$\tan(\Phi_{\mathbf{h}}) = \frac{\sum_{j=1}^p E_{3j} W_{\mathbf{k}_j} W_{\mathbf{h}-\mathbf{k}_j} \sin(\Phi_{\mathbf{k}_j} + \Phi_{\mathbf{h}-\mathbf{k}_j})}{\sum_{j=1}^p E_{3j} W_{\mathbf{k}_j} W_{\mathbf{h}-\mathbf{k}_j} \cos(\Phi_{\mathbf{k}_j} + \Phi_{\mathbf{h}-\mathbf{k}_j})}. \quad (10.4)$$

10.3 Direct methods in practice

The cosines of all triplets can be estimated from eqn (10.3), so the DM numerical problem can be formulated as extracting numerical values of p unknown phases given q cosine estimates of triplets. Even if $q \gg p$, this problem is not trivial, because only cosines of invariants, not the invariants themselves, can be estimated, and because the estimates are far from exact. Most DM programs proceed as follows (to be discussed in more detail below): First, observed $|F_{\mathbf{h}}|$ are normalized and the (semi-)invariants among the larger $|E_{\mathbf{h}}|$'s are identified and cosine estimates assigned. Then, one or more starting-sets of phases are taken. For each set, a limited phase extension, in which the phases of reflections with large $|E_{\mathbf{h}}|$'s are expressed successively in terms of the starting-set phases, is carried out. On the basis of (semi-)invariant consistency criteria, the phase sets developed this way are ranked and the most likely numerical solution is selected for a complete phase extension. With the latter set, an E -based Fourier map (E -map) is calculated and interpreted in terms of the atomic coordinates.

10.3.1 Normalization and setting up phase relations

A theoretical expectation value $\langle |F_{\mathbf{h}}|^2 \rangle$ can be calculated using the above mentioned model of N uniformly and independently distributed atoms with an overall isotropic displacement B . Setting $|F_{\mathbf{h}}|_{\text{obs}}^2 = K \cdot \langle |F_{\mathbf{h}}|^2 \rangle$ and rearranging gives:

$$\ln \left\{ \frac{|F_{\mathbf{h}}|_{\text{obs}}^2}{\varepsilon(\mathbf{h}) \sum_{j=1}^N f_j^2(\mathbf{h})} \right\} = \ln(K) - 2B \frac{\sin^2(\theta)}{\lambda^2} \quad (10.5)$$

with K an overall scale factor and $\varepsilon(\mathbf{h})$ a statistical weight due to the space-group symmetry. On the basis of eqn (10.5), a least-squares analysis can be set up for small ranges of $\sin^2(\theta)/\lambda^2$, and from the resulting Wilson plot (Wilson 1942)

estimates of K and B are derived. Subsequently, normalized structure factors $|E_{\mathbf{h}}|$ can be constructed:

$$|E_{\mathbf{h}}|^2 = \frac{|F_{\mathbf{h}}|_{\text{obs}}^2}{K \exp(-2B \sin^2(\theta)/\lambda^2) \varepsilon(\mathbf{h}) \sum_{j=1}^N f_j^2(\mathbf{h})}. \quad (10.6)$$

The $|E_{\mathbf{h}}| > 1$ are the most powerful ones for structure determination, because the Cochran- G_3 in eqn (10.3) (triplet product) in which they participate will be relatively large. Moreover, a large $|E_{\mathbf{h}}|$ deviates from the statistical average $|E_{\mathbf{h}}|^2 = 1$ so it carries specific structural information that is required to visualize the structure. Therefore, (semi-)invariants are set up only among the reflections with $|E_{\mathbf{h}}| > 1$ (the so-called ‘strong’ reflections). ‘Weak’ reflections with $|E_{\mathbf{h}}| \ll 1.0$ are not used actively in the phasing process but are still useful because they occur as cross-terms (see Section 10.5) of (semi-)invariants and as such they are essential for their correct estimation.

Because $\langle |E_{\mathbf{h}}|^2 \rangle = 1$, classes of reflections with $\langle |E_{\mathbf{h}}|^2 \rangle \ll 1$ (or $\gg 1$) (e.g. as a result of *pseudo*-translations) may cause problems in DM (e.g. in finding suitable origin-fixing reflections). Therefore, the $|E_{\mathbf{h}}|$ -statistics should be checked carefully for anomalies and, if necessary, a renormalization should be carried out. $|E_{\mathbf{h}}|$ -statistics of centrosymmetric and non-centrosymmetric structures are different. The former has more large and more small $|E_{\mathbf{h}}|$'s, but experimental statistics can be misleading because of *pseudo* centres of symmetry (e.g. heavy atom substructure in centrosymmetric configuration) or simply the lack of data, as often occurs with powder data.

10.3.2 Selection of starting-set phases

The selection of a small set of starting-set phases is often carried out with the convergence procedure of Germain *et al.* (1970). In this algorithm, reflections are removed one by one from a list on the basis of the smallest sum of G_3 values. Occasionally, the removal of one reflection implies the removal of another reflection (sometimes even two) that is linked via a single triplet. These reflections are potential starting-set reflections that have to be included in the starting set in order to avoid weak links in the phasing process. Some of the starting-set reflections may be phased freely to fix the origin, and sometimes even the enantiomorph in some acentric space groups, but the remaining starting-set phases may have any numerical phase value that is allowed by the space-group symmetry. In practice, the number of starting-set phases may vary from one to ten.

10.3.3 Active phase extension

In the active phasing process, the phases of the ‘strong’ reflections are expressed successively in terms of the starting-set phases using triplet relations only. Two

alternatives have been developed to deal with the phase values in the starting set that are not known in the beginning. In the numerical multi-solution technique, a multitude of numerical sets with different numerical values for the starting-set phases are generated and extended in parallel, usually by means of a weighted tangent expression. This technique has been implemented in many DM program systems, for example, MULTAN (Main 1985), SHELX (Sheldrick 1985), GENTAN (Hall 1985) and SIR88 (Burla *et al.* 1989). For a general review of DM systems available see Gilmore (1991). Various algorithms exist to select the numerical phase values, for example, systematically from the interval $[0, 2\pi]$ in steps of $\pi/4$ or $\pi/2$ or using the magic-integer representation (White and Woolfson 1975).

In symbolic phase determination, symbolic phase values, A , B , C , etc., are assigned to the phases of the starting-set reflections. Each symbol represents all numerical phase values allowed by the phase restriction of the reflection (Karle and Karle 1966). In principle, only one phase set (expressed in symbols) needs to be extended. Phases are accepted only if a unique symbolic phase indication is obtained. A multisolution-type symbolic phase determination has been implemented in SIMPEL88 (Peschar 1990), which is part of the POWSIM system to solve structures from powder data (see Section 10.6). In this approach, both the number of starting-set phases and the choice of starting-set reflections to which a symbolic phase is assigned are kept flexible during the phasing process.

10.3.4 Selection of most likely numerical starting set (criteria)

Throughout the numerical and at the end of the symbolic phase extension, consistency criteria are calculated in order to reject phase sets that are unlikely to be correct. Some criteria are based on the expected internal consistency of the triplet phase sums. The (semi-)invariants that have not been used actively nor implicitly in the phase-extension process play an (even more) important role, because they provide an independent statistical means to select the most likely numerical phase set. Examples include criteria based on negative quartets, one-phase and two-phase semi-invariants. Finally, on the basis of a combined figure of merit, a numerical solution is selected, and after a complete numerical phase extension, an E -map can be generated and interpreted.

10.4 Whole-pattern fitting

The first step towards a successful structure determination from powder data, the indexing of the pattern (see Chapter 7), is now well-established and will be considered to be solved from now on. A second prerequisite for using DM on powder data is that a sufficient number of reliable single-crystal-like intensities can be extracted from the powder pattern. As integrated intensities

are required, whole-pattern fitting techniques are an appropriate choice (see Chapter 8).

10.4.1 *The Pawley whole-pattern refinement*

Rietveld refinement, originally developed to refine a complete neutron-diffraction pattern as a function of a variety of parameters (Rietveld 1969), has spawned fruitful research in whole-pattern refinement techniques (see Post and Bish 1989). For our purposes, a procedure devised by Pawley (1981) to determine reliable cell parameters turned out to be a suitable starting point. The Pawley whole-pattern refinement minimizes R :

$$R = \sum_{\theta} |y(\text{obs}, \theta) - y(\text{calc}, \theta) - Bg(\theta)|^2, \quad (10.7)$$

in an iterative fashion. The variables $y(\text{obs}, \theta)$ and $y(\text{calc}, \theta)$ are the observed and calculated intensities at the angle θ respectively. $y(\text{calc}, \theta)$ depends on the intensity of the reflection(s) at position θ' and on its peak-shape function P . The background $Bg(\theta)$ can be modelled with a polynomial in θ of order q .

In a standard Pawley refinement, all parameters (intensities, background parameters, peak-shape parameters and cell parameters), are refined simultaneously. No structural parameters are required. As noted by Pawley himself, the refinement process, involving the Simplex (Nelder and Mead 1964) and Marquardt (1963) algorithms, can be unstable because of correlation between overlapping peaks. Pawley suggested the introduction of Waser constraints to improve the stability of the refinement, but this does not necessarily lead to more reliable intensities.

10.4.2 *The two-step LSQPROF whole-pattern fitting procedure*

By taking the derivative of eqn (10.7) with respect to the intensities and background parameters, Jansen *et al.* (1992a) showed that the minimization problem can be solved exactly for these parameters by means of a Simplex algorithm. This led to a revision of the Pawley refinement into a two-step process. The parameters are split in two sets with set one consisting of the intensities and the background parameters and set two of the cell, peak-shape and zero-point parameters. The latter are refined one-by-one while taking the parameters from set one as a starting point. The refinement of the second set is done with a Marquardt-type algorithm. In the computer program LSQPROF, these two steps are carried out iteratively, both in a block-diagonal way, until a final convergence has been obtained. Accurate standard deviations cannot be expected in this way but this is not critical since the extracted intensities are intermediates on the way to the structural atomic parameters. On the basis of

a comparison of peak-shape functions carried out by Young and Wiles (1982), the *pseudo*-Voigt function with eight refinable parameters (the Lorentzian (u_L , v_L and w_L) and Gaussian (u_G , v_G and w_G) peak-shape contributions, Lorentzian–Gaussian mixing parameter and an asymmetry parameter) has been implemented in LSQPROF.

Practical tests with LSQPROF showed that it is essential to start with correct initial estimates of intensities before undertaking the refinement of other parameters. Currently, in addition to the intensities, which are always refined, a refinement protocol is used in which the first refinement of the second-set parameters is cycle-dependent: zero-point (3–4), peak-shape parameters (5–8), cell-parameters (9–10). Progress in refinement is monitored via an R -factor that can converge towards values below 4 per cent in successful cases. Jansen *et al.* (1992a) showed that with LSQPROF individual intensities can be extracted of reflections with angles as close as 0.5 FWHM (Full Width at Half Maximum). The original Pawley algorithm only extracts reliably to 1.0 FWHM.

10.5 Estimation of the intensity of completely overlapping reflections: the DOREES program

If the diffraction angles of individual reflections differ by less than 0.5 FWHM, whole-pattern fitting programs like LSQPROF encounter increasing difficulties in extracting the correct individual reflection intensities.

DM probability distributions relate not only the invariant phase sums, but also the $|E_h|$'s. The latter feature can be exploited to estimate the $|E|$'s of overlapping reflections in terms of the $|E|$'s of resolved reflections. For example, it can be argued that for large products $|E_k||E_{h+k}|$, $|E_h|$ will have a tendency to be large as well. When averaged over all contributing triplets, this can be expressed in the Triplet Product Estimation of $|E_h|$. A similar procedure can be set up for quartet phase sums Ψ_4 , but the fact that the estimation of $\cos(\Psi_4)$ depends not only on the main-term magnitudes $|E_h|$, $|E_k|$, $|E_l|$ and $|E_{h+k+l}|$ but also on the cross-term magnitudes $|E_{h+k}|$, $|E_{h+l}|$ and $|E_{k+l}|$ must also be taken into account. Large cross-term $|E|$'s lead to $\langle \cos(\Psi_4) \rangle \approx 1$ (positive quartets) while $\langle \cos(\Psi_4) \rangle \approx -1$ is expected for small cross-term magnitudes (negative quartets, e.g. Hauptman 1974; Schenk 1974). After inserting an estimate of $\cos(\Psi_4)$ on the basis of six magnitudes $|E_h| - |E_{h+l}|$, the remaining $|E_{k+l}|$ can be expressed as being proportional to $|E_h E_k E_l E_{h+k+l}| \langle \cos(\Psi_4) \rangle$. After averaging over all quartets in which $|E_{k+l}|$ occurs with the six other magnitudes known, a Quartet Algebraic Estimation for $|E_{k+l}|$ is defined.

The Triplet Product Estimation and the Quartet Algebraic Estimation are two out of five techniques used in the program DOREES (Jansen *et al.* 1992b) to estimate the $|E|$'s of completely overlapping reflections. The quality of the estimates by each technique separately is not high and should be used only qualitatively to rank the estimates. On the basis of the individual ranking

numbers N_i , one for each estimation technique, and user-supplied weights w_i , an overall figure of merit $M_h = \sum w_i N_i / \sum w_i$ determines the classification of an $|E_h|$ as probably strong or weak.

On basis of the M_h and user-supplied values M_{strong} and M_{weak} , the overlapping reflections are divided into three groups: a 'strong' group consisting of the M_{strong} reflections with the smallest M_h values, a 'weak' group of M_{weak} reflections with the largest M_h while the remaining reflections form an 'intermediate' group. Subsequently, intensity redistribution is carried out in which, in comparison to the initial equipartitioned intensities, the M_{strong} reflections gain intensity, the M_{weak} intensities lose intensity and remaining intensities stay the same. Currently, 75 per cent of the intensity of a weak reflection is redistributed towards strong reflections (50 per cent) and intermediate ones (25 per cent). In this way, a strong reflection in a cluster of N reflections, of which N_s and N_w are strong and weak respectively, will gain intensity from the intermediate (i) and weak (w) reflections in its cluster according to the scheme:

$$I_s^{\text{new}}(\theta) = I_s^{\text{old}}(\theta) + \frac{\sum_i I_i(\theta_j) G_i(d_i)}{2N_s} + \frac{\sum_w I_w(\theta_j) G_w(d_w)}{(N - N_w)}, \quad (10.8)$$

where

$$G(d_j) = \begin{cases} 0 & d_j \geq d_{\min} \\ 1 - d/d_{\min} & d_j < d_{\min} \end{cases}$$

and

$$d_j = |2\theta - 2\theta_j|$$

with $d_{\min} = 0.5$ FWHM if LSQPROF is used. After one run of DOREES, the M_{strong} and M_{weak} reflections are included in the set of single reflections with an appropriate weight (Jansen *et al.* 1993). This also applies to intermediate reflections that remain as a single element of a cluster after the removal of strong and weak reflections. The resulting set of intensities can be processed again. This iteration continues until either a sufficient number of large $|E|$'s has been extracted to start a DM run or until no significant changes occur in the intensity distribution.

10.6 Direct methods for powder data in practice: the POWSIM package

The program package POWSIM has been designed to solve crystal structures from X-ray and neutron powder diffraction data. The main sequence of routines in POWSIM is LSQPROF, ITOF, NORMAL, SIMPEL88, EXFFT and DMS. In the routine LSQPROF, the powder pattern is fitted

into single-crystal-like integrated intensities for reflections that are at least 0.5 FWHM apart (Section 10.4). Subsequently, in ITOF (Jansen 1991), a Lorentz-polarization correction is applied, and in NORMAL (Main 1976), the $|F|$ -values are normalized to $|E|$'s using the Wilson plot. If LSQPROF results in a sufficient number of large $|E|$'s, the phase problem can be handled directly by the DM program SIMPEL88 (Peschar 1990). The structural model is then visualized by calculating an $|E|$ -Fourier-map with EXFFT (Ten Eyck 1977) and interpreted by means of DMS (Main and Hull 1978).

Starting at NORMAL, a second (optional) cycle of routines can be carried out: NORMAL, TRIQUA88 (+FOUR), DOREES, ITOF (and back to NORMAL). Very often many peaks overlap and the condition of a large number of large $|E|$'s is not satisfied. By means of DOREES, the number of single-crystal-like intensities, and thus the number of $|E|$'s, can be enlarged by estimating the latter on the basis of the reflections that are completely resolved. For this purpose, triplet and quartet relations are set up in TRIQUA88. In the later stages of DOREES, if approximately half of the reflections are single, peaks from an origin-removed Patterson (calculated with FOUR) can also be used together with the four DM-based techniques. This second cycle is repeated until either the structure can be solved or until the weights of the newly resolved $|E|$'s become too small.

Table 10.1 Some previously unknown structures solved by POWSIM

| | <i>a</i> | <i>b</i> / β | <i>c</i> | <i>Z</i> | Space group | <i>N</i> (asymm) | |
|---|-----------|--------------------|----------------|-----------------|-------------------------|------------------|-------------------|
| A | 13.20 | 7.58 | 8.554 | 2 | <i>Pnma</i> | 12 | |
| B | 13.66 | 12.05 | 7.63 | 4 | <i>Cmcm</i> | 9 | |
| C | 9.64 | 7.58 | 8.54 | 2 | <i>P2₁/m</i> | 11 | |
| D | 11.07 | 112.9 7.61 | 25.55 | 4 | <i>Pnma</i> | 27 | |
| | LSQPROF | | | DOREES | | | |
| | 2θ | <i>NTOT</i> | <i>NSINGLE</i> | <i>R</i> (in %) | <i>NSINGLE</i> | $ E > 1.0$ | <i>N</i> (out of) |
| A | 10–65 | 200 | 30 | 3.8 | 130 | 37 | 4(12) |
| B | 9–96 | 338 | 77 | 2.0 | 181 | 59 | 3(9) |
| C | 8–70 | 283 | 85 | 2.2 | 167 | 61 | 7(11) |
| D | 6–65 | 435 | 117 | 5.2 | 226 | 71 | 18(27) |

A: $\text{Ag}_2 \cdot 3\text{MoO}_3 \cdot 1.8\text{H}_2\text{O}$ Silver Trimolybdate (Lasocha *et al.* 1994)

B: $\text{K}_2 \cdot 3\text{MoO}_{10} \cdot 3\text{H}_2\text{O}$ Potassium Trimolybdate (Lasocha *et al.* 1995a)

C: $(\text{NH}_4)_2\text{O} \cdot 3\text{MoO}_3 \cdot \text{H}_2\text{O}$ Ammonium Trimolybdate (Lasocha *et al.* 1995b)

D: $2(\text{C}_6\text{H}_5\text{NH}_2) \cdot \text{Mo}_3\text{O}_{10} \cdot 4\text{H}_2\text{O}$ Anilinum Trimolybdate (Lasocha *et al.* 1995c)

NTOT is the total number of reflections in the 2θ interval.

NSINGLE is number of single-crystal(-like) reflections.

R(%) is the *R*-factor after the LSQPROF run.

N (out of) is the number of atoms (out of total number of atoms) found by POWSIM.

When applying DM to powder diffraction data rather than to single-crystal data, a conspicuous difference is that the B -value is often negative, in particular if the 2θ -range is limited. Data can be renormalized with a more realistic (positive) B , but recent indications exist that the renormalized $|E|$'s are not necessarily more suited for structure solution.

A practical rule in DM states that the number of strong $|E_h|$'s should be at least ten times the number of atoms (in the asymmetric unit with equal scattering power) to be visualized. In the case of powder data, the single-crystal limit of a 'strong' $|E_h|$ (≥ 1.2) is dropped to $|E| \geq 1.0$ and in the later stages of DOREES sometimes to even smaller values because otherwise too few $|E|$'s are available to generate (semi-)invariants. For example, in the case of some molybdates recently solved with POWSIM (Table 10.1, compounds A–C), the number of single reflections after LSQPROF (using 0.5 FWHM as the limit for peaks to be resolved) is only 30–85 and only 10–25 of them have an $|E| > 1.0$. This indicates that at most 1–2 atoms can be expected according to DM experience. The structures listed in Table 10.1 could not be solved after LSQPROF. Only after DOREES had been applied (five cycles, using $N_{\text{strong}} = 5$ and $N_{\text{weak}} = 10$, with the use of the Patterson criterion in the last two cycles) could partial structural models be obtained.

References

- Burla, M. C., Camalli, M., Cascarano, G., Giacovazzo, C., Polidori, G., Spagna, R. and Viterbo, D. (1989). *J. Appl. Crystallogr.*, **22**, 389–3.
- Cochran, W. (1955). *Acta Crystallogr.*, **8**, 473–8.
- Germain, G., Main, P. and Woolfson, M. M. (1970). *Acta Crystallogr. B*, **26**, 274–85.
- Giacovazzo, C. (1980). *Direct methods in Crystallography*, Academic Press, London.
- Gilmore, C. J. (1991). In *Direct methods of Solving Crystal Structures* (ed. H. Schenk), pp. 177–86. Plenum Press, New York.
- Hall, S. R. (1985). *J. Appl. Crystallogr.*, **18**, 263–4.
- Hauptman, H. (1974). *Acta Crystallogr. A*, **30**, 472–6.
- Heinerman, J. J. L. (1977). *Acta Crystallogr. A*, **33**, 100–6.
- Jansen, J. (1991). *Ph.D. Thesis*, Universiteit van Amsterdam.
- Jansen, J., Peschar, R. and Schenk, H. (1992a). *J. Appl. Crystallogr.*, **25**, 231–7.
- Jansen, J., Peschar, R. and Schenk, H. (1992b). *J. Appl. Crystallogr.*, **25**, 237–43.
- Jansen, J., Peschar, R. and Schenk, H. (1993). *Z. Kristallogr.*, **206**, 33–43.
- Karle J. and Hauptman, H. (1956). *Acta Crystallogr.*, **9**, 635–51.
- Karle, J. and Hauptman, H. (1958). *Acta Crystallogr.*, **11**, 264–9.
- Karle, J. and Karle, I. (1966). *Acta Crystallogr.*, **21**, 849–59.
- Lasocha, W., Jansen, J. and Schenk, H. (1994). *J. Solid. State Chem.*, **109**, 1–4.
- Lasocha, W., Jansen, J. and Schenk, H. (1995a). *J. Solid. State Chem.*, **115**, 225–8.
- Lasocha, W., Jansen, J. and Schenk, H. (1995b). *J. Solid. State Chem.*, **116**, 422–6.
- Lasocha, W., Jansen, J. and Schenk, H. (1995c). *J. Solid. State Chem.*, **117**, 103–7.
- Main, P. (1976). In *Crystallographic computing techniques* (ed. F. R. Ahmed) pp. 97–105. Munksgaard, Copenhagen.

- Main, P. (1985). In *Crystallographic Computing 3* (eds G. M. Sheldrick, C. Kruger, and R. Goddard), pp. 206–15. Clarendon Press, Oxford.
- Main, P. and Hull, S. E. (1978). *Acta Crystallogr.*, **34**, 353–61.
- Marquardt, D. W. (1963). *J. Soc. Ind. Appl. Math.*, **11**, 431–41.
- Nelder, J. A. and Mead, R. (1964). *Comput. J.*, **7**, 308.
- Pawley, G. S. (1981). *J. Appl. Crystallogr.*, **14**, 357–61.
- Peschar, R. (1990). In *MOLEN, Molecular structure solution procedures*, Vol. 3, pp.59–82. Enraf-Nonius, Delft.
- Post, J. E. and Bish, D. L. (1989). *Rev. Mineral.*, **20**, 277–308.
- Rietveld, H. M. (1969). *J. Appl. Crystallogr.*, **2**, 65–71.
- Schenk, H. (1974). *Acta Crystallogr. A*, **30**, 477–82.
- Schenk, H. (ed.) (1991). *Direct methods of solving crystal structures*, Plenum Press, New York.
- Sheldrick, G. M. (1985). In *Crystallographic computing 3* (eds G. M. Sheldrick, C. Kruger and R. Goddard), pp. 184–9. Clarendon Press, Oxford.
- Ten Eyck, L. F. (1977). *Acta Crystallogr. A*, **33**, 486–92.
- White, P. S. and Woolfson, M. M. (1975). *Acta Crystallogr. A*, **31**, 53–6.
- Wilson, A. J. C. (1942). *Nature*, **150**, 152
- Young, R. A. and Wiles, D. B. (1982). *J. Appl. Crystallogr.*, **15**, 430–8.

Direct methods in powder diffraction—applications

*Carmelo Giacovazzo, Angela Altomare,
Maria Cristina Burla, Benedetta Carrozzini,
Giovanni Luca Cascarano,
Antonietta Guagliardi, Anna Grazia G. Moliterni,
Giampiero Polidori and Rosanna Rizzi*

11.1 Introduction

In the last 10 years the number of structure determinations from powder data has increased surprisingly. Improvements in computational techniques and the use of high-resolution synchrotron facilities have made such progress possible. Nevertheless, *ab initio* structure solution from powder data is still a challenge in many cases. The combination of peak overlap, an uncertainty in the background signal and possible preferred orientation effects makes an unambiguous and accurate determination of the integrated intensities of the individual reflections difficult, if not impossible. This in turn makes crystal structure solution from powder data more complicated. In particular, the low accuracy of the estimated structure-factor moduli causes the application of Direct methods to be less than straightforward. The most recent advances in this field (Weeks and Miller 1996; Sheldrick 1998; Burla *et al.* 1999) show that even crystal structures with more than 2000 atoms in the asymmetric unit can be solved by a direct phasing procedure, provided high-quality single-crystal data up to about 1 Å resolution are available. Conversely, high-quality powder data do not necessarily transform into accurate structure-factor moduli and the real resolution of the information may be lower than 1 Å. The problems become more serious for organic compounds where the scattering at high angles rapidly decreases because of the presence of light atoms and because of thermal motion. One possible way of increasing the probability of successfully solving a structure from powder data is to improve the methods used to extract the integrated intensities from the diffraction pattern. Additional information can be exploited in the intensity extraction process, and methods for doing so will be described in the first part of this chapter. Then some successful applications of Direct methods will be discussed.

Table 11.1 Code name, crystal chemical information, and data details for the test structures. X: conventional X-ray data, N: neutron data, S: synchrotron data

| Code name | Space group | Unit cell content | 2θ range | Number of reflections | d (resolution) |
|------------------|--|---|-----------------|-----------------------|------------------|
| AGPZ (X) | <i>Pbca</i> | $\text{Ag}_8\text{N}_{16}\text{C}_{24}\text{H}_{24}$ | 5.0–80.0 | 258 | 1.198 |
| BACO (N) | <i>C 2/m</i> | $\text{Ba}_4\text{C}_8\text{O}_{20}\text{D}_8$ | 20.7–150.0 | 272 | 0.988 |
| BAMO (X) | <i>P 2₁</i> | $\text{Ba}_4\text{Mo}_{12}\text{O}_{40}$ | 10.0–119.0 | 1220 | 0.894 |
| BENZ (S) | <i>P2₁/a</i> | $\text{C}_{24}\text{F}_{12}$ | 5.0–100.0 | 716 | 0.916 |
| CF3BR (N) | <i>P2₁/a</i> | $\text{C}_4\text{Br}_4\text{F}_{12}$ | 6.0–150.0 | 375 | 0.989 |
| CFCL (N) | <i>Fdd2</i> | $\text{C}_8\text{F}_{16}\text{Cl}_{16}$ | 5.0–150.0 | 203 | 0.826 |
| CFI (N) | <i>Cmca</i> | $\text{C}_8\text{F}_{24}\text{I}_8$ | 10.0–150.0 | 428 | 0.826 |
| CIME (S) | <i>P 2₁/n</i> | $\text{S}_4\text{C}_{40}\text{N}_{24}\text{H}_{64}$ | 8.01–84.99 | 924 | 1.13 |
| CROX (X) | <i>P$\bar{1}$</i> | Cr_8O_{21} | 6.0–80.0 | 657 | 1.083 |
| CUPZ (X) | <i>Pbca</i> | $\text{Cu}_8\text{N}_{16}\text{C}_{24}\text{H}_{24}$ | 5.0–80.0 | 243 | 1.198 |
| DADA (X) | <i>P 2₁ 2₁ 2₁</i> | $\text{Ti}_8\text{K}_4\text{Si}_{12}\text{O}_{40}$ | 10.0–95.0 | 518 | 1.045 |
| LAMO (X) | <i>P 2₁/a</i> | $\text{La}_4\text{Mo}_{20}\text{O}_{32}$ | 11.0–69.0 | 271 | 1.357 |
| LASI (N) | <i>P 2₁/c</i> | $\text{La}_8\text{Si}_8\text{O}_{28}$ | 10.0–115.724 | 253 | 1.382 |
| LEV (S) | <i>R 3m</i> | $[\text{Si}_{54}\text{O}_{108}]_3\text{C}_8\text{NH}_{16}$ | 8.0–85.6 | 323 | 1.132 |
| MES (X) | <i>P 2₁/c</i> | $\text{C}_{24}\text{N}_4\text{O}_{20}\text{S}_4\text{H}_{52}$ | 5.0–88.0 | 719 | 1.109 |
| METYL (S) | <i>I 222</i> | $\text{Na}_{16}\text{C}_{16}\text{H}_{48}$ | 5.2–70.0 | 318 | 0.956 |
| NBPO (S) | <i>C 2/c</i> | $\text{Nb}_{20}\text{O}_{120}\text{P}_{28}$ | 3.0–60.0 | 1201 | 1.000 |
| NIZR (S) | <i>P 2₁/n</i> | $\text{Ni}_4\text{Zr}_8\text{P}_4\text{O}_{16}$ | 8.0–52.0 | 627 | 1.175 |
| PBS (S) | <i>Pbca</i> | $\text{Pb}_8\text{S}_{16}\text{O}_{24}$ | 7.5–79.8 | 477 | 0.961 |
| SAPO (X) | <i>Pnmm</i> | $\text{Si}_{32}\text{O}_{64}\text{N}_2\text{C}_{48}$ | 5.0–79.98 | 716 | 1.199 |
| SBPO (S) | <i>P 2₁/n</i> | $\text{Sb}_8\text{P}_{14}\text{O}_{48}$ | 6.0–100.0 | 1071 | 0.947 |
| SULPH (N) | <i>Pbcm</i> | S_8D_{16} | 7.0–150.0 | 220 | 0.947 |
| YONO (S) | <i>P 2₁</i> | $\text{Y}_8\text{O}_{26}\text{N}_2\text{H}_{18}$ | 7.0–80.0 | 680 | 0.959 |

11.2 A set of test structures

In addition to the theoretical aspects, a number of applications to real experimental data will be described in this paper. For the convenience of the reader, the code names and associated crystal chemical information for a set of test structures are given in Table 11.1.

11.3 Performance of extraction algorithms

The efficiency of the intensity extraction process depends on the quality of the data as well as on the mathematical algorithm used for the decomposition of the experimental profile. Two main methods have been used (see Chapter 8):

1. *The Pawley method* (Pawley 1981) minimizes the sum of the square of the differences between the observed and the calculated profiles. The integrated intensities, the background polynomial coefficients, the peak-shape

parameters, the unit cell etc. are all refined in a least-squares process. The system is often ill-conditioned and may return negative intensity values. Special techniques have been implemented to avoid such a wild variation of intensity (Jansen *et al.* 1992; Sivia and David 1994).

2. *The Le Bail method* (Le Bail *et al.* 1988) is based on an original proposal by Rietveld (1969). It does not require inversion of a least-squares matrix and is computationally efficient, but does not provide standard deviations for the intensity estimates.

The better the efficiency of the decomposition program, the smaller the discrepancy between the calculated and the *true* structure-factor moduli. It is expected that the smaller the discrepancy, the more straightforward the phasing process. It is reasonable to ask how accurate modern powder pattern decomposition programs are. A list of the R_D factors obtained by the Le Bail-based decomposition routine in EXPO (Altomare *et al.* 1999*a*) is given for the test structures in Table 11.2 (second column). We define:

$$R_F = \frac{\sum_{\mathbf{h}} ||F_{\mathbf{h}}(\text{calc})| - |F_{\mathbf{h}}(\text{true})||}{\sum_{\mathbf{h}} |F_{\mathbf{h}}(\text{true})|}. \quad (11.1)$$

Table 11.2 The R_F parameter corresponding to the EXTRA default run (R_D), to the run exploiting pseudo-translational information (R_{PSEUD}), Patterson information in the reciprocal space (R_{PROB}), and Patterson information in direct space (R_{PATT}) for some test structures

| Code name | R_D | R_{PSEUD} | R_{PROB} | R_{PATT} |
|-----------|-------|--------------------|-------------------|-------------------|
| AGPZ (X) | 0.52 | 0.33 | 0.47 | 0.39 |
| BACO (N) | 0.31 | — | 0.28 | 0.28 |
| BENZ (S) | 0.41 | — | 0.37 | 0.36 |
| CF3BR (N) | 0.30 | — | 0.27 | 0.27 |
| CFCL (N) | 0.21 | — | 0.19 | 0.16 |
| CFI (N) | 0.49 | — | 0.46 | 0.45 |
| CROX (X) | 0.37 | — | 0.31 | 0.33 |
| CUPZ (X) | 0.47 | 0.35 | 0.41 | 0.34 |
| LAMO (X) | 0.36 | — | 0.35 | 0.35 |
| LASI (N) | 0.38 | — | 0.36 | 0.37 |
| LEV (S) | 0.59 | — | 0.56 | 0.52 |
| MES (X) | 0.46 | — | 0.42 | 0.44 |
| METYL (S) | 0.30 | — | 0.27 | 0.27 |
| NBPO (S) | 0.39 | 0.33 | 0.30 | 0.24 |
| NIZR (S) | 0.42 | 0.42 | 0.36 | 0.37 |
| PBS (S) | 0.41 | — | 0.38 | 0.38 |
| SAPO (X) | 0.45 | — | 0.42 | 0.41 |
| SBPO (S) | 0.49 | 0.31 | 0.32 | 0.29 |
| SULPH (N) | 0.32 | — | 0.30 | 0.27 |
| YONO (S) | 0.32 | — | 0.25 | 0.27 |

For each test structure, $|F_h(\text{true})|$ is the structure-factor modulus which corresponds to the published refined structure, $|F_h(\text{calc})|$ is the corresponding modulus obtained by EXPO using default conditions. It is soon apparent that the performance of a powder decomposition program depends on: (a) the size of the unit cell and the space group (both affect the amount of peak overlap); (b) the radiation source and instrument (Chapters 3–5); and (c) the conditions under which the measurement is performed (Chapter 6).

The values in Table 11.2 indicate that, for normal-sized structures, R_D factors lower than 0.25 are rarely obtained. R_D factors between 0.35 and 0.50 are more common. How does this inaccuracy affect the triplet invariant estimates? Some statistics for triplet phase estimates for three test structures with high R_D values (**SAPO**, **LEV** and **LASI** with $R_D = 0.45, 0.59$ and 0.38 , respectively) are given in Tables 11.3–11.5.

The estimated structure-factor moduli have been normalized by a typical Direct methods program (in these cases by the EXPO section devoted to direct phasing) to obtain $|E|$ moduli. A subset of NLAR reflections has been isolated (those having the largest $|E|$ values) for **SAPO**, **LEV** and **LASI** (NLAR = 263, 125 and 84 respectively). Triplets found among the NLAR reflections have been estimated via the P_{10} formula (Casarano *et al.* 1984), which can identify positive and negative cosine triplets. A reliability factor G is associated with each triplet: large positive G 's correspond to triplet phases close to 2π , large negative G 's to triplet phases close to π , and small $|G|$ values to inaccurate estimates.

In Tables 11.3–11.5, two sets of statistics are shown: one for the true structure factor moduli (i.e. in absence of experimental errors, to simulate the statistics which would be obtained if single-crystal data were available), and one for the

Table 11.3 SAPO: triplet statistics

| ARG | Positive estimated triplets | | Negative estimated triplets | |
|---------------------------------|-----------------------------|-------|-----------------------------|-------|
| | Number | % | Number | % |
| Experimentally estimated moduli | | | | |
| 0.0 | 9859 | 60.7 | 0 | 0.0 |
| 0.4 | 1495 | 76.7 | 0 | 0.0 |
| 0.8 | 221 | 93.2 | 0 | 0.0 |
| 1.2 | 61 | 96.7 | 0 | 0.0 |
| 1.6 | 16 | 100.0 | 0 | 0.0 |
| True moduli | | | | |
| 0.0 | 5833 | 72.8 | 764 | 53.8 |
| 0.4 | 2207 | 85.9 | 22 | 63.6 |
| 0.8 | 826 | 95.4 | 2 | 100.0 |
| 1.2 | 382 | 99.5 | 0 | 0.0 |
| 1.6 | 217 | 100.0 | 0 | 0.0 |

Table 11.4 LEV: triplet statistics

| ARG | Positive estimated triplets | | Negative estimated triplets | |
|---------------------------------|-----------------------------|-------|-----------------------------|-------|
| | Number | % | Number | % |
| Experimentally estimated moduli | | | | |
| 0.0 | 3576 | 59.8 | 0 | 0.0 |
| 0.4 | 772 | 69.4 | 0 | 0.0 |
| 1.0 | 18 | 100.0 | 0 | 0.0 |
| 1.4 | 3 | 100.0 | 0 | 0.0 |
| True moduli | | | | |
| 0.0 | 1610 | 76.8 | 169 | 63.9 |
| 0.4 | 980 | 88.9 | 17 | 76.5 |
| 1.0 | 353 | 98.0 | 5 | 100.0 |
| 1.4 | 189 | 99.5 | 2 | 100.0 |
| 2.0 | 63 | 100.0 | 0 | 0.0 |

Table 11.5 LASI: triplet statistics

| ARG | Positive estimated triplets | | Negative estimated triplets | |
|---------------------------------|-----------------------------|-------|-----------------------------|------|
| | Number | % | Number | % |
| Experimentally estimated moduli | | | | |
| 0.0 | 484 | 58.5 | 0 | 0.0 |
| 0.4 | 243 | 63.0 | 0 | 0.0 |
| 1.0 | 35 | 74.3 | 0 | 0.0 |
| 1.4 | 15 | 60.0 | 0 | 0.0 |
| 2.0 | 5 | 60.0 | 0 | 0.0 |
| True moduli | | | | |
| 0.0 | 275 | 75.6 | 21 | 42.9 |
| 0.4 | 184 | 81.0 | 1 | 0.0 |
| 1.0 | 76 | 96.1 | 0 | 0.0 |
| 1.4 | 40 | 100.0 | 0 | 0.0 |
| 2.0 | 13 | 100.0 | 0 | 0.0 |

moduli originally obtained by EXPO. In each case, statistics for the negative estimated triplets are separated from the positive ones, because of the special role the latter play in the phasing process. For each value of ARG, the number of triplets (nr) with $|G|$ larger than ARG and the per cent of correctly estimated triplets are given. The examples show how the triplet estimates become less reliable as the accuracy of the estimated structure-factor moduli decreases. The worst situation occurs for **LASI**, where the total number of estimated triplets is very small (less than 500) and their accuracy quite

unsatisfactory (close to 60 per cent). This is due to the combined effect of the limited resolution (1.38 Å) of the experimental data and to the inefficient pattern decomposition. A further detail deserves to be stressed: when the true data were used, a number of negative triplets were always identified by the P_{10} formula. When experimental powder data were used, no negative triplet was found. The reason for this systematic feature is the overestimation of the weak reflection intensities. They frequently overlap with stronger reflections and EXPO is not able to evaluate them correctly. As a consequence, negative quartet estimates, which are based on weak reflection intensities, are also inaccurate. The data in Tables 11.3–11.5 also indicate that even quite simple crystal structures may not yield to phasing trials if only powder data are available.

11.4 Some warnings about the use of powder data

A short list of the main pitfalls a Direct methods user has to avoid when using powder data (Giacovazzo 1996) is given below.

1. Do not use Wilson statistics to establish whether or not the space group is centrosymmetric. Most of the features of the estimated normalized structure-factor moduli distribution are dependent upon the pattern-decomposition method rather than the crystal structure (Casarano *et al.* 1992; Estermann *et al.* 1992). For example, the Pawley technique generates amplitude distributions characterised by large percentages of very large and very small intensity values. This increases the distribution variance and simulates statistics indicative of a centrosymmetric structure even when it is actually non-centrosymmetric. Conversely, the Le Bail method tends to equipartition the intensities of the overlapping reflections to produce a rather uniform intensity distribution indicative of a non-centrosymmetric structure.
2. Do not be too confident about the overall thermal factor value obtained via a Wilson plot; sometimes it is even negative. The value depends on: (a) truncation of the experimental data at $\sin \theta/\lambda$ values where Debye effects are important; (b) imperfect modelling of the background and of the peak shape; (c) possible imperfect absorption correction for transmission geometry or surface roughness for reflection geometry.
3. Be suspicious of the information provided in the high-resolution region of the powder pattern. Structure factor moduli estimates can be markedly wrong in this region, where a high degree of reflection overlap occurs.
4. Do not apply Direct methods without first checking for the presence of preferred orientation. If this occurs, some $|E|$ normalized structure factor moduli will be systematically larger than their true values and some others systematically smaller, and this will have obvious consequences on the efficiency of the phasing process. A statistical check can be performed on

the $|E|$ distribution in order to reveal the possible presence of preferred orientation (Altomare *et al.* 1994, 1996a; Peschar *et al.* 1995). If this has been established, suitable corrections to the $|E|$ values can be applied.

5. Solving the structure with neutron data may be more difficult than with X-ray data if some heavy atoms are present. In this case, X-ray data can be used to locate the heavy atoms, and then the crystal structure can be completed/refined by combining the information contained in both datasets.
6. As a result of the uncertainty of the structure-factor moduli, the figures of merit defining the best trial solution in a direct phasing approach cannot be as discriminating as they are with single-crystal data.
7. The amount of information in the experimental pattern should be evaluated before a crystal structure determination or refinement is attempted. It may be that the information is not sufficient to guarantee success. An algorithm recently proposed by Altomare *et al.* (1995) (see also a more recent contribution by David (1999)) provides an estimate of the global information in terms of statistically independent observations. The larger their number (M_{ind}), the higher the information content of the pattern (see Table 11.6).

11.5 Powder pattern decomposition using supplementary prior information

The most important advantage of the Le Bail method is that it may profit from the use of supplementary information (Altomare *et al.* 1996b). The approach is sensitive to the starting point: if one starts from integrated intensity values closer to the true values rather than from arbitrary intensities, results can be improved and the accuracy increased.

Different types of information become available during the phasing process and can be used as prior information in a subsequent decomposition step:

1. Pseudo-translational symmetry (Altomare *et al.* 1996c).
2. The expected positivity of the Patterson function in reciprocal space (Carrozzini *et al.* 1997).
3. The expected positivity of the Patterson function in direct space (Altomare *et al.* 1997; Estermann *et al.* 1992; Estermann and Gramlich 1993).
4. A located molecular fragment (Altomare *et al.* 1999b).

Each can be used in a cyclic procedure in which the experimental pattern is decomposed to provide a first estimate of the structure-factor amplitudes. Once one of these types of information is available it can be included as prior information for a new pattern decomposition. EXPO is able to perform this cyclic process automatically. Brief descriptions of each category of information are given in the following sections.

Table 11.6 Summary of the structure solutions of the test structures

| Code name | NATS1 | NATS2 | $(\sin \theta/\lambda)_{\max}^2$ | M_{ind} | M | M_{ind}/M |
|------------------|-----------|-------|----------------------------------|------------------|------|--------------------|
| AGPZ (X) | 4 | 6 | 0.17 | 72 | 258 | 0.28 |
| BACO (N) | completed | 6 | 0.26 | 127 | 272 | 0.47 |
| BAMO (X) | 27 | 28 | 0.32 | 396 | 1220 | 0.32 |
| BENZ (S) | completed | 9 | 0.30 | 258 | 716 | 0.36 |
| CF3BR (N) | completed | 3 | 0.25 | 141 | 375 | 0.38 |
| CFCL (N) | completed | 3 | 0.37 | 106 | 203 | 0.52 |
| CFI (N) | completed | 3 | 0.37 | 149 | 429 | 0.35 |
| CIME (S) | completed | 17 | 0.19 | 484 | 924 | 0.52 |
| CROX (X) | completed | 15 | 0.21 | 202 | 657 | 0.31 |
| CUPZ (X) | 5 | 6 | 0.17 | 72 | 243 | 0.29 |
| DADA (S) | completed | 16 | 0.23 | 197 | 518 | 0.38 |
| LAMO (S) | 12 | 14 | 0.13 | 126 | 271 | 0.46 |
| LASI (N) | 8 | 11 | 0.13 | 105 | 253 | 0.42 |
| LEV (S) | 8 | 17 | 0.19 | 103 | 323 | 0.32 |
| MES (X) | 11 | 13 | 0.20 | 229 | 719 | 0.32 |
| METYL (S) | completed | 5 | 0.27 | 169 | 318 | 0.53 |
| NBPO (S) | completed | 22 | 0.25 | 481 | 1201 | 0.40 |
| NIZR (S) | 11 | 18 | 0.18 | 239 | 628 | 0.38 |
| PBS (S) | 5 | 6 | 0.27 | 179 | 477 | 0.38 |
| SAPO (X) | 9 | 21 | 0.17 | 183 | 717 | 0.25 |
| SBPO (S) | 13 | 17 | 0.28 | 337 | 1071 | 0.31 |
| SULPH (N) | completed | 3 | 0.26 | 93 | 220 | 0.42 |
| YONO (S) | completed | 18 | 0.27 | 203 | 680 | 0.30 |

NATS1 is the number of correct atomic positions localised by EXPO, NATS2 is the number of positions to be found, M_{ind} is the number of independent observations, M the number of reflections and M_{ind}/M their ratio.

11.5.1 Pseudo-translational symmetry

From the statistical analysis of the normalized structure factors, EXPO is able to reveal the presence of pseudo-translational symmetry effects. If the fractional scattering power (FSP) satisfying pseudosymmetry is larger than some minimum threshold, the EXPO user can decide to exploit the pseudoinformation in a new EXPO run. The FSP value is usually underestimated in the first run, so in the second run the information on pseudo-translational symmetry is used to modulate the starting intensities for the Le Bail algorithm. The rationale of the procedure is the following: if two reflections completely overlap and one is a superstructure and the other a substructure reflection, a sensible choice is to assign a larger intensity to the substructure reflection.

In Table 11.2, the R_F values in column 3 were obtained by using pseudoinformation for those structures revealing pseudoeffects. They can be compared with the default R_D values in column 2.

11.5.2 *Expected positivity of the Patterson function in reciprocal space*

The results of squaring a Patterson map from which the origin peak has been removed, viewed in reciprocal space, suggested the relations (Cascarano *et al.* 1991):

$$\langle |E_{\mathbf{h}}| | \dots \rangle \approx (\pi^{1/2}/2) \left[1 + (1/2N) \sum_{\mathbf{k}} (|E_{\mathbf{k}}|^2 - 1) (|E_{\mathbf{h}-\mathbf{k}}|^2 - 1) \right] \quad (11.2)$$

for non-centrosymmetric space groups, and:

$$\langle |E_{\mathbf{h}}| | \dots \rangle \approx (2/\pi)^{1/2} \left[1 + (1/2N) \sum_{\mathbf{k}} (|E_{\mathbf{k}}|^2 - 1) (|E_{\mathbf{h}-\mathbf{k}}|^2 - 1) \right] \quad (11.3)$$

for centrosymmetric space groups, where $E_{\mathbf{h}}$ is the normalized structure factor and N is the number of equivalent atoms in the unit cell.

Once the pattern decomposition has been performed, the extracted structure-factor moduli can be normalized and used to obtain the probabilistic estimates for each reflection by applying eqns (11.2) and (11.3). The estimates can then be input into the decomposition routine of EXPO and this improves the decomposition, because the starting point is more reliable. In Table 11.2 the R_F values in column 4 correspond to the extraction process exploiting the above relations.

11.5.3 *The expected positivity of the Patterson function in direct space*

The Patterson information in direct space is also used in EXPO. The default-structure factor moduli are used to calculate a Patterson map, and then the map is modified by reducing the origin peak and by deleting low-density points. The inverse Fourier transform of the modified map provides updated squared-structure-factor moduli to use for a new calculation of the Patterson map and so on cyclically. After a few cycles, the final updated diffraction intensities are used as a starting point for a new pattern decomposition. The results are shown in the column 5 of Table 11.2.

11.5.4 *A located molecular fragment*

The recognition of a partial structure solution by a default EXPO run can be taken into account in four different ways:

1. The structure-factor moduli calculated from the fragment are recycled for a new pattern decomposition process.
2. The structure-factor moduli calculated from the fragment are used to obtain a profile difference between the observed experimental pattern and the fragment-dependent calculated profile. Then the Le Bail algorithm,

suitably revised for taking into account the presence of negative regions in the difference profile, is run to decompose this profile and to extract the difference integrated intensities. These are then added to the integrated intensities calculated from the fragment and are used as prior information for a further EXTRA run.

3. The probabilistic relation:

$$\langle |F_{\mathbf{h}}| \mid |F_{p\mathbf{h}}| \rangle = |F_{p\mathbf{h}}|^2 + \sum_q f_j^2(\mathbf{h}) \quad (11.4)$$

is used. $|F_{p\mathbf{h}}|$ is the structure-factor modulus calculated from the fragment, and $\sum_q f_j^2(\mathbf{h})$ is the summation of the squared scattering factors extended to the atoms not yet localized. The relationship in eqn (11.4) supplies the structure-factor moduli estimates to be used as starting point for a better pattern decomposition.

4. The intensity values deduced in 1, 2 and 3 are averaged and exploited for a better pattern decomposition.

The R_F values corresponding to the four different procedures are shown in Table 11.7 for some test structures and some molecular fragments. Tables 11.2 and 11.7 show how recycling prior information can improve the powder pattern decomposition process. This means that the unavoidable loss of information due to overlapping, background, etc. can be partially recovered. The different types of information are correlated, so a choice is necessary. The following strategy seems to work well: if pseudoeffects are large, pseudoinformation must be preferred; Patterson information works well for heavy atom structures; otherwise the procedure using eqns (11.2) or (11.3) can be used; information on a located fragment can be usefully applied when a partial solution is obtained.

Table 11.7 Test structures solved using a selected fragment and the R_F values for each of the four procedures

| Code name | Selected fragment (%) | R_1 | R_2 | R_3 | R_4 |
|-----------------|-----------------------|-------|-------|-------|-------|
| AGPZ (X) | 1 Ag (97.2 %) | 29.15 | 30.96 | 29.26 | 29.47 |
| BAMO (X) | 2 Ba (37.8 %) | 39.06 | 41.37 | 38.92 | 38.06 |
| CUPZ (X) | 1 Cu (92.3 %) | 27.15 | 28.73 | 27.20 | 26.53 |
| DADA (X) | 1 Ti 2 K (54.4 %) | 35.81 | 30.95 | 35.83 | 31.92 |
| LAMO (X) | 1 La 2 Mo (55.8 %) | 33.51 | 33.73 | 33.43 | 32.75 |
| LASI (N) | 2 La (34.1 %) | 34.78 | 35.51 | 34.53 | 33.55 |
| NBPO (S) | 3 Nb (82.7 %) | 27.03 | 25.63 | 27.14 | 23.99 |
| NIZR (N) | 2 Zr (68.6 %) | 40.03 | 35.98 | 39.94 | 36.09 |
| SBPO (S) | 2 Sb (87.9 %) | 26.59 | 26.82 | 26.68 | 23.25 |
| YONO (S) | 4 Y (95.8 %) | 20.30 | 20.70 | 20.37 | 20.15 |

11.6 Applications

In Table 11.6, the number of correct atoms located by EXPO and the total number of positions to be found in the different test structures are given. Most structures are solved completely, but for some, only the heavy atoms were located: the light ones can be found by difference Fourier techniques. The structure solution failures can be correlated with small M_{ind}/M values or/and to small $(\sin \theta/\lambda)_{\text{max}}^2$, showing that a necessary condition for success is high quality experimental data. This is where synchrotron radiation can be helpful.

Two recent successes with EXPO (Knudsen *et al.* 1998; Chan *et al.* 1999) proved that the *ab initio* solution of organic crystal structures with a large number of atoms in the asymmetric unit is not impossible, provided high quality data are available. The first success was for fluorescein diacetate (31 non-hydrogen atoms in the asymmetric unit and $P\bar{1}$ space group), and the second for sulfathiazole polymorph V (32 non-hydrogen atoms in the asymmetric unit and $P2_1/n$ space group).

Ad hoc strategies are sometimes useful. For example, the paper by Chan *et al.* pointed out the influence of the high angle data in the solution process. The complete crystal structure solution was obtained only after several attempts: they systematically reduced the high angle 2θ limit, and refitted the background in order to have a better separation between diffraction peaks and background noise. Success with Direct methods for complex structures can also be obtained with laboratory data, provided the pattern decomposition is performed carefully (Neels and Stoeckli-Evans 1999).

References

- Altomare, A., Burla, M. C., Cascarano, G., Giacovazzo, C., Guagliardi, A., Moliterni, A. G. G. and Polidori, G. (1996a). *J. Appl. Crystallogr.*, **29**, 341–5.
- Altomare, A., Cascarano, G., Giacovazzo, C., Guagliardi, A., Moliterni, A. G. G., Burla, M. C. and Polidori, G. (1995). *J. Appl. Crystallogr.*, **28**, 738–44.
- Altomare, A., Cascarano, G., Giacovazzo, C. and Guagliardi, A. (1994). *J. Appl. Crystallogr.*, **27**, 1045–50.
- Altomare, A., Carrozzini, B., Giacovazzo, C., Guagliardi, A., Moliterni, A. G. G. and Rizzi, R. (1996b). *J. Appl. Crystallogr.*, **29**, 667–3.
- Altomare, A., Foadi, J., Giacovazzo, C., Guagliardi, A. and Moliterni, A. G. G. (1996c). *J. Appl. Crystallogr.*, **29**, 674–81.
- Altomare, A., Foadi, J., Giacovazzo, C., Moliterni, A. G. G., Burla, M. C. and Polidori, G. (1997). *J. Appl. Crystallogr.*, **31**, 74–7.
- Altomare, A., Burla, M. C., Camalli, M., Carrozzini, B., Cascarano, G., Giacovazzo, C., Guagliardi, A., Moliterni, A. G. G., Polidori, G. and Rizzi, R. (1999a). *J. Appl. Crystallogr.*, **32**, 339–40.
- Altomare, A., Giacovazzo, C., Guagliardi, A., Moliterni, A. G. G. and Rizzi, R. (1999b). *J. Appl. Crystallogr.*, **32**, 963–7.

- Burla, M. C., Camalli, M., Carrozzini, B., Cascarano, G. L., Giacovazzo, G., Polidori, G. and Spagna, R. (1999). *Acta Crystallogr. A*, **55**, 991–9.
- Carrozzini, B., Giacovazzo, G., Guagliardi, A., Rizzi, R., Burla, M. C. and Polidori, G. (1997). *J. Appl. Crystallogr.*, **30**, 92–7.
- Cascarano, G., Favia, L. and Giacovazzo, C. (1992). *J. Appl. Crystallogr.*, **25**, 310–317.
- Cascarano, G., Giacovazzo, C., Camalli, M., Spagna, R., Burla, M. C., Nunzi, A. and Polidori, G. (1984). *Acta Crystallogr. A*, **40**, 278–83.
- Cascarano, G., Giacovazzo, C., Guagliardi, A. and Steadman, N. (1991). *Acta Crystallogr. A*, **47**, 480–4.
- Chan, F. C., Anwar, J., Cernik, R., Barnes, P. and Wilson, R. M. (1999). *J. Appl. Crystallogr.*, **32**, 436–41.
- David, W. I. F. (1999). *J. Appl. Crystallogr.*, **32**, 654–63.
- Estermann, M. A., McCusker, L. B. and Baerlocher, Ch. (1992). *J. Appl. Crystallogr.*, **25**, 539–43.
- Estermann, M. A. and Gramlich, V. (1993). *J. Appl. Crystallogr.*, **26**, 396–404.
- Giacovazzo, C. (1996). *Acta Crystallogr. A*, **52**, 331–9.
- Jansen, I., Pescar, R. and Schenk, H. (1992). *J. Appl. Crystallogr.*, **25**, 231–6.
- Knudsen, K. D., Pattison, P., Fitch, A. N. and Cernik, R. J. (1998) *Angew. Chem. Int. Ed.*, **37**, No. 17, 2340–3.
- Le Bail, A., Duroy, H. and Fourquet, J. L. (1988). *Math. Res. Bull.*, **23**, 447–52.
- Neels, A. and Stoeckli-Evans, H. (1999). *Inorg. Chem.*, **38**, 6164–70.
- Pawley, G. S. (1981). *J. Appl. Crystallogr.*, **14**, 357–61.
- Peschar, R., Schenk, H. and Capková, P. (1995). *J. Appl. Crystallogr.*, **28**, 127–40.
- Rietveld, H. M. (1969). *J. Appl. Crystallogr.*, **2**, 65–71.
- Sheldrick, G. M. (1998). In *Direct methods for solving macromolecular structures*, (ed. S. Fortier), pp. 401–11. Kluwer, Dordrecht.
- Sivia, D. S. and David, W. I. F. (1994). *Acta Crystallogr. A*, **50**, 703–14.
- Weeks, C. M. and Miller, R. (1996). In *Proceedings of the macromolecular crystallography computing school*, (ed. P. Bourne and K. Watenpaugh), p. 17. Western Washington University.

Patterson methods in powder diffraction: maximum entropy and symmetry minimum function techniques

Michael A. Estermann and William I. F. David

12.1 Introduction

Patterson (1934) derived the autocorrelation function of a crystal structure in the form of a Fourier series depending on $|F_{\mathbf{h}}|^2$ alone and this is now generally known as the *Patterson function*. By exploiting the useful properties of this function, information about the crystal structure can be obtained. There are many ways to exploit the Patterson function, but they are specific to information that is available a priori, such as the presence of heavy atoms, anomalous scatterers, non-crystallographic symmetry, or known clusters of atoms and their relative orientations. The usefulness of the Patterson function in structure solution is determined primarily by the type of prior information available and the quality of the diffraction data. For example, the peaks in the Patterson map due to vectors between heavy atoms are selectively enhanced, and this ensures easy identification and interpretation of these Patterson peaks, which are used to derive the positions of the heavy atoms. The lighter atoms in the structure are then found by calculating Fourier maps based on the observed experimental intensities and the calculated phase values derived from the heavy-atom positions.

In fact, the heavy-atom technique is rather robust, even with incomplete and resolution-limited diffraction data. This is ideal for powder data, where limits in attainable resolution (minimum d -spacing) and the number of intensities suffering from reflection-overlap can seriously degrade the quality of the diffraction data. Not surprisingly, the early examples of structures determination from powder data were based either on trial-and-error methods or the Patterson function. For example, the Patterson function was used to solve the structures of uranyl chloride (Debets 1968), a molybdate(VI) complex (Berg and Werner 1977) and high pressure modifications of lithium wolframate (Waltersson *et al.* 1977*a,b*). In subsequent years, increasing numbers of structure solutions from powder diffraction data using heavy-atom methods were reported. Patterson techniques for locating molecular fragments were also applied successfully to poor quality powder data (Wilson 1989).

However, the ways in which Patterson maps were utilized remained unchanged, probably because these techniques were so successful that there was no immediate need for new developments in the area. Ideas presented in the context of single-crystal analysis, such as the use of the positivity of the Patterson map to interpolate experimental data beyond the measured range (Karle and Hauptmann 1964) and modification of the Patterson map itself (Nixon 1978), remained unused in the realm of powder diffraction until the late 1980s. It was first recognized by David (1987) that enforcing the positivity of the Patterson function is of use in unravelling overlapping reflections. Furthermore, he showed the benefits of employing maximum-entropy methods in producing Patterson maps of excellent quality without Fourier truncation effects. The application of systematic computerized Patterson vector-search techniques to such maps was another step in extending state-of-the-art Patterson techniques to powder data (David and Estermann 1993; Estermann 1995) as is the work of Rius described in Chapter 13.

12.2 The crystal structure and its Patterson function

The crystal structure is related to the diffraction data by a Fourier transform, the structure factor equation:

$$F_{\mathbf{h}} = \sum_{j=1}^N f_j \exp(2\pi i \mathbf{h} \cdot \mathbf{r}_j), \quad (12.1)$$

where f_j is the scattering factor (or scattering length in the case of neutron diffraction) of the j th atom and \mathbf{r}_j its position in a unit cell containing N atoms. The structure factor is a complex quantity:

$$F_{\mathbf{h}} = |F_{\mathbf{h}}| \exp(i\varphi_{\mathbf{h}}) \quad (12.2)$$

and the observed diffraction intensity $I_{\mathbf{h}}$ is proportional to the square of the structure-factor amplitude $|F_{\mathbf{h}}|$. In principle, a Fourier inversion of the complex structure-factor values $F_{\mathbf{h}}$ will reveal the scattering density:

$$\rho(\mathbf{r}) = \frac{1}{V} \sum_{\mathbf{h}} F_{\mathbf{h}} \exp(-2\pi i \mathbf{h} \cdot \mathbf{r}) = \frac{1}{V} \sum_{\mathbf{h}} |F_{\mathbf{h}}| \exp(i\varphi_{\mathbf{h}}) \exp(-2\pi i \mathbf{h} \cdot \mathbf{r}). \quad (12.3)$$

Normal diffraction experiments give the amplitude values, $|F_{\mathbf{h}}|^2$, but not the phase values $\varphi_{\mathbf{h}}$. The Patterson function is given as the autocorrelation function of the crystal:

$$P(\mathbf{u}) = \int_V \rho(\mathbf{x}) \rho(\mathbf{u} + \mathbf{x}) \, d\mathbf{x}, \quad (12.4)$$

where $\rho(\mathbf{x})$ is the scattering density in the real crystallographic cell. The Patterson function has two major advantages over Direct methods. Firstly, the Patterson function can be calculated from the experimentally derived diffraction intensities alone using:

$$P(\mathbf{u}) = \frac{1}{V^2} \sum_{\mathbf{h}} |F_{\mathbf{h}}|^2 \exp(2\pi i \mathbf{h} \cdot \mathbf{u}). \quad (12.5)$$

Secondly, no additional underlying assumptions (such as the positive scattering density assumption used in Direct methods) are made.

The vector \mathbf{u}_{ij} from the origin to a peak in the Patterson map corresponds to a vector $\mathbf{x}_i - \mathbf{x}_j$ between two atoms at positions \mathbf{x}_i and \mathbf{x}_j in the real crystal cell. The interatomic vectors together are referred to as the vector set in the classic book of Buerger (1959) on Patterson methods. The weight of a peak is proportional to the product of the scattering factors $f_i f_j$ or the neutron scattering lengths $b_i b_j$ of the two atoms involved, and can be negative if the neutron scattering lengths are of opposite signs. A unit cell containing N atoms will result in N^2 vectors in the Patterson cell, of which N will be located at the origin due to the convolution of each atom with itself. Since the Patterson cell is the same size as the real cell, the number of accidentally overlapping peaks increases with N . Wrinch (1939) showed that it is possible, in principle, to deduce the structure from the complete set of $N(N-1)$ non-origin Patterson vectors.

12.2.1 *Patterson maps calculated from X-ray powder diffraction data*

The quality of a Patterson map simply reflects the quality of the diffracted intensity data included in the Patterson function. For X-ray diffraction data in particular, the limit of attainable resolution affects both the resolution of electron density peaks in the unit cell as well as peaks in the Patterson cell. The width of a Patterson peak also increases with increasing thermal motion. In the case of powder diffraction data, equipartitioning the intensity of overlapping reflections results in a 'flatter' Patterson map with broader peaks and fewer features (Estermann and Gramlich 1993). Consequently, peak positions are less reliable and may be lost altogether, although the presence of heavy atoms may help to overcome these limitations via enhancement of selected Patterson peaks.

12.2.2 *Patterson maps calculated from neutron powder diffraction data*

In contrast to X-ray scattering factors, which fall off with increasing scattering angle, the neutron scattering length is constant and depends only upon the isotope. Therefore, the important limit of atomic resolution (about 1 Å) is much easier to attain with neutron diffraction data, and the resolution in the real cell as well as the Patterson cell will be improved accordingly. An atom with a negative neutron scattering length can play a pivotal role in recognizing the

structure. If only one of all the atoms in the cell has a negative scattering length, then the negative peaks in the Patterson map can only be due to vectors between that atom and all the others. Hence, the image of the structure seen from that atom is present exclusively in the negative regions (David 1990).

12.3 Conventional methods for improving the interpretability of the Patterson map

Patterson (1935) introduced the notion of origin peak removal and sharpening of the overall function in order to improve the interpretability of Patterson maps, with the ultimate aim of obtaining a Patterson map corresponding to a point atom structure.

Broadening of Patterson peaks due to thermal motion can be corrected by using normalized structure factors, $|E_{\mathbf{h}}|$. The degree of sharpening can be adjusted by choosing a different overall isotropic thermal parameter B for the calculation of the $|E_{\mathbf{h}}|$ values from the experimental $|F_{\mathbf{h}}|$ values. Other sharpening techniques have been suggested (for an overview, see Rossmann and Arnold 1993), but the choice of a particular sharpening technique is somewhat arbitrary. For example, Sheldrick (1991) uses $|E_{\mathbf{h}}^3 F_{\mathbf{h}}|^{1/2}$ as Fourier coefficients to sharpen the Patterson. Unfortunately, sharpening can cause serious Fourier truncation effects, which appear as large ripples in the Patterson map.

Removing the origin of the Patterson map is easily achieved by using $|E_{\mathbf{h}}|^2 - 1$ as coefficients. The shortest vectors between atoms are then no longer obscured by the large origin peak. Up to a radius comprising the minimum interatomic distance (which is generally known) the Patterson is expected to be zero. In an origin-removed Patterson, the values of the Patterson map in the vicinity of the origin may be set equal to zero (Karle and Hauptmann 1964).

12.4 Maximum entropy Patterson maps

For Patterson maps calculated from powder diffraction data, David (1987, 1990) presented an elegant way of handling reflection overlap, broadening due to thermal motion, and Fourier truncation effects within the same mathematical framework. The intensity of a group of overlapping Bragg peaks is treated as a single experimental observation D_i . That same intensity can be calculated from the Patterson function using:

$$G_i = \sum_{n=1}^{N_i} J_{\mathbf{h}_n} |F_{\mathbf{h}}|^2 = \int_V P(\mathbf{u}) \left[\sum_{n=1}^N \left\{ \sum_{j=1}^{J_{\mathbf{h}_n}} \cos(2\pi \mathbf{h}_n \cdot \mathbf{r}_j) \right\} \right] d\mathbf{u}, \quad (12.6)$$

where J is the number of overlapping reflections. By dividing the Patterson map into N_{pix} pixels, eqn (12.6) can be expressed in the form:

$$G_i = \sum_{k=1}^{N_{\text{pix}}} R_{ik} P_k \quad (i = 1, \dots, N_{\text{obs}}). \quad (12.7)$$

The calculation of the pixelized Patterson map P_k is defined as an image reconstruction problem with linear constraints. Given the above equations, the application of the maximum entropy method follows in a natural way by defining a Patterson entropy:

$$S = - \sum_{k=1}^{N_{\text{pix}}} P_k \ln \left(\frac{P_k}{Q_k} \right), \quad (12.8)$$

where Q_k is the a priori estimate of the Patterson map and it is assumed to be flat. Agreement with the observed data is controlled by the χ^2 -constraint:

$$\sum_{i=1}^{N_{\text{obs}}} \frac{1}{\sigma_i^2} (D_i - G_i)^2 = N_{\text{obs}}, \quad (12.9)$$

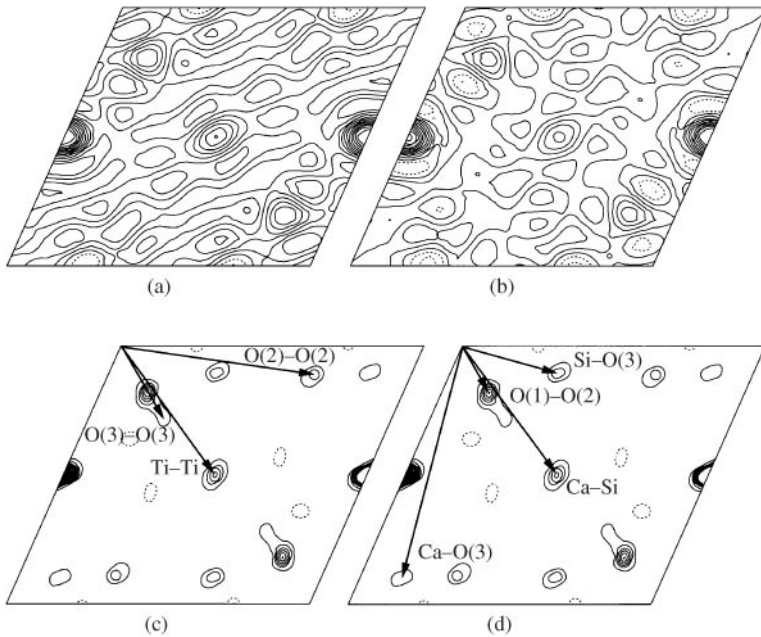


Fig. 12.1. CaTiSiO_5 : Harker section $v = 1/2$ of the (a) normal Patterson, (b) sharpened Patterson, and (c,d) maximum entropy Patterson, with (c) non-trivial Harker vectors, and (d) cross-vectors accidentally lying in the Harker section. The Patterson origin peak is also present at $(0, 1/2, 1/2)$ due to the A -centring of the lattice.

while the entropy S is maximized. The Patterson entropy equation requires an all positive Patterson map P_k . This is true for X-ray diffraction data, but as mentioned in Section 12.2.2, negative Patterson density may occur when using neutron diffraction data. David (1990) solved this problem by employing a two-channel all positive and all negative maximum entropy map. A comparison of a normal, sharpened and maximum entropy Patterson map is shown in Fig. 12.1. Only in the maximum entropy Patterson are the interatomic vectors clearly resolved.

12.5 Decomposition of overlapping Bragg peaks using the Patterson function

The successful application of Direct methods of structure solution depends crucially upon the availability of accurate integrated intensity data and so the problem of decomposing overlapping Bragg intensities must be addressed. In principle, it can be shown that equipartitioning (i.e. assigning equal $|E_{\mathbf{h}}|$) is the correct theoretical decomposition if no prior structural knowledge is available. However, the estimates of structure-invariant relationships, such as triplets and quartets, become systematically wrong and this tends to limit the success of Direct methods (Estermann and Gramlich 1993).

The use of the Patterson map for extrapolating data beyond the observed range had already been demonstrated by Karle and Hauptmann (1964) for single-crystal data. The basic idea is very simple: a Patterson function $P(\mathbf{u})$ is obtained from the available data, a non-linear modification is applied to the Patterson function, and the intensities for the reflections of interest are obtained by back-transformation of the modified map:

$$|\tilde{F}_{\mathbf{h}}|^2 = \int_V \tilde{P}(\mathbf{u}) \exp(-2\pi i \mathbf{h} \cdot \mathbf{u}) \, d\mathbf{u}. \quad (12.10)$$

Since an intensity value can be calculated for any arbitrary \mathbf{h} , the dataset can be extended beyond its observed range. The potential of this approach for extrapolating the intensity ratio of overlapping powder intensities was first recognized by David (1987) who proposed (a) the numerical back-transformation of the maximum entropy Patterson map, and (b) an analytical solution based on the squared Patterson which is discussed as follows.

David (1987) extended the squaring argument of Sayre (1952) to the Patterson map, that is, 'The square of the Patterson looks similar to the Patterson itself'. This assumption is true if the peaks in the Patterson are well-resolved. By assuming a Gaussian shape for the interatomic peaks in the Patterson, the following equation was derived to estimate the fractional

contribution of the n th of N overlapping reflections:

$$\frac{j_n |F_{\mathbf{h}_n}|^2}{\sum_{i=1}^N j_i |F_{\mathbf{h}_i}|^2} = \frac{j_n \sum_{\mathbf{k}} |F_{\mathbf{k}}|^2 |F_{\mathbf{h}_n - \mathbf{k}}|^2}{\sum_{i=1}^N j_i \left(\sum_{\mathbf{k}} |F_{\mathbf{k}}|^2 |F_{\mathbf{h}_i - \mathbf{k}}|^2 \right)}. \quad (12.11)$$

The results obtained for simulated data showed a clear advantage over simple equipartitioned $|F_{\mathbf{h}}|^2$ intensities. Motivated by the Sayre–Patterson approach, known algebraic and probabilistic relationships between structure-factor magnitudes (Bertaut 1959; Hauptmann 1972) were re-evaluated for their applicability to powder data by a number of authors (Bricogne 1991; Cascarano *et al.* 1991; Jansen *et al.* 1992) and are now part of Direct methods programs written to accommodate powder data (see also Chapters 10 and 11).

Squaring as a non-linear Patterson density modification can also be applied in an iterative and fully numerical way (Estermann and Gramlich 1993). A Patterson map is generated using an equipartitioned dataset, each point in the map is squared, the new map is back-transformed to obtain new Fourier coefficients and these coefficients are then extrapolated to give a new set of $|F_{\mathbf{h}}|^2$ for the overlapping reflections. The non-overlapping ones remain unaffected. This cycle is repeated until the statistical intensity distribution of the overlapping reflections is similar to that of the non-overlapping ones. Since the procedure is remarkably fast, it was named ‘fast iterative Patterson squaring’ (FIPS). Direct methods for structure determination are more likely to succeed with FIPS-improved data than with equipartitioned data. In the case of the molecular sieve SAPO-40, in which 65 per cent of the reflections were treated as overlapping, the *ab initio* solution with Direct methods was only possible after the redistribution of equipartitioned intensities with the FIPS method (Estermann *et al.* 1992).

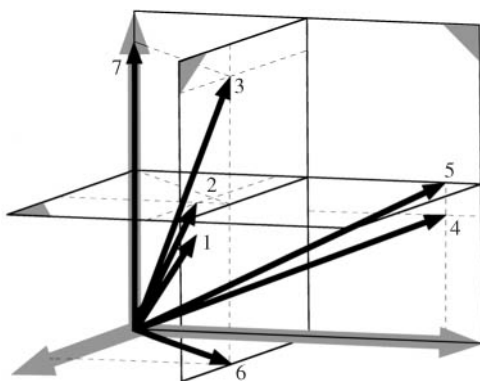
12.6 Solving a crystal structure directly from a powder Patterson map

The application of Patterson methods to structure solution is favoured by the presence of a small number of ‘outstanding’ scatterers that dominate the vector map. Typically, these are one or more heavy atoms, or atoms with a negative scattering length in a neutron diffraction experiment. Prandl (1994) suggested that multiwavelength anomalous-scattering experiments could be applied to powder data to highlight selected atoms and thus produce interpretable difference Patterson maps. Burger *et al.* (1997) obtained such maps for the known structure of iron garnet ($\text{Fe}_2\text{Ca}_3\text{Ge}_3$) by using the iron and germanium atoms as anomalous scatterers.

A systematic way to analyse a Patterson map is based on the use of Harker vectors (Harker 1936), that is, the interatomic vectors between symmetrically

Table 12.1 Unique Harker vectors u , v , w for the space group $Pbcm$ and a general position x , y , z in the crystal cell

| Number | u | v | w | Multiplicity |
|--------|------|------------|------------|--------------|
| 1 | $2x$ | $2y$ | $2z$ | 1 |
| 2 | $2x$ | $2y$ | $1/2$ | 2 |
| 3 | $2x$ | $1/2$ | $2z + 1/2$ | 2 |
| 4 | 0 | $2y + 1/2$ | $2z$ | 2 |
| 5 | 0 | $2y + 1/2$ | $1/2$ | 4 |
| 6 | $2x$ | $1/2$ | 0 | 4 |
| 7 | 0 | 0 | $2z + 1/2$ | 4 |

**Fig. 12.2.** The set of unique Harker vectors displayed for the position $x=0.8$, $y=0.2$, $z=0.7$ and the space group $Pbcm$ in the Patterson cell. The numbering 1 to 7 is the same as in Table 12.1.

equivalent atomic positions:

$$\begin{aligned}
 H(\mathbf{r}) &= \mathbf{r} - C_i \mathbf{r}, & C_i \mathbf{r} &= \mathbf{R}_i \mathbf{r} + \mathbf{t}_i \\
 &= i\text{th symmetry operator } (i = 1, \dots, n)
 \end{aligned}
 \tag{12.12}$$

where \mathbf{R}_i is the rotational component and \mathbf{t}_i the translation part of the i th symmetry operator of the space group, and \mathbf{r} is an atomic position in the crystal cell.

An example of a set of unique Harker vectors and their multiplicities for the space group $Pbcm$ and a general position x , y , z is given in Table 12.1, while Fig. 12.2 shows the set of unique Harker vectors inside the Patterson cell. Identifying the Harker vector $(2x, 2y, 2z)$ may be essential for manual analysis of the map, since it immediately reveals the position x , y , z . Unfortunately, the Harker vector $(2x, 2y, 2z)$ always has the multiplicity $m=1$, and therefore may be lost as it does not appear at the top of the list of the strongest Patterson peaks.

Once the Harker vectors have been identified in the Patterson map, they can be used directly to determine the atomic position \mathbf{r} . In fact, it is quite common to locate the position of one or more heavy atoms by manual inspection of the Patterson. However, manual analysis of the Harker vectors becomes increasingly difficult for Pattersons of lesser quality and structures of higher complexity. Interpreting the 'crossword puzzle' of interatomic vectors becomes tedious and may not discriminate between atomic positions. It is therefore desirable to have some objective measure that will quantify the likelihood that a heavy atom is sitting on a particular position.

12.7 Automatic location of atomic positions with the symmetry minimum function

Just such a measure was introduced by Kraut (1961) and Simpson *et al.* (1965), that is, the symmetry minimum function (SMF). It is based on the superposition of Patterson maps and is a natural extension of the systematic Patterson vector-search techniques developed in the early 1950s. A review of the early literature can be found in Buerger's (1959) book. Some of these techniques were implemented on computers by Richardson and Jacobson (1987), Pevclík (1990), Sheldrick (1991) and Chang and Lewis (1994). Only the SMF will be discussed in the context of structure solution from powder data as it systematically includes the space group symmetry and utilizes the entire Patterson map rather than just the identifiable vectors. In contrast to other superposition methods, the SMF can be justified on rigid Bayesian and statistical grounds. Indeed, Bricogne (1992) derived the SMF by a statistical analysis based on Wilson and Rice probability distributions in the form of a maximum likelihood function. However, here we follow the derivation of Kraut (1961) and Simpson *et al.* (1965), as it directly relates to the Harker theory and is based on geometrical arguments.

As mentioned above, it is advantageous to utilize the information in the entire Patterson map rather than restricting oneself to just the identifiable peaks. Thus, all positions \mathbf{r} in the crystal cell are tested as trial atomic positions. The term 'crystal cell' is used here to describe the unit cell of the crystal in order to distinguish it from the unit cell of the Patterson map, the 'Patterson cell'. The SMF is defined as:

$$\text{SMF}(\mathbf{r}) = \min_{i=1}^p \frac{1}{m_i} P(\mathbf{r} - \mathbf{C}_i\mathbf{r}) \quad (12.13)$$

and quantifies a position \mathbf{r} by automatically inspecting the Harker vectors. A trial atomic position \mathbf{r} in the crystal cell is ranked by comparing the heights of all unique Harker vectors $H(\mathbf{r}) = \mathbf{r} - \mathbf{C}_i\mathbf{r}$ ($i = 1, \dots, p$) in the Patterson cell (the origin vector is not included). The quantity m_i is the multiplicity of the Harker

vectors. The crystal cell is divided into N_{pix} grid points, and for each of these grid points with locus \mathbf{r} , the value of the SMF is calculated. The SMF map has the size of the crystal cell. The peaks in the SMF map are the possible atomic positions derived from the self-vectors due to crystal symmetry.

The SMF ensures a continuously low value for any position \mathbf{r} unless all Harker vectors $H(\mathbf{r})$ are above background. The minimum function, and the product and sum functions have all been described elsewhere (Buerger 1959; García-Granada *et al.* 1996).

There is however, an ambiguity due to the fact that the crystal structure, its enantiomorph structure and the structure shifted by a permissible origin shift have exactly the same vector set (homometric structures), and hence the same Patterson map. All the images of these structures are correct solutions of the Patterson map and are present in the SMF map. This is because eqn (12.13) evaluates each single-site independently. For a general discussion of the symmetry of the SMF see, for example Hirshfeld (1968), Zimmermann (1988), Pevclík (1990) and Koch and Fischer (1992).

Since all the origin-shifted images of the crystal structure are present in the SMF map, the peaks in the SMF map are not necessarily related by the same origin, and hence these positions cannot be used directly for a structure refinement. In order to retrieve a single image of the crystal structure, it is necessary to search the Patterson map for vectors between atoms that are not symmetrically equivalent. These vectors are called cross-vectors and provide information that supplements that provided by the Harker vectors.

In practice, one peak from the SMF map with position \mathbf{r}^* is selected as the pivotal peak. Each position \mathbf{r} in the crystal cell is tested in respect to the fixed position \mathbf{r}^* and its space group equivalent positions $\mathbf{C}_i\mathbf{r}^*$ ($i = 2, \dots, n$) by analysing the height of all the cross-vectors $\mathbf{r} - \mathbf{C}_i\mathbf{r}^*$ ($i = 1, \dots, n$) with the minimum function. The function:

$$\text{IMF}(\mathbf{r}) = \min_{i=1}^n P(\mathbf{r} - \mathbf{C}_i\mathbf{r}^*) \quad (12.14)$$

is called the image-seeking minimum function because it locates a single image out of all the ambiguous origin-shifted images. This is true if the structure is centrosymmetric. Otherwise, one of the two enantiomorphic solutions must also be eliminated. This can be done by extending the equation to:

$$\text{IMF}(\mathbf{r}) = \min_{i=1}^n (P(\mathbf{r} - \mathbf{C}_i\mathbf{r}_1^*), P(\mathbf{r} - \mathbf{C}_i\mathbf{r}_2^*)), \quad (12.15)$$

where a second suitable position \mathbf{r}_2^* has been selected (Buerger 1959). In a similar manner, information about fragments or not accessible volumes in the crystal cell, such as cavities and channels in molecular sieves, can be easily introduced as an additional term in the above equation.

12.8 Examples of structure solution using automated Patterson superposition techniques

Many of the *ab initio* structure solutions reported from powder data are actually based on the heavy-atom technique. In fact, some of these may even have been solved by Patterson superposition methods. Sheldrick (1991) adapted the vector superposition approach of Richardson and Jacobson (1987) in the popular computer program SHELXS-90. Although primarily aimed at high-resolution single-crystal data, it is often reported in the literature as being successful in solving structures from powder data. Here, we present two detailed examples which illustrate the application of maximum entropy and SMF techniques to powder diffraction data.

The symmetry minimum function techniques described here are implemented as a software module for the *Xtal System of Crystallographic Programs, Version 3.7* (Estermann 2000; Hall *et al.* 2000). The *Xtal System* is freely available under the terms of the GNU General Public Licence and can be accessed at <http://xtal.crystal.uwa.edu.au>.

12.8.1 Bismuth nitride fluoride Bi_3NF_6

Bismuth nitride fluoride Bi_3NF_6 belongs to the family of fluorite-type compounds with an anion excess and its crystal structure was previously unknown. As suitable single crystals could not be obtained, X-ray diffraction data were collected from a polycrystalline sample on a laboratory powder diffractometer using $\text{CuK}\alpha_1$ radiation. The diffraction pattern was indexed with an orthorhombic cell of dimensions $a = 5.817 \text{ \AA}$, $b = 5.702 \text{ \AA}$, $c = 18.511 \text{ \AA}$. Integrated intensities for reflections between 8° and 90° in 2θ (minimum d -spacing 1.1 \AA) were obtained with the program FullProf (Rodríguez-Carvajal 1992). Of the 260 reflections extracted, 117 lay within 15 per cent of the full width at half maximum of another reflection, and were thus considered to be severely overlapped. An approximation to a single-crystal-like dataset was obtained by equipartitioning the severely overlapping reflections. Systematic absences suggested the space groups $Pbc2_1$ or $Pbcm$, and as the intensities of the non-overlapping reflections had a statistical distribution indicative of a centrosymmetric structure, space group $Pbcm$ was chosen.

An examination of the X-ray scattering powers of the elements in the crystal structure (Bi = 83, F = 9, N = 7 electrons) indicates that it should be possible to locate the Bi atoms from the Patterson map. Accordingly, after normalization of the intensities with a Wilson plot, a sharpened Patterson map was calculated using $|E_{\mathbf{h}}F_{\mathbf{h}}|$ as coefficients. The entire Patterson map was sampled on a $48 \times 48 \times 152$ grid, with 0.12 \AA per grid point. The $|E_{000}F_{000}|$ coefficient was included in the calculation.

The SMF was calculated on the same grid as the Patterson map. The Harker vectors used were those listed in Table 12.1. The $x = 0.75$ layer of the SMF map

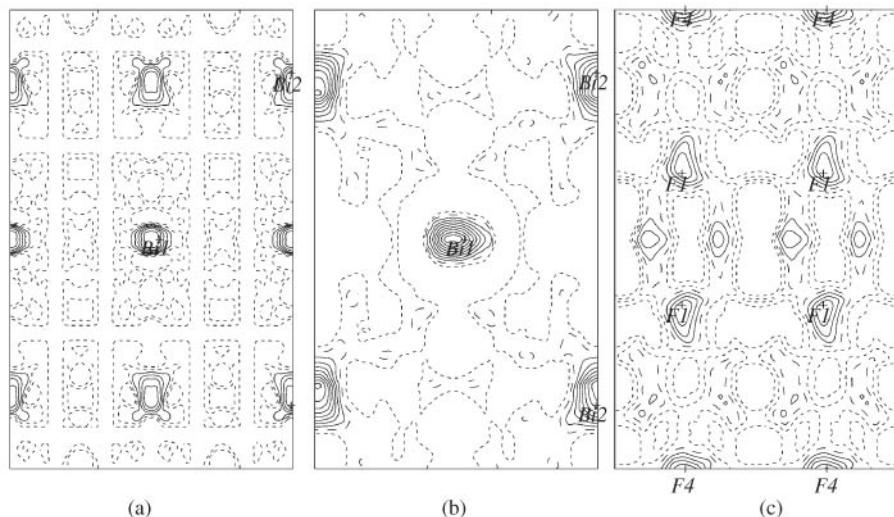


Fig. 12.3. Bi_3NF_6 : (a) section $x=0.75$ of the symmetry minimum function, (b) section $x=0.75$ of the image seeking minimum function, and (c) section $x=0.0$ of the image seeking minimum function. The refined atomic positions of Bi(1), Bi(2), F(1) and F(4) are included for comparison.

Table 12.2 Atomic coordinates of Bi_3NF_6 (Hofmann *et al.* 1995)

| Atom | x | y | z |
|-------|-------------|------------|-----------|
| Bi(1) | 0.2207(5) | -0.0296(7) | 0.25 |
| Bi(2) | 0.2923(3) | 0.5056(6) | 0.0688(1) |
| F(1) | -0.0180(8) | 0.7377(9) | 0.6778(1) |
| F(2) | 0.3716(6) | 0.5395(8) | 0.8722(2) |
| F(3) | 0.6046(9) | 0.1257(9) | 0.25 |
| F(4) | -0.0118(11) | 0.25 | 0.0 |
| N | 0.4983(9) | 0.25 | 0.0 |

is shown in Fig. 12.3(a). For comparison with the final structure solution, the refined positions of the Bi atoms are included (Table 12.2). The maxima in the SMF are the possible atomic positions, including the ones related by a permissible origin shift $(1/2, 0, 0)$, $(0, 1/2, 0)$ and $(0, 0, 1/2)$.

One of the strongest peaks in the SMF (afterwards assigned to Bi(1)) was selected as pivotal peak \mathbf{r}^* for the calculation of the IMF which was sampled again on the same grid as the Patterson map. The values of the Patterson function were retrieved by eight-point interpolation from a look-up table. This is necessary because the calculation of cross-vectors also inspects the Patterson between the pre-calculated grid points. As expected, the atoms Bi(1) and Bi(2)

then appeared at the correct positions and the ‘ghost’ positions disappeared (Fig. 12.3(b)). Rather unexpectedly, the $x = 0$ layer revealed the positions of all the F atoms (Fig. 12.3(c)). By accepting only one set of positions with consistent bond length and angles (distance B–F > 2.0 Å), the F and N atoms were selected from the list of IMF peaks.

As the F and N atoms could be neither distinguished nor refined satisfactorily with the X-ray data, the final structure refinement was carried out using time-of-flight neutron powder diffractometer data collected on the POLARIS instrument at the ISIS Facility of the Rutherford Appleton Laboratory. Hofmann *et al.* (1995) give full details of the neutron refinement.

12.8.2 Synthetic CaTiSiO_5

The known single-crystal structure of synthetic CaTiSiO_5 (Taylor and Brown 1976) was chosen as a good example of a structure that could be solved directly from neutron powder data. Examination of the neutron scattering lengths of the elements involved ($b(10^{-12} \text{ cm})$ Ti = -0.34 , Ca = 0.49 , Si = 0.41 , O = 0.58) clearly marked Ti as an ‘outstanding’ scatterer because of its negative sign. Accordingly, data were collected from a polycrystalline sample of synthetic CaTiSiO_5 on the time-of-flight neutron powder diffractometer HRPD at the ISIS Facility of the Rutherford Appleton Laboratory. The pattern was indexed with a monoclinic cell of dimensions $a = 7.068$ Å, $b = 8.714$ Å, $c = 6.562$ Å and $\beta = 113.82^\circ$. Using the Pawley-based intensity extraction program SR15LS (David *et al.* 1992) and assuming space group $A2/a$, 296 integrated intensities, (minimum d -spacing 0.9 Å) of which 62 were considered to be severely overlapping, were extracted. For a list of reference atomic coordinates see Table 12.3.

A normal Patterson map (Fig. 12.1(a)), a sharpened Patterson map (Fig. 12.1(b)) with Fourier coefficients $|E_{\mathbf{h}}F_{\mathbf{h}}|$ and a two-channel maximum entropy Patterson map (Fig. 12.1(c) and (d)) (David 1990) were calculated on a $32 \times 40 \times 28$ grid, with 0.22 Å per grid point. Their Harker sections, $v = 1/2$, are shown as contour plots. The difference in quality is remarkable, with the interatomic vectors clearly identified in the maximum entropy map. For clarity, the Harker vectors are drawn separately from the cross-vectors. The cross-vectors

Table 12.3 Atomic coordinates of CaTiSiO_5 (Taylor and Brown 1976)

| Atom | x | y | z |
|------|-----------|-----------|-----------|
| Ca | 1/4 | 0.4187(2) | 1/4 |
| Ti | 1/2 | 1/4 | 3/4 |
| Si | 3/4 | 0.4331(2) | 1/4 |
| O(1) | 3/4 | 0.3197(6) | 3/4 |
| O(2) | 0.9104(5) | 0.3160(4) | 0.4342(6) |
| O(3) | 0.3820(5) | 0.4600(4) | 0.6467(6) |

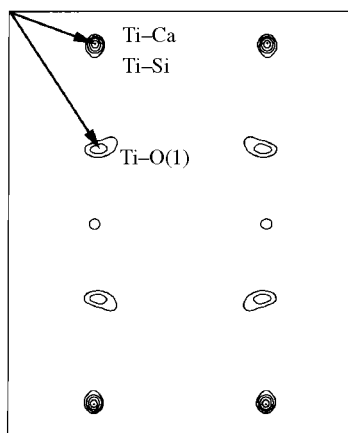


Fig. 12.4. CaTiSiO_5 : section $w=0$ of the negative regions in the maximum entropy Patterson map. The vectors between Ti (negative neutron scattering length) and Ca, Si, O(1) (positive neutron scattering lengths) are shown.

Table 12.4 Unique Harker vectors u , v , w for the space group $A2/a$ and a general position x , y , z in the crystal cell

| u | v | w | Multiplicity |
|------------|-------|-------|--------------|
| $2x$ | $2y$ | $2z$ | 1 |
| $2x + 1/2$ | $1/2$ | $2z$ | 2 |
| $1/2$ | $2y$ | $1/2$ | 2 |

are lying in the Harker section accidentally. The negative region of the two-channel maximum entropy Patterson map contains the information about the vectors between Ti (negative scattering length) and the other atoms (positive scattering length). The cross-vectors between Ti–Ca, Ti–Si, and Ti–O(1) can be found in the negative regions of the Patterson section $w=0$ (Fig. 12.4).

The SMF was calculated with the unique Harker vectors in Table 12.4. The layer $z=1/4$ is shown as a contour plot (Fig. 12.5). For comparison, the atomic positions are included. The SMF map is extremely sharp and the positions of Ca, Si, Ti and O(1) appeared in the top 10 of the peak list. All the correct atomic positions including the ones related by a permissible origin shift $(1/2, 0, 0)$, $(0, 1/2, 0)$ and $(0, 0, 1/2)$, appeared within the top 65 of the SMF peak list.

The top ten peaks from the SMF were then used as trial positions for the image-seeking minimum function (IMF). The top 20 peaks in the IMF were considered as candidates for atomic positions. Expected distances for Si–O bonds (1.6 \AA) and Ti–O bond (1.9 \AA) were used to select a set of consistent positions. The assignment of Si, Ti and O atoms was then made on the basis of tetrahedrally and octahedrally-coordinated positions.

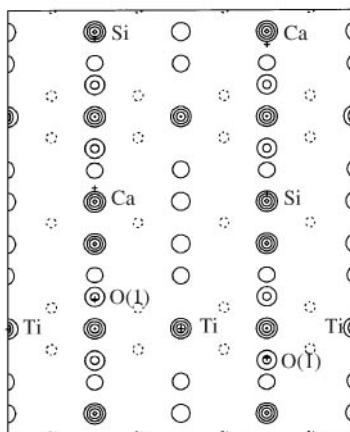


Fig. 12.5. CaTiSiO_5 : section $z=1/4$ of the symmetry minimum function. The atomic positions of Ti, Si, Ca and O(1) are shown for reference. All atomic positions including the ones related by a permissible origin shift $(1/2,0,0)$, $(0,1/2,0)$ and $(0,0,1/2)$ appear in the map.

Table 12.5 Additional atomic positions found by the image seeking minimum function

| Pivotal position | Type of cross-vectors | Additional atomic positions found (rank in peak list) |
|------------------|-----------------------|---|
| Ca | Positive | Si [8], O(3) [10], O(1) [14] |
| Si | Positive | O(3) [6], Ca [8], O(1) [9], O(2) [12] |
| O(1) | Positive | O(2) [2], Ca [3], O(3) [4], Si [7] |
| Ti | Positive | Ti [6] |
| Ca | Negative | Ti [6] |
| Si | Negative | Ti [6] |
| O(1) | Negative | Ti [1] |
| Ti | Negative | O(1) [2], Ca [3], Si [4], O(3) [5], O(2) [8] |

The number of new correct atomic positions which are generated in the IMF map depends on the pivotal position used (Table 12.5). As expected, only the search with negative cross-vectors found the entire structure, and also revealed the pivotal position as the Ti atom.

Acknowledgements

Part of this work was done by MAE during a stay as a visiting scientist at the ISIS facility of the Rutherford Appleton Laboratory.

References

- Berg, J.-E. and Werner, P.-E. (1977). *Z. Kristallogr.*, **145**, 310–20.
- Bertaut, E. F. (1959). *Acta Crystallogr.*, **12**, 541–9.
- Bricogne, G. (1991). *Acta Crystallogr. A*, **47**, 803–29.
- Bricogne, G. (1992). *Molecular Replacement. Proceedings of the CCP4 Study Weekend*, (ed. E. J. Dodson, S. Gover and W. Wolf), pp. 62–75. Daresbury Laboratory Publications.
- Buerger, M. J. (1959). *Vector Space*, pp. 252–68, Wiley, New York.
- Burger, K., Prandl, W. and Doyle, S. (1997). *Z. Kristallogr.*, **212**, 493–505.
- Cascarano, G., Giacovazzo, C., Giuagliardi, A. and Steadman, A. (1991). *Acta Crystallogr. A*, **47**, 480–4.
- Chang, G. and Lewis, M. (1994). *Acta Crystallogr. D*, **50**, 667–74.
- David, W. I. F. (1987). *J. Appl. Crystallogr.*, **20**, 316–19.
- David, W. I. F. (1990). *Nature (London)*, **346**, 731–4.
- David, W. I. F. and Estermann, M. A. (1993). *Acta Crystallogr. A*, **49** (Suppl.), C-37.
- David, W. I. F., Ibberson, R. M. and Matthewman, J. C. (1992). Rutherford Appleton Laboratory report, RAL-92-032.
- Debets, P. C. (1968). *Acta Crystallogr. B*, **24**, 400–2.
- Estermann, M. A., McCusker, L. B. and Baerlocher, Ch. (1992). *J. Appl. Crystallogr.*, **25**, 539–43.
- Estermann, M. A. (1995). *Nucl. Instr. and Meth. in Phys. Res. A*, **354**, 126–33.
- Estermann, M. A. and Gramlich, V. (1993). *J. Appl. Crystallogr.*, **26**, 396–404.
- Estermann, M. A. (2000). *Program SHAPE, Xtal3.7 System* (ed. S. R. Hall, D. J. du Boulay and R. Olthof-Hazekamp). University of Western Australia.
- García-Granada, S., Borge, J. and Gutiérrez-Rodríguez, A. (1996). *Anales de Química Int. Ed.*, **92**, 294–8.
- Hall, S. R., du Boulay, D. J. and Olthof-Hazekamp, R. (ed.) (2000). *Xtal3.7 System*. University of Western Australia.
- Harker, D. (1936). *J. Chem. Phys.*, **4**, 381–90.
- Hauptmann, H. (1972). *Crystal Structure Determination*. Plenum Press, New York.
- Hirshfeld, F. L. (1968). *Acta Crystallogr. A*, **24**, 301–11.
- Hofmann, M., Schweda, E., Strähle, J., Laval, J. P., Frit, B. and Estermann, M. A. (1995). *J. Solid State Chem.*, **114**, 73–8.
- Jansen, J., Peschar, R. and Schenk, H. (1992). *J. Appl. Crystallogr.*, **25**, 237–43.
- Karle, J. and Hauptmann, H. (1964). *Acta Crystallogr.*, **17**, 392–6.
- Koch, E. and Fischer, W. (1992). In *International Tables for Crystallography, Volume A, Space-Group Symmetry*, 3rd revised edn (ed. T. Hahn), pp. 856–69. Kluwer Academic Publishers, Dordrecht.
- Kraut, J. (1961). *Acta Crystallogr.*, **14**, 1146–52.
- Nixon, P. E. (1978). *Acta Crystallogr. A*, **34**, 450–3.
- Patterson, A. L. (1934). *Phys. Rev.*, **46**, 372–6.
- Patterson, A. L. (1935). *Z. Kristallogr.*, **90**, 517–42.
- Pevclík, F. (1990). *J. Appl. Crystallogr.*, **23**, 225–7.
- Prandl, W. (1994). *Acta Crystallogr. A*, **50**, 52–5.
- Richardson, J. W. and Jacobson, R. A. (1987). In *Patterson and the Pattersons* (ed. J. P. Glusker, B. K. Patterson and M. Rossi), pp. 310–17. Oxford University Press.

- Rodriguez-Carvajal, R. (1992). *FullProf*, version 2.2, ILL Grenoble.
- Rossmann, M. G. and Arnold, E. (1993). In *International Tables for Crystallography, Volume B, Reciprocal Space* (ed. U. Shmueli), pp. 230–63. Kluwer Academic Publishers, Dordrecht.
- Sayre, D. (1952). *Acta Crystallogr.*, **5**, 60–5.
- Sheldrick, G. M. (1991). In *Crystallographic Computing 5* (ed. D. Moras, A. D. Podjarny and J. C. Thierry), pp. 145–57. Oxford University Press.
- Simpson, P. G., Dobrott, R. D. and Lipscomb, W. (1965). *Acta Crystallogr.*, **18**, 169–79
- Taylor, M. and Brown, G. E. (1976). *Amer. Mineralogist*, **61**, 435–47.
- Waltersson, K., Werner, P.-E. and Wilhelmi, K.-A. (1977a). *Cryst. Struct. Comm.*, **6**, 225–30.
- Waltersson, K., Werner, P.-E. and Wilhelmi, K.-A. (1977b). *Cryst. Struct. Comm.*, **6**, 231–5.
- Wilson, C. C. (1989). *Acta Crystallogr. A*, **45**, 833–9.
- Wrinch, D. M. (1939). *Philos. Mag.*, **27**, 98–122.
- Zimmermann, H. (1988). *Z. Kristallogr.*, **183**, 113–22.

Solution of Patterson-type syntheses with the Direct methods sum function

Jordi Rius

13.1 Introduction

In the last decade, developments in Direct methods have been directed mainly towards extending their applicability to macromolecules and to the solution of crystal structures from powder diffraction data. In the case of macromolecular structure solution, two important limitations exist. Firstly, the need for data at atomic resolution often cannot be satisfied. Secondly, a large number of phases need to be refined, but this problem can be partially solved by assisting the phase refinement with direct-space filtering procedures. In the powder diffraction case, the principal limitation is due to reflection overlap, which in most cases produces incomplete sets of intensity data. Since the peak overlap tends to increase at higher 2θ , reliable intensity information can normally only be obtained at low or moderate resolution. This reflection overlap demands powerful deconvolution algorithms in order to extract as many accurate integrated intensities as possible and, in addition, requires effective and robust phase refinement strategies to work in extreme conditions.

Most modern Direct methods procedures for the solution of small crystal structures are based on the maximization (or minimization) of a certain target function expressed in terms of the phases of the large structure factors. Usually, random values are introduced as initial estimates for the phases. The simplest phase refinement function is the maximization of:

$$Z(\Phi_S) = \sum_{\mathbf{k}} \sum_{\mathbf{k}'} E(\mathbf{k})E(\mathbf{k}')E(\mathbf{k} - \mathbf{k}') \cos[\varphi(-\mathbf{k}) + \varphi(\mathbf{k}') + \varphi(\mathbf{k} - \mathbf{k}')], \quad (13.1)$$

where Φ_S generically denotes the phases φ of the subset of reflections \mathbf{k} with strong structure-factor magnitudes. As shown by Debaerdemaeker *et al.* (1985), maximization of the Z -function can be carried out iteratively applying the conventional tangent formula (Karle and Hauptman 1956):

$$\varphi(\mathbf{k}) = \text{phase of } \left\{ \sum_{\mathbf{k}'} E(\mathbf{k}')E(\mathbf{k} - \mathbf{k}') \exp[i(\varphi(\mathbf{k}') + \varphi(\mathbf{k} - \mathbf{k}'))] \right\}. \quad (13.2)$$

Refinement of phases with the tangent formula can lead to maxima of Z that are far from the desired local maximum, especially for crystal structures with symmorphic space groups (i.e. space groups without glide planes or screw axes). For such structures, the unconstrained global maximum reached is normally wrong, and the corresponding E -map only shows one or two very large peaks (i.e. the so-called 'uranium-atom' solution). Different solutions for this type of behaviour have been proposed. In practice, the most relevant ones have been the use of negative quartets (Schenk 1973, 1974; Hauptman 1974; Giacovazzo 1976; Sheldrick 1990) and the Sayre-equation tangent formula (Debaerdemaeker *et al.* 1985). More recently, Rius (1993) has introduced the Direct methods modulus sum function (i.e. a sum function based on the Patterson-type modulus synthesis, Ramachandran and Raman 1959). From this function, a tangent formula ($S' - TF$), which seems to be especially well-suited to coping with powder data, can be derived. Accordingly, a more formal derivation of this sum function is provided in this chapter.

13.2 Definition of the modulus sum function

Traditionally, the sum function has been used in connection with Patterson search methods to identify the correct solutions. For example, in the case of the shifted Patterson sum, it is used to measure the coincidence of a given set of interatomic vectors (the calculated Patterson function) with the observed Patterson function for different shifts. As indicated in Fig. 13.1, the procedure consists of multiplying the height at the end of each vector by the corresponding value of the observed Patterson function, and adding these products.

In general, the correct shift is indicated by a large value of the sum function. When the sum function is applied to Direct methods, the coordinates of the shift vector are replaced by the phases of the structure factors. Accordingly, the Direct methods modulus sum function is defined by the integral:

$$S'(\Phi_S) = \int_V P'(\mathbf{u})P(\mathbf{u}, \Phi_S) d\mathbf{u}, \quad (13.3)$$

where the integral extends over the volume V of the unit cell and should be a maximum for the true phases. $P'(\mathbf{u})$ denotes the observed modulus function without the origin peak and $P(\mathbf{u}, \Phi_S)$ the calculated modulus function expressed in terms of the collective Φ_S of phases of the strong reflections. One of the distinctive features of eqn (13.3) is the suppression of the origin peak of the observed modulus function; this peak is superfluous because the atomicity condition is introduced later as a restriction in $P(\mathbf{u}, \Phi_S)$. Although eqn (13.3) has been defined with the modulus synthesis, other Patterson-type functions giving related sum functions are imaginable (Rius *et al.* 1996a; Rius 1997).

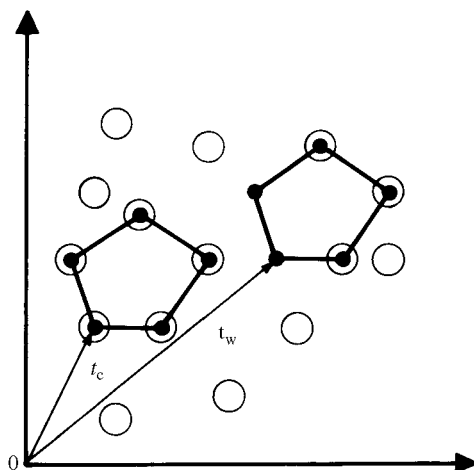


Fig. 13.1. Two dimensional example of the application of the sum function to the location of a vector set of five peaks (filled circles) in the observed Patterson function (empty circles). For simplicity, the heights of all peaks are assumed to be unity. For the wrong shift t_w , the value of the sum function is three, while for the correct one t_c , its value is five. While the correct shift always gives large sum function values, the reciprocal is not always true, especially for difficult cases.

The increased effectiveness of the S' function when compared to the Z function can be easily understood from purely physical considerations (Fig. 13.2). Effectively, the Z -function (eqn 13.1) is equivalent to the integral:

$$S(\Phi_S) = \int_V P(\mathbf{u})P(\mathbf{u}, \Phi_S) d\mathbf{u}, \quad (13.4)$$

where $P(\mathbf{u})$ possesses a large origin peak. Now, imagine a wrong Φ_S solution producing a very strong origin peak in $P(\mathbf{u}, \Phi_S)$. In this case, the sole product of both origin peaks will be a large quantity. This is precisely the 'uranium-atom' solution, as an E -map with only a dominant peak implies a $P(\mathbf{u}, \Phi_S)$ function with only a strong origin peak. In other words, the non-origin Patterson peaks play no significant role. Obviously, this difficulty disappears with the S' function. Physically, maximization of S' is equivalent to maximizing the coincidence between the non-origin peaks of $P(\mathbf{u})$ and $P(\mathbf{u}, \Phi_S)$. Since the uranium atom solution is no longer possible, the probability that the refined solutions with large S' values are correct increases dramatically for small structures.

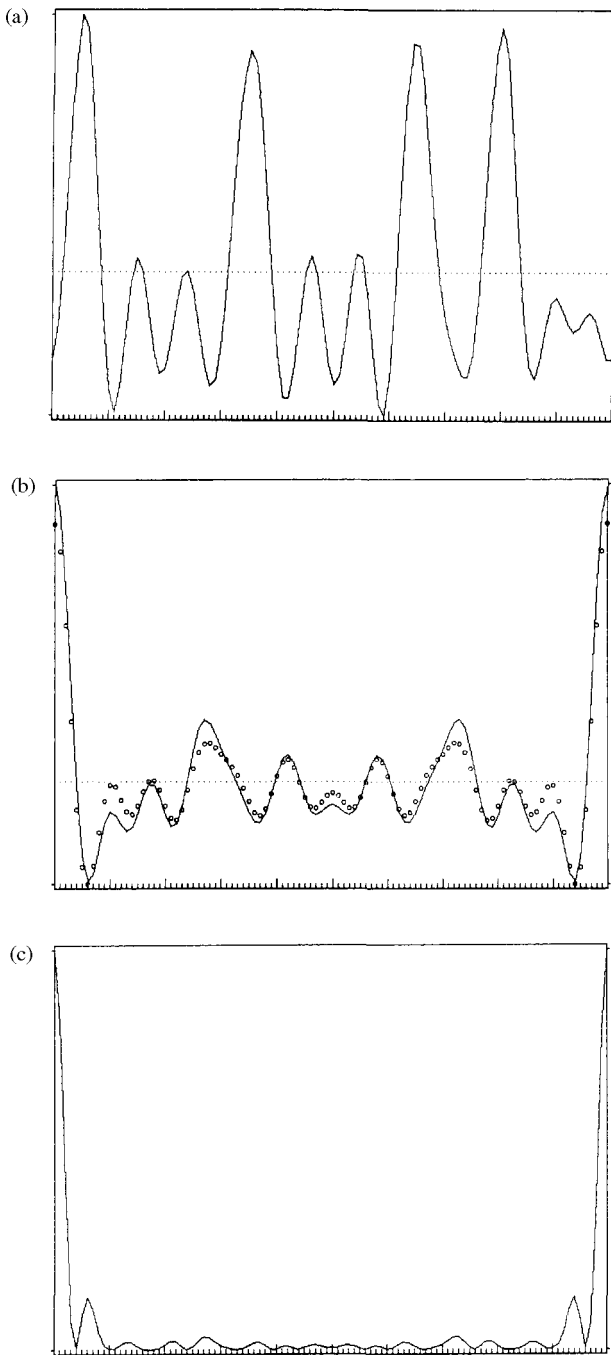


Fig. 13.2. See caption opposite.

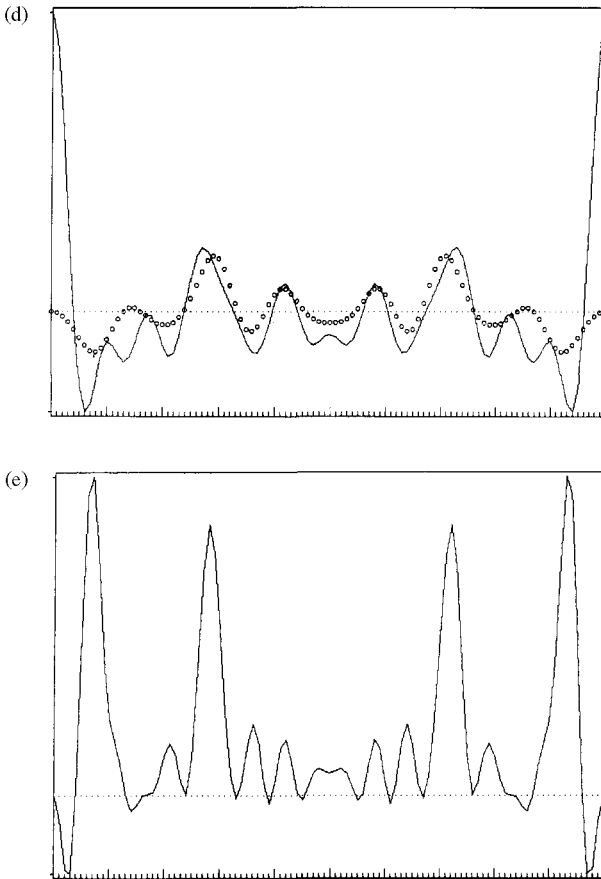


Fig. 13.2. (a): One dimensional test structure with four atoms in the unit period; (b) and (d): Observed modulus function (dots) and calculated modulus function with true phases (line) for the test structure (a). In (d) the origin peak of the observed modulus synthesis has been removed; (c) and (e): The products of the observed and calculated modulus functions given in (b) and (d), respectively. While (c) is dominated by the product of the origin peaks of the observed and calculated modulus functions, (e) is only sensitive to the non-origin peaks.

13.3 The modulus sum function in reciprocal space

The modulus function with the origin peak subtracted is evaluated by means of the Fourier synthesis:

$$P'(\mathbf{u}) = \frac{1}{V} \sum_{\mathbf{h}} [G(\mathbf{h}) - \langle G \rangle] \exp(-2\pi i \mathbf{h} \cdot \mathbf{u}), \quad (13.5)$$

where $G(\mathbf{h})$ is the structure factor of the squared-point atom structure and $\langle G \rangle$ is the corresponding value averaged over all reflections \mathbf{h} . For a structure satisfying the positivity criterion, the relationship between $G(\mathbf{h})$ and the structure factor $\xi(\mathbf{h})$ of the point atom structure is given by the approximation (Cochran and Woolfson 1955; Karle and Karle 1966):

$$G(\mathbf{h}) \cong \frac{\sigma_3}{\sigma_2^{3/2}} \xi(\mathbf{h}), \quad (13.6)$$

where, as usual, σ_n is equal to $\sum_j Z_j^n$ with Z_j being the atomic number of the j th atom. For an equal atom structure belonging to space group $P1$ with N atoms in the unit cell, the quasi-normalized structure factors ξ can be replaced by the normalized ones, E , and eqn (13.6) reduces to the equality:

$$G(\mathbf{h}) = \frac{1}{\sqrt{N}} E(\mathbf{h}), \quad (13.7)$$

so that:

$$\langle G \rangle = \frac{1}{\sqrt{N}} \langle E \rangle. \quad (13.8)$$

In view of eqn (13.7) and eqn (13.8), eqn (13.5) becomes:

$$P'(\mathbf{u}) = \frac{1}{V\sqrt{N}} \sum_{\mathbf{h}} [E(\mathbf{h}) - \langle E \rangle] \exp(-2\pi i \mathbf{h} \cdot \mathbf{u}). \quad (13.9)$$

For practical purposes, let the modulus sum function S' be expressed in the form of a sum instead of an integral. This can be done by transforming it to reciprocal space (i.e. by applying Parseval's theorem to eqn (13.3)), so that:

$$S'(\Phi_S) = \frac{1}{V\sqrt{N}} \sum_{\mathbf{h}} [E(\mathbf{h}) - \langle E \rangle] G(\mathbf{h}, \Phi_S). \quad (13.10)$$

Now let the reflections be divided into two subsets: \mathbf{S} being the subset of reflections \mathbf{k} with large E values, and \mathbf{W} the subset containing the rest of reflections, \mathbf{I} . Introducing this partitioning in eqn (13.10) yields:

$$S'(\Phi_S) = \frac{1}{V\sqrt{N}} \left\{ \sum_{\mathbf{k}} [E(\mathbf{k}) - \langle E \rangle] G(\mathbf{k}, \Phi_S) + \sum_{\mathbf{l}} [E(\mathbf{l}) - \langle E \rangle] G(\mathbf{l}, \Phi_S) \right\}. \quad (13.11)$$

$G(\mathbf{h}, \Phi_S)$ is the Fourier transform of ρ^2 , and must necessarily be an approximation to $G(\mathbf{h})$ because only the phases of the reflections in \mathbf{S} participate in its

calculation. Using the convolution theorem (which states that the Fourier transform of the product of two functions is the convolution of the Fourier transforms of the individual functions) the structure factor:

$$\mathbf{G}(\mathbf{h}, \Phi_S) = G(\mathbf{h}, \Phi_S) \exp(i\phi(\mathbf{h})) \tag{13.12}$$

can be expressed as:

$$\mathbf{G}(\mathbf{h}, \Phi_S) = \frac{1}{V} \sum_{\mathbf{k}'} E(\mathbf{k}') E(\mathbf{h} - \mathbf{k}') \exp[i(\varphi(\mathbf{k}') + \varphi(\mathbf{h} - \mathbf{k}'))], \tag{13.13}$$

where \mathbf{k}' and $\mathbf{h} - \mathbf{k}'$ belong to \mathbf{S} . In view of eqn (13.12), the best approximation to $\mathbf{G}(\mathbf{h}, \Phi_S)$ is:

1. for the reflections in \mathbf{S} :

$$G(\mathbf{k}, \Phi_S) = \frac{1}{V} \sum_{\mathbf{k}'} E(\mathbf{k}') E(\mathbf{k} - \mathbf{k}') \exp[i(\phi(-\mathbf{k}) + \varphi(\mathbf{k}') + \varphi(\mathbf{k} - \mathbf{k}'))] \tag{13.14}$$

$$= \frac{1}{V} \sum_{\mathbf{k}'} E(\mathbf{k}') E(\mathbf{k} - \mathbf{k}') \exp[i(\varphi(-\mathbf{k}) + \varphi(\mathbf{k}') + \varphi(\mathbf{k} - \mathbf{k}'))], \tag{13.15}$$

where, due to the atomicity and positivity of ρ , the equality $\phi(\mathbf{k}) = \varphi(\mathbf{k})$ has been introduced in eqn (13.15);

2. for the reflections in \mathbf{W} :

$$G(\mathbf{l}, \Phi_S) = \frac{1}{V} \sum_{\mathbf{k}} E(-\mathbf{k}) E(\mathbf{l} + \mathbf{k}) \exp\{i[\phi(-\mathbf{l}) + \varphi(-\mathbf{k}) + \varphi(\mathbf{l} + \mathbf{k})]\}. \tag{13.16}$$

Substitution of eqn (13.15) and eqn (13.16) in eqn (13.11) gives:

$$S'(\Phi_S) = \frac{2}{V^2 \sqrt{N}} \left\{ \sum_{\mathbf{k}} \sum_{\mathbf{k}'}^A [E(\mathbf{k}) - \langle E \rangle] E(\mathbf{k}') E(\mathbf{k} - \mathbf{k}') \cos[\varphi(-\mathbf{k}) + \varphi(\mathbf{k}') + \varphi(\mathbf{k} - \mathbf{k}')] + \sum_{\mathbf{l}} \sum_{\mathbf{k}}^A [E(\mathbf{l}) - \langle E \rangle] E(\mathbf{k}) E(\mathbf{l} + \mathbf{k}) \cos[\phi(-\mathbf{l}) + \varphi(-\mathbf{k}) + \varphi(\mathbf{l} + \mathbf{k})] \right\}, \tag{13.17}$$

where A denotes the asymmetric unit in reciprocal space. For the reflections in \mathbf{S} , there are three different terms in the summation with the same $\cos[\varphi(-\mathbf{k}) + \varphi(\mathbf{k}') + \varphi(\mathbf{k} - \mathbf{k}')] values. Hence the abbreviation,$

$$X(\mathbf{k}, \mathbf{k}') = 1 - \frac{\langle E \rangle}{3} \left[\frac{1}{E(\mathbf{k})} + \frac{1}{E(\mathbf{k}')} + \frac{1}{E(\mathbf{k} - \mathbf{k}')} \right] \tag{13.18}$$

can be introduced in eqn (13.17) and this leads to the definitive form of $S'(\Phi)$:

$$S'(\Phi_S) = \frac{2}{V^2\sqrt{N}} \left\{ \sum_{\mathbf{k}} \sum_{\mathbf{k}'} E(\mathbf{k})E(\mathbf{k}')E(\mathbf{k}-\mathbf{k}')X(\mathbf{k},\mathbf{k}') \cos[\varphi(-\mathbf{k}) + \varphi(\mathbf{k}') + \varphi(\mathbf{k}-\mathbf{k}')] + \sum_{\mathbf{k}} \sum_{\mathbf{l}} E(\mathbf{k})[E(\mathbf{l}) - \langle E \rangle]E(\mathbf{l}+\mathbf{k}) \cos[\varphi(-\mathbf{k}) + \phi(-\mathbf{l}) + \varphi(\mathbf{l}+\mathbf{k})] \right\} \quad (13.19)$$

13.4 The sum function tangent formula, $S' - TF$

According to its definition, the Direct methods modulus sum function should be a maximum for the true phases. Consequently, the practical application of $S'(\Phi)$ requires an easy and effective maximization procedure. By following the conventional tangent formula derivation of Debaerdemaeker *et al.* (1985), it can be shown, that $S'(\Phi)$ can be maximized with a new tangent formula called $S' - TF$. The condition for an extremum is:

$$\frac{\partial S'(\Phi_S)}{\partial \varphi(\mathbf{k})} = 0 \quad (13.20)$$

for every \mathbf{k} , and application of this condition to eqn (13.19) gives:

$$\frac{\partial S'(\Phi_S)}{\partial \varphi(\mathbf{k})} = -\frac{2K}{V^2\sqrt{N}} E(\mathbf{k}) \left\{ \sum_{\mathbf{k}'} E(\mathbf{k}')E(\mathbf{k}-\mathbf{k}')X(\mathbf{k},\mathbf{k}') \sin[\varphi(-\mathbf{k}) + \varphi(\mathbf{k}') + \varphi(\mathbf{k}-\mathbf{k}')] + \sum_{\mathbf{l}} [E(\mathbf{l}) - \langle E \rangle]E(\mathbf{l}+\mathbf{k}) \sin[\varphi(-\mathbf{k}) + \phi(-\mathbf{l}) + \varphi(\mathbf{l}+\mathbf{k})] \right\} = 0, \quad (13.21)$$

which, after some manipulation, results in the definitive form of the $S' - TF$:

$$\varphi(\mathbf{k}) = \text{phase of} \left\{ \sum_{\mathbf{k}'} X(\mathbf{k},\mathbf{k}')E(\mathbf{k}')E(\mathbf{k}-\mathbf{k}') \exp\{i[\varphi(\mathbf{k}') + \varphi(\mathbf{k}-\mathbf{k}')]\} + \sum_{\mathbf{l}} [E(\mathbf{l}) - \langle E \rangle]E(\mathbf{l}+\mathbf{k}) \exp\{i[\phi(-\mathbf{l}) + \varphi(\mathbf{l}+\mathbf{k})]\} \right\}. \quad (13.22)$$

Notice that $\phi(-\mathbf{l})$ must be updated from the refined Φ_S value using the expression:

$$\phi(\mathbf{l}) = \text{phase of} \left\{ \sum_{\mathbf{k}'} E(\mathbf{k}') E(\mathbf{l}-\mathbf{k}') \exp\{i[\varphi(\mathbf{k}') + \varphi(\mathbf{l}-\mathbf{k}')]\} \right\} \quad (13.23)$$

with \mathbf{k}' and $\mathbf{1} - \mathbf{k}'$ belonging to \mathbf{S} . Unlike most tangent formulae, the $S' - TF$ needs no weights for optimal use, a property that confers increased stability upon it. Inspection of eqn (13.22) indicates that the principal contributors are those terms with $|E(\mathbf{h}) - \langle E \rangle|$ large. Since the contributions of the reflections with E magnitudes close to the average value are rather small, they are normally left out of the phase refinement. In practice, the best results are achieved by introducing a similar number of strong and weak reflections. The calculation of the average value $\langle E \rangle$ is then carried out with these reflections only.

To show the capability of the $S' - TF$ to refine phases, a series of test calculations using single-crystal diffraction data collected from organic compounds to atomic resolution ($d \simeq 1 \text{ \AA}$) were performed (Rius *et al.* 1995a). The test calculations were computed with the program XLENS (Rius 1994) using the NES strongest and the NWEAK ($= \text{NES} - \sqrt{NES}$) weakest reflections. The tests were selected to cover the following situations:

- (1) low- and high-symmetry space groups;
- (2) space groups with fixed and non-fixed origins;
- (3) equal-atom structures with the same symmetry but with different numbers of atoms in the unit cell.

The tests showed that refinement of phases with the $S' - TF$ function was very effective in all cases. However, the most spectacular results (with success rates in the range between 10–70 per cent) were obtained for structures in which the origin can float in at least one direction. These tests also allowed assessment of the decisive influence of the size of the crystal structure upon the success rate. By using three structures belonging to $P2_12_12_1$ but with N values equal to 108, 188 and 340, the respective success rates gradually decreased (10, 1 and 0.1 per cent respectively). Finally, comparison of the results of the $S' - TF$ with those obtained using the tangent formula incorporating the most reliable negative quartets (Sheldrick 1990) indicates that the success rate of the former is, in general, an order of magnitude higher.

13.5 Application of the sum function tangent formula to powder diffraction data

In the application of Direct methods to powder data, the most decisive parameter is the upper resolution limit of the set of extracted integrated intensities. Experience shows that for structures with no systematic overlap or pseudo-symmetry, the set of extracted intensities is very often almost complete up to a certain upper resolution limit. The latter depends on (a) the size and symmetry of the crystal structure, (b) the quality of the sample and (c) the experimental conditions. If the set of extracted integrated intensities is assumed to be accurate enough then, before the $S' - TF$ can be applied, the influence of the upper resolution limit must be understood. As has already been shown

(Rius *et al.* 1995*b*, 1996*b*) the required data resolution for applying the $S' - TF$ largely depends on the closest separation S_D between dominant scatterers in the structure; that is, for a given S_D the required intensity data resolution expressed in terms of the minimum d -spacing d_{\min} is given by

$$d_{\min} = \frac{S_D}{1.44}. \quad (13.24)$$

Obviously, the corresponding E -map will reveal principally the partial structure of the dominant scatterers. According to the maximum d_{\min} value required, the crystal structures can be classified into:

1. *Organic compounds.* This is the most unfavourable case for X-ray powder data. As the C atoms are typically the dominant scatterers, and they are only 1.4–1.5 Å apart, the corresponding maximum d_{\min} value will be close to 1 Å resolution. This demands the combination of rather well crystallized samples with the use of synchrotron radiation. To date, no purely organic compounds (C,N,O,H) have been solved from powder data by means of the $S' - TF$.
2. *Compounds with heavy atoms.* This is the most favourable case. In such compounds, the separation S_D between heavy atoms is rather large, so that the $S' - TF$ can locate them even with data at low resolution. One example is provided by the zeolite RUB-10. Crystal data: monoclinic with space group $P2_1/a$ and $a = 13.112(2)$, $b = 12.903(1)$, $c = 12.407(2)$ Å, $\beta = 113.50^\circ$, $V = 1925$ Å³, unit cell content: $[\text{Si}_{32}\text{B}_4\text{O}_{72}][\text{N}(\text{CH}_3)_4]_4$. The general connectivity pattern of the silicate framework which belongs to the clathrasil family was determined by Patterson search methods (Gies and Rius 1995) using laboratory powder diffraction data up to 2 Å resolution (Fig. 13.3). Since the

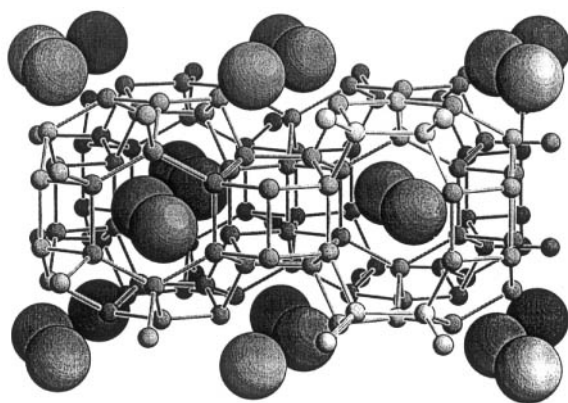
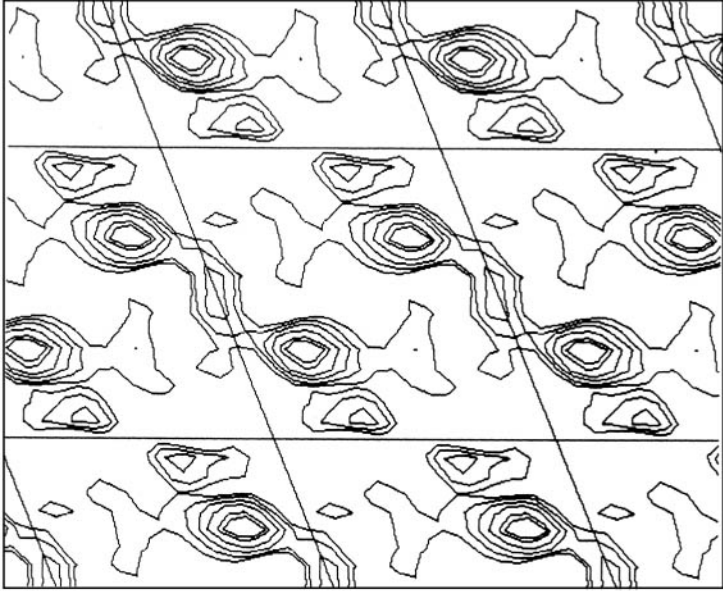


Fig. 13.3. Perspective view of zeolite RUB-10 showing the arrangement of the template cations within the double cages. Small circles: T-atoms (Si,B). Large circles: Template cations showing rotational disorder. For clarity the bridging oxygen atoms have been left out.

(a)



(b)

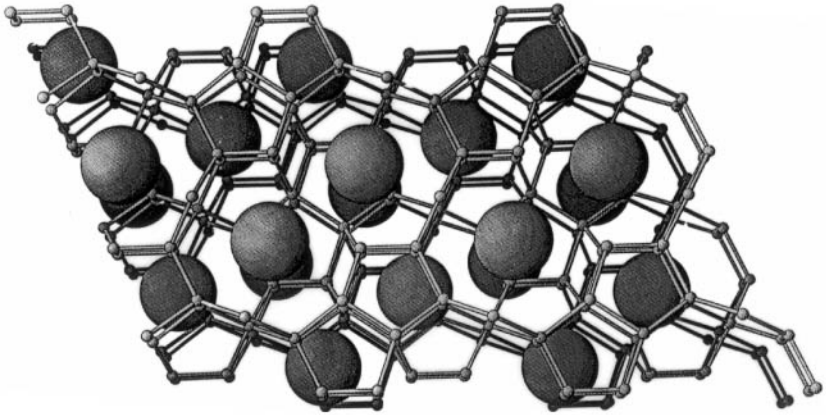


Fig. 13.4. (a): Section $y=0$ of the E -map of RUB-10 obtained from phase refinement with the $S' - TF$ using data up to $d \simeq 2 \text{ \AA}$ resolution; (b) Perspective view along b of approximately the same portion of the unit cell showing the correct location of the template cations.

template cations show rotational disorder at room temperature, they can be regarded as heavy scatterers, and consequently, this example represents the ideal case for testing the power of the $S' - TF$. By introducing the 30 strongest and 20 weakest reflections (from a total of 83 observed reflections at 2 \AA resolution) into XLENS, the set with the best FOM clearly shows the correct template cation arrangement (Figs 13.4(a,b)).

3. *Zeolite-like compounds*. This case is less favourable. Fortunately, experience has shown that the Si atoms can be regarded to some extent as dominant scatterers (i.e. the bridging oxygen atoms play no significant role). Since the Si-Si distance in zeolites is approximately 3.1 \AA , values of d_{\min} up to approximately 2 \AA can be tolerated, and the Si tetrahedra will show up as single peaks in the corresponding E -map. This is illustrated in the structure solution of the layer silicate RUB-15 (Oberhagemann *et al.* 1996). Crystal data: orthorhombic with space group $Iba2$ and $a = 27.905(6)$, $b = 8.404(1)$, $c = 11.518(2)$, $V = 2702 \text{ \AA}^3$, unit cell content: $[\text{Si}_{24}\text{O}_{52}(\text{OH})_4] [\text{N}(\text{CH}_3)_4]_8 \cdot 20\text{H}_2\text{O}$. The 76 low resolution reflections up to $2\theta \simeq 41^\circ$ ($\text{Cu K}\alpha_1$) were introduced in XLENS with the overall B fixed at 3.5 \AA^2 . The phases of the 20 strongest reflections were refined with the $S' - TF$ using the 16 weakest reflections as additional information. The projection of the E -map corresponding to the solution with the best combined figure of merit is shown in Fig. 13.5(a). For clarity, the same projection of part of the structure is reproduced in Fig. 13.5(b). Inspection of both figures allows one

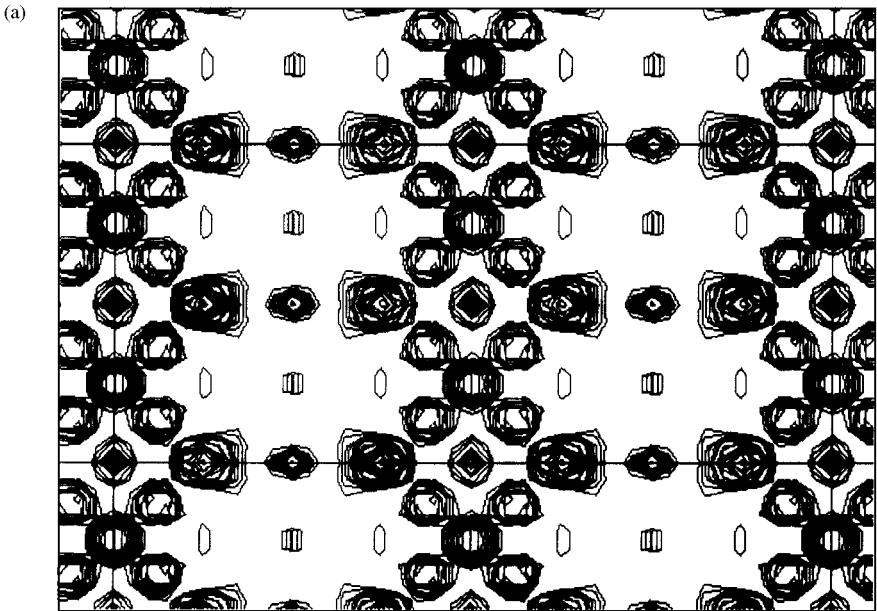


Fig. 13.5. See caption opposite.

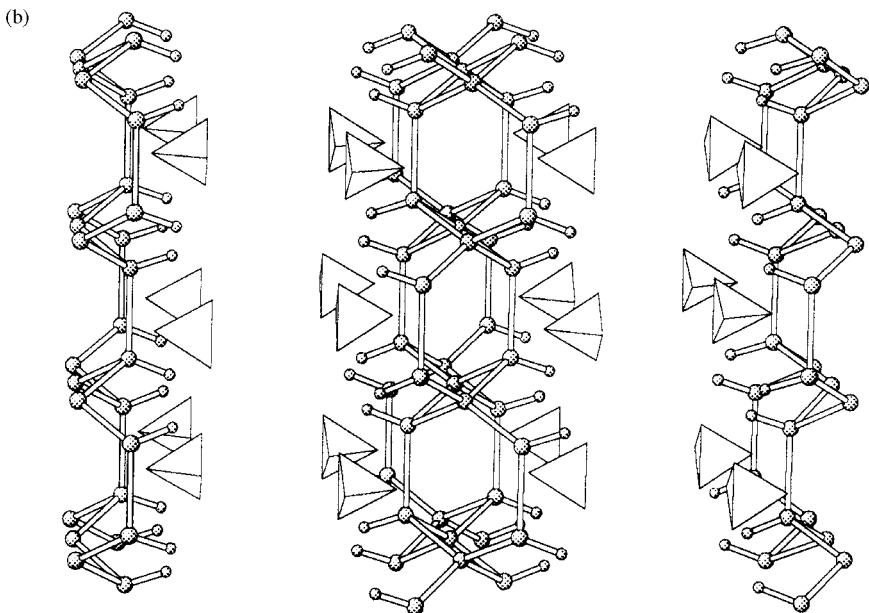


Fig. 13.5 (a): (010) projection of the E -map of RUB-15 obtained from phase refinement with the $S' - TF$ ($d \geq 2 \text{ \AA}$) showing the silicate sheets normal to [001] and the template cations; (b): Perspective view along b of the same portion of the unit cell (without the water molecules). It can be clearly seen that both the tetrahedral Si units as well as the tetramethylammonium cations appear as spheres.

to confirm that, at this resolution, the Si tetrahedra appear as well-resolved peaks and may be considered as dominant scatterers together with the template cations.

Some recent relevant applications of the $S' - TF$ to powder data have been the crystal structure solution of the microporous material RUB-18 (Vortmann *et al.* 1997), of the hydrous layer silicate kanemite, a precursor of the industrial ion exchanger SKS-6 (Vortmann *et al.* 1999), and of the three large-pore zeolites ITQ-21 (Corma *et al.* 2002), ITQ-22 (Corma *et al.* 2003) and ITQ-32. The crystal structure of the last material was solved combining the origin-free modulus sum function with the isomorphous replacement technique (Rius-Palleiro *et al.* 2005). The $S' - TF$ has also been applied successfully to the solution of the structure of the dominant crystalline phase present in the hydrated high alumina cement i.e. the phase determining the valuable cementing properties (Guirado *et al.* 1998) as well as to the determination of the structure of the mineral aerinite used as blue pigment in the middle ages (Rius *et al.* 2004). Both structures belong to hemihedral space groups and may be regarded as tests examples to demonstrate the feasibility of solving structures belonging to hemihedral space groups with the $S' - TF$ (Rius *et al.* 1999).

Acknowledgements

This work was partially supported by the Spanish 'Ministerio de Cultura' (Project PB98-0483) and the Direcció Gral de Recerca de la Generalitat de Catalunya (Grant No. SGR 00460, 1995).

References

- Cochran, W. and Woolfson, M. M. (1955). *Acta Crystallogr.*, **8**, 1–12.
- Corma, A., Diaz-Cabañas, M. J., Martínez-Triguero, J., Rey, F. and Rius, J. (2002). *Nature*, **418**, 1, 514–17.
- Corma, A., Rey, F., Valencia, S., Jordá, J. L. and Rius, J. (2003). *Nature Materials*, **2**, 493–97.
- Debaerdemaeker, T., Tate, C. and Woolfson, M. M. (1985). *Acta Crystallogr. A*, **41**, 286–90.
- Giacovazzo, C. (1976). *Acta Crystallogr. A*, **32**, 91–9.
- Gies, H. and Rius, J. (1995). *Z. Kristallogr.*, **210**, 475–80.
- Guirado, F., Galí, S., Chinchón, S. and Rius, J. (1998). *Angew. Chem. Int. Ed.*, **37**, 72–5.
- Hauptman, H. (1974). *Acta Crystallogr. A*, **30**, 822–9.
- Karle, J. and Hauptman, H. (1956). *Acta Crystallogr.*, **9**, 635–51.
- Karle, J. and Karle, I. (1966). *Acta Crystallogr.*, **21**, 849.
- Oberhagemann, U., Bayat, P., Marler, B., Gies, H. and Rius, J. (1996). *Angew. Chem. Int. Ed. Engl.*, **35**, 2869–72.
- Ramachandran, G. N. and Raman, S. (1959). *Acta Crystallogr.*, **12**, 957–64.
- Rius, J. (1993). *Acta Crystallogr. A*, **49** 406–9.
- Rius, J. (1994). *XLENS. A program for crystal structure determination*. ICMAB-CSIC, Catalunya, Spain.
- Rius, J., Sañé, J., Miravittles, C., Amigó, J. M. and Reventós, M. M. (1995a). *Acta Crystallogr. A*, **51**, 268–70.
- Rius, J., Sañé, J., Miravittles, C., Gies, H., Marler, B. and Oberhagemann, U. (1995b). *Acta Crystallogr. A*, **51**, 840–5.
- Rius, J., Miravittles, C. and Allmann, R. (1996a). *Acta Crystallogr. A*, **52**, 634–9.
- Rius, J., Sañé, J., Miravittles, C., Amigó, J. M., Reventós, M. M. and Louér, D. (1996b). *Anales de Química Int. Ed.*, **92**, 223–7.
- Rius, J. (1997). *Acta Crystallogr. D*, **53**, 535–9.
- Rius, J., Miravittles, C., Gies, H. and Amigó, J. M. (1999). *J. Appl. Crystallogr.*, **32**, 89–97.
- Rius, J., Elkaim, E. and Torrelles, X. (2004). *European Journal of Mineralogy*, **16**, 127–34.
- Rius-Palleiro, J., Peral, I., Margiolaki, I. and Torrelles, X. (2005). *J. Appl. Crystallogr.*, **38**, 906–11.
- Schenk, H. (1973). *Acta Crystallogr. A*, **29**, 77–82.
- Schenk, H. (1974). *Acta Crystallogr. A*, **30**, 477–81.
- Sheldrick, G. M. (1990). *Acta Crystallogr. A*, **46**, 467–73.
- Vortmann, S., Rius, J., Siegmann, S. and Gies, H. (1997). *J. Phys. Chem. B.*, **101**, 1292–6.
- Vortmann, S., Rius, J., Marler, B. and Gies, H. (1999). *Eur. J. Mineral.*, **11**, 125–34.

A maximum entropy approach to structure solution

Christopher J. Gilmore, Kenneth Shankland and Wei Dong

14.1 Introduction

Direct methods of crystal structure analysis are one of the great success stories of twentieth century science, with the enormous number of solved single-crystal structures available today giving testament to their power. Traditional Direct methods require data at atomic resolution coupled with a complete sampling of reciprocal space. It therefore comes as no surprise that these methods perform less well with powder diffraction data, where the inevitable reflection overlap represents an information loss that can be critical.

In 1984, Bricogne proposed an alternative solution to the crystallographic phase problem involving a combined multi-solution, maximum entropy, log-likelihood estimation approach. Following its first practical implementation in 1990 (Bricogne and Gilmore 1990; Gilmore *et al.* 1990), it quickly became apparent that the maximum entropy approach was particularly useful when the input structure factors were few in number or poorly estimated. Accordingly, an extension of the theory to cover the specific problems of powder diffraction data was a natural progression (Bricogne 1991). Here, we outline the application of these ideas within the context of the maximum entropy in a Crystallographic Environment (MICE) computer program and use powder diffraction examples to illustrate specific points. For more detailed reviews see Shankland (1994) and Gilmore (1996).

14.2 Data collection, range and overlap

For any Direct methods structure solution attempt, the best possible data should be collected to high resolution, at least 1.5 \AA where possible. In the case of molecular organic compounds, diffracted intensity is typically weak at higher resolution and so it is advantageous to collect at low temperature and count for longer at higher 2θ in order to improve the signal-to-noise ratio (see Chapter 6). Extraction of structure-factor intensities from the powder diffraction pattern is typically achieved by either the Pawley or the Le Bail methods (see Chapter 8). An important step here is the definition of an *overlap set*; when two or more reflections lie so close together in 2θ that their individual structure-factor magnitudes cannot be reliably deconvoluted, they are often output as a

single clumped intensity. Thus extracted structure factors are automatically split into two distinct sets, *overlapped* and *non-overlapped*. The extent of overlap encountered depends upon a number of factors such as instrumental resolution, sample broadening, space group and unit cell size and shape. For example, in the case of laboratory X-ray data collected on a sample of Mg_3BN_3 to $\sim 0.9 \text{ \AA}$ ($P6_3/mmc$, $V = 174 \text{ \AA}^3$), fewer than 3 per cent of the reflections were classified as overlapped and the data thus approaches single-crystal quality. In contrast, with laboratory X-ray data collected from a sample of the organic compound $\text{C}_4\text{O}_2\text{S}_4$ ($P2_1/a$, $V = 138 \text{ \AA}^3$), approximately 60 per cent of the reflections were classified as overlapped. Subsequent sections will show that these overlaps, which are often

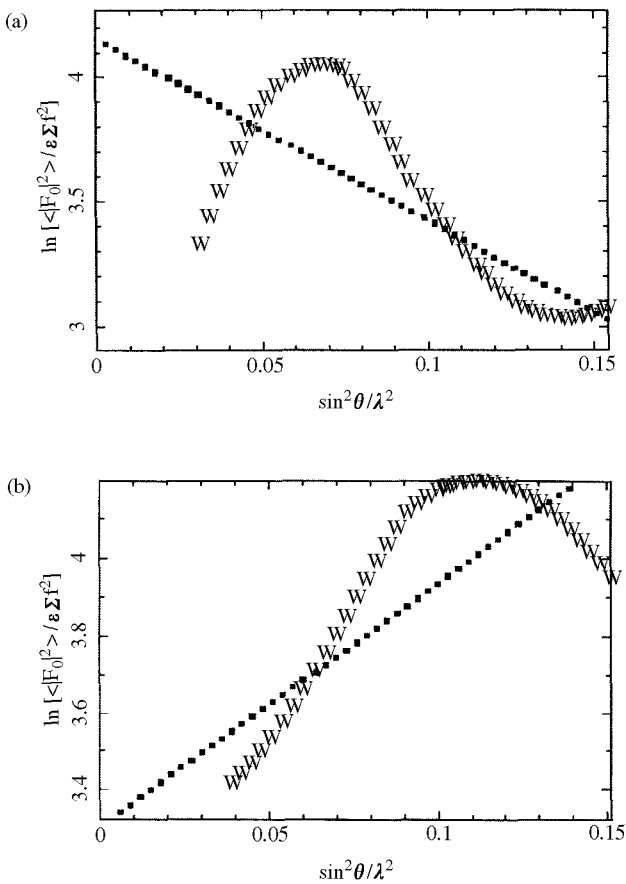


Fig. 14.1. Wilson plots for $\text{Li}_6\text{Zr}_2\text{O}_7$. The straight line is the least-squares fit of the data points represented by the curve of 'w' symbols. (a) Includes the non-overlapped and overlapped reflections and gives an overall temperature factor of $B = 3.6$. (b) Includes only the non-overlapped reflections and gives the physically meaningless value of $B = -3.1$.

discarded or simply equipartitioned in preparation for a Direct methods structure solution attempt, can be used more effectively, and the maximum entropy (ME) method is particularly suited to this purpose.

The first step of most direct method procedures, including the ME method, is the normalization of structure factors to E - or U -magnitudes and this is typically achieved by using a standard Wilson plot. However, the dearth of reflections in a powder pattern compared to the single-crystal case means that the quality of the Wilson plot is often poor, resulting in a meaningless negative temperature factor. Nevertheless, the $|E|$ or $|U|$ values can still be used in a successful structure solution without the need to enforce a positive temperature factor. By including overlapped reflections in the normalization process, the number of data points is increased, as is the $\sin \theta/\lambda$ range, and, as can be seen in Fig. 14.1, the quality of the Wilson plot is improved significantly.

14.3 Starting set choices: defining the origin and enantiomorph

In the ME method, an origin is normally defined by assigning appropriate phases to a set of strong reflections that constitute a legal origin. Where

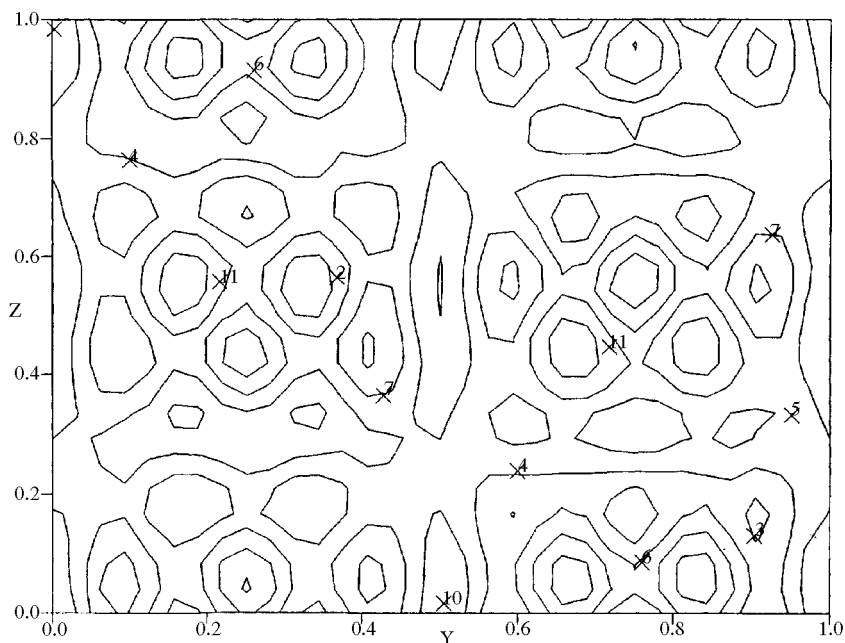


Fig. 14.2. A centroid map for KAIP_2O_7 based on three origin defining reflections used as constraints in entropy maximization. Note that the map includes these three reflections as well as the extrapolates suitably weighted. Atomic positions are shown by crosses.

appropriate, the enantiomorph is also defined. If this poses problems, then an incomplete or deferred origin/enantiomorph definition can be made; the building of a phasing tree will usually complete the process *de facto*. Ideally, the reflections should all be non-overlapped in order to avoid any intensity ambiguities, but this is not essential. At this stage, the set of n phased reflections constitutes the *basis set* $\{H\}$ and these reflections, both their amplitudes and phases, are used as constraints in an entropy maximization to generate a maximum entropy map, $q^{ME}(\mathbf{x})$ using a highly damped exponential modelling algorithm (Bricogne 1984; Bricogne and Gilmore 1990). The Fourier transform of this map reproduces the constraints to within experimental error, but also generates estimates of amplitudes and phases for reflections that were not included in the original calculation, that is, reflections that lie in the non-basis set $\{K\}$ via a process of extrapolation. A typical map for $KAlP_2O_7$ generated with just three origin-defining reflections is shown in Fig. 14.2.

14.4 Basis set expansion and the phasing tree

In order to improve the strength and reliability of maximum entropy extrapolation, new reflections are introduced into the basis set $\{H\}$ from $\{K\}$. For a given basis set $\{H\}$ containing n reflections, the second neighbourhood of $\{H\}$ consists of the N_2 symmetry unique set of reflections distinct from the basis set, $\mathbf{k} = \mathbf{h}_1 \pm {}^t\mathbf{R}_g \mathbf{h}_2$ for $\mathbf{h}_1, \mathbf{h}_2 \in \{H\}$, where ${}^t\mathbf{R}_g$ is the transpose of the rotation matrix for the space group. Reflection \mathbf{k} can also be defined via a second writing of the form $\mathbf{k} = \mathbf{h}_3 \pm {}^t\mathbf{R}_g \mathbf{h}_4$ for $\mathbf{h}_3, \mathbf{h}_4 \in \{H\}$. Reflections are then transferred from $\{K\}$ to $\{H\}$ such that the quantity

$$\sum_{\mathbf{k}} |E_{\mathbf{k}}^2 - 1| |U_{\mathbf{h}_1}| |U_{\mathbf{h}_2}| |U_{\mathbf{h}_3}| |U_{\mathbf{h}_4}| \quad (14.1)$$

is maximized. It can now be stated that origin-defining reflections are preferably chosen in a similar fashion: one starts with a complete set of strong reflections and eliminates them stepwise using the sum in eqn (14.1) as the measure of strength.

Of course, reflections cannot be introduced into the basis set without assigning them phases. To do this, centric reflections may be assigned each of the two possible phase choices, for example, $0, \pi$ or $\pm\pi/2$, while acentric reflections are assigned $\pm\pi/4, \pm3\pi/4$, that is, the quadrant is fixed. A *node* is created for every possible phase combination; introducing n_c centric reflections creates 2^{n_c} new nodes each with distinct basis sets, with n_a acentric reflections giving 4^{n_a} nodes. The nodes comprise a phasing tree; the root node, on the first level, is defined by the origin-fixing reflections, and the second level is defined by those reflections for which phase choices have been made by phase permutation. Subsequent levels are built by further phase permutation.

14.5 Log-likelihood gain

Permuting six centric and six acentric phases in a given level generates $2^6 \cdot 4^6 = 262\,144$ nodes, and further reflections may need to be permuted. To contain the combinatorial explosion that can arise from this process, the phasing tree needs to be pruned and nodes that contain incorrect phase choices removed from the calculation. Entropy cannot do this (see, for example, Gilmore 1996 and Table 14.1). More appropriate is a calculation of the probability that the distribution of observed structure factors in the non-basis set ($|U_{\mathbf{h}}|^{\text{obs}}$) has arisen from the phase choices made in a particular basis set. This is conveniently evaluated via an appropriate likelihood function (Bricogne 1984, 1991, 1997*a*).

For a general expression for the likelihood function, let a given overlap comprise R_i , $i = 1, m$ observed intensities, $|U_{\mathbf{h}}|^{\text{obs}}$, and r_i , $i = 1, m$ the calculated intensities produced as a result of extrapolation from a maximum entropy optimization, $|U_{\mathbf{h}}^{\text{ME}}|$. A single, non-overlapped reflection is treated by simply setting $m = 1$. For each overlap or single reflection, define:

$$R = \sum_{i=1}^m p_i R_i^2 \quad (14.2)$$

and

$$r = \sum_{i=1}^m p_i r_i^2. \quad (14.3)$$

Let

$$z = \frac{Rr}{\Sigma}, \quad (14.4)$$

where p is the reflection multiplicity and Σ is a refinable parameter related to the unit cell contents via $\Sigma \approx 1/N$, where there are N non-hydrogen atoms, assumed

Table 14.1 LLGs for $\text{Li}_6\text{Zr}_2\text{O}_7$. Entropy is a poor figure of merit, but the LLG performs well when overlaps are included, with node 135 having its entire basis set phases correct

| Node number | Entropy | LLG excluding overlaps | LLG including overlaps |
|-------------|---------|------------------------|------------------------|
| 135 | -2.03 | 7.10 | 15.11 |
| 109 | -1.75 | 5.93 | 12.78 |
| 97 | -2.90 | 7.51 | 12.51 |
| 99 | -1.87 | 4.89 | 11.28 |

equal, in the unit cell. Define:

$$X_n(z) = e^{-z} {}_0F_1(-; n/2; z^2/4), \quad (14.5)$$

where ${}_0F_1$ is a confluent hypergeometric function (Abramowitz and Stegun 1970). The log likelihood, LH, is written:

$$\text{LH} = \sum_{\substack{\text{all} \\ \text{extrapolates}}} \left[\frac{-n}{2 \log \Sigma} - \frac{(R-r)^2}{2\Sigma} + \log X_n(z) \right]. \quad (14.6)$$

For the null hypothesis, LH_0 , we set r , and hence z , equal to 0 so that:

$$\text{LH}_0 = \sum_{\substack{\text{all} \\ \text{extrapolates}}} \left[\frac{-n}{2 \log \Sigma} - \frac{R^2}{2\Sigma} \right]. \quad (14.7)$$

The log-likelihood gain (LLG) is then:

$$\text{LLG} = \text{LH} - \text{LH}_0 \quad (14.8)$$

Clearly, the higher the value of LLG, the more closely the process of entropy maximization has predicted the pattern of observed intensities and hence the more likely it is that our phase choices are correct. The refinement of Σ is carried out by maximization of LLG.

The LLG can be computed with or without the inclusion of overlapped reflections. The inclusion of overlapped data in the LLG calculation is the preferred option, as it usually has a marked effect upon the rank order of nodes. For example, consider four nodes obtained from the second level of phasing for the compound lithium zirconate ($\text{Li}_6\text{Zr}_2\text{O}_7$) which has space group $C2/c$, 148 non-overlapping reflections, and 109 overlapping reflections in 47 groups. Table 14.1 shows that node 135 generates a centroid map corresponding to the correct solution and it is identified by the highest LLG only when the overlapped data is included (Tremayne 1995).

In principle, those 8–16 nodes which have the highest LLGs are selected from a given level of the phasing tree for subsequent enlargement. However, except for the simplest cases, selecting nodes simply on the criterion of maximum LLG is unreliable since we have no estimates of their variances. LLGs need to be analysed with more care, and the following algorithm has proved successful (Gilmore *et al.* 1997).

First, tests of significance are used (Shankland *et al.* 1993; Bricogne 1993, 1997b) in which the LLGs are analysed for phase indications using the Student t -test. The simplest example involves the detection of the main effect associated with the sign of a single centric phase. The LLG average, μ^+ , and its associated variance V^+ is computed for all those nodes in a given level of the phasing tree

in which the sign of this permuted phase under test is positive. The calculation can then be repeated for those nodes in which the sign is negative, thus giving the corresponding μ^- , and variance V^- . The t -test statistic is:

$$t = \frac{|\mu^+ - \mu^-|}{\sqrt{V^+ + V^-}} \quad (14.9)$$

and this is used with the standard, two-tailed tables of significance.

The use of the t -test enables a sign choice to be derived with an associated significance level, s . The calculation is repeated for all the single phase indications, and is then extended to combinations of two and three phases where appropriate.

A simple example involves the solution of the structure of Mg_3BN_3 (Shankland *et al.* 1993). The data consisted of 63 non-overlapped reflections and two sets of overlapped reflections, with an effective resolution of 0.9 Å. The origin node was defined by assigning a phase of 0 to the 1 0 7 and the basis set was expanded by permuting the 1 0 12, 2 0 12, 3 -1 1, 3 -1 4, 3 1 5, 3 1 6 and 3 1 7 reflections. LLGs were calculated for the 128 nodes generated and analysed for significant phase indications (Table 14.2).

In general, only phase interactions with associated significance levels <0.02 are used in the analysis, but this is often relaxed to 0.05 - 0.10 if few significant interactions can be found at a particular level or error correcting codes are being used. Each of the m phase relationships with associated significance levels above the preset significance limit is given an associated weight:

$$w_i = \left(1 - \frac{I_1(s_i)}{I_0(s_i)} \right) \quad (14.10)$$

where I_1 and I_0 are Bessel functions and s_i is the significance level of the i th relationship from the t -test. Each node n is now given an overall score, s_n :

$$s_n = \text{LLG}_n \sum_{j=1}^m w_j \quad (14.11)$$

Table 14.2 t -test results for Mg_3BN_3 . The 1, 2 and 3 phase interactions with a significance level <0.02 are listed

| Refl. 1 | Refl. 2 | Refl. 3 | Sign | Type | Significance |
|---------|---------|---------|------|-------------|------------------------|
| 3 -1 7 | | | + | Main effect | 0.98×10^{-19} |
| 3 -1 1 | 3 -1 4 | 1 0 12 | - | 3-phase | 0.43×10^{-3} |
| 1 0 12 | 2 0 12 | | + | 2-phase | 0.67×10^{-3} |
| 3 1 1 | | | - | Main effect | 0.15×10^{-1} |

The summation in eqn (14.11) spans only those phase relationships where there is agreement between the basis set phases and the t -test.

For Mg_3BN_3 , eight nodes were retained on the basis of these relationships and the map from the node with the highest score revealed the position of all the atoms as shown in Fig. 14.3.

A question that arises naturally is: 'Why not take strongly extrapolated reflections and put them into the basis set with their observed magnitudes and extrapolated phases?' This procedure usually ends with the solution trapped in a local entropy maximum in phase space (Gilmore *et al.* 1990). To see this in the context of Mg_3BN_3 , the origin was again defined using the 1 0 7. After a constrained entropy maximization, the inverse Fourier transform yielded extrapolated structure factors. For those reflections where $|U_{\mathbf{h}}^{\text{ME}}| \geq 0.5|U_{\mathbf{h}}|^{\text{obs}}$ the phase angles predicted by extrapolation were assigned to the observed U magnitudes, and the process of entropy maximization repeated. Successive cycles of this procedure were performed until all the 54 reflections used were phased. The results are summarized in Table 14.3.

A Fourier map based on the 54 phased reflections is incorrect, with the majority of the density placed on a single nitrogen atom site. It is clear that the algorithm never recovers from the early acceptance of incorrect phases. In contrast, the MICE node with the highest score had correct phases for the seven permuted basis set reflections and 36 of the 42 extrapolated reflections with $|U_{\mathbf{h}}^{\text{ME}}||U_{\mathbf{h}}|^{\text{obs}} \geq 0.001$.

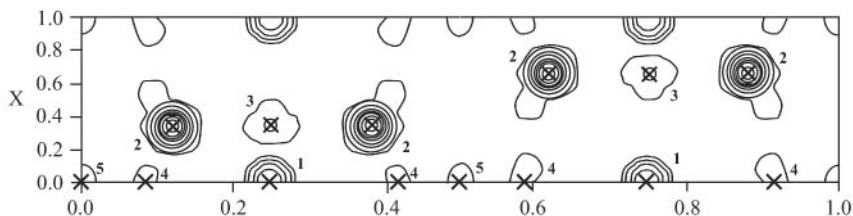


Fig. 14.3. The best centroid map for Mg_3BN_3 . The atoms labelled 1 and 2 are Magnesiums; 3 and 4 are Nitrogens; 5 is Boron.

Table 14.3 The results of incorporating ME extrapolated phases into the basis set for Mg_3BN_3

| Cycle | No. of reflections | No. of correct phases phased |
|-------|--------------------|------------------------------|
| 1 | 4 | 2 |
| 2 | 8 | 3 |
| 3 | 26 | 12 |
| 4 | 54 | 27 |

For other successes of this part of the ME formalism with powder data, see for example, Gilmore *et al.* (1991), Tremayne *et al.* (1992a, b), and Gilmore *et al.* (1999).

14.6 Centroid maps

The maps which are most useful in an ME-phasing environment are *centroid maps* (Bricogne and Gilmore 1990; Bricogne 1991; Gilmore *et al.* 1991) in which the overlapped reflections are included. These have the following coefficients:

1. Basis set reflections are included with unit weights, the observed U magnitudes and phases from the relevant node on the tree.
2. Non-basis set reflections incorporate the observed U magnitudes, phase angles resulting from the ME extrapolation process, and Sim-type weights w_i (Sim 1959) computed via:

$$w_i = \frac{R^2_0 F_1(-; n/2 + 1; z^2/4)}{n \Sigma_0 F_1(-; n/2; z^2/4)}. \quad (14.12)$$

All the maps in this chapter are of this type.

14.7 Fragments and partial structures

It is often the case that some fragment of the structure under investigation is already known, perhaps from a Patterson map or from a partial structure detected via the ME formalism (Fig. 14.4). In such cases, three U magnitudes are considered: $|U_{\mathbf{h}}|^{\text{obs}}$, $|U_{\mathbf{h}}^{\text{ME}}|$, $|U_{\mathbf{h}}^{\text{frag}}|$. The constraints to be fitted in the entropy maximization process incorporate the fragment information and the whole

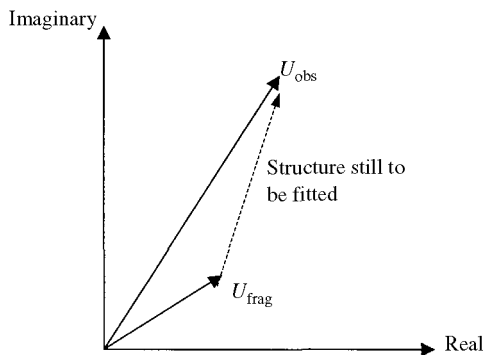


Fig. 14.4. The contribution of a partial structure to an observed structure factor.

Table 14.4 Light atom location in $\text{Li}_6\text{Zr}_2\text{O}_7$ using the ME formalism

| Peak number in map | Atom | Distance from refined position (\AA) |
|-----------------------|------|--|
| 1 | Zr | 0.12 |
| 2 | O | 0.31 |
| 3 | O | 0.91 |
| 4 | O | 0.54 |
| 5 | Li | 0.48 |
| 6 | O | 0.45 |
| 8 | Li | 0.51 |
| 11 | Li | 0.22 |

ME process works as before, with the fragment contribution subtracted from the observed U magnitude, and phase information from the fragment incorporated.

In the case of the $\text{Li}_6\text{Zr}_2\text{O}_7$ structure mentioned earlier, the Zr position was obtained from node 135. To find the rest of the structure, the data was renormalized so as to incorporate the Zr atom and a new phasing tree generated with the permutation of five centric reflections to generate another 32 nodes. All nodes generated centroid maps that revealed the entire structure, with the node exhibiting the highest score giving the best approximation of the final refined structure (Table 14.4).

14.8 Using likelihood to partition overlapped reflections

14.8.1 *The overlap problem defined in terms of hyperphases and pseudophases*

In the above cases, no attempt has been made to predict the relative magnitudes of the reflections under a given overlap. In fact the combined ME/LLG method can predict these splittings in favourable cases (Dong and Gilmore 1998). Let a given overlap contain m_a acentric and m_c centric reflections. The net intensity, I , is:

$$I = \sum_{i=1}^{m_a} p_i (A_i^2 + B_i^2) + \sum_{j=1}^{m_c} p_j C_j^2, \quad (14.13)$$

where p_j is the multiplicity of reflection j , A and B are the real and imaginary parts of an acentric structure factor, and C the structure factor component for centric reflections. Multiplicities are readily derived from point group symmetry, so that the problem is one of determining the A , B and C coefficients in eqn (14.13). It is profitable to rephrase this problem in terms of hyperphases. To do this we define the overlap as a vector \mathbf{F} in an n -dimensional space R^n

(Bricogne 1991) as:

$$\mathbf{F} = \begin{bmatrix} p_1^{1/2} A_1 \\ p_1^{1/2} B_1 \\ p_2^{1/2} A_2 \\ p_2^{1/2} B_2 \\ \vdots \\ p_{m_a}^{1/2} A_{m_a} \\ p_{m_a}^{1/2} B_{m_a} \\ p_{m_a+1}^{1/2} C_{m_a+1} \\ \vdots \\ p_m^{1/2} C_m \end{bmatrix} \tag{14.14}$$

where $n = 2m_a + m_c$, is the number of degrees of freedom, and $m = m_a + m_c$ is the number of reflection moduli under the overlap. \mathbf{F} can be visualized as a hypersphere in R^n and we wish to parameterize it. A total of $m - 1$ splitting angles, $\Psi_{j,j=1,m-1}$, $0 \leq \psi \leq \pi/2$, called *pseudophases* define a point on the positive unit hypersphere. This is best seen via an example: consider an overlap of net intensity $I^{1/2}$ comprising two acentric and one centric reflection. The radius of the hypersphere is $R = \|\mathbf{F}\| = I^{1/2}$. Defining R_1 , R_2 and R_3 as the individual intensities of these three reflections, then:

$$\begin{aligned} R' &= R \sin \psi_1 & 0 \leq \psi_1 \leq \pi/2 \\ R_1 &= R' \cos \psi_2 & 0 \leq \psi_2 \leq \pi/2 \\ R_2 &= R' \sin \psi_2 \\ R_3 &= R \cos \psi_1 \end{aligned} \tag{14.15}$$

The angles ψ_1 and ψ_2 are the two pseudophases; once they are known the individual intensities of the reflections are determined. It is then necessary to derive the associated phase angles to fully characterize the overlap, and this is the process of determining *hyperphases*. The whole process is now defined exclusively in terms of angles.

14.8.2 Duncan's procedure for multiple significance tests

In order to determine the necessary pseudophases, a sequence of *t*-tests is carried out to decide which ratios of intensities lying under an overlap are the most likely. However, a simple application of such methods leads to a serious overestimate of the associated level of significance and hence introduces damaging systematic errors. Consider an overlap in which there are three reflections of intensity I_1 , I_2 and I_3 . To estimate these, various partitions of the net intensity are tried, and each permutation has associated with it some figure of merit

(in this case the LLG), and a measure of its variance. A total of nineteen t -tests are performed on various combinations of LLGs and their associated standard deviations, that is (Duncan 1955):

1. Six decisions of the form: LLG_1 is significantly less than LLG_2 ; LLG_2 is significantly less than LLG_3 etc. In the usual shorthand we write these six choices as (1, 2, 3), (1, 3, 2), (2, 1, 3), (2, 3, 1), (3, 1, 2) and (3, 2, 1).
2. Six decisions of the form: LLG_1 is significantly less than LLG_2 and LLG_3 , but LLG_2 and LLG_3 are not significantly different from each other. This is written (1, 2, 3), and the other possible choices are (2, 1, 3), (3, 1, 2), (1, 3, 2), (1, 2, 3) and (2, 3, 1).
3. Six decisions of the form LLG_1 is significantly less than LLG_3 , but LLG_1 and LLG_2 do not differ significantly and LLG_2 and LLG_3 do not differ significantly either. This is written as (1, 2, 3), with the remaining decisions written as (1, 3, 2), (2, 1, 3), (2, 3, 1), (3, 1, 2) and (3, 2, 1).
4. One decision of the form (1, 2, 3), that is, there are no significant differences among the intensities.

While computationally these tests are trivial, a situation arises that if several t -tests are performed at, say, a 5 per cent significance level, the probability that one of these gives an erroneous indication is greater than 0.05 (see, for example, Cochran and Cox 1957; Duncan 1955). If the t -tests are independent, this probability of error is surprisingly large: 0.23 for 5 tests, 0.40 for 10 and 0.64 for 20 tests. In order to protect against such errors, Duncan (1955) has provided a procedure in which the t -test tables in the form of studentized ranges (Pearson and Hartley 1966) are modified to include variable protection levels that are adjusted against incorrect indications of significance.

The LLGs are ranked in order, and an initial analysis of variance carried out. A standard error of the mean LLG, S_{error} , is computed along with the number of degrees of freedom, n . Duncan's tables are then used: the number of degrees of freedom and the significance level define the necessary entries. A studentized range statistic is computed:

$$q_r = \frac{(T_i - T_j)}{(n \cdot S_{\text{error}})^{1/2}}, \quad (14.16)$$

where T_i and T_j are two means to be compared. A critical value for each degree of freedom and the range r can be found from the tables prepared by Duncan. The hypothesis of equality of the two means will be rejected if q_r is greater than the specified level. These are the *significant studentized ranges*. Each of these is multiplied by the standard error to form what Duncan calls the *shortest significant ranges*. Each difference is then tested in the order: largest minus smallest, largest minus second smallest, ..., second largest minus smallest, second largest minus second smallest, ..., finishing with second smallest minus

smallest. Each difference is significant only if it exceeds the corresponding shortest significance range. There is an exception to this rule: no difference is significant if the two LLGs concerned are both contained in a subset (which can be the complete set) of the mean LLG which has a non-significant range.

14.8.3 *The determination of pseudophases using the maximum entropy-likelihood method and Duncan's procedure*

The ME method needs only minor modifications to use this procedure. Following origin definition, a set of reflections, both overlapped and non-overlapped, is selected via the standard algorithm of optimum second neighbourhood extension. The incorporation of overlaps is carried out in the same way as for non-overlaps except that for the former, all the reflections in a given set must be considered simultaneously. If one reflection is selected from an overlap set for the basis set, then all the reflections under the same overlap are included. Pseudophases arising from overlapped intensities are constrained to lie between 0 and $\pi/2$ in steps of $\pi/10$ (18°) that is, working as 18° , 36° , 54° and 72° . This appears to give the finest grid to which this formalism is sensitive. Zero and ninety degrees are not used since these correspond to a situation where one intensity is zero, and this introduces computational difficulties as well as being unlikely when the overlap is large. Conventional phases are permuted in the usual way. Each choice of conventional and pseudophase defines a node on the second level of the phasing tree, and each node is subjected to constrained entropy maximization. At convergence, each node has associated with it an LLG computed using the generalized form of likelihood when powder overlaps are present.

The likelihood estimates are then analysed. When pseudophase permutation is involved, the LLG analysis is divided into two stages: pseudophases and conventional phases. Since a four-point sampling method is used for the splitting angles instead of the coarse binary sampling for conventional phases, an *F*-test is first invoked to test if pseudophase permutations have a statistical effect on the LLG at a given significance level. When significant differences do exist, the LLG means for all permuted pseudophase values are compared using Duncan's procedure at either the 1 per cent or 5 per cent level. If no significant differences are found, then the LLG is not sensitive to the relevant pseudophases. If this is the case then the overlaps can be deconvoluted by multiplicity-weighted, equipartitioning (pseudophase = $\pi/4$). This is surprisingly frequent, and may possibly arise from our use of likelihood in its simplest diagonal approximation (Bricogne and Gilmore 1990). Other, more sophisticated likelihood formalisms (Bricogne 1993, 1997a) may prove more sensitive.

If the significance test indicates suitable pseudophases, then the conventional phase angles are extracted by the methods described above. If necessary, another cycle of tree-building and entropy maximization can then be carried out.

An example: SAPO-40. SAPO-40 $[(\text{Si}, \text{Al}, \text{P})_{64}\text{O}_{128} \cdot 4\text{TPAOH}]$ is a large pore molecular sieve. Its structure has been reported by Dumont *et al.* (1993) and McCusker and Baerlocher (1995). The data were collected at a synchrotron source, and only 18 per cent of the reflections present could be treated as being 'independent' in the intensity extraction stage, the remainder falling into numerous clumps of overlapped reflections. The space group $Pm\bar{m}n$ was used with cell parameters $a = 21.9410$, $b = 13.6912$, $c = 7.1244 \text{ \AA}$. As McCusker and Baerlocher have shown, this is acceptable until atom-type designation is imposed for P and Al; this causes a doubling of the c -axis and the space group becomes $Pccn$. However, as a starting point for Rietveld refinement, the smaller cell is sufficient. In general, the LLGs were not sensitive to overlap partitioning, but some phasing sequences were successful, and the following demonstration of the feasibility of magnitude partitioning is typical:

1. An origin was defined in the usual way to generate the root node. Eight non-overlapped reflections were given permuted phases, generating a 256 node second level. As this was simply a feasibility test, the node corresponding to a zero degree phase error (with respect to the known phases from the known crystal structure) was chosen at this point for subsequent tree building.
2. Fourteen reflections were given permuted phases, and the strongest overlap involving the (240) and (601) reflections was given true and pseudophase permutation. Since this would generate $2^{16} \times 4 = 65,536$ nodes in a full factorial design, a Nordström–Robinson code was used as a source of phase

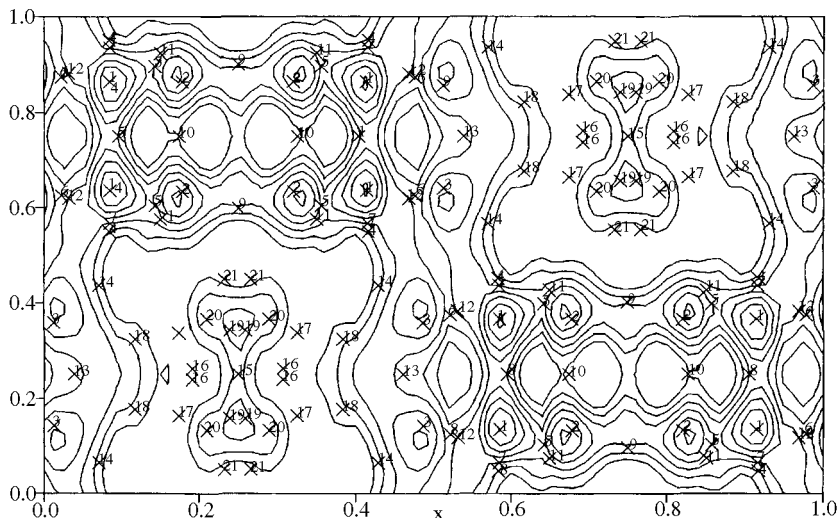


Fig. 14.5. The best centroid map for SAPO-40 projected down the c -axis. The pore is clearly visible. The crosses numbered 15–21 are the tetrapropylammonium hydroxide ions in the 12-ring channel.

permutation (Bricogne 1993, 1997*b*; Gilmore and Bricogne 1997; Gilmore *et al.* 1999). This procedure is discussed further in the next section. The use of the Nordström–Robinson code plus pseudophase permutation generated only 1024 nodes.

3. The Duncan procedure operating at a 5 per cent confidence level indicated a pseudophase angle of 72° for the overlap; a value of 54° was not significantly different although it had a lower average LLG. The mean of these indications, 63° , is in excellent agreement with the true value of 61° established from the refined structure. Analysis at the 1 per cent level instead of 5 per cent indicated no significant differences. The best map shown in projection down the z -axis with the atomic coordinates indicated as crosses is shown in Fig. 14.5. It is of high quality, with most of the density in correct places and the pore clearly visible.

14.9 The maximum entropy method and the need for experimental designs

There is an obvious computational problem associated with the ME formalism. If n nodes are retained at a given level, and there are m degrees of freedom for each of the p reflections that are about to be phase permuted, then any full factorial permutation will generate $n \cdot m^p$ phase sets, all of which need to be subjected to constrained entropy maximization. The problem is significantly worsened if pseudophases are used and, magnitude of the computational problem aside, it can be difficult to interpret the results due to the sheer number of phase sets generated. A highly effective way of reducing the number of sets that need to be generated in order to cover the same phase space is to use suitable error-correcting codes (ECCs) as a source of experimental design (Bricogne 1993, 1997*b*; Gilmore *et al.* 1999). ECCs are a part of digital communication, a subject on which there is a huge volume of literature. A discussion of ECCs and the origin of their properties lies outside the scope of this chapter, but a good introduction comes from Hill (1993), while the classic book is by MacWilliams and Sloane (1977). Outside the world of communications, the relationship between some ECCs, experimental designs and combinatorics is well documented (see, for example, Anderson 1989). Furthermore, there is a link between certain ECCs and experimental designs (Bricogne 1993, 1997*b*) which can be used as an efficient source of phase permutation in *ab initio* phasing.

14.9.1 Error correcting codes and their use in MICE

Most ECCs are unsuitable for our purposes; useful ones contain a suitable experimental design that balances both the main reflection phases and the interactions between them, as well as covering the phase space with optimum efficiency. Selecting suitable candidates is a non-trivial task, but those listed in Table 14.5 have suitable properties and were first employed in the BUSTER computer program (Bricogne 1993).

Table 14.5 Properties of certain ECCs selected as a source of phase permutation. The last column indicates the maximum number of incorrect phase indications guaranteed to be present in one of the generated sets

| Name of code | Degrees of freedom | No. sets generated | No. sets generated in full factorial | Maximum no. wrong phases in best set |
|---|--------------------|--------------------|--------------------------------------|--------------------------------------|
| [8, 4, 4] Hadamard | 8 | 16 | 256 | 2 |
| [7, 4, 3] Hamming | 7 | 16 | 128 | 1 |
| [15, 11, 3] Hamming | 15 | 2048 | 32 768 | 1 |
| [16, 11, 4] Hadamard | 16 | 2048 | 65 536 | 2 |
| [16, 256, 6] Nordström–Robinson | 16 | 256 | 65 536 | 4 |
| [15, 256, 5] punctured Nordström–Robinson | 15 | 256 | 32 768 | 3 |
| [24, 12, 8] Golay | 24 | 4096 | 16 777 216 | 4 |
| [23, 12, 7] punctured Golay | 23 | 4096 | 8 388 608 | 3 |

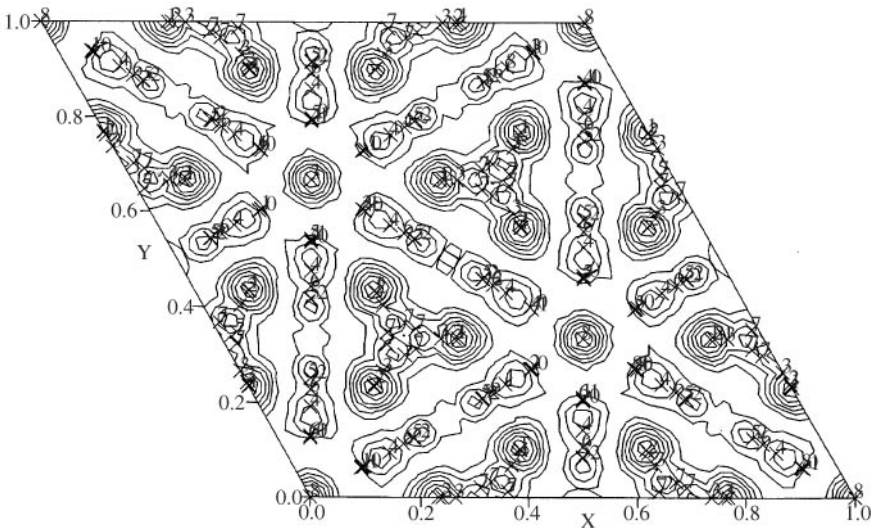


Fig. 14.6. The NU-3 structure projected down the *c*-axis for node 3349.

To use codes for phase permutation is straightforward. For centric phases the binary digit ‘0’ represents one possible choice, and ‘1’ the alternative, *e.g.* for a phase restricted to 0 or π , 0 represents a phase angle of 0 and 1 represents an angle of π . In the acentric situation two bits are used to assign the quadrant of the phase; one bit describes the sign of the real part of the phase and the second the imaginary part, that is, 0, 0 = $\pi/4$, 1, 0 = $3\pi/4$, 1, 1 = $5\pi/4$ and 0, 1 = $7\pi/4$.

The [24, 12, 8] Golay code and the NU-3 powder dataset. McCusker and Baerlocher have reported two forms of the zeolite NU-3 (McCusker 1993; Baerlocher and McCusker 1994) which has the LEV-type framework. In one case 1-aminodiamantane (ADAM) was used in the synthesis and in the other N-methylquinuclidinium iodide (QUIN). We have used the ADAM form. The space group is $R\bar{3}m$ with $a = 13.2251$ and $c = 22.2916$ Å. There are 373 reflections in total of which 199 are in 80 overlap sets with up to seven under a single overlap envelope; the maximum resolution is 1.1 Å. The origin was defined by the 1 0 7 reflection with a U magnitude of 0.345. Twenty-four reflections were given permuted phases using the [24, 12, 8] Golay code, generating 4096 nodes. The resulting LLG analysis based on values that included the overlapped reflections at the 5 per cent significance level produced a centroid map for the top ranked solution that is shown in Fig. 14.6. The entire zeolite framework and the envelope of the ADAM guest molecule are clearly visible.

14.10 Conclusions and other possibilities

The power of the ME method in solving structures from powder diffraction data has been demonstrated. Some future developments that are currently under investigation are:

1. *Phase refinement.* Errors naturally accumulate with ECCs when building phasing trees, and phase refinement is therefore a necessary development. In general, the tangent formula is unstable with much of the data under investigation, because it is sparse or of low resolution. The Bayesian method based on likelihood optimization that we have sometimes employed (Bricogne and Gilmore 1990; Gilmore *et al.* 1990) can be useful, but is sometimes unstable or unable to refine phases very far from their initial values.

2. *Better use of overlaps.* In the powder diffraction case, ECCs can be used as a source of spherical designs for hyperphase permutation (Bricogne 1991, 1997*b*). This means that both phases and amplitudes of overlapped reflections can be permuted using the appropriate codes, and *both* can be recovered with suitable analysis of the associated LLGs.

3. *Fragment searching.* There has been a great deal of activity in using structural fragments translated and rotated through the unit cell to solve organic crystal structures from powder data (see, for example, Harris and Tremayne 1996; Kariuki *et al.* 1997; Shankland *et al.* 1997). These methods use various search procedures (e.g. genetic algorithms, simulated annealing) to carry out the search. Codes provide an efficient way of defining the initial search parameters (Bricogne 1997*b*) and could potentially be used to increase the power of these methods by providing more efficient starting points. We have used codes to define molecular envelopes as a starting point in modelling studies of this type with considerable success (Tremayne *et al.* 1997).

4. *Envelope determination.* The ME method is often very effective with low resolution data (see, for example, Gilmore *et al.* 1996) and can produce maps that effectively define a molecular envelope. This can be used as a starting point for modelling calculations, and can be used more rigorously by incorporating the envelope as a penalty function in an optimization procedure (Brenner *et al.* 1997).

5. *Codes.* The literature on coding theory is enormous. Other codes, not necessarily binary, may well exist with excellent design and covering properties that could extend the scope of ECCs.

Acknowledgements

We thank Lynne McCusker and Christian Baerlocher for the SAPO-40 and NU-3 datasets, Phil Lightfoot, Maryjane Tremayne and Peter Bruce for the remaining datasets used here, and the EPSRC and Eastman Kodak, USA for financial support.

References

- Abramowitz, M. and Stegun, I. A. (1970). *Handbook of Mathematical Functions*. Dover Publications Inc., New York.
- Anderson, I. (1989). *A First Course in Combinatorial Mathematics*. Ch. 6 and 7. Oxford University Press.
- Baerlocher, Ch. and McCusker, L. B. (1994). *Studies in Surface Science and Catalysis*, **85**, 391–428.
- Brenner, S., McCusker, L. B. and Baerlocher, Ch. (1997). *J. Appl. Crystallogr.*, **30**, 1167–72.
- Bricogne, G. (1984). *Acta Crystallogr. A*, **40**, 410–45.
- Bricogne, G. (1991). *Acta Crystallogr. A*, **47**, 803–29.
- Bricogne, G. (1993). *Acta Crystallogr. D*, **49**, 37–60.
- Bricogne, G. (1997a). *Methods in Enzymol.*, **276**, 361–423.
- Bricogne, G. (1997b). *Methods in Enzymol.*, **276**, 424–48.
- Bricogne, G. and Gilmore, C. J. (1990). *Acta Crystallogr. A*, **46**, 284–97.
- Cochran, W. G. and Cox, G. M. (1957). *Experimental Designs*, pp. 75–6. John Wiley, New York.
- Dong, W. and Gilmore, C. J. (1998). *Acta Crystallogr. A*, **54**, 438–46.
- Dumont, N., Gabelica, Z., Derouane, E. G. and McCusker, L. B. (1993). *Microporus Mater.*, **1**, 149–60.
- Duncan, D. B. (1955). *Biometrics*, **11**, 1–42.
- Gilmore, C. J., Bricogne, G. and Bannister, C. (1990). *Acta Crystallogr. A*, **46**, 297–308.
- Gilmore, C. J., Henderson, K. and Bricogne, G. (1991). *Acta Crystallogr. A*, **47**, 830–41.
- Gilmore, C. J. (1996). *Acta Crystallogr. A*, **52**, 561–89.
- Gilmore, C. J., Nicholson, W. V. and Dorset, D. L. (1996) *Acta Crystallogr. A*, **52**, 937–46.
- Gilmore, C. J. and Bricogne, G. (1997). *Methods Enzymol.*, **277**, 65–78.

- Gilmore, C. J., Marks, L. D., Grozea, D., Collazo, C., Landree, E. and Twesten, R. (1997). *Surface Sci.*, **381**, 77–91.
- Gilmore, C. J., Bricogne, G. and Dong, W. (1999). *Acta Crystallogr. A*, **55**, 70–83.
- Harris, K. D. M. and Tremayne, M. (1996). *Chem. Mater.*, **8**, 2554–70.
- Hill, R. (1993). *A First Course in Coding Theory*, Oxford University Press.
- Kariuki, B. M., Serrano-González, H., Johnston, R. L. and Harris, K. D. M. (1997). *Chem. Phys. Lett.*, **280**, 189–95.
- MacWilliams, F. J. and Sloane, N. J. A. (1977). *The Theory of Error-Correcting Codes*, North-Holland, Amsterdam.
- McCusker, L. B. (1993). *Mater. Sci. Forum*, **133–136**, 423–34.
- McCusker, L. B. and Baerlocher, Ch. (1995). *Microporus Materials*, **6**, 51–4.
- Pearson, E. S. and Hartley, H. O., (ed.) (1966). *Biometrika Tables for Statisticians, Volume I.*, Table 29, Cambridge University Press, Cambridge.
- Shankland, K., Gilmore, C. J., Bricogne, G. and Hashizume, H. (1993). *Acta Crystallogr.*, **A49**, 493–501.
- Shankland, K. (1994). *Trans. Amer. Crystallogr. Assoc.*, **30**, 29–39.
- Shankland, K., David, W. I. F. and Csoka, T. (1997). *Z. Kristallogr.*, **212**, 550–2.
- Sim, G. A. (1959). *Acta Crystallogr.*, **12**, 813–15.
- Tremayne, M., Lightfoot, P., Glidewell, C., Mehta, M. A., Bruce, P. G., Harris, K. D. M., Shankland, K., Gilmore, C. J. and Bricogne, G. (1992a). *J. Solid State Chem.*, **100**, 191–6.
- Tremayne, M., Lightfoot, P., Harris, K. D. M., Shankland, K., Gilmore, C. J., Bricogne, G. and Bruce, P. G. (1992b). *J. Mater. Chem.*, **2**, 1301–2.
- Tremayne, M. (1995). PhD Thesis, Ab-initio Structure Determination from X-ray Powder Diffraction Data. St. Andrews University.
- Tremayne, M., Dong, W. and Gilmore, C. J. (1997). American Crystallographic Association Meeting, St. Louis, Abstract SuB06.

Global optimization strategies

Kenneth Shankland and William I. F. David

15.1 Introduction

Global optimization methods that involve the assessment of multiple trial crystal structures in real space offer a powerful method of structure solution from powder diffraction data. High quality atomic-resolution density maps are difficult to obtain for even moderately complex structures using powder diffraction data because of Bragg peak overlap. This makes the direct location of atomic positions from density maps a far more difficult exercise for powder data than it is for traditional single-crystal Direct methods and Patterson techniques. With global optimization methods, this process is circumvented because the task is not to identify atomic density from first principles but to match atomic density with atomic positions in a trial crystal structure.

One large class of important materials that lends itself to this approach is that of molecular organic compounds. These materials generally possess low symmetry and have relatively large unit cells and no particularly strongly scattering atoms. Over the past few years, a growing number of crystal structures of organic, and particularly pharmaceutical, compounds have been solved using these real-space techniques. The principal advantage of the real-space global optimization approach can be understood in terms of basic information theory. The information content in a powder diffraction pattern is small compared with a single-crystal measurement and often too small compared with the information required to describe the crystal structure itself. Real-space global optimization strategies that involve the incorporation of sufficient additional chemical knowledge can shift the information balance from a deficit to a surplus. This chemical knowledge can take a number of forms (Chapter 17). One of the most convenient and easiest to exploit is the known molecular topology, or polyhedral connectivity and coordination of the system under study.

In the direct-space approach, adjustments are made in real space to a trial model of the crystal structure in order to maximize the agreement between the calculated and the measured diffraction data.¹ As such, these real space

¹ This assumes that the unit cell and space group have already been determined; this is not always a straightforward task (see Chapters 7 and 8).

approaches have many of the hallmarks of traditional structure refinement. Conventional refinement, however, requires a good approximate starting model and thus is not usually regarded as a structure solution technique. What, one might then ask, differentiates global optimization structure solution from conventional structure refinement? This chapter shows that these trial-and-error methods may indeed be viewed as *global* Rietveld refinements, and outlines the significant number of variants on this theme that have been developed in recent years.

15.2 Background

Given a known unit cell, space group, and a set of atomic coordinates with corresponding atom types, the structure factors for a trial crystal structure may be calculated according to the standard formula:

$$F_{\mathbf{h}} = \sum_{j=1}^N f_j \exp(2\pi i \mathbf{h} \cdot \mathbf{r}_j). \quad (15.1)$$

The agreement between the calculated structure factors and a set of 'single-crystal' structure factors, or structure factors of non-overlapped reflections extracted from a powder diffraction pattern may be calculated using any of a number of Bragg R -factors such as the $|F|$ R -factor:

$$R = \frac{\sum_{\mathbf{h}} \left| |F_{\mathbf{h}}^c| - |F_{\mathbf{h}}^o| \right|}{\sum_{\mathbf{h}} |F_{\mathbf{h}}^o|}. \quad (15.2)$$

Although some early implementations of global optimization strategies used only non-overlapped reflections, most current approaches now also include overlapped reflections. This is most conventionally achieved using an agreement factor based upon the full diffraction profile. Alternatively (and equivalently) an agreement factor based upon the correlated integrated intensities extracted from the full profile may also be used (Section 15.6).

The chances of randomly placing all of the atoms in a crystal structure in their correct positions are vanishingly small, even if some assumptions are made about the way in which the atoms are related to one another (Section 15.4). Accordingly, the trial structure must be adjusted in some manner in order to explore the function that describes the agreement between the calculated and measured diffraction data. For the purposes of this discussion, this function can be thought of in terms of an N -dimensional hypersurface, where N is the number of structural parameters that must be varied to describe all the possible trial structures that make chemical sense. Structure solution is then equivalent to searching for, and locating the position of, the minimum value of the N -dimensional hypersurface. If the optimization procedure involves matching

the full diffraction pattern, then the surface to be searched would be either the Rietveld χ^2 or a profile R -factor. These surfaces exhibit multiple minima (Fig. 15.1) as a function of the N variable parameters.

These minima may be divided into two sets: (a) the *global* minimum that corresponds to the fully determined crystal structure and (b) *local* minima that correspond to incorrectly determined crystal structures. In a structure *refinement*, it is generally assumed that an initial model has been obtained from a similar structure in a database, or from a Patterson or Direct methods structure solution. Furthermore, for a successful refinement, it must also be the case that the initial model is sufficiently close to the true crystal structure in order that the current function value lies within the radius of convergence of the N -dimensional well that surrounds the global minimum. If these conditions hold, then conventional least-squares methods of refinement are able to locate quickly the precise global minimum. However in the absence of a well-positioned starting model (as is the case with a random trial structure), standard least-squares refinement simply locates the closest local minimum and terminates at that point. This is a fruitless strategy for structure determination. Global optimization algorithms on the other hand, possess the ability to escape

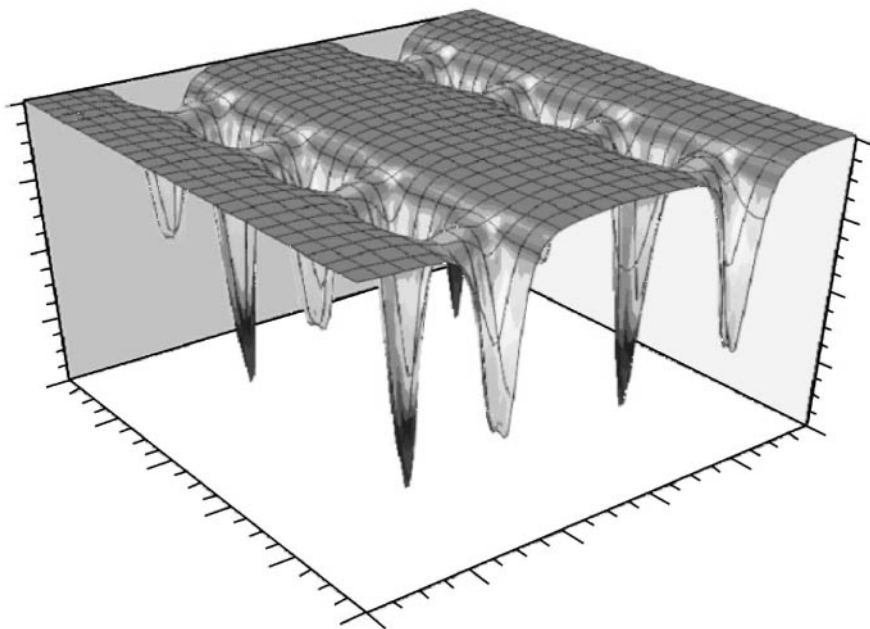


Fig. 15.1. A two-dimensional section through the 12-dimensional χ^2 hypersurface of famotidine form B. The flat regions of the surface correspond to χ^2 values of approximately 1000, while the deepest minima correspond to χ^2 values of approximately 200.

from local minima and are thus able, in principle, to locate the global minimum from any random starting point. As such, they have great significance for structure determination and are discussed in more detail in Section 15.5.

Figure 15.2 shows a flow chart of a generic global optimization strategy; each of the heavily outlined blocks is described in the following pages.

There is a certain amount of confusing terminology employed in some powder diffraction papers regarding global optimization. For example, a distinction might be drawn between a ‘Monte Carlo’ method and simulated annealing. To avoid confusion, we state that ‘Monte Carlo’ implies a method that involves some element of random sampling, while noting that its use in the simulation of crystal structures almost always implies use of importance sampling. Note that the term ‘Reverse Monte Carlo’ is also employed by some

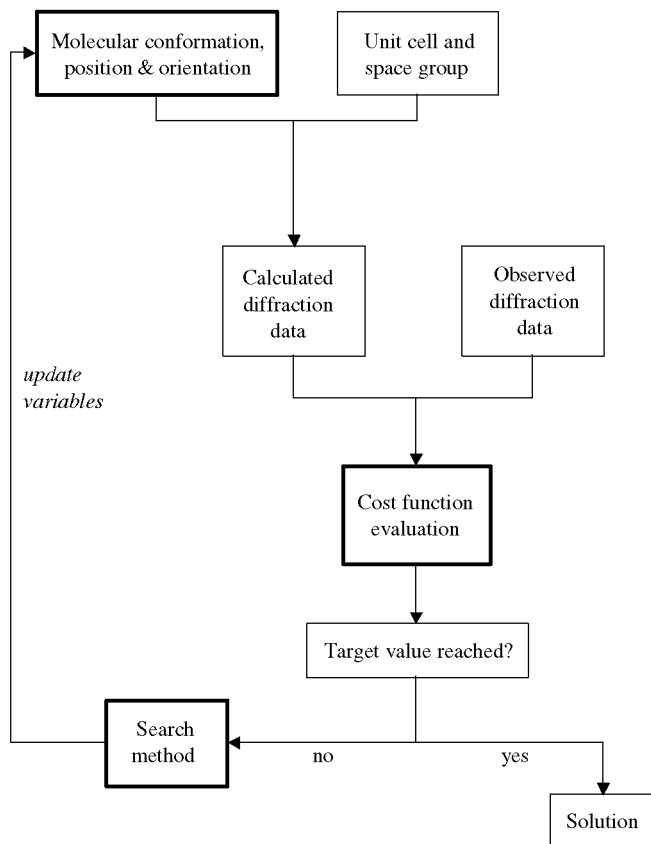


Fig. 15.2. A generic flow chart for implementing a global optimization approach to crystal structure solution. The heavily outlined blocks represent the key components discussed in the chapter.

authors to describe a particular Monte Carlo computational methodology developed for the solution of disordered crystal structures and liquid structures (see Keen 1998, for a concise description of RMC). Furthermore, we use the term 'global optimization' throughout this chapter to represent both *search* and *optimization* algorithms, bearing in mind that 'global search' and 'global optimization' are normally used interchangeably in the literature (Hazelrigg 1996).

15.3 Describing a crystal structure

The most straightforward description of a crystal structure consists of specifying N independent atoms located with fractional coordinates (x, y, z) in the asymmetric unit of a unit cell. With such a description, any configuration of atoms can be generated, whether physically reasonable or otherwise, and it is then the task of the cost function to discriminate between reasonable and unreasonable solutions. This cost function can gradually impose chemical sense through evaluation of energy terms such as those derived from bond valence rules (Pannetier *et al.* 1990; Bush *et al.* 1995), calculation of the level of agreement with a powder diffraction pattern (Solovyov and Kirik 1993), or some combination thereof (Putz *et al.* 1999). Geometry refinement of tentative atomic arrangements is possible through distance-least-squares refinement (Baerlocher *et al.* 1976; Deem and Newsam 1989). This description is not confined to ordered crystal structures but has also found applicability in modelling disordered structures, such as vitreous silica (Keen 1997). Intuitively, the N independent atom formulation seems best suited to the solution of inorganic crystal structures, where the extended connectivity of the crystal structure is generally unknown at the outset. In cases where the molecular connectivity of a compound under study is known, it is possible to transform these $3 \cdot N$ parameters into a smaller set by describing the molecule as a series of connected atoms. One simple way of doing this is to describe the molecule in terms of bond lengths, bond angles and torsion angles. For example, an internal coordinate description of a famotidine molecule (Fig. 15.3) is given in Table 15.1.

Given that the covalent bond lengths and bond angles for famotidine can be estimated with sufficient accuracy,² one may construct a three-dimensional molecular description in which the only unknowns are the values of six torsion angles. By inserting trial torsion angle values into these points in this Z -matrix, different molecular conformations can be generated. Recognizing that the position and orientation of a famotidine molecule within the asymmetric unit can be described by a single x, y, z position and three Euler angles, each trial

² Values for covalent bond lengths and bond angles may be obtained from published tables, or by analysing polymorphs or other related crystal structures in the Cambridge Structural Database.

Table 15.1 An internal coordinate description of the famotidine molecule shown in Fig. 15.3

| # | Atom | Length | Angle | | Torsion | | Bond to | Angle with | Torsion with |
|----|------|--------------|----------|--------------|----------|--------------|----------|------------|--------------|
| 1 | C | 0.900 | 0 | 0.0 | 0 | 0.0 | 0 | 0 | 0 |
| 2 | H | 0.900 | 0 | 0.0 | 0 | 0.0 | 0 | 1 | 0 |
| 3 | H | 0.900 | 0 | 109.5 | 0 | 0.0 | 0 | 1 | 2 |
| 4 | C | 1.540 | 0 | 109.5 | 0 | 120.0 | 0 | 1 | 2 |
| 5 | C | 1.510 | 0 | 109.5 | 0 | 0.0 | 1 | 4 | 1 |
| 6 | H | 0.900 | 0 | 109.5 | 0 | 120.0 | 0 | 4 | 1 |
| 7 | H | 0.900 | 0 | 109.5 | 0 | 240.0 | 0 | 4 | 1 |
| 8 | N | 1.310 | 0 | 115.0 | 0 | 180.0 | 1 | 5 | 4 |
| 9 | N | 1.310 | 0 | 117.0 | 0 | 180.0 | 0 | 5 | 4 |
| 10 | H | 0.900 | 0 | 120.0 | 0 | 0.0 | 0 | 8 | 5 |
| 11 | H | 0.900 | 0 | 120.0 | 0 | 180.0 | 0 | 8 | 5 |
| 12 | S | 1.610 | 0 | 120.0 | 0 | 180.0 | 0 | 9 | 5 |
| 13 | O | 1.440 | 0 | 109.5 | 0 | 180.0 | 1 | 12 | 9 |
| 14 | O | 1.440 | 0 | 109.5 | 0 | 120.0 | 0 | 12 | 9 |
| 15 | N | 1.630 | 0 | 109.5 | 0 | 240.0 | 0 | 12 | 9 |
| 16 | H | 0.900 | 0 | 109.5 | 0 | 60.0 | 0 | 15 | 12 |
| 17 | H | 0.900 | 0 | 109.5 | 0 | 180.0 | 0 | 15 | 12 |
| 18 | S | 1.810 | 0 | 109.5 | 0 | 120.0 | 0 | 1 | 4 |
| 19 | C | 1.830 | 0 | 102.0 | 0 | 180.0 | 1 | 18 | 1 |
| 20 | C | 1.490 | 0 | 109.5 | 0 | 180.0 | 1 | 19 | 18 |
| 21 | H | 0.900 | 0 | 109.5 | 0 | 120.0 | 0 | 19 | 18 |
| 22 | H | 0.900 | 0 | 109.5 | 0 | 240.0 | 0 | 19 | 18 |
| 23 | C | 1.357 | 0 | 126.0 | 0 | 180.0 | 1 | 20 | 19 |
| 24 | S | 1.726 | 0 | 110.0 | 0 | 180.0 | 0 | 23 | 20 |
| 25 | C | 1.756 | 0 | 90.0 | 0 | 0.0 | 0 | 24 | 23 |
| 26 | N | 1.317 | 0 | 113.0 | 0 | 0.0 | 0 | 25 | 24 |
| 27 | H | 0.900 | 0 | 125.0 | 0 | 180.0 | 0 | 23 | 20 |
| 28 | N | 1.356 | 0 | 130.0 | 0 | 180.0 | 0 | 25 | 26 |
| 29 | C | 1.335 | 0 | 120.0 | 0 | 0.0 | 0 | 28 | 25 |
| 30 | N | 1.330 | 0 | 125.0 | 0 | 0.0 | 0 | 29 | 28 |
| 31 | N | 1.330 | 0 | 118.0 | 0 | 180.0 | 0 | 29 | 28 |
| 32 | H | 0.900 | 0 | 120.0 | 0 | 0.0 | 0 | 30 | 29 |
| 33 | H | 0.900 | 0 | 120.0 | 0 | 180.0 | 0 | 30 | 29 |
| 34 | H | 0.900 | 0 | 120.0 | 0 | 0.0 | 0 | 31 | 29 |
| 35 | H | 0.900 | 0 | 120.0 | 0 | 180.0 | 0 | 31 | 29 |

The six rows highlighted in bold correspond to the torsion angles flagged for optimization. The description, in Z-matrix format, is read as follows, taking the first highlighted line as an example: atom five is bonded to atom four at a distance of 1.51 Å; it makes a bond angle of 109.5° with atoms four and one, and a torsion angle of 0° with atoms four, one and three. The zeros and ones following each distance or angle entry denote whether or not the corresponding entry is to be optimized.

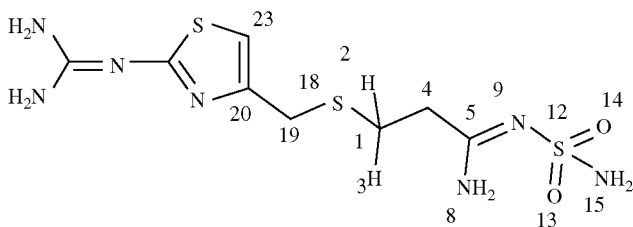


Fig. 15.3. The molecular structure of famotidine, with the atom numbering scheme corresponding to the scheme used in Table 15.1.

crystal configuration can now be described in terms of only 12 independent variables³ rather than the 105 needed for an individual atom description. All solutions are restricted to this 12-dimensional sub-space of the 105-dimensional atomic coordinate space such that only these 12 variables need be altered in order to optimize the fit to the measured diffraction data and thus solve the crystal structure. Note that those fragment rotations that have little impact upon the overall diffraction pattern, for example the rotation of a methyl group, are typically ignored. The transformations required to convert a stereochemical description of a molecule in Cartesian space into a trial crystal structure are discussed in Chapter 16. This type of stereochemical description can accommodate variation of bond lengths or bond angles equally well, although sensible bounds on the variable parameters are required (see Chapter 16). While torsion angles are normally allowed to rotate in the range 0–360°, appropriate bounds may be placed if required. For example, the rotation of a carboxylic acid group, while properly described by a 0–360° rotation, can be approximated by 0–180° rotation since the H-atom makes a negligible contribution to the overall scattering of the group. Similarly, an amide group might be constrained to adopt a *trans* planar configuration with $\pm 10^\circ$ latitude, based on observation of the preferred configuration of this bond in known crystal structures.

A related approach (Favre-Nicolin and Cerny 2004) that may offer advantages in terms of the efficiency with which the global minimum is located defines molecules through a series of restraints rather than the more ‘rigid’ Z-matrix approach just described.

15.4 Calculating the odds

Given the infinite number of trial crystal structures that may be randomly generated for a particular structure solution problem, the probability of

³ If quaternion numbers are used to describe the orientation of the molecule then the number of variables increases by one to 13, although the number of independent variables is still 12 (see Leach 1996).

obtaining the correct crystal structure by chance is vanishingly small. However, it is an interesting exercise to calculate exactly how small this probability is, given certain assumptions. Consider firstly a method of structure solution that involves placing atoms at random into a unit cell. Taking the case of an organic molecule, ignoring the hydrogen atoms and treating all the remaining atoms as equal scatterers, then the structure might be said to be solved if all atoms are positioned within approximately $r = 0.4 \text{ \AA}$ of a correct atomic position. Given that each atom in an organic structure occupies a volume of around 20 \AA^3 and enforcing the condition that atoms are not permitted to be closer than $s \approx 1.5 \text{ \AA}$ of one another, then the probability of obtaining the correct structure is of order

$$p \approx N! \left(\frac{\frac{4}{3} \pi r^3}{20 - \frac{4}{3} \pi s^3} \right)^N \approx \frac{Nr^3}{(5 - s^3)e} \approx \left(\frac{N}{200} \right)^N. \quad (15.3)$$

For a 10-atom structure, $p \approx 10^{-13}$, about a million times less likely than the chances of winning the UK national lottery. In the same way that one is guaranteed to win the lottery if one purchases all of the possible tickets, this type of problem can be solved by a *grid search* in which the atoms are moved systematically around the x, y, z space of the asymmetric unit on a number of discrete grid points, in such a way that all feasible atomic configurations are explored. For example, one might choose to divide the asymmetric unit into a $10 \times 10 \times 10$ grid, giving 10^3 possible atomic locations for each atom and a total (ignoring the possibility of atomic overlap) of 10^{30} atomic configurations. Grid searches are therefore not to be recommended even in this crystallographically simple case. For a 50-atom structure, $p \approx 10^{-30}$ and the situation is even worse.

Building in the molecular topology as outlined in Section 15.3 improves the odds of obtaining a correct crystal structure by many orders of magnitude. For example, imagine that the 10-atom structure mentioned above is in fact the non-H atom structure of naphthalene; the only degrees of freedom for this problem are the position and orientation of the rigid body within the unit cell. Working on the assumption that the radius of convergence for the location of a molecule is of order of 0.7 \AA , the probability of locating the correct molecular position is then $(0.7 \text{ \AA})^3 / 200 \text{ \AA}^3 \approx 1/600$. Given that determining the molecular orientation is a problem of similar complexity, then solving the 10-atom problem reduces to a $\approx 10^6$ point grid search. Suddenly, the grid search has become tractable and rigid structures may be solved using this approach (Section 15.5). However, noting that each additional degree of freedom (typically a torsion angle) increases the number of trial structures by a power of *at least* 10 (the figure of 10 assumes sampling the torsion angle in coarse steps of 36°) then a 10 torsion angle problem requires the evaluation of an enormous number (10^{16}) of structures. Even if 10 000 structures could be calculated and tested every second, the grid search process would take around 30 000 years. How then, can more sophisticated global optimization algorithms render these calculations feasible? The broad answer to this question is that, although algorithms such as simulated annealing can in principle visit every

trial structure, they never do. Instead, they may be regarded as ‘a random walk among the good solutions’. Taking this analogy further, a one in 10^{16} probability approximates to finding the highest square metre on the surface of the Earth. While a grid search laboriously tests each point on the earth’s surface in turn, an algorithm such as simulated annealing is predisposed to searching the mountain ranges, with a bias always for going uphill.

By way of confirming the empirical orders of magnitude discussed above, the nature of the χ^2 hypersurface associated with the structure solution of famotidine form B was investigated. This problem is discussed fully in Section 15.8 but for the moment, it suffices to say that famotidine has six internal degrees of freedom. Using the simple arguments outlined above, the chances of randomly finding the correct trial structure should be around one in 10^{12} . To check these probabilities, 10^5 trial structures were generated and their calculated powder diffraction patterns compared with the observed data. The resultant decaying exponential χ^2 distribution is shown on a logarithmic scale in Fig. 15.4.

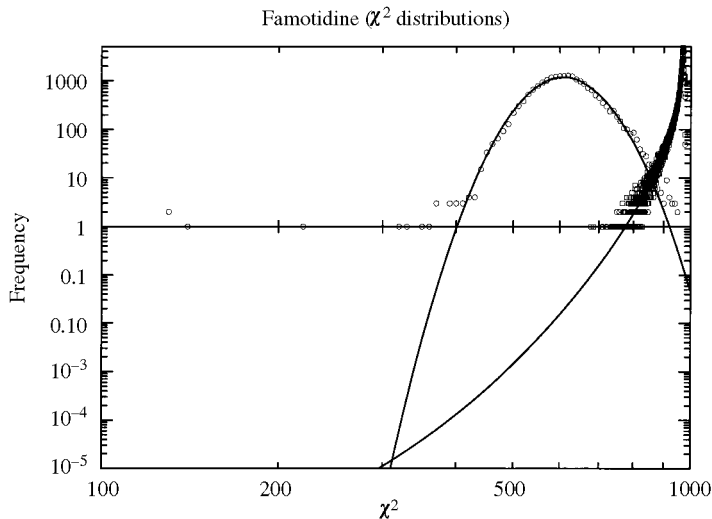


Fig. 15.4. The log–log frequency distributions of simplex-optimized and randomly chosen chi-squared values for famotidine. Nearly all the χ^2 values of the 100 000 random structures are located between 900 and 1000. The fit to the rapidly decaying exponential distribution associated with the random structures indicates that low χ^2 values are extremely unlikely. The 20 000 simplex-optimized structures, obtained from random start positions, follow a log-normal distribution. These structures and their associated χ^2 values represent the distribution of semi-global minima. A few structures (*c.* 14) have χ^2 values that are anomalously low and deviate significantly from the log-normal distribution. All of these structures have some of the characteristics of the correct structure. Only two simplex minimizations, however, give the correct structure, indicating that it is very difficult to obtain the global minimum in among a complex topology of multiple local minima.

Unsurprisingly, the correct solution ($\chi^2 \approx 124$) was not among any of the trial structures, with the majority of solutions corresponding to symmetry equivalent molecules lying on top of one another. The distribution falls off exponentially and based upon this, one may calculate that the chances of obtaining the correct structure are ~ 1 in 10^{13} , a figure in good agreement with the empirical estimates made earlier. Further insight into the nature of the structure solution χ^2 hypersurface may be obtained by plotting sections of this surface. Figure 15.1 is in fact a plot of the two-dimensional centre-of-mass x - z section of the 12-dimensional χ^2 space taken at the correct solution point. There are two sets of four identical minima corresponding to four equivalent correct and four incorrect solutions belonging to the four different asymmetric units in the unit cell. The incorrect solutions are related to the correct solutions by a pseudo-symmetry element, which is often found to occur in global optimization methods. The minima are deep, with the plateaux between the correct solutions corresponding to some of the very worst fits with $\chi^2 \sim 1000$. The proximity of such poor fits to the correct solution highlights the difficulties in locating the correct solution; all but two of the twelve parameters can be correct and yet the goodness of fit is still very poor. Finally, the hypersurface is very smooth with no high frequency features. This is a general feature of direct space approaches to structure solution. The width of these features may be estimated by noting that the Rietveld χ^2 is equivalent to the correlated integrated intensities χ^2 (see Section 15.6.1). Through Parseval's theorem, this χ^2 is the same as the volume integral of the squared difference between the sharpened, observed and calculated Patterson maps. This correlation function has features that are similar in shape and width to a vector peak in a Patterson map and this corroborates the observation in Fig. 15.1 that the χ^2 hypersurface has smooth Gaussian features with a full width at half maximum of around 2 \AA .

15.5 Beating the odds—global optimization algorithms

Global optimization problems are ubiquitous and a large number of different strategies have been developed for tackling them (Horst and Pardalos 1995; Floudas 1999). The global optimization problem in powder diffraction is analogous to the conformational search problem in molecular modelling (Leach 1996), with the additional complication that the position and orientation of a molecule in the unit cell must also be identified. It is therefore unsurprising that many of the optimization methods employed in molecular modelling are transferable to the crystal structure solution problem.

The simplest approach is to perform an exhaustive grid search over the parameter space of interest. This approach, although naïve, at least has the merit of guaranteeing that the global minimum will be found providing that a suitably fine grid is employed, and has been applied successfully to some problems in powder diffraction where the parameter space is relatively small

(Hammond *et al.* 1997; Chernyshev and Schenk 1998). However, more efficient search methods are required to deal with the ‘combinatorial explosion’ that arises when dealing with torsionally complex molecular structures. We focus here almost exclusively upon *stochastic* approaches that can also be classified as *heuristic*, in that they produce non-exact, good quality solutions in a reasonable amount of time.

15.5.1 *A search method with a physical basis—simulated annealing*

Simulated annealing (SA) is the Monte Carlo method that is currently the most widely used optimization method for solving structures from powder diffraction data (Andreev *et al.* 1997; David *et al.* 1998; Engel *et al.* 1999; Putz *et al.* 1999; Coelho 2000; Pagola *et al.* 2000; Stephenson 2000; Coelho 2000; Le Bail 2001; Favre-Nicolin and Cerny 2002; Stephens and Huq 2002). The Monte Carlo method employed by Tremayne (Tremayne and Glidewell 2000) and first described a few years earlier (Harris *et al.* 1994) equates to SA at a fixed, elevated temperature. Chapter 16 details the essential elements of the SA approach in a powder diffraction context, and the underlying algorithm is not discussed further here. The interested reader is referred to two comprehensive books (van Laarhoven and Aarts 1987; Aarts and Korst 1988) for more detailed discussions of SA.

Simulated annealing possesses several distinct advantages as an optimization approach: it is an effective algorithm that is straightforward to translate into computer code and possesses only a limited number of control parameters. The resultant ease-of-use has undoubtedly contributed to its popularity. Theoretically, SA is only guaranteed to find the global minimum after an infinite number of temperature steps. In practice, the global minimum can often be located in a finite number of steps. Typical SA strategies normally involve multiple annealing runs—if the same answer is found repeatedly, then there is a good chance that the global minimum has been located. Furthermore, in the specific case of structure solution from powder data, the quality of fit to the diffraction data provides an objective figure of merit with which to judge the reliability of the structures found by the SA algorithm.

There are many variants on the basic SA algorithm. For example, rather than simply reduce the temperature of the system at a preset rate (Putz *et al.* 1999; Chapter 16), the rate of cooling can be linked to function value fluctuations (David *et al.* 1998). Thus, as the system approaches a region where the function values (e.g. χ^2) fluctuate significantly as a function of the variable parameters, the rate of cooling drops in order to allow the system to explore this region. This is intuitively obvious, as large fluctuations indicate a region where both bad and good fits to the data exist and care is therefore required in its exploration. Conversely, in regions where there is little χ^2 discrimination, the rate of cooling can be much higher. This variable rate of cooling has a physical interpretation in terms of statistical mechanics. The energy fluctuations are linked to the specific heat of the system and the occurrence of a large specific heat is the hallmark of

a structural phase transition. Care must be taken in cooling through, for example, a liquid–solid phase transition to avoid quenching into a thermodynamically unfavourable configuration. By analogy, a reduced rate of temperature reduction in an SA run increases the probability of locating the global minimum configuration. A further simple modification is to introduce a sampling algorithm for the generation of new parameter values that allows large perturbations from the current parameter values with an exponentially decreasing probability (David *et al.* 1998). A more complex modification to the parameter shift criterion is to introduce the notion of biased sampling which takes into account the local environment around the current position in parameter space and proposes moves that are more likely to be accepted. This approach, coupled with parallel tempering, has been used to good effect in a validation exercise in which the structures of all publicly known zeolite materials were solved using a figure of merit that incorporates both geometric and diffraction terms (Falcioni and Deem 1999).

Despite the fact that SA is intrinsically a sequential process and thus difficult to parallelize at a low level, it can still benefit from parallel computing in the context of *parametric execution*. For example, multiple SA runs can be started in parallel, in order to ensure that the same function minimum can be located several times from different random starting points. This has proven to be a powerful tool in characterizing the chemical, crystallographic and control variables that impact upon a particular implementation of SA in structure solution (McBride 2000; Section 15.8)

15.5.2 *A search method with a biological basis—genetic algorithms*

Genetic algorithms (GAs) are an approach to global optimization that borrow heavily from the Darwinian theory of evolution. For a detailed discussion of their history, their place in the larger scheme of *evolutionary strategies* and the correct use of the often-confusing terminology surrounding the subject, the reader is referred to Michalewicz (1996). GAs have been widely applied to optimization problems ranging from circuit design (Arslan *et al.* 1996) to conformational searching (McGarrah and Judson 1993) and molecular docking (Jones *et al.* 1997).

Evolutionary strategies maintain a population of potential solutions to a problem, employ a selection process based upon the fitness of each of the individual solutions and have genetic operators that serve to recombine and vary the initial solutions. Taking the structure solution example, each trial crystal structure is treated as an individual defined by a collection (‘chromosome’) of variables (‘genes’). A characteristic of the individual is its ‘fitness’, which is in some way related to how well its associated model diffraction pattern agrees with the measured diffraction data. By applying the genetic operators of crossover and mutation, new structures can be produced from a population of individuals and their relative fitness assessed. By the principle of ‘survival of the

fittest', the population evolves towards a point where one or more individuals reach the global minimum. However, in the majority of GAs, it is not only the fittest individuals that survive and proceed into the next generation. Rather, it is the fittest individuals that have the highest *probability* of survival, given a selection procedure containing some random element. Indeed, unless one employs an *elitist* strategy, there is no guarantee that the fittest individual will pass into the next generation. Classical GAs use fixed length binary strings as their chromosomes and employ only two genetic operators: binary crossover and binary mutation. This is illustrated in Fig. 15.5(a).

However, structure solution is a problem best described in terms of real numbers rather than discrete binary approximations. Faced with the possibility of adapting the problem to suit the conventional GA approach, or adapting the GA to suit the problem, the latter is a much more attractive option (Fig. 15.5(b)). Hence it is a modified GA (classified by Michalewicz as an *evolutionary program*) that has found a use in structure solution (Kariuki *et al.* 1997, 1999; Shankland *et al.* 1997a, 1998a).

That GAs are effective optimizers is therefore not in doubt. What is less clear however, is exactly why they are so effective. For example, one study of the use of a GA designed to assist in the selection of a detection method for ion chromatography (van Kampen and Buydens 1997a) found that the recombination operator (i.e. crossover) was ineffective in improving fitness and that mutation was therefore the dominant operator in this problem. A similar conclusion was reached for the use of a GA in the macromolecular folding problem (van Kampen and Buydens 1996). However, the authors emphasize that such findings are highly problem-specific and implementation dependent and wisely confine themselves to the overall conclusion that the effectiveness of the crossover operator should not be taken for granted. These findings are in line with the general principle that the behaviour of a GA is somewhat difficult to understand and control. Control parameters for a typical GA include: population size, crossover rate, crossover type (single-point, multi-point, simple, arithmetic, heuristic), mutation rate, mutation type (single-point, multi-point, uniform, non-uniform, each possessing an individual rate) and the selection rule by which survivors are chosen from the population. Careful control of parameters can yield good results. For example, the use of a relatively large percentage of non-uniform mutations was a key element in fine-tuning the structure solution of ibuprofen using a GA (Shankland *et al.* 1998a). With an overall mutation rate of around five per cent, 40 per cent of these mutations were uniform and 60 per cent were non-uniform. In a uniform mutation, the bounds on the allowable values for the genes are fixed for the duration of the GA run. In a non-uniform mutation, the bounds on the gene progressively contract around the current value for that gene. Thus, the non-uniform operator introduced an increasing amount of local searching as the population aged and ensured that the resultant GA solutions were extremely close to the final refined structure. Some authors (Srinivas and Patnaik 1994) have

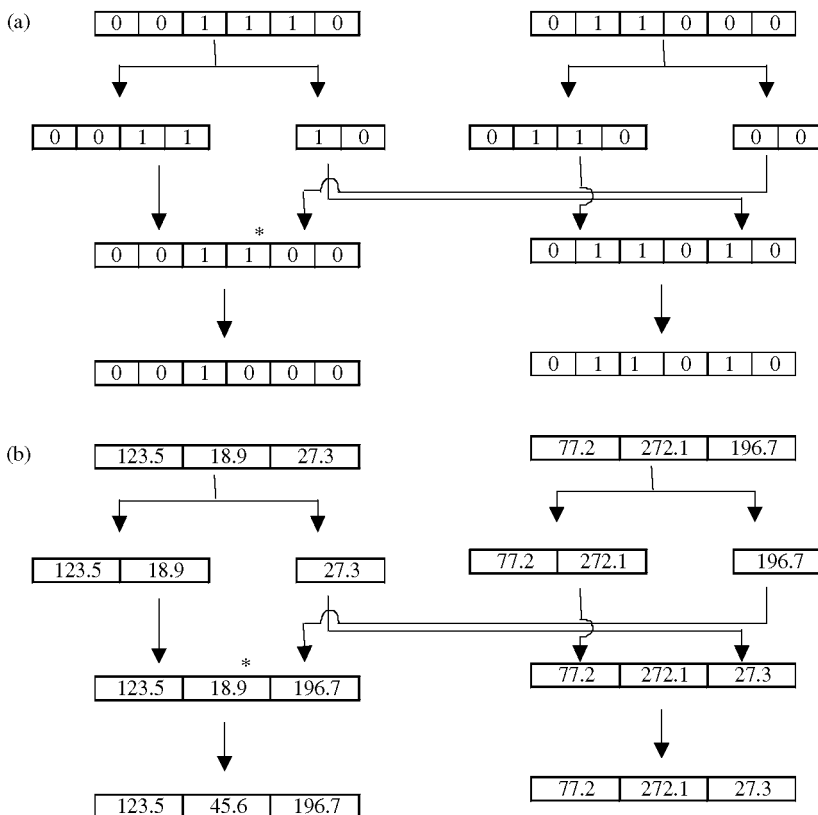


Fig. 15.5. A simple example of (a) a binary encoded genetic algorithm for a molecular conformation and (b) a corresponding real valued GA. The molecule in question possesses three torsion angles that can take any value in the range $0-360^\circ$. In the binary example, each torsion angle is encoded using only two bits: '00' = 0° , '01' = 90° , '10' = 180° and '11' = 270° . Two parent molecules consisting of three genes each undergo a crossover operation involving the exchange of their rightmost genes to create two new child molecules. The left-hand child subsequently undergoes a mutation in which a single bit (indicated by the *) is changed to its alternate value. The right-hand child remains unaltered and both children pass onto the selection process for the next generation. The corresponding real-valued description follows the same process, except that all possible torsion angle values are allowed.

suggested that an adaptive GA, which utilizes adaptive (i.e. variable) probabilities of crossover and mutation to realize the twin goals of maintaining population diversity and sustaining the convergence capacity of the GA, is appropriate when locating the global optimum in a multimodal landscape. Others (Michalewicz 1996) have explored the option of adaptive population

sizes. The permutations are almost endless—in fact, it is not unheard of to use one GA to optimize the parameters that control another GA (Freisleben and Hartfelder 1993). Subdivision of a population (the ‘island model’) is another variant, in which discrete population clusters are only allowed to communicate periodically with one another via a process of ‘migration’. This model is an ideal candidate for parallelization on a modest ‘Beowulf’ style cluster of computers, as each ‘island’ can be mapped easily onto a single processor. Communication between processors, carried out via shared memory or fast ethernet, is kept to a minimum and thus the traditional bottleneck of commodity supercomputing is largely circumvented. Such parallel calculations have been used to good effect in the GA structure solution of ibuprofen (Shankland *et al.* 1998a).

All of the GA strategies mentioned so far assume that once an individual has been created by a crossover operation and altered by a mutation operator, it is an unchanging entity until the point that its fitness has been evaluated and it passes onto the next generation or is destroyed. Lamarckian evolution on the other hand is a ‘nature and nurture’ approach that assumes that an individual improves during its lifetime and that such improvements are coded back into the chromosome (Michalewicz 1996). In practice, these improvements are realized via invocation of a *local* optimizer, which quickly pulls each candidate GA solution to the location of the closest function minimum before the genetic operators are applied. Unsurprisingly, this can improve the convergence rate of a GA significantly (Turner *et al.* 2000).

It is clear that GAs constitute a somewhat beguiling topic. Undoubtedly, one of the reasons for their success is the ease with which highly problem-specific information can be incorporated (Grefenstette 1987; Michalewicz 1996). For example, one could envisage encoding cis-trans isomerism capability into a GA via the use of a specific mutation, where a fixed rotation of 180° is applied to the relevant bond at an appropriate rate. Alternatively, the search space can be bounded with additional problem-specific information. For example, the use of torsion angle bounds derived from structure-correlation analyses using the Cambridge Structural Database greatly improved the success rate and convergence rate of a GA used to solve the crystal structure of ibuprofen (Shankland *et al.* 1998b).

McCrone (1963) has stated that ‘every compound has different polymorphic forms and the number of forms known for a given compound is proportional to time and the energy spent in research on that compound’. In analogous fashion, it seems equally fair to say that the success of GAs as an optimization method is proportional to the amount of effort that is put into adapting them to the problem in hand.

15.5.3 *Search methods with a social basis—the swarm*

The behaviour of a flock of birds or a swarm of bees bears a striking resemblance to the way in which many global optimization procedures work. It is

therefore unsurprising to find that particle swarm optimization (Kennedy and Eberhart 1995) has been proposed as a method for solving multidimensional non-linear function optimization problems and has found applications ranging from the location of skiers buried under an avalanche (Robinette 2000) to solving crystal structures from powder diffraction data (Section 15.7). The algorithm can be described in a series of concise steps.

1. The system is initialized with a population of potential solutions in random positions \underline{x} in the search space. Each solution is henceforth referred to as a particle.
2. Each particle is assigned a randomized velocity \underline{v} and an inertia \underline{w} .
3. The current objective function value (e.g. χ^2) is evaluated for each particle and each particle is endowed with a memory of its best ever position, **myBest**, together with a knowledge of the best position visited by the swarm as a whole, **gpBest**.
4. At each time step, the velocity of each particle is adjusted to have a component that takes it towards its previous best position and a component that takes it towards the best position visited by the whole swarm. This acceleration is weighted by a random term to prevent the swarm getting trapped in a local minimum.

$$\underline{v} = \underline{w} \cdot \underline{v} + 2.0 \cdot \text{rand}() \cdot (\underline{\text{myBest}} - \underline{x}) + 2.0 \cdot \text{rand}() \cdot (\underline{\text{gpBest}} - \underline{x}). \quad (15.4)$$

5. A new position in the solution space is calculated for each particle by adding the new velocity value to each component of the particle's position vector.
6. Eventually, the swarm of potential solutions hovers around the best solution position.

A simple example that demonstrates the application of such an algorithm in a powder structure solution context (Csoka and David 1999) is discussed further in Section 15.7.

15.5.4 *The downhill simplex algorithm—a 'semi-global' optimizer*

The well-known downhill simplex algorithm (Nelder and Mead 1965) is an optimization method that requires only function evaluations, not derivatives. The radius of convergence of the simplex algorithm is determined by the size of the initial step length allowed for each variable. If the step length is sufficiently large then this approach can be viewed as a local optimizer that has the capability to 'look beyond' local minima in the immediate vicinity of the current solution.

The utility of the simplex algorithm in structure solution was evaluated using the famotidine problem mentioned earlier and discussed in more detail in Section 15.8. Twenty thousand simplex structure solutions were started from random initial configurations. The χ^2 values obtained from these trials

are plotted in Fig. 15.4 and closely follow a log-normal distribution. This distribution is quite different from the other distribution shown in Fig. 15.4, which was obtained from the random trials (see Section 15.4), in that it is shifted quite substantially to lower values of χ^2 and indicates that the number of local minima in the χ^2 hypersurface is very large. Despite this, the simplex algorithm returned two correct structures from the 20 000 trials. Given that each of the 12 degrees of freedom are equally difficult to obtain, this one in 10 000 chance can be written as ~ 1 in 2^{12} . This means that the simplex minimization is indeed *semi-global* in nature since each variable initially need only be in the correct half of its parameter space for the correct structure to be obtained. This impressive convergence makes simplex minimization a worthwhile approach for small problems. Indeed, rigid body structures should solve with around a one in 64 success rate. Note, however, that each simplex minimization run requires of the order of $\sim 5N^2$ function evaluations (N = number of parameters) so that, even in the rigid body case, around 10 000 structures are assessed in order to return a correct answer. Nevertheless, this relatively small number is easily calculated and for small rigid structures, the direct minimization simplex approach offers some speed advantages over the random walk approach of SA. However, for torsionally complex structures, the simplex method becomes unwieldy. In the case of famotidine ($N = 12$), the number of structure evaluations is around 7×10^6 . At an evaluation rate of 1000 structures per second on a DEC 433 MHz Alphastation, the total calculation time was around two hours, roughly five times slower than an equivalent single SA run. For molecules with 10 internal torsion angles, the problem becomes progressively worse and the simplex approach requires $\sim 10^8$ trials, taking around a day. In contrast to this, our findings indicate that the number of trial structures required in an SA run is of the order of $\sim 100 \times 2^N$. For $N = 16$, $M_{SA} \sim 6 \times 10^6$ leading to gains of around 15 over the simplex approach and to calculation times of around two hours on a DEC 433 MHz Alphastation.

15.5.5 Other approaches

The above-mentioned methods have all been employed in solving crystal structures from powder diffraction data. However, there still remain many global optimization strategies that are used elsewhere in chemistry and physics and are likely to be applicable to the powder problem. For example, the Hybrid Monte Carlo method originally introduced for numerical simulation in lattice field theory has been successfully applied to the solution of the crystal structure of capsaicin from powder diffraction data (Johnston *et al.* 2002). The interested reader is referred to a recent review of global optimization approaches in protein folding and peptide docking (Floudas *et al.* 1999) for a concise summary of some relevant methods.

15.5.6 Which algorithm is best?

Many comparisons between GAs and SA exist (see, for example, de Groot *et al.* 1990; Ingber and Rosen 1992; Manikas and Cain 1996; van Kampen and Buydens 1996; van Kampen and Buydens 1997b), but they are usually hampered by the fact that they are comparisons of particular implementations of SA and GA for particular problems. For example, a comparison of the performance of very fast simulated reannealing (VFSR) with a simple binary coded GA on a suite of six standard test functions found that VFSR was significantly more efficient than the GA (Inger and Rosen 1992). In contrast, a comparison of a simple GA with SA in circuit partitioning problems found that the GA gave better results than the SA in two out of the three test problems (Manikas and Cain 1996). Much depends upon the level of problem-specific information incorporated into the search algorithm.

In the context of structure solution from powder diffraction data, there is little doubt that SA has the advantage of being straightforward to code and has relatively few control parameters. The only parameter that varies significantly from dataset to dataset is the initial temperature of the system, and this can be calculated automatically via an initial sampling of the χ^2 hypersurface. Simulated annealing is highly effective even in the absence of a great deal of problem-specific information and as such, it comes close to a 'black-box' approach that appeals to many structural chemists.

It remains to be seen whether hybrid SA-GA algorithms (Ackley 1987; Mahfoud and Goldberg 1995; Renyuan *et al.* 1996) which take the best features of both approaches and are already well-adapted to parallel computing environments find applicability in structure solution.

15.5.7 Use of molecular envelope information

It was mentioned in Section 15.5.2 that incorporation of torsion angle bounds could improve the performance of a GA-structure solution. However, bounds need not be limited to intramolecular degrees of freedom. It has been shown (Brenner *et al.* 1997) that the use of a structure envelope, calculated from a periodic nodal surface based upon a few low-resolution reflections, can be employed to effectively bound the region of space that should be explored by a search algorithm. Significant improvements in the performance of zeolite structure solutions have been achieved and the approach has recently been extended to organic materials (Brenner 1999).

15.5.8 Hybrid DM–global optimization approaches

The latest releases of EXPO (Altomare *et al.* 2000; Altomare *et al.* 2004) take elements of the global optimisation strategies outlined above and incorporate them into a Direct Methods framework. It seems entirely logical that continuing software developments will see an equivalent flow of important features from DM into the global-optimization-based programs.

15.6 Structure evaluation—the cost function

15.6.1 Efficiency of function evaluations

Regardless of the description of the system under study or the search method employed, the crystal structure solution process inevitably involves the evaluation of a large number of trial crystal structures. The efficiency of the function called in order to perform this evaluation is critical and impacts upon the overall time performance of the structure solution process. Clearly, the most efficient approach is to extract a set of structure factors from the diffraction data and then work with this set. Thus an early approach used to solve 6-methyl-uracil from powder diffraction data (Reck *et al.* 1988) utilized a small number of fully resolved (mostly low order) reflections in the calculation of figures of merit for discrete orientation and translation searches. Similarly, only low-angle reflections (typically $2\theta < 40^\circ$, $\lambda = 1.54 \text{ \AA}$, $d = 2.25 \text{ \AA}$) were employed in the structure solution of several organic compounds by a process that involved the translation and rotation of rigid fragments throughout the regions of space which were bounded by limits derived from Cheshire groups (Masiocchi *et al.* 1994). Crucially, overlapping reflections were not excluded from this analysis. Rather, they were treated as clumps (multiplets) with a net intensity that could be compared directly with the sum of the equivalent calculated intensities.

However, there are two main reasons why it is still common practice to use the weighted profile R -factor or χ^2 . The first of these is pragmatic and is concerned with the ease with which existing Rietveld refinement codes can then be adapted for structure solution use. The second is largely anecdotal and is based on the belief that the intensity extraction stage is an unreliable process (Kariuki *et al.* 1997). In fact, all global optimization approaches of necessity use a Le Bail or Pawley refinement at the outset of the structure solution process, if only to obtain accurate lattice parameters and peak widths.⁴ However, there is a strong body of opinion that believes that the utility of the intensity extraction stage ends at this point and that structure solution should then be undertaken as a sequence of full profile Rietveld refinements in which, typically, only the scale

⁴ Although it is possible to perform ‘scale-factor only’ Rietveld refinements without prior refinement of the lattice parameters, zero point, background description and peak shape, the chances of solving the structure in this way are greatly reduced.

factor is refined (see, for example: Kariuki *et al.* 1997; Tremayne and Glidewell 2000). This is based upon the correct presumption that Rietveld refinement is the optimal method of fitting a structural model to a diffraction pattern but also upon the incorrect presumption that there is no equivalent approach. As hinted at by the work of Masiocchi *et al.* (1994), stated explicitly by Prince (1985) and expanded upon here, use of the correlated integrated intensity χ^2 function:

$$\chi^2 = \sum_h \sum_k [(I_h - c|F_h|^2)(V^{-1})_{hk}(I_k - c|F_k|^2)], \quad (15.5)$$

where I_{hk} is the extracted intensity from a Pawley refinement of the diffraction pattern, V_{hk} is the covariance matrix from the Pawley refinement, c is the scale factor and F_{hk} is the calculated structure factor from the current trial structure, is mathematically equivalent to the Rietveld method. There is in fact a simple relationship between the unnormalized χ^2 values for the Rietveld, Pawley and correlated integrated intensity methods: within statistical errors

$$\chi_{\text{Rietveld}}^2 = \chi_{\text{Pawley}}^2 + \chi_{\text{Correlated integrated intensities}}^2 \quad (15.6)$$

It is apparent from the eqn (15.5) that one requires access to a covariance matrix in order to evaluate χ^2 . For the Pawley method, which is based upon conventional least-squares, this is straightforward. Although the iterative Le Bail approach does not automatically generate such a matrix, it is possible to adapt it to do so (Pagola *et al.* 2000; Chapter 8) and obtain an expression similar to eqn (15.5).

Any argument that the structure factor contributions of overlapping reflections are not correctly partitioned in this approach misunderstands the fact that, in the global optimization structure solution stage, the relevant partitioning of the structure factors *is derived from the trial structure*, in exactly the same way as it is with the Rietveld method. Even if unphysical negative intensities are produced in the decomposition of a group of strongly overlapping reflections, eqn (15.5) preserves the sum of the integrated intensities for that group; under these conditions, this is the only significant value for the structure solution process. That eqn (15.5) holds well in practice has now been demonstrated in numerous publications (see, for example, Shankland *et al.* 1997a; David *et al.* 1998; Shankland *et al.* 1998a; Bell *et al.* 1999; Admans 2000; Dinnebier *et al.* 2000; McBride 2000; Smrčok *et al.* 2001). The mathematical proof of eqn (15.5) was established by David (2004).

Problems with either Le Bail or Pawley extracted intensities can arise in high-angle regions of strong overlap, when the background parameters are also being refined and the background is poorly determined. Under such conditions, it is probably best to either eliminate this higher angle data from the fit (as it contains little information of value to the solution process) or perform a preliminary background subtraction. It should be noted however,

that the weight matrix in the correlated integrated intensities χ^2 can be modified to allow implicit background refinement during the structure solution process.

Use of the correlated integrated intensities χ^2 in a structure solution context allows for the extremely rapid evaluation of trial crystal structures. For example, the DASH structure solution program (David *et al.* 2001), which employs SA as the global optimization method, uses eqn (15.5) as the evaluation function on which optimization is performed. Taking the structure solution of hydrochlorothiazide from synchrotron powder diffraction data as an example (23 atoms, 8 degrees of freedom, 204 reflections to 1.5 Å resolution, 9726 points in the profile) the program evaluates approximately 3500 trial structures per second when running on a single processor 800 MHz Intel Pentium III based computer.

15.6.2 *Multi-objective optimization*

For moderately complex molecular organic crystal structures, structure solution methods based upon the agreement between observed and calculated diffraction data have so far proven to be adequate. For example, it has been shown that such crystal structures can be solved quickly and reliably from powder data without resort to intra- or inter-molecular distance checks (Shankland *et al.* 1997a; David *et al.* 1998; Shankland *et al.* 1998a; Bell *et al.* 1999; Admans 2000; Dinnebier *et al.* 2000; McBride 2000; Smrčok *et al.* 2001). However, as increasingly complex structures are tackled, it seems likely that the information content of the diffraction pattern may need to be 'topped up' still further with additional information from other sources. One obvious such source is an empirical potential energy function appropriate to the system under study (Hammond *et al.* 1997; Putz *et al.* 1999; Lanning *et al.* 2000). In the context of global optimization strategies, the search algorithm roams a hypersurface that is a combination of the potential energy and diffraction hypersurfaces. An obvious advantage of such a strategy is that local minima in the diffraction hypersurface may not coincide with local minima in the potential energy surface, and as such, the combined hypersurface may be simpler to explore. There is however, the risk that the global minimum of the empirical potential hypersurface may not coincide with the global minimum of the diffraction function hypersurface, particularly if the empirical potential is poorly parameterized. Thus appropriate weighting of the relative contributions to the combined figure of merit is an important consideration. Such an approach to structure solution has been used for the simple example of L-glutamic acid, solved by the use of a GA-based search (Lanning *et al.* 2000) and the solution of numerous ionic compounds using an SA-based search (Putz *et al.* 1999).

15.6.3 *Maximum likelihood*

The concept of maximum likelihood based methods for evaluating the cost function has recently been introduced (Markvardsen *et al.* 2002; Favre-Nicolin and Cerny 2004) and this offers substantial benefits in cases where incomplete structural models are present e.g. a hydrate structure where the main moiety is optimised and the water molecules are not.

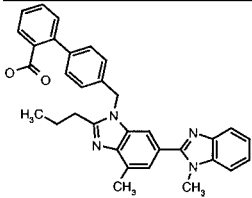
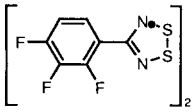
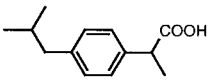
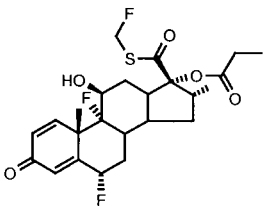
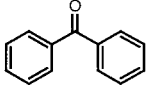
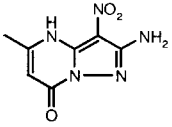
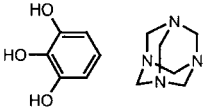
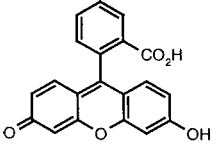
15.7 Examples

The number of crystal structures appearing in the literature that have been solved by the application of global optimization methods has grown substantially over the past five years and Table 15.2 lists two representative examples for each of the commonly employed optimization methods.

Here, we discuss the only example that we are aware of involving the application of a swarm algorithm (Csoka and David 1999). The compound is chlorothiazide ($C_7H_6ClN_3O_4S_2$, $P1$, $a=6.372\text{ \AA}$, $b=8.916\text{ \AA}$, $c=4.855\text{ \AA}$, $\alpha=96.132^\circ$, $\beta=99.476^\circ$, $\gamma=74.412^\circ$), a thiazide diuretic whose crystal structure had previously been solved by DM (Shankland *et al.* 1997b). The molecule was parameterized using an internal coordinate description and Eulerian angles were employed to describe its orientation. Being in $P1$, its location within the unit cell may be fixed by specifying an arbitrary xyz position for one of the atoms in the molecule. A swarm algorithm of the type described in Section 15.5.3 was coded in the 'C' programming language and the method of correlated integrated intensities, eqn (15.5), was used to evaluate the best configurations in χ^2 space. Each swarm run consisted of 70 particles, with a maximum of 1000 cycles per run. The effect of the inertial weight on the structure solution process was investigated by performing 20 runs at each inertia value, and the results are shown in Fig. 15.6(a).

The best results were obtained with an inertia value of 0.9, where the success rate was ~ 80 per cent. Figure 15.6(b) shows that use of low particle inertia results in a search with predominantly 'local' optimizer characteristics; the relatively low success rate indicates that the algorithm frequently becomes trapped in local minima. In contrast, Fig. 15.6(c) shows that higher particle inertia results in a search with a good balance of 'global' and 'local' characteristics. With inertia values of one or more, the 'local' search characteristics are lost and the algorithm bypasses promising search areas, resulting in a low success rate. Accordingly, by time-varying the inertial weight of the particles from a high initial inertia to a low final inertia, the algorithm can be tuned to improve performance in a manner that is strongly analogous to temperature reduction in SA.

Table 15.2 Some recent examples of structures solved by the application of global optimization methods

| Molecular structure | Compound name | Methodology | Reference |
|--|---|-------------|---------------------------------|
|  | Telmisartan | SA | Dinnebier <i>et al.</i> (2000) |
|  | 4-(2,3,4-trifluorophenyl)-1,2,3,5-dithiadiazolyl | SA | Bell <i>et al.</i> (1999) |
|  | Ibuprofen | GA | Shankland <i>et al.</i> (1998a) |
|  | Fluticasone propionate | GA | Kariuki <i>et al.</i> (1999) |
|  | Benzophenone | Grid | Hammond <i>et al.</i> (1997) |
|  | 3-amino-4-nitro-6-methyl-8-oxopyrazolol [1,5-b]-pyrimidine | Grid | Chernyshev and Schenk (1998) |
|  | 1,2,3-trihydroxybenzene: hexamethylenetetramine cocrystal (1 : 1) | MC | Tremayne and Glidewell (2000) |
|  | fluorescein | MC | Tremayne <i>et al.</i> (1997) |

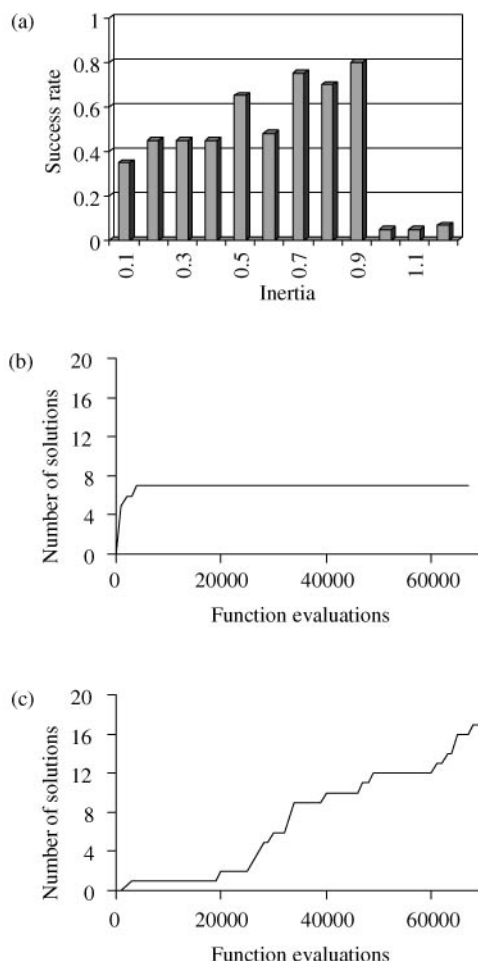


Fig. 15.6. The results of multiple swarm runs for the structure solution of chlorothiazide, showing (a) the overall success rate as a function of inertia, with 20 runs performed at each inertial value, (b) the cumulative number of solutions obtained as a function of the number of χ^2 evaluations at inertia = 0.1 and (c) a corresponding plot for inertia = 0.8.

15.8 Influence of crystallographic factors

It was stated in Section 15.5.6 that SA comes close to a ‘black box’ approach to solving structures. Nonetheless, small changes in the individual elements that make up an SA strategy can still have a significant bearing on the chances of reaching the correct solution. This has been demonstrated convincingly in the case of famotidine form B (McBride 2000), using synchrotron X-ray diffraction

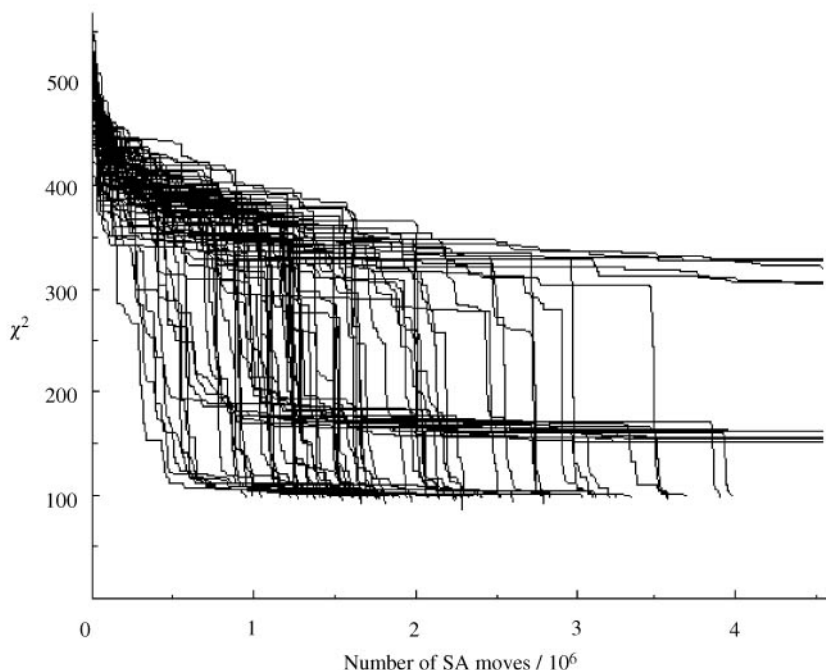


Fig. 15.7. A plot of the correlated integrated intensities χ^2 vs the number of SA moves for 80 repeat runs of the SA structure solution of famotidine form B. The plot shows the wide variation in the number of moves taken to reach the target χ^2 value of 100, corresponding to the correctly solved structure. A few of the runs fail to reach this target, becoming trapped instead in local minima.

data collected at low temperature and an implementation of an SA structure solution algorithm. In addition to assessing the impact of obvious algorithmic factors such as the choice of initial temperature and cooling rate, three other important factors that impact on the structure solution strategy were investigated systematically: the data resolution, the choice of boundary conditions and the exact Z -matrix description of the molecule. The impact of a change was assessed in terms of both the overall success rate achieved in solving the structure from a large number of replicate SA runs, and the number of SA moves required to reach each solution. The requirement for the replicate runs is easily explained by the intrinsically random aspect of the SA process (Fig. 15.7)

The conclusions of the study are reported in detail elsewhere (McBride 2000). Here we summarize the final refinement (Table 15.3) and highlight two of the more generally applicable conclusions relating to the crystallographic aspects of the work.

Firstly, by performing eighty repeat structure solution runs in which the location of the centre-of-mass of the molecule was restricted to either the unit cell or the asymmetric unit, it was found that there were no significant

Table 15.3 Rietveld refinement details for famotidine form B

| | |
|----------------------------|---|
| Space group | $P2_1/c$ |
| Z | 4 |
| Unit cell refinement | whole pattern |
| Unit cell constants | $a = 17.6547 \text{ \AA}$, $b = 5.2932 \text{ \AA}$, $c = 18.2590 \text{ \AA}$, $\beta = 123.56^\circ$ |
| Data range | 3–53° |
| Observations | 10 001 |
| Refined parameters | 124 |
| Restraints | |
| slack (distance) | restrained to Z -matrix values ± 0.001 |
| slack (angle) | restrained to Z -matrix values ± 0.1 |
| Constraints | |
| strict (B_{iso}) | all H = 3.00 O13 = O14 = N15 = N9 = C5 = N8 = C4 = C1 = C19 = N28 = C29 = N30 = N31 S12 = S18 C20 = C23 = S24 = C25 = N26 |
| Thermal parameters | all atoms isotropic |
| Rietveld agreement factors | |
| profile | $\chi^2 = 1.6634$, $R_p = 12.22$, $R_{wp} = 12.45$, $R_E = 9.65$ |
| constraints | $\chi^2 = 3.53$ |

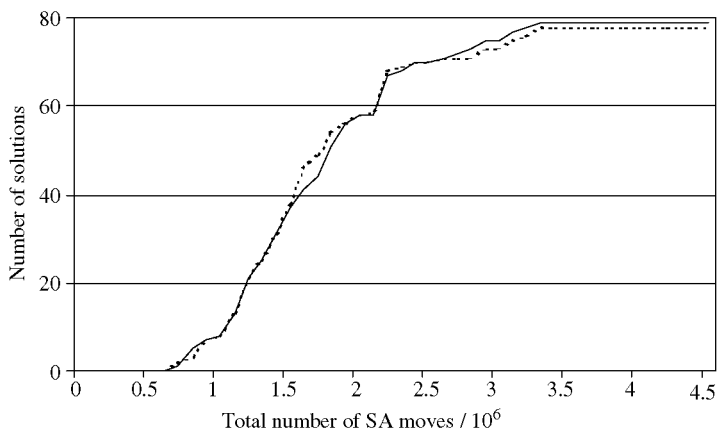


Fig. 15.8. A plot of the cumulative number of correct solutions vs the number of SA moves for the structure solution of famotidine form B in which the location of the centre-of-mass of the molecule was restricted to either the unit cell (dotted line) or the asymmetric unit (solid line). Eighty repeat runs were performed for both conditions.

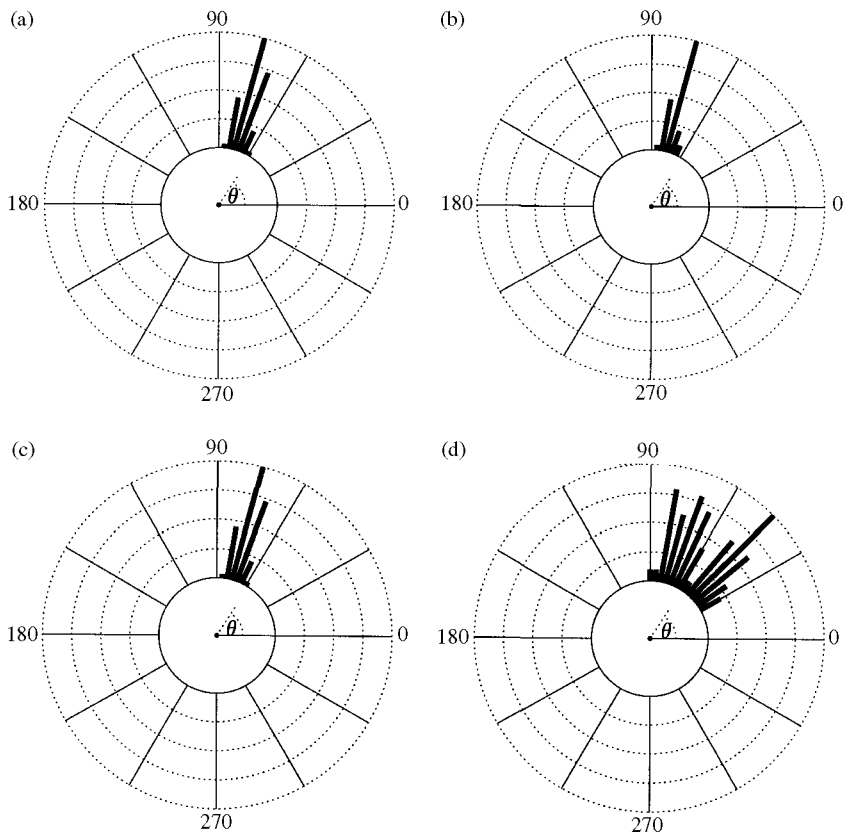


Fig. 15.9. Polar plots of torsion angle τ_1 (designated '5-4-1-18' in Fig. 15.3) determined from diffraction data measured to (a) 1.5 Å, (b) 2.0 Å, (c) 2.5 Å and (d) 3.0 Å resolution. The maximum histogram values correspond to 35, 43, 29 and 10 structures respectively. The angle θ is $+60^\circ$ from the horizontal at 0° . Thus, the histogram on the 1.5 Å plot falls between $+60^\circ$ and $+90^\circ$. In the refined crystal structure, $\tau_1 = +67.5^\circ$.

differences in either the overall success rates or the number of moves required to solve the structure (Fig. 15.8).

This is to be expected, as all possible solutions are contained within an asymmetric unit and other parts of the unit cell must give identical solutions. Put another way, allowing the trial structure to roam freely within the unit cell must be equivalent to the process where the solution is mapped back on to its equivalent position within the asymmetric unit. Since the unit cell boundaries are always much simpler to define than the boundaries of the asymmetric unit, it is simplest to employ unit cell boundary conditions.

Secondly, it was found that decreasing the resolution of the set of input reflections from 1.5 to 3 Å resulted in a ~ 30 per cent decrease in the number of

structures reaching a target χ^2 (i.e. the χ^2 corresponding to a correct solution) within a 4.5 million move limit. More significantly, the structures reaching this target χ^2 at 3.0 Å resolution were less accurate than those obtained at 1.5 Å resolution when compared to the single-crystal structure of famotidine. In order to quantify this effect, for each structure reaching the target χ^2 at one of four input data resolutions studied (1.5 Å, 2.0 Å, 2.5 Å and 3.0 Å), six torsion angles in the famotidine molecule were measured and their values collated on a series of polar plots. Figure 15.9 shows the results obtained for one of these torsion angles ($^{\circ}5\text{-}4\text{-}1\text{-}18^{\circ}$ in Fig. 15.3).

The SA algorithm correctly and consistently located the value of this torsion angle with data as limited as 2.5 Å spatial resolution. However, with the 3.0 Å dataset, the spread of values in Fig. 15.9 indicates that the reliability of the solutions is severely compromised. This implies that for a problem of the complexity of famotidine, diffraction data should be collected to a minimum of ~ 2.5 Å.

15.9 Caveats and pitfalls

It is clear that the inclusion of a large amount of chemical knowledge in the form of the known chemical connectivity of a molecule is the key factor contributing to the striking successes obtained with global optimization methods in recent years. However, therein lies the principle weakness of the method—the chemical connectivity must be known and the bond lengths and bond angles must be known with sufficient accuracy if the method is to converge successfully. If the input structure is incorrect in some significant degree, structure solution will usually fail. That it not to say that some molecular approximations cannot be made. For example, in the case of famotidine form B, the inclusion/exclusion of hydrogen atoms in the structure factor calculations had no discernible impact upon the overall success rate of the structure solution process. Indeed, the omission of a relatively small amount of scattering power is sometimes a useful strategy for eliminating some torsional degrees of freedom. Once the main fragment is located, it is then generally a simple matter to locate the remaining groups either by Fourier recycling or by subsequent global optimization runs in which the main fragment is held in its previously determined position.

The random nature of the majority of search methods employed means that multiple runs are essential in order to establish that the true global minimum has been located. That this is a necessary step is confirmed by the seductive nature of the false minima that lie close to the global minimum—see, for example, Fig. 15.10 where two incorrect SA structure solutions for famotidine form B are compared with the refined crystal structure.

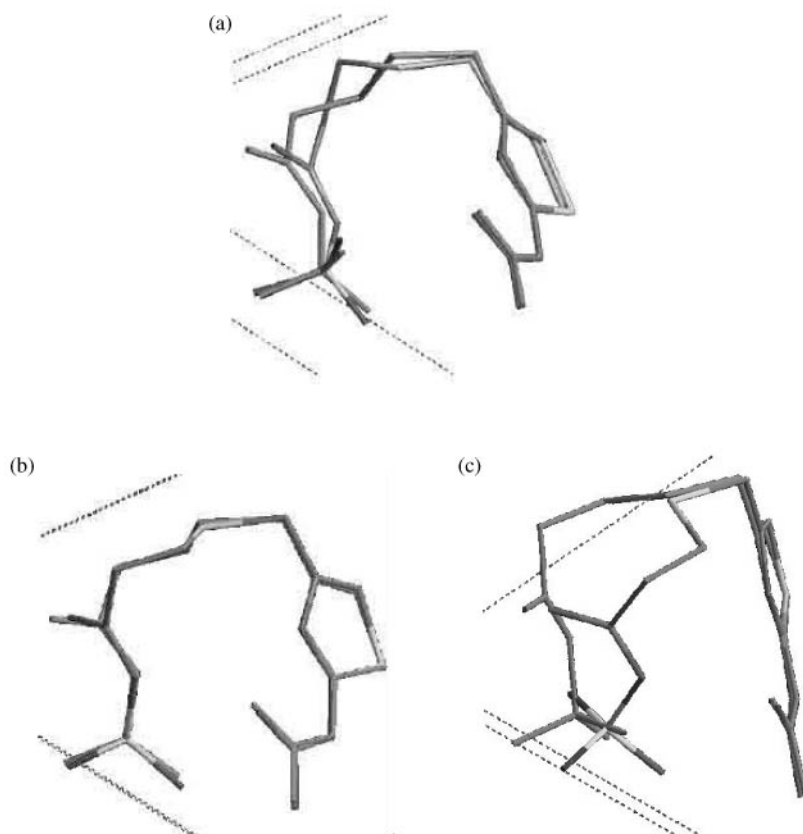


Fig. 15.10. A comparison of the refined crystal structure of famotidine form B with (a) an SA structure solution trapped at a false minimum of $\chi^2 = 224$, (b) an SA structure solution trapped at a false minimum of $\chi^2 = 325$, viewed down the *b*-axis, and (c) the same solution as in '(b)', but with the viewing angle rotated $\sim 45^\circ$.

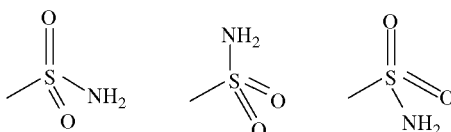


Fig. 15.11. Three orientations of the SO_2NH_2 group that are observed in the SA structure solutions of famotidine form B.

The structure with $\chi^2 = 224$ (Fig. 15.10(a)) is clearly very close to the true one, except for the central section which clearly 'zig-zags' in the wrong direction. In reality, this equates to only two badly placed atoms, and the structure can certainly be refined from this position. The same cannot be said of the structure with $\chi^2 = 325$ which looks excellent in projection (Fig. 15.10(b)) but in actuality,

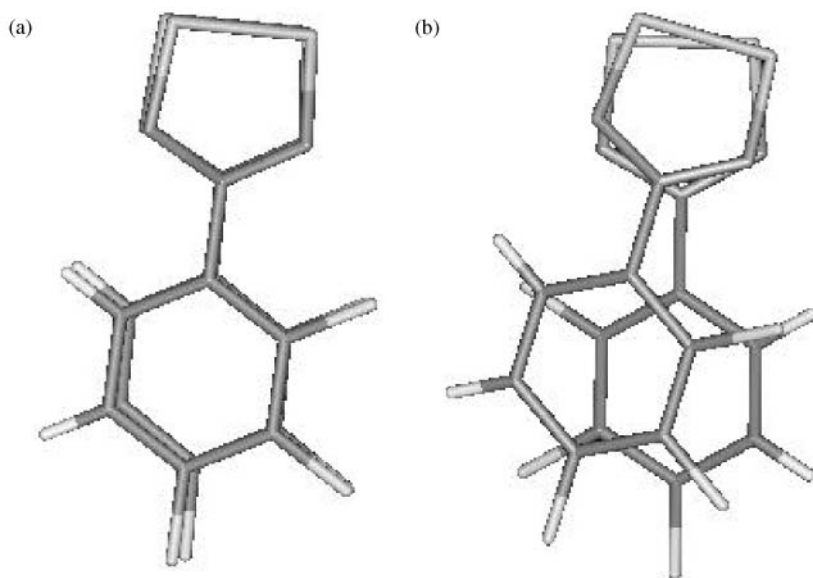


Fig. 15.12. The relative positions of the two independent molecules of 4-(2,3,4-trifluorophenyl)-1,2,3,5-dithiadiazolyl in (a) the correct crystal structure (b) a deep false minimum with intensity χ^2 approximately four times higher than that of the correct crystal structure.

has the backbone appearing almost as a mirror image of the true structure (Fig. 15.10(c)). It is clear that only a subset of the structure factors has been well-fitted and that the structure cannot be refined from this position. However, in both these cases, significant portions of the molecule have been essentially correctly located, suggesting that Fourier recycling methods may be an appropriate approach for obtaining the correct structure from these wrong solutions. Nevertheless, as stated above, the most straightforward approach remains multiple attempts at structure solution. With the advent of efficient global optimization programs such as DASH (David *et al.* 2001), the ability to repeat tens of structure solution attempts is recommended.

One problem that arises during the structure solution of famotidine relates to the orientation of the SO_2NH_2 group. The X-ray scattering power of an NH_2 group is on a par with that of an O-atom, and these three orientations, shown in Fig. 15.11, are essentially indistinguishable with relatively low spatial resolution data. Thus, it is not at all surprising to observe a number of structure solutions in which the value of the torsion angle that determines the orientation of this group is found to be $\pm 120^\circ$ removed from the correct answer. In such instances, the correct orientation can usually be determined from careful Rietveld refinement, and/or intermolecular bonding considerations. If a definitive result is essential then long wavelength, high-resolution neutron powder diffraction (Chapter 5) can be used to discriminate between these orientations because nitrogen scatters substantially more strongly

than oxygen, and hydrogen atoms are also easily located by virtue of their negative scattering length.

It has been our experience that false minima are even more of a problem in structures that possess more than one molecule in the asymmetric unit. For example, in the structure solution of 4-(2,3,4-trifluorophenyl)-1,2,3,5-dithiadiazolyl ($P2_1/n$, $Z' = 2$), several deep local minima with broadly reasonable crystal structures were located in the vicinity of the correct crystal structure. An example of one of these minima is shown in Fig. 15.12. Multiple SA runs were therefore required to ensure that the structure with the lowest value of χ^2 could be consistently obtained and that no lower point on the hypersurface could be reached. Of course, the ultimate arbiter of any structure determination is satisfactory Rietveld refinement to a chemically sensible structure.

15.10 Conclusions

Global optimization methods of structure solution are certainly now competitive with DM when applied to powder diffraction data collected from molecular organic compounds. The same may be true of inorganic compounds, though it is not the remit of this chapter to discuss this. While the methods are undoubtedly computationally intensive, it is pleasing to see that it is algorithmic development rather than raw computing power that has transformed global optimization methods from a niche interest into a mainstream approach.

How these methods will compare with Direct methods in the long run remains to be seen. Both approaches are still being intensively developed. Any direct comparisons are likely to be frustrated by the same problems that, for example, haunt comparisons of SA and GA.

In the rush to adopt these powerful approaches to structure solution, the importance of the prior stages of structure determination must not be forgotten. This extends back as far as data collection, where a little time spent recrystallizing a sample in order to produce sharper diffraction peaks, or a little time invested in calculating an appropriate data collection strategy (Chapter 6; Shankland *et al.* 1997b) will be rewarded many times over at all subsequent stages. Nor should it be forgotten that prior information from other analytical methods can also be usefully employed in combination with the diffraction data; see, for example, Middleton *et al.* 2002, for a description of how conformational information derived from SS-NMR was used to facilitate a powder structure determination.

Acknowledgements

We gratefully acknowledge the work of Tony Csoka, whose contribution during the time he spent at the Rutherford Appleton Laboratory in 1996–97 was crucial in developing the genetic algorithm/correlated integrated intensity approach. The many successful structure solutions obtained by Lorraine McBride and her work on characterizing the behaviour of both the GA and SA

approaches is gratefully acknowledged. We are also most grateful to Dr. Gerry Steele of AstraZeneca R&D Charnwood for introducing us to many challenging problems as a direct result of his role as Lorraine's industrial supervisor.

Our long-standing collaboration with Dr. Norman Shankland of the Department of Pharmaceutical Sciences at the University of Strathclyde in Glasgow has been a key element in maintaining the momentum behind the development of this approach and its application to pharmaceuticals and we gratefully acknowledge his contribution. Finally, we acknowledge the many other people who have provided us with interesting structures to solve.

References

- Aarts, E. and Korst, J. (1988). *Simulated Annealing and Boltzmann Machines*, John Wiley and Sons, Chichester.
- Ackley, D. (1987). *Stochastic Iterated Genetic Hillclimbing*, PhD thesis, Carnegie Mellon University.
- Admans, G. (2000). *ESRF Highlights 1999*, p. 23, ESRF, Grenoble.
- Altomare, A., Burla, M. C., Giacovazzo, C., Guagliardi, A., Moliterni, A. G. G., Polidori, G. and Rizzi, R. (2000). In *Abstracts of the 19th European Crystallographic Meeting, Nancy, France*, p. 133, Université Henri Poincaré, Nancy.
- Altomare, A., Caliandro, R., Camalli, M., Cuocci, C., Giacovazzo, C., Moliterni, A. G. G. and Rizzi, R. (2004). *J. Appl. Crystallogr.*, **37**, 1025–8.
- Andreev, Y. G., MacGlashan, G. S. and Bruce, P. G. (1997). *Phys. Rev. B*, **55**, 12011–7.
- Arslan, T., Horrocks, D. H. and Ozdemir, E. (1996). *IEEE Electronics Lett.*, **32**, 651–2.
- Baerlocher, Ch., Hepp, A. and Meier, W. M. (1976). *DLS-76: A Program for the Simulation of Crystal Structures by Geometric Refinement*. Institut fuer Kristallographie, ETH, Zurich.
- Bell, A. M. T., Smith, J. N. B., Attfield, J. P., Rawson, J. M., Shankland, K. and David, W. I. F. (1999). *New J. Chem.*, **23**, 565–7.
- Brenner, S., McCusker, L. B. and Baerlocher, C. (1997). *J. Appl. Crystallogr.*, **30**, 1167–72.
- Brenner, S. (1999). PhD Thesis, Structure Envelopes and their Application in Structure Determination from Powder Diffraction Data. ETH, Zürich, Switzerland.
- Bush, T. S., Catlow, C. R. A. and Battle, P. D. (1995). *J. Mater. Chem.*, **5**, 1269–72.
- Chernyshev, V. V. and Schenk, H. (1998). *Z. Krist.*, **213**, 1–3.
- Coelho, A. A. (2000). *J. Appl. Crystallogr.*, **33**, 899–908.
- Csoka, T. and David, W. I. F. (1999). *Acta Crystallogr. A*, **55** Supplement.
- David, W. I. F., Shankland, K. and Shankland, N. (1998). *J. Chem. Soc. Chem. Commun.*, 931–2.
- David, W. I. F., Shankland, K., Cole, J., Maginn, S., Motherwell, W. D. S. and Taylor, R. (2001). *DASH User Manual*, Cambridge Crystallographic Data Centre, Cambridge, UK.
- David, W. I. F. (2004). *J. Appl. Crystallogr.*, **37**, 621–8.
- Deem, M. W. and Newsam, J. M. (1989). *Nature*, **342**, 260–2.
- de Groot, C., Wuertz, D. and Hoffmann, K. H. (1990). *Helvetica Physica Acta*, **63**, 843.
- Dinnebier, R. E., Wagner, M., Peters, F., Shankland, K. and David, W. I. F. (2000). *Z. Anorganische Und Allgemeine Chemie*, **626**, 1400–5.

- Engel, G. E., Wilke, S., Konig, O., Harris, K. D. M. and Leusen, F. J. J. (1999). *J. Appl. Crystallogr.*, **32**, 1169–79.
- Falcioni, M. and Deem, M. W. (1999). *J. Chem. Phys.*, **110**, 1754–66.
- Favre-Nicolin, V. and Cerny, R. (2002). *J. Appl. Crystallogr.*, **35**, 734–43.
- Favre-Nicolin, V. and Cerny, R. (2004). *Z. Kristallogr.*, **219**, 847–56.
- Floudas, C. A. (1999). *Deterministic Global Optimization: Theory, Algorithms and Applications*, Kluwer, Dordrecht.
- Floudas, C. A., Klepeis, J. L. and Pardalos, P. M. (1999). *Global Optimization Approaches in Protein Folding and Peptide Docking*, DIMACS Series in Discrete Mathematics and Theoretical Computer Science, (ed. F. Roberts), Vol. 47, pp. 141–71.
- Friesleben, B. and Hartfelder, M. (1993). *Optimization of Genetic Algorithms by Genetic Algorithms*. In *Proc of the 1993 Int. Conf. on Artificial Neural Nets and Genetic Algorithms*. Springer-Verlag, Vienna.
- Grefenstette, J. J. (1987). ‘Incorporating Problem Specific Knowledge into Genetic Algorithms’. In *Genetic Algorithms and Simulated Annealing* (ed. L. Davis), Morgan Kaufmann Publishers.
- Hammond, R. B., Roberts, K. J., Docherty, R. and Edmondson, M. (1997). *J. Phys. Chem. B.*, **101**, 6532–6.
- Harris, K. D. M., Tremayne, M., Lightfoot, P. and Bruce, P. G. (1994). *J. Am. Chem. Soc.* **116**, 3543–47.
- Hazelrigg, G. A. (1996). *Systems Engineering: An Approach to Information-based Design*. Prentice-Hall International.
- Horst, R. and Pardalos, P. M. (ed.) (1995). *Handbook of Global Optimization*, Kluwer, Dordrecht.
- Ingber, L. and Rosen, B. (1992). *Mathematical and Computer Modelling*, **16**, 87–100.
- Johnston, J. C., David, W. I. F., Markvardsen, A. J. and Shankland, K. (2002). *Acta Crystallogr. A*, **58**, 441–7.
- Jones, G., Willett, P., Glen, R. C., Leach, A. R. and Taylor, R. (1997). *J. Molec. Biol.*, **267**, 727–48.
- Kariuki, B. M., Serrano Gonzalez, H., Johnston, R. L. and Harris, K. D. M. (1997). *Chem. Phys. Lett.*, **280**, 189–95.
- Kariuki, B. M., Psallidas, K., Harris, K. D. M., Johnson, R. L., Lancaster, R. W., Staniforth, S. E. and Cooper, S. M. (1999). *J. Chem. Soc. Chem. Commun.*, 1677–8.
- Keen, D. A. (1997). *Phase Transitions*, **61**, 109–24.
- Keen, D. A. (1998). In *Local Structure From Diffraction* (ed. S. J. L. Billinge and M. F. Thorpe). Plenum Press, New York.
- Kennedy, J. and Eberhart, R. (1995). *Proc. IEEE Int. Conf. Neural Networks IV*, 1942–8.
- Lanning, O. J., Habershon, S., Harris, K. D. M., Johnson, R. L., Kariuki, B. M., Tedesco, E. and Turner, G. W. (2000). *Chem. Phys. Lett.*, **317**, 296–303.
- Leach, A. R. (1996). *Molecular Modelling Principles and Applications*. Longman.
- Le Bail, A. (2001). *Material Science Forum*, **378–383**, 65–70.
- Mahfoud, S. W. and Goldberg, D. E. (1995). *Parallel Computing*, **21**, 1–28.
- Manikas, T. W. and Cain, J. T. (1996). *Technical Report 96–101*, Department of Electrical Engineering, University of Pittsburgh.
- Markvardsen, A. J., David, W. I. F. and Shankland, K. (2002). *Acta. Crystallogr. A*, **58**, 316–26.
- Masciocchi, N., Bianchi, R., Cairati, P., Mezza, G., Pilati, T. and Sironi, A. (1994). *J. Appl. Crystallogr.*, **27**, 426–9.

- McBride, L. (2000). *Determination of Organic Crystal Structures by X-ray Powder Diffraction*, PhD Thesis, Strathclyde University, Glasgow.
- McCrone, W. C. (1963). In *Physics and Chemistry of the Organic Solid State*, Vol 2 (ed. D. Fox, M. M. Labes and A. Weissberger) pp. 725–67. Interscience, New York.
- McGarrah, D. B. and Judson, R. S. (1993). *J. Comp. Chem.*, **14**, 1385–95.
- Michalewicz, Z. (1996). *Genetic Algorithms + Data Structures = Evolution Programs*, 3rd edn, Springer-Verlag, Berlin.
- Middleton, D. A., Peng, X., Saunders, D., Shankland, K., David, W. I. F. and Markvardsen, A. J. (2002). *J. Chem. Soc. Chem. Commun.*, 1976–7.
- Nelder, J. A. and Mead, R. (1965). *Comp. J.*, **7**, 308–13.
- Pagola, S., Stephens, P. W., Bohle, D. S., Kosar, A. D. and Madsen, S. K. (2000). *Nature*, **404**, 307–10.
- Pannetier, J., Bassas-Alsina, J., Rodriguez-Carvajal, J. and Caignaert, V. (1990). *Nature*, **346**, 343–5.
- Prince, E. (1985). In *Structure in Statistics in Crystallography* (ed. A. J. C. Wilson) pp. 95–103. Adenine Press.
- Putz, H., Schön, J. C. and Jansen, M. (1999). *J. Appl. Crystallogr.*, **32**, 864–70.
- Reck, G., Kretschmer, R. G., Kutschabsky, L. and Pritzkow, W. (1988). *Acta Crystallogr. A*, **44**, 417–21.
- Renyan, T., Shiyu, Y., Yan, L., Geng, W. and Tiemin, M. (1996). *IEEE Trans. Mag.*, **32**, 1326–9.
- Robinett, R. D. (2000). *Sandia National Laboratories News Release*, 19th January.
- Shankland, K., David, W. I. F. and Csoka, T. (1997a). *Z. Kristallogr.*, **212**, 550–2.
- Shankland, K., David, W. I. F. and Sivia, D. S. (1997b). *J. Mater. Chem.*, **7**(3), 569–72.
- Shankland, K., David, W. I. F., Csoka, T. and McBride, L. (1998a). *Int. J. Pharm.*, **165**, 117–26.
- Shankland, N., Florence, A. J., Cox, P. J., Wilson, C. C. and Shankland, K. (1998b). *Int. J. Pharm.*, **165**, 107–16.
- Solovyov, L. A. and Kirik, S. D. (1993). *Mater. Sci. Forum*, **133–136**, 195–200.
- Smrčok, L., Koppelhuber-Bitschnau, B., Shankland, K., David, W. I. F., Tunega, D. and Resel, R. (2001). *Z. Kristallogr.*, **216**, 63–6.
- Srinivas, M. and Patnaik, L. M. (1994). *IEEE Trans. Sys., Man Cybernetics*, **24**, 656–67.
- Stephens, P. W. and Huq, A. (2002). *Transactions of the American Crystallography Assn.*, **37**, 125–42.
- Stephenson, G. (2000). *J. Pharm. Sci.*, **89**, 958–66.
- Tremayne, M., Kariuki, B. M. and Harris, K. D. M. (1997). *Angew Chem. Int. Edn.*, **36**, 770–2.
- Tremayne, M. and Glidewell, C. (2000) *J. Chem. Soc. Chem. Commun.* 2425–6.
- Turner, G. W., Tedesco, E., Harris, K. D. M., Johnson, R. L. and Kariuki, B. M. (2000). *Chem. Phys. Lett.*, **321**, 183–90.
- van Kampen, A. H. C. and Buydens, L. M. C. (1996). In *Proceedings of the Second Nordic Workshop on Genetic Algorithms and their Applications* (ed. J. T. Alander) pp. 115–30, University of Vaasa, Finland.
- van Kampen, A. H. C. and Buydens, L. M. C. (1997a). *Comp. Chem.*, **21**, 153–60.
- van Kampen, A. H. C. and Buydens, L. M. C. (1997b). *Chemom. Intell. Lab. Sys.*, **36**, 141–52.
- van Laarhoven, P. J. M. and Aarts, E. H. L. (1987). *Simulated Annealing: Theory and Applications*. Kluwer Academic Publishers, Dordrecht.

Solution of flexible molecular structures by simulated annealing

Peter G. Bruce and Yuri G. Andreev

16.1 Introduction

The simulated annealing (SA) approach to structure determination from powder diffraction data described in this chapter differs fundamentally from the methods adapted from single-crystal crystallography. No attempt is made to extract individual intensities and treat them in a single-crystal sense. Instead effort is concentrated on generating chemically plausible, but random, structural models, whose calculated powder patterns are tested against the experimental data.

Rietveld recognized the inevitable limitation of any approach that relies on obtaining individual reflection intensities from powder data, and in response introduced whole-pattern fitting (Rietveld 1969). His method has been used successfully to refine the details of partially known structures in many hundreds of cases. The only barrier to structure determination, as opposed to refinement, with the Rietveld approach is the use of the least-squares method of minimization, which requires that the starting structural model be close to the correct structure. This is because structural parameters can only be adjusted in the direction of decreasing χ^2 , that is, a downhill move, improving the fit between the calculated and observed profiles. In other words, the Rietveld method can only locate the local minimum in the goodness of fit, hence the necessity to start from a structural model for which the local minimum coincides with the global minimum. By definition, the starting structural model for a structure determination is unlikely to bear much relationship to the correct structure. The probability is negligible that starting from a random structural model, the true structure (corresponding to the global minimum in the goodness of fit) can be obtained.

A summary of the minimization methods capable of finding the global minimum in the presence of multiple local minima is given in Chapter 15. In the SA method, a Monte-Carlo procedure is used to generate random models for the structure. This is achieved by making stepwise increments, random in size and direction, of the structural parameters. The models may yield a better fit (downhill, i.e. lower χ^2) or worse fit (uphill, higher χ^2) between the

calculated and observed profile. The latter is critical as it permits escape from local minima. As the minimization progresses, tolerance for the uphill steps is gradually decreased until steps in both directions are exhausted. At this point, the set of adjustable structural parameters corresponds to the lowest possible value of the figure-of-merit function, that is, the global minimum. The potential of SA in the realm of molecular structure determination was first demonstrated by Newsam *et al.* (1992), who solved the previously known crystal structure of benzene using a modified Rietveld method. In addition to an SA minimization, the authors included a rigid-body representation of the benzene ring. This allowed a significant reduction in the number of variable structural parameters. The crystallographic coordinates of all the constituent atoms used to calculate the powder pattern were computed using only the positional and orientation parameters of the rigid body as a whole (six parameters).

The rigid-body approach has been further exploited in the structure solution of molecular structures that are marginally more complex than that of benzene (Harris *et al.* 1994; Harris and Tremayne 1996; Tremayne *et al.* 1997). However, the authors did not utilize minimization of the full-pattern goodness-of-fit function but instead generated trial rigid-body structures in a Monte Carlo fashion and then analysed all the moves in a subsequent step to select several low minima. The implementation of such an approach involves multiple subsequent refinements in order to identify the structure that corresponds to the lowest value of the figure-of-merit function. While successful for relatively rigid structures, it is likely that this approach will not allow structures with a larger number of intramolecular degrees of freedom to be solved.

For structure solution from powder diffraction data to become of general utility, the development of a robust approach capable of tackling both flexible and rigid structures was vital. Determination of flexible structures by SA is much more challenging, because at first sight the number of possible structural permutations appears to be enormous. Indeed it has been estimated that the computation required to perform an exhaustive search of possible structural models would take up to 10^9 years, even for a relatively simple structure (Shankland *et al.* 1998). The SA approach used successfully for benzene can be extended to embrace the much larger range of crystals containing highly flexible moieties. Flexibility may be in the bond lengths, bond angles or torsion angles and in some cases it is essential to vary all of these in order to achieve a successful structure solution. The modified SA method is also capable of tackling the solution of polymeric structures in which a single molecule straddles more than one asymmetric unit. The problem here is that random models of the asymmetric unit are only valid if they generate chain continuity. Thus the interatomic connectivity at the junctions of neighbouring asymmetric units is determined merely by the relevant symmetry operator of the space group and cannot be maintained by random variation of the relevant bond length, bond angle and torsion angle.

The key to this approach is the development of a stereochemical description that permits the atomic positions of the molecular structural model to be defined in terms of bond lengths, bond angles and torsion angles, rather than individual atomic coordinates (Andreev *et al.* 1996, 1997*a*). This, in turn, permits attention to be restricted to chemically plausible structural models and thereby reduces the number of trial structures significantly and renders tractable the otherwise impossible task of solving the crystal structures of flexible molecules. The approach to the geometrical description of flexible molecules via stereochemical parameters is suitable for describing a molecular fragment of any kind.

16.2 Simulated annealing

The principles behind the SA approach and its distinctive features in comparison with other methods of continuous minimization are best understood by analogy with the process of forming a solid by cooling from a melt. Let us assume that the solid phase can be either amorphous or crystalline. At temperatures above the melting point, atoms have a high mobility and are in chaotic motion; the total energy of the ensemble is also high. The minimum energy of this system corresponds to a crystalline solid. There are two extreme routes by which the melt may be solidified: slow cooling or quenching. During the latter process, a random atomic configuration is immediately frozen, forming a glass with a total energy somewhat higher than that of the crystalline state. If the rate of the temperature decrease is low enough, such cooling corresponds to an annealing process in which the chaotic motion of free atoms in the melt is gradually reduced allowing the ensemble to explore the energy space fully and hence to adopt the most energetically favourable (crystalline) configuration. Applying this thermodynamic reasoning to crystal structure solution from powder data requires the substitution of the atoms of the melt with the variable structural parameters of the ensemble (e.g. the atomic coordinates or bond lengths) and energy by the value of a figure-of-merit function (χ^2).

The most frequently used method of minimization is 'conventional' gradient least-squares, which is based on an iterative linearization of a target function using its Taylor series expansion in the vicinity of a minimum (e.g. Wilson 1995). This is akin to quenching. It does not allow any chaotic changes in the structural parameter values and adopts only those changes that are in the downhill direction of the figure-of-merit function. Such a procedure is useful for refinement tasks only when a model is already known with sufficient accuracy and is already close to the global minimum. In a situation where the initial set of structural parameters describing the system is a poor estimate of the true values (a situation implicit in the context of structure solution), the minimization algorithm must allow random steps in the uphill direction of the figure-of-merit function in order to escape local minima in the search for the global minimum.

The number of uphill steps representing chaotic behaviour of the figure-of-merit function should however be slowly decreased by introducing a varying attenuation factor so that minimization towards the global minimum may occur. This procedure is analogous to that of the slow cooling (annealing) with the attenuation factor acting as the temperature.

A convenient way of introducing random steps, which includes the possibility of uphill moves, is known as the standard importance sampling algorithm (Metropolis *et al.* 1953). Application of this procedure to the minimization of a figure-of-merit function, $\chi^2(\mathbf{P})$, whose value is determined by a set of the crystallographic parameters \mathbf{P} , may be outlined as follows. A new set of parameter values \mathbf{P}^i is accepted if either

$$\chi^2(\mathbf{P}^i) < \chi^2(\mathbf{P}^{i-1}) \quad (16.1)$$

or if

$$\exp(-(\chi^2(\mathbf{P}^i) - \chi^2(\mathbf{P}^{i-1}))/\Delta\chi_{\text{cur}}^2) > R, \quad (16.2)$$

where \mathbf{P}^{i-1} is a previously accepted set of parameters, $\Delta\chi_{\text{cur}}^2$ is a current marginal value of the χ^2 variation serving as a temperature analogue, R is a random number in the range from 0 to 1. In the case of continuous minimization, each j th component P_j^i of the \mathbf{P}^i vector is calculated via the P_j^{i-1} value of the \mathbf{P}^{i-1} vector in a Monte-Carlo fashion:

$$P_j^i = P_j^{i-1} + r_j \cdot \Delta p_j, \quad (16.3)$$

where Δp_j is a predefined maximum step width and r_j is a random number in the range from -1 to 1 . Once \mathbf{P}^i is accepted, \mathbf{P}^{i-1} is set to \mathbf{P}^i and the process reiterates.

An account of various types of 'temperature-reduction' procedures is given by Press *et al.* (1992). Here we mention only one, which was used successfully in the examples of the structure solutions presented in Section 16.4. At a given value of $\Delta\chi_{\text{cur}}^2$, the sampling algorithm reiterates as long as the total number of rejected and accepted \mathbf{P}^i vectors (referred to as moves from here on) exceeds the pre-set value of N_{tot} or until the number of accepted moves becomes greater than $f_1 \cdot N_{\text{tot}}$, with the f_1 value also chosen in advance. As soon as this happens the value of $\Delta\chi_{\text{cur}}^2$ is reset to $(1 - f_2) \cdot \Delta\chi_{\text{cur}}^2$ with a predetermined value of f_2 and the whole procedure continues. Minimization terminates when there are no downhill moves at a current value of $\Delta\chi_{\text{cur}}^2$.

16.3 Constraints and restraints

Reduction of the number of adjustable parameters and narrowing parameter-space are favourable procedures for any optimization task. This can be

accomplished by imposing hard constraints and soft constraints (restraints) on the number of parameters or on their values. In this way, only chemically plausible molecular models (e.g. ones with no unrealistic bond lengths) need to be explored.

16.3.1 *Non-structural constraints*

The most obvious constraint to be used in the course of structure solution by a full-pattern fitting approach is fixing the values of those profile-defining parameters that are not directly related to the arrangement of atoms sought-for within the unit cell. The values of cell constants, peak-shape and half-width parameters, background, peak asymmetry etc. are readily determined with reasonable accuracy using full-pattern decomposition methods without reference to a structural model (see Chapter 8). The only parameter that has no effect on the structure, but cannot be fixed in advance, is the scale factor for the calculated pattern. However, its value is easily computed for each new trial structural model using the linear-least-squares method. The effect of introducing these constraints is two-fold. First, there is the advantage of a reduction in the number of variable parameters. Second, the disadvantage is that it is unreasonable to expect the fixed values to provide the best fit to the experimental powder pattern when the profile is calculated using the structural parameters instead of the integrated intensities of individual Bragg peaks used during the full-pattern decomposition. In this case the restrained structure solution terminates in the vicinity of the 'true' global minimum rather than at the minimum itself. To reach the minimum, a subsequent refinement of all parameters using the Rietveld method is required.

16.3.2 *Structural restraints*

Structural restraints are an integral part of modern software for structure refinement by the Rietveld method and are a means of taking into account our knowledge about the atomic arrangement (Baerlocher 1993). Restraints are usually introduced into the calculation of the figure-of-merit function as a sum of residuals for additional 'observations'. Each 'observation' is typically the most probable value of an interatomic distance or angle, while its corresponding term in the residual is the actual value calculated from the current set of atomic coordinates. Such restraints do not eliminate unreasonable structural models from the refinement process, but do impose a severe penalty on the minimized quantity (χ^2) when there is a deviation from the most probable value. Although applicable in the case of structure solution, such an approach is rendered unattractive because of the more computationally demanding nature of the SA method and because of the problems encountered in weighting the penalty terms of the figure-of-merit function. An entirely different approach to the imposition of restraints on structures containing fragments of an approximately known geometry (e.g. molecules) not only preserves all the attributes of the

established procedure but, in addition, allows randomized minimization by SA strictly within the pre-determined limits of the structural parameters.

16.3.3 Molecular crystals

In the case of molecular crystals, the connectivity of atoms within the molecule is generally known. By describing the positions of the atoms in terms of their bond lengths, bond angles, and torsion angles, rather than atomic coordinates, only chemically plausible structural models need be explored. The values of these stereochemical descriptors are simply restrained to lie within certain limits. This greatly reduces the number of trial structures. The number can be reduced still further by checking for unfavourable contacts between non-bonding atoms and for the spatial continuity of an infinite moiety (e.g. polymer chain) at the junction of neighbouring asymmetric units. The imposition of these chemical constraints makes the process of minimizing $\chi^2(\mathbf{P})$ by SA much more tractable. Although it is the stereochemical descriptors that are altered to generate each new chemically plausible model, the crystallographic coordinates for each model are still required in order to calculate the powder profile using the conventional mathematical formalism. However these can be obtained from the stereochemical descriptors (bond lengths l , bond angles ϕ , and torsion angles τ) by expressing initially the atomic coordinates in a local Cartesian frame whose origin is fixed on an atom from the molecule's framework which has at least two bonds attached to it. If the X -axis of the frame is chosen to lie along one of the bonds, the Y -axis is then set perpendicular to the X and belongs to the plane formed by the first bond and any other second bond attached to the origin. The Z -axis completes a right-handed orthogonal set, then the coordinates of atoms that are one bond length from the origin are calculated using trigonometric functions and values of corresponding bond lengths and bond angles. When the origin coincides with the position of the $(N-1)$ th atom of a molecule containing N atoms, the coordinates x_m^l, y_m^l, z_m^l of each m th ($m=1, N-3$) atom positioned on a bonded pathway originating from the bond $l_{N-2, N-1}$ between the $(N-1)$ th and $(N-2)$ th atoms, through which the X -axis is drawn, can be computed with the recurrent formula put forward by Arnott and Wonacott (1966)

$$\begin{bmatrix} x_m^l \\ y_m^l \\ z_m^l \end{bmatrix} = \sum_{i=m}^{N-3} \left(\left(\prod_{j=N-3, -1}^i [\mathbf{A}^j] \right) \cdot \begin{bmatrix} l_{i, i+1} \\ 0 \\ 0 \end{bmatrix} \right) + \begin{bmatrix} l_{N-2, N-1} \\ 0 \\ 0 \end{bmatrix}. \quad (16.4)$$

Elements of the rotational matrices $[\mathbf{A}^j]$ are defined by

$$[\mathbf{A}^j] = \begin{bmatrix} -\cos \phi^j & -\sin \phi^j & 0 \\ \sin \phi^j \cos \tau^j & -\cos \phi^j \cos \tau^j & \sin \tau^j \\ -\sin \phi^j \sin \tau^j & \cos \phi^j \sin \tau^j & \cos \tau^j \end{bmatrix}, \quad (16.5)$$

$$\phi^j \equiv \phi_{j, j+1, j+2}, \quad \tau^j \equiv \tau_{j, j+1, j+2, j+3},$$

where $l_{i, i+1}$, $\phi_{j, j+1, j+2}$ and $\tau_{j, j+1, j+2, j+3}$ denote the bond lengths, bond angles, and torsion angles formed by the atoms whose numbers are listed in the subscripts. When, in addition to the m th atom, the $(m-1)$ th atom has k bonded neighbours it is sometimes more convenient to calculate the coordinates of the $(m+k)$ th atom by rotating the $(m-1)$ - m bond around the $(m-2)$ - $(m-1)$ bond while assigning the length of the former to $l_{m-1, m+k}$

$$\begin{bmatrix} x_{m+k}^l & y_{m+k}^l & z_{m+k}^l \end{bmatrix} = \begin{bmatrix} x_m^l(l_{m-1, m+k}) & y_m^l(l_{m-1, m+k}) & z_m^l(l_{m-1, m+k}) \end{bmatrix} \cdot [\mathbf{R}], \quad (16.6)$$

$$[\mathbf{R}] = \begin{bmatrix} \cos \alpha + l_1^2(1 - \cos \alpha) & l_1 l_2(1 - \cos \alpha) + l_3 \sin \alpha & l_3 l_1(1 - \cos \alpha) - l_2 \sin \alpha \\ l_1 l_2(1 - \cos \alpha) - l_3 \sin \alpha & \cos \alpha + l_2^2(1 - \cos \alpha) & l_2 l_3(1 - \cos \alpha) + l_1 \sin \alpha \\ l_3 l_1(1 - \cos \alpha) + l_2 \sin \alpha & l_2 l_3(1 - \cos \alpha) - l_1 \sin \alpha & \cos \alpha + l_3^2(1 - \cos \alpha) \end{bmatrix}, \quad (16.7)$$

where l_1, l_2, l_3 are the Cartesian direction cosines of the rotation axis ($(m-2)$ - $(m-1)$ bond). The angle of rotation, α , is a function of the bond angles $\phi_{m-2, m-1, m+k}$ and $\phi_{m-1, m, m+k}$ (Andreev *et al.* 1997a), whose values in most cases can be constrained more readily than the value of τ^j in eqn (16.5). Transformation of the atomic coordinates from the local Cartesian to the crystallographic frame introduces a set of additional parameters which determine the position and orientation (defined by the Eulerian angles Θ, Φ and Ψ) of the molecular fragment as a whole in the unit cell (Goldstein 1980; *International Tables for X-ray Crystallography* 1959).

Once this procedure is introduced into a Rietveld-type algorithm in which the original least-squares procedure is substituted by the method of SA, the restraints are imposed in a straightforward manner by allowing the parameters to accept only reasonable values within predetermined limits instead of penalizing the value of $\chi^2(\mathbf{P})$ when the limits are violated. The range of acceptable values for bond lengths and bond angles in most classes of compounds is well-known, torsion angles vary between $-\pi$ and π and the coordinates of the reference N th atom are kept within the dimensions of the asymmetric unit. The limits on the Eulerian angles are $0 < \Theta, \Psi < 2\pi$ and $0 < \Phi < \pi$. Such a description allows the introduction of further constraints, which reduce the total number of parameters to be varied. For example, chemical knowledge can indicate that all like bond lengths or bond angles (e.g. all l_{C-C} and all ϕ_{C-C-C} in a benzene ring) can be treated as variable but equal to each other, or that a certain part of the molecule is flat implying that corresponding torsion angles can be kept at fixed values 0 or π , or the whole molecular fragment is rigid, in which case only the values of the Eulerian angles and of the reference-atom coordinates are to be varied. More sophisticated constraints on the conformation of molecules, such as for example either the *boat* or *chair* arrangement of atoms in a six-membered

ring, can also be imposed. Although introduction of the above constraints is computationally beneficial, it must be done with caution, because in certain cases (see Section 16.4) even a slight reduction of the molecular flexibility can mislead the structure solution.

16.4 Examples

The following structure solutions were performed using X-ray powder diffraction patterns collected in steps of 0.02° in transmission mode on a STOE STADI/P diffractometer with Cu $K\alpha_1$ radiation. The computer code implementing the full-profile-fitting procedure with minimization by the SA method was written in Visual C++. The code for pattern calculation was adapted from the CPSR software package (Andreev *et al.* 1995). For each new structure solution, a customized subroutine was written to define the coordinates of the atoms in a local Cartesian frame via stereochemical descriptors following the general approach described in Section 16.3.3. The program was implemented on a PC under Windows NT. Final structure refinements were performed using the Rietveld procedure included in the GSAS program package (Larson and Von Dreele 1987).

All the structures presented here are described in the monoclinic space group, $P2_1/c$. Details concerning indexing and space group determination are given in the references (Andreev *et al.* 1997*a, b*; MacGlashan *et al.* 1999). Profile parameters and lattice constants were fixed at the values obtained from profile-fitting using the CPSR program suite. The background was subtracted manually. The set of variable parameters used in the SA runs included the overall isotropic displacement factor, B . Hydrogen atoms were ignored during the structure solution and were added only at the refinement stage. Unless otherwise stated, the minimization of $\chi^2(\mathbf{P})$ by SA was performed using a value of five for the initial 'temperature' parameter ($\Delta\chi_{\text{cur}}^2$), $N_{\text{tot}} = 5000$, and $f_1 = f_2 = 0.1$.

The three examples below serve to illustrate the basic approach, the effect of molecular flexibility and the level of structural complexity that can be tackled. All of the examples are poly(ethylene oxide): salt complexes, which are composed of salts, for example, LiCF_3SO_3 dissolved in the solid high molecular weight polymer poly(ethylene oxide) (PEO). The polymer is a continuous linear chain with the repeat unit ($\text{CH}_2\text{-CH}_2\text{-O}$). Previous studies indicate that in complexes with ethylene oxide: salt ratios of 3:1 and 4:1, the polymer chain adopts a helical conformation (Chatani and Okamura 1987; Lightfoot *et al.* 1993, 1994), while in the case of complexes with a 1:1 ratio, the chain forms a stretched zig-zag conformation (Yokoyama *et al.* 1969; Chatani *et al.* 1990). The cations in all the above complexes are coordinated to the oxygens of the chain and to the oxygens of the anion. No structures of complexes with PEO:salt ratios higher than 4:1 had been reported prior to our work. $(\text{PEO})_3:\text{LiN}(\text{SO}_2\text{CF}_3)_2$ is of interest because the PEO-imide system has one of

the highest levels of ionic conductivity for a PEO-based polymer electrolyte at room temperature.

16.4.1 (PEO)₃:LiN(SO₂CF₃)₂

Similarity between the lattice parameters of (PEO)₃:LiN(SO₂CF₃)₂ ($a = 12.034 \text{ \AA}$, $b = 8.660 \text{ \AA}$, $c = 19.139 \text{ \AA}$, $\beta = 128.5^\circ$) and the previously determined (PEO)₃:LiCF₃SO₃ ($a = 10.064 \text{ \AA}$, $b = 8.613 \text{ \AA}$, $c = 16.77 \text{ \AA}$, $\beta = 121.0^\circ$, Lightfoot *et al.* 1993) suggested that the orientation and conformation of the PEO chain in (PEO)₃:LiN(SO₂CF₃)₂ might be similar to that found in the (PEO)₃:LiCF₃SO₃, where the helical axis is parallel to the b -axis and coincides with the 2₁ screw axis. However, all attempts to refine the structure of (PEO)₃:LiN(SO₂CF₃)₂ on the basis of the known structure of (PEO)₃:LiSO₃CF₃, adjusted to the new dimensions of the unit cell, failed, as did attempts to solve the structure by approaches based on Direct methods and difference Fourier synthesis.

Density measurements suggested the presence of one formula unit in the asymmetric unit of the cell. Initially an SA run was performed using fixed coordinates for the atoms of the three EO units comprising the PEO chain (adapted from the (PEO)₃:LiCF₃SO₃ crystal structure). The Li⁺ cation was placed inside the helix and its coordinates were allowed to vary. The coordinates of the atoms comprising the imide anion N(SO₂CF₃)₂⁻ (Fig. 16.1(a)) were expressed in terms of stereochemical descriptors. The total number of variable parameters required to describe the flexible structural model was reduced from 55 to 24 by invoking the approximation that in the imide anion, all bond lengths of a given bond type (e.g. all C–F or S–O bonds), all bond angles of a given type (e.g. all S–C–F or C–S–O angles), and all like torsion angles (N–S1–C1–F1 and N–S2–C2–F2) are equal. The **P** vector used to calculate $\chi^2(\mathbf{P})$ included the positional parameters for Li⁺ and for the imide defined through the C1 carbon (x_{Li} , y_{Li} , z_{Li} , x_{C1} , y_{C1} , z_{C1}), the orientation of the imide (Θ_{imide} , Φ_{imide} , Ψ_{imide}), the bond lengths ($l_{\text{C F}}$, $l_{\text{S C}}$, $l_{\text{S O}}$, $l_{\text{S N}}$), the bond angles ($\phi_{\text{C S O}}$, $\phi_{\text{S C F}}$, $\phi_{\text{O S O}}$, $\phi_{\text{F C F}}$, $\phi_{\text{C S N}}$, $\phi_{\text{N S O}}$, $\phi_{\text{S N S}}$), the torsion angles ($\tau_{\text{N S C F}}$, $\tau_{\text{C1 S1 N S2}}$, $\tau_{\text{S1 N S2 C2}}$) and the overall displacement parameter B . The initial values of the bond lengths and angles were taken from a crystallographic database. The SA minimization analysed ~200 000 chemically plausible structural models. Approximately 15 000 of these were accepted while the rest were rejected either on the basis of the test for closest approach (model rejected if atoms closer than the sum of their Van der Waals radii) or by the Metropolis algorithm (uphill move). The structural model, frozen at $\Delta\chi_{\text{cur}}^2 = 0.02$, after subsequent refinement gave the fit to the experimental pattern shown in Fig. 16.1(b). Although the quality of fit is reasonably good, a noticeable mismatch is clearly seen in the inset of Fig. 16.1(b) indicating that the model is still inadequate.

To tackle the problem of the unsatisfactory fit, the SA procedure was revisited, this time with extra flexibility added to the structural model. The

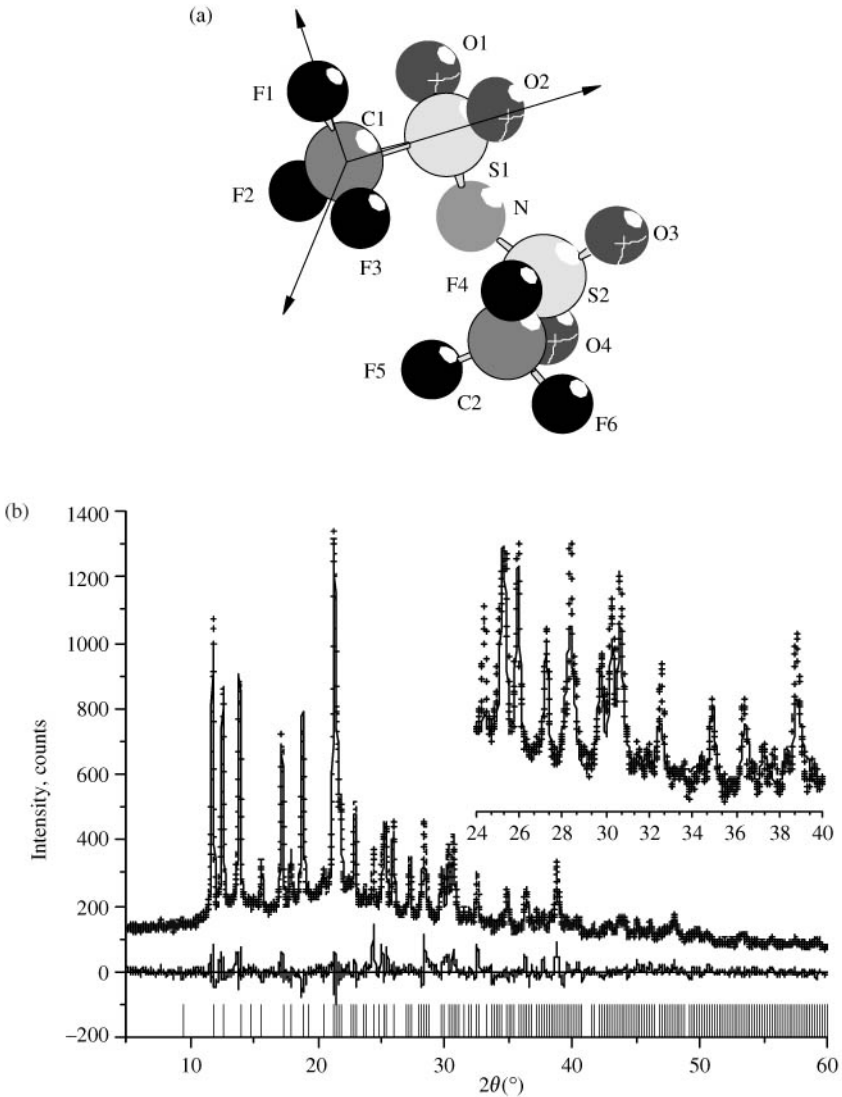


Fig. 16.1. (a) Imide anion in a local Cartesian frame. (b) Observed (crosses), calculated (solid line) and difference X-ray powder diffraction patterns for $(\text{PEO})_3 : \text{LiN}(\text{SO}_2\text{CF}_3)_2$ after refinement and following the SA run with fixed coordinates for the atoms belonging to the PEO chain. The insert shows an expansion of the region from 24° to 40° in 2θ .

polymer chain was allowed to vary its position and conformation in addition to the set of parameters involved in the first run. The coordinates of the atoms comprising the chain (Fig. 16.2(a)) were calculated with all bond lengths and bond angles fixed at the values obtained in the course of the last refinement.

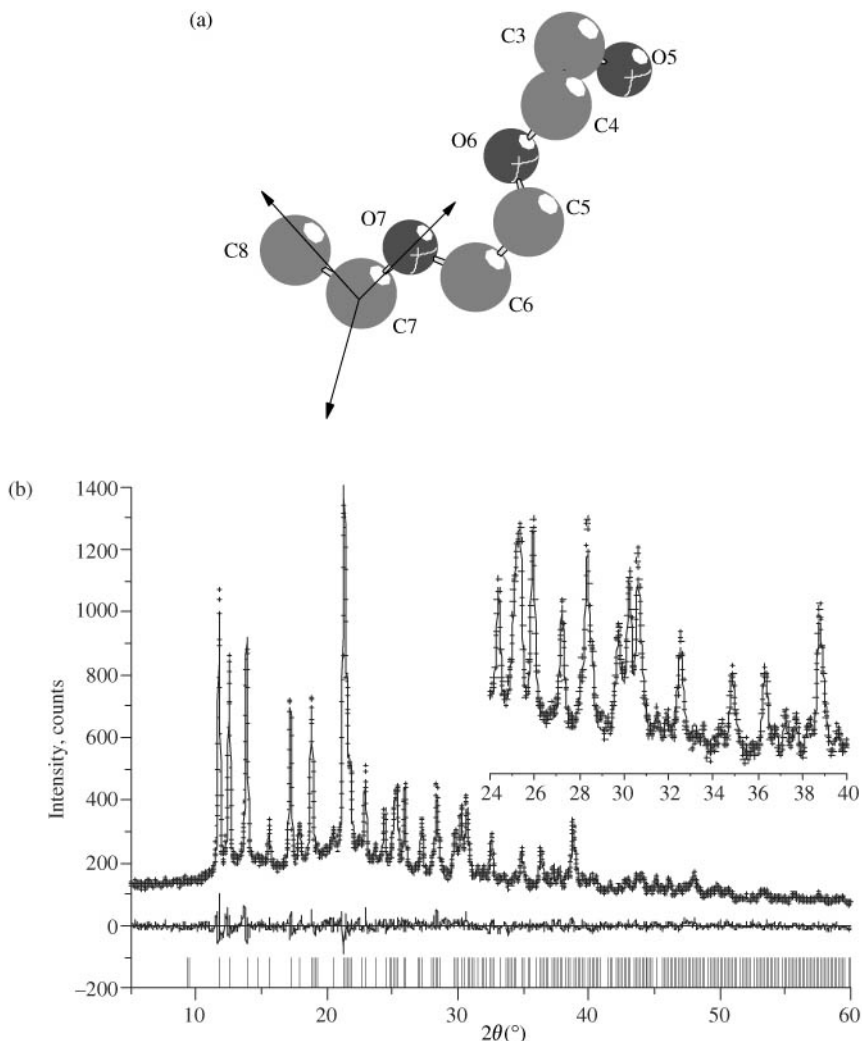


Fig. 16.2. (a) A fragment of the PEO chain in a local Cartesian frame. (b) Observed (crosses), calculated (solid line) and difference X-ray powder diffraction patterns for $(\text{PEO})_3 : \text{LiN}(\text{SO}_2\text{CF}_3)_2$ after refinement and following the SA run in which the position and conformation of the PEO chain were varied. The insert shows an expansion of the region from 24° to 40° in 2θ .

Such a description added 12 parameters to the \mathbf{P} vector: $x_{C7}, y_{C7}, z_{C7}, \Theta_{\text{PEO}}, \Phi_{\text{PEO}}, \Psi_{\text{PEO}}, \tau_{O5\ C3\ C4\ O6}, \tau_{C3\ C4\ O6\ C5}, \tau_{C4\ O6\ C5\ C6}, \tau_{O6\ C5\ C6\ O7}, \tau_{C5\ C6\ O7\ C7}, \tau_{C6\ O7\ C7\ C8}$. The total number of rejected and accepted trial configurations at each ‘temperature’ was chosen to be $N_{\text{tot}} = 7000$ while the initial

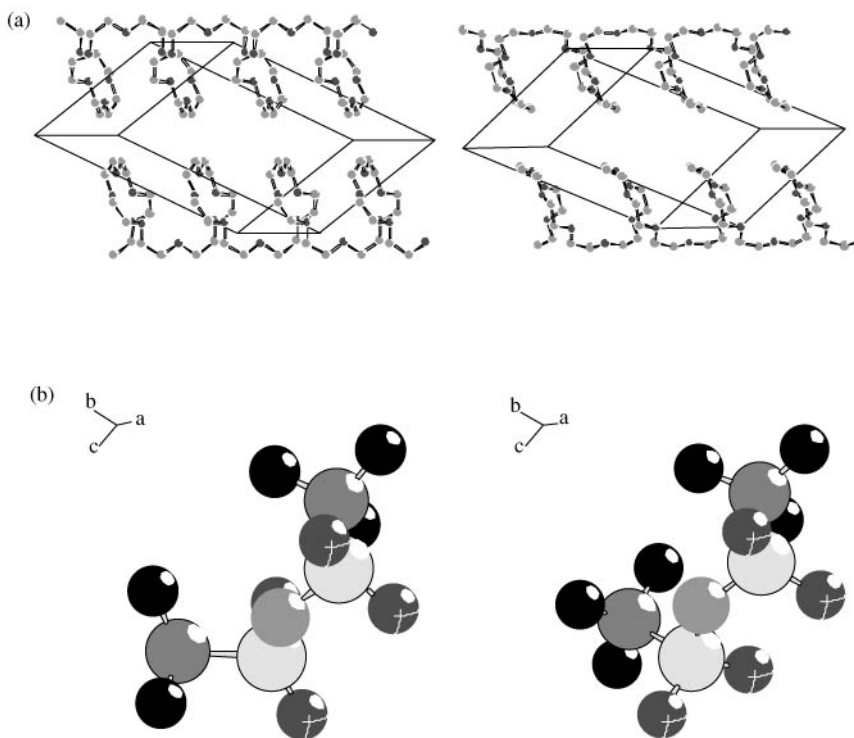


Fig. 16.3. (a) PEO chain and (b) a single imide anion from the structural models corresponding to the fits shown in Fig. 16.1(b) (left) and Fig. 16.2(b) (right).

value of $\Delta\chi_{\text{cur}}^2$ was set to 0.5, preventing large variations of the parameter values when making an uphill step in $\chi^2(\mathbf{P})$. Over 100 000 random structural models were generated with only 861 being accepted. Approximately 90 per cent of the rejected trial models were discarded on the grounds of breaking the continuity of the PEO chain at the junctions of neighbouring asymmetric units. The best structural model was used in a new refinement, which gave an excellent fit to the observed pattern (Fig. 16.2(b)). Apart from a somewhat different chain conformation, the second SA run has revealed a different conformation for the SO_2CF_3 fragments of the imide group about the $\text{S}_2\text{-N}$ bond (Fig. 16.3), which did not appear during the first run with the chain fixed and could not be established in the course of the first refinement by the Rietveld method. The final structure of $(\text{PEO})_3:\text{LiN}(\text{SO}_2\text{CF}_3)_2$ is shown in Fig. 16.4. As in other 3 : 1 complexes, one cation is located in each turn of the PEO helix and is coordinated by oxygen atoms. Further discussion of the structure and computational details are given in Andreev *et al.* (1996, 1997a).

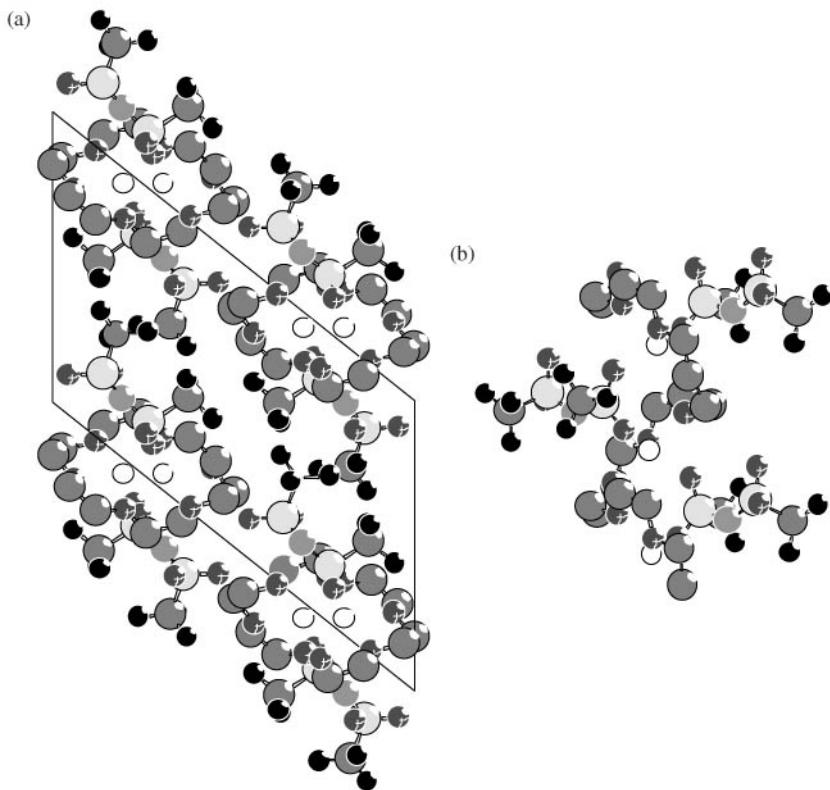


Fig. 16.4. (a) View of the $(\text{PEO})_3:\text{LiN}(\text{SO}_2\text{CF}_3)_2$ structure down the *b*-axis. (b) Part of the structure showing a single polymer chain with associated ions (hydrogen atoms are not shown).

16.4.2 PEO : NaCF_3SO_3

Based on the observed density and unit cell volume, the asymmetric unit of PEO : NaCF_3SO_3 comprises a single EO unit, a sodium cation, and a triflate, CF_3SO_3^- , anion. The stereochemical description of the anion coincides with that of the NSO_2CF_3 moiety (see Fig. 16.1(a)) of the imide anion but with the nitrogen atom substituted by an oxygen.

The initial trial structure for the SA run was chosen at random and did not provide a match between the calculated and observed diffraction patterns. During the minimization, 27 parameters were varied simultaneously with all bond lengths and bond angles associated with particular bond types in the triflate set to be equal. This constrained SA run produced a structural model (Fig. 16.5(a)) with a continuous PEO chain along the shortest cell axis giving a reasonable profile fit after subsequent refinement by the Rietveld method

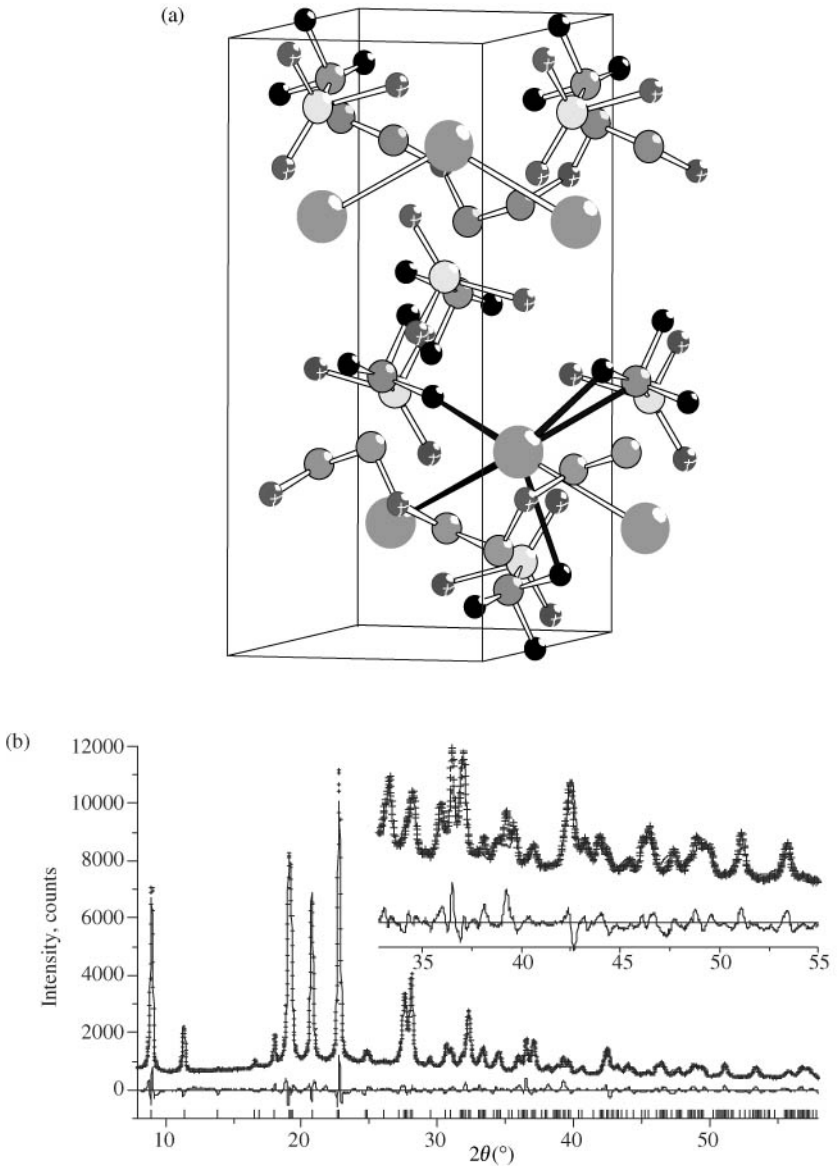


Fig. 16.5. (a) Refined structural model of PEO:NaCF₃SO₃ after the SA run with all like bond lengths and bond angles in the triflate ion treated as equal. Solid lines connect the Na⁺ cation to its nearest neighbours. (b) Observed (crosses), calculated (solid line) and difference powder diffraction profiles for the above structural model of PEO:NaCF₃SO₃.

(Fig. 16.5(b)). However all attempts to improve the fit further by refinement failed, leaving the best χ^2 equal to six and a noticeable misfit in the 2θ range from 33° to 55° (see insert in Fig. 16.5(b)). The refined model placed fluorines rather than the more negatively charged oxygens of the triflate anion adjacent to the Na^+ cation and did not ensure coordination of the sodiums by the chain oxygens (see Fig. 16.5(a)). In addition, the separation of adjacent Na^+ ions was only 3.26 \AA which is highly unlikely based on the Coulombic repulsion. Negative values of the displacement parameter B for some of the atoms provided further evidence indicating the inappropriateness of the structural model.

Successful structure determination was achieved after removing the constraint that all like bond lengths and bond angles in the triflate were equal. A new SA minimization was performed allowing all such lengths and the angles to vary independently. During this run, 37 parameters were varied in a random fashion but with the imposition of chain continuity. The structural model obtained after further refinement (Fig. 16.6(a)) revealed six-fold coordination of the Na^+ ion and provided an excellent match between the observed and calculated patterns with $\chi^2 = 1.1$ (Fig. 16.6(b)) and all B values positive.

The dramatic deleterious effect of averaging the bond lengths and angles on the structure solution could not have been anticipated in advance because the same constraint did not negate finding the internal conformation and position of the imide ion (see Section 16.4.1) with almost twice as many like bond lengths and bond angles set to be equal. Nevertheless, the distribution of the scattering power

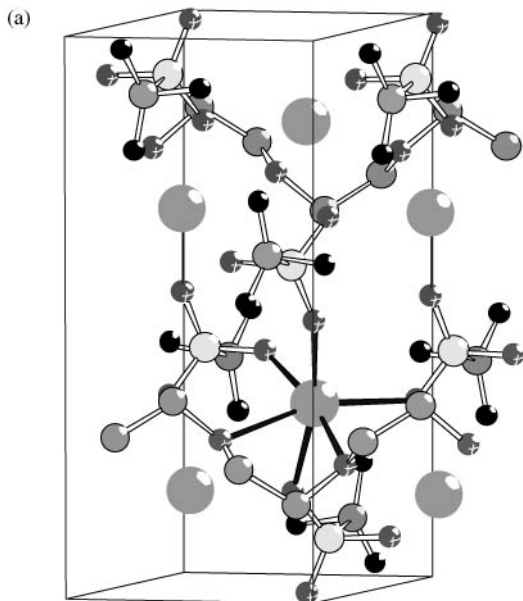


Fig. 16.6. See caption opposite.

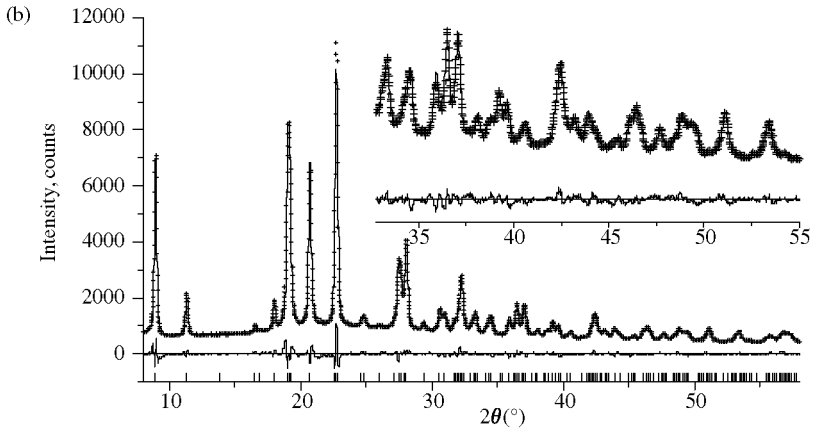


Fig. 16.6. (a) Refined structural model of PEO:NaCF₃SO₃ after the SA run in which all like bond lengths and bond angles in the triflate ion were varied independently. Solid lines connect the Na⁺ cation to its nearest neighbours. (b) Observed (crosses), calculated (solid line) and difference powder diffraction profiles for the above structural model of PEO:NaCF₃SO₃.

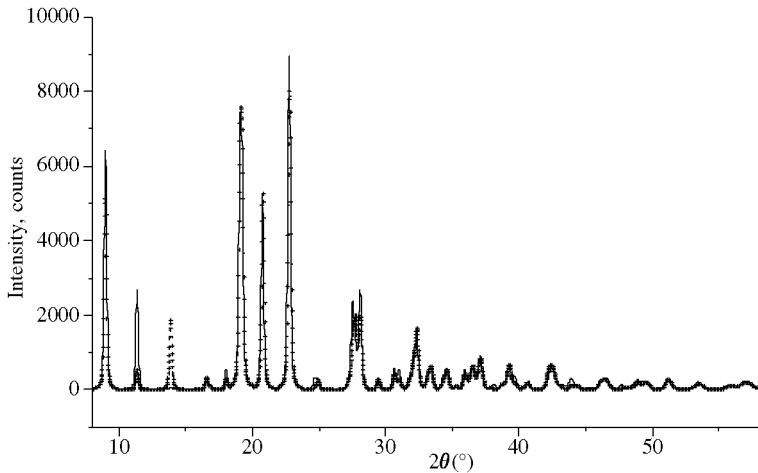


Fig. 16.7. Solid line—calculated powder diffraction pattern of PEO:NaCF₃SO₃ based on atomic coordinates obtained in the final refinement. Crosses—calculated powder diffraction pattern of the modified PEO:NaCF₃SO₃ structure by averaging all like bond lengths and bond angles in the triflate ion.

among the constituent atomic species in the case of PEO:NaCF₃SO₃ was such that a random search using the constrained model was biased from the start and could not yield the correct solution. As an illustration of the effect of imposing too high a level of constraints, Fig. 16.7 shows a significant change in the appearance

of the calculated diffraction pattern upon averaging the bond lengths and bond angles of the triflate in the final structural model. Further computational details and discussion of the structure can be found in Andreev *et al.* (1997b).

16.4.3 PEO₆:LiAsF₆

In the preceding sections, the dangers of over-constraining the molecular moieties during the structure solution of polymer:salt complexes were demonstrated. Therefore, for the structure solution of the first 6:1 complex, all molecular fragments were treated as fully flexible from the outset. Analogous to the previous examples, the asymmetric unit consisted of a single formula unit of

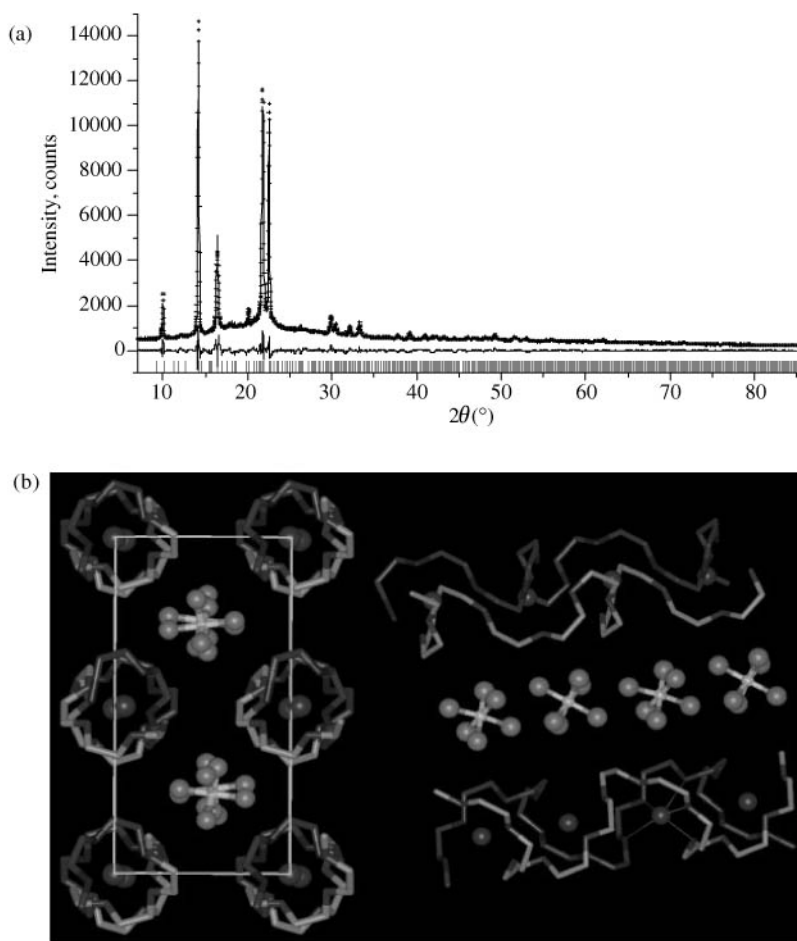


Fig. 16.8. (a) Observed, calculated and difference powder diffraction patterns of PEO₆:LiAsF₆ (b) The structure of PEO₆:LiAsF₆.

PEO₆:LiAsF₆. The anion in this case may be described as a near-perfect octahedral arrangement of fluorines around the As atom. Seventy-nine stereochemical parameters, including 15 torsion angles, were varied simultaneously in the SA procedure. The initial position and orientation of all fragments along with the conformation of the PEO chain were chosen at random and provided no match between the calculated and observed diffraction patterns. This SA run, during which 7000 out of 160 000 moves were accepted, produced a structural model with a much improved profile fit. The location of the Li⁺ ion was verified using routine Rietveld refinement of neutron diffraction data collected on the OSIRIS diffractometer at ISIS, Rutherford Appleton Laboratory on a deuterated sample. The final structural model (50 atoms in the asymmetric unit) obtained after refinement produced an excellent fit to the diffraction pattern (Fig. 16.8(a)) with $\chi^2 = 3.2$ ($R_p = 4.9$ per cent, $R_{wp} = 6.6$ per cent, 3899 data points, 1370 reflections, 168 variables, 135 soft constraints).

The structure is completely different from any previously known polymer electrolyte. The Li⁺ cations are located within cylinders formed by interlocking double, non-helical, polymer chains (Fig. 16.8(b)). Each cation is coordinated simultaneously by both chains giving a total coordination around Li⁺ of five. In contrast to other known PEO complexes, the anions do not coordinate the cations but instead are located outside the cylinder in the interchain space. Further discussion of the structure may be found in MacGlashan *et al.* (1999).

16.5 Discussion

The SA method based on a full-profile fit of the experimental pattern is capable of determining relatively complex crystal structures containing highly flexible molecules. Recently it has been suggested that instead of calculating a complete powder diffraction pattern for each random structure and fitting it directly to the observed pattern, the process could be divided into two steps. Step 1 involves extracting integrated intensities from the observed pattern, using either the Pawley (1981) (Shankland *et al.* 1997; David *et al.* 1998) or the Le Bail (1988) (Pagola *et al.* 2000) approach. In step 2, the randomly generated structures are tested against the set of intensities rather than the entire profile. Molecular structures, with up to 16 degrees of freedom, have been solved using SA minimization of the figure-of-merit function based on integrated intensities (David *et al.* 1998). The advantage of this approach is that it offers a significant reduction of over 100 fold in the computational time. Typically the full-profile SA method requires between 12 and 24 hours on a 450 MHz Pentium PC. As is frequently the case in modern crystallography, the computational efficiency is much greater than that of the other essential steps in the process of structure determination. Often the time taken to prepare the compound, collect high quality data, index the powder pattern and write the paper, considerably

exceeds the computation time! In the case of relatively complex structures, peak overlap is likely to be severe and there has been considerable debate whether, in such circumstances, the fashion in which group-overlapped intensities are dealt with in the two-step method is valid or leads to a loss of information compared with full-profile fitting. It is, of course, in the structure solution of such complex compounds that the increased computational efficiency would be particularly advantageous.

Perhaps the most interesting question is what level of structural complexity can be tackled successfully. In the context of the SA method, the issue is not the size of the structure measured by the number of atoms in the asymmetric unit, but the degree of flexibility that has to be allowed in order to determine the crystal structure of the molecule. If the structure is permitted to be fully flexible (i.e. all bond lengths, bond angles, torsion angles and positional and orientation parameters of each fragment in the asymmetric unit are independent variables), it is possible to reach the global minimum corresponding to the best possible fit to the data provided that the temperature reduction is sufficiently slow and the number of moves explored at each temperature is sufficiently large. If the asymmetric unit of the structure consists of a single isolated molecule, for which interatomic connectivity is well-established and the bond lengths and angles are particularly well defined (e.g. Harris and Tremayne 1996; Harris *et al.* 1994; Shankland *et al.* 1998; David *et al.* 1998; Pagola *et al.* 2000), then only a few variables are required in the SA minimization in order to solve the structure. The required parameters are those defining the position and orientation of the molecule as well as the torsion angles. The bond lengths and angles can be fixed at typical values. However, such an approach may be insufficient if the asymmetric unit consists of more than a single molecule. For each possible conformation and position of one molecule there exist numerous possible conformations and positions of the other. As a result, there may be many more local minima in the goodness-of-fit function that are sufficiently deep to be confused with the global minimum. In such circumstances, a final discrimination between different fits of the calculated and observed data is essential before refinement can be expected to yield the correct structural model. Such discrimination may require bond lengths and angles to be varied independently in addition to torsion angles. The presence of ionic bonding between separate moieties in the structure may be particularly troublesome since such bonding is stronger than van der Waals' forces and can perturb the internal dimensions of covalently bonded moieties compared with the case of two or more neutral molecules. The examples of structure determination we have presented here constitute a particularly severe test of the methodology in the context of these difficulties because the asymmetric unit comprises several independent moieties that interact via both van der Waals forces and ionic bonding. In the case of $(\text{PEO})_3 : \text{LiN}(\text{SO}_2\text{CF}_3)_2$ it was sufficient to set all similar bond lengths, bond angles and torsion angles in the imide anion as single variables while changing only the conformation of the polymer chain with fixed bond lengths and angles.

However, for PEO:NaCF₃SO₃ the correct model was found only when all stereochemical restraints were removed and all parameters were varied in a random fashion.

The solution of structures containing different atoms of comparable scattering power (e.g. C, N, O) is often regarded as presenting the greatest challenge. This task is readily tackled for molecular structures by the SA approach described in this chapter. The successful structure solution of compounds requiring the independent variation of 79 parameters and up to 26 symmetry-unrelated non-hydrogen atoms has been demonstrated. The upper limit for structure solution by whole-pattern fitting using SA minimization combined with a stereochemical description of the problem should be comparable to the limit of structural complexity found for Rietveld refinement.

Acknowledgements

The authors are grateful to Dr P. Lightfoot for his collaboration during the structure solution of (PEO)₃:LiN(SO₂CF₃)₂ and to Mr G. S. MacGlashan for his work on structure solution of (PEO)₆:LiAsF₆. Thanks are also due to Dr L. J. M. Sawers, Dr D. Martin and Dr D. Engberg. The financial support of this work by the EPSRC and The Leverhulme Trust is gratefully acknowledged.

References

- Andreev, Y. G., Lundström, T. and Sorokin, N. I. (1995). *Nucl. Instr. and Meth. in Phys. Res.*, **A354**, 134–8.
- Andreev, Y. G., Lightfoot, P. and Bruce, P. G. (1996). *Chem. Comm.*, 2169–70.
- Andreev, Y. G., Lightfoot, P. and Bruce, P. G. (1997a). *J. Appl. Crystallogr.*, **30**, 294–305.
- Andreev, Y. G., MacGlashan, G. S. and Bruce, P. G. (1997b). *Phys. Rev. B*, **55**, 12011–17.
- Arnott, S. and Wonacott, A. J. (1966). *Polymer*, **7**, 157–66.
- Baerlocher, Ch. (1993). In *The Rietveld Method* (ed. R. A. Young), pp. 186–96. Oxford University Press.
- Chatani, Y., Fujii, Y., Takayanagi, T. and Honma, A. (1990). *Polymer*, **31**, 2238–44.
- Chatani, Y. and Okamura, S. (1987). *Polymer*, **28**, 1815–20.
- David, W. I. F., Shankland, K. and Shankland, N. (1998). *J. Chem. Soc. Chem. Comm.*, 931–2.
- Goldstein, H. (1980). *Classical Mechanics*. Addison-Wesley.
- Harris, K. D. M., Tremayne, M., Lightfoot, P. and Bruce, P. G. (1994). *J. Am. Chem. Soc.*, **116**, 3543–7.
- Harris, K. D. M. and Tremayne, M. (1996). *Chem. Mater.*, **8**, 2554–70.
- International Tables for X-ray Crystallography* (1959). Vol. II. Birmingham: Kynoch Press. (Present distributor Kluwer Academic Publishers, Dodrecht).

- Larson, A. C. and Von Dreele, R. B. (1987). *Los Alamos Natl. Lab. Rep.* No. LA-UR-86-748.
- Le Bail, A., Duroy, H. and Fourquet, J. L. (1988). *Mat. Res. Bull.*, **23**, 447–52.
- Lightfoot, P., Mehta, M. A. and Bruce, P. G. (1993). *Science*, **262**, 883–5.
- Lightfoot, P., Nowinski, J. L. and Bruce, P. G. (1994). *J. Am. Chem. Soc.*, **116**, 7469–70.
- MacGlashan, G. S., Andreev, Y. G. and Bruce, P. G. (1999). *Nature*, **398**, 792–4.
- Metropolis, N., Rosenbluth, A. W., Rosenbluth, M. N., Teller, A. H. and Teller, E. (1953). *J. Chem. Phys.* **21**, 1087–92.
- Newsam, J. M., Deem, M. W. and Freeman, C. M. (1992). *NIST Spec. Publ.*, **846**, 80–91.
- Pagola, S., Stephens, P. W., Bohle, D. S., Kosar, A. D. and Madsen, S. K. (2000). *Nature*, **404**, 307–10.
- Pawley, G. S. (1981). *J. Appl. Crystallogr.*, **14**, 357–61.
- Press, W. H., Teukolsky, S. A., Vetterling, W. T. and Flannery, B. P. (1992). *Numerical Recipes in C: the Art of Scientific Computing*. Cambridge University Press.
- Rietveld, H. M. (1969). *J. Appl. Crystallogr.*, **2**, 65–71.
- Shankland, K., David, W. I. F., Csoka, T. and McBride L. (1998). *Int. J. Pharmaceutics*, **165**, 117–26.
- Shankland, K., David, W. I. F. and Csoka, T. (1997). *Z. Kristallogr.*, **220**, 550–2.
- Tremayne, M., Kariuki, B. M. and Harris, K. D. M. (1997). *Angew. Chem., Int. Ed.*, **36**, 770–2.
- Wilson, A. J. C. (ed.). (1995). *International tables for crystallography, Vol. C, Mathematical, Physical and Chemical Tables*. Kluwer Academic Publishers, Dodrecht.
- Yokoyama, M., Ishihara, H., Iwamoto, R. and Tadokoro, H. (1969). *Macromolecules*, **2**, 184–92.

Chemical information and intuition in solving crystal structures

Lynne B. McCusker and Christian Baerlocher

17.1 Introduction

In attempting to solve a structure from powder diffraction data, we tend to become so absorbed in the details of the diffraction pattern that we forget that this is not the only information we have on the material under investigation. In general, we know quite a lot more. For example, we almost always know its approximate chemical composition and its relevant physical properties (e.g. optical, magnetic, electronic, catalytic, thermal), and we know the structural features of related compounds. We may also have the results of other (non-diffraction) experiments, such as IR, UV-visible, EXAFS, NMR and/or ESR spectroscopy, electron microscopy or theoretical calculations, at our disposal.

In the early days of single-crystal structure analysis, it was common practice to use such information in the structure solution process. However, as crystallographic methods became more and more powerful, access to increased computing capacity became routine, and instrumentation improved, this additional crystal chemical information became redundant and fell into disuse. Now, in the world of structure analysis of polycrystalline materials, where the information content of the powder pattern is significantly lower than that of a single-crystal dataset, we have to reinstate the use of such information. It can mean the difference between solving and not solving a structure.

Crystal chemical information can be put to good use at several stages of the structure determination process. In the following sections, examples of how chemical information (and intuition) can facilitate structure determination and refinement are discussed. Many of the examples are taken from the realm of zeolite structures, because that is our particular sphere of interest and because these structures quite often challenge the limits of powder methods, but the principles involved can be applied to any class of material. The order of presentation parallels that of the structure solution process: the collection of the data, the determination of the unit cell and space group, the generation of an approximate model, the completion of the model, the refinement of the structure, and the evaluation of the final structure.

17.2 Data collection

Even at the data collection stage (see Chapter 6), crystal chemical information can play an important role. The optimization of data-collection parameters depends significantly on the composition and nature of the sample. For example, if the material is strongly absorbing, reflection rather than transmission geometry should be used in the laboratory, or specific wavelength(s) should be selected or avoided at a synchrotron, or the possibility of using neutrons should be considered. If a sample contains a potential anomalous scatterer, absorption edge experiments at a synchrotron may be advantageous. If the material shows a tendency towards preferred orientation or the compound contains both light and heavy atoms, a neutron experiment may be indicated. If the sample is highly crystalline and displays sharp diffraction peaks in the laboratory, a synchrotron or high-resolution neutron experiment might produce even higher quality data and thereby provide more information.

It is not the purpose of this chapter to delve into the many aspects of data collection optimization, but the few examples given above should serve to suggest that a little thought given to the diffraction experiment itself is worthwhile. The selection of optimal data collection parameters for the specific material under investigation can only have a beneficial effect on the quality of the data that emerges, and this may prove to be critical in subsequent structure analysis.

Example 1. A prime example of the importance of carefully selected data collection conditions was illustrated in the structure solution of $\text{La}_3\text{Ti}_5\text{Al}_{15}\text{O}_{37}$ (Morris *et al.* 1994). With 60 atoms in the asymmetric unit, this is one of the most complex structures solved from powder data to date, and the availability of both synchrotron and neutron data was essential to the structure solution and subsequent refinement.

17.3 Indexing and choice of space group

Indexing programs (see Chapter 7) have become so reliable in recent years that if accurate peak positions are input, the correct unit cell is generally found relatively easily. However, in difficult cases, the inclusion of density information can help the programs and can be used as a check (the cell volume should correspond to an integral number of formula units) of an indexing solution (Louer 1992).

The determination of the correct space group, however, is rarely unambiguous, and this can be a serious limitation in structure analysis using powder diffraction data. The number of probable space groups is usually limited by the geometry of the unit cell (though lower symmetries are always possible), but overlap of reflections often prevents systematic absences from being established satisfactorily, and intensity symmetry of potentially equivalent reflections

cannot be evaluated. It is important to keep the uncertainty of the assumed space group in mind in subsequent steps. Independent experimental data can be extremely useful in narrowing the choice. For example, electron diffraction or solid state NMR can provide additional symmetry information, or physical properties can limit the choice (e.g. an optically active crystal or one displaying piezoelectric properties cannot be centrosymmetric). Similarly, for a molecular crystal, consideration of the symmetry of the molecule and possible packing arrangements can eliminate some space groups. For example, given a hexagonal unit cell with no observable systematic absences, 16 space groups are equally probable (and 17 more only have conditions on $00l$ reflections and these might easily be obscured). However, if the maximum symmetry of the molecule is three, and there are two molecules per unit cell, nine of the sixteen space groups can be eliminated immediately.

Example 2. In the structure determination of $((\text{CH}_3)_4\text{N})_2\text{Ge}_4\text{MnS}_{10}$, Achak and co-workers (1995) had eight body-centred, tetragonal space groups to choose from. They used the knowledge that the Ge and Mn would probably be tetrahedrally coordinated to S to limit the choice to the three space groups containing $\bar{4}$ axes.

17.4 Model building

The classical approach to solving the structure of a polycrystalline material is to build a physical model that is consistent with all the information known about the compound. This model is then used to simulate a powder diffraction pattern for comparison with the measured one. A multitude of information (see Table 17.1 for a short list of potential sources) is used, some of it intuitively, in this process. It is difficult, if not impossible, to describe the complex thought processes that lead to the production of a feasible structural model, but perhaps the few examples below can illustrate some of the more tangible aspects of this approach to structure determination. Although model building is inefficient and prone to failure, it is often the only option available for complex structures and therefore deserves special attention.

Example 3. Cyclo- β -peptide (Seebach *et al.* 1997). A series of cyclic β -peptide tetramers were synthesized, but because they are virtually insoluble in both organic solvents and water, single crystals could not be grown. All were found to be thermally stable up to at least 300°C. These properties were thought to be due to strong intermolecular hydrogen-bonding. The powder diffraction pattern of the (*R, R, S, S*) stereoisomer derived from 3-aminobutanoic acid (see Fig. 17.1(a)) could be indexed on a monoclinic unit cell ($a = 12.69 \text{ \AA}$, $b = 4.98 \text{ \AA}$, $c = 18.64 \text{ \AA}$ and $\beta = 129.7^\circ$ volume = 906 \AA^3), and the systematic absences were consistent with the space group $P2_1/c$. However, the quality of the data did not allow solution by Direct methods.

Table 17.1 Some sources of information useful in model building

| Source | Information |
|---------------------------------|--|
| Powder diffraction pattern | Dimensions of the unit cell Possible symmetry Intensities for checking a simulated pattern |
| Electron microscopy | Morphology Dimensions of the unit cell Possible symmetry Presence/absence of faulting |
| Structures of related compounds | Interatomic distances Coordination numbers and geometries Structural subunits (e.g. SiO ₄ tetrahedron, phenyl ring, peptide linkage) |
| Density | Number of formula units per unit cell |
| NMR | Connectivity Symmetry |
| Physical measurements | Optical activity Magnetic behaviour Conductivity Elasticity Thermal stability Sorption capacity |

The volume of the unit cell and the size of the molecule (24 non-hydrogen atoms at *c.* 15–20 Å³ per atom) suggest that there are probably two molecules per unit cell. Since the geometry of the peptide linkage and the configurations of the four asymmetric C atoms were known, building models of the molecule was straightforward. The short axis dictates that the disk-shaped molecules lie approximately perpendicular to the *b*-axis, and the symmetry elements of the space group further require that the molecules lie on a centre of inversion. Rotation of the molecule around the inversion centre is sterically hindered by the methyl groups of neighbouring molecules (Fig. 17.1(c)), but there are two possible orientations of the molecule (related to one another by a rotation of *c.* 90°) and four conformations of the ring that are consistent with the chemical and symmetry information. Only one combination yields a powder diffraction pattern that approximates the observed one. The molecules are stacked in such a way that all NH groups form a hydrogen bond with a CO group of a neighbouring molecule (Fig. 17.1(b)). In this case, only a limited number of models were feasible, and the powder pattern could be used to distinguish the correct one. Using this model as a starting point, the finer details of the structure were determined via Rietveld refinement.

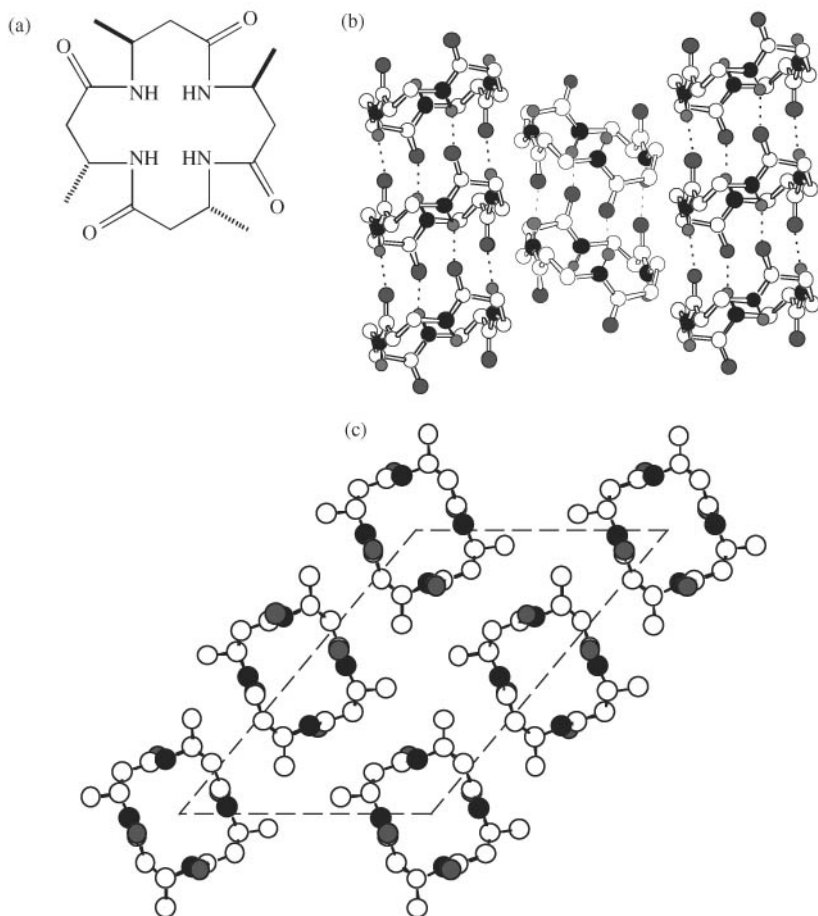


Fig. 17.1. (a) stick drawing of the (R,R,S,S) stereoisomer of the β -peptide tetramer derived from 3-aminobutanoic acid, (b) $[0\ 1\ 0]$ projection of the refined structure, and (c) $[1\ 0\ 1]$ projection (methyl groups deleted for clarity) showing the stacking of the molecules and the hydrogen bonding between them.

Example 4. Zeolite A (Breck et al. 1956). Zeolite A was one of the first zeolites to be synthesized in the laboratory. Initial characterization of the polycrystalline material yielded the information given in Table 17.2. The dehydration, sorption and ion-exchange properties indicated that it was, in fact, a zeolite, and using all the information and their knowledge of other zeolite crystal structures, Breck and co-workers were able to build a model of the framework structure.

The chemical formula per unit cell ($\text{Na}_{12}\text{Al}_{12}\text{Si}_{12}\text{O}_{48} \cdot 27\text{H}_2\text{O}$) could be calculated from the chemical composition and density information. From other

Table 17.2 Initial characterization of zeolite A

| | |
|----------------------|---|
| Chemical composition | $\text{NaAlSiO}_4 \cdot 2.25\text{H}_2\text{O}$ |
| Density | 1.99 g/cm^3 |
| Indexing | Primitive cubic unit cell with $a = 12.3 \text{ \AA}$ (no systematic absences) |
| Dehydration | Reversible |
| Sorption | $c.4.5 \text{ \AA}$ pore openings |
| Ion exchange | Na^+ easily exchanged |

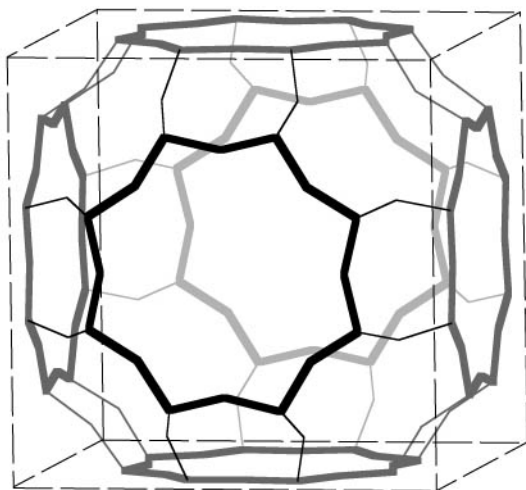


Fig. 17.2. The framework structure of the aluminosilicate zeolite A showing the cubic unit cell, the eight rings on the faces (thick lines), and the connections (thin lines) between them.

zeolite structures, it was known that Al and Si are tetrahedrally coordinated (therefore called T-atoms) to bridging oxygens to form a three-dimensional framework structure. It could be assumed that the X-ray diffraction experiment would not distinguish between Al and Si, so they could be treated as being equivalent. The sorption data were indicative of an eight-ring (eight oxygen and eight T-atoms) pore opening. Given the cubic symmetry, the size of the unit cell, the number of T-atoms per unit cell, the size of an eight-ring, and the requirement that the aluminosilicate framework be three-dimensional and four-connected, the number of possible structures is extremely limited. Only by placing the eight-rings on the faces of the cubes and connecting them to one another via oxygen bridges, can a model consistent with all the information be built (see Fig. 17.2).

Another way of looking at this puzzle would be to use the symmetry information for $Pm\bar{3}m$ in the *International Tables for Crystallography* (Hahn 1983). Assuming that the 24 T-atoms in the unit cell are equivalent, they must lie on

a mirror plane, and of the three possibilities (at $x=0$, at $x=1/2$, and along the diagonal $x=y$), only one set of symmetry equivalent coordinates $(0, y, z)$ generates T-atom positions consistent with tetrahedral geometry, eight-ring channels, and a three-dimensional, four-connected net.

Example 5. Tetramethylammonium gismondine (Baerlocher and Meier 1970). The powder pattern of this zeolite, synthesized in the presence of tetramethylammonium (TMA^+) ions, could be indexed on a body-centred, tetragonal unit cell with $a = 10.46$ and $c = 9.73$ Å. Chemical analysis indicated that there were four TMA^+ ions per unit cell, and given the symmetry and size of that cell, there was only one sensible way of arranging them: at 000 , $0\ 1/2\ 1/4$, $1/2\ 1/2\ 1/2$ and $1/2\ 0\ 3/4$ (see Fig. 17.3(a)). This arrangement yields an N-N distance of 5.77 Å, which agrees well with the 5.53 Å found in $(\text{CH}_3)_4\text{NCl}$, but which excludes the possibility of the framework atoms being located between neighbouring TMA^+ cations. That is, the aluminosilicate cage around each cation must have windows, presumably eight rings, arranged in a tetrahedral fashion. This reasoning leads automatically to the framework structure shown in Fig. 17.3(b).

Example 6. Some complex zeolite structures. The zeolite structure literature is rich in impressive examples of model building, starting with the very early single crystal studies of cancrinite, natrolite and sodalite by Pauling (1930*a, b*) and of analcime, edingtonite and thompsonite by Taylor and co-workers (Taylor 1930; Taylor and Jackson 1933; Taylor *et al.* 1933). Some more recent examples that are too complex to describe in detail here but that provide some

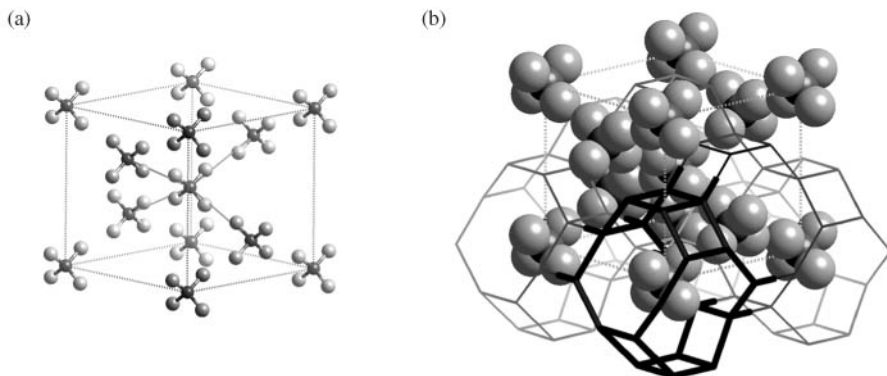


Fig. 17.3. (a) Body-centred, tetragonal arrangement of tetramethylammonium ions (TMA^+) in the unit cell of TMA-gismondine. The lines show the closest contacts to the central ion and indicate where windows in the aluminosilicate framework must be. (b) The aluminosilicate framework (bridging oxygens have been omitted for clarity) built around the TMA^+ ions.

thought-provoking reading, include the framework structures of ZSM-5 with 38 framework atoms in the asymmetric unit (Flanigen *et al.* 1978; Kokotailo *et al.* 1978), EU-1 with 31 (Briscoe *et al.* 1988), CIT-1 with 24 (Lobo and Davis 1995), NU-87 with 21 (Shannon *et al.* 1991) and VPI-8 with 14 (Freyhardt *et al.* 1996). The number of framework atoms in the topological (highest possible) symmetry are included as an indication of the complexity involved, but the real structures often deviate significantly from this high symmetry and usually contain additional non-framework atoms as well.

17.5 Computer generation of structural models

An obvious way to expedite the model building process would be to exploit the power of a computer, and, in fact, several programs have been developed with this in mind. These can be of tremendous assistance to a model builder. For example, computer graphics software such as Cerius² (Accelrys) can be used to build a molecule, optimize its geometry, put it in a unit cell with the appropriate symmetry, optimize its packing, and monitor the effect of various manipulations on the simulated powder diffraction pattern.

Other programs have been designed to generate models based on some set of criteria. Bennett and Shomaker (Bennett 1988), Brunner (1990), Treacy, Rao and Riven (1993), Akporiaye and Price (1989), and Shannon (1993) have all developed approaches to zeolite structure solution using this idea. The models generated are then evaluated for consistency with other experimental information by hand.

17.6 Using chemical information actively in an automated structure determination process

The use of computers to generate structural models for organic compounds has been developed further in the Monte Carlo, simulated annealing and genetic algorithm approaches, which are described in detail in separate chapters (see Chapters 15 and 16). These methods tackle the problem of structure solution from powder data in direct (i.e. model-building space) rather than reciprocal space. Structural models are generated according to criteria derived from chemical information, and the diffraction pattern is then considered in an automatic evaluation process.

In these methods, chemical information is used actively, and the powder diffraction data passively (in contrast to conventional crystallographic methods). The obvious question is whether it is possible to use both the chemical *and* the diffraction data actively (i.e. to incorporate the model builder's knowledge into an algorithm that also uses the information in the diffraction pattern). While it is perhaps difficult to convert the intuitive thought processes and all the knowledge of an experienced model builder into the strict logic of a computer

program, some quantifiable characteristics (e.g. chemical composition, expected coordination geometries and typical bond distances and angles) would seem to lend themselves to such an approach.

Of course, once such knowledge is incorporated into a structure determination procedure, that procedure becomes specific to the selected class of materials, so care must be taken that the information is, in fact, relevant to the sample under study. An elegant way of introducing such information into a structure determination procedure would be to use a Bayesian approach (see Chapters 8 and 14), where the data can be included as 'prior information' in the same way that the positivity of electron density is. However, the encoding required is far from trivial.

Another possibility is to tailor a program to the class of materials of interest. This has been done for zeolites and zeolite-like molecular sieves in the program *focus* (Grosse-Kunstleve *et al.* 1997). The input to the program includes the chemical composition per unit cell and minimum interatomic distances for all atoms. This information is then used by the program to search for possible framework structures. To start with, random phases are assigned to the observed structure factors (obtained from extracted integrated intensities) to generate an electron density map, which is then interpreted automatically using the chemical information. A new phase set is calculated from the structure or fragment of the structure resulting from this interpretation and a Fourier recycling procedure started. Once the phases have converged, a new set of starting phases is generated and the procedure repeated. A flow diagram of the program is given in Fig. 17.4.

The key to the success of *focus* lies in the search for a three-dimensional, four-connected net (framework topology) with appropriate interatomic distances within each electron density map generated. Even if some of the reflection intensities are wrong (because of reflection overlap) and some of the phases are wrong (because they have been generated randomly), the electron density map is likely to have some indication of the correct structure. Given the information that a framework structure must be present, weaker peaks that complete a net can be included in a model while stronger peaks that do not can be ignored. Of course, the prerequisite is that the phase set be at least partially correct, so the generation of many starting phase sets is an integral part of the program. The Fourier recycling loop is also an essential part of the procedure, since it allows a more correct phase set to be generated from different starting points. Alternating between map interpretation in terms of atoms (based on peak height and interatomic distances) and map interpretation in terms of the largest framework fragment found has proven to be the most effective strategy.

The framework topology search, based on a backtracking algorithm, is exhaustive. Each time an electron density map is generated, possible topologies are sought, and any found are written to a file. These topologies are then analysed for their uniqueness and the one that occurs most frequently is generally the

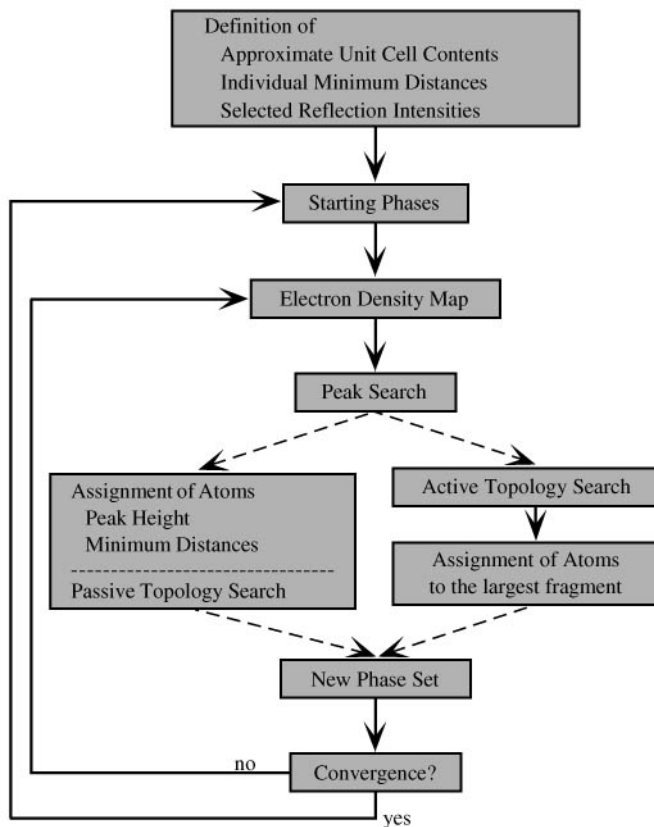


Fig. 17.4. Flow diagram for the program *focus*.

correct one (assuming the space group is correct). The program has been applied successfully to many test examples (Grosse-Kunstleve 1996; Grosse-Kunstleve *et al.* 1999), and to several real structure solutions. The latter include the zincosilicate VPI-9 (seven T-atoms in the asymmetric unit of the topological unit cell and 15 T-atoms and 30 oxygens in the true cell, McCusker *et al.* 1996), the high-silica zeolites SSZ-44 (eight T-atoms, Wagner *et al.* 1999) and MCM-61 (three T-atoms, Schantz *et al.* 1999), and the aluminophosphate $\text{AlPO}_4\text{-53(C)}$ (six T-atoms, Kirchner *et al.* 2000). This is one way of incorporating chemical knowledge into an automated procedure. A similar approach using different criteria for other classes of structures can be imagined, but has not yet been realized.

17.7 Recognizing a structure solution

One of the difficulties in solving a structure from powder data is in recognizing the solution when it is offered. Direct methods applied to the limited set of

reflection intensities that can be extracted reliably from a powder pattern are likely to produce a solution with an approximately oriented, distorted fragment of the structure, but the small displacements of the atoms from their true positions can easily lead to bonds being drawn where there are none and bonds being omitted where they are present. Furthermore, atoms might be missing or false peaks present. This combination can disguise the correct solution beyond recognition, and standard figures-of-merit are not reliable indicators (see, however, Chapters 10 and 11 on Direct methods programs written specifically for powder data). How then should possible solutions be analysed in order to identify feasible candidates?

Again, the answer lies in the chemistry of the material and consistency with other experimental results, but there is no foolproof recipe. Obviously, the solution should reveal the positions of the heavier atoms. The interatomic distances must make sense. Peak heights should approximate the relative scattering powers of the atoms. The coordination numbers may be too low, because some atoms are missing, but shouldn't be too high. The geometry should be within reason, but some deviation due to the approximate nature of the model should be tolerated. Missing atoms should be anticipated (e.g. if a benzene ring is expected, perhaps only three or four of the C's will appear, and these might not be neighbouring ones). If the material is a zeolite, channels or cavities should be around the points of highest symmetry (Brunner 1990). It is possible that no single solution is correct, but comparison of several models may reveal common features that can be developed further using Fourier methods.

This may all seem very vague and unsatisfactory to the reader. That is because one cannot, by definition, describe intuition. All the pieces of information may be present, but it still takes an intuitive leap on the part of the crystallographer to recognize the solution. In other words, flexible thinking is essential.

Example 7. The structure of the zeolite RUB-10 was determined from low-resolution (2 \AA) powder diffraction data by Gies and Rius (1995). They applied a Patterson search technique (see Chapter 13), using a tetrahedral Si_5 fragment as the search model, and the best solution produced the electron density projection shown in Fig. 17.5. Without any knowledge of zeolite structures, the interpretation of that map would be virtually impossible, but, because of their experience with these structures, they were able to discern two potential zeolite framework fragments (A and A'). Although each produced a framework, only A had a reasonable geometry, and subsequent refinement showed this to be the correct structure. The amount of imagination and intuitive thinking required for this structure solution is readily apparent.

17.8 Interpretation of Fourier maps

Once an approximate model has been deduced, it often needs to be completed, and this is normally done using Fourier techniques. Although difference

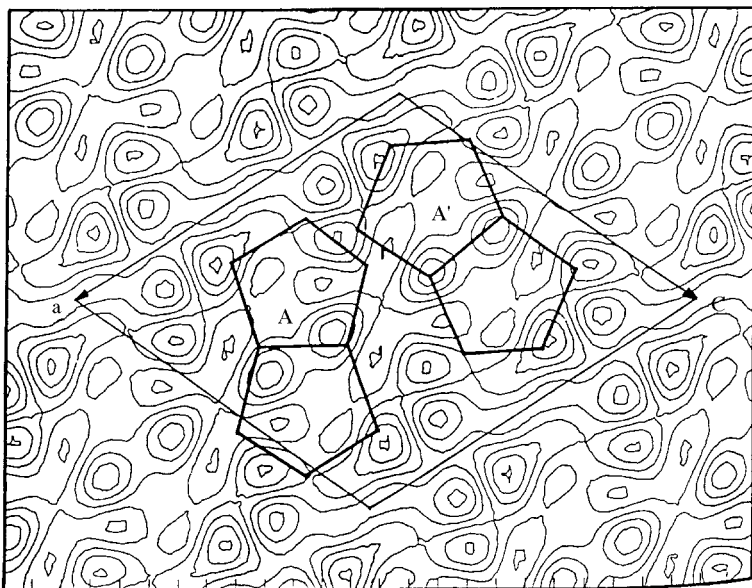


Fig. 17.5. Contour map of the (010) electron density projection obtained for RUB-10 from the result of a Patterson search calculation. Possible interpretations consistent with zeolite chemistry are indicated (A and A'). Reprinted with permission from *Z. Kristallogr.*, 1995, **210**, 476. Copyright 1995, R. Oldenbourg Verlag, München.

electron density maps can be generated from powder data in the same way as they can from single crystal data, they tend to be diffuse and require interpretation. It should always be borne in mind that these maps are doubly biased towards the model used to generate them. Not only are the phases for the observed F 's taken from the model (as they are in the single-crystal case), the partitioning of the intensities of overlapping reflections is also assumed to be the same as for the model. This partitioning and the inexact scaling of the observed to the calculated pattern causes the peaks in the electron density map to be less well-defined and poorly resolved. The electron density often appears as a diffuse cloud rather than as discrete peaks, so the results of peak-finding routines should be treated with caution. It is advisable to look at a three-dimensional contour map rather than at a list of peak positions. An even better approach is to perform a maximum entropy reconstruction instead of a Fourier synthesis. Such maps are generally less noisy and more definitive than their Fourier counterparts. Examples of their successful application include the location of non-framework species in zeolites (Papoular and Cox 1995; Hasegawa *et al.* 1999) and charge density studies of a series of fullerenes (Takata *et al.* 1999) and of the Laves phase $MgCu_2$ (Kubota *et al.* 2000).

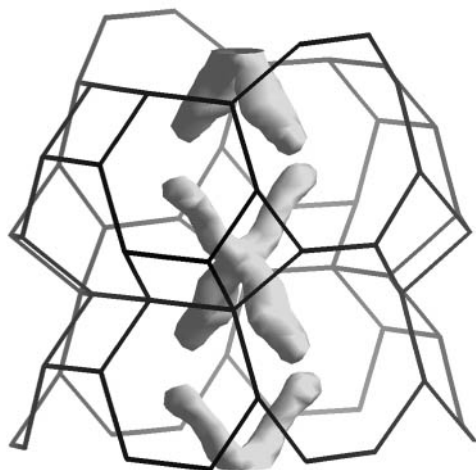


Fig. 17.6. A single contour level of the difference electron density within the channels of the zeolite-like silicoaluminophosphate SAPO-40 (bridging oxygens have been omitted for clarity). The form indicates clearly how the tetrapropylammonium ion is oriented, but the positions of the individual atoms are not resolved into discrete peaks.

Example 8. For zeolites, the framework structure is often known, but the location of non-framework species in the channels and cavities usually has to be determined from difference Fourier maps. In Fig. 17.6, a single contour level of the difference electron density found in the channels of the zeolite-like silicoaluminophosphate SAPO-40 is shown. The organic cation was known to be tetrapropylammonium (TPA^+), and the contour map shows the location and conformation of the molecule very clearly. However, the positions of the individual atoms are not at well-defined maxima that would be found by a peak search program. In this case, additional information from solid state NMR experiments was also considered. It indicated that two of the four 'arms' of the TPA^+ ion were different from the other two, and the orientation found is consistent with that observation: two propyl groups point towards 'pockets' in the framework and two point towards open channels.

A further problem that can lead to confusion in the interpretation of an electron density map is that of disorder. Atoms not found in the initial structure solution may well be disordered and therefore appear as weaker peaks. For example, a functional group in an organic molecule may assume two different orientations in a random fashion, waters of crystallization may be statistically distributed over several sites, or non-framework atoms of a zeolite may not obey the higher symmetry of the framework. Such cases make the interpretation of a difference Fourier map difficult and require some imagination (and additional knowledge) on the part of the interpreter.

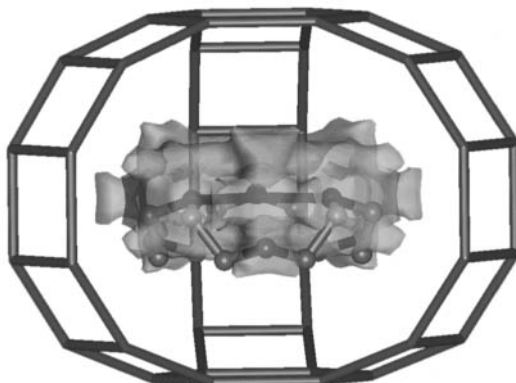


Fig. 17.7. A single contour level of the difference electron density within the medium-sized cages of the zeolite EMC-2 (bridging oxygens omitted for clarity). The horizontal mirror plane causes a mirror image to be created, so the cloud is almost twice as thick as the 18-crown-6 molecule.

Example 9. The zeolite EMC-2 is synthesized in the presence of 18-crown-6 ether molecules, and because these molecules have a strong structure directing effect in the synthesis, it is of interest to know where they are located within the framework. The difference electron density in the medium-sized cage of EMC-2 is shown in Fig. 17.7. The electron density cloud is almost twice as high as the molecule, but two molecules cannot sensibly be so close to one another. The problem is that the electron density lies on a mirror plane. Although only one molecule is in fact present (on one side of the mirror plane or the other), the mirror plane automatically generates a mirror image. In other words, the non-framework positions can only be described in the higher symmetry of the framework structure and they must be assumed to be statistically distributed over the two positions (i.e. half occupied).

17.9 Elucidation of refinement difficulties

It is not the purpose of this book to go into the details of Rietveld refinement, but a structure cannot be considered solved until it has been satisfactorily refined. Inadequacies in the structural model often remain undetected until a refinement is attempted. If a structure does not refine well, it may be because there is something wrong with the data (preferred orientation, non-random orientation due to an insufficient number of crystallites in the beam, absorption effects, instability in the beam, etc.), but it is more likely to be due to the (incorrect) model.

One of the first things to check is the space group. As noted earlier, the determination of the correct space group is notoriously difficult with powder data (Markvardsen *et al.* 2001; Chapter 8), so alternatives often need to be

tested. If the calculated diffraction pattern approximates the observed one, but refinement does not progress beyond a certain point (yielding relatively small but significant discrepancies between observed and calculated patterns), or if interatomic distances deviate significantly from known values, a subgroup of the assumed space group may be indicated.

A second potential source of error is the chemistry assumed. Although the structures of related materials may serve as very useful guides in the structure solution process, they can also lead us astray. A new material always has the potential to surprise us. Similarly, results of non-diffraction experiments may be inaccurate (e.g. chemical analysis), based on solution measurements (e.g. optical activity), or misinterpreted (e.g. EXAFS or NMR), so a certain amount of caution is recommended. All assumptions need to be re-evaluated if refinement does not progress satisfactorily.

Example 10. The aluminophosphate VPI-5 was thought to have a zeolite-like framework structure with tetrahedrally coordinated Al and P atoms, and this prejudice hindered refinement of the structure for several years. One of the Al atoms was eventually shown to be octahedrally coordinated to four framework oxygens and two water molecules (McCusker *et al.* 1991).

17.10 Evaluation of the final structure

The final test as to the validity of a structural model is that it accounts for all of the data available. Not only must the calculated powder diffraction pattern match the observed one, the structure must also be consistent with any spectroscopic data (e.g. IR, Raman, NMR, ESR, Mössbauer, EXAFS) and with the physical properties of the material. Furthermore, the structure should be compatible with the structures of related materials. Any unusual features should be given special attention, and, if possible, further experiments devised to confirm or refute them.

17.11 Conclusion

It is clear that the use of crystal chemical information can have a significant impact upon the structure determination process, whether it is used at the data collection stage, in the critical evaluation of the final structure, or in any of the steps in between. Its exploitation is highly recommended. Chemical intuition is a less tangible concept. The human thought process that makes the key connection between seemingly unrelated facts, that we call intuition, does not just happen. Just as lightning does not strike 'out of the blue', intuition requires extensive groundwork and considerable devotion to the problem. While a structure solution via a computer program is fast, comfortable and usually quite useful, one requiring intuitive intervention also leaves the crystallographer with

a most satisfying sense of accomplishment. Fortunately, there are still many structures that challenge the limits of our computer programs, so intuition will continue to play a critical role in structure determination from powder diffraction data.

References

- Achak, O., Pivan, J. Y., Maunaye, M., Louër, M. and Louër, D. (1995). *J. Alloys & Compd.*, **219**, 111–15.
- Akporiyaye, D. E. and Price, G. D. (1989). *Zeolites*, **9**, 23–32.
- Baerlocher, Ch. and Meier, W. M. (1970). *Helv. Chim. Acta*, **53**, 1285–93.
- Bennett, J. M. (1988). *Am. Chem. Soc. Symp. Ser.*, **368**, 162–76.
- Breck, D. W., Eversole, W. G., Milton, R. M., Reed, T. B. and Thomas, T. L. (1956). *J. Am. Chem. Soc.*, **78**, 5963–71.
- Briscoe, N. A., Johnson, D. W., Shannon, M. D., Kokotailo, G. T. and McCusker, L. B. (1988). *Zeolites*, **8**, 74–6.
- Brunner, G. O. (1990). *Zeolites*, **10**, 612–14.
- Flanigen, E. M., Bennett, J. M., Grose, R. W., Cohen, J. P., Patton, R. L., Kirchner, R. M. and Smith, J. V. (1978). *Nature*, **271**, 512–16.
- Freyhardt, C. C., Lobo, R. F., Khodabandeh, S., Lewis, J. E., Tsapatsis, M., Yoshikawa, M., Cambor, M. A., Pan, M., Helmkamp, M. M., Zones, S. I. and Davis, M. E. (1996). *J. Am. Chem. Soc.*, **118**, 7299–310.
- Gies, H. and Rius, J. (1995). *Z. Kristallogr.*, **210**, 475–80.
- Grosse-Kunstleve, R. W. (1996). *Ph.D. Thesis*, ETH, Zürich, Switzerland.
- Grosse-Kunstleve, R. W., McCusker, L. B. and Baerlocher, Ch. (1997). *J. Appl. Crystallogr.*, **30**, 985–95.
- Grosse-Kunstleve, R. W., McCusker, L. B. and Baerlocher, Ch. (1999). *J. Appl. Crystallogr.*, **32**, 536–42.
- Hahn, T. (ed). (1983). *International tables for crystallography*, Vol. A, Reidel, Dordrecht.
- Hasegawa, K., Nishibori, E., Takata, M., Safata, M., Togashi, N., Yu, J. H. and Terasaki, O. (1999). *Jap. J. Appl. Phys. Part 1*, **38**, 65–8.
- Kirchner, R. M., Grosse-Kunstleve, R. W., Pluth, J. J., Wilson, S. T., Broach, R. W. and Smith, J. V. (2000). *Microporous Mesoporous Mater.*, **39**, 319–22.
- Kokotailo, G. T., Lawton, S. L., Olson, D. H. and Meier, W. M. (1978). *Nature*, **272**, 437–8.
- Kubota, Y., Takata, M., Sakata, M., Ohba, T., Kifune, K. and Tadaki, T. (2000). *J. Phys.: Condens. Matter*, **12**, 1253–9.
- Lobo, R. F. and Davis, M. E. (1995). *J. Am. Chem. Soc.*, **117**, 3764–79, and references therein.
- Louër, D. (1992). *NIST Spec. Publ.*, **846**, 92–104.
- Markvardsen, A., David, W. I. F., Johnson, J. C. and Shankland, K. (2001). *Acta Crystallogr. A*, **57**, 47–54.
- McCusker, L. B., Baerlocher, Ch., Jahn, E. and Bülow, M. (1991). *Zeolites*, **11**, 308–13.
- McCusker, L. B., Grosse-Kunstleve, R. W., Baerlocher, Ch., Yoshikawa, M. and Davis, M. E. (1996). *Microporous Materials*, **6**, 295–309.
- Morris, R. E., Owen, J. J., Stalick, J. K. and Cheetham, A. K. (1994). *J. Solid State Chem.*, **111**, 52–7.

- Papoular, R. J. and Cox, D. E. (1995). *Europhys. Lett.*, **32**, 337–42.
- Pauling, L. (1930a). *Proc. Natl Acad. Sci. USA*, **16**, 453–9.
- Pauling, L. (1930b). *Z. Kristallogr.*, **74**, 213–25.
- Schantz, D. F., Burton, A. and Lobo, R. F. (1999). *Microporous and Mesoporous Mater.*, **31**, 61–73.
- Seebach, D., Matthews, J. L., Meden, A., Wessels, T., Baerlocher, Ch. and McCusker, L. B. (1997). *Helv. Chim. Acta*, **80**, 1–10.
- Shannon, M. D. (1993). In *Proc. 9th Int. Zeolite Conf.* (ed. R. von Ballmoos, J. B. Higgins and M. M. J. Treacy), pp. 389–98, Butterworth-Heinemann, Boston, MA.
- Shannon, M. D., Casci, J. L., Cox, P. A. and Andrews, S. J. (1991). *Nature*, **353**, 417–20.
- Takata, M., Machida, N., Nishibori, E., Umeda, B., Sakata, M., Tanigaki, K., Kosaka, M., Hirose, I. and Mizuki, J. (1999). *Jap. J. Appl. Phys. Part 1*, **38**, 122–5.
- Taylor, W. H. (1930). *Z. Kristallogr.*, **74**, 1–19.
- Taylor, W. H. and Jackson, R. (1933). *Z. Kristallogr.*, **86**, 53–64.
- Taylor, W. H., Meeks, C. A. and Jackson, W. W. (1933). *Z. Kristallogr.*, **84**, 373–98.
- Treacy, M. M. J., Rao, S. and Rivin, I. (1993). In *Proc. 9th Int. Zeolite Conf.* (ed. R. von Ballmoos, J. B. Higgins and M. M. J. Treacy), pp. 381–8, Butterworth-Heinemann, Boston, MA.
- Wagner, P., Zones, S. I., Davis, M. E. and Medrud, R. C. (1999). *Angew. Chem., Int. Ed.*, **38**, 1269–72.

This page intentionally left blank

Index of symbols

| | |
|--|---|
| $\mathbf{a}, \mathbf{b}, \mathbf{c}$ | basis vectors of the direct lattice |
| $\mathbf{a}^*, \mathbf{b}^*, \mathbf{c}^*$ | basis vectors of the reciprocal lattice |
| a, b, c | lengths of the basis vectors of the direct lattice |
| a^*, b^*, c^* | lengths of the basis vectors of the reciprocal lattice |
| B | isotropic atomic displacement (Debye-Waller) factor |
| C_{ij} | covariance matrix |
| d or d_{hkl} | interplanar spacing of neighbouring (hkl) planes |
| d^* | $1/d$ |
| $E_{\mathbf{h}}$ or E_{hkl} | normalized structure factor |
| $ E_{\mathbf{h}} $ or $ E_{hkl} $ | modulus of $E_{\mathbf{h}}$ |
| f | atomic scattering factor |
| f^r | real part of the anomalous scattering factor |
| f^i | imaginary part of the anomalous scattering factor |
| $f_{hkl}(2\theta)$ | sample line-broadening function |
| $F_{\mathbf{h}}$ or F_{hkl} | structure factor corresponding to the Bragg reflection hkl |
| $ F_{\mathbf{h}} $ or $ F_{hkl} $ | modulus of $F_{\mathbf{h}}$ |
| F_N | Smith & Snyder figure of merit for an indexing solution |
| $g(2\theta)$ | instrumental line-broadening function |
| \mathbf{h} or hkl | indices of the Bragg reflection from the (hkl) planes |
| $H(2\theta)$ | peak-shape function |
| $I_{\mathbf{h}}$ or I_{hkl} | intensity of the Bragg reflection hkl |
| K | scale factor |
| M_{20} | de Wolff figure of merit for an indexing solution |
| $P(xyz)$ | Patterson function at point xyz |
| $P_{\mathbf{h}}(\chi, \phi)$ | pole figure value for reflection hkl at sample orientation (χ, ϕ) |
| Q_{hkl} | $10^4/d_{hkl}^2$ or $1/d_{hkl}^2$ |
| \mathbf{r} or \mathbf{r}_{xyz} | position vector of a point xyz in the unit cell |
| \mathbf{r}^* or \mathbf{r}_{hkl}^* | reciprocal lattice vector with coefficients hkl |
| R_p | profile R -value (agreement factor) |
| R_{wp} | weighted profile R -value (agreement factor) |
| R_B | R -value based on Bragg intensities |
| R_F | R -value based on structure factors |
| T | temperature |
| $U_{\mathbf{h}}$ or U_{hkl} | unitary structure factor |
| $ U_{\mathbf{h}} $ or $ U_{hkl} $ | modulus of $U_{\mathbf{h}}$ |
| V | cell volume of the direct lattice |
| V^* | cell volume of the reciprocal lattice |
| w | weighting factor |
| x, y, z | fractional coordinates of a point in the unit cell |
| y_i | intensity at point i in a powder diffraction pattern |
| Z | number of formula units per unit cell |
| Z' | number of formula units in the asymmetric unit |

| | |
|-------------------------------|---|
| α, β, γ | interaxial angles of the direct lattice |
| $\alpha^*, \beta^*, \gamma^*$ | interaxial angles of the reciprocal lattice |
| η | mixing parameter in the pseudo-Voigt peak-shape function |
| 2θ | diffraction angle |
| Θ, Φ, Ψ | Eulerian angles |
| λ | wavelength |
| μ | linear absorption coefficient |
| $\rho(\mathbf{r})$ | (electron) density at point \mathbf{r} in the unit cell |
| σ | standard deviation |
| $\varphi_{\mathbf{h}}$ | phase angle of $F_{\mathbf{h}}$ or $E_{\mathbf{h}}$ |
| ϕ | sample rotation angle (for texture measurements) |
| χ | sample tilt angle (for texture measurements) |
| χ^2 | goodness of fit |

Index of abbreviations

| | |
|--------|--|
| e.s.d. | estimated standard deviation |
| D2B | high resolution powder diffractometer at ILL |
| DM | direct methods |
| ECC | error correcting code |
| ESR | electron spin resonance |
| ESRF | European Synchrotron Radiation Facility (Grenoble, France) |
| EXAFS | extended X-ray absorption fine structure |
| FWHM | full width at half maximum |
| GA | genetic algorithm |
| HOLZ | higher order Laue zones |
| HRPD | high resolution powder diffractometer at RAL |
| ILL | Institut Laue Langevin (Grenoble, France) |
| IMF | image-seeking minimum function |
| IRF | instrument resolution function |
| LLG | log-likelihood gain |
| ME | maximum entropy |
| NIST | National Institute of Standards and Technology |
| NMR | nuclear magnetic resonance |
| NSLS | National Synchrotron Light Source (Brookhaven, USA) |
| ODF | orientation distribution function |
| RAL | Rutherford Appleton Laboratory (Oxfordshire, UK) |
| SA | simulated annealing |
| SDPD | structure determination from powder diffraction data |
| SMF | symmetry minimum function |
| SG | space group |
| SRS | Synchrotron Radiation Source (Daresbury, UK) |
| UKAEA | UK Atomic Energy Authority |
| VCT | variable counting time |

Computer programs

- ALLHKL *Intensity extraction*
Pawley, G. S. (1981). *J. Appl. Crystallogr.*, **14**, 357–361
- BEARTEX *Texture analysis using the WIMV method*
Wenk, H.-R., Matthies, S., Donovan, J. and Chateigner, D. (1998). *J. Appl. Crystallogr.*, **31**, 262–269
<http://eps.berkeley.edu/~wenk/TexturePage/beartex.htm>
- CIFTOOLS *Working with pdCIF files*
Toby, B.
<http://www.ncnr.nist.gov/programs/crystallography/software/cif/>
- CMPR *Multipurpose program for displaying diffraction data, indexing, peak fitting*
Toby, B.
<http://www.ncnr.nist.gov/programs/crystallography/software/cmpr/>
- CPSR *Rietveld refinement*
Andreev, Y. G., Lundström, T. and Sorokin, N. I. (1995). *Nucl. Instr. and Meth. in Phys. Res.*, **A354**, 134–138
- CRYSFIRE *A collection of indexing programs*
Shirley, R.
<http://www.ccp14.ac.uk/solution/indexing/>
- DASH *Structure solution—simulated annealing*
David, W. I. F., Shankland, K., Cole, J., Maginn, S., Motherwell, W. D. S. and Taylor, R. (2001). *DASH User Manual*, Cambridge Crystallographic Data Centre, Cambridge, UK
http://www.ccdc.cam.ac.uk/products/powder_diffraction/dash/
- DBWS *Rietveld refinement*
Wiles, D. B. and Young, R. A. (1981). *J. Appl. Crystallogr.*, **14**, 149–151
http://www.physics.gatech.edu/downloads/young/download_dbws.html
- DICVOL91 *Indexing*
Boultif, A. and Louër, D. (1991). *J. Appl. Crystallogr.*, **24**, 987–993
see CCP14 web site
- DICVOL04 *Indexing*
Boultif, A. and Louër, D. (2004). *J. Appl. Crystallogr.*, **37**, 724–731
see CCP14 web site
- DOREES *Treatment of overlapping reflections*
Jansen, J., Peschar, R. and Schenk, H. (1992). *J. Appl. Crystallogr.*, **25**, 237–243
- ENDEAVOUR *Structure solution—simulated annealing with chemical potentials*
Putz, H., Schön, J. C. and Jansen, M. (1999). *J. Appl. Crystallogr.*, **32**, 864–870
<http://www.crystalimpact.com/endeavour/>
- ESPOIR *Structure solution—simulated annealing*
Le Bail, A. (2001). *Mater. Sci. Forum*, **378–381**, 65–70
<http://www.cristal.org/sdpd/espoir/>
- ESYM *Extinction symbol / space group determination*
Markvardsen, A. J., David, W. I. F., Johnston, J. and Shankland, K. *Acta Crystallogr. A.*, **57**, 47–54.
<http://www.markvardsen.net/space-group.html>
- EXPGUI *Graphical user interface (GUI) for GSAS*
Toby, B.
<http://www.ncnr.nist.gov/programs/crystallography/software/expgui/>

- EXPO *Structure solution—direct methods for powder diffraction data (includes intensity extraction and treatment of overlapping reflections)*
Altomare, A., Burla, M. C., Camalli, M., Carrozzini, B. Cascarano, G. L., Giacovazzo, C., Guagliardi, A. Moliterni, A. G. G., Polidori, G. and Rizzi, R. (1999). *J. Appl. Crystallogr.*, **32**, 339–340
<http://www.ic.cnr.it/>
- EXTRA *Intensity extraction*
see EXPO
- FIPS *Treatment of overlapping reflections*
Estermann, M. A. and Gramlich, V. (1993). *J. Appl. Crystallogr.*, **26**, 396–404
- FOCUS *Zeolite-specific structure determination*
Grosse-Kunstleve, R. W., McCusker, L. B. and Baerlocher, Ch. (1999). *J. Appl. Crystallogr.*, **32**, 536–542
- FOX *Free objects for crystallography: a modular approach to ab initio structure determination from powder diffraction*
Favre-Nicolin, V. and Cerny, R. (2002). *J. Appl. Crystallogr.*, **35**, 734–743.
<http://objcryst.sourceforge.net/Fox/>
- FullProf *Rietveld refinement*
J. Rodriguez-Carvajal, Laboratoire Leon Brillouin (CEA-CNRS)
<http://www-llb.cea.fr/fullweb/fp2k/fp2k.htm>
- GSAS *Rietveld refinement (includes intensity extraction and single-crystal refinement)*
Larson, A. C. and Von Dreele, R. B. (1987). *GSAS, Los Alamos National Laboratory Report No. LA-UR-86-748*
<http://www.ccp14.ac.uk/solution/gsas>
- ITO *Indexing*
Visser, J. W. (1969). *J. Appl. Crystallogr.*, **2**, 89–95
see CRYSFIRE entry for download details
- LSQPROF *Intensity extraction*
Jansen, J., Peschar, R. and Schenk, H. (1992). *J. Appl. Crystallogr.*, **25**, 231–236
- MAUD *Materials analysis using diffraction (includes texture analysis)*
Lutterotti, L. and Bortolotti, M. (2003). *IUCr: Compcomm Newsletter*, **1**, 43–50
<http://www.ing.unitn.it/~maud/>
- MICE *Structure solution—maximum entropy*
Gilmore, C. J., Bricogne, G. and Bannister, C. (1990). *Acta Crystallogr.*, **A46**, 297–308
- NBS*AIDS83 *Aid to space group determination*
Mighell, A. D., Hubbard, C. R. and Stalick, J. K., “NBS*AIDS80: A FORTRAN Program for Crystallographic Data Evaluation.” US Technical Note 1141, National Bureau of Standards, Washington, DC, 1981
- PowderSolve *Structure solution—simulated annealing*
Engel, G. E., Wilke, S., König, O., Harris, K. D. M., and Leusen, F. J. J. (1999). *J. Appl. Crystallogr.*, **32**, 1169–1179
<http://www.accelrys.com/products/mstudio/modeling/crystallization/reflexplus.html>
- POWSIM *Structure solution—direct methods*
see DOREES and LSQPROF
- PSSP *Simulated annealing approach to structure solution*
<http://powder.physics.sunysb.edu/programPSSP/pssp.html>
- SHELX *Single-crystal structure determination*
Sheldrick, G.
<http://shelx.uni-ac.gwdg.de/SHELX/>
- SIMPEL *Direct methods for powder diffraction data*
Jansen, J., Peschar, R. and Schenk, H. (1993). *Z. Kristallogr.*, **206**, 33–43
- SIRPOW
see EXPO

- TOPAS *Profile analysis, Rietveld refinement, structure solution, intensity extraction, indexing*
Coelho, A. A. (2000). *J. Appl. Crystallogr.*, **33**, 899–908
<http://www.bruker-axs.de/index.php?id=topas>
<http://members.optusnet.com.au/~alancoelho/>
- TREOR90 *Indexing*
Werner, P.-E., Eriksson, L. and Westdahl, M. J. (1985).
J. Appl. Crystallogr., **18**, 367–370
Note that TREOR90 has now been replaced by N_TREOR
<http://www.fos.su.se/~pew>
- XLENS *Structure solution—direct methods*
Rius, J. (1994). XLENS. A program for Crystal Structure Determination.
ICMAB-CSIC, Catalunya, Spain
- WPPF *Intensity extraction*
Toraya, H. (1986). *J. Appl. Crystallogr.*, **19**, 440–447
- ZEFSAI *Zeolite framework structure solution*
Falcioni, M. and Deem, M. W. (1999).
J. Chem. Phys. **110**, 1754–1766
<http://www.mwdeem.rice.edu/zefsaII/>

Useful web sites and mailing lists

Due to the dynamic nature of the WWW, the following addresses are subject to change

- <http://www.ccp14.ac.uk/>
Collaborative Computational Project Number 14
(CCP14) for single crystal and powder diffraction
- <http://www.cristal.org/iniref.html>
A sporadically updated SDPD Database
- <http://www.crystallography.net>
The Crystallography Open Database
- <http://www.powderdata.info/>
A collection of high-quality XRPD patterns available for download
- <http://www.iucr.org/sincris-top/>
Information server for crystallography
- <http://groups.yahoo.com/group/sdpd/>
A mailing list dedicated to the subject of SDPD
- <http://lachlan.bluehaze.com.au/stxnews/riet/>
A mailing list dedicated to the subject of Rietveld refinement

Index

- absorption
 - heavily absorbing materials 34, 103
 - X-ray 34, 103, 106, 109, 110–11, 195
- agreement factors
 - full profile 253, 270–1, 286, 303
 - integrated intensity 158, 271
- anisotropic thermal expansion 2, 7, 15, 162–8
- anomalous scattering 8, 57–9, 69, 80, 106, 308
- atom–atom potential method 45
- autoindexing, *see* indexing
- axial divergence 56, 111

- background 37, 53, 105–6, 142, 148, 184, 190–1, 195, 200, 271, 290
- Bayesian analysis 249, 315
 - dealing with negative intensities 146, 148, 175
 - incorporating fragment information 156
 - space group determination 149
 - see also* maximum entropy
- beam divergence 30, 102–3

- Cambridge Structural Database 10, 256, 266
- chemical information 2, 7–9, 45, 252, 291, 307–8, 310, 314
- chemical potentials 9
- Cochran distribution 180–1
- computer programs
 - ALLHKL 20
 - BEARTEX 177
 - BUSTER 247
 - CPSR 293
 - CRYSFIRE 133
 - DASH 272, 281
 - DBWS 13
 - DICVOL 19, 40, 124, 126–8, 129–31
 - DMS 186–7
 - DOREES 21, 179, 185–6, 187–8
 - ENDEAVOUR 9
 - EXFFT 186–7
 - EXPO 12, 20, 73, 74, 192–200, 270
 - EXTRA 20, 192, 199
 - FIPS 21, 152, 208
 - FOCUS 9, 77, 315–16
 - FOUR 187
 - FullProf 56, 212
 - GENTAN 183
 - GSAS 13, 20, 56, 58, 63, 83, 293
 - ITO 19, 124, 125–6, 129–33
 - ITOF 186–7
 - LSQPROF 20, 179, 184–5, 186–8
 - MICE 20, 233, 247
 - MODCELL 133
 - MULTAN 43, 68, 81, 183
 - NBS*AIDS83 40
 - NORMAL 186–7
 - PIRUM 133
 - PowderSolve 73
 - POWSIM 179, 183, 186–8
 - PSSP 80
 - REDUCT 133
 - SHELX 73, 75, 76, 78, 81, 183, 212
 - SIMPEL 20, 179, 183, 186–7
 - SIR 71, 183
 - SIRPOW 43, 74, 78
 - SR15LS 214
 - TREOR 19, 69, 81, 76, 82, 124, 128–9, 130–3
 - TRIQUA88 187
 - WPPF 20
 - XLENS 227, 230
 - XTAL 69, 183, 212
- coordinate transformations 292
- crystallite size 33, 35, 64, 66, 83, 101–4

- Darwin width 54, 57
- data collection 17, 29–48, 98–117, 173, 308
 - constant-wavelength 113–14
 - counting time 33, 99, 100, 113–16, 233
 - external standard 124
 - fluorescence 52, 53, 106
 - high angle data 114, 200
 - internal standard 70, 100, 111, 121, 123–4
 - monochromatic radiation 35–8, 39, 43
 - parameters 5, 308
 - step size 99, 100, 113–14, 146
- de Wolff figure of merit 120, 121–2
- detectors
 - analyser crystal 52, 54, 56, 58, 68, 71, 172, 173

- detectors (*cont.*):
 CCD 26, 61
 dead time 53, 105
 imaging plate 53, 54, 61, 65, 99, 108, 172
 parallel-blade collimator 52–3, 71
 position-sensitive 34, 43–4, 53–4, 61, 99, 108, 110
 scintillation 52, 53
 diamond-anvil cell 65
 dichotomy method 126–8
 differential thermal expansion 2, 7, 15, 162–8
 diffraction data
 background 37, 53, 105–6, 142, 148, 170, 184, 190–1, 195, 200, 271, 290
 density of reflections 106, 137
 number of independent reflections 40, 108, 196
 resolution (d_{\min}) 114, 190, 195, 200, 219, 227–8, 233, 279
 resolution (2θ) 33–8, 52–5, 56–7, 233
 direct methods 2, 7, 15, 20, 40, 91, 106, 116, 270
 basics 179–81
 comparison with global optimization 282
 figure-of-merit 196
 negative quartets 183, 195, 220, 227
 normalization 181–2, 187–8, 193, 235
 origin definition 179–80, 235
 P_{10} formula 193, 195
 phase extension 181, 182–3
 phase refinement 219, 227
 phase sum relations 179–80, 183
 quartets 180
 structure invariants 180–3, 207
 sum function 7, 211, 220–31
 symbolic addition 183
 tangent formula 181, 183, 219–20, 226–31, 249
 triplets 180–3, 193–5
 Z -function 219–21
 direct-space methods 7–9, 46
 model building 2, 8, 21, 76, 309–14
see also global optimization
 disorder 3, 7, 24, 59, 90, 175, 230, 256, 319
- electron diffraction 20, 26, 309
 electron microscopy 21, 26, 64, 307
 enantiomorph definition 182, 235
 energy minimization 22, 25, 45
 error correcting codes 247–9
 Euler angles 256, 292
 evolutionary strategies, *see* genetic algorithms
 EXAFS 25, 76, 307, 321
 extinction 99, 105
 extinction symbol 148, 149, 150, 151
- F figure of merit 39, 121
 fluorescence 52, 53, 102, 106
- Fourier methods 317
 difference maps 7, 8, 21, 159, 177, 200, 317–20
 electron density map 159, 315, 317
 recycling 3, 8, 41, 92, 241, 279, 315
 Friedel pairs 108
- genetic algorithms 9, 22, 263–6, 314
 comparison with simulated annealing 269
 global optimization 3, 9, 45, 116, 249
 comparison with Direct methods 282
 cost function 22, 270–2
 examples of local minima 279–81
 global minimum 286, 299, 290
 hypersurface 253
 local minimum 286
 multi-objective optimization
 parameter bounds 258, 264, 266
 pitfalls 148, 279
 probability of obtaining a structure solution 258–61, 286
 structural complexity 259, 287, 293, 304
 swarm algorithm 273
 variable parameters 9, 256–8, 288, 290–3, 300
see also genetic algorithms and simulated annealing
 grid search 9, 22, 73, 259, 261, 287
- heavy atom methods 3, 106, 158, 159, 196, 202, 212, 308
 hydrogen atom location 92
 hyperphase permutation 153
- image-seeking minimum function 211, 213, 214, 215, 216
 indexing 5, 19, 29, 30, 37–9, 54, 61, 82, 89, 98–100, 110, 308
 central zone 125
 de Wolff figure of merit 120, 121–2
 dichotomy method 126–8
 dominant zone 121, 122, 129–30
 F figure of merit 39, 121
 M_{20} figure of merit 39, 66, 120, 121–2, 125–6, 128–30
 Q values 39, 119, 120–1, 124–6
 trial and error methods 128
 instrument geometry 5, 30, 34–5, 51–4, 99, 101, 108
 aberrations 32, 98, 100–1, 103, 109, 110, 111, 114, 172
 axial divergence 56, 111
 beam divergence 30, 102–3
 Bragg–Brentano 31–2, 34–5, 39, 40–1, 43, 100, 103, 105, 111, 172

- Debye–Scherrer 43–5, 101, 110–11, 123–4
 diffracted beam monochromator 102
 focused beam 111
 focusing cameras 34, 121, 123
 Gandolfi spinner 65, 109
 Guinier 34, 123
 Guinier–Hägg 123
 incident beam monochromator 36, 43, 111
 multi-layer mirrors 36, 111
 parallel beam 36, 110–11
 reflection mode 34, 37, 105, 109, 172, 195
 sample displacement 54, 111, 172
 Soller slits 111
 transmission mode 34, 53, 99, 106, 172, 195
- instrument related error 111–12
- integrated intensities 16, 30, 100, 113, 140, 164, 174, 175, 186, 190, 271, 303
 correlations 6, 51, 114, 145, 148, 156, 159, 163, 165, 174, 184
 covariance matrix 142, 145, 149, 164
 use of prior information 196–9, 202
- intensity extraction 5–6, 20–1, 30, 61, 100, 108, 113–14, 136, 179, 183–5, 190, 191–5
 equipartitioning 6, 185
 LeBail method 6, 20, 41, 43, 136, 138–43, 160, 174, 175, 192, 195–8
 multi-pattern deconvolution 174, 175
 multiple datasets 3, 6, 164
 Pawley method 6, 20, 136, 142, 143–8, 158, 160, 168, 174, 175, 179, 184, 185, 191–2, 195, 214
 dealing with negative intensities 146, 163, 184–5, 192
 Sayre’s squaring method 151, 152, 153, 207
 use of prior information 142, 156, 196–9, 202
- internal coordinates 256–8, 291
- internal standard 70, 100, 111, 121, 123
- joint refinement 13, 24–5, 196
- laboratory X-ray diffraction 2, 5, 17, 22, 100, 107, 111
 comparison with synchrotron X-ray diffraction 22–5, 31, 39, 49–50
 instrument geometry 34–5
 instrument related error 111
 instrumental resolution 30–32
 monochromatic radiation 35–8
- Le Bail method, *see* intensity extraction
- limitations in structure solution 138, 148, 200
- line broadening 29, 30–3, 111, 172
 anisotropic 24, 33
 anisotropic strain 33, 63
 instrumental 30–2, 111
 sample 32–3, 56, 138
 size 17, 32–3, 55, 104
 strain 17, 33, 55, 104
see also peak shape
- Lorentz-polarization factor 114, 187
- M_{20} figure of merit 39, 66, 120, 121–2, 125–6, 128–30
- magnetic structures 88
- maximum entropy 7, 25
 experimental design 247–9
 extrapolation 236
 hyperphases and pseudophases 242–5
 likelihood expressions 237–8
 maps 214, 236, 241, 318
 Patterson maps 151, 152, 205–7
 phase permutation 236, 245, 248
 phase refinement 249
 positive/negative maps 94–7, 214
 structure completion 159, 318
 tests of significance 238–40, 243–5
 treatment of overlapping reflections 238, 242–3, 249
 ‘uranium atom’ solution 240
see also Bayesian analysis
- microcrystal 2, 20, 25–6, 32, 101
- microstructure 17, 30, 32–3
- molecular connectivity 256
- molecular envelope 94, 250
- monochromator
 diffracted beam 102
 incident beam 36, 43, 111
- Monte Carlo method 22, 255, 287, 314
- multi-layer mirrors 36, 111
- multiple diffraction 105
- NBS Crystal Data File 118
- neutron diffraction 5, 16–18, 23–5, 41, 78, 80, 81, 88, 99, 100, 105–6, 110, 191, 195, 202, 207, 208, 214, 281, 308
- neutron facilities
 ILL 24, 89
 ISIS 89, 95, 214, 303
 NIST 92, 93
- NMR 21, 25, 77, 81, 307, 309, 319, 321
- normalization
see Direct methods and synchrotron data
- origin definition
see Direct methods
- overlapping reflections 2, 6, 15, 20, 29–30, 50, 103, 108, 113, 137–8, 146, 149, 179, 193–5, 234, 318
 describing using hyperphases and pseudophases 242–3
 estimation using anisotropic thermal expansion 7, 162–8

- overlapping reflections (*cont.*):
 estimation using Bayesian methods 154–6
 estimation using Direct methods 153, 185–6
 estimation using Patterson methods 151–3, 198, 207–8
 estimation using texture 7, 168–77
 equipartitioning 6, 153, 185–6, 195, 204, 207, 208, 212, 245
 negative quartets 185
 quantification 29–30, 40, 108, 196
 quartets 185, 187, 207
 systematic and accidental 20, 227
 triplets 185, 187, 207
 use in global optimization 270–1, 303–4
- parallel computing 263, 266, 269
 Parseval's theorem 224, 261
 pattern decomposition, *see* intensity extraction
 Patterson methods 7, 15, 20, 41, 69, 91, 152, 153, 158, 202, 203, 204, 317
 Harker sections 41, 214
 Harker vectors 41, 208, 210, 211, 214, 215
 image-seeking minimum function 211, 213, 214, 215, 216
 maximum entropy map 7, 205–7
 origin peak removal 187, 198, 205, 220–3
 positive/negative map 205, 207
 separating overlapping reflections 188, 196, 198, 203
 sharpened map 205, 212, 214
 symmetry minimum function 7, 210–11, 212, 215
 use of anomalous scattering 208
 vector-search techniques 24, 203, 210, 220, 228, 317
- Pawley method, *see* intensity extraction
 PDF 2 database 118, 121, 124, 131, 133
 peak shape 17–18, 32–3, 37, 54–6, 61, 64, 99, 139, 184–5, 191, 195, 290
 half width 17, 31, 33, 37, 52, 61, 114, 138, 146, 185
 instrumental contribution 30, 31, 54
 peak asymmetry 56, 185
 sample contribution 17, 30
see also line broadening
 peak shift 71, 111
 peak/background ratio 123
 peak-shape function 31
 fundamental parameters approach 32–3
 Gaussian 17, 32–3, 54, 185
 Lorentzian 17, 32–3, 54, 185
 Pearson VII 33
 pseudo-Voigt 17, 32–3, 61, 185
 phase extension 181, 182–3
 phase refinement 219, 227
 preferred orientation 7, 24, 34–5, 65, 71, 101, 105, 110, 195–6
 profile parameters 6, 17, 184
 pseudo-translational symmetry 182, 192, 196, 197
 reflection multiplicity 114, 237
 resonant scattering 8, 57–9, 69, 80, 106, 308
 restraints, structural and non-structural 209
 Reverse Monte Carlo 255
 Rietveld calculation of F(obs) 140
 Rietveld method 1, 13, 16–19, 25, 50, 113–14, 138, 140, 142, 148, 270–1, 286, 320
- sample
 absorption 65, 173, 195
 capillary 34, 43, 46, 64, 65, 68, 71, 99, 102–3, 110–11, 165
 characteristics 99
 displacement 54, 111, 172
 flat plate 108–110
 grinding 83, 104–5, 170
 mosaic size 105
 particle statistics 64, 102, 105, 110
 preparation 169
 random orientation of crystallites 105
 surface roughness 65, 102, 105, 114, 195
 thin 34, 110
 thin-film 34, 99, 100
 transparency 30, 52, 54, 71, 105, 109, 111, 173
- SDPD Round-Robin challenge 93
 Sheldrick's rule 138
 simplex method 184, 267–8
 simulated annealing 9, 22, 46, 267–8, 288, 314
 accept–reject criterion 289
 applied to zeolites 22, 76
 comparison with genetic algorithms 269
 cooling schedule 262, 275, 288, 289
 importance sampling 289
 parallel tempering 9, 263
 quenching 288
- space group
 determination 5, 19, 20, 29, 90, 148–51, 158, 195, 308, 320
 hemihedral 231
 optically active crystal 309
 systematic absences 20, 29, 120, 122, 148, 150
 structure completion 89
 structure envelope 9
 structures
 inorganic
 $\text{Ag}_2 \cdot 3\text{MoO}_3 \cdot 1.8\text{H}_2\text{O}$ 187
 $\text{Ag}_8\text{N}_{16}\text{C}_{24}\text{H}_{24}$ 191
 $\text{Al}_2\text{Y}_4\text{O}_9$ 23, 68
 $\beta\text{-Ba}_3\text{AlF}_6$ 24, 36
 $\text{BaBiO}_{2.5}$ 23
 $\text{Ba}_4\text{C}_8\text{O}_{20}\text{D}_8$ 191

- $\text{Ba}_2\text{Mo}_5\text{O}_{17}$ 134
 $\text{Ba}_4\text{Mo}_{12}\text{O}_{40}$ 191
 $\text{BaTiO}(\text{C}_2\text{O}_4)_2 \cdot 4.5\text{H}_2\text{O}$ 39
 BeH_2 23, 68
 $\text{Bi}_{12}\text{Ni}_{58}\text{S}_{30}$ 134
 Bi_3NF_6 212–13
 Bi_3ReO_8 21
 $((\text{CH}_3)_4\text{N})_2\text{Ge}_4\text{MnS}_{10}$ 309
 $((\text{CH}_3)_4\text{N})_4\text{Ge}_4\text{S}_{10}$ 39
 $2(\text{C}_6\text{H}_4\text{NH}_3)\text{Mo}_3\text{O}_{10} \cdot 4\text{H}_2\text{O}$ 187
 CaTiSiO_5 91, 214–16
 CeH_{2+x} 21
 Cr_8O_{21} 191
 $\alpha\text{-CrPO}_4$ 18, 23, 24, 66
 $\text{Cs}_2\text{V}_6\text{O}_{16}$ 133
 $\text{Cu}_8\text{N}_{16}\text{C}_{24}\text{H}_{24}$ 191
 CuPt_3O_6 23
 $\text{Eu}_2\text{O}(\text{CO}_3)_2 \cdot \text{H}_2\text{O}$ 134
 FeAsO_4 91
 $\text{Fe}_{0.923}\text{O}$ 16
 fullerenes 318
 $\text{Ga}_2(\text{HPO}_3)_3 \cdot 4\text{H}_2\text{O}$ 23, 81, 92
 $\text{Gd}_2\text{O}(\text{CO}_3)_2 \cdot \text{H}_2\text{O}$ 134
 I_2O_4 23, 68
 KAlP_2O_7 236
 $\text{K}_2 \cdot 3\text{MoO}_{10} \cdot 3\text{H}_2\text{O}$ 187
 kanemite 231
 LaMo_5O_8 23
 $\text{La}_4\text{Mo}_{20}\text{O}_{32}$ 191
 $\text{La}_8\text{Si}_8\text{O}_{28}$ 191
 $\text{La}_3\text{Ti}_5\text{Al}_{15}\text{O}_{37}$ 23, 81, 93, 308
 $\text{LiB}_2\text{O}_3(\text{OH}) \cdot \text{H}_2\text{O}$ 34, 43
 LiCF_3SO_3 34
 LiZnPO_4 75, 92
 $\text{Li}_6\text{Zr}_2\text{O}_7$ 234, 238, 242
 lithium wolframate 202
 $\text{Mg}(\text{H}_2\text{PO}_4)_2$ 134
 Mg_3BN_3 234, 239
 $\text{Mg}_6\text{Co}_2\text{H}_{11}$ 80
 MgCu_2 318
 $\text{MnPO}_4 \cdot \text{H}_2\text{O}$ 23, 66
 $(\text{NH}_4)_2\text{O} \cdot 3\text{MoO}_3 \cdot \text{H}_2\text{O}$ 187
 $(\text{NH}_4)_4[(\text{MoO}_2)_4\text{O}_3](\text{C}_4\text{H}_3\text{O}_5)_2 \cdot \text{H}_2\text{O}$ 34
 $\text{NaAl}(\text{HPO}_4)_2$ 133
 NaGaH_5 133
 $\text{Na}_4\text{Ti}_2\text{Si}_8\text{O}_{22} \cdot 4\text{H}_2\text{O}$ 75
 $\text{Nb}_{20}\text{O}_{120}\text{P}_{28}$ 191
 $\text{Nd}(\text{OH})_2\text{NO}_3 \cdot \text{H}_2\text{O}$ 36
 $\text{Ni}_4\text{Zr}_8\text{P}_4\text{O}_{16}$ 191
 PbC_2O_4 23
 $\text{Pb}_8\text{S}_{16}\text{O}_{24}$ 191
 $\beta\text{-plutonium}$ 2, 15
 ReF_7 91
 RUB-15 230–1
 RUB-18 231
 S_8D_{16} 191
 $\text{Sb}_8\text{P}_{14}\text{O}_{48}$ 191
 $\text{Sr}_6\text{Co}_5\text{O}_{15}$ 91
 SrSO_4 69
 $\text{Ti}_8\text{K}_4\text{Si}_{12}\text{O}_{40}$ 191
 $(\text{Tl}_{0.47}\text{Pb}_{0.53})(\text{Sr}_{1.58}\text{Ca}_{0.42})(\text{Ca}_{1.94}\text{Tl}_{0.06})\text{Cu}_3\text{O}_9$ 59
 $(\text{Tl}_{1.72}\text{Cu}_{0.28})\text{Ba}_2(\text{Ca}_{1.86}\text{Tl}_{0.14})\text{Cu}_3\text{O}_{10}$ 59
 tenticite 3
 tourmaline 116
 $\text{U}(\text{UO}_2)(\text{PO}_4)_2$ 41
 $\text{U}_2\text{O}(\text{PO}_4)_2$ 37, 38
 UCl_3 14
 UCl_4 15
 UO_2Cl_2 15
 UPd_2Sn 23
 uranium halides 15
 uranium oxohalides 15
 uranyl chloride 202
 $(\text{VO})_3(\text{PO}_4)_2 \cdot 9\text{H}_2\text{O}$ 23
 $\text{Y}_8\text{O}_{26}\text{N}_2\text{H}_{18}$ 191
 $\text{YK}(\text{C}_2\text{O}_4)_2 \cdot 4\text{H}_2\text{O}$ 37
 $\text{Zr}(\text{HPO}_4)_2 \cdot \text{H}_2\text{O}$ 36
 $\text{Zr}(\text{OH})_2\text{SO}_4 \cdot 3\text{H}_2\text{O}$ 40
 organic
 acetaldehyde 91
 4-amidinoindanone guanylhydrazone 45
 3-amino-4-nitro-6-methyl-8-oxopyr-
 azolol[1,5-b]-pyrimidine 274
 5-aminovaleric acid 71
 benzophenone 274
 bicyclo [2.2.1] heptane- C_7H_{12} 72
 $\text{C}_6\text{H}_6\text{-C}_6\text{F}_6$ adduct 71
 $\text{C}_2\text{H}_4\text{N}_2\text{O}_2$ 34
 $\text{C}_5\text{H}_{11}\text{NO}_2$ 23
 $(\text{CH}_3)_2\text{S}$ 91
 $(\text{CH}_3)_2\text{SBr}_2$ 81
 $(\text{CH}_3)_2\text{SBr}_{2.5}$ 82
 $(\text{CH}_3)_2\text{SBr}_4$ 82
p- $\text{CH}_3\text{C}_6\text{H}_4\text{SO}_2\text{NH}_2$ 34
 $\text{C}_{24}\text{F}_{12}$ 191
 $\text{C}_4\text{Br}_4\text{F}_{12}$ 191
 $\text{C}_4\text{O}_2\text{S}_4$ 234
 CBr_3F 91
 CCl_3F 91
 CF_3Br 91
 $\text{C}_8\text{F}_{16}\text{Cl}_{16}$ 191
 CFH_3 91
 CF_3I 91
 $\text{C}_8\text{F}_{24}\text{I}_8$ 191
 $\text{C}_{24}\text{N}_4\text{O}_{20}\text{S}_4\text{H}_{52}$ 191
 $\text{C}_{10}\text{N}_6\text{SH}_{16}$ 23
 chlorothiazide 156, 158, 159, 165–8, 273
 cyanamide 91
 cyclo- β -peptide 34, 309
 1,4-diethynyl-2,5-bis(octyloxy)benzene
 2, 3
 1,4-dimethanol benzene 150
 dimethyl acetylene 91
 dopamine hydrobromide 149, 150
 famotidine 24, 254, 258, 260, 275–80

- structures (*cont.*):
- organic (*cont.*):
- fluorescein 274
 - fluorescein diacetate 3, 73, 200
 - fluticasone propionate 274
 - L-glutamic acid 272
 - hexamethylenetetramine cocrystal (1:1) 274
 - hydrochlorothiazide 272
 - ibuprofen 264, 266, 274
 - malonic acid 91
 - 1-methylfluorene 22
 - 6-methyluracil 270
 - (PEO)₃:LiN(SO₂CF₃)₂ 294
 - (PEO)₃:LiCF₃ SO₃ 294
 - PEO:NaCF₃SO₃ 298
 - (PEO)₆:LiAsF₆ 302
 - Ph₂P(O)(CH₂)₇P(O)Ph₂ 4, 24
 - piracetam 22, 34, 44–5
 - remacemide 24
 - RS-camphor 73
 - S₄C₄₀N₂₄H₆₄ 191
 - sodium para-hydroxybenzoate 63
 - sotalol 39
 - sulphamide 94–7
 - sulfathiazole 2, 200
 - telmisartan 274
 - 4-(2,3,4-trifluorophenyl)-1,2,3,5-dithiadiazolyl 274
 - m*-xylene 94
 - o*-xylene 91, 92
- organometallic
- bipyridine polymer 4
 - copper bipyridyl complex 24
 - β-haematin 4, 78
 - [HgRu(CO)₄]₄ 24
 - human insulin-zinc complex 83
 - methylammonium tin chloride 90
 - NaCD₃ 23, 78
 - Na₁₆C₁₆H₄₈ 191
 - nickel bipyridyl complex 24
 - RbC₅H₅ 78
 - tetraferrocenyl-[3]-cumulene 24
 - uranyl phenylphosphonate 3
- zeolites
- AlPO₄-53C (**AEN**) 316
 - aluminophosphate VPI-5 (**VFI**) 321
 - aluminophosphate VPI-8 (**VET**) 314
 - Beryllphosphate-H (**BPH**) 75
 - CIT-1 (**CON**) 314
 - EMC-2 (**EMT**) 320
 - EU-1 (**EUO**) 314
 - gismondine (**GIS**) 313
 - MAPSO-46 (**AFS**) 75
 - MCM-61 (**MSO**) 316
 - NU-3 (**LEV**) 249
 - NU-87 (**NES**) 314
 - RUB-10 (**RUT**) 228–9, 317
 - SAPO-40 (**AFR**) 208, 246, 319
 - [Si₅₄O₁₀₈]₃C₈NH₁₆ (**LEV**) 191
 - Si₃₂O₆₄N₂C₄₈ (**AFR**) 191, 208
 - Sigma-2 (**SGT**) 23, 68
 - SSZ-44 (**SFF**) 316
 - UiO-7 (**OSV**) 76
 - UTD-1F (**DON**) 3, 175
 - zeolite A (**LTA**) 2, 311
 - zincosilicate VPI-9 (**VNI**) 4, 77, 316
 - ZSM-23 (**MTT**) 21
 - ZSM-5 (**MFI**) 2, 314
- sublattice 123
- superlattice 123
- swarm algorithm 273
- symmetry information 309–11
- symmetry minimum function 202, 210–11, 212, 215
- symmetry 211
- synchrotron X-ray diffraction 17, 106–7 121, 123, 138, 172, 200, 228, 308
- anomalous scattering 8, 57–9, 69, 80, 106, 308
 - choice of wavelength 56–9, 106
 - comparison with laboratory X-ray diffraction 22–5, 31, 39, 49–50
 - instrumental resolution 54–6
 - instrumentation 51–4
 - normalization 59
 - undulator 49
- synchrotron radiation facilities
- ESRF 6, 25, 52, 54, 56, 138
 - NLSL 23, 54, 56, 92
 - Photon Factory 52, 54
 - SRS 26, 31, 52, 165
- systematic absences 20, 29, 120, 122, 148, 150, 151
- texture, *see* preferred orientation
- texture approach to structure solution 3, 168–77
- data analysis 174
 - data collection 173
 - inducing texture 169
 - instrumentation 171
 - orientation distribution function
 - harmonic method 174
 - WIMV method 174, 177
 - pole figures 170–4
 - theoretical description 170
- torsion angle
- description 256–8
 - polar plot 278
- undulator 49
- uranium-atom solution 220–1

- Waser restraints 184
- whole-pattern fitting 179, 183–5, 286, 303
- Wilson plot 181, 187, 195, 212, 235
- Wilson statistics 195

- X-n structure solution 92–3
- X-ray absorption 34, 65, 103, 106, 109, 110–11, 173, 195

- Z function 219–21
- Z-matrix format 257
- zeolite 2, 9, 152, 175, 230, 311, 313, 317–19
- zero-background sample holder 110
- zone
 - central 125
 - dominant 121, 122, 129–30